Faculty of Pharmaceutical, Biomedical and Veterinary Sciences
Department of Pharmaceutical Sciences
University of Antwerp

Faculty of Medicine and Pharmacy
Department of Pharmaceutical and Pharmacological Sciences
Vrije Universiteit Brussel

Untargeted metabolomics to study ethanol-induced hepatotoxicity in HepaRG cells

Doctoral thesis submitted for the degree of
Doctor of Pharmaceutical Sciences at the University of Antwerp
and
Doctor of Pharmaceutical Sciences at the Vrije Universiteit Brussel
to be defended by

Elias ITURROSPE

Supervisors:
Prof. dr. Adrian Covaci (University of Antwerp)
Prof. dr. Alexander L.N. van Nuijs (University of Antwerp)
Prof. dr. Ir. Tamara Vanhaecke (Vrije Universiteit Brussel)

Antwerp, 2023

Disclaimer

Faculteit Farmaceutische, Biomedische en Diergeneeskundige Wetenschappen
Departement Farmaceutische Wetenschappen
Universiteit Antwerpen

Faculteit Geneeskunde en Farmacie
Departement Farmaceutische en Farmacologische Wetenschappen
Vrije Universiteit Brussel

Untargeted metabolomics om ethanol-geïnduceerde hepatotoxiciteit in HepaRG cellen te bestuderen

Proefschrift voorgelegd tot het behalen van de graad van
Doctor in de Farmaceutische Wetenschappen aan de Universiteit Antwerpen
en
Doctor in de Farmaceutische Wetenschappen aan de Vrije Universiteit Brussel
te verdedigen door

Elias ITURROSPE

Promotoren:
Prof. dr. Adrian Covaci (Universiteit Antwerpen)
Prof. dr. Alexander L.N. van Nuijs (Universiteit Antwerpen)
Prof. dr. Ir. Tamara Vanhaecke (Vrije Universiteit Brussel)

Antwerpen, 2023

Members of the jury

Promotors

Prof. dr. Adrian Covaci
University of Antwerp, Department of Pharmaceutical Sciences
Toxicological Centre, Antwerp, Belgium

Prof. dr. Alexander L.N. van Nuijs
University of Antwerp, Department of Pharmaceutical Sciences
Toxicological Centre, Antwerp, Belgium

Prof. dr. Tamara Vanhaecke
Vrije Universiteit Brussel, Department of Pharmaceutical Sciences
In Vitro Toxicology and Dermato-Cosmetology, Brussels, Belgium

Internal jury members

Prof. dr. Luc Pieters
University of Antwerp, Department of Pharmaceutical Sciences
Natural Products & Food Research and Analysis, Antwerp, Belgium

Prof. dr. Luisa Vonghia
University of Antwerp, Department of Medicine
Laboratory of Experimental Medicine and Pediatrics, Antwerp, Belgium
Antwerp University Hospital, Department of Gastroenterology & Hepatology, Antwerp, Belgium

Prof. dr. Ann van Eeckhaut
Vrije Universiteit Brussel, Department of Pharmaceutical Sciences
Laboratory of Pharmaceutical Chemistry, Drug Analysis and Drug Information, Center for Neurosciences, Brussels, Belgium

External jury members

Prof. dr. Pim E.G. Leonards
Vrije Universiteit Amsterdam, Department of Environment and Health
Amsterdam Institute for Life and Environment, Amsterdam, The Netherlands

Prof. dr. Jef Verbeek
Catholic University of Leuven, Department of Chronic Diseases and Metabolism
Laboratory of Hepatology, Leuven, Belgium
University Hospitals Leuven, Department of Gastroenterology and Hepatology, Leuven, Belgium

LIST OF ABBREVIATIONS

A	
Ach	Acetylcholine
ACN	Acetonitrile
ADP	Adenosine diphosphate
AFLD	Alcoholic fatty liver disease
AH	Alcoholic hepatitis
AIF	All-ions fragmentation
ALD	Alcoholic liver disease
ALT	Alanine aminotransferase
AMP	Adenosine monophosphate
AMPK	Adenosine monophosphate-activated protein kinase
AOP	Adverse outcome pathway
AOP-KB	AOP knowledge database
ASH	Alcoholic steatohepatitis
AST	Aspartate aminotransferase
ATP	Adenosine triphosphate
AUC	Area under the curve
AWS	Alcohol withdrawal syndrome
B	
BBD	Box-Behnken design
BEH	Ethylene bridged hybrid
BHT	Butylated hydroxytoluene
C	
CAP	Controlled attenuation parameter
CAR	Carnitine
Carn	Carnosine
CCS	Collision cross section
CDC	Center for disease control and prevention
CDP-choline	Cytidine diphosphocholine
CDP-E	CDP-ethanolamine
Cer	Ceramide
CHAT	Choline O-acetyltransferase
ChoP	Phosphorylcholine
CID	Collision-induced dissociation
cIMS	Cyclic ion mobility spectrometry
CoA	Coenzyme A
COT	Carnitine octanoyltransferase
CPT-1	Carnitine palmitoyltransferase 1
Cr	Creatine
CT	Computed tomography
CV	Coefficient of variation
CYP	Cytochrome P450
CYP2E1	Cytochrome P450 2E1
D	
DAMPs	Damage-associated molecular patterns
DBE	Double bond equivalent
DDA	Data-dependent acquisition
DEV	Drift entrance voltage
DG	Diglyceride
DGAT2	Diglyceride acyltransferase 2
DHCer	Dihydroceramide
DIA	Data-independent acquisition
DIMS	Direct infusion mass spectrometry
DOE	Design of experiments
DT	Drift time
DTIMS	Drift tube ion mobility spectrometry
DXV	Drift exit voltage
E	
EASL	European association for the study of the liver
EC	Extracellular
EDTA	Ethylenediaminetetraacetic acid
EI	Electron impact
EIEIO	Electron impact excitation of ions from organics
ELF	Enhanced liver fibrosis
EMA	European medicines agency
EPT1	Ethanolaminephosphotransferase 1
ER	Endoplasmatic reticulum
ES	Electrospray
ESI	Electrospray ionization
EtG	Ethylglucuronide
EtOChoP	Ethylated phosphorylcholine
EtOH	Ethanol
EtoP	O-phosphoethanolamine
EtS	Ethylsulfate

LIST OF ABBREVIATIONS

F	
FA	Fatty acid
FAHFA	Fatty acyl esters of hydroxy fatty acid
FAIMS	Field asymmetric ion mobility spectrometry
FAS	Fatty acid synthetase
FC	Fold change
FDA	Food and drug administration
FIA	Flow injection analysis
FID	Flame ionization detection
FWHM	Full width at half maximum
G	
G3P	Glycerol 3-phosphate
GAA	Guanidinoacetate
GAHS	Glasgow alcoholic hepatitis score
GAMT	Guanidinoacetate methyltransferase
GC	Gas chromatography
GDE1	Glycerophosphodiester phosphodiesterase 1
GGT	Gamma-glutamyl transferase
GNMT	Glycine N-methyltransferase
GPC	Glycerophosphocholine
GPCPD1	Glycerophosphocholine phosphodiesterase 1
GSH	Glutathione (reduced)
GSR	Glutathione reductase
GSSG	Glutathione (oxidized)
H	
HCC	Hepatocellular cancer
HCD	Higher-energy C-trap dissociation
HILIC	Hydrophilic interaction liquid chromatography
HMDB	Human metabolome database
HPLC	High-performance liquid chromatography
HRMS	High-resolution mass spectrometry
HS	Headspace
HSCs	Hepatic stellate cells
HSS	High strength silica
I	
IC	Intracellular
ICF	Informed consent form
IC_X	Inhibitory concentration X (X = number)
IM	Ion mobility
IMS	Ion mobility spectrometry
INR	International normalized ratio
IPA	Isopropanol
IPB	Institute of plant biochemistry
IRS-1	Insulin receptor substrate-1
ISF	In-source fragmentation
K	
KE	Key event
L	
LC	Liquid chromatography
LE	Liquid extraction
LLE	Liquid-liquid extraction
LPC	Lysophosphatidylcholine
LPCAT	Lysophosphatidylcholine acyltransferase
LPE	Lysophosphatidylethanolamine
LPI	Lysophosphatidylinositol
LPS	Lipopolysacharides
LRMS	Low resolution mass spectrometry
LS	Least square
LSECs	Liver sinusoidal endothelial cells
LYPLA1	Lysophospholipase 1
M	
m/z	Mass-to-charge
MAFLD	Metabolic dysfunction-associated fatty liver disease
MAT	Methionine adenosyltransferase
MBOAT7	Membrane-bound O-acyltransferase domain-containing protein 7
mc-CAR	Medium chain-carnitine
mc-COA	Medium chain-coenzyme A
MCP-1	Monocyte chemoattractant protein-1

LIST OF ABBREVIATIONS

MCV	Mean corpuscular volume
MDA	Mean decrease in accuracy
MDF	Maddrey discriminant function
MELD	Model for end-stage liver disease
MeOH	Methanol
Met	Methionine
mfn2	Mitochondrial protein mitofusin 2
MG	Monoglyceride
MIE	Molecular initiating event
MoA	Mode of action
MPA	Mobile phase A
MPB	Mobile phase B
mQACC	Metabolomics quality assurance and quality control consortium
MRI	Magnetic resonance imaging
MRM	Multiple reaction monitoring
mRSD	Median relative standard deviation
MS	Mass spectrometry
MSI	Metabolomics standards initiative
MSMLS	Mass spectrometry metabolite library of standards
MTA	Methylthioadenosine
MTBE	Methyl tert-butyl ether
MTT	3-(4,5-dimethylthiazol-2-yl)-2,5-diphenyltetrazolium bromide
N	
NADH	Nicotinamide adenine dinucleotide
NADPH	Nicotinamide adenine dinucleotide phosphate
NAE	N-acyl ethanolamine
NAFLD	Non-alcoholic fatty liver disease
NASH	Non-alcoholic steatohepatitis
NIAAA	American national institute on alcohol abuse and alcoholism
NMR	Nuclear magnetic resonance
NRU	Neutral red uptake
O	
O-DG	Alkyl ether diglyceride
O-PC	Alkyl ether phosphatidylcholine
O-PE	Alkyl ether phosphatidylethanolamine
O-TG	Alkyl ether triglyceride
P	
PA	Phosphatidic acid
PAG	Phenylacetylglutamine
PAP	Phosphatidate phosphatase
PBS	Phosphate-buffered saline
PC	Phosphatidylcholine
PCA	Principal component analysis
PCDL	Personal compound database and library
PCYT2	Phosphoethanolamine cytidylyltransferase
PE	Phosphatidylethanolamine
PEEK	Polyether ether ketone
PEMT	Phosphatidylethanolamine-N-methyltransferase
PE-P	Alkenyl ether phosphatidylethanolamine
PEth	Phosphatidylethanol
PG	Phosphatidylglycerol
PGA1	Prostaglandin A1
PGE1	Prostaglandin E1
PGE2	Prostaglandin E2
PHH	Primary human hepatocytes
PI	Phosphatidylinositol
PLA2	Phospholipase A2
PLD	Phospholipase D
PLD1_2	Phospholipase D1/2
PLS-DA	Partial least squares-discriminant analysis
PNPLA3	Patatin-like phospholipase domain-containing protein 3
P-PC	Alkenyl ether phosphatidylcholine
P-PE	Alkenyl ether phosphatidylethanolamine
PQN	Probabilistic quotient normalization
PR	Prenol lipid
PRM	Parallel reaction monitoring
PS	Phosphatidylserine
PT	Prothrombin time
P-TG	Alkenyl ether triglyceride
PUFA	Polyunsaturated fatty acid
PVA	Polyvinyl alcohol

LIST OF ABBREVIATIONS

Q	
QA	Quality assurance
QC	Quality control
QMS	Quality management system
QqQ	Triple quadrupole
R	
RF	Random forest
RFE	Rear funnel entrance
RFX	Rear funnel exit
RMSE	Root mean square error
ROC	Receiver operating characteristic
ROS	Reactive oxygen species
RPLC	Reversed-phase liquid chromatography
RSD	Relative standard deviation
RT	Retention time
S	
S/N	Signal-to-noise ratio
SAH	S-adenosyl-homocysteine
SAM	S-adenosylmethionine
SI	Supplementary information
SM	Sphingomyelin
SMA	Sphingomyelinase
SMILES	Simplified molecular-input line-entry system
SOD	Superoxide dismutase
SOP	Standard operating procedure
SPDS	Spermidine synthase
SPE	Solid-phase extraction
Sph	Sphingosine
SREBP-1c	Sterol regulatory element-binding protein-1c
SRM	Selected reaction monitoring
SS	System suitability
ST	Sterol lipid
SWATH	Sequential window acquisition of all theoretical mass spectra
T	
Tau	Taurine
TCA	Tricarboxylic acid
TF	Trap filling
TG	Triglyceride
TIMS	Trapped ion mobility spectrometry
TLR4	Toll-like receptor 4
TM6SF2	Transmembrane 6 superfamily member 2
TMS	Trimethylsilyl
TNF-R	TNF-α receptors
TNF-α	Tumor necrosis factor alpha
TQ	Triple quadrupole
TR	Trap release
TWIMS	Traveling-wave ion mobility spectrometry
U	
UDPGA	Uridine 5'-diphosphoglucuronic acid
UDPGDH	UDP-glucose dehydrogenase
UDP-Glu	Uridine diphosphate glucose
UGT	UDP-glucuronosyltransferase
UHPLC	Ultra-high performance liquid chromatography
URL	Upper reference limit
V	
VAD	Vlaams expertisecentrum alcohol en andere drugs
VIM	Variable importance measure
VIP	Variable importance in projection
W	
WHO	World Health Organization
X	
XB	Cross-butyl

TABLE OF CONTENTS

CHAPTER 1:
GENERAL INTRODUCTION

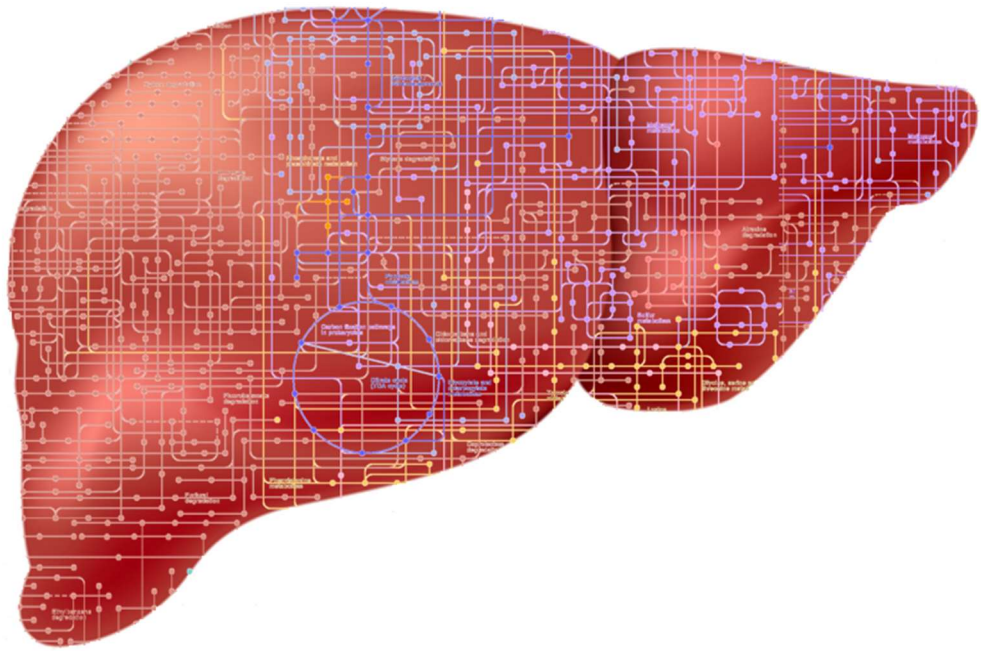

Based on the following publications

Iturrospe E, Da Silva KM, Van de Lavoir M, Robeyns R, Cuykx M, Vanhaecke T, van Nuijs A, Covaci A. Mass spectrometry-based untargeted metabolomics and lipidomics platforms to analyze cell culture extracts. In: González-Domínguez, R. (eds) Mass Spectrometry for Metabolomics. Methods in Molecular Biology, Springer Nature. 2023; 2571, 189-206. Humana, New York, NY. (DOI: 10.1007/978-1-0716-2699-3_19).

Da Silva KM, **Iturrospe E,** Bars C, Knapen D, Van Cruchten S, Covaci A, Van Nuijs A. Mass Spectrometry-Based Zebrafish Toxicometabolomics: A Review of Analytical and Data Quality Challenges. Metabolites 2021; 11(9), 635. (DOI: 10.3390/metabo11090635).

1.1. Alcoholic liver disease

The causal impact of ethanol (often referred to as 'alcohol' in layman's term) on liver disease has been known for a long time. As early as in 1785, physician Benjamin Rush listed liver conditions as a disease consequence of habitual drinking of spirits in his book 'Inquiry into the Effects of Ardent Spirits upon the Human Body and Mind'. Rush compared the hepatic effects of ethanol with the punishment of Prometheus by Zeus, who would have chained Prometheus to a high mountain, where a vulture would prey on his liver (Rush, 1785).

Excessive ethanol use is a major causality of liver disease worldwide and is the most common cause of acute-on-chronic liver failure (Asrani et al., 2019). About 2 billion people worldwide consume ethanol and upwards of 75 million are diagnosed with alcohol-use disorders and are at risk of developing alcoholic liver disease (ALD) (Asrani et al., 2019). In 2016, the harmful use of ethanol resulted in 3.3 million deaths (5.3% of all deaths) worldwide (World Health Organization, 2018). In the same year, the Global Burden of Disease project estimated the number of deaths due to cirrhosis and chronic liver disease to be 1,256,900, of which 334,900 deaths (27%) were attributable to ethanol (Naghavi et al., 2017).

ALD is caused by chronic excessive consumption of ethanol. However, the important question of 'how much ethanol is too much', or 'how much can I safely drink' has been often addressed in the past and the answers are not straightforward (Bellentani & Tiribelli, 2001). First of all, thresholds can be reported in either grams of ethanol per day or week, or in the number of alcoholic drinks. Although the quantification in grams of ethanol is more precise, it is time-consuming and frequently difficult to obtain during questionnaires, since patients are not able to recall the different types of drinks and their amount. For this latter reason, it might be more useful to quantify by the number of drinks, although the amount of ethanol can vary significantly between alcoholic drinks from 8 to 16 g (European Association for the Study of the Liver, 2018). According to the Dietary guidelines for Americans, one standard alcoholic drink is defined to contain 14 g of ethanol (U.S. Department of Health and Human Services & U.S. Department of Agriculture, 2020), while the European association for the Study of the Liver (EASL) suggests standardizing the measure to 10 g.

The threshold of daily ethanol consumption and the duration of excessive ethanol consumption needed to develop ALD varies considerably between individuals (Seitz et al., 2018). The world health organization (WHO) defined heavy episodic drinking as ≥ 60 g ethanol on at least one occasion at least once per month (World Health Organization, 2018). The American center for disease control and prevention (CDC) defines heavy drinking as ≥ 15 alcoholic drinks per week for men or ≥ 8 alcoholic drinks per week for

women (Bohm et al., 2021), while the American National Institute on Alcohol Abuse and Alcoholism (NIAAA) defines heavy drinking as > 4 drinks per day or > 14 drinks per week for men and > 3 drinks per day or > 7 drinks per week for women (NIAA, 2010). While no general European guidelines are available on low-risk drinking behavior, the European Commission published a list with guidelines per European country, showing disagreement in these local recommendations (European Commission, 2021). For example, the Flemish expertise center on alcohol and other drugs (VAD) of Belgium recommends to not consume more than 10 standard glasses of ethanol per week. When ethanol is being consumed, the VAD recommends to spread the consumption and to have a few ethanol-free days (VAD, 2016). These recommendations are in disagreement with for example those in Ireland, where the lower risk limits were set at 17 standard drinks per week for men and 11 for women (European Commission, 2021).
Differences in thresholds are mainly due to heterogeneity in sampling population and lack of reliable records for ethanol consumption (Bellentani & Tiribelli, 2001).

1.1.1. Stages of alcoholic liver disease

Chronic exposure to ethanol can lead to a broad spectrum of pathological liver conditions (Figure 1.1). Rather than being distinct disease entities, these pathologic processes frequently overlap (Chacko & Reinus, 2016).

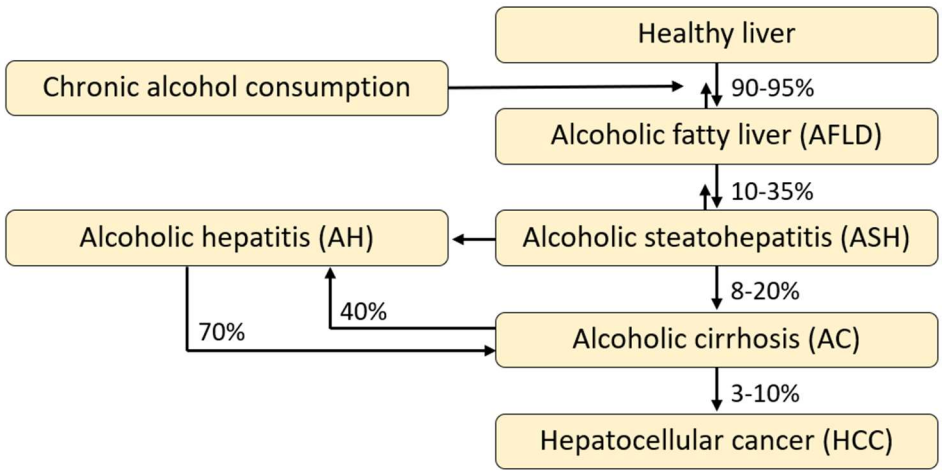

Figure 1.1 Stages of alcoholic liver disease. Overlap between shown pathologic entities can occur. Adapted from Seitz et al., 2018 and European Association for the Study of the Liver, 2018.

Ethanol is known to alter fat metabolism processes, followed by progressive intracellular lipid accumulation in hepatocytes, resulting in alcoholic fatty liver disease (AFLD) (Sakhuja, 2014; Seitz et al., 2018). The development of AFLD may occur in up to 90-95% of heavy drinkers and it can be induced in a short time period (3-7 days) after

heavy ethanol consumption (Chacko & Reinus, 2016; Seitz et al., 2018). AFLD can progress to alcoholic steatohepatitis (ASH), which is characterized by hepatic inflammation, mostly accompanied by hepatocellular ballooning. Hepatocellular ballooning is usually defined as cellular enlargement 1.5-2 times the diameter of a normal hepatocyte, with rarefied cytoplasm (Brunt et al., 2004). Chronic ASH can eventually lead to progressive fibrosis and cirrhosis and in some cases to hepatocellular cancer (HCC). (Chacko & Reinus, 2016; Liangpunsakul et al., 2016; Sakhuja, 2014; Seitz et al., 2018; World Health Organization, 2018). Besides the slow chronic progression of ASH to fibrosis and cirrhosis, a rapid progression to alcoholic hepatitis (AH) associated with poor prognosis can occur (Seitz et al., 2018). Acute AH represents a severe type of ASH, which is characterized by abdominal pain, fever, increased white blood cell count, impaired blood clotting and jaundice (Vonghia et al., 2014). Occurrence of AH in cirrhotic patients is an example of acute-on-chronic disease (Seitz et al., 2018).

1.1.2. Mechanism of alcoholic liver disease

The susceptibility to develop ethanol dependence and ALD is determined by constitutional, environmental and genetic factors, although the nature and level of interplay between them remains unclear (Stickel et al., 2017). The heritability of ethanol dependence is well-documented, but no strong candidate genes related to increased dependence risk have emerged. Concerning ethanol-related cirrhosis, three candidate genes are thought to have an important influence, although the mechanisms by which genetic variants increase pathological risks and their interplay remain to be determined. These latter genes are patatin-like phospholipase domain-containing protein 3 (PNPLA3), transmembrane 6 superfamily member 2 (TM6SF2) and membrane-bound O-acyltransferase domain-containing protein 7 (MBOAT7) (Stickel et al., 2017).
In addition to genetic factors, ethanol-induced epigenetic changes in the liver can lead to dysregulated hepatocyte and immune cell functions (Seitz et al., 2018). For example, ethanol can modulate acetylation of histones and lead to DNA hypomethylation through depletion of hepatic S-adenosylmethionine (SAM) (S. C. Lu et al., 2000; Park et al., 2005).

Hepatic alcohol dehydrogenase oxidizes ethanol to form acetaldehyde, which is further biotransformed to acetate in mitochondria by aldehyde dehydrogenase (Figure 1.2). In addition, acetaldehyde is also formed through conversion catalyzed by peroxisomal catalase and cytochrome P450 2E1 (CYP2E1) in the endoplasmic reticulum and mitochondria of hepatocytes (Hyun et al., 2021; Lieber et al., 1970). Acetaldehyde can bind to proteins and alter their structure and/or function, induce production of reactive oxygen species (ROS) and neoantigens, and can interact with DNA causing point mutations and chromosomal damage. In addition, ethanol can generate ROS e.g.,

through induction of CYP2E1 and by stimulating production of tumor necrosis factor alpha (TNF-α) (Hyun et al., 2021; Seitz et al., 2018). A small amount of ethanol is non-oxidatively conjugated to phosphatidylcholine to form phosphatidylethanol (PEth), to glucuronic acid and sulfate to form ethyl glucuronide (EtG) and ethyl sulfate (EtS), respectively and fatty acids to form fatty acid ethyl esters (FAEE) (Hyun et al., 2021).

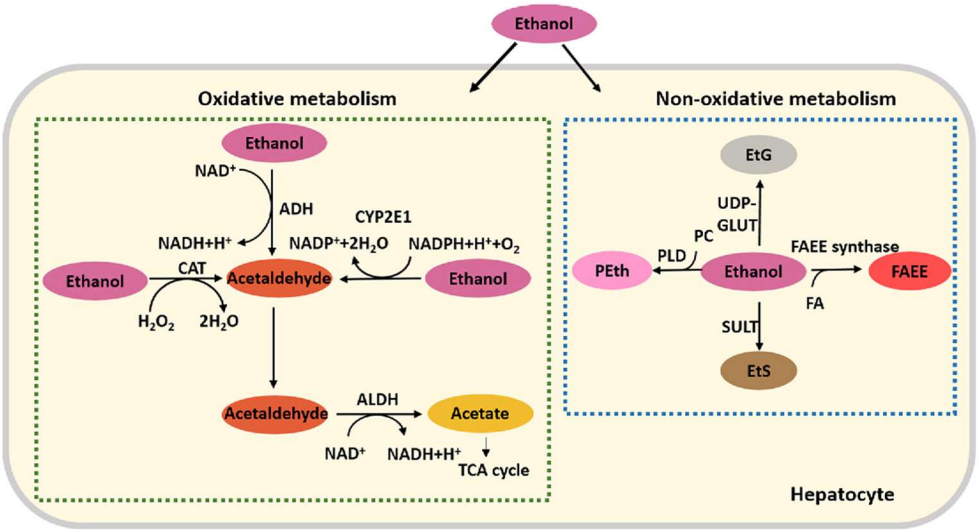

Figure 1.2 Biotransformation of ethanol in hepatocytes. The majority of ethanol is biotransformed via oxidative metabolism (±95%), while a minority through non-oxidative metabolism (±5%) (J. Sun et al., 2018). ADH: Alcohol dehydrogenase. ALDH: Aldehyde dehydrogenase. CAT: Catalase. CYP2E1: Cytochrome P450 2E1. EtS: Ethyl sulfate. EtG: Ethyl glucuronide. FAEE: Fatty acid ethyl esters. FA: Fatty acids. NAD: Nicotinamide adenine dinucleotide. NADP: Nicotinamide adenine dinucleotide phosphate. PC: Phosphatidylcholine. PLD: Phospholipase D. PEth: Phosphatidylethanol. SULT: Sulfotransferases. TCA: Tricarboxylic acid. UDP-GLUT: UDP-glucuronosyl-transferase. NADH: Nicotinamide adenine dinucleotide (reduced).

Acetate, the biotransformation product of acetaldehyde is believed to contribute to ALFD as it can be converted to acetyl-CoA which can fuel fatty acid synthesis. However, the contribution of acetate to fat accumulation would be minimal as acetate is rapidly secreted from hepatocytes (Seitz et al., 2018). More important factors in the development of AFLD are (i) elevation of the hepatocyte ratio of NADH/NAD+ interrupting mitochondrial β-oxidation of fatty acids (Baraona & Lieber, 1979), (ii) upregulation of sterol regulatory element-binding protein-1c (SREBP-1c) which stimulates lipogenic genes (You et al., 2002) and (iii) inactivation of peroxisome proliferator- activated receptor-α (PPARα), affecting genes involved in transport and oxidation of fatty acids (Galli et al., 2001). In addition, consumption of ethanol can result in lipolysis of adipose tissue and adipocyte death (Parker et al., 2017) and increase

intestinal uptake of lipids (Baraona & Lieber, 1979), both fueling hepatic fat accumulation.

The development of ASH is triggered by gut-derived pathogen-associated molecular patterns (PAMPs; for example, lipopolysaccharides (LPS) and bacterial DNA) resulting in release of cytokines and chemokines from Kupffer cells and damage-associated molecular patterns (DAMPs) released by dying hepatocytes (Seitz et al., 2018). In addition, neoantigens, resulting from protein adducts formed with acetaldehyde and ROS, can contribute to inflammation (Seitz et al., 2018).

Chronic liver damage results in liver fibrosis, which is induced as a wound-healing response. The key event in hepatic fibrogenesis is production of extracellular matrix by activated hepatic stellate cells (HSCs). HSCs can be activated by pro-fibrotic mediators secreted by immune cells. For example, Kupffer cells which are stimulated by gut-derived endotoxins, can stimulate HSCs (Paik et al., 2003). Advanced fibrosis results in cirrhosis, disturbing hepatic blood flow and causing portal hypertension, which may occur together with other complications such as ascites and esophageal varices (Seitz et al., 2018).

1.1.3. Diagnosis of alcoholic liver disease

A major challenge exists in the clinical diagnosis of ALD (Seitz et al., 2018; Sheron et al., 2013). Alcohol-related disorders, which put individuals at high risk of developing ALD, are highly prevalent, but poorly identified and characterized (Seitz et al., 2018). Unfortunately, most patients are diagnosed at advanced stages of ALD and data on the prevalence and profile of patients with early stages of disease are limited (Singal et al., 2018). Another important issue in clinical diagnosis is that patients with ethanol use disorders are generally treated by psychiatrists, and hepatic evaluation is often not performed (Seitz et al., 2018).

Symptoms of ALD tend to develop late in the course of disease progression and may only be apparent at the stage of irreversible cirrhosis (Seitz et al., 2018; Sheron et al., 2013). At present, there are no early and specific biomarkers for the diagnosis of ALD. Current guidelines advice to perform laboratory tests for general markers of liver damage, such as serum transaminases (aspartate transaminase (AST) and alanine transaminase (ALT)) activity and gamma-glutamyl transferase (GGT) activity, as well as tests reflecting liver function (e.g., blood coagulation and bilirubin) (Seitz et al., 2018). In advanced ALD, prolonged prothrombin time (PT), increased bilirubin levels or thrombocytopenia can occur. The inexpensiveness of measurements of GGT, ALT, AST and the mean corpuscular volume (MCV) makes them the most frequently used markers for the detection of ALD. However, these markers suffer from low sensitivity and specificity and no single marker or combination of markers can be used to differentiate

between different causes of liver disease and stages of ALD (Thursz et al., 2018; Vonghia et al., 2014). An example of a low specificity marker is serum GGT activity, which is elevated not only in cholestatic liver disease, but also in cardiac insufficiency, drug-induced liver injury and many more diseases (Seitz et al., 2018; Sheron et al., 2013).

In the case of acute alcoholic hepatitis, prognostic scores are useful to assess short-term survival and/or to guide pharmacotherapeutical initiation. The Maddrey discriminant function (MDF) score, which uses the patient's PT and total bilirubin, is mostly used (Owens et al., 2016; Vonghia et al., 2014). An MDF score ≥ 32 is used to initiate corticosteroid treatment and indicates severe AH with a 1-month mortality rate up to 30-50% (Oshea et al., 2010). Other scores, such as the Model for End-Stage Liver Disease (MELD), which includes bilirubin, creatinine, and the international normalized ratio (INR), and the Glasgow Alcoholic Hepatitis Score (GAHS), which includes age, white blood cell count, urea, bilirubin, and PT value, have been proposed, but need further validation in the context of ALD (Vonghia et al., 2014).

The abovementioned issues with biochemical markers for diagnostic purposes leaves imaging as an important tool during diagnosis. Ultrasonography, magnetic resonance imaging (MRI) and computed tomography (CT) may allow quantification of steatosis (European Association for the Study of the Liver, 2018). For example, abdominal ultrasonography using bright echo pattern can be used to screen for AFLD, but it has only moderate sensitivity and specificity (65% sensitivity, 81% specificity) (Thiele et al., 2018; Y. Zhang et al., 2018) and has little value when steatosis is below 20-30% (European Association for the Study of the Liver, 2018). Ultrasonography techniques based on attenuation of shear waves such as controlled attenuation parameter (CAP) are more accurate for the quantification of severe steatosis (Thiele et al., 2018). The diagnostic sensitivity of CT ranges from 52-62% in mild steatosis with a fat fraction of 10-20% (Y. Zhang et al., 2018). MRI is considered superior to ultrasonography and CAP due to its high accuracy for detecting steatosis (sensitivity 77-90%, specificity 87-91%) (Q. Li et al., 2018). However, the high cost and low availability of this technique are major bottlenecks.

Patients with severe ASH or advanced fibrosis and/or cirrhosis may develop AH, which is considered as a distinct clinical syndrome characterized by the recent onset of jaundice with or without other signs of liver decompensation such as ascites and/or encephalopathy (European Association for the Study of the Liver, 2018). Jaundice is often associated with fever, malaise, weight loss and malnutrition (Seitz et al., 2018). Typical laboratory abnormalities in AH include neutrophilia, hyperbilirubinemia and serum AST > two times the upper reference limit (URL). Prolonged PT, hypoalbuminemia and thrombocytopenia can occur in severe forms (European Association for the Study of the Liver, 2018).

Liver fibrosis is graded in five histological stages, with F0 representing no fibrosis and F4 representing the most severe stage with cirrhosis. The measurement of liver stiffness by transient elastography, such as fibroscan, can be used to classify fibrosis stages (Seitz et al., 2018). Liver stiffness values <6 kPa are generally considered as normal and exclude even mild fibrosis (F1-F2). Usage of liver stiffness for clinical differentiation between F1 and F2 is not recommended as there exists a grey area between 6 to 8 kPa and interferences such as positioning, breathing and eating can have an influence (Seitz et al., 2018). It is not recommended to use liver stiffness as a stand-alone diagnostic tool as inflammation, hepatic perfusion and hepatocyte ballooning affect the outcome (Seitz et al., 2018). In addition, ethanol intake and increased transaminase levels (especially AST > 100 IU/L) can modify measurements of liver stiffness, independent of the fibrosis stage (Vonghia et al., 2014). For improved assessment of liver stiffness, patients should withdraw from ethanol for 1-2 weeks and liver stiffness should be redetermined after normalization of transaminases or inflammation-adapted cut-off values should be used (Seitz et al., 2018). Serum markers for fibrosis, such as Fibrotest and enhanced liver fibrosis (ELF) test, are inferior to liver stiffness measurements, but can be used to differentiate between mild and advanced fibrosis when elastography is not available (Seitz et al., 2018).

Histological evaluation of a liver biopt remains the golden standard to confirm ALD. Early stages can only be diagnosed properly through liver biopsy, since noninvasive tests do not show an increase in the liver parameters (Singal et al., 2018). The disadvantage of liver biopsy is the possibility to cause complications, such as hepatic bleeding (Seitz et al., 2018; Singal et al., 2018) and liver biopsy is generally only recommended in cases of aggressive forms of ALD requiring intervention (Vonghia et al., 2014). During ALFD, hepatocytes show accumulation of lipid droplets in the cytoplasm. This accumulation may start with the formation of small droplets of fat (microvesicular), which later enlarge to large fat droplets (macrovesicular), which push the nucleus to the periphery (Sakhuja, 2014). In ASH, steatosis is accompanied by hepatic injury. This latter is mostly visible under the form of hepatocyte ballooning, but also neutrophil rich inflammation in the lobular parenchyma and/or Mallory Denk bodies (i.e., intracellular deposition of misfolded protein aggregated into ubiquitin-rich cytoplasmic inclusions in ballooned hepatocytes) might be observed (Sakhuja, 2014). Unfortunately, about half of the patients with seemingly early ALD already have advanced fibrosis or cirrhosis on liver biopsy (Singal et al., 2018). There is a need for new diagnostic tools to detect ALD in an early stage, as is stated in the clinical guidelines for ALD of 2018 by the American College of Gastroenterology and by the European Association for the Study of the Liver (Singal et al., 2018; Thursz et al., 2018). A specific interest lies in the discovery of specific biomarkers that can be used for an early diagnosis of ALD in patients with risky drinking

behavior, in order to advise and treat patients before progression to irreversible stadia occurs. A similar call for specific biomarkers has been launched also for the early detection of non-alcoholic steatohepatitis (NASH) (Francque & Vonghia, 2017).

1.1.4. Treatment of alcoholic liver disease

The treatment options for ALD have not changed in the last four decades, and in fact ethanol abstinence is still the cornerstone of treatment (Singh et al., 2017). Abstinence is critical, even after diagnosis of cirrhosis, as it significantly improves long-term prognosis (Chacko & Reinus, 2016). Several pharmacotherapeutical options are available to assist in the cessation of ethanol consumption such as disulfiram, naltrexone and acamprosate (Seitz et al., 2018). However, solely acamprosate can be used without concerns of hepatotoxicity (Burnette et al., 2022). Only baclofen has been tested for ethanol cessation in the context of ALD (Addolorato et al., 2007) and its use remains controversial as there were studies that could not show superiority over placebo (Reynaud et al., 2017). After abrupt cessation of ethanol consumption, patients can develop an alcohol withdrawal syndrome (AWS), which occurs 6-24 h after cessation and can last up to 24-48 h (Vonghia et al., 2014). Clinical manifestations of AWS include increased blood pressure, tremors, sweating, anxiety, headache, nausea, emesis, and more severely delirium tremens, seizures, coma, cardiac arrest and death (Leggio et al., 2008). Benzodiazepines can be administered to prevent seizures and decrease other symptoms such as anxiety, while antipsychotics might be used in patients with excess agitation or psychotic symptoms (Singh et al., 2017). Alcoholics are usually malnourished and deficient in vitamins. For example, vitamin B1 deficiency is frequently observed in alcoholics due to inadequate nutritional intake, impaired gastrointestinal absorption and impaired cellular utilization (Martin et al., 2003). In case of vitamin B1 deficiency, parenteral thiamine can be administered to prevent Wernicke encephalopathy, in addition to general nutritional support (Singh et al., 2017). Parenteral thiamine is preferred over oral thiamine because in addition to impaired gastrointestinal absorption in alcoholics, oral thiamine has poor bioavailability that does not allow for attaining a sufficient concentration in cerebrospinal fluid (Singh et al., 2017). The need of a multidisciplinary clinical team, including hepatologists and addiction therapists managing patients with ALD should be emphasized (Seitz et al., 2018). For treatment of ALD, there are no targeted therapies available, nor European Medicine Agency (EMA)- or Food and Drug Administration (FDA)-approved drugs (Burnette et al., 2022; Singh et al., 2017; Vuittonet et al., 2014). Corticosteroids (or pentoxifylline in case steroids are contraindicated) can be used to reduce hepatic inflammation for patients with severe AH (MDF ≥ 32) (European Association for the Study of the Liver, 2018; Singh et al., 2017).

The only long-term management option for decompensated cirrhosis is liver transplantation, which requires to abstain from ethanol consumption for 6 months prior to surgery in most countries (Seitz et al., 2018). Liver transplantation should also be considered in severe AH non-responsive to pharmacotherapy. Liver transplantation is the second most common solid organ transplantation, yet less than 10% of global transplantation needs are met at current rates (Asrani et al., 2019). After one year, post-transplant survival was determined to be 80-85% (European Association for the Study of the Liver, 2018).

1.2. Models to study alcoholic liver disease

1.2.1. Animal models

Most animal experiments studying the effects of ALD are performed using rodents, as rodent models are time- and cost-efficient and facilitate easy manipulation of the study subjects. For example, rodents can be genetically modified (e.g., 'knockout mice'), in order to directly test specific hypotheses (Arteel, 2010). One of the simplest models of ALD in rodents is to provide ethanol-mixed drinking water combined with a normal chow-diet (i.e., grain- or cereal-based diet) *ad libitum*. The issue with this model is that rodents show a natural aversion to ethanol and this model only causes low increase in blood ethanol levels and mild liver injury (Dilley et al., 2018; Lamas-Paz et al., 2018). The Lieber-DeCarli liquid diet partially overcomes aversion of ethanol by feeding rodents solely an ethanol-containing liquid diet formula *ad libitum*. This latter diet showed to markedly elevate aminotransferases and induce steatosis. However, inflammation is mild and fibrosis rarely occurs (DeCarli & Lieber, 1967; Lamas-Paz et al., 2018; Wilkin et al., 2016). To fully overcome the aversion of ethanol, the Tsukamoto–French model was developed in which intragastric infusion is used instead of *ad libitum* feeding (Tsukamoto et al., 1984). This model can be used to achieve higher levels of blood ethanol and more severe liver injury. However, the achievable levels of hepatic inflammation and fibrosis are still inadequate to mimic the human situation. In addition, the model suffers from technical difficulties and higher expenses (Louvet & Mathurin, 2015). A fourth animal model of ALD which is commonly used is the Gao-binge model, which is also known as the NIAAA model. In this model, the Lieber–DeCarli liquid diet is used *ad libitum* for consecutive days (≥ 10), followed by a single binge or multiple binges (Bertola et al., 2013). The combination of chronic feeding with one or multiple binge(s) would synergistically mimic acute-on-chronic alcoholic liver injury with fatty liver and inflammation (Bertola et al., 2013). To generate late stages of ALD in rodents, such as advanced fibrosis, the Lieber–DeCarli liquid diet can be used while other hepatotoxins (e.g., carbon tetrachloride (CCl_4) or lipopolysacharides (LPS)) are added during the

chronic feeding to create a second hit of liver damage (Karaca et al., 2015; Muñoz et al., 2014).

Despite the advances in animal models, there are still no rodent models that fully mimic the spectrum of human ALD, which slows down the progress in research and treatment of ALD (Hyun et al., 2021; Lamas-Paz et al., 2018). Although there are several rodent models, differences exist between humans and rodents, especially in mild forms and early stages of ALD. In human ALD, high levels of ALT and AST are observed in addition to steatosis, hepatocyte ballooning, neutrophil infiltration and Mallory-Denk bodies. Murine models of early-stage ALD do not reflect the human pathology at each stage and often lack one or more characteristics of human ALD (Lamas-Paz et al., 2018). Due to obvious species differences in physiology and pathology between rodents and humans, translation of results from rats or mice to humans is problematic (Lamas-Paz et al., 2018).

Indeed, there are fundamental differences in physiological and biological processes for ethanol between rodents and humans (Hyun et al., 2021). First of all, as mentioned above, there is the natural aversion of rodents towards ethanol (Brandon-Warner et al., 2012). In addition, ethanol catabolism is up to 5 times faster in rodents, and they will stop consuming ethanol when blood acetaldehyde levels increase (Brandon-Warner et al., 2012). Neutrophil infiltration, which is considered a key feature during ASH, is hardly detected in rodents (Hyun et al., 2021; Ramaiah & Jaeschke, 2007). Human blood is neutrophil rich, 50–70% of leukocyte balance, compared to only 10–25% in mice, where lymphocytes comprise 75–90% of leukocytes (Mestas & Hughes, 2004).

There are also marked differences between humans and rodents in inflammatory and innate immune responses and how they are influenced by translocation of intestinal LPS (Brandon-Warner et al., 2012). Rodents exhibit a tolerance to LPS that is higher in several degrees of magnitude compared to humans (Ramaiah & Jaeschke, 2007). In addition, at high LPS exposure, mice express more chemokines compared to humans, which is possibly a result of differences in myeloid and lymphoid-derived cell populations (Copeland et al., 2005). High variability between animal studies and within individual animals impede interpretation of research outcomes. This inter-variability is attributed to, for example, differences in sex, age, genetic background and animal facility environment (Gao et al., 2017).

Primates are considered the ideal animal species to develop a model for human ALD. For example, baboons maintained on ethanol-containing drinking water for 3-4 years developed all stadia of ALD, closely resembling human ALD pathology (Lieber et al., 1985). However, high cost, long study duration and ethical difficulties impede the use of primates as model organism.

In general, animals including rodents remain important to obtain models of ALD for research purposes. However, the abovementioned disadvantages and the recent advances in bioengineering techniques have increased the interest in *in vitro* and *ex vivo* models, which could comprise limitations of animal models (Hyun et al., 2021). Reducing the use of animal modes falls within the scope of the 3R principles (i.e., replacement, reduction and refinement), defined by Russell and Burch in 1959 in response to an increase in laboratory animal science (Aske & Waugh, 2017). Although the 3R principles was mainly introduced for social and ethical reasons, these principles improved bio-medical scientific research e.g., by improving reproducibility and reliability using cell systems. Expansion of 3R to 5R principles, including 'robustness' and 'reproducibility', may highlight the contribution of these principles to advances in fundamental and applied research in general (Aske & Waugh, 2017).

1.2.2. Cellular models

In vitro hepatic metabolic research enables mechanistic elucidation at the cellular level and circumvents the difficult accessibility of the liver through biopsies. Zeilinger *et al.* (2016) defined four criteria for evaluation of hepatic cells in basic research. These criteria include: (i) metabolism of endogenous substrates and exogenous compounds; (ii) regulation of amino acids, carbohydrates, and fatty acids, (iii) synthesis of proteins, such as albumin or transferrin; and (iv) activation of inflammatory and immune reactions upon liver injury due to disease, drug, or toxin exposure. The more criteria are met, the better the cells will reflect the situation in the native organ *in vivo*. Furthermore, hepatocyte functionality has to be preserved over the time period of the study, which can be several hours up to days or even weeks (Zeilinger et al., 2016).

Primary human hepatocytes (PHH) are considered to be the gold standard for hepatic *in vitro* models because they closely mimic the *in vivo* liver's functionality (Guillouzo et al., 2007; Zeilinger et al., 2016). However, they suffer from limitations, such as difficult standardization due to high inter-donor metabolic variability and alterations due to the isolation procedure, limited *in vitro* stability, differences in medication history of the donor, scarcity and unpredictable availability (Guillouzo et al., 2007; Zeilinger et al., 2016). When cultured over extended time periods, PHH show a progressive loss of the hepatocellular phenotype at the level of morphology, as well as functionality. This de-differentiation starts already during the isolation process (Treyer & Müsch, 2013). Liver cell lines generated from hepatomas or by genetic manipulation are widely used due to their good availability, high proliferation activity and stable metabolic performance (Zeilinger et al., 2016).

Oncogenic immortalization of adult hepatocytes received a lot of scientific interest, although the results are rather disappointing as the immortalized cells tend to be

genetically unstable and lose their phenotype characteristics (Guguen-Guillouzo & Guillouzo, 2010). Most of the used human hepatocyte cell lines (e.g., HepaRG, HepG2, Hep3B, Huh7, HBG) are derived from hepatoma (Guguen-Guillouzo & Guillouzo, 2010). Of the hepatic cell lines developed for *in vitro* studies of hepatic functions as alternatives to PHH, many have lost major liver-like functions, but not HepaRG cells (Tascher et al., 2019). HepG2 cells are well characterized and abundant data is available on the use of these cells for the analysis of toxicity pathways. However, major differences in metabolic properties compared to PHH, for example loss of crucial CYP enzymes, make this cell line less interesting for metabolomics purposes and toxicity evaluations (Zeilinger et al., 2016).

Compared to PHH, HepaRG cells, derived from a female suffering from liver carcinoma, are a promising alternative due to low variability and long-term stability while maintaining expression of most liver-specific functions, such as CYP activity and bile acid synthesis. In addition, HepaRG cells are capable of differentiating toward hepatocyte-like cells and biliary-like cells, mimicking the *in vivo* situation (Guillouzo et al., 2007; Marion et al., 2010). This trans-differentiation from a bipotent progenitor is one of the advantages compared to PHH (Tascher et al., 2019). Zooming in at different hepatoma cell lines, the HepaRG cell line shows a phenotype most close to that of the *in vivo* organ (Guguen-Guillouzo & Guillouzo, 2010). The close resemblance to PHH was further evidenced by genomic microarrays showing around 85% identity in genes expressed in both models (Guguen-Guillouzo & Guillouzo, 2010). Tascher *et al.* found HepaRG cells to be highly differentiated, with functional mitochondria, hepatokine secretion abilities, and an adequate response to insulin (2019). HepaRG cells appear as a robust surrogate for PHH, a versatile cell system to study xenobiotic detoxification, control of hepatic energy metabolism, secretory function and disease-related mechanisms (Tascher et al., 2019).

1.3. Metabolomics

Metabolomics is a systems biology discipline that has grown tremendously over the past 20 years. It concerns the holistic investigation of endogenous metabolites, low molecular weight (< 1500 Da) biomolecules (e.g., lipids and amino acids) that provide information on the biochemical activities of cells. The metabolome is often referred to as the molecular phenotype of living organisms because it is the most downstream level of cellular organization (i.e., more downstream than DNA, RNA or proteins) (Barnes et al., 2016a; Su Jung et al., 2016). Subdisciplines of metabolomics include, among others, lipidomics, which focuses on lipids (K. Yang & Han, 2016) and fluxomics, which studies metabolic fluxes for example using ^{13}C-labeled molecules (Emwas et al., 2022).

The analysis of metabolites can be performed using untargeted, semi-targeted/semi-quantitative, and/or targeted/quantitative approaches. In most cases, an untargeted method can be used as a first screening approach (i.e., hypothesis-generating), as this technique is less biased towards certain metabolite classes (Ivanisevic & Want, 2019). Once the metabolites of interest have been annotated, a (semi-)targeted method (hypothesis-driven) can be used in order to detect changes in the concentration of specific metabolites using reference standards (Ivanisevic & Want, 2019). While quantification in targeted methods is performed using one calibration curve per metabolite, one calibration curve per class of metabolites is used during semi-targeted metabolomics (Malm et al., 2021).

The metabolome consists of a heterogeneous variety of molecules, ranging from small polar organic acids to relatively large apolar triglycerides. The complexity of the metabolome is reflected in the 222,860 metabolite entries listed in the Human Metabolome Database (HMDB) as of May 2023 (Wishart et al., 2022). In addition, Alseekh *et al*. (Alseekh et al., 2021) estimated that up to 1,000,000 different metabolites occur across living organisms with approximately up to 40,000 metabolites in a single species. To cover this vast array of metabolites in untargeted experiments, comprehensive sample preparation combined with highly sensitive and specific analytical methods using complementary techniques are required (Patti, 2011). To increase metabolite coverage, samples can be fractionated during sample preparation in order to analyze the fractions with different analytical platforms (da Silva, Iturrospe, Heyrman, et al., 2021; Iturrospe et al., 2021). The typical workflow of an untargeted metabolomics experiment is presented in Figure 1.3 and discussed in detail below.

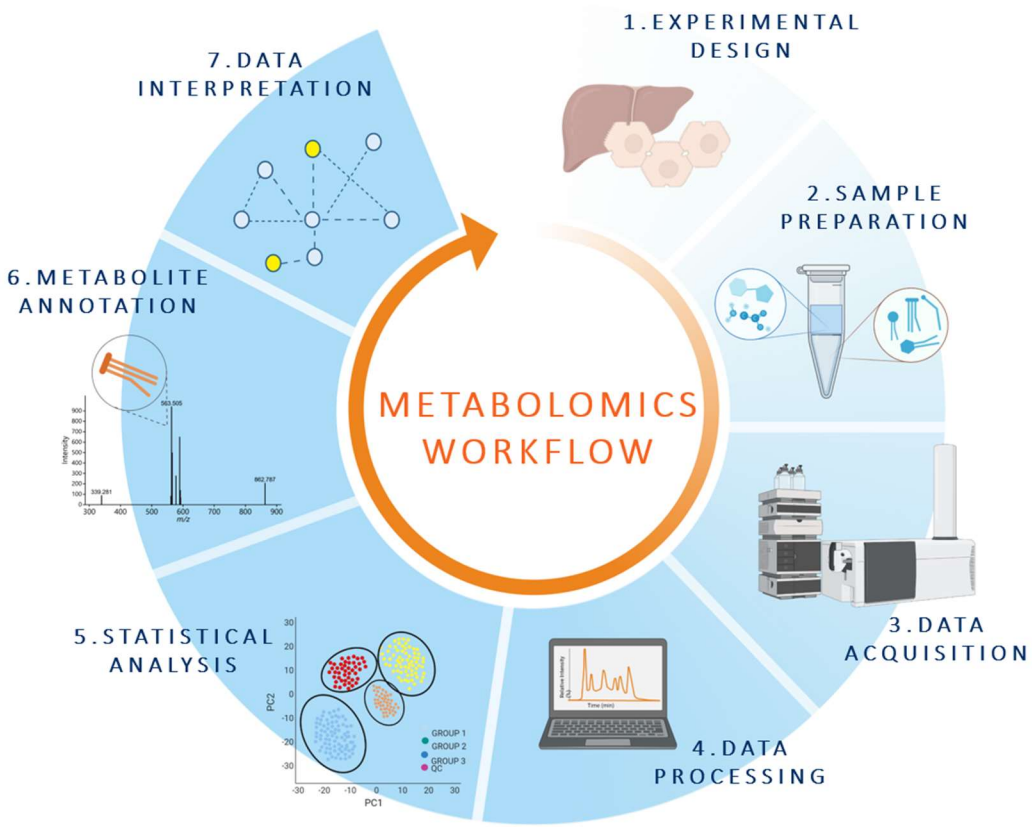

Figure 1.3 Overview of an untargeted metabolomics workflow.

1.3.1. Experimental design

Developing a planned approach is the most critical part of a metabolomics experiment. The number of samples and/or size of the groups needed for a metabolomics experiment depend on the biological variability associated with the system being studied compared with the analytical variability of the analytical system (Barnes et al., 2016a). As a result, the needed sample size will depend primarily on the study design (e.g., choice to use *in vitro* or *in vivo* systems) and the expected outcome (Faber & Fonseca, 2014).

As the growth of cells in culture can be carefully controlled, a sample size of three to five per group may give useful data (Barnes et al., 2016a). The majority of experiments report no more than 6 replicates per group and although 3 replicates is considered as the minimum, ≥ 5 replicates are generally recommended for reliable *in vitro* metabolomics applications (Martano et al., 2014; Sumner et al., 2007). Laboratory animals on controlled diets are more complex and require a larger sample size of at least 6-12 (Barnes et al., 2016a). Highly controlled clinical trials may be able to be carried out

with as few as 10-20 patients, depending on the variance of the disease traits, drug response or the type of interventional procedure (Barnes et al., 2016a). For epidemiological studies, where the samples were collected from a general population, often over long periods of time, variance is a substantial issue and may require patient numbers in the thousands (Barnes et al., 2016a).

For *in vitro* assessment of hepatotoxicity by metabolomics, experiments are usually conducted in short time frames (< 48 h) at sub-toxic dosages (Cuykx, Rodrigues, et al., 2018). The majority of studies report an exposure time of 24 h and/or 48 h. Determination of exposure concentrations are usually performed using viability assays. The most popular assay applies the bioconversion of 3-(4,5-dimethylthiazol-2-yl)-2,5-diphenyltetrazolium bromide (MTT). However, this bioconversion assay is biased towards lower concentrations, since it is linked to mitochondrial metabolism pathways, which can be specifically inhibited by the tested compound, thereby providing a biased indication of cell viability (Cuykx, Rodrigues, et al., 2018). The neutral red uptake (NRU) assay, which is based on lysosomal storage of the cationic dye, is an alternative method often applied when the energy metabolism is suspected to be part of the toxicant's mechanism of action (Ates et al., 2017; S. Z. Zhang et al., 1990). Within the NRU assay, cytotoxicity is expressed as a concentration-dependent reduction of the uptake of neutral red after exposure to the xenobiotic under investigation (Ates et al., 2017). Using viability assays, inhibitory concentration (IC_X) values can be calculated. For example, exposing cells for 24 h to the IC_{10} value of a certain toxicant will cause a decrease of 10% in cell viability. Although low IC_X values are considered to be sub-cytotoxic, the toxicological insult can be considered to be significant. Toxic concentrations, such as IC_{30} and IC_{50} are sometimes used. However, these high concentrations have such a strong impact that only alterations to general toxicity can be observed, impeding mechanistic fingerprinting (Cuykx, Rodrigues, et al., 2018). Combination of two exposure concentrations (e.g., IC_{10} and 1/10 of IC_{10}) is therefore recommended to investigate the trends of toxicity markers through the toxicological process (Cuykx, Rodrigues, et al., 2018).

Avoiding unintended bias in any sort of -omics analysis is a critical issue. Each step of a metabolomics experiment should be well documented and include measurements to avoid generation of non-biological variance. For example, in metabolomics to study cell exposure, samples should be randomized before exposure and sample collection has to be performed in the same way for each sample. In addition, analytical data should be acquired using a randomized order of the samples (Barnes et al., 2016a).

1.3.2. Sample preparation

Sample collection and preparation should be performed as quickly as possible to reduce the effect of additional metabolism and compound biotransformation (W. Lu et al., 2017). Thus, quenching strategies are essential to ensure that detected metabolites reflect the metabolism of the organism at the time of sampling. Importantly, for highly metabolically active matrices, such as tissues or cells, any remaining enzymatic activity should be stopped by snap-freezing the sample with liquid nitrogen immediately after sample collection (W. Lu et al., 2017). Although some metabolites, such as adenosine triphosphate (ATP) and glucose-6-phosphate, can turnover in terms of seconds, which is almost impossible to avoid, butylated hydroxytoluene can be added to reduce metabolite degradation (Ulmer et al., 2021).

Preferably, freeze–thaw cycles of collected samples should be limited, and analysis should be performed on fresh samples. However, analysis of fresh samples is often not feasible. Therefore, samples should be stored at −80 °C for as little time as possible and thawed only once for analysis (Barnes et al., 2016a).

Depending on the goal of the study, the extraction method can be designed for "global" metabolomics (Want et al., 2013), polar (primary) metabolomics (Fiehn, 2016), or lipidomics (Le Faouder et al., 2021), which can be further subdivided and tailored for less abundant lipid classes, such as polyunsaturated fatty acids (Le Faouder et al., 2013), steroids (Olesti et al., 2021), or the epilipidome (L. Li et al., 2019). In addition, the extraction method is highly dependent on the sample matrix and the platform used for analysis. For instance, gas chromatography–mass spectrometry (GC-MS)-based metabolomics often requires a derivatization step (e.g., oximation of ketone groups followed by silylation of hydroxy-, carboxyl-, amino- and thiol-groups for a wide range of small polar metabolites (Fiehn, 2016) or single silylation for sterols (Jenner & Brown, 2017)) after metabolite extraction to increase thermal stability and volatility.

For liquid chromatography–mass spectrometry (LC-MS) analysis, liquid extraction (LE) is often used to extract and concentrate metabolites (Figure 1.4). Single-phase extraction by adding more of the same solvent used for protein precipitation (e.g., methanol (MeOH) and/or acetonitrile (ACN)) is commonly applied (J. Shi et al., 2016; Vorrink et al., 2017; Y. Wang et al., 2015). However, to extract and dissolve non-polar lipids, a more apolar organic solvent, such as methyl tert-butyl ether (MTBE), dichloromethane (CH_2Cl_2), or chloroform ($CHCl_3$), is usually required (Ramani Venkata & Ramesh, 2021). Single-phase methods are attractive because they reduce the time and complexity of the extraction, but they are also subject to a higher matrix effect and a smaller detection range due to the polarity diversity of the molecules in the metabolome (e.g., LogP for citric acid is −1.64, while LogP for triacylglycerol (54:6) is 22.2) (Gong et al., 2017; Ivanisevic & Want, 2019; Kim et al., 2021; W. Lu et al., 2017). In order to improve the

efficiency of the extraction methods, two-phase LE or two-step LE can be used to increase the range of extracted molecules. Popular two-phase extraction techniques for untargeted metabolomics include the classic Bligh and Dyer ($CHCl_3$/MeOH/H_2O, 2/2/1.8, v/v/v) and Matyash *et al.* (MTBE/MeOH/H_2O, 10/3/2.5, v/v/v) extraction procedures (Bligh & Dyer, 1959; Matyash et al., 2008).

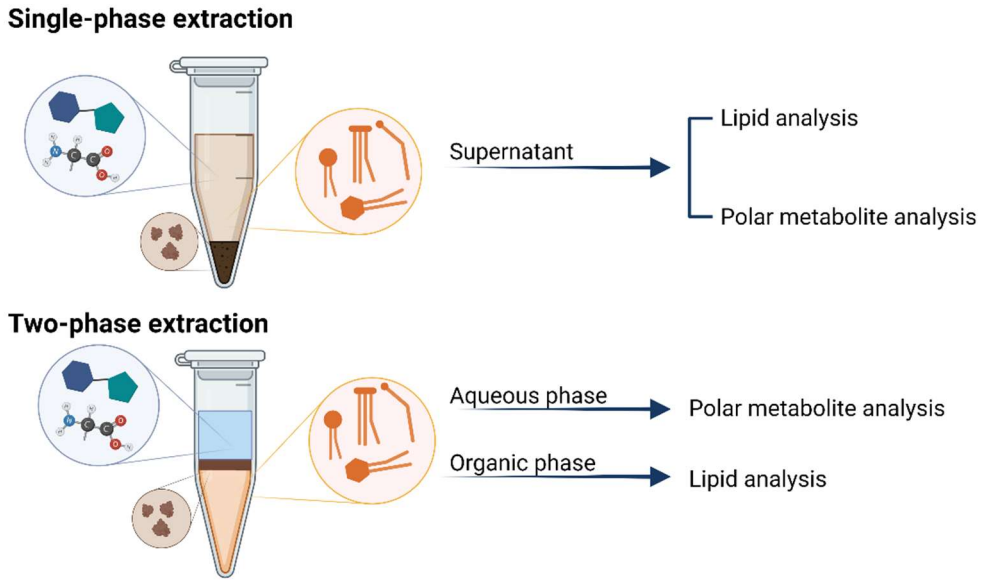

Figure 1.4 Single-phase versus two-phase liquid extraction. Polar metabolites are shown in blue, lipids in orange and proteins in brown. Graphical icons in this figure were provided by BioRender, license n. 2641-5211.

In addition to LE, solid-phase extraction (SPE) methods can be necessary to concentrate specific classes present in low concentrations, such as eicosanoids, oxylipins, and steroids (Olesti et al., 2021; Strassburg et al., 2012). SPE cartridges commonly used for lipid removal in fat-rich samples, such as Captiva-EMR (Agilent Technologies, Santa Clara, USA), can also be applied in a two-step method for extraction of polar and lipid metabolites. This latter cartridge traps lipids based on acyl chains, allowing small molecules to be eluted in a cleaner extract, which would allow higher concentration factors due to less interference of lipids. The second step includes the elution of lipids, in a different fraction, with a stronger organic solvent, such as $CHCl_3$. However, its application for lipidomics and metabolomics workflows still needs to be evaluated, since most of the non-commercial applications are used for food analysis (Han et al., 2016).

1.3.3. Analytical platforms

Most analytical platforms in metabolomics are based on either mass spectrometry (MS) or nuclear magnetic resonance (NMR) spectroscopy. Although MS can be used without any prior separation (i.e., direct MS analysis), the technique is often hyphenated to liquid or gas chromatography (Gika et al., 2019).

^{1}H NMR is based on the principle that protons resonate between energy states in a high magnetic field. Every metabolite has its own unique NMR spectrum that represents the environment of each proton in the metabolite (Barnes et al., 2016a). The advantages of NMR include its non-destructive nature and a higher robustness compared to LC-MS. A major disadvantage is the low sensitivity, explaining the large sample volume needed. For example, for cell culture experiments, it is recommended to use 10 million cells per sample (Barnes et al., 2016a).

During shotgun metabolomics, no chromatographic separation is performed prior to MS detection. Direct MS techniques include direct infusion MS (DIMS) and flow injection analysis (FIA). During DIMS, a syringe pump is used to constantly deliver sample extracts into the MS in order to generate a single summed or averaged mass spectrum per sample. During FIA, samples are injected using an LC system without chromatographic column. FIA generates a data profile with a maximum after a few seconds, and then tails off towards background levels in order to avoid carry-over between consecutive injections (González-Domínguez et al., 2016). The main advantage of direct MS methods for metabolomics is the reduced time of analysis (typically < 60 s per sample), enabling high-throughput screening (Bravo-Veyrat & Hopfgartner, 2022; González-Domínguez et al., 2016). Drawbacks include chemical isomers remaining to be unresolved and the need for ultrahigh resolution instruments, such as Orbitrap-MS or Fourier-transform ion cyclotron resonance-MS (FTICR-MS) to be able to distinguish peaks with small differences in mass-to-charge (*m/z*) value (e.g., in the mDa range for FTICR-MS, which can achieve a resolution up 3,000,000 at *m/z* 200 (Bahureksa et al., 2022)). However, the largest disadvantage remains ion suppression (i.e., reduced ionization efficiency for analytes of interest due to competition between chemical species), impeding meaningful data analysis (González-Domínguez et al., 2016).

Coupling GC to MS has been the most suitable method for detection of volatile metabolites (Su Jung et al., 2016). These metabolites can have intrinsic volatile properties or they can be rendered volatile and/or thermally more stable by derivatization (Alseekh & Fernie, 2018). Advantages of GC-MS include its high robustness and sensitivity (Alseekh & Fernie, 2018). GC-MS is usually the preferred

platform for small and volatile metabolites, including steroids and fatty acids (FA) (Su Jung et al., 2016). As GC-MS often requires chemical derivatization to improve volatility, and its application has limitations in terms of the molecular size, volatility, and polarity, LC-MS has become the most popular choice in metabolomics. Sample derivatization is generally not required in LC-MS, and metabolites with more diverse chemical structures and increased molecular sizes can be detected (Su Jung et al., 2016).

For targeted metabolomics (Figure 1.5), LC-MS-based multiple reaction monitoring (MRM) platforms are often used. This type of analysis is typically carried out on a triple quadrupole (QqQ) or Qtrap mass spectrometer. Calibration curves for each metabolite can be prepared and therefore the concentrations of these metabolites in the biological samples can be accurately determined (Barnes et al., 2016a). These latter instruments can also be used for semi-targeted metabolomics (Figure 1.5), in which one standard is used per subset of metabolites. Due to structural similarities between the standard and the metabolites within the subset, a semi-quantitative concentration can be determined (Malm et al., 2021).

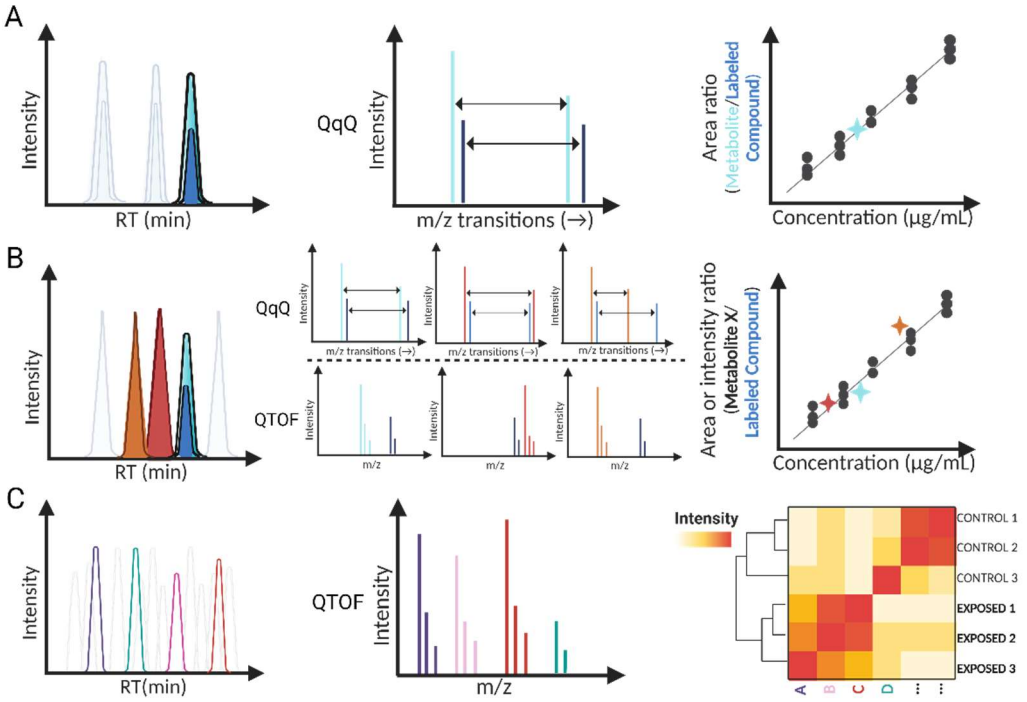

Figure 1.5 Overview of analytical strategies within LC-MS-based metabolomics. In targeted analysis (A), quantification is performed using one calibration curve per metabolite. The calibration curves are based on the area ratio of the standards and the labelled internal standards. Instruments, such as triple quadrupole (QqQ)-MS are used with multiple reaction monitoring (MRM) methods. During semi-targeted analysis (B), calibration curves are generated using one standard per class of metabolites. As with targeted analysis, QqQ instruments can be used as well as the high-resolution QTOF. Untargeted metabolomics (C) aims to separate and detect as many metabolites as possible and uses high resolution MS instruments, such as QTOF or Orbitrap. Relative differences in signal intensity between study groups (e.g., exposure versus unexposed controls) can be used to perform statistics, distinguish altered metabolites and visualize results e.g., using heatmaps. Graphical icons in this figure were provided by BioRender, license n. 2641-5211.

Liquid chromatography coupled to high-resolution mass spectrometry (HRMS, e.g. Orbitrap or QTOF) remains one of the most widely used hyphenated techniques in untargeted metabolomics (Figure 1.5) with a constantly increasing number of applications (da Silva, Iturrospe, Bars, et al., 2021). This latter is due to, for instance, the evolution of the development of chromatographic stationary phases (e.g., improved particle size, stability, and selectivity), the increase in resolution of mass spectrometry instrumentation (e.g., resolving power at full width at half maximum (FWHM) of an Orbitrap can reach up to 240,000 at *m/z* 400), and the LC-MS versatility in being able to

be coupled to additional techniques (e.g., ion mobility spectrometry) (da Silva, Iturrospe, Heyrman, et al., 2021; Ghaste et al., 2016; Iturrospe et al., 2021).

Hyphenating LC to MS reduces co-elution and ion suppression hence improving metabolite coverage and the quality of detected features (i.e., an entity with assigned *m/z* and retention time (RT) associated with a response signal (peak intensity or area)). Next to MS/MS fragmentation spectra, the RT behavior of lipids obtained by reversed-phase separation offers additional information for annotation of features (i.e., structural elucidation) (Xu et al., 2020).

In LC-MS analysis, the combination of hydrophilic interaction liquid chromatography (HILIC, e.g., bare silica, amide, diol, amido, zwitterionic columns) and reversed-phase liquid chromatography (RPLC, e.g., C18, C8, C30 columns) methods is one the most comprehensive strategies for untargeted metabolomics, providing a broad metabolite coverage (Cuykx, Negreira, et al., 2017; da Silva, Iturrospe, Heyrman, et al., 2021; Iturrospe et al., 2021). Currently, C18 columns with sub-2-µm particle size are often used for untargeted metabolomics and lipidomics as a stand-alone technique, and rarely combined with HILIC (J. Shi et al., 2016; Van den Eede et al., 2015; Vorrink et al., 2017). Furthermore, the complementarity of HILIC to RPLC methods is a highly powerful strategy for polar metabolites that should not be overlooked, especially when a multiplatform strategy is not employed (Cuykx, Negreira, et al., 2017; Tang et al., 2016).

In addition, MS data can be acquired in positive and negative mode with electrospray ionization (ESI+ and ESI−, respectively) which benefits both acidic and basic functional groups (Banerjee & Mazumdar, 2012). Consequently, with the same chromatographic column, two datasets can be obtained (ESI+ and ESI-). If two chromatographic columns are used (e.g., HILIC and RPLC), four datasets are obtained which require parallel processing (Cuykx, Negreira, et al., 2017).

Furthermore, the separation of isomers and isobars, and consequently, the acquisition of well-resolved fragmentation spectra is a challenge especially for lipidomics applications (Blaženović et al., 2018; Xu et al., 2020). In order to obtain a less time-consuming but comprehensive platform, ion mobility spectrometry (IMS, a separation technique based on the mobility of ions through a buffer gas under the influence of an electric field) has been successfully integrated into LC-MS-based lipidomics and metabolomics workflows (Burnum-Johnson et al., 2019; da Silva, Iturrospe, Heyrman, et al., 2021). One of the key advantages of the IMS technique is that it can separate ions in milliseconds based on their shape and size, which is highly convenient for linking LC separations (minutes) and time-of-flight (TOF)-MS detection (microseconds) for the separation of isomers, and increasing annotation confidence with the addition of collision cross section values (Blaženović et al., 2018; Burnum-Johnson et al., 2019). Disadvantages of IMS include the increased complexity of data acquisition and -analysis,

as well as reduced sensitivity and incompatibility with data-dependent acquisition (DDA) (da Silva, van de Lavoir, et al., 2022; Paglia et al., 2021).

1.3.4. Data preprocessing

Data derived from untargeted metabolomics workflows are of great complexity since they usually englobe thousands of features (e.g., for LC-MS, an entity with an attributed *m/z*, retention time, fragmentation spectra, and a response signal). The workflow for untargeted data preprocessing includes several steps to obtain a feature signal response matrix (e.g., features in rows versus samples in columns). These steps are dependent on the instrument (e.g., GC-MS, LC-MS, NMR) used to acquire the data. For MS-based instrumentation, if vendor-specific software is not used, data files need to be converted to an open file format (e.g., mzML, netCDF, ABF) to be further processed with open-source software packages, such as MS-DIAL, XCMS, MZmine, or OpenMS (Misra, 2021; Spicer et al., 2017). The software can be used to perform peak picking, deconvolution, alignment across samples, and in some cases, the same software can perform metabolite annotation with experimental and/or *in silico* libraries (e.g., MS-DIAL (Tsugawa et al., 2020)). Peak picking, deconvolution, and alignment processes are performed to detect ions in a specific region of interest above pre-defined instrumental noise levels, to handle overlapping peaks, fragments and to align those signals across different samples. Considering peak picking of LC-MS data in more detail, chromatographic peaks are detected by defining peaks by a finite number of MS points acquired in consecutive MS scans in the time domain. Peak picking will generate a peak list without correspondence across samples, i.e., the samples do not necessarily have the same number of peaks (Karaman et al., 2018). RT alignment is necessary as the physical interaction of analytes with the chromatographic column stationary phase can create variability in the peak position for metabolites across the samples. During RT alignment, peaks are aligned to reference peaks from a selected reference sample, based on similarity in the *m/z* and RT window. Alignment creates a peak list where each sample contains the same number of peaks, although some of these have missing values when no peak has been detected (Karaman et al., 2018). Values in a dataset can be missing either at random or not at random (Wei et al., 2018). Values which are missing not at random can originate from low concentrated metabolites that can fall below the limit of detection, where the signal cannot be distinguished from noise. Random missing values can occur due to incomplete ionization, inaccurate peak detection or deconvolution of co-eluting peaks (Wei et al., 2018). Feature tables do not contain unique signals corresponding to a specific metabolite, but also redundant features (e.g., different isotopes, charges, and adducts in soft ionization techniques such as ESI), background signals, etc. (Treutler & Neumann, 2016). Computational techniques can

address the challenge of isotope and adduct annotation, including the recent web application MS-FLO (based on several parameters such as peak height, RT alignment and mass similarities to detect adducts, isotopes and duplicate features in a preprocessed dataset) (DeFelice et al., 2017).
Following data preprocessing, signal drift correction, data cleaning (feature reducing) (e.g., removal of background ions and features with low precision and detectability), and imputation of missing values are commonly applied (Klåvus et al., 2020; Riquelme et al., 2020; Schiffman et al., 2019). Then, data pretreatment and statistical analysis (univariate and/or multivariate techniques) are performed to identify relevant features for a specific condition, followed by further structural elucidation and biological interpretation. Depending on the type of statistical analysis (univariate/ multivariate), different data pretreatment methods are necessary. Statistical analysis of metabolomics data is a complex workflow and requires tailored approaches.

1.3.5. Data pretreatment and statistics

Often applied pretreatment methods of metabolomics data include normalization, transformation and scaling. The overall goal of these methods is to improve the biological information content of the data (van den Berg et al., 2006). Normalization can be applied to correct for variation in the intensity of features that is unrelated to biological differences between sample groups. Sources of variations that can be corrected by normalization include small changes in volume applied during sample preparation and sample injection and in instrument performance (e.g., changes in ionization, ion transfer and detector efficiency) (Di Guida et al., 2016). Transformation of data (e.g., to a logarithmic scale) is mostly used to correct for data heteroscedasticity and/or skewed distributions (Di Guida et al., 2016). Scaling is performed to adjust for differences in fold change between metabolites which may be caused by large differences in the variation of the measured responses (Di Guida et al., 2016). For example, during Pareto scaling, the square root of the standard deviation is used as a scaling factor, reducing the relative importance of large fold changes in feature intensities between sample groups (van den Berg et al., 2006).

Univariate and multivariate analysis techniques are routinely used to extract relevant information from metabolomics data with the aim of providing biological knowledge on the problem studied. However, most studies either use univariate or multivariate statistical methods (Saccenti et al., 2014). Where univariate methods focus on independent changes in metabolite levels, multivariate methods can be used to zoom in on the relations between metabolites and their orchestrated or complementary behavior in relation to biological processes. Because of their complementary nature, it

is recommended to use both univariate and multivariate statistics and never to seek validation of univariate results by means of multivariate analysis and vice versa (Saccenti et al., 2014).

A serious problem encountered in applying univariate statistical analysis to all –omics data is that the number of samples is smaller than the number of observed variables (Barnes et al., 2016b). Taking a univariate approach such as a Student's t-test comparing the amount of a single metabolite ion in a control group with the amount in an exposed group and selecting significant metabolites based on p-values is fraught with problems due to multiple testing issues (Barnes et al., 2016b). The multiple testing problem refers to the increasing risk of wrongly rejecting a null hypothesis, when the number of hypothesis tests increases (i.e., the larger the list of metabolite ions used for univariate statistics, the higher the chance of obtaining false positive results) (Vinaixa et al., 2012). Therefore, it is important to correct for multiple testing, e.g., using the Benjamini-Hochberg procedure (Benjamini & Hochberg, 1995) in order to avoid false positive and false negative results.

The two major multivariate methods used in metabolomics are the unsupervised principal components analysis (PCA) and the supervised partial least squares discriminant analysis (PLS-DA), both dimensionality reduction techniques (Barnes et al., 2016b; Ruiz-Perez et al., 2020). PCA allows high dimensional datasets to be reduced to a few major principal components by projecting the maximal variance without any awareness of the class labels (Barnes et al., 2016b; Ruiz-Perez et al., 2020). As the technique is unsupervised, it is often used during exploration of data (Bernardo-bermejo et al., 2021; Cuykx, Claes, et al., 2018; Iturrospe et al., 2022). On the other hand, PLS-DA uses a binary class group (Y) to explain the variables in the data matrix (X) and aims to maximize the covariance between X and Y. A variable importance in projection (VIP) score can be assigned to each feature, which is a measure for the importance of that feature in the PLS-DA class separation (Barnes et al., 2016b; Gromski et al., 2015). As supervised multivariate approaches are prone to overfitting (i.e., the discriminatory capacity of the statistical model works well for the training data, but subsequent samples will be very often incorrectly classified), cross-validation of PLS-DA models are important. Cross-validation procedures use a fraction of the data-set as an independent test-set to estimate the performance of discriminative capacity of the model (Ruiz-Perez et al., 2020). Another multivariate method that is often used in metabolomics is random forest (RF). During RF, data are divided in training and test sets using bootstrapping. The training sets are used to build a large collection of decorrelated decision trees. Each tree is generated from a root node, in which small subsets of input

variables (i.e., features) are selected randomly. Starting from the root node, internal nodes are generated, where the samples are split based on the values of different variables (i.e., intensities of the features). The internal nodes proceed to leaf nodes when the sample classes are recognized. In the last step, the classification accuracy of the constructed forest is estimated using the test data. The importance of each variable can be determined as mean decrease in accuracy (MDA), which expresses the magnitude of accuracy loss of the model when the variable is excluded (Gromski et al., 2015).

1.3.6. Annotation

During annotation, structural elucidation of features is performed (i.e., instrumental signals are converted to metabolites). For annotation of metabolites, the most commonly used approach is to compare the exact mass of the precursor ion (MS1, *m/z*) and the tandem mass spectra (MS/MS spectrum) against standard spectral libraries (Kind et al., 2018; Vinaixa et al., 2016). Commonly used spectral libraries include MassBank (Horai et al., 2010), NIST (Yan et al., 2020), METLIN (Smith et al., 2005b) and GNPS (Nothias et al., 2020). Metabolomics software such as MS-DIAL also provides the option to include personal or public MS/MS databases for annotation and enables manual confirmation of MS/MS matches using mirror plots (Figure 1.6) (Tsugawa et al., 2020).

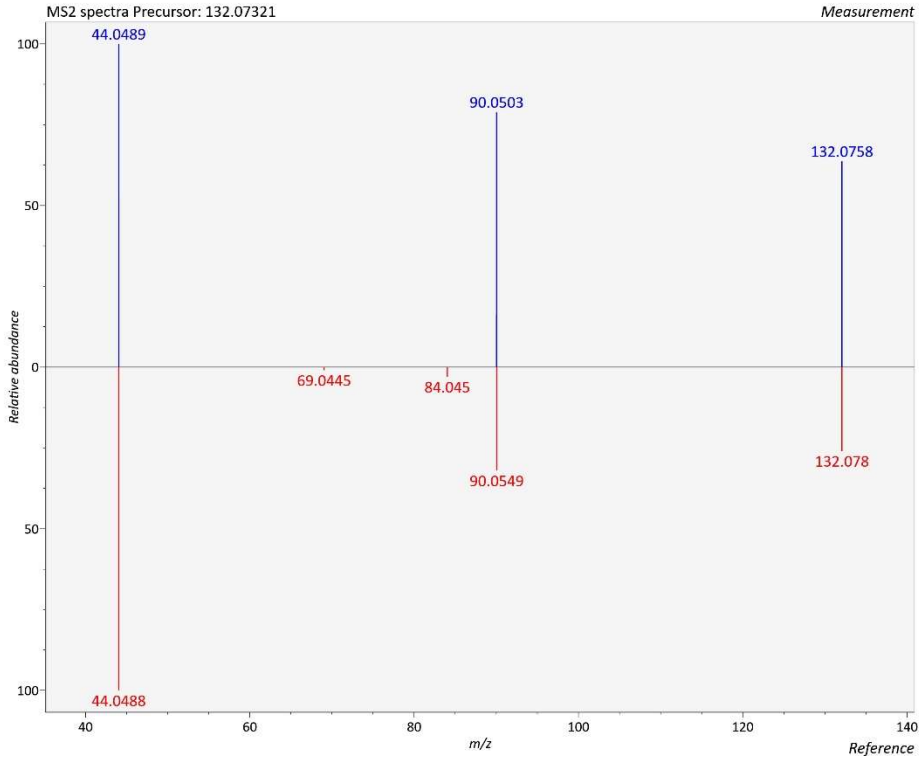

Figure 1.6 Example of a mirror plot to confirm MS/MS spectra matching in MS-DIAL (Tsugawa et al., 2020). In this example, the MS/MS spectra of creatine $[M+H]^+$ are shown.

When the MS/MS spectra of a feature cannot be matched to a metabolite in a spectral library, *in silico* fragmentation software can help to provide structural information. For example, for the prediction of ESI-MS/MS spectra, CFM-ID is widely used for compound-to-mass-spectrum prediction and *in silico* mass-spectrum-to-compound annotation (F. Wang et al., 2021). Concerning lipidomics, specific databases and software were developed for annotation such as LipidMatch (Koelmel, Kroeger, Ulmer, et al., 2017), LipidHunter (Ni et al., 2017), and Lipostar (Goracci et al., 2017). As opposed to polar metabolites, fragmentation of lipids follows certain rules. This rule-based fragmentation facilitates the annotation process and was extensively described by Lange *et al*. (2021a) and Pi *et al.* (2016).

Next to MS/MS spectra and accurate mass, the isotopic pattern and RT can help during the annotation process (Vinaixa et al., 2016). For example, using C18 columns for separation, analytes will be retained based on hydrophobic interactions that are dependent on their carbon chain length and the level of saturation (Lange et al., 2019). As a result, different classes can be mapped within RT ranges. These class-specific RT

windows can then be used to filter false positive lipid annotations in complex matrices (da Silva, Iturrospe, et al., 2022; Lange et al., 2021).

In addition to *m/z*, MS/MS spectra, and RT, ion mobility provides CCS values as an additional molecular descriptor, to further increase annotation confidence (Celma et al., 2020; Pičmanová et al., 2022). In addition, CCS values can also be used as a class annotation filter (Qian Wu et al., 2020). When plotting CCS values in function of *m/z* values, metabolites within the same class will cluster together as their similarity in the chemical space is reflected in their ion mobility behavior. As a result of this clustering behavior, metabolites that show a large deviation in CCS within their class can be flagged as possible false positive annotations. In addition, CCS values can help in the structural characterization of lipids. Lipid species within the same class show increasing CCS values with increasing fatty acyl chain length as their increased size will cause slower passage through the ion mobility spectrometer. In contrast to the direct relation between CCS value and fatty acyl chain length, there is an inverse relation with the degree of unsaturation (da Silva, Iturrospe, Heyrman, et al., 2021).

Ideally, a reference standard is used to confirm annotations. For this latter purpose, the reference standard is analyzed in the same conditions as the acquired metabolomics data. Comparison of RT, CCS, accurate mass and MS/MS spectra for the standard and the annotated metabolite can be used for confirmation. However, as many reference standards are expensive and often unavailable, this confirmation strategy is not always possible (da Silva, Iturrospe, Bars, et al., 2021).

As confidence in HRMS-based annotations varies between studies and substances, confidence levels for annotations have been proposed to facilitate reporting (Schymanski et al., 2014). An example of annotation confidence levels was published by Schymanski *et al.* (2014) and is given in Figure 1.7. The latter annotation confidence level system remains widely used and was updated for IMS-HRMS data by Celma *et al.* (2020). Several confidence level systems were published including those from the Metabolite Identification Task Group, in which confidence levels are based on the metabolite complete structure level. As a high level of confidence in this system includes information on stereochemistry and chirality, additional techniques for structural elucidation are needed (e.g., ozonolysis or photochemical derivatization to determine the position of double bonds in glycerolipids) (Sumner et al., 2007).

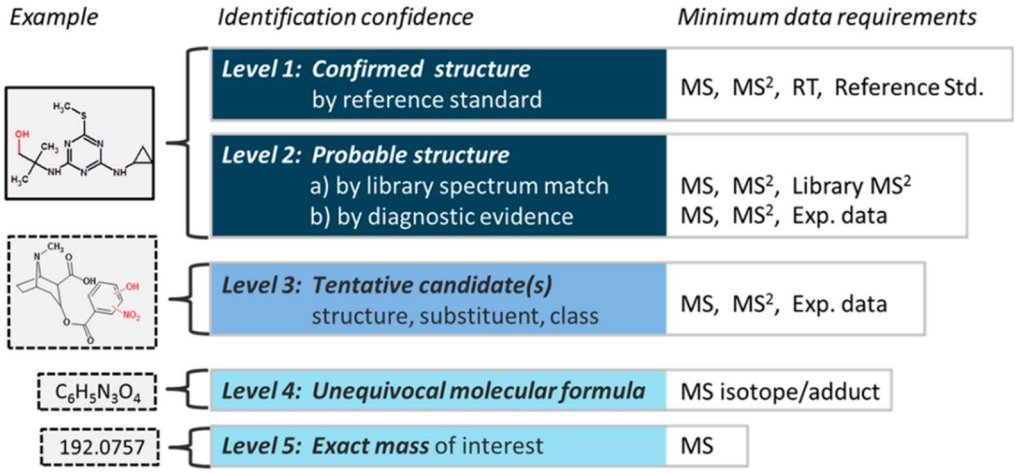

Figure 1.7 Annotation confidence levels as proposed by Schymanski *et al.* (2014).

1.3.7. Quality assurance and quality control

The implementation of a quality management system (QMS), including quality assurance (QA) and quality control (QC) measures, is imperative to ensure the collection of high-quality data and, subsequently, reliable data interpretation (Broadhurst et al., 2018). QA procedures include the development and continuous improvement of standard operating procedures for sample collection, preparation, data acquisition, and data processing. These procedures also include the use of a chromatographic column inventory and avoidance of using freeze-thaw cycles for samples. However, when freeze-thaw cycles cannot be avoided, samples with the same amount of cycles should be used for comparison purposes (Barnes et al., 2016a). QC activities are undertaken during and after the experiment to monitor and report quality requirements. For metabolomics applications, these include the acquisition of system suitability samples with documented performance over time, blank extraction samples, intra-study QC pooled samples (e.g., mixed aliquots of biological samples representative of the entire sample set), spiking of samples with labeled internal standards (IS) to assess precision during the analysis, and reference materials for inter-laboratory and long-term studies (Gika et al., 2016). However, there is currently no agreement on which quality metrics should be used and reported.

The metabolomics quality assurance and quality control consortium (mQACC) began to address the lack of guidelines and nomenclature by collecting detailed information on QA and QC practices used by different laboratories using LC-MS-based untargeted analysis (Evans et al., 2020). Pooled QC samples were identified as one of the most commonly applied quality measurements in untargeted LC-HRMS-based metabolomics studies (Evans et al., 2020). The importance of QC pooled samples for instrumental

source conditioning, carry-over assessments, data filtering, signal correction, and determination of precision has been shown by recent software developments and applications (Beger et al., 2019; Broadhurst et al., 2018; Riquelme et al., 2020). Furthermore, the main consensus that resulted from the mQACC consortium group was the prospect of creating a set of minimum QA and QC practices for metabolomics. Meanwhile, the current guidelines for QA/QC management processes proposed by Broadhurst *et al.* can be used for metabolomics studies, since they present good application and reporting practices, including the use of system suitability samples, process blanks (extraction blanks), pooled QC samples, QC conditioning samples, and order of analytical batches (Broadhurst et al., 2018). The reasons for implementing these latter QC measures are summarized in Table 1.1.

Table 1.1 Analytical quality control strategies in untargeted metabolomics. MS: Mass spectrometry. RT: Retention time. QC: Quality control. RSD: Relative standard deviation.

Quality control measure	Reason of implementation
Solvent blanks	Controlling contaminations originating from the solvent Assessment of carryover
System suitability sample (i.e., mixture of standards)	Evaluation of the system condition (e.g., mass accuracy of MS, chromatographic resolving power, RT stability, peak area/intensity)
Labeled internal standards spiked to samples	Assessment of extraction efficiency (if spiked before extraction) and/or ionization efficiency (if spiked after extraction) Evaluation of mass accuracy, deviation of RT, peak area/intensity Signal correction for (semi-)quantification purposes
Extraction blanks	Removal of contaminants originating from the sample preparation
Pooled QC samples	Conditioning of the analytical system Correction of signal drift Filtering of datasets (e.g., based on RSD cutoff) Normalization of data
Randomization of injection order	Reducing false correlations

In the work of Broadhurst et al., the authors did not advise the use of pooled QC serial dilution to filter data based on correlations, since it does not consider a non-linear response, but they mentioned that further work is required to extend the use of this approach (Broadhurst et al., 2018). Nevertheless, one of the most important aspects of QA/QC practices is the description of data acquisition and processing strategies, which includes feature-reducing strategies (Goodacre et al., 2007).

1.3.8. Interpretation

Metabolomics has two principal goals: to identify (i) a useful biomarker or panel of biomarkers that accurately predicts a particular phenotype, and/or (ii) the metabolic pathways and hence the underlying proteins and/or genes that lead to the phenotype (Barnes et al., 2016b). Network modelling and pathway-mapping tools can help us to understand the parts that metabolites play in relation to each other and in biological aberrations (C. H. Johnson et al., 2016). Databases of known pathways, such as the Kyoto Encyclopedia of Genes and Genomes (KEGG) are publicly available and can be used to link metabolomics outcomes to biochemical pathways (Kanehisa & Goto, 2000). Annotated metabolites can be projected on known metabolic pathways such as the Krebs cycle. Over-representation analysis (ORA, also known as enrichment analysis) can be used to identify significantly impacted pathways as it identifies pathways or metabolite sets that have a higher overlap with a set of molecules of interest than expected by chance (Wieder et al., 2021). Metabolic pathway maps currently include ~2,000 metabolites, and, similar to metabolite databases, they are incomplete, as some metabolites have not yet been characterized (C. H. Johnson et al., 2016).

Next to pathway analysis, metabolic networks can be used to explore and possibly interpret metabolomics data. Network-based analysis is an established method that allows the identification of non-intuitive metabolic relationships as well as the identification of unknown compounds in mass spectrometry (Perez De Souza et al., 2020). Multiple network strategies can be applied in metabolomics, including correlation-based networks relying on quantitative information and mass spectra similarity networks to assist metabolite annotation (Perez De Souza et al., 2020). Unlike pathway analysis, correlation-based analysis builds metabolite networks according to the relationship patterns observed in the experiment data. In the resulting network, each metabolite is represented by a network node and the links between nodes represent the level of mathematical correlation between each pair of metabolites (Alonso et al., 2015).

1.4. Principles of liquid chromatography

The phenomenon of chromatography was discovered by the Russian scientist Michael Tswett at the beginning of the 20th century (Sakodynskii, 1972). Chromatography is an overarching research domain consisting of techniques used to separate complex mixtures on the basis of different physical interactions between the individual molecules and the stationary phase of the system. A mobile phase carries samples through a column, which is packed with a stationary phase. Molecules within the sample can be separated based on the distribution between the stationary and the mobile phase (Bishop et al., 2017). During high-performance liquid chromatography (HPLC), high pressure (up to 400 bar) is used to enable fast separations. The size of the stationary phase particles in the column is an important variable. To take advantage of the increased peak resolution that occurs with decreases in particle size, ultra-high performance LC (UHPLC) uses sub-2-µm particles. However, a penalty for this is a substantial increase in backpressure, which can go up to 1200 bar (Barnes et al., 2016a). Recent advances in UHPLC engineering include the generation of LC pumps able to perform at pressures up to 1500 bar, which would be suitable for columns with even smaller particle sizes (R. Zheng et al., 2022). At the high pressures of (U)HPLC, loop injectors can be used to inject samples with high reproducibility. Samples are injected into a fixed-volume loop using a needle. When the loop is switched, the sample is placed in the path of the flowing mobile phase and is flushed onto the column, which contains the stationary phase (Bishop et al., 2017).

When coupling LC to an MS detector, the chromatographic separation enhances analytical capabilities of MS, by facilitation deconvolution and reducing ion suppression, leading to improved detection, especially for low abundant metabolites or in case of metabolites that suffer from low ionization efficiency (Harrieder et al., 2022). In addition, LC methods can be used to separate isomers, which could not be differentiated by fragmentation spectra. A third advantage is that the obtained RT represents orthogonal information to MS and MS/MS, as RT is dependent on the polarity of the analyte under investigation (e.g., in RPLC, early eluting metabolites are more polar) (Harrieder et al., 2022).

Since metabolites show a wide range of hydrophobicities/hydrophilicities, it is impossible to separate them all on a single LC column. An in-depth analysis of a metabolomics sample typically involves both RPLC, for separation of mid- to non-polar metabolites, and HILIC, for the separation of polar metabolites, which are the most used LC-methods in metabolomics (Barnes et al., 2016a; Harrieder et al., 2022). In RPLC, apolar modified stationary phases (e.g., C18) are used in combination with more polar mobile phases, such as water, methanol (MeOH), acetonitrile (ACN), isopropanol (IPA),

or a combination of these (Bishop et al., 2017; Harrieder et al., 2022). HILIC, on the other hand uses both a polar stationary phase and a polar mobile phase. Polar stationary phases are used to bind a layer of water on the stationary support and the separation is based on partitioning between this polar water layer and the more hydrophobic mobile phase, such as ACN or MeOH. In general, HILIC separations are difficult to predict, as the different ligands that can be used to immobilize the water, generate secondary interactions such as dipole-dipole interactions, electrostatic interactions and/or hydrogen bonding (Harrieder et al., 2022).

1.5. Principles of mass spectrometry

During MS analysis, ions are separated according to their *m/z* ratio and measured by an ion detector. To enable MS analysis, eluting analytes from the LC system, which are present in the liquid phase need to be converted to ions in the gas-phase. This latter process is commonly performed using electrospray ionization (ESI), which is a soft ionization technique (i.e., the molecular ions remain largely intact in the source) (Bishop et al., 2017). Analytes present in the LC eluents can already be ionized or ionization can be driven by the strong electrostatic field in the spray chamber. Ions are formed by deprotonation, protonation or adduct formation (Kebarle & Verkcerk, 2009). ESI can be used either in positive or negative ionization mode (ESI (+) and ESI (-), respectively). For example, in ESI (+) the nozzle will function as positive electrode and the sampling capillary as negative electrode (Figure 1.8). The electric field leads to an enrichment of positive ions near the surface of the meniscus. This polarization will cause distortion of the meniscus and dispersion of the sample solution into an aerosol of highly positively charged electrospray (ES) droplets (Banerjee & Mazumdar, 2012; Kebarle & Verkcerk, 2009). Super-heated nitrogen gas can be used as a sheath gas to focus the beam of droplets and improve ion generation (e.g., in Agilent Jet Stream ESI) (Banerjee & Mazumdar, 2012). A drying gas, consisting of heated nitrogen, will shrink the droplets by desolvation. When the repulsive electrostatic forces exceed the cohesive forces of the droplet, Coulomb fission will occur, leading to gas phase ions that are passed to the mass analyzer (Banerjee & Mazumdar, 2012; Kebarle & Verkcerk, 2009).

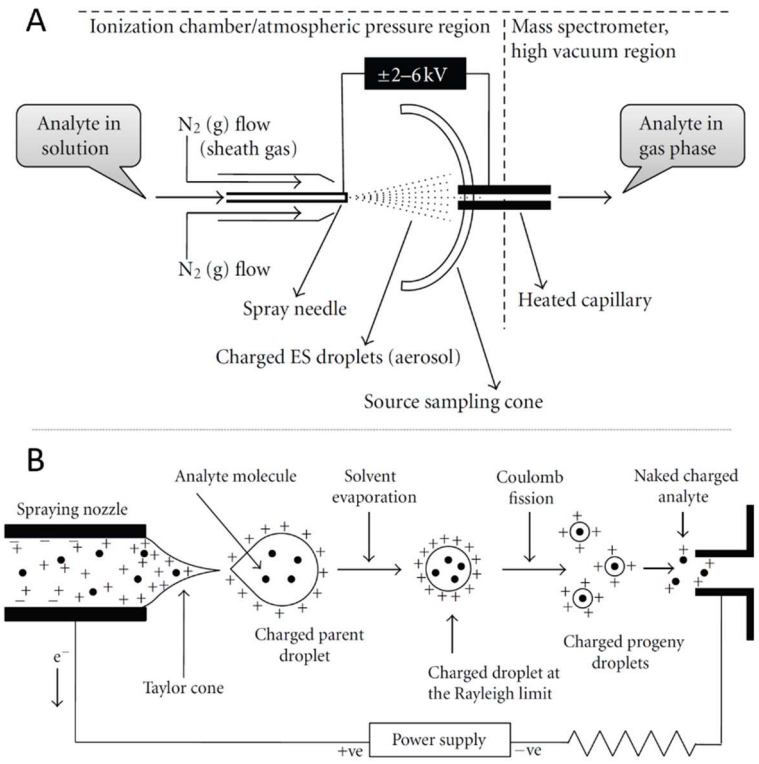

Figure 1.8 Schematic representation of electrospray ionization (A) and detailed overview of the ionization process (B). Adapted from Banerjee & Mazumdar, 2012. ES: Electrospray.

In untargeted metabolomics, HRMS instruments are used such as QTOF. Compared with traditional or 'low resolution' mass spectrometers that determine masses to approximately 0.5 Da, QTOF mass spectrometers operate at resolutions that allow the exact mass of an unknown molecule to be calculated to approximately 0.001 Da (Bishop et al., 2017). Resolution in MS is defined as the mass of a given molecule divided by the width of the corresponding peak and is commonly designated by the term full width at half maximum (FWHM). Many commercial QTOF MS instruments can achieve resolutions of 40,000 and more (e.g., the Agilent 6560 QTOF system can reach a resolution of >42,000 at *m/z* 2,722) (Agilent Technologies, 2016; Bishop et al., 2017; Fjeldsted, 2016). The basic principle of time-of-flight (TOF) instruments relies on velocity-dependent separation and subsequent detection of ions as they travel through a flight tube (García-Reyes et al., 2017). Analytical ions enter the vacuum chamber of the QTOF instrument through the sampling capillary (Figure 1.9) and will be guided towards the octopole. The octopole guide will continue to focus the ions toward the quadrupole and allows the removal of neutral species.

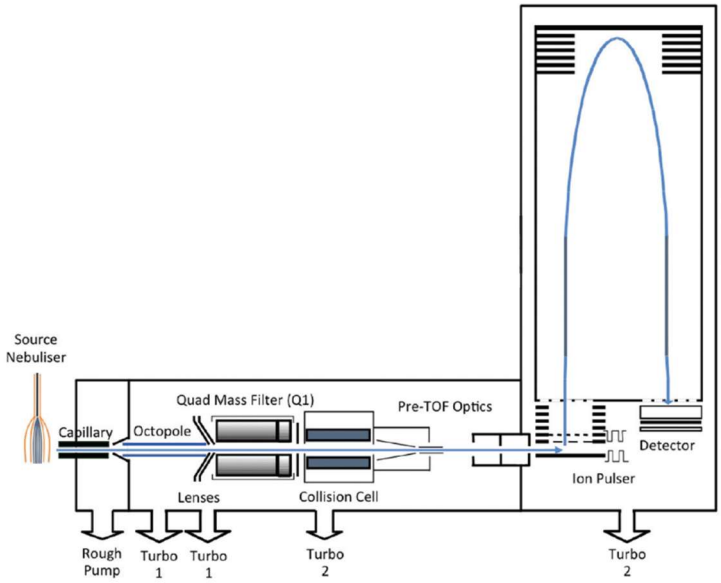

Figure 1.9 Schematic overview of the key elements of a quadrupole time-of-flight mass spectrometer with an electrospray ionization source (Klein, 2020).

Within the quadrupole, an oscillation electric field is used to scan across a preselected *m/z* range and select ions of interest. The oscillating forward movement of ions through the quadrupole is guided by radio frequency and direct current voltages, which are applied to the four parallel rods. Depending on the set of voltages, only a certain set of ions (*m/z* values) can pass through the quadrupole to the detector. Ramping of the voltages allows other *m/z* values to pass through. Undesirable ions will have large oscillatory amplitudes and will hit the metal rods, get neutralized and fail to reach the collision cell (Fjeldsted, 2016; García-Reyes et al., 2017; Ho et al., 2003). The collision cell consists out of a hexapole that focuses and transmits ions while introducing nitrogen gas into the flight path of the ions. The energy transfer from this collision gas to the ionized analytes causes bond cleavages, resulting in fragmentation or collision-induced dissociation (CID) and rearrangements of the selected ions (Agilent Technologies, 2017; A. R. Johnson & Carlson, 2015). Ions that exit the collision cell are pulsed into the flight tube. At the top of the flight tube, a reflectron will change the course of the ions towards the detector. Another function of the reflectron is to minimize kinetic energy variations in arrival time that originated from ions with the same mass, but different kinetic energies or ions of the same mass that left the pulser at different positions. As the use of a reflectron enables doubling the flight path length, longer flight times can be achieved and therefore increased resolution (García-Reyes et al., 2017). Ions arrive at the detector in order of increasing mass and the *m/z* values can be calculated as the flight time is proportional to the square root of the *m/z* value (García-Reyes et al., 2017).

During HRMS analysis, full-scan (MS1) mode, data-dependent acquisition (DDA, MS2), and data-independent acquisition (DIA, MS2) are common data acquisition modes (Guo & Huan, 2020). In DDA mode, the selection of precursor ions for MS2 analysis is intensity dependent, while in DIA mode, the MS instrument cycles through the precursor ion *m/z* range with a large precursor ion mass width to fragment more than one precursor ion simultaneously. DIA can theoretically generate MS2 spectra for all metabolites in a sample, while during DDA, metabolic features with a low abundance may never be selected for fragmentation. However, DDA provides higher quality of MS/MS spectra and deconvolution of DIA data is challenging. In DIA, the link between precursors and their fragment ions is dissociated due to the complexity of the resulting MS/MS spectra (Guo & Huan, 2020). In order to obtain high quality MS/MS spectra with increased metabolite coverage, DDA mode can be used with iterative exclusion. During iterative exclusion DDA, precursors selected based on their intensity (i.e., topN) are excluded in sequential injections. In each sequential injection, unique precursors are fragmented until HR-MS/MS spectra of all ions above a user-defined intensity threshold are acquired (Koelmel, Kroeger, Gill, et al., 2017).

1.6. Principles of ion mobility spectrometry

Hyphenation of IMS to LC and HRMS adds an additional dimension of gas-phase separation based on shape, size, charge and mass. As IMS separation takes place in the millisecond timescale, it is compatible with both chromatographic separation (second timescale) and QTOF ion detection (μs timescale) (García-Reyes et al., 2017). Just as chromatographic separations add significantly to both the selectivity and specificity of HRMS, in the same way IMS increases selectivity and specificity beyond what LC-HRMS can achieve (Fjeldsted, 2016). Firstly, addition of IMS to LC-HRMS may offer a reduction in interferences and improves separation of isomers and close isobars, increasing selectivity. Secondly, IMS leads to increased confidence in annotation (specificity) by qualifying the measured collision cross section (CCS) (Fjeldsted, 2016). The CCS value is a physicochemical property of an ion in a specific gas environment, determined by its three-dimensional gas-phase structure. CCS values can be calculated from the drift time in ion mobility spectrometry using the Mason-Schamp equation (equation 1.1) (Fjeldsted, 2016; Stow et al., 2017).

$$CCS = \frac{\sqrt{18\pi}}{16} \times \frac{ze}{\sqrt{Tk_b}} \times \sqrt{\left[\frac{1}{m_i} + \frac{1}{m_B}\right]} \times \frac{760ETt_A}{273.15LPN}$$

Equation 1.1 Mason-Schamp equation to calculate CCS values (Å²) in ion mobility. A fundamental assumption of the equation is that the separation is performed under low-field conditions and hence do not excite the molecule to change its cross section. T: drift tube temperature in kelvin, k_b: Boltzmann's constant, z: ion charge state, e: charge of an electron, m_i: ion mass, m_B: buffer gas mass, E: electric field, t_A: measured arrival time, L: drift tube length, P: drift tube pressure, and N: buffer gas number density at standard temperature and pressure (Stow et al., 2017).

Several IMS instruments are commercially available, including drift tube IMS (DTIMS), traveling-wave IMS (TWIMS), trapped IMS (TIMS), cyclic IMS (cIMS) and field asymmetric IMS (FAIMS). These IMS technologies can be classified according to three modes of separation: (i) temporary dispersive (DTIMS, TWIMS), (ii) trapping and selective release (TIMS, cIMS), and (iii) spatially dispersive release (FAIMS) (Paglia et al., 2021).

In temporally dispersive methods, all ions drift along a similar path and an arrival time spectrum is generated. In DTIMS, ions migrate through a stationary buffer gas, directed by a constant and homogeneous electric field (Ibrahim et al., 2015). A downside is that DTIMS suffers from lower sensitivity as some ions never reach the MS detector due to a high gas diffusion coefficient, causing ions to diverge from the axial path (Paglia et al., 2021). In TWIMS, ion movement is directed by an oscillating electric field and diffusional ion losses are restricted by use of RF confinement fields (K. Richardson et al., 2018).

During ion trapping and selective release IMS, ions are trapped in pressurized regions and ejected based upon differences in mobility. In TIMS, ions are kept stationary against a moving gas before being released by selectively lowering the electrical forces (Michelmann et al., 2014). cIMS is based on the same principle, with the difference that a cyclic TWIMS chamber is used, allowing multiple ion passes to increase resolving power (Giles et al., 2019).

Spatially dispersive IMS methods separate ions along different drift paths based on differences in their mobility (Paglia et al., 2021). FAIMS is mostly used in targeted experiments, as it can filter selected ions based on their specific mobility, and as the instrument operates at high electric fields, experimental CCS determination is not possible (May & McLean, 2015).

During DTIMS, ion funnel sampling is combined with a uniform low-field drift tube (Figure 1.10). Ions move forward through the drift tube under influence of an applied electric field and are slowed down by a countercurrent drag force, due to collisions with a stationary buffer gas. Separation is achieved as the magnitude of the drag force is

dependent on the collision cross sections of the analytes, which is a function of size, shape, charge and mass (García-Reyes et al., 2017).

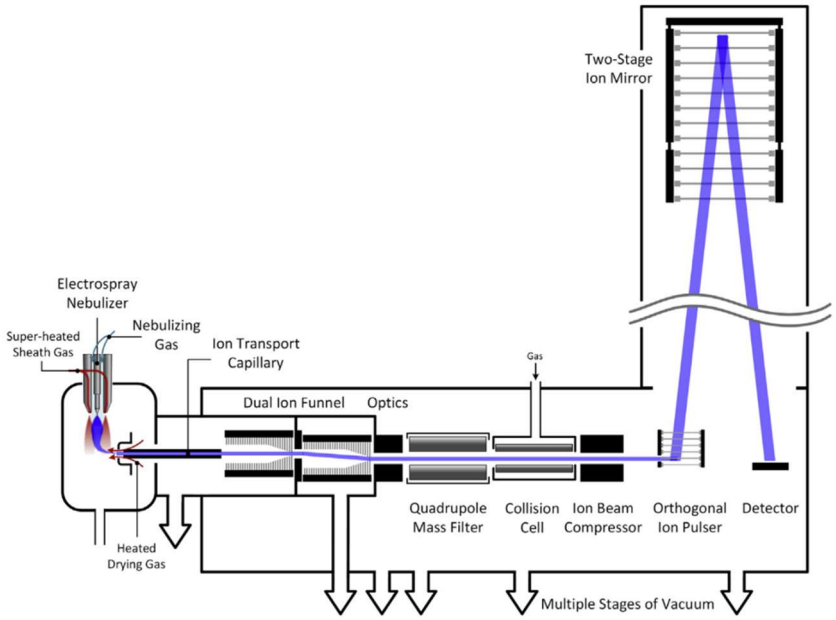

Figure 1.10 Drift tube ion mobility spectrometry hyphenated to a quadrupole time-of-flight mass spectrometer. Ions generated in the ionization source are carried out into the front ion funnel through a sampling capillary. The trapping funnel accumulates ions and releases ions packets into the drift tube. Separated ions exiting the drift tube enter a rear ion funnel, which compresses the ion beam before transmission to the QTOF mass spectrometer (Fjeldsted, 2016).

It should be noted that DTIMS can be coupled with DIA to acquire MS/MS fragmentation, but is incompatible with DDA (da Silva, van de Lavoir, et al., 2022). Complex deconvolution of DIA data becomes more straightforward when using DTIMS separation prior to DIA acquisition, as precursors and fragments can be matched based on drift times (Pezzatti et al., 2020).

DTIMS can be run in different modes, such as single pulse and Hadamard transform multiplexing with 4-bit pseudo-random pulsing sequence (Figure 1.11) (Causon et al., 2019). In single pulse mode, one ion packet is measured per IMS cycle. Ions are trapped in the trapping funnel (e.g., for 60 ms) before they get released into the drift tube for their separation (i.e., one time every 60 ms). No additional ion packets are introduced until the preceding ion populations exit the drift tube (Demelenne et al., 2022; Prost et al., 2014). The combination of a continuous ionization source and the pulsed nature of IMS causes low duty cycles and thus impairment of analytical sensitivity. IMS multiplexing mode allows to increase duty cycles and to decrease the risk of detector saturation, which would impair mass accuracy (Prost et al., 2014; Reinecke et al., 2019).

In the 4-bit multiplexing mode, the trapping time is reduced (e.g., 4 ms) and smaller packets of ions are sent into the drift tube in a particular sequence (i.e., a sequence of 15 open-closed events; 8 open, 7 closed; ion packets are released 8 times every 60 ms). The pseudorandom nature of multiplexing allows elimination of systematic noise. This release of a sequence of ion packets implies that within one IM cycle, signals of the same feature reach the detector at different drift times, generating multiple signals for the same feature. Post-acquisition, these separately recorded signals are mathematically combined during the process of demultiplexing (Demelenne et al., 2022; Prost et al., 2014).

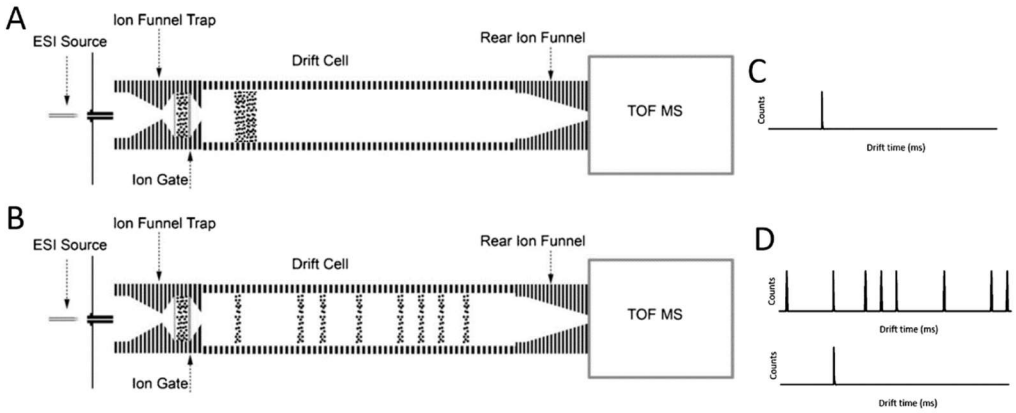

Figure 1.11 Schematic explanation of ion mobility single pulse mode (A) and 4-bit Hadamard multiplexing mode (B). At the right, the arrival time distribution is shown for one feature in single pulse mode (C), in multiplexed mode (D, up) and in demultiplexed mode (D, down). Adapted from Demelenne et al., 2022 and Prost et al., 2014. ESI: Electrospray ionization. TOF MS: Time-of-flight mass spectrometry.

CHAPTER 2:
OBJECTIVES

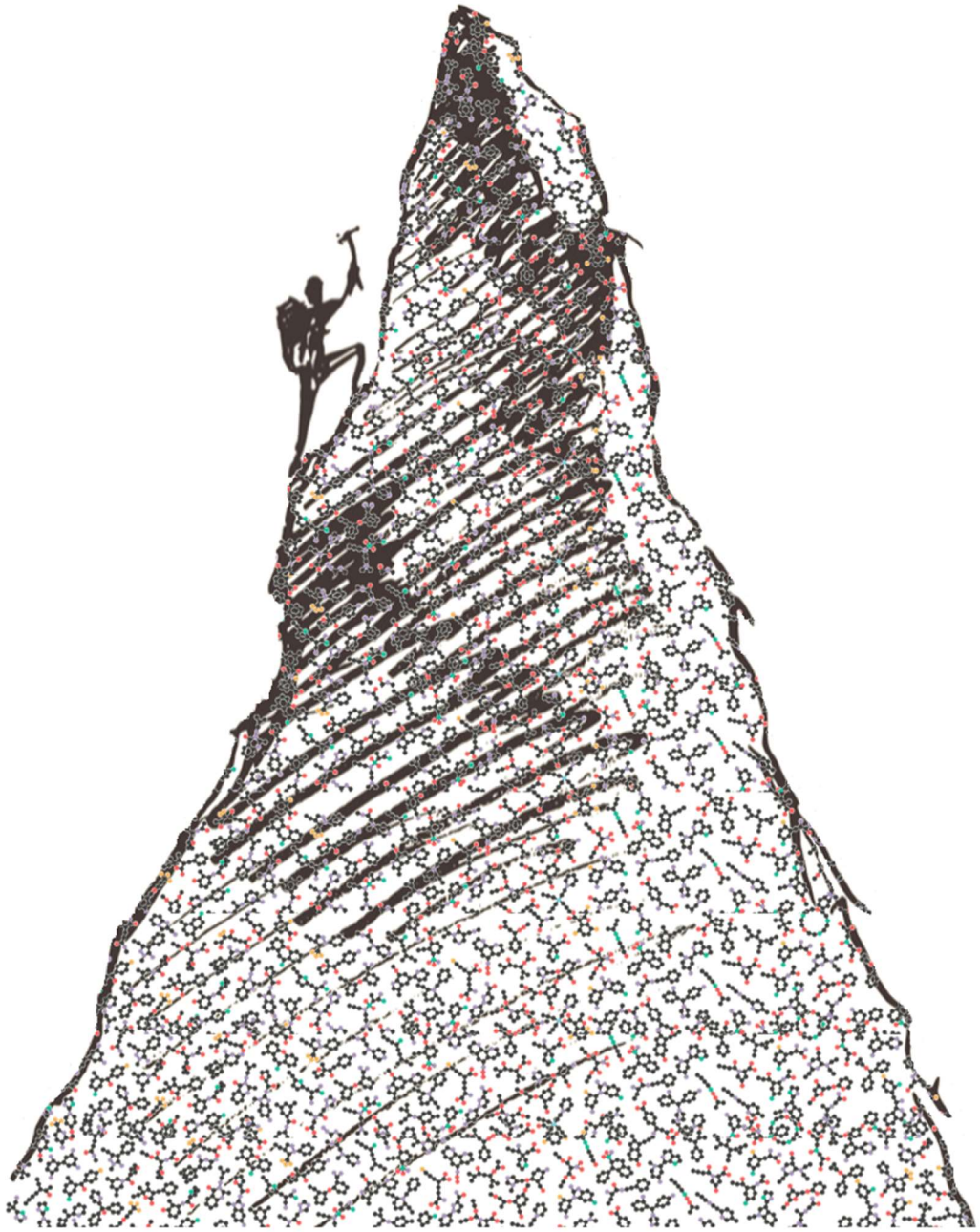

The overarching goal of this PhD thesis is the identification of a panel of small molecule biomarkers to characterize early stages of alcoholic liver disease (AFLD and ASH) in an *in vitro* setting, through an advanced metabolomics workflow (Figure 2.1). This research goal was set as the mechanisms of ALD pathogenesis remain unclear because of the lack of ALD patient samples and reliable animal models for ALD that reflect human ALD. The limited understanding of ALD hampers development of novel therapies and diagnostic improvements (Hyun et al., 2021). By using HepaRG cells as a human-based cell model, biochemical biomarkers can be identified to elucidate the mechanism of ethanol-induced hepatotoxicity at a mechanistic cellular level.
To achieve this goal, the research was based on a close collaboration between (i) the Toxicological Center of the University of Antwerp with its main expertise in analytical chemistry, bioanalysis applications and analytical method development, and (ii) the *In Vitro* Toxicology and Dermato-Cosmetology research group of the Vrije Universiteit Brussel, with its extensive expertise in *in vitro* (hepatic) modeling. This project further intensified the exchange of information and technology between both universities.

The hypothesis of this project is based on the concept of Adverse Outcome Pathways (AOPs), which is well-accepted in modern toxicology (Ankley et al., 2010; Corradi et al., 2022; Vinken et al., 2017). The adverse outcomes in ALD (e.g., steatosis and steatohepatitis) are established through different Modes of Action (MoA), involving a molecular initiating event (MIE) leading to a series of key events (KEs), which imply alterations in specific metabolic pathways. MIEs induce specific intracellular alterations, resulting in different metabolic profiles. Based on the up- or downregulation of intra- and extracellular metabolites, biomarkers could be identified for the characterization of the early stages of ALD. In addition, alterations in metabolites can be used to visualize changes in metabolic pathways, to offer new toxicological insights in the MoAs of ethanol-induced hepatotoxicity. Characterization of ALD at a mechanistic cellular level can provide a better understanding of pathogenesis, boost research to improve clinical diagnosis and pinpoint possible pharmacotherapeutic targets (Hyun et al., 2021).
In vitro identified biomarkers can be used for future *in vivo* studies using samples of patients suffering from ALD for verification. For this latter verification, liver biopsy samples can be used. However, the research within this thesis is not limited to elucidation of intracellular metabolic alterations in hepatocytes, but also aimed to include extracellular metabolomics, and thus plasma and/or serum of ALD patients could be used for verification purposes.

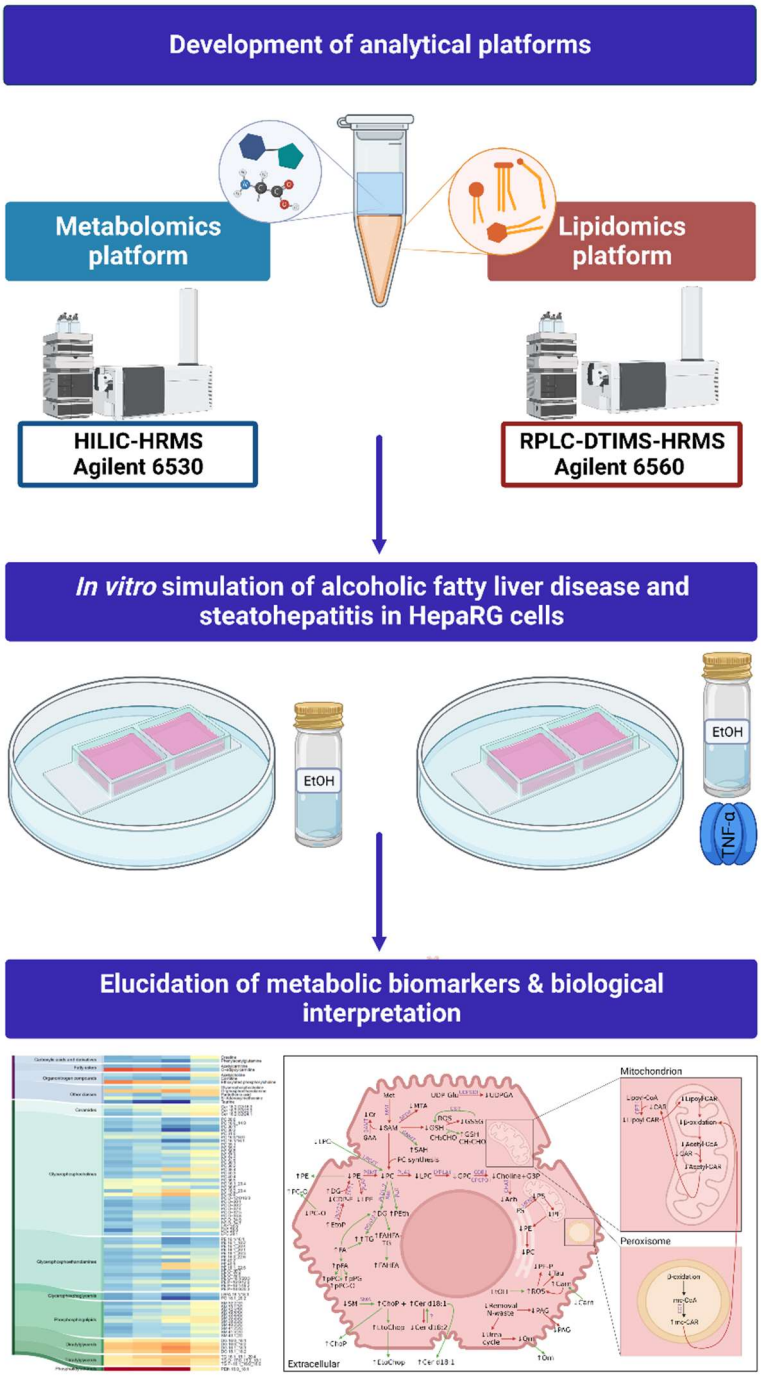

Figure 2.1 Overview of the objectives of this PhD thesis.

The **first major objective** is the development of untargeted metabolomics and lipidomics platforms using LC-HRMS. A high-quality and high-end metabolomics

platform using state-of-the-art technology and bioinformatics is crucial in order to obtain reliable data to be used to address the second major objective. Chapter 3 of this thesis was dedicated to the development of an untargeted HILIC-MS platform for polar metabolites in biological matrices using an exploratory approach.
Chapter 4 is dedicated to the development of an RPLC-DTIM-HRMS lipidomics platform. Experiments were designed to determine the optimal LC methodology, and the value of DTIMS was evaluated as an extra dimension of separation. As hyphenation of DTIMS to LC-HRMS results in reduced sensitivity due to impaired duty cycles, strategies to improve sensitivity were explored.
As feature annotation remains a major challenge in untargeted metabolomics and lipidomics, guidelines and considerations for building multidimensional MS-based metabolite libraries were described in Chapter 5. The usefulness of implementing RT and CCS information, in addition to accurate mass and MS/MS spectra, for feature annotation was explored. In addition, an easy-to-use workflow for the creation of in-house metabolite libraries was provided.

The **second major objective** is the application of the constructed analytical platforms to investigate AFLD and ASH in an *in vitro* model using the HepaRG liver cell line. This objective was subdivided in two minor aims: (i) optimization of the workflow/protocols of the *in vitro* model and (ii) the selection of biomarkers, based on the alteration of metabolites. HepaRG liver cells were subject to ethanol exposure in different experiments. The differences between the observed metabolic profiles against a negative control group allowed the detection and identification of biomarkers specific for ethanol-induced hepatotoxicity. While Chapter 6 provides a general overview of the experimental exposure, sample preparation methods and analytical procedures, Chapters 7 and 8 were dedicated to the use of metabolomics to investigate ethanol-induced hepatotoxicity. In Chapter 7, AFLD was simulated and metabolic alterations in response to ethanol exposure at different concentrations and for different exposure times were elucidated with extensive discussion of the results. However, as the extrahepatic environment was lacking in these experiments, ethanol exposure could not generate the inflammatory response caused by extrahepatic cytokines as seen in human ASH (Nagy, 2015). In Chapter 8, follow-up experiments were performed in which HepaRG cells were co-exposed to tumor necrosis factor alpha (TNF-α) in order to obtain an improved *in vitro* simulation of ASH. TNF-α is considered the most important inflammatory cytokine in the progression of ALD (Kawaratani et al., 2013; Nagy, 2015; Seo & Jeong, 2016; Yin et al., 1999). Metabolic alterations were elucidated comparing exposure to ethanol and TNF-α with negative controls and with solely ethanol exposure.

PART A: DEVELOPMENT OF ANALYTICAL PLATFORMS FOR UNTARGETED METABOLOMICS

CHAPTER 3:
DEVELOPMENT OF UNTARGETED PLATFORMS FOR POLAR METABOLITES

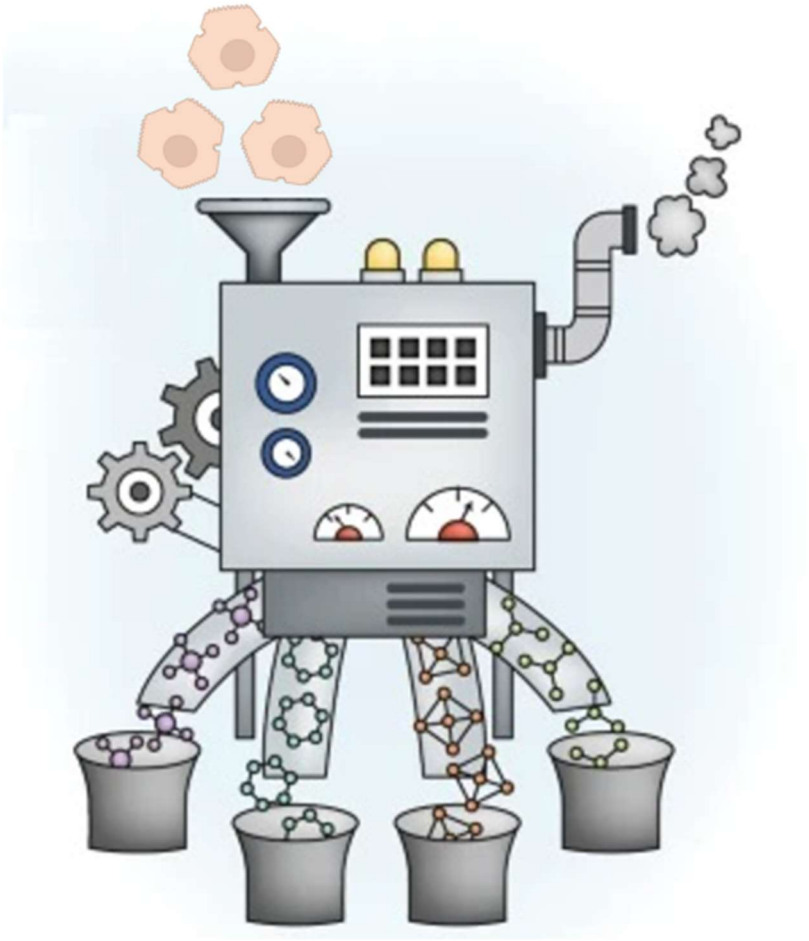

Based on the following publication

Iturrospe E*[,$], Da Silva KM*[,$], Andujar BT, Cuykx M, Boeckmans J, Vanhaecke T, Covaci A, Van Nuijs A. An exploratory approach for an oriented development of an untargeted hydrophilic interaction liquid chromatography-mass spectrometry platform for polar metabolites in biological matrices. Journal of Chromatography A. 2021; 1637, 461807. (DOI: 10.1016/j.chroma.2020.461807).

*Shared first authors.

[$]Contribution as in the publication. E.I.: Conceptualization, Methodology, Investigation, Writing - original draft, Visualization. K.M.d.S.: Conceptualization, Methodology, Investigation, Writing - original draft, Visualization.

3.1. Introduction

Due to the heterogeneity of molecules in the metabolome, varying from small polar organic acids to apolar triglycerides, a single LC-MS method is not capable to capture this broad variety of metabolites (W. Lu et al., 2017). Traditionally, reversed-phase liquid chromatography (RPLC) is used for the separation of apolar to slightly polar metabolites, resulting in a wide lipid coverage, useful for lipidomics research (Cajka & Fiehn, 2014). Hydrophilic interaction liquid chromatography (HILIC), a technique compatible with electrospray ionization (ESI)-MS, has become the separation technique of choice for polar compounds such as organic acids and sugars (Cajka et al., 2017; Sillner et al., 2019). In HILIC, a polar stationary phase is used in combination with an aqueous-organic mobile phase, which creates a water-rich layer around the stationary phase, in which various hydrophilic interaction mechanisms occur (Gritti et al., 2015; McCalley, 2017). HILIC methods have the potential to retain and separate polar metabolites that show no retention or co-elute in RPLC and can lead to an increased MS sensitivity for polar compounds. However, HILIC has some disadvantages (e.g., limited choice of mobile phase compositions, long equilibration times) and it cannot be used for an untargeted metabolomics experiment without proper method development and validation of its actual metabolome coverage (Buszewski & Noga, 2012).

In this chapter, different HILIC-columns and chromatographic settings were tested for an untargeted approach that can be applied for the polar metabolite fraction of different biological matrices. By employing HILIC-QTOF-MS in ESI (-) and ESI (+) ionization modes to analyze standard mixtures of polar metabolites and various biofluids (plasma, urine) as well as HepaRG cells, the capabilities and limitations of HILIC chromatography were explored.

3.2. Chemicals and materials

Analytical standards were purchased from Sigma Aldrich (St. Louis, Missouri, USA), Merck (Darmstadt, Germany) and Janssen Chimica (Beerse, Belgium). A total number of 72 panel standards was used during the experiments covering a wide range of metabolic classes including amino acids (19), amino acid metabolites (5), phosphorylated amino acid metabolites (2), peptides (5), sugars (4), amino sugars (1), phosphorylated sugars (1), organic acids (6), phosphorylated organic acids (2), tricarboxylic acid cycle (TCA) intermediates (6), nucleobases or analogues (4), nucleosides (3), nucleotides (3), cofactors or -enzymes (6) and small chain acylcarnitines (5). Using the final optimized methods, 13 additional analytical panel standards (3 amino acids, 3 amino acid metabolites, 2 sugars, 1 organic acid, 1 nucleobase or analogue, 2 cofactors or -enzymes and 1 amine oxide) were analyzed, bringing the total number to 85 panel standards. In

Figure 3.1, 65 out of 85 panel standards were used for pathway mapping to visualize the metabolic coverage. All chemical standards used during method optimization are listed in the supplementary information (Table SI-3.1). L-glutamic acid-2,3,3,4,4-D_5, L-leucine-5,5,5-D_3, L-lysine-$^{13}C_6$-$^{15}N_2$, succinic acid-2,2,3,3-D_4, D-tryptophan-2,4,5,6,7-D_5 and glucose-$^{13}C_6$ were used as internal standards during the sample preparation of biological samples. All internal standards were purchased from Sigma Aldrich, except for D-tryptophan-2,4,5,6,7-D_5, which was bought from CDN isotopes (Pointe-Claire, Quebec, Canada). Methanol ultrapure (MeOH), acetonitrile (ACN) and formic acid (99%) (HCOOH), all ULC/MS-CC/CSF grade, were purchased from Biosolve (Valkenswaard, The Netherlands). Ammonium formate (≥ 99%, LC-MS grade) ($HCOONH_4$), ammonium carbonate HPLC grade ($(NH_4)_2CO_3$) and ammonium acetate LC-MS grade (CH_3COONH_4) were obtained from Sigma Aldrich. Acetic acid (100%) (CH_3COOH), ammonia solution (25%) ($NH_{3(aq)}$) and ethanol (EtOH), all LC-MS grade, isopropanol for analysis (ACS reagent) (IPA) and chloroform (analytical grade) ($CHCl_3$) were purchased from Merck. Ultrapure water (H_2O) used throughout the experiments was obtained from an Elga Pure Lab apparatus (Tienen, Belgium).

For the experiments with HepaRG cells, differentiated HepaRG cells, Basal Hepatic Medium, HepaRG Thaw, Seed and General-Purpose Supplement and HepaRG Maintenance and Metabolism Supplement were acquired from Biopredic International (Rennes, France). HepaRG cells were seeded in Permanox 2-well Lab-Tek chamber slides from Nunc, Thermo Scientific (Rochester NY, USA) and incubated using a Galaxy 170 S incubator acquired from Eppendorf (Hamburg, Germany). Rat tail collagen for coating was provided by Corning (New York, USA). Eppendorf Safe-Lock tubes and 0.2 µm nylon centrifugal filters were acquired from respectively Eppendorf and VWR (Pennsylvania, USA) and used during sample preparation. Pure, dry nitrogen (AZOTE N28, N_2) used for solvent evaporation was obtained from Air Liquide Belge (Liège, Belgium). 384 well plates (PS, small volume) were bought from Greiner Bio-One (Vilvoorde, Belgium). Human blood was collected in sterile Vacuette K_3EDTA premium tubes acquired from Greiner Bio-One and aseptic polypropylene urine recipients from Disera (Izmir, Turkey) were used for urine collection.

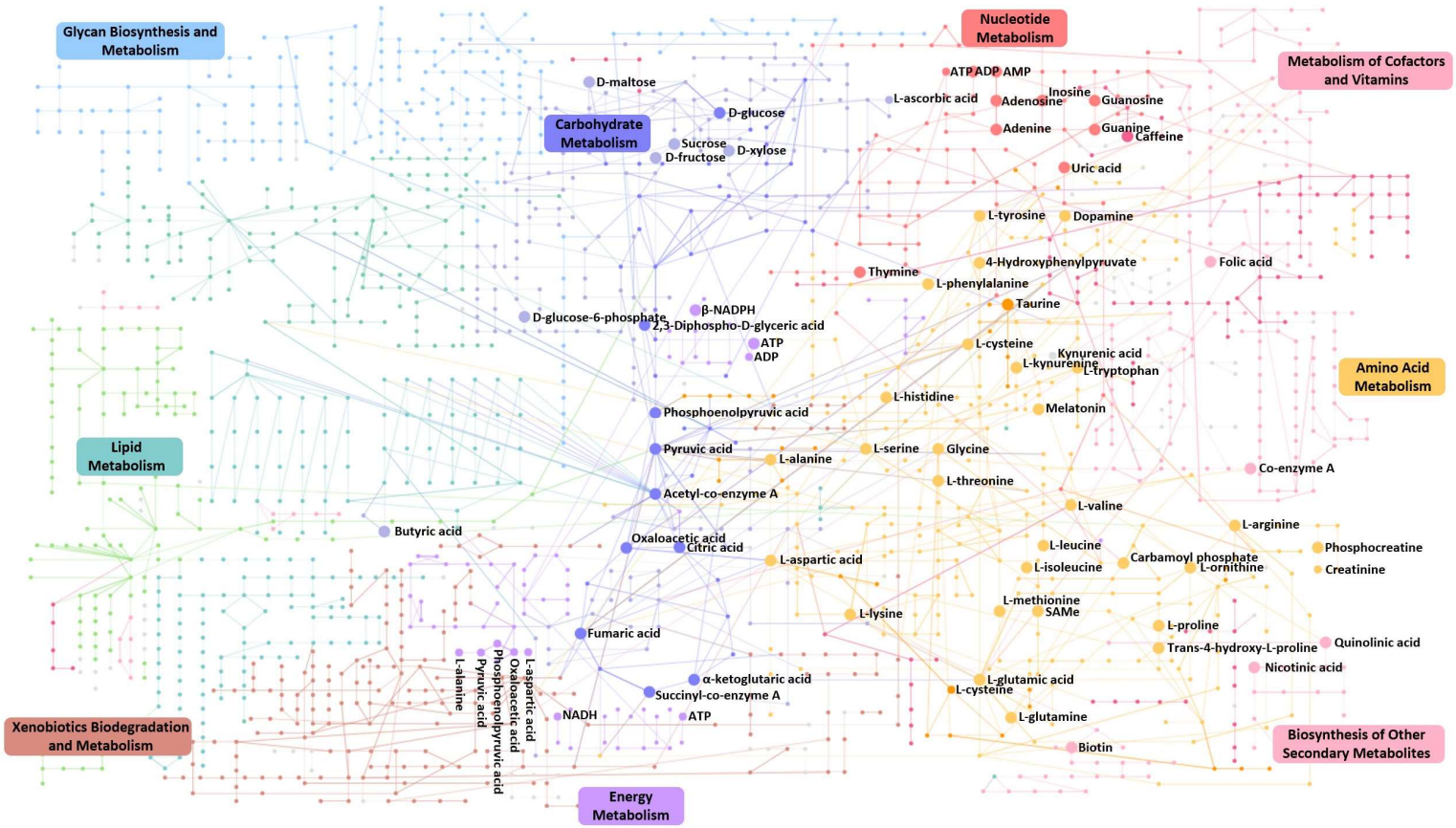

Figure 3.1 Pathway coverage for 65 analytical panel standards used for method development. Standards were selected based on their polarity to cover the polar side of the pathway map. ATP: Adenosine triphosphate. ADP: Adenosine diphosphate. AMP: Adenosine monophosphate. β-NADPH: β-Nicotinamide adenine dinucleotide phosphate. SAM: S-adenosyl-L-methionine. NADH: Nicotinamide adenine dinucleotide.

3.3. Sample preparation

The used sample preparation technique has an important influence on the metabolite coverage in biological samples (W. Lu et al., 2017). Therefore, the extraction methods were carefully chosen. The sample preparation for the liver cell extracts was adapted from a previously in-house method using two-phase liquid-liquid extraction (Cuykx, Mortelé, et al., 2017). The sample preparation for plasma and urine samples were chosen based on literature screening of validated methods which had a good coverage for polar metabolites (Benito et al., 2018; Bruce et al., 2009; Chen et al., 2016; Fernández-Peralbo & Luque de Castro, 2012; Qiong Wu et al., 2014).

3.3.1. Analytical standard solution

Analytical standard solutions were prepared by dissolving solids or diluting liquid standards in H_2O, MeOH, EtOH or a combination of H_2O with MeOH or EtOH (50/50, v/v), depending on the solubilization properties of the compounds, to obtain a stock solution of 50 µg/mL. All panel standards were combined in a mixture, the solvent was evaporated to dryness using a stream of N_2 at room temperature, and reconstituted in H_2O/ACN (35/65, v/v) to obtain a final concentration of 1 µg/mL. The final mixtures were stored at -20 °C before injection.

3.3.2. Intracellular extracts of HepaRG cells

Ethical approval for the use of HepaRG cells was provided by the Medical Ethics Committee of the University Hospital Brussels (reference number 143201941214).
Differentiated HepaRG cells were seeded (N = 6) in collagen-coated Permanox 2-well Lab-Tek chamber slides at a concentration of 1 x 10^6 cells per well (day 0). For seeding of the cells, Basal Hepatic Medium with HepaRG Thaw, Seed and General-Purpose Supplement was used. The cells were incubated for 8 days at 37 °C, 5% CO_2 and saturated humidity using a Galaxy 170 S incubator. On day 1 of incubation, the medium was replaced by Basal Hepatic Medium with HepaRG Maintenance and Metabolism Supplement. On day 3, 6 and 7, the medium was renewed. Blanks (N = 4) did not contain the HepaRG cells and were treated identically to other samples. After eight days of incubation of HepaRG cells, the incubation medium was collected for extraction (see 3.3.3.) and the chamber slides were washed twice using PBS (37 °C) before snap-freezing with liquid N_2. 300 µL of a quenching solution was added. The quenching solution consisted out of 80% MeOH (v/v) and 20% (v/v) of 10 mM CH_3COONH_4 (at -80 °C). After 2 min, the cells were scraped and extracted in an LLE-vial, which contained 500 µL of a polar mixture and 420 µL of an apolar mixture (at -20 °C). The polar mixture consisted out of 1 mM $(NH_4)_2EDTA$ and 0.5 mM ascorbic acid in 5 mM CH_3COONH_4 with 0.1% (v/v)

CH_3COOH (pH 4.2). The apolar mixture consisted out of 1 mM butylated hydroxytoluene (BHT) in $CHCl_3$. Another 300 µL of the quenching solution was used for rinsing and was collected in the same LLE-vial. 20 µL of an internal standard mixture was added. The mixture contained 7 µg/mL of internal standards (L-glutamic acid-2,3,3,4,4-D_5, L-leucine-5,5,5-D_3, D-Tryptophan-2,4,5,6,7-D_5 and Glucose $^{13}C_6$) in H_2O/MeOH (1/1, v/v) to obtain a final concentration of 1 µg/mL. The LLE-vial was subsequently vortexed for 90 s, equilibrated for 10 min (4 °C), centrifuged at 2,200 g for 7 min at room temperature and again equilibrated for 10 min (4 °C). 960 µL of the polar fraction (upper phase) was transferred to an Eppendorf tube, without transferring solid particles from the protein disk. After vortexing for 20 s, 480 µL was transferred to a second Eppendorf tube after which the liquid of both Eppendorf tubes was evaporated using pure, dry nitrogen at room temperature. Each sample was divided in two fractions right before the evaporation step, in order to analyze each fraction using a different ionization mode during LC-MS acquisition. Dried extracts were stored at -80 °C and reconstituted directly before analysis. Each sample was reconstituted on ice, using 60 µL ACN/H_2O (65/35, v/v). After vortexing for 90 s, samples were filtered using a 0.2 µm nylon centrifugal filter and centrifugated at 14,000 g for 2 min at room temperature. Ten µL of each filtered sample was transferred to an LC-vial to create a QC pool. Another 20 µL of each sample was transferred to a Greiner Bio-One 384 well plate. Surrounding wells were filled with solvent blanks and the well plate was sealed using aluminum adhesive. Both the well plate and the QC pool were transferred to the autosampler (4 °C) right before analysis.

3.3.3. Extracellular extracts of HepaRG cells

In order to analyze the extracellular metabolome of HepaRG cells, the used incubation medium was collected at the same day as the extraction of the HepaRG cells. The sample preparation was based on the method of Cuykx *et al.* (Cuykx, Mortelé, et al., 2017) and Dettmer *et al.* (Dettmer et al., 2013).

After eight days of incubation of HepaRG cells in Permanox 2-well Lab-Tek chamber slides, the incubation medium (1.2 mL per well) was extracted in separate Eppendorf tubes (N = 6). Blank media (N = 4) were obtained after incubation without HepaRG cells and were treated identically to other samples. 320 µL of the collected medium was transferred to a second Eppendorf tube, to which 725 µL of a quenching solution was added (see 3.3.2. for composition). After vortexing for 60 s, 980 µL of quenched medium was transferred to an LLE-vial, which contained 500 µL of a polar mixture and 420 µL of an apolar mixture (-20 °C, see 3.3.2. for composition). 20 µL of the same internal standard mixture as in 3.3.2. was added. This time, the mixture contained 9 µg/mL of internal standards to obtain a final concentration of 1 µg/mL. The LLE-vial was

subsequently vortexed for 90 s, equilibrated for 10 min (4 °C), centrifuged at 2,200 g for 7 min at room temperature and again equilibrated for 10 min (4 °C). 1000 µL of the polar fraction (upper phase) was transferred to an Eppendorf tube, without transferring solid particles from the protein disk. After vortexing for 20 s, 500 µL was transferred to a second Eppendorf tube. Subsequent sample preparation steps were identical to those for the intracellular samples.

3.3.4. Human plasma

Blood samples were collected from 6 healthy volunteers, 3 males and 3 females, aged 24-31 years. The sampling was approved by the Ethical Committee of the University Hospital Antwerp (EC/PC/avl/2018.039). The sample preparation protocol was adapted from Benito *et al*. (2018), Chen *et al.* (2016) and Bruce *et al.* (2009). Extraction was performed using K_3EDTA tubes, which were centrifuged at 1,000 g for 5 min, within 15 min after collection. The obtained plasma samples were separated from the red blood cell pellet and stored at -80 °C until further sample preparation and LC-MS analysis. Frozen plasma samples were thawed on ice on the day of the analysis. Aliquots of 50 µL plasma were transferred to an Eppendorf tube and mixed with 150 µL of -80 °C MeOH/EtOH (1/1, v/v). Samples were vortexed for 60 s, kept on ice for 5 min, then centrifuged at 15,500 g for 10 min at room temperature. The supernatant was transferred to a new Eppendorf tube and evaporated to dryness under a stream of N_2. Dried samples were reconstituted to 120 µL of ACN/H_2O (65/35, v/v) spiked with a 1 µg/mL internal standard mixture (L-lysine-$^{13}C_6$-$^{15}N_2$, succinic acid-2,2,3,3-D_4, L-glutamic acid-2,3,3,4,4-D_5, L-leucine-5,5,5-D_3, D-tryptophan-2,4,5,6,7-D_5 and glucose-$^{13}C_6$). Reconstituted samples were transferred to a 0.2 µm nylon centrifugal filter and centrifuged at 14,000 g for 2 min. A pooled QC sample was obtained by combining equal volumes of the extracts.

3.3.5. Human urine

Urine samples were collected from 6 healthy volunteers, 3 males and 3 females aged 24-48 years. The donation was approved by the Ethical Committee of the University Hospital Antwerp (18/31/357). Sample preparation was based on the method of Wu *et al.* (2014) and the recommendations of Fernández-Peralbo *et al.* (2012). Urine samples were stored at -80 °C directly after collection. Frozen urine samples were thawed on ice and vortexed for 60 s. A volume of 133 µL of urine was diluted with 300 µL ACN and stored on ice for 5 min. Samples were centrifuged at 15,000 g for 10 min at room temperature. A volume of 67 µL of an internal standard mixture (L-lysine-$^{13}C_6$-$^{15}N_2$, succinic acid-2,2,3,3-D_4, L-glutamic acid-2,3,3,4,4-D_5, L-leucine-5,5,5-D_3, D-tryptophan-2,4,5,6,7-D_5 and glucose-$^{13}C_6$) was added to the supernatant (final concentration 1

µg/mL). Before injection, samples were filtered using 0.2 µm nylon centrifugal filters with centrifugation at 14,000 g for 2 min at room temperature. A pooled QC sample was obtained by combining equal volumes of the extracts.

3.4. Mass spectrometry parameters

Mass spectrometry detection was performed on an Agilent 6530 QTOF-MS with Agilent Jet Stream Electrospray Ionization (Agilent Technologies, Santa Clara, USA). In ESI (+) mode, nitrogen was used as drying and sheath gas at 250 °C and 350 °C with flow rates of 8 L/min and 11 L/min, respectively. The nebulizer gas pressure was set at 45 psig, the MS capillary voltage at 2000 V, the nozzle voltage at 0 V and the fragmentor at 150 V. In ESI (-) mode, the drying and sheath gas had a temperature of 250 °C and a flow of 10 L/min and a temperature of 350 °C and a flow of 10 L/min respectively. The nebulizer gas pressure was set at 45 psig, the MS capillary voltage at 2000 V, the nozzle voltage at 0 V and the fragmentor at 100 V. For both ionization modes, data were acquired in 2 GHz extended dynamic mode with a scan range of 60-1000 *m/z* and a scan rate of 2 spectra/s. Full scan data were stored in profile mode. Calibration of the mass axis was performed within run using purine (*m/z* 121.0508 in ESI (+) mode and *m/z* 119.0363 in ESI (-) mode) and hexakis (1H, 1H, 3H-tetrafluoropropoxy) phosphazine (*m/z* 922.0097 in ESI (+) mode and *m/z* 980.0163 in ESI (-) mode). The calibrant solution was constantly infused during the run with an additional isocratic pump (Agilent 1200 series G1310A) and mixed with the effluent using a T-piece connected to the ESI source. Data-dependent MS/MS (auto-MS/MS) acquisition was obtained at collision energies of 10, 20 and 40 eV using a separate method with a scan rate of 2 spectra/s and 6.67 spectra/s for MS and MS/MS spectra, respectively. The maximum precursors/scan cycle was set at 12.

3.5. Analytical method optimization

3.5.1. Liquid chromatography column screening

Liquid chromatography was performed on an Agilent 1290 Infinity UPLC system. The injection volume was set at 3 µL and the thermostat of the autosampler at 4 °C. Firstly, several chromatographic columns were screened using generic HILIC methods based on the recommendations of the supplier and previous publications (Buszewski & Noga, 2012; Cuykx, Negreira, et al., 2017). Details concerning these generic methods are specified in Table 3.1. In addition to HILIC-QTOF-MS, one RPLC-QTOF-MS method was tested in parallel to evaluate the coverage of a reversed-phase method with an ACQUITY UPLC HSS T3 column previously used for metabolomics applications (Zhi Zhou et al., 2017).

Table 3.1 Generic LC methods used for column screening. Void time (t_0) was estimated using the elution time (min) of naphthalene (*), thiourea (**) or toluene (***). For Shodex columns, a theoretical estimation of t_0 (****) was calculated using the formulas published by Wernisch *et al.* (Wernisch & Pennathur, 2016). U(H)PLC: Ultra (high) performance liquid chromatography. HSS: High strength silica. HILIC: Hydrophilic interaction liquid chromatography. RPLC: Reversed-phase liquid chromatography. PVA: Polyvinyl alcohol. PEEK: Polyether ether ketone. ACN: Acetonitrile. MeOH: Methanol. MS: Mass spectrometry. ESI: Electrospray ionization.

Column	A	B	C	D	E	F	G	H
Commercial name	HILICON iHILIC-Fusion UHPLC	Waters ACQUITY UPLC HSS T3	Waters ACQUITY UPLC HSS T3	Phenomenex Luna HILIC	HILICON iHILIC-Fusion(+) UHPLC	HILICON iHILIC-Fusion(P)	Shodex HILICpak VT-50 2D	Shodex HILICpak VG-50 2D
Separation mode	HILIC	RPLC	RPLC	HILIC	HILIC	HILIC	HILIC	HILIC
Chemistry	Zwitterionic, Charge modulated hydroxyethyl amide	C18	C18	Dihydroxy-propane	Zwitterionic, Permanent positive charged modulated hydroxyethyl amide	Zwitterionic, Charge modulated amide	Quaternary ammonium	Amino
Solid support	Silica	Silica	Silica	Silica	Silica	Polymer	Polymer (PVA)	Polymer (PVA)
Material	Stainless steel	Stainless steel	Stainless steel	Stainless steel	Stainless steel	PEEK	PEEK	PEEK
Dimensions (mm)	100 x 2.1	100 x 2.1	100 x 2.1	100 x 3.0	100 x 2.1	100 x 2.1	150 x 2.0	150 x 2.0
Particle size (µm)	1.8	1.8	1.8	3	1.8	5	5	5
Pore size (Å)	100	100	100	200	100	200	100	100
Temperature (°C)	30	30	30	30	30	30	30	30

Table 3.1 Continuation.

Column	A	B	C	D	E	F	G	H
Commercial name	HILICON iHILIC-Fusion UHPLC	Waters ACQUITY UPLC HSS T3	Waters ACQUITY UPLC HSS T3	Phenomenex Luna HILIC	HILICON iHILIC-Fusion(+) UHPLC	HILICON iHILIC-Fusion(P)	Shodex HILICpak VT-50 2D	Shodex HILICpak VG-50 2D
Flow rate (mL/min)	0.3	0.2	0.2	0.2	0.2	0.2	0.2	0.2
Mobile phase A	H_2O	H_2O	H_2O	H_2O	H_2O	H_2O	H_2O	H_2O
Mobile phase B	ACN/MeOH (98/2, v/v)	ACN	ACN	ACN/H_2O (9/1, v/v)	ACN/H_2O (9/1, v/v)	ACN/H_2O (9/1, v/v)	ACN/H_2O (9/1, v/v)	ACN/H_2O (9/1, v/v)
Modifier	10 mM $HCOONH_4$+ 0.1% (v/v) HCOOH (pH 3) (A)	0.1% (v/v) HCOOH (pH 3) (A) + (B)	0.003% (v/v) NH_4OH (pH 8) (A) + (B)	10 mM CH_3COONH_4 + NH_4OH (pH 8) (A)	10 mM CH_3COONH_4 + NH_4OH (pH 9) (A)	10 mM CH_3COONH_4 + NH_4OH (pH 9) (A)	10 mM CH_3COONH_4 + NH_4OH (pH 9) (A)	10 mM CH_3COONH_4 + NH_4OH (pH 9) (A)
Gradient	Min - %B 0 – 95 2 – 95 8 – 65 13 – 25 15 – 25 17 – 95 23 – 95	Min - %B 0 – 2 1 – 2 4 – 10 6 – 35 7.3 – 95 9.3 – 95 9.4 – 2 12 – 2	Min - %B 0 – 2 1 – 2 4 – 10 6 – 35 7.3 – 95 9.3 – 95 9.4 – 2 12 – 2	Min - %B 0 – 100 2.5 – 100 12 – 50 17 – 50 20 – 100 30 - 90	Min - %B 0 – 90 2 – 90 12 – 10 17 – 10 20 – 90 30 – 90	Min - %B 0 – 90 2 – 90 12 – 10 17 – 10 20 – 90 30 - 90	Min - %B 0 – 90 2 – 90 12 – 10 17 – 10 20 – 90 30 – 90	Min - %B 0 – 90 2 – 90 12 – 10 17 – 10 20 – 90 30 – 90
Void time (t_0) (min)	0.7*	1.4**	1.4**	2.5***	1.1*	1.4*	1.9****	1.9****
MS mode	ESI+	ESI+	ESI-	ESI-	ESI-	ESI-	ESI-	ESI-

A graphical representation of the stationary phases of the columns mentioned in Table 3.1 is shown in Figure 3.2.

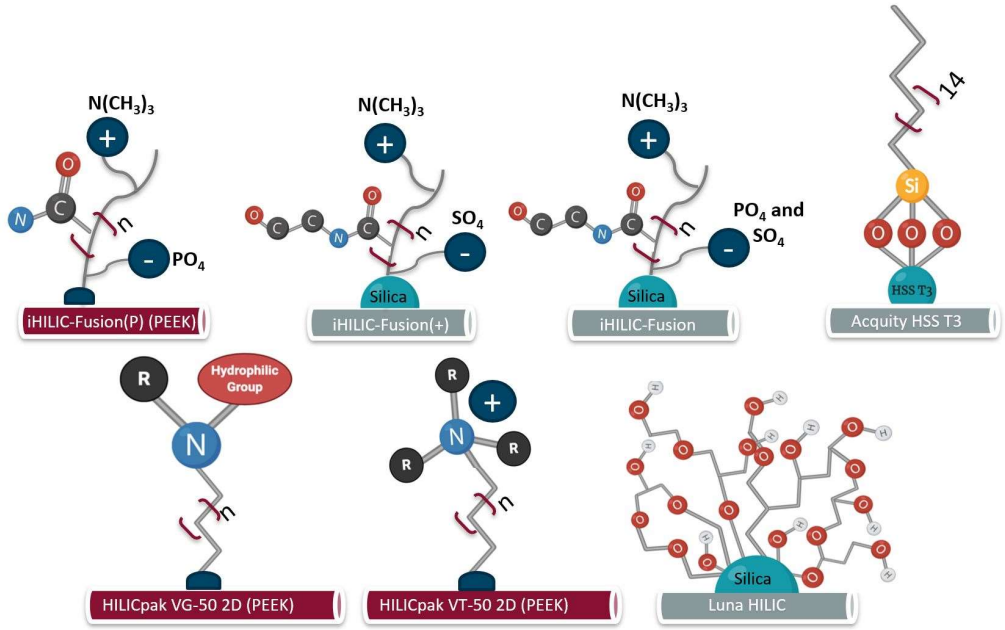

Figure 3.2 Stationary phases of the columns used for screening. The text highlighted in red refers to polymer-based columns and the one in grey refers to silica-based columns. HILIC: Hydrophilic interaction liquid chromatography. PEEK: Polyether ether ketone. HSS: High strength silica.

3.5.2. Liquid chromatography method optimization

HILIC interactions are highly dependent on the used stationary phase, mobile phase composition and several other factors, such as temperature, gradient and flow rate (Dinh et al., 2011; McCalley, 2017; Sampsonidis et al., 2015). A decision tree optimization was chosen based on the influence of these factors in the following order: stationary phase > mobile phase pH and modifier > modifier concentration > additional parameters (temperature, gradient, flow) (Chirita et al., 2010; Ikegami, 2019). After the selection of the most suitable stationary phases, the solvent and pH effects were tested with ACN, MeOH or a combination of both as organic eluent and buffered H_2O as aqueous eluent. LC-MS analysis was performed in both ESI (+) and ESI (-) modes. Generally, high pH values were tested to ionize compounds in ESI (-) mode and low pH values in ESI (+) mode. In the starting conditions in ESI (-) mode, $(NH_4)_2CO_3$ was added to the aqueous mobile phase until the maximum tolerable pH value for each column. Following the recommendations of the manufacturer, a maximum pH ≈ 8 was tested for the Waters ACQUITY UPLC HSS T3 column and pH ≈ 9 for HILIC columns in ESI (-) mode. In ESI (+) mode, aqueous mobile phases were buffered with 10 mM of $HCOONH_4$ and

0.1% HCOOH (pH ≈ 3.5). In addition, the effect of the pH was tested by injecting the mixture of panel standards at a basic pH with the above-mentioned restrictions, an acidic pH and neutral pH in both polarities, adjusting the pH with $NH_{3(aq.)}$, $(NH_4)_2CO_3$ or HCOOH when necessary. Salt modifiers affect the eluent strength, causing a greater impact on columns with dominant ionic interactions (Buszewski & Noga, 2012). The modifier effect was tested using different modifiers, including CH_3COONH_4, $HCOONH_4$ and $(NH_4)_2CO_3$ in ESI (-) mode and CH_3COONH_4, $HCOONH_4$ in ESI (+) mode at different concentrations ranging from 1 mM to 30 mM.

Gradient conditions in HILIC were optimized based on starting conditions of 95% organic phase, slowly decreasing to 20% at 10 min and keeping this condition for 4 min before returning to the initial conditions for a 5 min equilibration. In reversed-phase mode, starting conditions of 80% aqueous phase were slowly decreased to 15% at 8 min and kept at this condition for 5 min before returning to the initial conditions for a 5 min equilibration. Subsequently, the initial flow rate of 0.2 mL/min was increased to 0.25 mL/min and 0.3 mL/min. Higher flows were avoided to not exceed the maximum tolerable backpressure for the used columns. The effect of the column temperature was tested in the range of 30 °C to 60 °C. For ESI (-) mode, the bypassing of certain metal parts, such as the heat exchanger, inline filter and MS diverter valve was tested to determine the effect on the detection of anionic compounds (Pesek et al., 2011; Soga et al., 2009). Due to the purpose of this work, the optimization was performed by changing chromatographic parameters one by one. The results of each method guided the next tier in the method optimization. A flow chart with the factors explored for method development is shown in Figure 3.3. Detailed information regarding tested LC conditions for each column and ionization mode is shown in Figure 3.4 to Figure 3.7.

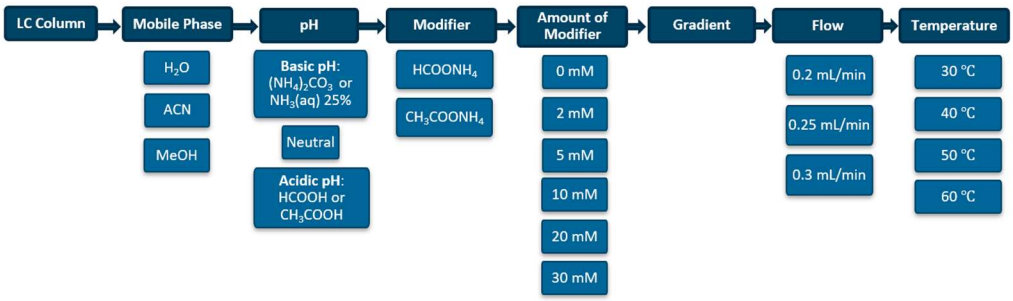

Figure 3.3 Method optimization flowchart. LC: Liquid chromatography. ACN: Acetonitrile. MeOH: Methanol.

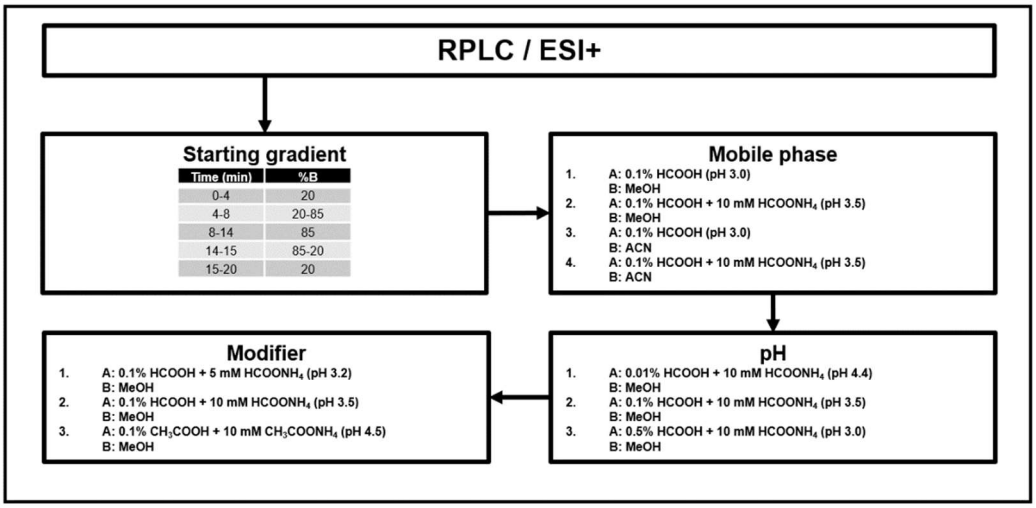

Figure 3.4 Univariate factor optimization for reversed-phase liquid chromatography (RPLC) in positive electrospray ionization (ESI) mode. All shown percentages are based on the volume/volume ratio. ACN: Acetonitrile. MeOH: Methanol.

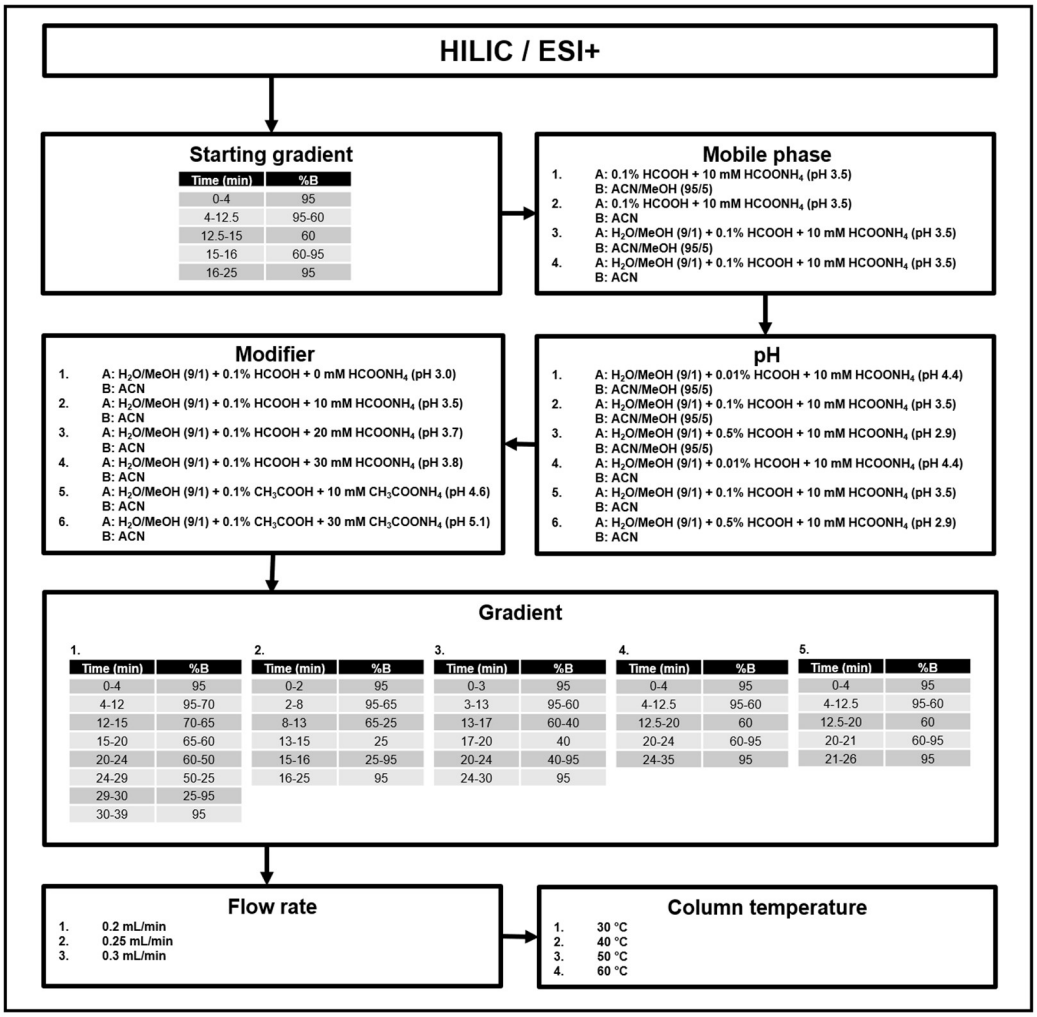

Figure 3.5 Univariate factor optimization for hydrophilic interaction liquid chromatography (HILIC) in positive electrospray ionization (ESI) mode. All shown percentages are based on the volume/volume ratio. ACN: Acetonitrile. MeOH: Methanol.

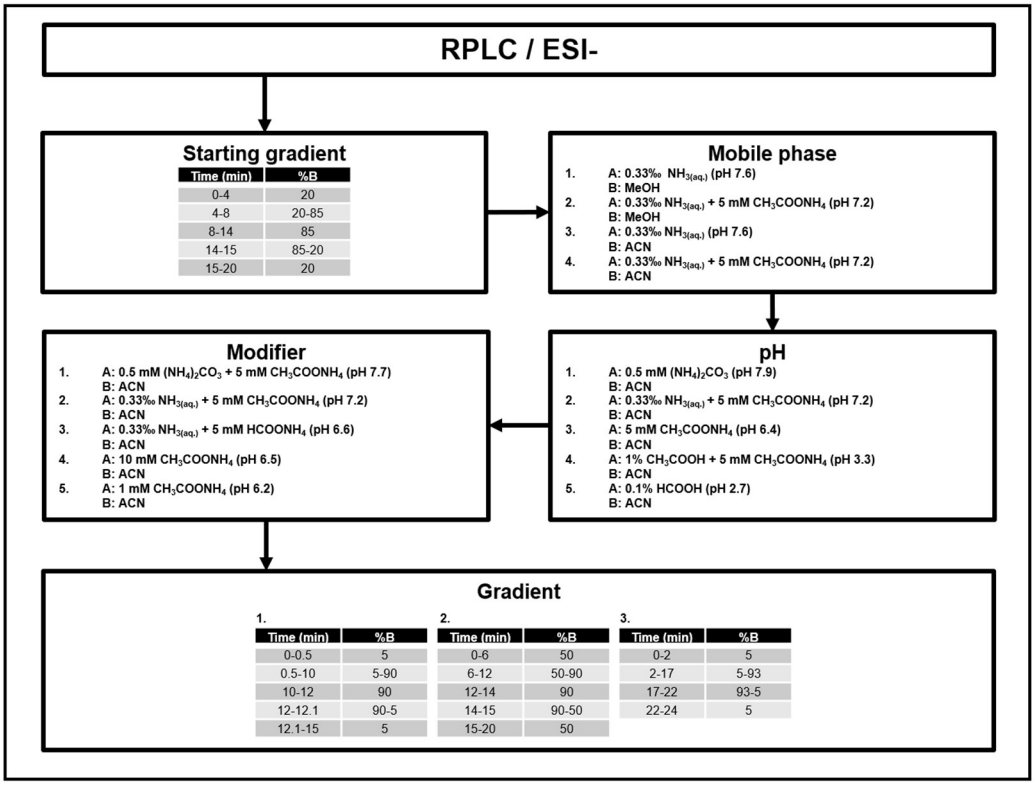

Figure 3.6 Univariate factor optimization for reversed-phase liquid chromatography (RPLC) in negative electrospray ionization (ESI) mode. All shown percentages are based on the volume/volume ratio. ACN: Acetonitrile. MeOH: Methanol.

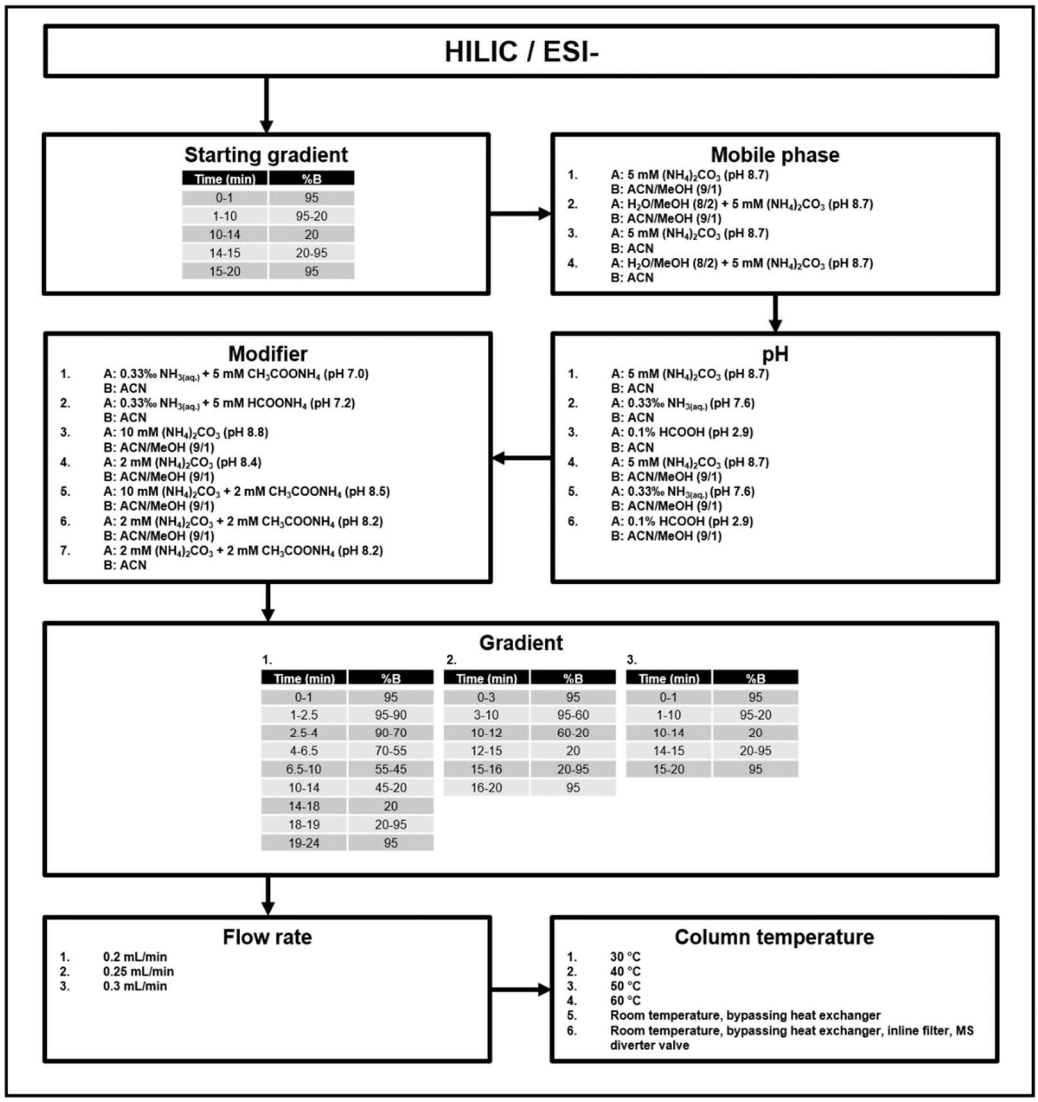

Figure 3.7 Univariate factor optimization for hydrophilic interaction liquid chromatography (HILIC) in negative electrospray ionization (ESI) mode. All shown percentages are based on the volume/volume ratio. ACN: Acetonitrile. MeOH: Methanol. MS: Mass spectrometry.

3.5.3. Data analysis of analytical standards

The structure-based predictions for chemical properties and abundances of different ion forms at specific pH values were calculated using the online tool Chemicalize (ChemAxon, Hungary). The *m/z* values of common ESI adducts (i.e., $[M+H]^+$, $[M+NH_4]^+$, $[M+Na]^+$, $[M-H_2O+H]^+$, $[M-H]^-$, $[M-H_2O-H]^-$, $[M+HCOO]^-$, $[M+CH_3COO]^-$) were calculated for each compound using the Mass Spectrometry Adduct Calculator of Fiehn Lab (UC Davis) (Fiehn Lab, 2020). To obtain reliable, high-quality results and avoid peak misidentification, individual chromatograms originating from standard mixtures were

manually extracted using a 5 ppm mass tolerance in MassHunter Qualitative Software 10.0 (Agilent Technologies). Each adduct ion of the standards was inspected in three instrumental replicates. To eliminate false positive results, ion chromatograms were compared to solvent blanks and the isotopic distribution of each adduct was investigated by manually comparing the experimentally obtained distribution in MassHunter Qualitative Software 10.0 with the theoretical distribution, calculated with the Isotope Distribution Calculator B7024.0 (Agilent Technologies).

For ESI (-) mode, ions were extracted for deprotonated ions and chloride adducts. Depending on the mobile phase composition, carbonate, formate and/or acetate adducts were additionally considered. For ESI (+) mode, ions were extracted for protonated, sodium and potassium adducts. Likewise, depending on mobile phase modifiers, ammonium adducts were additionally considered. Neutral losses were investigated depending on the compound class, for instance, water and carbon dioxide losses for compounds with a carboxylic acid function or phosphate loss for compounds with a phosphate group (Levsen et al., 2007).

During column screening and method optimization experiments, the best signal was selected out of the different detected adducts by applying a scoring system to evaluate the peak shape, retention time and peak intensity for each analytical panel standard, as explained in Table 3.2. The scores were calculated according to Equation 3.1 per analytical panel standard and per method. Similar strategies were previously applied to evaluate different LC-MS conditions by assigning individual scores to metabolites and combining the values (Pezzatti et al., 2019). This highlights the applicability of the scoring system to the analytical method development and evaluation of untargeted methods. Eluting compounds were confirmed by comparison of their MS/MS fragmentation spectra with MassHunter METLIN Metabolite PCDL (Agilent Technologies).

Table 3.2 Scoring system to evaluate peak shape, peak intensity and retention time. The scoring system was used for each analytical panel standard to guide the choice of LC column and the method optimization. FWHM: Full width at half maximum. S/N: Signal-to-noise ratio. RT: Retention time.

	Peak shape score		Peak intensity score		Retention time score
0	No peak	**0**	S/N < 3	**0**	No peak
1	Multiple peaks*	**1**	3 ≤ S/N < 10	**1**	RT = 1 to 1.1t_0
2	Single peak with FWHM ≥ 0.2 and/or tailing factor ≥ 2 or ≤ 0.8	**2**	10 ≤ S/N ≤ 50	**2**	RT > 1.1t_0
3	single peak with FWHM < 0.2 and tailing factor < 2 and > 0.8	**3**	S/N > 50		

*Multiple peaks refer to splitted peaks and/or peaks with multiple retention, which can occur when the mobile phase conditions are at the iso-electric point of zwitterions under investigation.

$$Quality\ Score = \sum_{i=1}^{n} Peak\ shape\ score + \sum_{i=1}^{n} Peak\ intensity\ score + \sum_{i=1}^{n} Retention\ time\ score$$

Equation 3.1 Quality score equation based on the quality score sum of Table 3.2.

3.5.4. Data analysis of biological samples

During data acquisition of each dataset of biological samples, the injection order was randomized, and the QC sample was injected six times at regular intervals. Data acquired in profile mode was centroided using the vendor's algorithm and converted to mzML format with MSConvert (Holman et al., 2014). The converted files were exported to R (R Core Team, 2018). Untargeted data of biological samples was pre-processed with XCMS 3.11 and feature quality was inspected with the MetaboMeeSeeks package in R (Beirnaert, Peeters, et al., 2019; Smith et al., 2006). Internal standards were inspected for intensity, area, mass accuracy and peak width in order to guide the choice of XCMS parameters. Peak picking was performed using *CentWav*e with a peak width ranging from 5 to 60 s for HILIC-MS ESI (-) mode and 5 to 30 s for HILIC-MS ESI (+) mode, maximum tolerated mass error of 20 ppm, minimum difference in *m/z* of 0.01 for peaks with the same retention time, S/N threshold equal to 5 and noise set to 500 based on the noise signal of the Agilent 6530 QTOF. Alignment was performed with the *Orbiwarp* algorithm using a pooled QC as center sample. Features were grouped with the *PeakDensity* algorithm, followed by integration of missing peaks with chromatogram filling. Subsequently, blank filtration (fold change of 3) was performed with the BlankCheckR function of the MetaboMeeSeeks package. Features showing MS/MS spectra were annotated by comparison of accurate mass, retention time and MS/MS fragmentation with in-house libraries, using MS-DIAL (v.4.24) with the All Public MS/MS library (v.15) for ESI (+) and (-) modes (Tsugawa et al., 2015), HMDB (Wishart et al., 2022) and METLIN (Smith et al., 2005a). Annotated features assigned with a level 1 or 2 confirmation according to the recommendations of Schymanski *et al.*, were considered in detail (Schymanski et al., 2014). A general overview of the method performance was illustrated through the numbers and chromatographic distribution of detected features, in combination with their respective data quality represented by their peak width and relative standard deviation.

3.6. Results and discussion

3.6.1. Screening of LC columns

The selection of the appropriate LC column is a critical step in the method development of LC-MS based metabolomics platforms. The tested columns in this study varied in terms of the chemistry of the stationary phase and the column dimensions. For this

latter reason, the columns were not compared based on their full potential, which would require the use of hydrodynamics equations for comparison and in-depth evaluation of kinetic parameters (Desmet et al., 2005), but rather on the results obtained during a first screening experiment (*cf. infra*) based on the column chemistry in the scope of further method optimization. The main goal of this latter optimization was to study the effect of different LC parameters (e.g., mobile phase composition, type of modifier,…) on the retention mechanisms of polar metabolites in combination with MS analysis.

The stationary phase of the iHILIC-Fusion column contains negatively charged sulfate and phosphate groups, and a charged quaternary amine, resulting in a slightly negative net surface charge. For this reason, this column was only used in ESI (+) mode, since anionic compounds, such as organic acids, are not expected to be retained efficiently on this stationary phase due to repulsive effects. The opposite applies for the iHILIC-Fusion(+) column, which was tested only in ESI (-) mode due to its permanent positive net surface charge which would repel protonated basic metabolites (Cuykx, Negreira, et al., 2017; Greco & Letzel, 2013; Vosse et al., 2018). The iHILIC-Fusion(P) column was tested in ESI (-) mode due to its polymeric material stable at high pH (≈ 10), which might improve the retention and ionization of acidic metabolites.

Figure 3.8 summarizes the panel of analytical standards used for the column screening with their summed scores based on peak shape, intensity and retention time. Using the ACQUITY HSS T3 column, 34% of detected analytes eluted close to the void time ($t_0 \leq RT \leq 1.1\ t_0$) in ESI (-) mode. For the HILIC methods, there were no analytical standards eluting close to the void time, highlighting the applicability of HILIC for the retention and separation of polar compounds.

The number of detected analytes was dependent on the used LC column and ionization mode. In ESI (-) mode, the percentage of detected compounds varied between 40% for HILICpak VT-50 2D and 84% for iHILIC-Fusion(P), while in ESI (+) mode, the percentage varied between 55% for ACQUITY HSS T3 and 63% for iHILIC-Fusion. The limited detection rate can be explained by the wide range of different properties of the analytes and the need of ionization before MS detection, since some metabolites are more easily converted to cations than anions (e.g., carnitines), while the opposite applies for other metabolites such as organic acids. Detailed results can be found in Table 3.3.

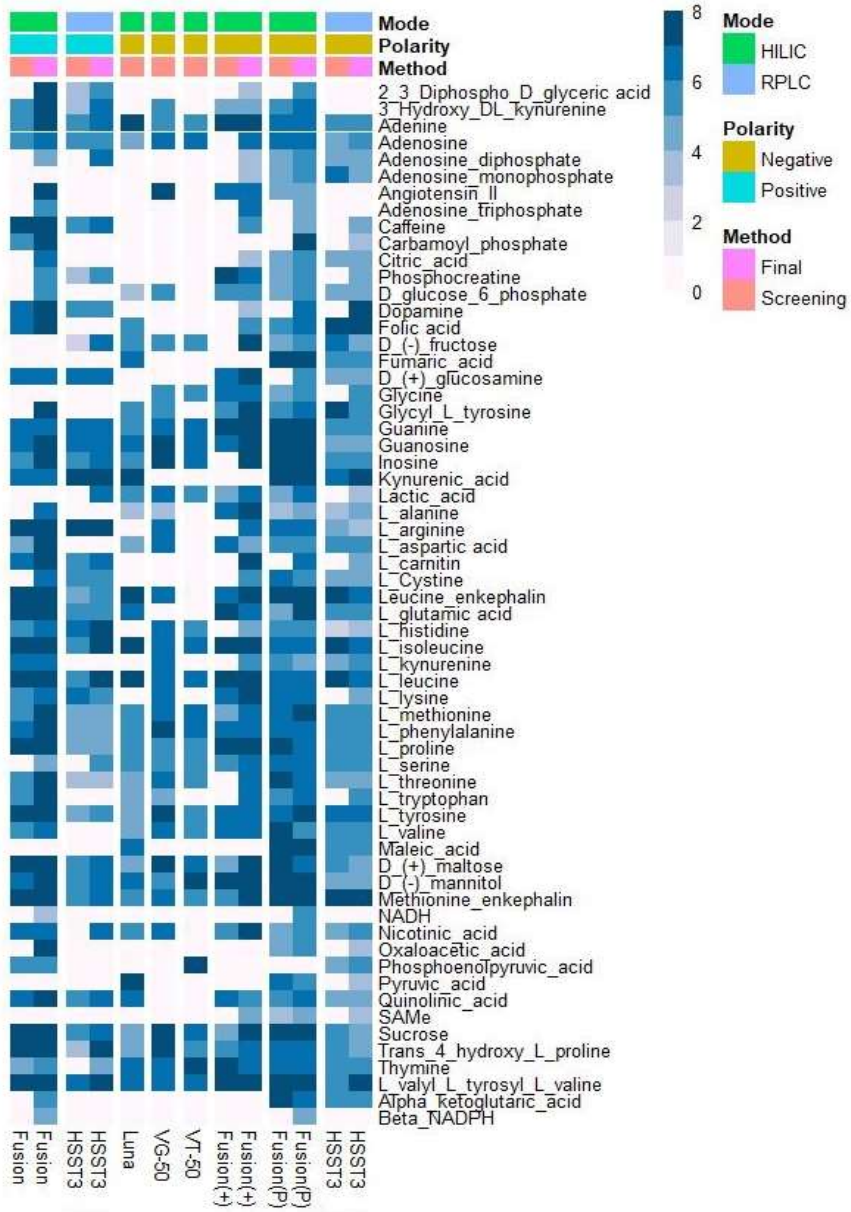

Figure 3.8 Heatmap showing the coverage of the standard mixture during column screening and acquisition with the final optimized methods. Scores are based on peak shape, peak intensity and retention time. The higher the score, the better the peak quality. Note that the Luna, VG-50 and VT-50 column were only used during the column screening experiment. Column's legend: Fusion: iHILIC-Fusion, HSST3: ACQUITY UPLC HSS T3, Luna: Luna HILIC, VG-50: HILICpak VG-50 2D, VT-50: HILICpak VT-50 2D, Fusion(+): iHILIC-Fusion(+),Fusion(P): iHILIC-Fusion(P). HILIC: Hydrophilic interaction liquid chromatography. RPLC: Reversed-phase liquid chromatography. SAM: S-adenosyl-L-methionine. NADH: Nicotinamide adenine dinucleotide. β-NADPH: β-Nicotinamide adenine dinucleotide phosphate.

Table 3.3 Percentage of analytical panel standards detected using different LC-columns during column screening experiments. Details on the used columns and methods can be found in Table 3.1. HILIC: Hydrophilic interaction liquid chromatography. U(H)PLC: Ultra (high) performance liquid chromatography. HSS: High strength silica. RPLC: Reversed-phase liquid chromatography. ESI: Electrospray ionization.

Column	A	B	C	D	E	F	G	H
Commercial name	HILICON iHILIC-Fusion UHPLC	Waters ACQUITY UPLC HSS T3	Waters ACQUITY UPLC HSS T3	Phenomenex Luna HILIC	HILICON iHILIC-Fusion (+) UHPLC	HILICON iHILIC-Fusion(P)	Shodex HILICpak VT-50 2D	Shodex HILICpak VG-50 2D
Separation mode	HILIC	RPLC	RPLC	HILIC	HILIC	HILIC	HILIC	HILIC
MS mode	ESI+	ESI+	ESI-	ESI-	ESI-	ESI-	ESI-	ESI-
%detected standards	63	55	71	60	53	84	40	60
Summed quality score	270	196	261	221	225	342	152	250

The ACQUITY HSS T3 column showed a substantial degree of co-elution between 1.5-4 minutes, both in ESI (+) and (-) modes. Broad peaks were observed, especially for basic compounds, due to secondary interactions with residual silanol groups of the stationary phase. The HILICpak VG-50 2D column showed good separation for most analytes, but broad peaks for amino acids e.g., L-aspartic acid and L-histidine, while some small organic acids, such as fumaric acid and maleic acid, could not be detected. Both the Luna HILIC column and the HILICpak VT-50 2D column showed a poor quality for eluting panel standards with substantial tailing. For example, L-arginine, L-aspartic acid, L-histidine and quinolinic acid had a peak tail of over four minutes using the Luna HILIC column. Broad peak shapes are a common issue in HILIC mode, due to the complex interactions such as proton donor and/or acceptor interactions. In addition, significant tailing for positively charged metabolites can be induced by their adsorption on the negatively charged silica. This effect can be anticipated through adjustment of the eluent strength according to the type of interaction of the stationary phase; or by using polymeric columns. During the column screening, the iHILIC-Fusion(+) and iHILIC-Fusion showed the least tailing.

The interaction mechanisms in HILIC, especially zwitterionic columns, are extremely diverse. They involve physical, intermolecular and chemical interactions between analyte and eluent and analyte and stationary phase (Buszewski & Noga, 2012). Due to the complementarity of ESI (+) and (-) modes, some compounds were only detected in

ESI (+) mode (e.g., acylcarnitines, caffeine) and others only in ESI (-) mode (e.g., small organic acids, nucleotides). Based on the summed quality scores, the number of detected standards and the method complementarity showed in Figure 3.8, the iHILIC-Fusion (ESI (+) mode), ACQUITY UPLC HSS T3 (ESI (+) and (-) mode), iHILIC-Fusion(+) (ESI (-) mode) and iHILIC-Fusion(P) (ESI (-) mode) were selected for further method optimization.

3.6.2. Method optimization for selected columns

Full factorial designs are extremely useful to investigate the main effects on the response, covering all possible combinations of the investigated factors at the selected levels. However, a decision tree-based univariate method optimization was chosen due to its time-saving properties and straightforward interpretation compared to a multiple-response full factorial approach. Furthermore, the factors that most significantly affect analysis were already known (i.e., solvent polarity and pH). In comparison, approximately 10 to 40 standard injections were needed with each LC column using the knowledge-based univariate method optimization, while a full-factorial design with 6 factors at only 3 levels (3^6) would correspond with 729 standard injections per LC column resulting in approximately 292 hours of data acquisition per column (not including blank injections, replicates, column equilibration and cleaning). Response surface designs were also considered, but due to the number of factors to be considered (> 4), lack of information about quadratic effects, and the exploratory goal of this work, the decision tree was still more adequate. The decision tree procedure allowed to change the chromatographic settings based on metabolite-stationary phase-mobile phase interactions in real time. In addition, this approach assisted in the decision to stop the optimization for one given column at a certain moment, allowing more time to optimize methods for more promising columns, when results are more dependent on the column chemistry than on the chromatographic settings. The results of iHILIC-Fusion (ESI (+) mode), ACQUITY UPLC HSS T3 (ESI (+) and (-) mode), iHILIC-Fusion (+) (ESI (-) mode) and iHILIC-Fusion(P) (ESI (-) mode) after optimization are shown in Figure 3.8. Based on these results, two zwitterionic columns were selected as the best fit for polar metabolites, the iHILIC-Fusion(P) in ESI (-) mode and the iHILIC-Fusion in ESI (+) mode (Figure 3.9). The effect of different factors, such as solvent, modifiers and temperature, is discussed in detail for the columns selected for the final methods in the following paragraphs. The results of the method optimization for the iHILIC-Fusion(+) column and RPLC column can be consulted in the supplementary information of this chapter (3.8.2. and 3.8.3.).

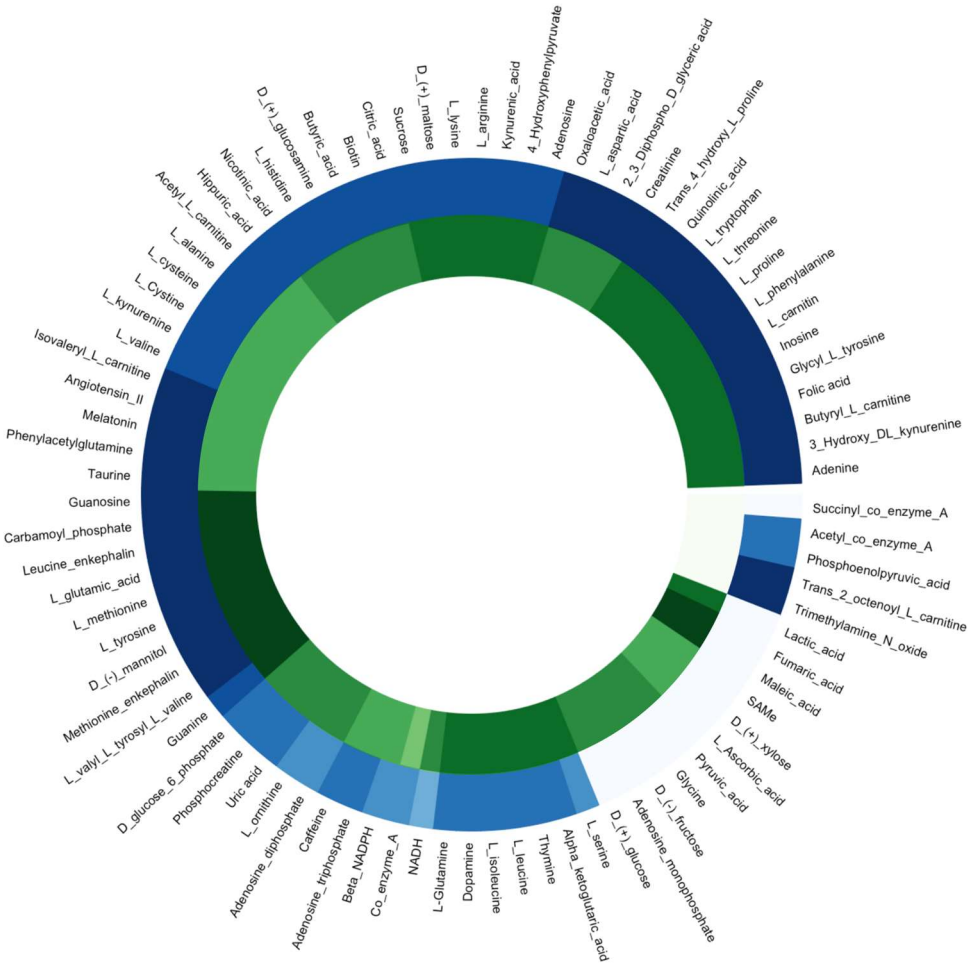

Figure 3.9 Circular heatmap showing the coverage of the standard mixture with the final optimized methods. Positive ionization mode is shown in a blue based color pallet and negative mode in a green based color pallet. The darker the color, the higher the summed score quality based on peak shape, intensity and retention time ranging from 0 to 8. Abbreviations: SAM: S-adenosyl-L-methionine. NADH: Nicotinamide adenine dinucleotide. β-NADPH: β-Nicotinamide adenine dinucleotide phosphate.

3.6.2.1. Mobile phase solvent composition

Using the iHILIC-Fusion column in ESI (+) mode, a buffered aqueous mobile phase A (0.1% (v/v) HCOOH + 10 mM $HCOONH_4$, pH 3.5) was initially combined with ACN as mobile phase B. The addition of 10% (v/v) MeOH to mobile phase A slightly increased the summed quality score, increasing retention and slightly increasing the intensity of the chromatographic peaks. Longer retention times can be explained by the lower elutropic strength of MeOH compared to H_2O, while higher intensities are observed due

to a higher ionization efficiency. Addition of 5% (v/v) MeOH to mobile phase B decreased the summed quality score by 8%. This latter decrease in quality score was mainly due to a deteriorated peak shape of some amino acids, such as L-arginine, L-leucine and L-isoleucine. In addition, most analytes showed a slightly earlier retention time when MeOH was added to mobile phase B, due to the higher elutropic strength of MeOH, compared to ACN (Buszewski & Noga, 2012). By adding MeOH to the mobile phase A and B, the summed quality score decreased further by 14%. Next to the deteriorated peak shape for the previously mentioned amino acids, a similar effect was observed for nucleosides, such as adenosine and inosine.

For the iHILIC-Fusion(P) in ESI (-) mode, H_2O with 5 mM $(NH_4)_2CO_3$ (pH 8.7) was initially used as mobile phase A and ACN as mobile phase B. The addition of 10% (v/v) MeOH to mobile phase B and addition of 20% (v/v) MeOH to mobile phase A caused a decrease of the summed quality score of 14% and 10% respectively. The addition of MeOH to both mobile phase A and B decreased the summed quality score by 19%. The addition of MeOH to mobile phase B mainly influenced the start of the run, due to the applied HILIC gradient, starting at a composition with a high organic content. MeOH caused peak splitting for peptides, such as leucin enkephalin and methionine enkephalin and tailing for amino acids (e.g., L-threonine) and small peptides (e.g., glycyl-L-tyrosine). The peak shape deterioration could partly be explained by the mismatch of mobile phase and sample solvent, which could be solved by changing the reconstitution solvent. In addition, alcohols such as MeOH can compete for active polar sites on the stationary surface and analytes, forming hydrogen bonding interactions and interfering with the retention mechanisms. After all, polar protic solvents can be both donors and acceptors of hydrogen bonds, while aprotic solvents, such as ACN, can be only hydrogen bond acceptors. Hydrogen-bonding interactions between MeOH and analytes may introduce extra resonance structures and cause broad or tailing peaks (Hao et al., 2008). A decrease in the intensity of several panel standards was observed when MeOH was added to the mobile phase. The decrease was especially significant for organic acids and amino acids. L-serine and phosphocreatine were not detected, since the S/N ratio of their corresponding signal dropped below 3. The decrease in peak intensity could be caused by a lower ionization efficiency, due to the higher content of MeOH. In comparison to MeOH, ACN has a lower viscosity, facilitating a higher ionization efficiency in ESI due to production of finer droplets (Yanes et al., 2011). In addition, the retention time of most panel standards was reduced slightly, due to the stronger elutropic strength of MeOH compared to ACN and to the MeOH-induced decrease of the polarity of the dynamically immobilized aqueous layer on the stationary phase, impeding the retention of polar compounds (Hao et al., 2008). Using MeOH in both mobile phase A and B, no improvement was observed in peak shape or intensity for a

single panel standard. In addition, peak shape deterioration, such as tailing and peak splitting, was observed for several panel standards. The decrease in intensity of organic acids and amino acids became more intense with an increasing content of MeOH.

3.6.2.2. Mobile phase pH and modifiers

A significant number of metabolites in important metabolic pathways are ionizable compounds, such as amino acids and TCA cycle intermediates. Salts present in the mobile phase, such as ammonium acetate, can precipitate in some organic-aqueous compositions, depending on their solubility and concentration, causing drastic damage to mass spectrometers (Schellinger & Carr, 2004). Therefore, the concentration of salts and its combination with organic solvents during the chromatographic run were taken into account during the development of the methods.

Using the iHILIC-Fusion in ESI (+) mode, the aqueous mobile phase was firstly modified with 0.1% HCOOH in H_2O/MeOH (9/1, v/v). The addition of 10 mM of $HCOONH_4$ increased the total summed quality score by 20%, reducing peak splitting for compounds such as 3-OH-DL-kynurenine, maltose, fructose and other panel standards with hydroxyl groups. This can be explained by the stationary phase of iHILIC-Fusion which contains hydrogen bond acceptors (S=O and P=O) and buffering with $HCOONH_4$ can affect hydrogen bond interactions positively. However, an increase in its concentration to 20 and 30 mM did not improve the total score, on the contrary, the peak shape score decreased by 30% and 35%, respectively. Additionally, an aqueous mobile phase (0.1% of CH_3COOH in H_2O) in ESI (+) mode was buffered with CH_3COONH_4 with concentrations ranging from 10-30 mM and pH 4.6-5. The use of CH_3COONH_4 decreased the quality score by approximately 19%, due to the increase of alkalinity of the mobile phase which can deprotonate acidic compounds. The iHILIC-Fusion column has a net charge varying between 0 and -1 depending on the pH of the mobile phase. A negative net charge can cause repulsive interaction between deprotonated compounds and the stationary phase, which can explain the poor peak shape at pH > 4. Therefore, 10 mM $HCOONH_4$ with 0.1% HCOOH (v/v) at pH 3.5 was chosen to proceed as the buffer solution in ESI (+) mode.

Using the iHILIC-Fusion(P) in ESI (-) mode, the starting conditions included a mobile phase A at pH 8.7, pH 7.6 or pH 2.9, adjusted with $NH_{3(aq.)}$ and HCOOH. The acidic pH resulted in a 34% decrease of the total summed quality score, in contrast with the results for pH 7.6, where the quality score increased by 10%. The effect at low pH can be explained by the protons in the mobile phase that can protonate anionic compounds, giving them a more hydrophobic character, reducing the interactions with the iHILIC-Fusion(P) column. At low pH, the intensity score decreased, especially for L-valine and L-phenylalanine that would be positively charged. They were not detected due to poor

ionization efficiency in ESI (-) mode at acidic pH. The addition of 2 mM of $(NH_4)_2CO_3$ to the mobile phase (pH 8.4) increased the total score by 20%, since it keeps a more stable pH over injections compared to NH_3, due to a lower volatility. Different modifiers ($HCOONH_4$, CH_3COONH_4) and concentrations (2-10 mM) were tested. Higher concentrations of modifiers are generally used to increase the polar eluent strength and improve the peak shape, but it also can suppress the electrostatic interactions by titrating the stationary phase ions (Chirita et al., 2010; Jiang et al., 2006). Anionic compounds, especially organic acids could benefit from higher concentrations of buffers to decrease repulsive effects with the column stationary phase which has a net charge varying between 0 and -1. However, chromatographic runs tested with higher amounts of salts in the mobile phase (>20 mM) caused significant signal decrease over approximately ten injections. The combination of 2 mM CH_3COONH_4 and 2 mM $(NH_4)_2CO_3$ as mobile phase A and ACN as mobile phase B showed the highest total quality score with a chromatographic signal for 85% of the analyzed panel standards. After optimization of the pH and the modifier concentration, additional analytical runs were performed using 10% (v/v) MeOH in mobile phase B. Addition of MeOH enabled the detection of a higher number of organic acids with a better peak shape. The summed quality score increased by 16%, highlighting the complexity of interactions between the chosen modifier and mobile phase and its influence on retention of analytes. Most undetected compounds, such as caffeine and acylcarnitines, could be detected in ESI (+) mode, pointing out the power of method complementarity.

3.6.2.3. Column temperature

Column temperature is an important parameter to optimize because of its influence on mobile phase viscosity, analyte diffusivity and amount of energy for the analyte partitioning between the mobile phase and the aqueous layer on the stationary phase within HILIC (Letzel, 2019).

In ESI (+) mode, no significant differences were observed when the column temperature was increased from 30 °C to 40 °C. However, the summed quality score increased slightly at 50 °C and 60 °C with 3% and 4%, respectively. The increase in the temperature reduced tailing and FWHM for amino acids, sugars, and small chain acylcarnitines. This latter effect can be explained by the temperature induced increase of the diffusion coefficient, resulting in narrower peaks (Hao et al., 2008). Additionally, butyric acid was only detected using a high column temperature of 50 °C or above, which might be due to enhancement of electrostatic interactions between the anion and the charged stationary phase at higher temperatures (Letzel, 2019). No significant differences were observed regarding signal intensity.

Increasing temperature can decrease the retention time of neutral molecules due to the exothermic nature of partitioning of analytes between the organic mobile phase with a high ACN content and the hydrophilic aqueous layer. For charged analytes separated on a charged surface, a temperature increase can result in stronger retention due to strong electrostatic interactions. Depending on the analyte and the contribution of partitioning or electrostatic interactions, column temperature could change the elution order and selectivity (Hao et al., 2008; Letzel, 2019). For the zwitterionic iHILIC-Fusion column in ESI (+) mode, the retention of the panel standards was more or less independent of temperature, with a negligible median reduction in retention time of 0.06 min at 60 °C. This behavior suggests a low enthalpic contribution and a high entropic contribution to the retention.

In ESI (-) mode, elevating the column temperature from 30 °C to 40 °C, 50 °C and 60 °C increased the summed quality score slightly by 2%, 4%, and 1%, respectively. As with the iHILIC-Fusion in ESI (+) mode, no significant temperature dependent differences were observed regarding signal intensity and the peak shape improved with increasing temperature. However, a column temperature of 60 °C caused peak splitting for several organic acids, such as pyruvic acid, L-ascorbic acid and α-ketoglutaric acid and fronting for kynurenic acid. These latter effects were not observed at lower temperatures and were reproducible. The true reason behind the peak shape deterioration of organic acids is unknown but might be affected by the lower thermal conductivity of the PEEK column material compared to stainless steel. At high temperatures, the lower thermal conductivity might cause a temperature gradient within the column, causing peak shape deterioration. Increasing the column temperature from 30 °C to 60 °C slightly shortened the retention time for the panel standards with a median reduction of 0.1 min. The decrease in retention time showed a maximum at 0.46 min. Based on the column temperature experiment, 50 °C was selected as optimal temperature.

In addition, the method using a temperature of 50 °C was compared to the same method at room temperature (25 °C), bypassing the heat exchanger and/or the inline filter and MS diverter valve. Bypassing the heat exchanger decreased the summed peak shape score by 10% but increased the summed intensity score by 7%. Bypassing the heat exchanger, inline filter and MS diverter valve decreased the summed peak shape score further by 16% and increased the summed intensity score with 12%. For example, for carbamoyl phosphate and α-ketoglutaric acid, the S/N value increased with 103% and 121%, respectively, when the heat exchanger was bypassed and with 135% and 162% when the heat exchanger, inline filter and MS diverter valve were bypassed. Bypassing the heat exchanger did negatively impact the peak shape through elimination of the increased diffusion coefficients induced by high column temperatures. This latter effect was seen as e.g., tailing for some amino acids (L-tryptophan, L-serine) and L-

carnitine. The rationale behind the bypassing of the heat exchanger, inline filter and MS diverter valve was based on the chelating interaction of anionic metabolites, such as carboxylic acids and phosphorylated anions with trace metals from the concerned hardware, resulting in a negative impact on the peak shape and lower peak intensities impairing sensitivity (Pesek et al., 2011; Soga et al., 2009). For the same reason, a polyether ether ketone (PEEK) iHILIC-Fusion(P) column was used instead of a stainless steel column. Alternatively, addition of a strong metal chelator such as EDTA as a mobile phase additive could enhance the detection of acidic metabolites and phosphorylated analytes. However, EDTA is highly ionizable and can cause substantial ion suppression (Pesek et al., 2011). Based on the results of the temperature experiment, bypassing the heat exchanger at room temperature was selected for the final method due to the sensitivity improvement. Despite the higher signal intensities acquired when the heat exchanger, inline filter and MS diverter valve were bypassed, the inline filter and MS diverter valve were retained in the method in order to avoid system contamination during analysis of complex biological samples.

3.6.2.4. Gradient and flow

Several gradients were tested to result in an evenly distribution of the analytical panel standards in the retention time dimension. Generic HILIC gradients started with a high amount of organic solvent, which was kept for 1-4 min depending on the column length, followed by a gradual increase in the amount of polar solvent (water) to a maximum of 80%. The re-equilibration step is crucial for HILIC columns to allow its return to the initial layer conditions in the entire column. The generic and optimized gradients are described in Table 3.1 and Table 3.4, respectively.

In parallel with gradient optimization, flow rates of 0.20–0.30 mL/min were tested; higher flow rates were not considered taking maximal tolerable backpressures into account. For the iHILIC-Fusion(P) and the iHILIC-Fusion column, flow rates of 0.20 mL/min and 0.25 mL/min were selected respectively, based on the balance between analytical speed and chromatographic resolution, which increased and decreased respectively when higher flow rates were applied. The larger decrease of chromatographic resolution with increasing flow rate for the iHILIC-Fusion(P) column compared to the iHILIC-Fusion column can be explained by the smaller particle size of the latter.

Table 3.4 Final liquid chromatography conditions obtained after method optimization. U(H)PLC: Ultra (high) performance liquid chromatography. HSS: High strength silica. HILIC: Hydrophilic interaction liquid chromatography. ACN: Acetonitrile. MeOH: Methanol. MS: Mass spectrometry. ESI: Electrospray ionization.

Column	A	B	C	E	F
Commercial name	HILICON iHILIC-Fusion UHPLC (100 x 2.1 mm; 1.8 µm)	Waters ACQUITY UPLC HSS T3 (100 x 2.1 mm; 1.8 µm)	Waters ACQUITY UPLC HSS T3 (100 x 2.1 mm; 1.8 µm)	HILICON iHILIC-Fusion(+) UHPLC (100 x 2.1 mm; 1.8 µm)	HILICON iHILIC-Fusion(P) (100 x 2.1 mm; 5 µm)
Temperature (°C)	60	30	30	30	25, bypassing heat exchanger
Flow rate (mL/min)	0.25	0.20	0.20	0.20	0.20
Mobile phase A	H_2O/ MeOH (9/1, v/v)	H_2O	H_2O	H_2O	H_2O
Mobile phase B	ACN	MeOH	ACN	ACN	ACN/MeOH (9/1, v/v)
Modifier mobile phase A	10 mM $HCOONH_4$ + 0.1% (v/v) HCOOH (pH 3.5)	10 mM CH_3COONH_4+ 0.1% (v/v) CH_3COOH (v/v) (pH 4.5)	5 mM CH_3COONH_4 + 0.33%(v/v) $NH_{3(aq.)}$ (pH 7.2)	0.1% (v/v) HCOOH (pH 2.9)	2 mM $(NH_4)_2CO_3$ + 2 mM CH_3COONH_4 (pH 8.4)
Gradient	Min - %B 0 – 95 4 – 95 12.5 – 60 20 – 60 21 – 95 26 – 95	Min - %B 0 – 20 4 – 20 8 – 85 14 – 85 15 – 20 20 – 20	Min - %B 0 – 5 0.5 – 5 10 – 90 12 – 90 12.1 – 5 15 – 5	Min - %B 0 – 95 1 – 95 10 – 20 14 – 20 15 – 95 20 – 95	Min - %B 0 – 95 1 – 95 10 – 20 14 – 20 15 – 95 20 – 95
MS mode	ESI+	ESI+	ESI-	ESI-	ESI-

3.6.3. Optimized methods

The optimized methods, which are described in Table 3.4, increased the number of detected analytes and the overall quality score of chromatographic peaks compared to the column screening experiment (Figure 3.8). In ESI (+) mode, the optimized methods enabled the detection of 14 and 3 additional panel standards, using the iHILIC-Fusion and the ACQUITY HSS T3 column respectively. In addition, the quality score increased with 46% and 32% respectively. In ESI (-) mode, the optimized methods enabled the detection of 9, 19 and 11 additional panel standards, using the iHILIC-Fusion(P), the iHILIC-Fusion(+) and the ACQUITY HSS T3 column respectively, while the quality score increased with 20%, 58% and 21% respectively. The circular heatmap in Figure 3.9 shows the coverage of the standard mixture using the final two methods, which are described in Table 3.4 in column A and F. Using the iHILIC-Fusion(P) column in ESI (-) mode, 80 out of 85 panel standards could be separated and detected, while using the iHILIC-Fusion column in ESI (+) mode, 73 standards could be separated and detected. Combining both ionization modes, 84 out of 85 panel standards could be separated and detected, highlighting the complementarity of ESI (+) and (-) ionization modes. The method using ESI (-) mode clearly showed better results for organic acids, such as lactic acid, fumaric acid and L-ascorbic acid, which were undetected in ESI (+) mode. On the other hand, the method using ESI (+) mode enabled the separation and detection of acylcarnitines, such as trans-2-octanoyl-L-carnitine, and amine oxides, such as trimethylamine N-oxide, which were undetected by ESI (-) mode. Succinyl-co-enzyme A was the only standard which was undetected using either method. A single standard of succinyl-co-enzyme A was prepared in a concentration of 1 µg/mL. Subsequent analysis showed the presence of co-enzyme A, suggesting degradation of succinyl-co-enzyme A, which could be caused by compound hydrolysis (Wagner et al., 2017).

Figure 3.10 shows chromatographic peak shapes for metabolites from various metabolic classes using the final two selected methods. For the optimized method applying the iHILIC-Fusion(P) column in ESI (-) mode, kynurenic acid has a negative charge at the alkaline pH of the mobile phase. Consequently, negatively charged compounds showed short retention time due to repulsive effects with the stationary phase. Amino acids such as L-isoleucine, L-leucine and L-lysine are zwitterionic at the mobile phase pH ≈ 8, thus their quadrupolar electrostatic interactions with the stationary phase became significant. An increasing number of nitrogen atoms in zwitterionic amino acids resulted in an increased retention. As a result, the retention time of L-lysine was approximately 10 min longer than the retention time of L-leucine. Neutral compounds, such as guanine, showed retention mechanisms based on hydrogen bond interactions and hydrophilic partition, eluting close to the region of most amino acids.

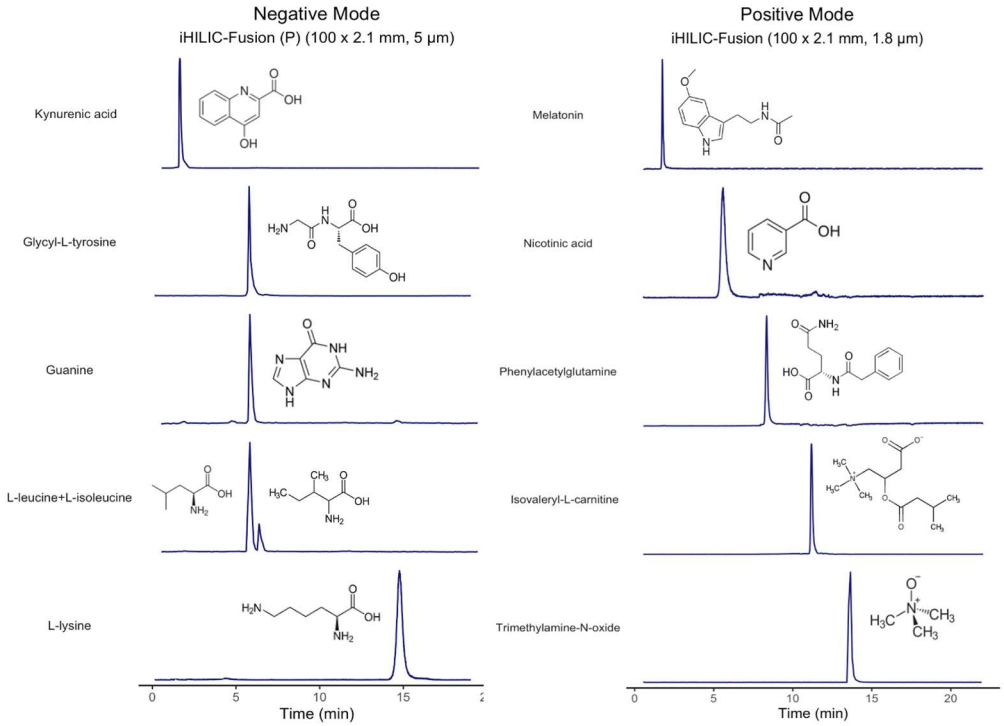

Figure 3.10 Extracted ion chromatograms of panel standards from various metabolic classes. The standards were separated and detected using the optimized methods in negative ionization mode (left) and positive ionization mode (right).

Using the optimized method with the iHILIC-Fusion column in ESI (+) mode, the acidic mobile phase conditions caused nicotinic acid to be neutral or partially positively charged, showing stronger interactions with the stationary phase and a better peak shape compared to the alkaline conditions using the iHILIC-Fusion(P) in ESI (-) mode. Trimethylamine N-oxide and isovaleryl-L-carnitine are positively charged compounds at low pH, thus ion exchange mechanisms will be dominant. In addition, the higher the carbon chain, the shorter the retention time due to hydrophobicity, for instance, butyryl-L-carnitine eluted approximately 1 min after isovaleryl-L-carnitine. Additional chromatograms for all optimized methods can be consulted in the supplementary information (Figure SI-3.1 and Figure SI-3.2).

3.6.4. Untargeted analysis of biological samples

Biological matrices containing high amounts of salts (e.g., urine and cellular extracts) and high amounts of lipids (e.g., plasma) were analyzed in order to test the analytical performance and the coverage of small polar metabolites with key biological functions. The precision of the dataset was defined by calculating the relative standard deviation (RSD) of the intensity of the features in each matrix and for each ionization mode (Figure

3.11). The median RSD (mRSD) is often used to evaluate the overall quality of the features for untargeted data analysis (Cuykx, Negreira, et al., 2017). The mRSD of the QC pooled samples in Figure 3.11 was used to assess the repeatability of the analytical method in the matrices.

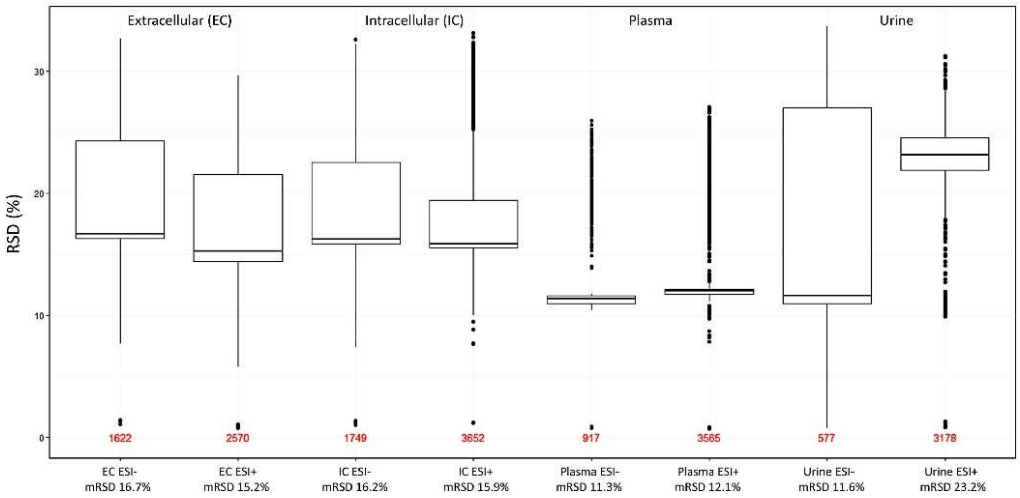

Figure 3.11 Boxplot with relative standard deviation (RSD) for QC pooled of *in* vitro (HepaRG EC and IC extracts) and *in vivo* (human plasma and urine) samples. mRSD: Median relative standard deviation. ESI: Electrospray ionization.

The mRSD of the six analytical replicates of the pooled QC sample was 15.2% for extracellular extracts of HepaRG cells (HepaRG EC) in ESI (+) mode and 16.7% in ESI (-) mode. For intracellular extracts (HepaRG IC), the mRSD was approximately 16.0% for both ionization modes. For urine, the mRSDs were 23.2% in ESI (+) mode and 11.6% in ESI (-) mode while 12.1% and 11.3% for plasma in ESI (+) and ESI (-) modes, respectively. Relative standard deviations values below 30% define a high-quality dataset for untargeted analysis which reflects a good method stability over runs with different matrices (Cuykx, Negreira, et al., 2017; Naz et al., 2014). The number of features in the QC pooled sample after blank subtraction were always higher in ESI (+) mode compared to ESI (-) mode. For HepaRG IC, HepaRG EC, plasma and urine, the number of detected features amounted 3652, 2570, 3565 and 3178 respectively in ESI (+) mode, while 1749, 1622, 917 and 577 features were detected in ESI (-) mode. In addition to mRSD and number of features, data-dependent (auto-MS/MS) acquisition was included during the analysis of each matrix to support annotations.

Features with available MS/MS spectra were matched against METLIN, MS-DIAL and HMDB databases. Urine samples showed the highest number of matches with polar metabolites. As a proof of concept, in urine samples, 90 compounds were identified at

identification level 1 or 2, including metabolites such as adenosine, L-proline, citric acid, taurine, uric acid, L-glutamine, estrone and a small number of exogenous compounds, such as bisphenol A, caffeine and vanillin.
In intra- and extracellular extracts of HepaRG cells, several amino acids, acylcarnitines and organic acids were identified, but no exogenous compounds. This was expected based on the origin of the samples and highlights a rigorous sample preparation and column cleaning, avoiding cross-contamination.
For plasma samples, in addition to amino acids such as L-tyrosine, L-proline, L-histidine, some phospholipids were detected, such as lysophosphatidylcholine 18:2 and lysophosphatidylethanolamine 18:1. This demonstrates that the sample preparation method should be optimized in order to remove lipids for matrices such as plasma, since they can cause ion suppression for small molecules.
The table with the annotations for each biological matrix with their HMDB identifier and database used for MS/MS spectra matching can be found in the supplementary information (Table SI-3.2-3.5).

3.7. Conclusions

This study handled the optimization of HILIC-MS methods using a decision tree-based univariate method optimization approach, with the objective of developing a platform that can be used to investigate polar metabolites during untargeted metabolomics experiments, applicable for different biological matrices. During method optimization, the mix-mode interaction mechanisms of two generations of HILIC columns were investigated using 85 representative analytical standards for polar metabolites from various metabolic pathways. Combining the final optimized HILIC-MS method in ESI (+) and ESI (-), almost 100% of polar standards could be separated and detected, covering key pathways of the polar human metabolome. The methods were successfully applied using different biological matrices of human origin, including urine, plasma and extracts of hepatic cells.

3.8. Supplementary information

3.8.1. Chemical standards used during method optimization

Information concerning chemical standards used during method optimization can be consulted in Table SI-3.1 of the electronic supplementary information, which is available on the link below. Extracted ion chromatograms of these analytical panel standards, analyzed using the optimized methods, are provided in Figure SI-3.1 and Figure SI-3.2 of the electronic supplementary information.
https://www.dropbox.com/sh/bvxln6vaf00q3hk/AABt5gt5XbDgsROqKY4w7ZnIa?dl=1

3.8.2. LC method optimization for the HILICON iHILIC-Fusion(+) column

3.8.2.1. Mobile phase solvent composition

For the iHILIC-Fusion(+) in ESI (-), initially H_2O with 5 mM $(NH_4)_2CO_3$ (pH 8.7) was used as mobile phase A and ACN as mobile phase B. Addition of 10% (v/v) MeOH to mobile phase B and addition of 20% (v/v) MeOH to mobile phase A caused minor changes to the summed quality score. However, addition of MeOH to both mobile phase A and B, decreased the summed quality score by 19%. Addition of MeOH to mobile phase B mainly influenced the start of the run, due to the applied HILIC gradient, starting at a composition with a high organic content. MeOH caused peak splitting for peptides such as leucin enkephalin and methionine enkephalin and tailing for amino acids (e.g., L-threonine) and small peptides (e.g., glycyl-L-tyrosine). The peak shape deterioration could partly be explained by the mismatch of mobile phase and sample solvent. In addition, alcohols such as MeOH can compete for active polar sites on the stationary surface and analytes, forming hydrogen bonding interactions and interfering with the retention mechanisms. After all, polar protic solvents can be both donors and acceptors of hydrogen bonds, while aprotic solvents such as ACN, can be only hydrogen bond acceptors. Hydrogen-bonding interactions between MeOH and analytes may introduce extra resonance structures and cause broad or tailing peaks (Hao et al., 2008). A decrease in the intensity of several standards was observed when MeOH was added to the mobile phase. The decrease was especially significant for organic acids such as pyruvic acid, α-ketoglutaric acid, lactic acid and amino acids. The lower peak intensities could be caused by an impaired ionization efficiency, due to the higher content of MeOH. In comparison to MeOH, ACN has a lower viscosity, facilitating a higher ionization efficiency in ESI due to production of finer droplets (Yanes et al., 2011). In addition, the retention time of most standards reduced slightly, which can be explained by the stronger elutropic strength of MeOH compared to ACN and by a MeOH induced decrease of the polarity of the dynamically immobilized aqueous layer on the stationary phase, impeding the retention of polar compounds (Hao et al., 2008). Addition of MeOH

to mobile phase A resolved peak splitting for nicotinic acid, kynurenine and butyric acid. Using MeOH both in mobile phase A and B, no improvement was observed in peak shape or intensity for a single standard. In contrary, there was no detection of pyruvic acid, D-glucose-6-phosphate, phosphocreatine, adenosine monophosphate, L-ornithine and L-alanine, which were all detected using the initial mobile phase composition. In addition, peak shape deterioration, such as tailing and peak splitting was observed for several standards. The decrease in intensity of organic acids and amino acids became more profound as the content of MeOH increased.

3.8.2.2. Mobile phase pH and modifiers

The starting conditions included a mobile phase A at pH 8.7, pH 7.6 or pH 2.9, adjusted with $NH_{3(aq.)}$ and HCOOH. The acidic pH resulted in a 6% increase of the total summed quality score, in contrast with the results for pH 7.6, where the quality score decreased by 11%. A pH of 8.7 showed superior intensities for organic acids such as fumaric acid, butyric acid, and kynurenic acid, while the acidic pH improved the peak shape and intensity for several sugars such as D-glucose-6-phosphate, glucosamine and fructose and amino acids such as L-arginine and L-lysine. The iHILIC-Fusion(+) has a stationary phase which is permanently positively charged, thus electrostatic interactions will play an important role in increasing the retention of anionic species at alkaline pH values. Contrarily, at an acidic pH, the peak shape of compounds with a neutral net charge were improved by reducing strong ionic interactions, for instance, nicotinic and quinolinic acid in Figure SI-3.3. For zwitterionic amino acids, the retention mechanisms are especially complex and based on quadrupolar electrostatic interactions (Dinh et al., 2011). Moreover, it was noted that π-π interactions can play a role in the retention, since L-tyrosine (containing aromatic double bonds) had a slightly longer retention time compared to L-lysine, even though L-lysine has an additional nitrogen, which usually increases retention.

The addition of a salt modifier to the mobile phase did not improve the summed quality score. Thus, the method with aqueous mobile phase at pH 2.9 modified with HCOOH and ACN as organic solvent was classified as a suitable method for polar metabolites, especially for sugars and related polyols.

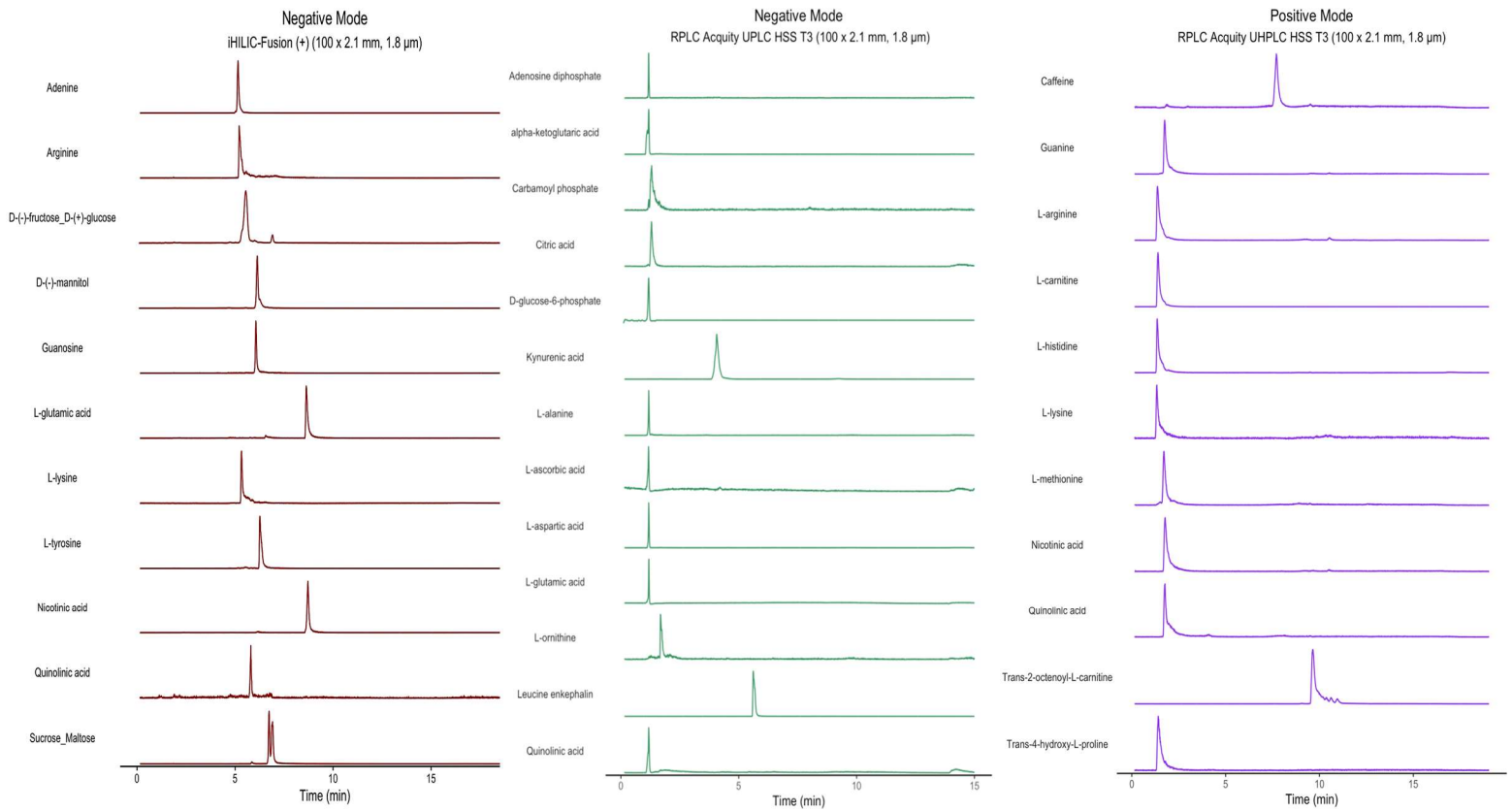

Figure SI-3.3 Extracted ion chromatograms for analytical panel standards analyzed using the optimized method for the iHILIC-Fusion(+) column in negative electrospray ionization (ESI) mode (left), the ACQUITY HSS T3 column in negative electrospray ionization (ESI) mode (middle) and the ACQUITY HSS T3 column in positive electrospray ionization (ESI) mode (right).

3.8.2.3. Gradient

Several gradients were tested to result in an evenly distribution of the analytical panel standards in the retention time dimension. HILIC generic gradients started with a high amount of organic solvent, which was kept for 1-4 min depending on the column length, followed by a gradual increase in the amount of polar solvent to a maximum of 80%. The re-equilibration step is crucial for HILIC columns to allow its return to the initial layer conditions in the entire column. The generic and optimized gradients are described in Table 3.1 and Table 3.4, respectively.

3.8.2.4. Column temperature and flow

Since, the most suitable HILIC columns were selected for further method optimization, no flow rate or column temperature experiments were conducted for the iHILIC-Fusion(+) column.

3.8.3. LC method optimization for the Waters ACQUITY HSS T3 column

3.8.3.1. Mobile phase solvent composition

In ESI (+), MeOH was preferred over ACN as the organic mobile phase since ACN caused greater tailing factor values for most compounds under investigation. Some of the most extreme differences in tailing factor were observed for the protonated adducts of L-kynurenine, trans-2-octenoyl-L-carnitine and glycyl-L-tyrosine with an average tailing factor of 4.2, 4.2 and 4.0 using ACN and 0.9, 0.9 and 1.5 using MeOH, respectively. This latter effect can be explained by the ability of methanol to form hydrogen bonds with residual silanol groups, a property lacked by ACN (Nawrocki, 1997). The formation of these hydrogen bonds can prevent tailing by impeding the interaction between residual silanol groups and basic moieties of analytes. A disadvantage of using MeOH as the organic mobile phase is the higher backpressure, compared to ACN, which puts more strain on the LC system components and column. During the initial gradient, a pressure difference of 150 bar was observed at 85% of the organic mobile phase, at a flow of 0.2 mL/min, due to the higher viscosity of MeOH mixtures compared to ACN.

In ESI (-) mode, the column performed slightly better when MeOH was used as organic mobile phase compared to ACN, when combined with a slightly alkaline aqueous mobile phase ($NH_{3(aq.)}$, pH 7.6). Using MeOH, a better separation and longer retention times were observed especially for peptides. For example, methionine enkephalin, leucine enkephalin and L-valyl-L-tyrosyl-L-valine had retention times of 8.7, 9.1 and 5.9 minutes respectively, using MeOH as organic solvent. In comparison, using ACN, the retention times were 3.5, 4.9 and 1.4 minutes respectively. However, the small difference in quality score was mostly due to the elution of some small polar compounds, such as glycine and L-carnitine, close to the void time ($t_0 \leq RT \leq 1.1\ t_0$), when ACN was used as

organic solvent. The shorter retention times are a direct effect of the higher elutropic strength of ACN compared to MeOH. Surprisingly, when 5 mM CH_3COONH_4 was added to the aqueous mobile phase, ACN outperformed MeOH as organic solvent, with a summed quality score difference of 11%. This latter highlights the complexity of interactions between the analytes and the stationary and the mobile phase and the importance of the mobile phase composition. When using 5 mM CH_3COONH_4 in the aqueous mobile phase, ACN or MeOH as the organic solvent had only little influence on the peak intensity score or retention time score, but a rather large difference on the peak shape score. While MeOH provided less tailing for small organic acids such as fumaric acid and maleic acid, ACN improved the peak shape of several amino acids, nucleobases and nucleosides by resolving the problem of peak splitting. In addition, slightly higher intensities were observed when ACN was used. The improved quality score could be explained by a combination of effects. Firstly, using ACN as organic mobile phase, there was a higher similarity with the sample solvent, avoiding peak shape distortion due to mismatches. Secondly, ACN has a lower viscosity compared to MeOH, which can increase the ionization efficiency in ESI due to production of finer droplets. Thirdly, ammonium acetate promotes the formation of deprotonated analytes in the gas phase during ESI (Yanes et al., 2011).

3.8.3.2. Mobile phase pH and modifiers

The RPLC column did not provide enough retention for most panel standards, including nucleosides, nucleobases and various organic acids, indicated by their elution close to the void, despite the use of different mobile phase pH values and modifiers. An acidic pH of aqueous mobile phase (A) was achieved using 0.1% (v/v) of HCOOH in ESI (+) mode which was enough to provide high ionization (S/N ≥ 50) for 60% of panel standards, but with poor retention and peak width often higher than 1 min. An aqueous ammonia solution and $(NH_4)_2CO_3$ were used to adjust the pH to values ranging from 7.2 to 8 in ESI (-) mode. For example, compounds with pKa < 3 will be neutral at pH < 3, which would theoretically improve the retention of acidic compounds on reversed-phase columns. However, a neutral pH buffered with 5 mM of $HCOONH_4$ and aqueous ammonia solution (pH 6.6) showed better results for most classes, including amino acids and peptides, increasing the retention of several panel standards. For example, the retention time of L-proline increased by 0.5 min, for L-leucine the retention increased by 0.4 min and for leucine enkephalin, the retention time increased by 2 min in addition to the better peak shape score. This effect can be explained by the distribution of different ion forms of amino acids at different pH values. For instance, in the pH range from 5 to 7, amino acids such as L-glutamic acid and L-leucine have a predominant zwitterionic ion form with a prevalence higher than 90%.

Ammonium acetate and ammonium formate were tested in amounts ranging from 5 to 10 mM and in combination with 0.1% (v/v) of HCOOH in ESI (+) mode. Ammonium acetate affected the ionization efficiency of several panel standards, including dopamine in ESI (+) mode, by decreasing the S/N ratio and increasing the tailing factor. The addition of 5 mM of $HCOONH_4$ and 0.1% (v/v) of HCOOH (pH 3.2) provided the best summed quality score. Compounds started eluting later and showed less tailing. However, several panel standards still co-eluted around 2 min, which is far from ideal for an untargeted approach, when co-elution should be avoided as much as possible, since it can lead to significant ion suppression.

3.8.3.3. Gradient

In ESI (+) and (-) modes, a generic gradient was tested with a constant flow rate of 0.2 mL/min. The gradient profile started with 20% of organic mobile phase for 4 min, followed by an increase to 85%, which was kept for 6 min before returning to the initial conditions. In order to explore the interaction of the reversed-phase column with the analytical panel standards, three additional gradients were tested. A lower amount of water (50% instead of 95%) resulted in more co-elution in the beginning of the run. However, a high amount of water (95%) kept for 2 min in the beginning of the run showed similar co-elution profiles.

3.8.3.4. Column temperature and flow

Since the most suitable HILIC columns were selected for further method optimization, no flow rate or column temperature experiments were conducted for the Waters ACQUITY HSS T3 column.

3.8.4. Library matching results for biological samples

Information concerning library matching results for untargeted analyses can be consulted in Table SI-3.2 (intracellular extracts of HepaRG cells), Table SI-3.3 (extracellular extracts of HepaRG cells), Table SI-3.4 (human plasma), and Table SI-3.5 (human urine) of the electronic supplementary information, which is available on the link below.

https://www.dropbox.com/sh/bvxln6vaf00q3hk/AABt5gt5XbDgsROqKY4w7Znla?dl=1

CHAPTER 4:
DEVELOPMENT OF UNTARGETED PLATFORMS FOR LIPIDS

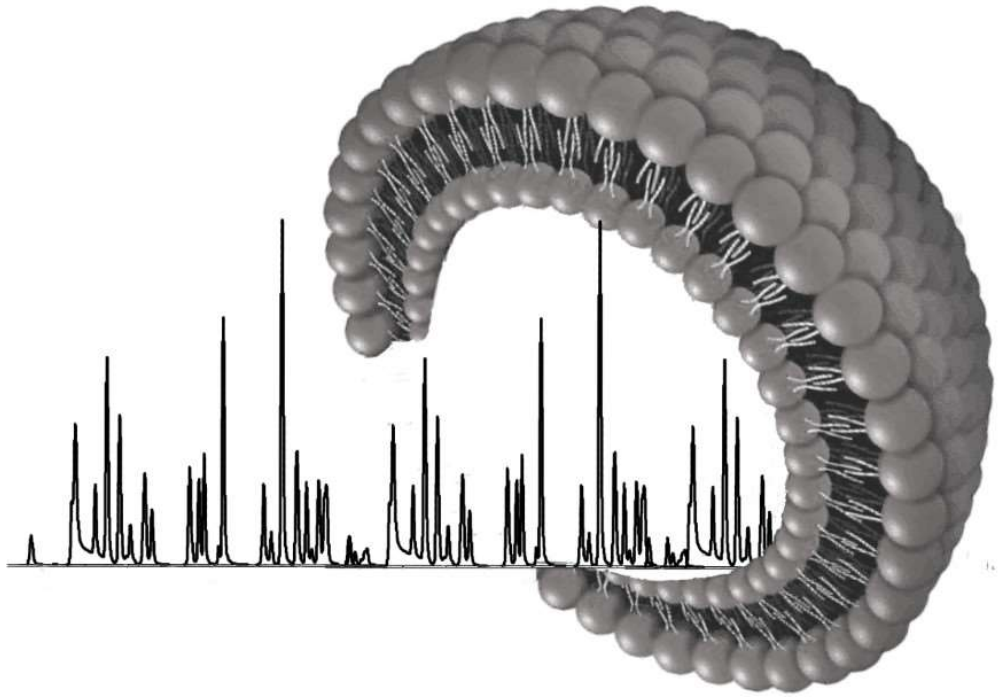

Based on the following publication

Da Silva KM*,$, **Iturrospe E*,$**, Heyrman J, Koelmel JP, Cuykx M, Vanhaecke T, Covaci A, Van Nuijs A. Optimization of a Liquid Chromatography-Ion Mobility-High Resolution Mass Spectrometry Platform for Untargeted Lipidomics and Application to HepaRG Cell Extracts. Talanta. 2021; 235, 122808. (DOI: 10.1016/j.talanta.2021.122808).

*Shared first authors.

$Contribution as in the publication. K.M.d.S.: Conceptualization, Methodology, Formal analysis, Investigation, Writing, Visualization. E.I.: Conceptualization, Methodology, Formal analysis, Investigation, Writing, Visualization.

4.1. Introduction

In recent years, lipidomics, the full characterization of the lipid molecular species of a biological system (i.e., the lipidome), has grown in popularity due to advances in instrumental detection and identification and the myriad of applications in pathogenesis elucidation, biomarker discovery and toxicity testing (Öztas & Bosgelmez, 2017). As of January 2023, the LIPID MAPS portal lists 25,756 unique curated lipid structures, divided into eight main categories: fatty acyls, glycerolipids, glycerophospholipids, sphingolipids, saccharolipids, polyketides, sterol, and prenol lipids (Figure 4.1) (O'Donnell et al., 2019). This list is non-exhaustive, with millions of possible lipid species, especially when including oxidized lipids, and other portions of the lipidome currently not fully characterized, as well as subtle isomeric details such as double bond positions, position of oxygen additions, backbone substitution, and stereochemistry (Koelmel, Aristizabal-Henao, et al., 2021; Yetukuri et al., 2008).

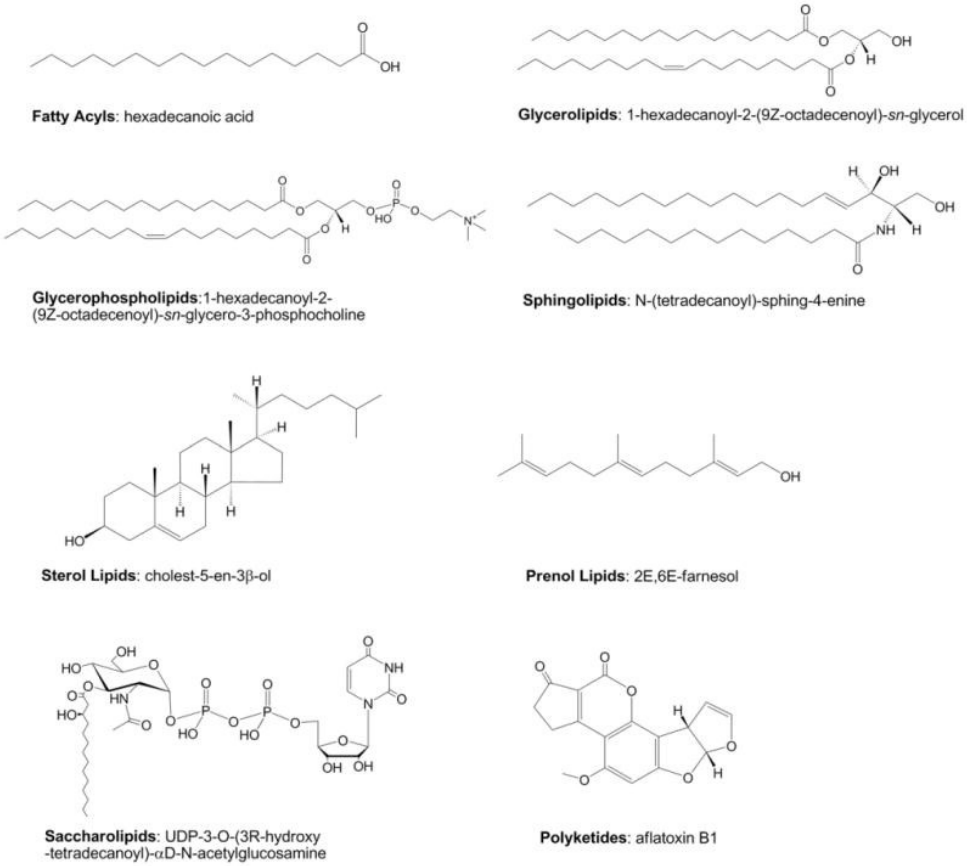

Figure 4.1 Eight main lipid categories as defined by LIPID MAPS. Representative structures for each of the lipid categories are shown (Fahy et al., 2011).

Regardless of the key role played by lipids in many physiological processes and diseases, it is often not known which specific lipids or lipid classes are affected by a specific biological condition, and the interplay of these changes across the entire lipidome largely remain to be elucidated. This latter shortcoming requires an untargeted analytical approach (e.g., fingerprinting) rather than a targeted approach of selected biomarkers. The main objective of an untargeted lipidomics method is the unbiased measurement of a wide range of lipids within a biological system. Liquid chromatography coupled to high resolution mass spectrometry (LC-HRMS) can provide near-comprehensive lipidome profiles and has therefore been widely applied in untargeted lipidomics analyses (Xu et al., 2020). The LC separation reduces co-elution of compounds and ion suppression, thus improving the compound coverage and quality of features (Xu et al., 2020). However, many lipids with the same fatty acyl chain length and level of unsaturation can have different structural isomers that might co-elute and can often not be distinguished by HRMS or MS/MS spectra alone. In this light, the hyphenation of ion mobility spectrometry (IMS) to LC-HRMS adds an additional dimension of separation, which improves the peak capacity. Certain isobaric and isomeric species not separated by LC-HRMS can be separated using ion mobility and identified through collision cross section (CCS) values derived from size and shape-dependent ion mobility behavior of analytes migrating through an inert gas (Causon & Hann, 2015; Kyle et al., 2016).

Although the implementation of IMS provides several advantages, it also faces challenges. Disadvantages of LC-IM-HRMS include reduced duty cycles and large and complex data compared to LC-HRMS data, resulting in lower sensitivity and demand for high computing power, respectively (Prost et al., 2014). Optimized instrumental acquisition and lipid identification remain fundamental steps of the lipidomics workflow to reduce the effect of interferences, expand lipid annotation coverage and accuracy and expand the linear range in lipidomics profiling (L. Li et al., 2019).

The goal of the experiments documented in this chapter was to optimize an LC-IM-HRMS platform with high lipid coverage and annotation confidence for untargeted *in vitro* cell-based experiments. An in-depth sensitivity optimization of IMS was performed by evaluating the drift tube and rear funnel voltages with a chemometrics approach and trap filling/release events with single pulse and Hadamard multiplexed modes, in the scope of finding a balance between sensitivity and detector saturation (for linear range considerations). The obtained CCS values were compared with *in silico* and experimental publicly available libraries in order to evaluate CCS error thresholds for lipid annotation.

4.2. Chemicals and materials

Methanol (MeOH), acetonitrile (ACN) and formic acid (99%) (HCOOH) UPLC/MS grade were purchased from Biosolve (Valkenswaard, The Netherlands). Ammonium formate (≥ 99%, LC-MS grade) ($HCOONH_4$), ammonium acetate LC-MS grade (CH_3COONH_4), ethylenediaminetetraacetic acid (EDTA) (99%), L-ascorbic acid (99%) and butylated hydroxytoluene (BHT, 99%) were obtained from Sigma Aldrich (St. Louis, Missouri, USA). Acetic acid (100%) (CH_3COOH) and ethanol (EtOH), both LC-MS grade, isopropanol for analysis (IPA, ACS reagent), ammonia solution (25%, LC-MS grade) and chloroform ($CHCl_3$, analytical grade) were purchased from Merck (Merck KGaA, Darmstadt, Germany). Ultrapure water (H_2O) used throughout the experiments was obtained from an Elga Pure Lab apparatus (Tienen, Belgium). Fifty lipid analytical standards were purchased from Sigma Aldrich, Avanti Polar Lipids (Alabaster, USA), Cayman Chemical Company (Michigan, USA), and Honeywell Fluka (Charlotte, NC, USA) to cover a broad variety of human lipids originating from different categories including fatty acyls (15), glycerolipids (5), glycerophospholipids (11), prenol lipids (1), sphingolipids (7) and sterol lipids (11). A detailed list of the lipid panel standards can be found in Table SI-4.1. Glyceryl tri(palmitate-1-^{13}C) and cholic acid-2,2,4,4-D_4 were purchased from Sigma Aldrich, while lauric acid-12,12,12-D_3 was bought from CDN Isotopes (Pointe-Claire, Quebec, Canada), 18:1-D_7 lyso PE from Avanti Polar Lipids and octanoyl-L-carnitine-(N-methyl-D_3) and ceramide (d18:1/18:1(9Z)-$^{13}C_{18}$) from Cambridge Isotope Laboratories (Massachusetts, USA). For the *in vitro* experiments with liver cells, differentiated HepaRG cells were acquired from Biopredic International (Rennes, France).

4.3. Sample preparation

Intracellular extracts of HepaRG cells were prepared as described in 3.3.2. The same liquid-liquid extraction (LLE) procedure was performed. Instead of adding polar internal standards during LLE, apolar internal standards were added (i.e., 20 µL of 11 µg/mL of lauric acid-12,12,12-D_3, cholic acid-2,2,4,4-D_4, glyceryl tri(palmitate-1-^{13}C), 18:1-D_7 lyso PE, octanoyl-L-carnitine-(N-methyl-D_3) and ceramide (d18:1/18:1(9Z)-$^{13}C_{18}$) in $CHCl_3$ to obtain a final concentration of 1 µg/mL). After LLE, a volume of 240 µL of the apolar fraction (lower phase) was transferred to a thermo reacti-vial. After vortexing for 20 s, 120 µL was transferred to a second thermo reacti-vial, after which the liquid was evaporated using pure, dry N_2 at room temperature. Dried extracts were stored at -80 °C and reconstituted directly before analysis. As in 3.3.2, each sample was divided in two fractions right before the evaporation step, in order to analyze each fraction using a different polarity during LC-DTIMS-HRMS acquisitions. Each sample was reconstituted on ice using 60 µL IPA/MeOH (35/65, v/v). After vortexing for 90 s, samples were filtered

using 0.2 µm nylon centrifugal filters and centrifugated at 14,000 g for 2 min at room temperature. Equal volumes of filtered sample were combined to create a quality control (QC) pool.

4.4. LC-DTIMS-HRMS data acquisition

The analytical measurements were carried out on an Agilent 1290 Infinity II LC system coupled to an Agilent 6560 drift tube-ion mobility-quadrupole-time-of-flight high resolution mass spectrometer (DTIM-QTOF-HRMS) (Agilent Technologies, Santa Clara, USA) using Agilent Dual Jet Stream Electrospray Ionization (ESI) in positive (+) and negative modes (-). Previously in-house optimized ESI source parameters for lipids in positive and negative mode were slightly adapted from Cuykx *et al.* (2017). In ESI (+) mode, nitrogen was used as drying and sheath gas, both at 325 °C with a flow rate of 8 L/min. The nebulizer gas pressure was set at 30 psig, the MS capillary voltage at 3500 V, the nozzle voltage at 500 V and the fragmentor at 200 V. In ESI (-) mode, the drying and sheath gas both had a temperature of 350 °C with a flow rate of 8 L/min. The nebulizer gas pressure was set at 30 psig, the MS capillary voltage at 3750 V, the nozzle voltage at 500 V and the fragmentor voltage at 200 V.

An LC-based lipidomics method (Cuykx, Negreira, et al., 2017) (Table 4.1) was used to screen 3 different columns: a) Kinetex XB-C18 (2.1 x 150 mm, 1.7 µm), b) ACQUITY UPLC HSS T3 C18 (2.1 x 100 mm, 1.8 µm) and c) ACQUITY UPLC BEH C18 (2.1 x 150 mm, 1.7 µm). The standard mixture of 50 lipids was injected in ESI (+) and ESI (-) modes to evaluate the column performance. As in chapter 3, a quality score system was used to select one column for further LC method optimization (Table 4.2 and Equation 4.1). For this latter LC method optimization (i.e., mobile phase composition, flow, and gradient), the lipidomics method described in Table 4.1 was used a starting point. The evaluation criteria were based on signal-to-noise (S/N) ratio, peak shape (i.e., full width at half-maximum (FWHM) and tailing factor), retention factor, and resolution (Iturrospe et al., 2021).

Table 4.1 LC-parameters used for column screening.

Parameter	Positive ionization mode	Negative ionization mode
Mobile phase A	ACN/H_2O (1/1, v/v)	MeOH/H_2O (1/1, v/v)
Mobile phase B	H_2O/ACN/IPA (2/10/88, v/v/v)	H_2O/MeOH/IPA (2/10/88, v/v/v)
Modifier	5 mM CH_3COONH_4 + 0.1% (v/v) CH_3COOH	10 mM CH_3COONH_4
Flow rate (mL/min)	0.25	0.25
Temperature (°C)	55	55
Gradient	0 min: 55% B 1 min: 55% B 5 min: 70% B 25 min: 98% B 29 min: 100% B 38 min: 55% B	0 min: 55% B 1 min: 55% B 5 min: 70% B 25 min: 98% B 29 min: 100% B 38 min: 55% B

Table 4.2 Scoring system to evaluate peak shape, peak intensity and retention time. The scoring system was used for each analytical panel standard to guide the choice of LC column and the method optimization. To calculate retention time scores, the void time (t_0) of each column was used (Kinetex XB-C18: 0.91 min, based on elution time of uracil, ACQUITY UPLC HSS T3: 1.4 min, based on elution time of thiourea, ACQUITY UPLC BEH C18: 1.1 min, based on elution time of uracil). FWHM: Full width at half maximum. S/N: Signal-to-noise ratio. RT: Retention time.

	Peak shape score		Peak intensity score		Retention time score
0	No peak	**0**	S/N < 3	**0**	No peak
1	Single peak with FWHM ≥ 0.2 and/or tailing factor ≥ 2 or ≤ 0.8	**1**	3 ≤ S/N < 10	**1**	RT = 1 to 1.1t_0
2	Single peak with FWHM < 0.2 and tailing factor < 2 and > 0.8	**2**	10 ≤ S/N ≤ 50	**2**	RT > 1.1t_0
		3	S/N > 50		

$$Quality\ Score = \sum_{i=1}^{n} Peak\ shape\ score + \sum_{i=1}^{n} Peak\ intensity\ score + \sum_{i=1}^{n} Retention\ time\ score$$

Equation 4.1 Quality score equation based on the quality score sum of Table 4.2

In the final method, the ACQUITY UPLC BEH C18 was maintained at 60 °C at a flow rate of 0.2 mL/min. The injection volume was set at 2 µL and the thermostat of the autosampler at 4 °C. The mobile phase in ESI (-) consisted of (A) ACN/H_2O (30/70, v/v) with 5 mM of CH_3COONH_4 and (B) IPA/ACN/H_2O with 5 mM of CH_3COONH_4 (88/10/2, v/v/v). In ESI (+), 0.1% (v/v) of CH_3COOH was added to the aqueous fraction. 15% (B) was kept constant for 2 min and increased to 30% at 3 min, to 60% at 5 min, which was kept constant for 3 min, to 100% at 20 min, which was kept constant for 10 min and back to 15% at 35 min for a 5 min equilibration.

For both ionization modes, data were acquired in 2 GHz extended dynamic mode with a scan range of 100-1500 *m/z.* Consecutive runs were used for data-independent acquisition (DIA) based on All-ions fragmentation with alternating frames switching between no collision energy and high collision energy (10, 20, or 40 eV). The calibrant solution was constantly infused during the run with an isocratic pump (Agilent 1260 Infinity II Isocratic Pump (G7110B)) and introduced in the ESI source by a second nebulizer. The LC-IM-HRMS data was post-processed for calibration of the mass axis using purine (*m/z* 121.0508 in ESI (+) mode and *m/z* 119.0363 in ESI (-) mode) and hexakis (1H, 1H, 3H-tetrafluoropropoxy) phosphazine (*m/z* 922.0097 in ESI (+) mode and *m/z* 980.0163 in ESI (-) mode) in IM-MS Reprocessor software (Agilent). In addition to acquired LC-DTIMS-MS/MS data-independent spectra, LC-DTIMS-MS and LC-MS/MS using data-dependent acquisition (DDA) were acquired for offline alignment (Agilent Mass Profiler). DDA was used with an MS1 scan rate of 2 spectra/sec and an MS2 scan rate of 6.67 spectra/sec, a maximum set of precursors per scan cycle of 12, and collision energies of 10, 20, and 40 eV. Ion mobility multiplexed data files were de-multiplexed using the vendor-supplied software Agilent deMP. Data files were smoothed with a kernel size of 3 for both drift and retention time and saturation repaired for points over 40% of the abundance limit using PNNL Preprocessor (Prost et al., 2014). The $^{DT}CCS_{N2}$ values were calculated using single-field calibration coefficients obtained by infusing the Agilent Tune Mix before the sequence worklist in IM-MS Browser B.08.00 (Agilent) (Stow et al., 2017).

4.5. LC-DTIMS-HRMS data processing

Data files were processed per ionization mode for peak detection, alignment, and blank filtering in Agilent Mass Profiler to obtain a feature table. Minimum peak intensity was set at 200 counts (i.e., close to the noise level of the instrument). Isotopic models were based on common organic formula without halogens. Alignment parameters included retention time (RT) tolerance ± 15% + 0.2 min, drift time (DT) tolerance ± 2.0%, and mass tolerance ± 15 ppm + 2.0 mDa. The MS/MS files were exported as Mascot Generic Format (.mgf) together with the feature tables to LipidIMMS Analyzer for a broader lipid annotation (Zhiwei Zhou et al., 2019). Moreover, the lipidomic database of MS-DIAL (v. 4.6) was used to narrow the LipidIMMS Analyzer results based on accurate mass and MS/MS fragmentation (Tsugawa et al., 2020). Converted data files (IBF format) were imported and processed using MS-DIAL. The following parameters were used for peak detection and alignment. Mass range: 100-1500 Da; retention time range: 0.5-30 min; accurate mass tolerance (MS1): 0.01 Da; MS2 tolerance: 0.025 Da; linear weighted moving average as smoothing method: 3 and 5 scans for smoothing level and minimum

peak weight, respectively; minimum peak height: 1000; mass slice width: 0.07 Da; sigma window value: 0.5; retention time tolerance for alignment: 0.05 min; MS1 tolerance for alignment: 0.015 Da; mobility tolerance for alignment: 0.2 ms; adduct ion setting: $[M+H]^+$, $[M+NH_4]^+$, $[M+Na]^+$, $[M-H_2O+H]^+$ in positive ion mode and $[M-H]^-$, $[M-H_2O-H]^-$, $[M+HCOO]^-$, $[M+CH_3COO]^-$ in negative ion mode.

In addition, MassHunter Lipid Annotator v.1.0 (Agilent) was used for annotation of DIA spectra and LipidMatch for annotation of DDA spectra (Koelmel et al., 2020; Koelmel, Kroeger, Ulmer, et al., 2017). Matched MS/MS spectra were manually evaluated to improve annotation confidence. Different data analysis pipelines were tested and combined in order to find results that are not biased towards a specific software (Figure 4.2).

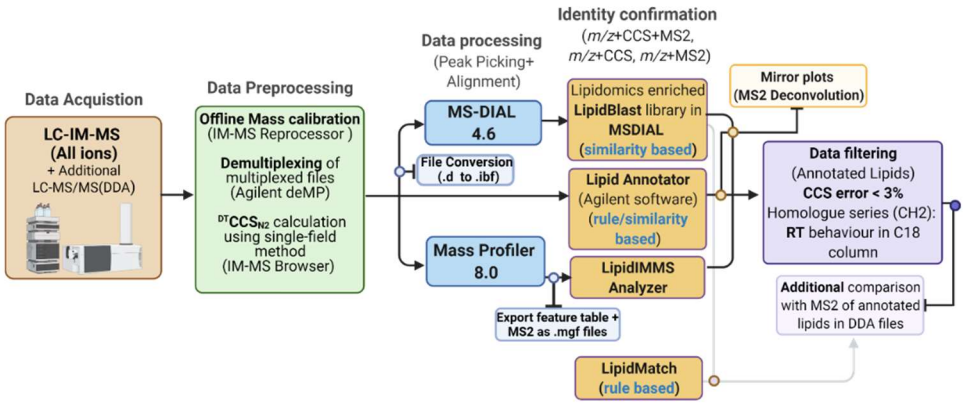

Figure 4.2 Data analysis workflow applied in this work for LC-DTIMS-MS/MS data.

To assess CCS error thresholds for annotation and to find the most accurate and accessible library for untargeted lipidomics applications, the panel lipid standard mixture was injected in both ESI (+) and ESI (-) modes with single pulse and 4-bit Hadamard multiplexing modes. The resulting $^{DT}CCS_{N2}$ values were compared to (i) experimental values found in public databases (LIPID MAPS (Sud et al., 2007), CCS compendium (Picache et al., 2019), CCSbase (Ross et al., 2020)), preferably obtained with DTIMS instruments or databases with *in silico* predicted values (CCSbase (Ross et al., 2020), LipidCCS (Zhiwei Zhou, Tu, et al., 2017), MetCCS (Zhiwei Zhou, Xiong, et al., 2017), DeepCCS (Plante et al., 2019)), when experimental values were unavailable and (ii) CCS values predicted using AllCCS (Zhiwei Zhou et al., 2020), in order to estimate the prediction performance of a single *in silico* tool.

4.6. Ion mobility spectrometry optimization

In the DTIM-QTOF-HRMS instrument, the electrodynamic ion trap funnel, located before the drift tube, radially accumulates ions by applying a radio frequency field on the stacked ring electrodes. Direct current (DC) voltages are used to axially trap and eject accumulated ions towards the drift tube (Clowers et al., 2008). The DTIMS analysis was carried out under uniform electric field conditions using high-purity nitrogen (99.999% N_2) as a buffer gas. CCS measurements were based on a single electric field calibration derived from the Mason-Schamp equation (Equation 4.2).

$$t_A = t_D + t_{fix} = \frac{\beta}{z}\left[\frac{m_i}{m_B + m_i}\right]^{1/2} CCS + t_{fix}$$

Equation 4.2 Single field equation (Stow et al., 2017). Full arrival time (t_A), drift time (t_D), slope (β), and intercept (t_{fix}) from the regression using tune mix calibrant ions, analyte mass (m_i), buffer gas mass (m_B), and ion charge state (z).

Analyses of tune mix calibrant and samples were acquired under the same conditions. To find the optimal parameters for lipidomics, a multivariate design of experiments (DOE) was applied and combined with desirability functions. This has been proven to be a valuable tool for the development of analytical methods when multiple responses need to be optimized simultaneously for a single method (Candioti et al., 2014). Since the information was already available on the main parameters and the range of the electric field to obtain accurate and precise CCS values, a two-level full factorial design screening study was discarded (Stow et al., 2017).

To optimize sensitivity for lipidomics purposes, a Box-Behnken design (BBD) was used with four key factors, including drift entrance voltage (DEV), drift exit voltage (DXV), rear funnel entrance (RFE), and rear funnel exit (RFX) voltages. BBD is a multivariate optimization technique for second order response surface modeling of numerical and categorical factors with three levels. The number of experiments (*N*) for BBD is determined by the number of factors (*k*) and central points (*Cp*) with the following formula $2k(k-1)+Cp$ (Candioti et al., 2014). For this study, a total of 27 methods including three central points were analyzed with electric fields varying from approximately 9.6 to 19.2 V/cm, rear funnel voltages varying from 200-300 V for the entrance, and 30-50 V for the exit. In addition, ion trap funnel filling and release times were investigated in single pulse and Hadamard 4-bit multiplexing mode. In single pulse mode, tested trap filling (TF) times included 10,000 µs, 20,000 µs, 30,000 µs, and 40,000 µs, while in multiplexing mode, 2500 µs, 3000 µs, 3500 µs, and 3900 µs were investigated. Tested trap release (TR) times included 150 µs, 200 µs, and 250 µs in both modes. The responses were evaluated based on the intensity of 50 panel lipids representing six lipid

classes in both ESI (+) and ESI (-) modes. A mathematical model fitting a second order polynomial equation was built for each detected lipid from the standard mixture and combined into a single composite equation called desirability in Minitab 19 (Candioti et al., 2014). The function was maximized to obtain the highest intensity values for all features in each polarity separately (Equation 4.3).

$$d_i\left(\widehat{y}_1(x)\right) = \begin{bmatrix} 0 & \text{if } \widehat{y}_1(x) < L_i \\ \left(\dfrac{\widehat{y}_1(x) - L_i}{U_i - L_i}\right)^s & \text{if } L_i \leq \widehat{y}_1(x) \leq U_i \\ 1 & \text{if } \widehat{y}_1(x) > U_i \end{bmatrix}$$

Equation 4.3 Individual desirability function (d_i) for a maximized response (Derringer & Suich, 1980). U_i is the upper limit (~10,000) and L_i is the lower limit (instrument noise intensity of ~ 200). The weight s was set to 1 for all individual equations (no factor was prioritized over another).

The desirability approach converts all function results to a numerical scale ([0,1]) and combines the responses using the geometric mean called composite desirability (Equation 4.4).

$$D = \left(\prod_{i=1}^{n} d_i\right)^{1/n}$$

Equation 4.4 Composite desirability function (D) expressed as the geometric mean of the individual desirabilities.

4.7. Results and discussion

4.7.1. Liquid chromatography

Reversed-phase liquid chromatography (RPLC) remains a valuable technique for lipidomics analysis. In addition to reduction of ion suppression, RPLC provides retention times for the lipids under investigation, which can improve annotation confidence. After lipid annotation, filtering by elution profile (within the same class, larger carbon chain and saturation number result in increasing and decreasing retention times, respectively) provides a data quality tool to reduce the number of incorrectly annotated species. This approach is especially valuable for saturated and monounsaturated fatty acids that often undergo low fragmentation in LC-ESI-QTOF-MS/MS (Ovčačíková et al., 2016).

After injection of the panel lipid standard mixture, an overall chromatographic quality score was calculated for each tested LC column and both ionization modes separately. Signal-to-noise (S/N) ratio, peak shape (i.e., FWHM and tailing factor), and retention

factor were used for calculation of the quality score. Detailed results on the overall quality score can be found in Table 4.3.

Table 4.3 Percentage of analytical panel standards detected and overall quality score of chromatographic peaks during screening of LC columns and during analysis using the optimized LC method. XB: Cross-butyl. UPLC: Ultra performance liquid chromatography. HSS: High strength silica. BEH: Ethylene bridged hybrid. ESI: Electrospray ionization.

	----------COLUMN SCREENING----------						OPTIMIZED METHOD	
Column	Kinetex XB C18		ACQUITY UPLC HSS T3 C18		ACQUITY UPLC BEH C18		ACQUITY UPLC BEH C18	
Ionization mode	ESI+	ESI-	ESI+	ESI-	ESI+	ESI-	ESI+	ESI-
Detected standards per ESI mode (%)	70	38	74	64	77	64	85	72
Total detected standards in both ESI modes (%)	83		91		91		100	
Overall quality score	240	116	256	199	272	208	309	264

The ACQUITY HSS T3 C18 and the ACQUITY BEH C18 columns outperformed the Kinetex XB-C18 column. This latter column performed similarly in ESI (+) mode, except for substantial tailing for carnitines and phosphocholines. In addition, the Kinetex XB-C18 column showed low retention for several polar lipids (eluting between 1-2 min), relatively close to the void time (t_0) of 0.91 min. The ACQUITY HSS T3 C18 column showed good retention and peak shapes for most tested lipids in ESI (+) with exception of small chain acylcarnitines, which eluted close to the t_0 (< 1.1 t_0). In ESI (-), eicosanoids, bile acids, and steroids eluted close to t_0, and eicosanoids such as PGE1 and PGE2 showed a tailing factor above 2. The ACQUITY BEH C18 column performed slightly better in comparison to the ACQUITY HSS T3 C18 column. In ESI (+), the retention of small chain acylcarnitines improved and the signal-to-noise ratio (S/N) increased for all carnitines. Only in ESI (-), chromatographic separation of the isomers PGA1 and LTB4 was obtained. None of the lipids eluted close to t_0 (< 1.1 t_0) in contrast to the ACQUITY HSS T3 C18 column. In addition, eicosanoids did not show tailing and higher S/N values were obtained for bile acids and steroids in ESI (-).

Based on the column screening experiment, the ACQUITY BEH C18 column was selected for method optimization. Further, a step-by-step approach was used to optimize each LC parameter. In comparison to the methods used during column screening (Table 4.1), the optimized methods used a higher temperature (60 °C instead of 55 °C) and the gradients were changed according to the elution profile of the panel lipid standards. To improve chromatographic resolution and reduce backpressure, the flow rate was

decreased from 0.25 to 0.2 mL/min. In both ionization modes, the aqueous fraction in mobile phase A was increased from 50% to 70%, to avoid elution close to t_0. In ESI (-), MeOH was replaced by ACN in both mobile phase A and B, and the CH_3COONH_4 concentration was lowered from 10 mM to 5 mM. The results of the optimized LC method showed an increased detection number. For example, PA (17:0/17:0) and C17 sphingosine-1-phosphate were detected, while these lipids remained undetected during column screening. Higher S/N values were obtained for eicosanoids in ESI (+) and ESI (-) and for bile acids, glycerophosphoethanolamines, and steroids in ESI (-).

Combining both ionization modes of the optimized method, all panel lipid standards could be detected with an excellent peak shape (FWHM < 0.2, tailing factor < 2 and > 0.8, and no elution close to t_0) (Figure 4.3). In addition, the BEH column was able to separate *sn*-positional isomers of e.g., MG(18:0/0:0/0:0), LPE(18:1(9Z)), and LPC(18:0). 24 lipids could be detected in either ESI (+) or ESI (-), while some lipid species such as carnitines were only detected and separated in ESI (+) and others such as fatty acids were only detected and separated in ESI (-).

Figure 4.3 shows the overlayed normalized extracted ion chromatogram (EIC) of each lipid standard, including highly polar lipids (e.g., CAR (2:0) and CAR (4:0)) and more apolar lipids (e.g., TG (16:0/16:0/16:0) and CE (18:1)). The abbreviations of the lipids mentioned in Figure 4.3 are explained in the supplementary information (Table SI-4.1).

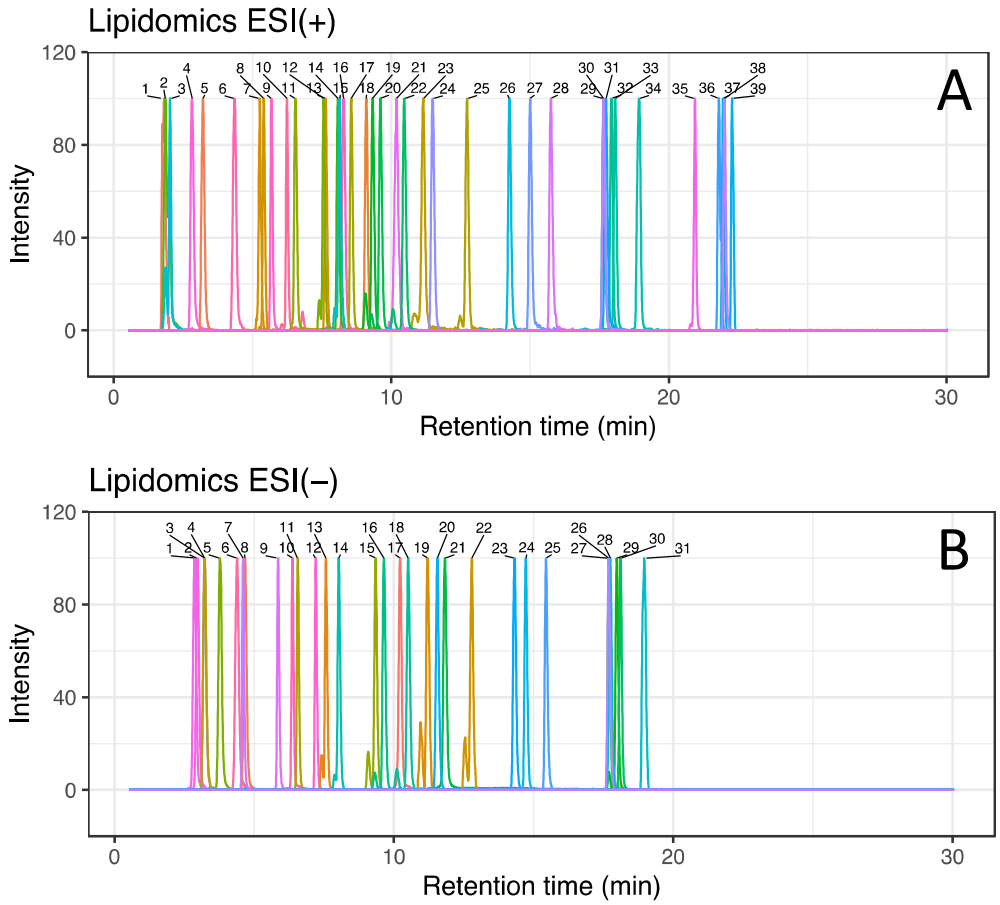

Figure 4.3 Chromatographic separation of panel lipid standards in positive (A) and negative (B) ionization modes. Doubled peaks denote separation of *sn*-positional isomers. **A)** (1): CAR(2:0), (2): CAR(4:0), (3): CAR(5:0), (4): CAR(8:1), (5): ST 21:3;O5, (6): ST 21:3;O4, (7): FA 20:4;O3, (8): FA 20:3;O3, (9): ST 19:2;O2, (10): FA 20:4;O2, (10): FA 20:4;O2, (11): Misoprostol, (12): LPE(13:0), (13): CAR(14:0), (14): CAR(18:2), (15): LPI(18:1), (16): SPB 18:1;O2, (17): CAR(16:0), (18): DG(8:0/8:0), (19): LPE(18:1), (20): LPC(17:0), (21): ST 18:3;O2, (22): LPC(18:0), (23): MG(18:1), (24): LacCer(18:1/8:0), (25): MG(18:0), (26): SM(d18:1/12:0), (27): PG(15:0/15:0), (28): PI(16:0/16:0), (29): PC(18:1/18:1), (30): Cer(d18:1/16:0), (31): PE(16:0/16:0), (32): Cer(d18:0/16:0), (33): Cer(d18:1/17:0), (34): DG(16:0/16:0), (35): Coenzyme Q10, (36): CE(20:4), (37): CE(18:2), (38): TG(16:0/16:0/16:0), (39): CE(18:1). **B)** (1): FA 20:4;O3, (2): FA 20:3;O3, (3): ST 18:3;O2, (4): ST 21:3;O5, (5): ST 24:1;O5;T, (6): ST 21:3;O4, (7): FA 20:4;O2, (8): ST 24:1;O5, (9): FA 20:4;O2, (10): ST 24:1;O4, (11): Misoprostol, (12): ST 24:1;O3, (13): LPE(13:0), (14): LPI(18:1), (15): LPE(18:1), (16): LPC(17:0), (17): FA 18:1, (18): LPC(18:0), (19): MG(18:1), (20): LacCer(18:1/8:0), (21): FA 18:0, (22): MG(18:0), (23): SM(d18:1/12:0), (24): PG(15:0/15:0), (25): PI(16:0/16:0), (26): Cer(d18:1/16:0), (27): PC(18:1/18:1), (28): PE(16:0/16:0), (29): Cer(d18:0/16:0), (30): Cer(d18:1/17:0), (31): DG(16:0/16:0).

In Figure 4.3, the lipid with the highest retention time was CE (18:1), which eluted before 25 min. To avoid carry-over, the time spent at a high percentage of organic solvent and equilibration conditions were optimized for samples with a high lipid content, as suggested by Martínez-Sena et al. (2019).

4.7.2. Drift tube ion mobility spectrometry

The BBD design considers the interactions between factors and the non-linear relations with responses, avoids extreme combination of factors (keeping the values inside the experimental region), and requires fewer experiments than a central composite design. To predict optimal values for multiple responses, the algorithm in Minitab software searches for values between -1 and +1 at which the parameter yields the maximal result for the overall desirability (Equation 4.4) and the corresponding optimized voltages could be back-calculated (Table 4.4).

Table 4.4 Optimized drift tube values obtained from response surface methodology (Box-Behnken design) combined with a desirability approach with a maximized response. DEV: Drift entrance voltage. DXV: Drift exit voltage. RFE: Rear funnel entrance voltage. RFX: Rear funnel exit voltage.

ESI	DEV (V)	DXV (V)	RFE (V)	RFX (V)
Positive	1221	300	200	49
Negative	-1273	-300	-216	-47

To validate the model, the mixture of standards was reinjected, and the responses were compared to all combinations of voltages used for the model. The predicted values showed the best results for both ESI (+) and ESI (-) experiments, highlighting the power of combining BBD with a desirability approach for multi-response method optimization. The least square (LS) methodology was chosen to describe the data because it provides easily interpretable results (Candioti et al., 2014). Moreover, different methods can be tested to assist in the choice of the best model for prediction that explains a significant amount of the data variation, e.g., artificial neural networks and generalized linear models. In addition to the regression significance and coefficient of determination (R^2), model predictions were compared with experimental values. The experimental design points were randomly re-injected in the same batch in which the optimized values were evaluated to prevent bias. The interaction between these variables does not always follow well-defined rules, making model predictions challenging. Thus, this former strategy was found to be essential to validate the results obtained with the optimized parameters of Table 4.4.

4.7.3. Ion trap funnel

The combination of a continuous ion source (e.g., ESI) with DTIMS, operated under pulsed conditions (trap, accumulation, and release events) results in reduced duty cycles, impairing sensitivity (Causon et al., 2019). Multiplexing techniques, such as Hadamard transform, have been investigated to improve the sensitivity for compounds with low *m/z*. In multiplexing mode, multiple ion packets enter the drift cell instead of one single packet, which requires shorter trap filling times to release ions in pulsed sequences (Reinecke et al., 2019). Recent findings showed a sensitivity gain factor of 2-8 for *m/z* values below 250 and an apparent improvement in signal-to-noise ratio (S/N) (Baker et al., 2014; Causon et al., 2019; Reinecke et al., 2019). Multiplexing techniques have not been fully explored for lipidomics applications, as well as the comparison with single pulse experiments with different ion trap conditions. A 4-bit sequence with 8 pulses was explored with different TF and TR times. Figure 4.4 shows a heatmap with the LC-DTIM-HRMS intensities of 67 ions, representing different detected adducts of the lipid panel mixture, in both ESI modes.

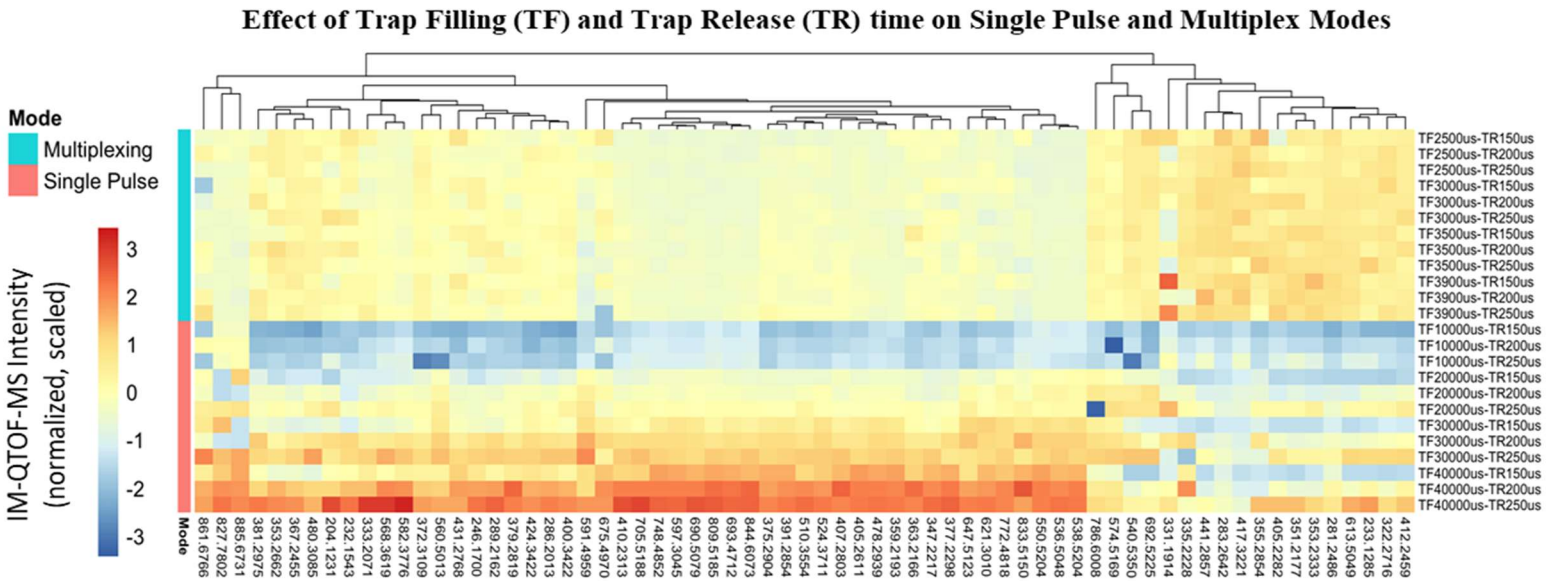

Figure 4.4 Effect of the trap filling and trap release times on single pulse and 4-bit Hadamard multiplexed drift tube ion mobility modes. The heatmap shows combined positive and negative electrospray ionization mode analysis of a mixture of 50 panel lipid standards. The intensities were column-scaled with a built-in function in the pheatmap R package. A scaled intensity color closer to value 3 (red) shows highly saturated signals. Scaled intensity color closer to value -3 (dark blue) shows low intensity values close to instrumental noise (approximately 200 counts).

Higher LC-DTIM-HRMS intensity signals were observed for higher TF times, e.g., 30,000 µs and 40,000 µs in single pulse mode (Figure 4.4), due to the higher duty cycle. However, as the TF time increases, the detector saturation also increases, and some chromatographic peaks started to show a squared profile instead of a Gaussian peak shape. For most compounds, different TF times (2,500-3,900 µs) had no significant effect on sensitivity in multiplexing mode, within the tested range ($p > 0.05$, ANOVA). In single pulse mode, the mean intensities of the compounds in the different conditions were significantly different ($p < 0.05$). No significant effects were found using different TR times within the 150-250 µs range for both single pulse and multiplexing modes.

Overall, higher TF times resulted in higher signal intensities in single pulse mode for the evaluated standard mixture, while no significant differences were detected in multiplexing mode. This could be due to the relatively high *m/z* values of lipids (*m/z* values usually ≥ 250). In addition, the effect of the tested range of TF times might be too small on the theoretical duty cycle in multiplexing mode to show a significant effect. However, there are other benefits when using multiplexing mode for lipid species, such as reduced detector saturation and the ability to provide a broader linear range. Figure 4.5 shows the difference in signal intensity between single pulse and multiplexed mode for a mixture of lipid standards in the 200-900 *m/z* range.

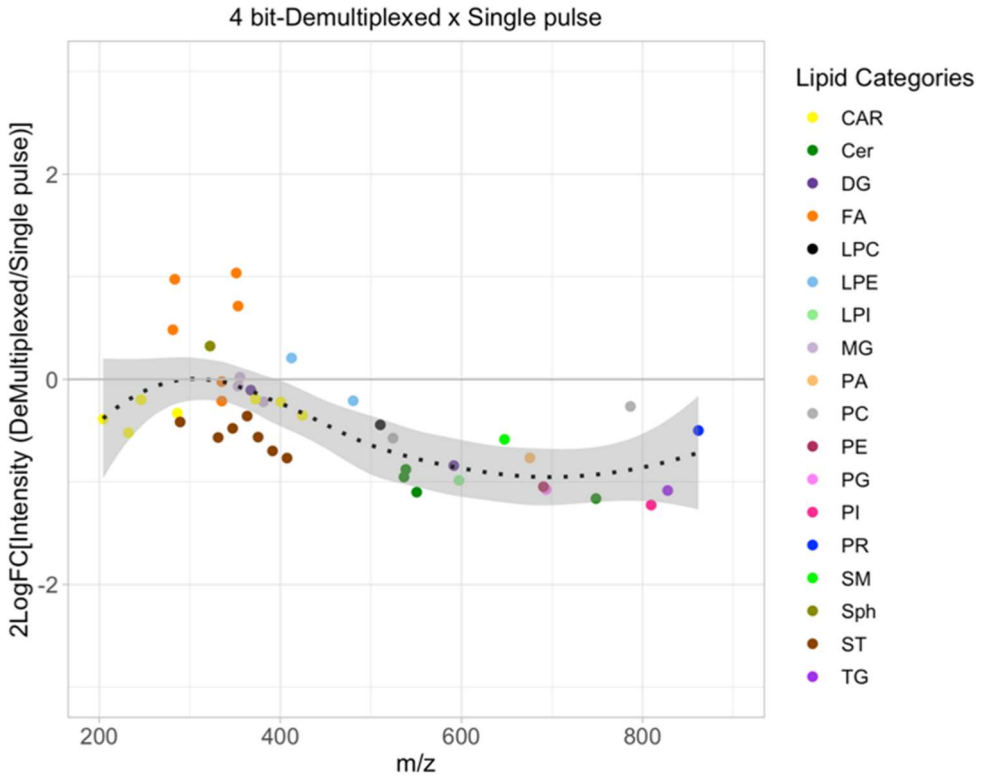

Figure 4.5 Effect of 4-bit Hadamard multiplexing and single pulse drift tube ion mobility mode on 18 categories of lipid standards in a 200-900 *m/z* range. The trap filling times were 30,000 µs and 3,000 µs in single pulse and multiplexed mode, respectively. For both modes, a trap release time of 200 µs was used. The dotted line and grey area represent the smoothed function (y=f(m/z)) with confidence interval at 95%. CAR: Carnitine. Cer: Ceramide. DG: Diglyceride. FA: Fatty acyl. LPC: Lysophosphatidylcholine. LPE: Lysophosphatidylethanolamine. LPI: Lysophosphatidylinositol. MG: Monoglyceride. PA: Phosphatidic acid. PC: Phosphatidylcholine. PE: Phosphatidylethanolamine. PG: Phosphatidylglycerol. PI: Phosphatidylinositol. PR: Prenol lipid. SM: Sphingomyelin. Sph: Sphingosine. ST: Sterol lipid. TG: Triglyceride.

The intensity gain of multiplexing mode was more prominent for *m/z* values around 300, more specifically for smaller fatty acids. On the other hand, carnitines showed higher sensitivity in single pulse mode in the same *m/z* range, which suggests that the lipid structure plays a meaningful role.

To further evaluate the effect of single pulse and multiplexing mode on lipids, intracellular extracts of HepaRG cells were analyzed as a proof-of-concept. Figure 4.6 shows the intensity comparison of annotated lipids between these two modes.

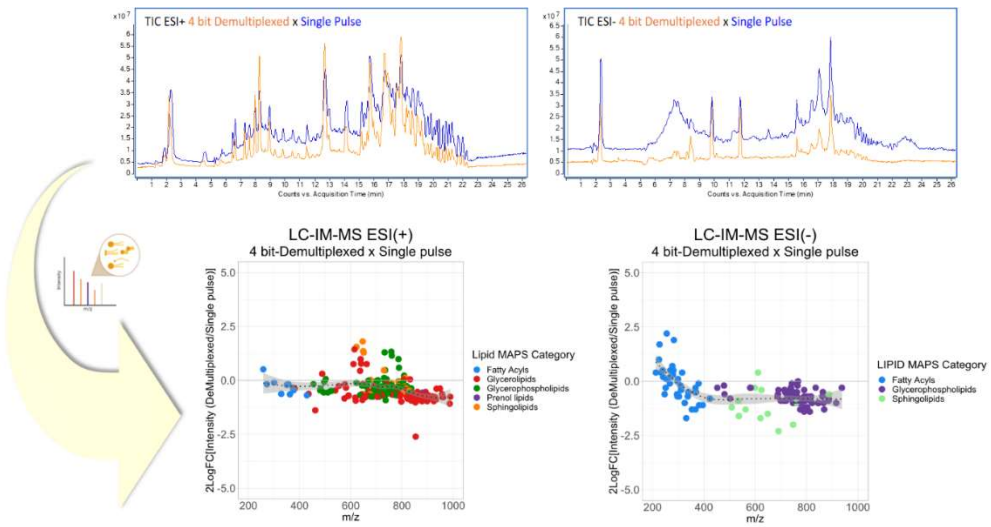

Figure 4.6 Effect of DTIMS 4-bit Hadamard multiplexing and single pulse mode on the intensity of different lipid categories measured in HepaRG extracts. A trap filling time of 20,000 µs and 3,000 µs was used in single pulse and multiplexing mode, respectively. Trap release times were set to 200 µs for both modes. The dotted line represents the smoothed function (y=f(*m/z*)).

Most lipids showed higher intensities in single pulse mode. No trend between intensity and *m/z* value or lipid category could be observed. DTIMS multiplexing mode can be beneficial for the analysis of samples with diverse lipid contents, such as plasma and tissues. These samples contain a substantial amount of lipid species that can saturate the detector and affect the dynamic linear range. In general, the multiplexed mode reduced the detector saturation for a wide range of *m/z* values. The latter can result in better peak deconvolution facilitating statistical evaluation and possibly improving mass accuracy. In addition, low abundant lipids, such as eicosanoids, could benefit from multiplexing mode by decreasing saturation from abundant lipids if these cannot be separated by LC or IMS and have a similar *m/z* value. However, the influence of ion suppression on sensitivity cannot be overlooked.

Although IMS software tools (e.g., PNNL PreProcessor (Prost et al., 2014)) have major advantages for data handling by removing data artifacts and reducing signal saturation, adequate data acquisition based on the study objective and matrix can assist in increasing the quality of the dataset and the throughput of the analysis. Multiplexing mode needs high computing power for data acquisition (pulsed sequence acquisition mode) and data processing. The additional data demultiplexing step also increases the data processing time, especially for long analytical runtimes, which are necessary for lipidomics. The application of LC-DTIMS-HRMS based untargeted lipidomics for a large number of samples would benefit from a simple method, such as single pulse mode with

a short TF time (e.g., 20,000 µs) to reduce saturation and avoid using other post-processing tools (e.g., demultiplexing) in large cohort studies.

4.7.4. CCS database matching

Although the CCS value is described as a physicochemical property of a compound, it can vary significantly among different libraries. This variation can be due to different instrumentation (e.g., drift tube and traveling wave IMS show CCS deviations from 1% up to 6% (Hinnenkamp et al., 2018)) and data source (prediction models versus experimental values). Currently, most of these libraries have different formats and are not integrated with data processing tools, which makes the manual comparison between obtained experimental CCS values and CCS values reported in libraries highly time-consuming, especially in an untargeted setting.

The $^{DT}CCS_{N2}$ values for each lipid standard matched with freely available libraries were reported in the supplementary information (Table SI-4.2). In addition, the AllCCS prediction tool was evaluated in order to (i) obtain *in silico* predicted CCS values coming from the same source and (ii) test the accuracy of the CCS values predicted by AllCCS. Figure 4.7 shows the distributions of CCS errors for different LIPID MAPS (O'Donnell et al., 2019) categories comparing AllCCS machine-learning-based prediction with experimental single field $^{DT}CCS_{N2}$ values acquired in-house.

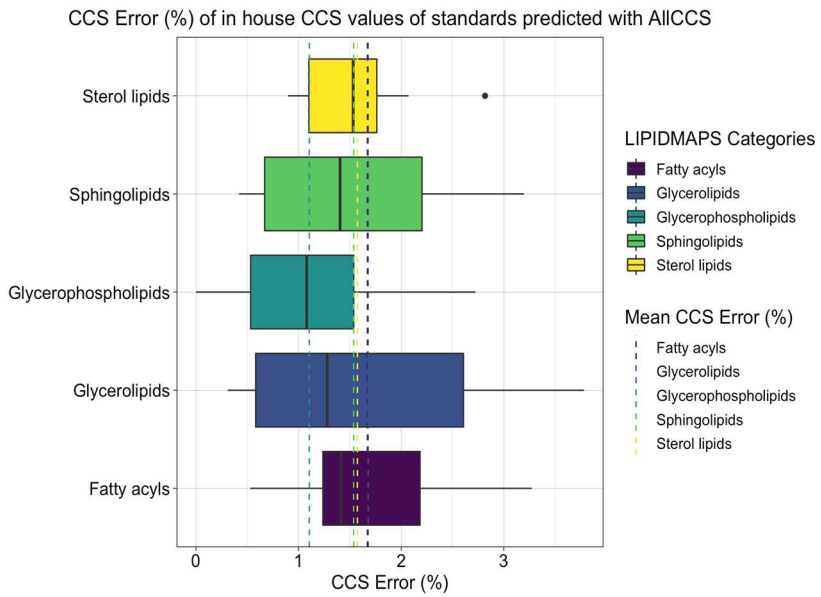

Figure 4.7 CCS relative error (%) comparing in-house acquired single-field $^{DT}CCS_{N2}$ values of lipid standards with CCS values predicted with the AllCCS prediction tool. CCS: Collision cross section.

Based on the comparison of experimental $^{DT}CCS_{N2}$ values with AllCCS predictions, the accuracy of CCS values predicted by AllCCS is acceptable for annotation in untargeted lipidomics using a threshold of 3% for the five lipid categories shown in Figure 4.7. However, experimental values produced with the same instrumentation are preferable, especially if a compound can be a potential biomarker. Some lipids with different *sn*-positions can be separated by chromatography and/or ion mobility. In practice, however, lipid standards with known *sn*-positions are needed to observe the effect on CCS-values measured with the same instrument for information that may be relevant for a specific study, since instrumental variation and CCS prediction errors can be larger than the influence of these specific structural differences on the CCS value (Cao et al., 2020; Stow et al., 2017). For untargeted analysis, CCS class-based filtering can be applied to exploratory lipidomics studies applying ion mobility. For in-depth annotation, the full structure level is necessary for biomarker identification. In addition, depending on the lipid category, additional techniques are necessary (e.g., ozonolysis for elucidation of double bond positions) (Liebisch et al., 2020).

4.7.5. Analysis of HepaRG extracts and CCS database matching

Intracellular HepaRG extracts were analyzed with the optimized LC-DTIMS-HRMS platform. The precision of the dataset was defined by calculating the relative standard deviation (RSD) of the intensity of the features for each ionization mode (Figure 4.8). The median RSD (mRSD) of the QC pooled samples in Figure 4.8 was used to assess the 24 h repeatability of the analytical method in the matrices. The mRSD of the six analytical replicates of the pooled QC sample was 19.6% for intracellular extracts of HepaRG cells (HepaRG IC) in ESI (+) mode and 13.3% in ESI (-) mode. Relative standard deviation values below 30% define a high-quality dataset for untargeted analysis which reflects a good method stability over runs with different matrices (Cuykx, Negreira, et al., 2017; Naz et al., 2014). The number of features in the QC pooled sample after blank subtraction and deisotoping were always higher in ESI (+) mode compared to ESI (-) mode and amounted 1982 in ESI (+) mode, while 1930 features were detected in ESI (-) mode.

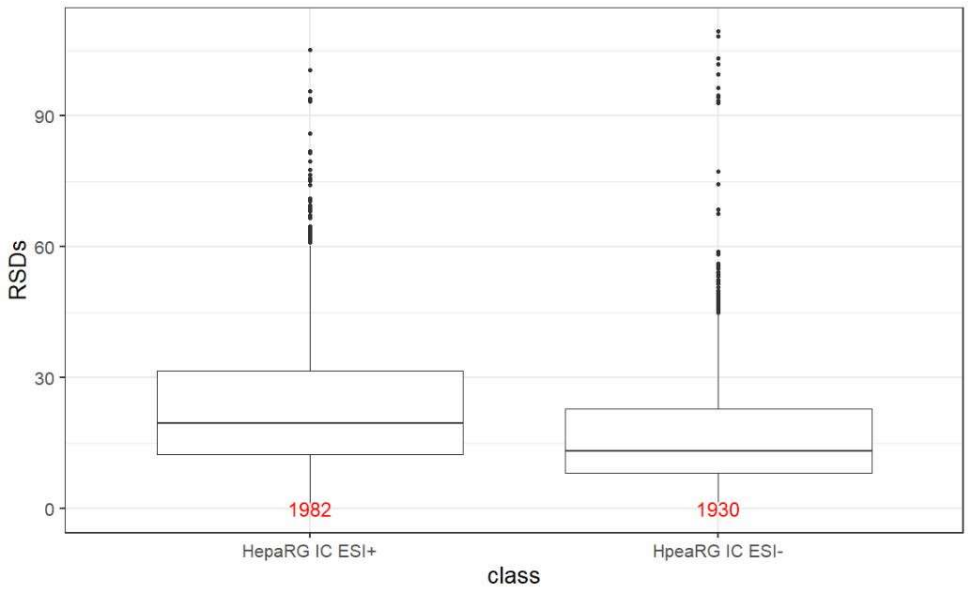

Figure 4.8 Relative standard deviation (RSD) of the intensity of features during analysis of intracellular extracts of HepaRG samples (HepaRG IC). RSD values were calculated based on the intensities of 6 injections of QC pooled samples in 24 h. The total number of detected features per biological matrix and per ionization mode, shown below the boxplots, were derived after preprocessing of acquired data (i.e., peak picking, alignment, blank subtraction, gap filling, and deisotoping).

A maximal CCS error of 3% compared to the AllCCS prediction was used as an annotation filter. All matched MS/MS spectra were manually double-checked within the MS-DIAL or Lipid Annotator interface considering the fragmentation rules for lipids (Lange et al., 2021). The reversed-phase model for retention time based on the carbon chain and the number of double bonds was used for further filtering. When in-house standards were available, annotated lipids were confirmed by comparison of their empirical MS/MS fragmentation spectra, RT and $^{DT}CCS_{N2}$ value (Table SI-4.3 and SI-4.4). Figure 4.9 shows the $^{DT}CCS_{N2}$ value and *m/z* value of different lipids species annotated in intracellular HepaRG extracts.

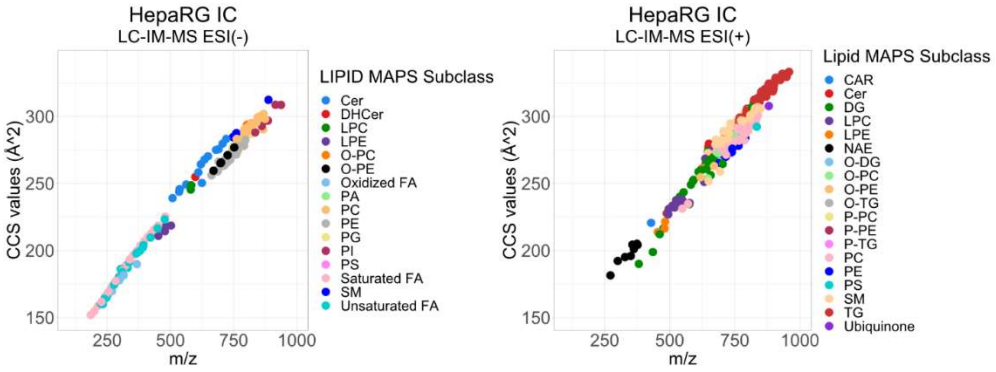

Figure 4.9 Lipid species annotated in intracellular extracts of HepaRG cells. Single-field $^{DT}CCS_{N2}$ values were plotted against the *m/z* values. One adduct per polarity was kept. IC: Intracellular. CAR: Carnitine. Cer: Ceramide. DHCer: Dihydroceramide. DG: Diglyceride. LPC: Lysophosphatidylcholine. LPE: Lysophosphatidylethanolamine. NAE: N-acyl ethanolamine. O-DG: Alkyl ether diglyceride. O-PC: Alkyl ether posphatidylcholine. O-PE: Alkyl ether phosphatidylethanolamine. O-TG: Alkyl ether triglyceride. P-PC: Alkenyl ether posphatidylcholine. P-PE: Alkenyl ether phosphatidylethanolamine. P-TG: Alkenyl ether triglyceride. FA: Fatty acid. PA: Phosphatidic acid. PC: Phosphatidylcholine. PE: Phosphatidylethanolamine. PG: Phosphoglycerol. PI: Phosphatidylinositol. PS: Phosphatidylserine. SM: Sphingomyelin. TG: Triglyceride.

Supplementary tables SI-4.3 and SI-4.4 contain the unique annotated lipids structures. Annotations were based on *m/z* values (< 5 ppm), isotopic distributions, the retention time of homologue series (CH_2), CCS values (< 3%) and the use of fragmentation spectra (DDA and/or DIA) when available. Overall, 169 lipid species were annotated in ESI (-) and 267 in ESI (+) in HepaRG extracts. In ESI (+), 46 features were annotated without acquiring their $^{DT}CCS_{N2}$ values. Annotation of these latter features was based on DDA spectra since the lower sensitivity of LC-DTIMS-MS and IM-All ions did not enable the calculation of their CCS value.

Most saturated and monounsaturated fatty acids (FA) did not show significant fragmentation. Based on the CCS values shown in Figure 4.9, both saturated and unsaturated fatty acids do not assume an elongated structure when colliding with N_2 gas with the experimental conditions in this study (estimated from CCS values of possible gas-phase conformations of fatty acids) (Stow et al., 2017). More compact conformations can result in higher variability for CCS values, especially for polyunsaturated species. From the annotated fatty acids, the same trend as for retention time was followed for CCS values, the higher the unsaturation level, the lower the retention time and CCS value (observed for the annotated FA ranging from 10 to 32 carbons). However, FA 20:4 (putatively eicosatetraenoic acid) showed a higher CCS value (186.2 $Å^2$) than both FA 20:0 (185.3 $Å^2$) and FA 20:1 (184.1 $Å^2$). This latter

information was not sufficient to remove FA (20:4) as an annotation since the number of gas-phase conformations assumed by this species can result in CCS values ranging from 170.3 Å^2 (most compact structure) to 220.7 Å^2 (elongated conformation) (Stow et al., 2017). In addition, oxidized fatty acids showed higher CCS values compared to their saturated and unsaturated analogue species (i.e., FA 18:1;O and FA 18:1 had measured CCS values 177.7 Å^2 and 176.1 Å^2) (X. Zheng et al., 2017).

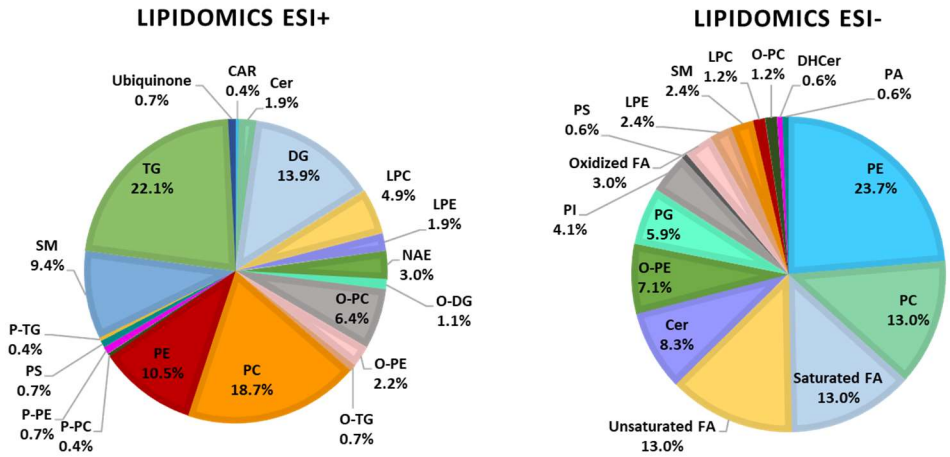

Figure 4.10 Lipid composition of HepaRG extracts annotated by the optimized LC-DTIMS-HRMS lipidomics platform. IC: Intracellular. CAR: Carnitine. Cer: Ceramide. DHCer: Dihydroceramide. DG: Diglyceride. LPC: Lysophosphatidylcholine. LPE: Lysophosphatidylethanolamine. NAE: N-acyl ethanolamine. O-DG: Alkyl ether diglyceride. O-PC: Alkyl ether posphatidylcholine. O-PE: Alkyl ether phosphatidylethanolamine. O-TG: Alkyl ether triglyceride. P-PC: Alkenyl ether posphatidylcholine. P-PE: Alkenyl ether phosphatidylethanolamine. P-TG: Alkenyl ether triglyceride. FA: Fatty acid. PA: Phosphatidic acid. PC: Phosphatidylcholine. PE: Phosphatidylethanolamine. PG: Phosphoglycerol. PI: Phosphatidylinositol. PS: Phosphatidylserine. SM: Sphingomyelin. TG: Triglyceride.

Figure 4.10 shows a detailed LIPID MAPS sub-class distribution of the annotated lipids. Glycerophospholipids, as key components in cellular membranes, were the most prevalent lipids in HepaRG extracts, next to glycerolipids. Overall, LC-DTIMS-HRMS can provide valuable information and can help in the separation of lipid classes that can co-elute in reversed-phase liquid chromatography (e.g., some sphingolipids, PEs, and PCs in reversed-phase columns). Ion mobility spectrometry enables the possibility to separate unresolved species in different features for untargeted analysis (same *m/z* and RT, different mobilities) (Blaženović et al., 2018). However, *m/z*, RT, and CCS values are not enough to provide in-depth information for structural elucidation of lipids, which contain a high number of isomeric species. The rule-based fragmentation is crucial for confirming lipid species and *in silico* and experimental libraries for lipid fragmentation

in IM-All ions mode are still lacking (including the incorporation of in-source fragmentation, adducts, and multimers) (Tada et al., 2019). It is important to note that even with MS/MS evidence certain isomers cannot be distinguished (Koelmel, Ulmer, et al., 2017).

Currently, the data analysis workflow for IM data is still highly complex and deconvolution algorithms to obtain clear fragmentation spectra are still advancing (Koelmel et al., 2020; Tsugawa et al., 2020; Zhiwei Zhou et al., 2019). Therefore, the confirmation of annotated compounds relies immensely on manual verification. The pipeline used in this study can be successfully applied for exploratory lipidomics studies to select statistically significant features. Furthermore, to obtain cleaner fragmentation spectra combined with LC-DTIMS-MS data, a validation experiment is necessary. During this latter experiment, the *m/z* values of statistically significant compounds can be used as a target list in the data acquisition software to enable the quadrupole to select features of interest for fragmentation. As a result, more conclusive information about the structure of the compound can be obtained for generation of hypotheses.

4.8. Conclusions

The ACQUITY UPLC BEH C18 column provided satisfactory results in terms of lipid coverage and its ability to separate critical pairs. A Box-Behnken design combined with a maximized desirability function was able to improve DTIMS sensitivity for lipidomics, while 4-bit Hadamard multiplexing provided variable sensitivity for different lipid species not following specific *m/z* rules. Sensitivity and saturation were not significantly affected by the trap release time, only by the trap filling time in single pulse mode. 4-bit Hadamard multiplexing ion mobility mode resulted in less saturated peaks which can improve mass accuracy and accuracy of quantitation for high abundant compounds. The optimized LC-DTIMS-QTOF-HRMS platform was successfully applied to HepaRG liver cell extracts to annotate 436 unique lipid species.

4.9. Supplementary information

The tables described below are available in the electronic supplementary information, which is accessible using the link below.

https://www.dropbox.com/sh/bvxln6vaf00q3hk/AABt5gt5XbDgsROqKY4w7Znla?dl=1

Table SI-4.1 Composition of the lipid panel mixture.

Table SI-4.2 Comparison of experimental $^{DT}CCS_{N2}$ values of the panel lipid standard mixture with database CCS values.

Table SI-4.3 Annotated lipids in intracellular extracts of HepaRG cells in ESI (-) mode

Table SI-4.4 Annotated lipids in intracellular extracts of HepaRG cells in ESI (+) mode

CHAPTER 5:
BUILDING MULTIDIMENSIONAL LIBRARIES FOR UNTARGETED MS-BASED METABOLOMICS

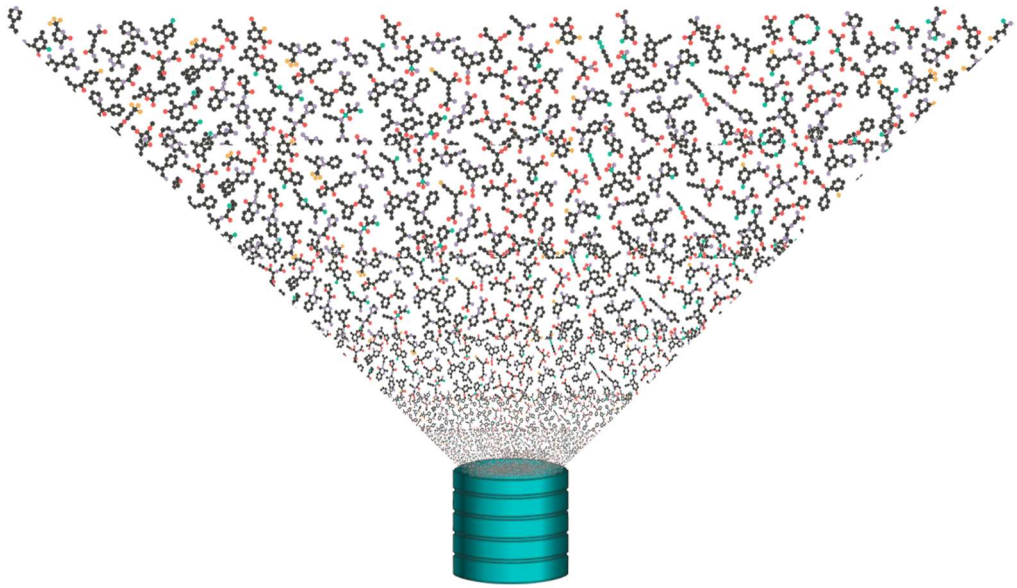

Based on the following publication

Da Silva KM*,$, Van de Lavoir M*,$, Robeyns R*,$, **Iturrospe E*,$**, Verheggen L, Covaci A, Van Nuijs A. Guidelines and considerations for building multidimensional libraries for untargeted MS-based metabolomics. Metabolomics. 2023; 19, 4. (DOI: 10.1007/s11306-022-01965-w).

*Shared first authors.

$Contribution as in the publication. K.M.d.S.: conceptualized the study, designed the analytical methods, performed experiments, and wrote the manuscript. M.v.d.L.: conceptualized the study, performed experiments, and wrote the manuscript. R.R.: conceptualized the study, performed experiments, and wrote the manuscript. E.I.: conceptualized the study, designed the analytical methods, performed experiments, and wrote the manuscript.

5.1. Introduction

In a typical LC-HRMS-based metabolomics experiment, information required for structural elucidation (e.g., MS/MS spectra) is acquired using a set of pooled quality control (QC) samples (Rathahao-Paris et al., 2015). During data processing, MS/MS spectra are deconvoluted and aligned to features (i.e., RT-*m/z* combinations associated with a response abundance) in the individual samples acquired in full scan mode. The MS/MS spectra are tentatively matched in experimental databases and/or through *in silico* prediction tools.

Despite advances in metabolomics, annotation remains one of the bottlenecks in the field due to the limited availability of high-quality MS/MS spectra (and CCS values) in public databases (Ivanisevic & Want, 2019). Reliable annotations are crucial for drawing conclusions in the biochemical interpretation of data. While dedicated databases, such as METLIN, have MS/MS data for over 850,000 compounds, the coverage of the (un)known chemical space is still very limited (Xue et al., 2020). Furthermore, constructing such databases is a costly and time-demanding task which resulted in the development of software applications that can simulate mass spectra by performing theoretical, so called *in silico* fragmentations of compounds (Krettler & Thallinger, 2021). Community efforts, such as MassBank, are a valuable resource to share spectral data from different platforms and compounds since there is still an open debate on the (dis)similarity of spectra generated from QTOF and Orbitrap systems (Paglia et al., 2021; Stravs et al., 2013). However, the creation of metabolite libraries with multidimensional information is a time-consuming and expensive process but still necessary for untargeted workflows. Different software can be used to create metabolite libraries, some of which are described in Table 5.1.

Table 5.1 Software for handling LC-(IM)-MS/MS data and summary of workflows for building metabolite libraries. CID: Collision-induced dissociation. DDA: Data dependent acquisition. DIA: Data independent acquisition. DTIM: Drift tube ion mobility. ESI: Electrospray ionization. HCD: Higher-energy C-trap dissociation. HRMS: High resolution mass spectrometry. IM: Ion mobility. LC: Liquid chromatography. LRMS: Low resolution mass spectrometry. MRM: Multiple reaction monitoring. PRM: Parallel reaction monitoring. QTOF: Quadrupole Time-of-Flight. QqQ: Triple-quadrupole. SRM: Selected reaction monitoring. TIMS: Trapped ion mobility spectrometry. TWIMS: Traveling wave ion mobility spectrometry.

SOFTWARE	AVAILABILITY	TOOL(S)*	WORKFLOW FOR CREATING IN HOUSE LIBRARY	REFERENCES
NIST 20	Commercial	**Database** MS/MS spectra from Ion trap (MS^n), CID from QTOF, QqQ and HCD from Orbitrap. 6000 human metabolites with different ionization species $[M+H]^+$, $[M-H]^-$, $[M-2H]^{2-}$, $[M+Na]^+$, dimers, and in source fragments. **In house library creation** The software can be used for library building.	1. Generate consensus spectra based on a clustering algorithm using dot product similarity of multiple scans. The data is processed for each instrument, polarity and collision energy separately. Merging of the above-mentioned parameters is not recommended. 2. Create high quality spectra by using noise removal, annotation of fragment ions and evaluation of collision energy dependence trends. 3. Manual inspection by an expert.	(X. Yang et al., 2014)
GNPS	Freely available	**Database** MS/MS spectra from QTOF, Orbitrap, QqQ, ToF, Ion Trap, Hybrid FT. 587,122 spectra. **In house library creation** A GNPS workflow (MSMS-Chooser) can be used for building and validating in house libraries.	1. Fill out the MSMS-Chooser Template. 2. Import .mzXML/.mzML file from MassIVE using ProteoSAFe. 3. Review MSMS-Chooser results. 4. Inspection by an expert.	(M. Wang et al., 2016)

Table 5.1 Continuation.

SOFTWARE	AVAILABILITY	TOOL(S)*	WORKFLOW FOR CREATING IN HOUSE LIBRARY	REFERENCES
MAVEN	Freely available	**Database** *In silico* lipidomics library. **Software** Multiple MS/MS libraries can be searched simultaneously.	1. Import .mzML file. 2. MSMS-based peak grouping. 3. Inspection by an expert.	(Seitzer et al., 2022)
Mass Bank (EU)	Freely available	**Database** MassBank EU contains data from several LRMS and HRMS instruments: 29% LC-ESI-QTOF. Not all spectra were generated by RMassBank. 15,075 unique compounds (v 2.2). **In house library creation** Script-based (R language). RMassBank workflow is indicated for high-resolution LC-MS/MS data. It can also handle direct injections. Automated recalibration and annotation of fragment ions.	1. Conversion of raw data to .mzML. 2. Load .mzML, compound smiles, ID and analytical information. 3. Formula assignment for fragment ions. 4. Recalibration and formula reassignment. 5. Noise filtering (multiplicity filtering optional). 6. Generation of Mass Bank records (.txt).	(Stravs et al., 2013)
SKYLINE	Freely available	**Software** Multidimensional data processing and visualization with windows client application. MS/MS data from LRMS and HRMS using different types of acquisition including SRM, MRM, PRM, DIA/SWATH. LC-IM-HRMS data (DTIMS, TIMS, TWIMS). **In house library generation** Libraries can be created based on predefined transition list.	1. Transition lists generation based on experimental data or *in silico* predictions (e.g., LipidCreator).	(K. J. Adams et al., 2020; Peng et al., 2020)

Table 5.1 Continuation.

SOFTWARE	AVAILABILITY	TOOL(S)*	WORKFLOW FOR CREATING IN HOUSE LIBRARY	REFERENCES
MS-DIAL 5	Freely available	**Data-processing and statistics** Program supports all untargeted data processing steps from raw data import to statistical analysis. **Database** MS/MS data from 16,481 unique standards in ESI+ and 15,245 in ESI−. *In silico* LipidBlast v.68 (377,313 predicted molecules in ESI+ and 792,757 in ESI−). EIEIO fragmentation for lipids. **In house library generation** It can handle and generate libraries for MS/MS data from HRMS including DDA, DIA (All-ions fragmentation, SWATH) and IM.	1.The data is processed with selected filtering thresholds. 2. The deconvoluted spectrum is selected and exported to MS-FINDER. 3. *In silico* predictions based on formula and SMILES notation of the neutral structure or spectral databases can be used for fragment annotations. 3. Add metadata such as instrument and collision energy. 3. Data can be exported as .msp file.	(Lai et al., 2017; Tsugawa et al., 2020)
MZmine	Freely available	**Data-processing and statistics** Data processing of raw data, visualization and interpretation of results by providing statistical analysis methods. Annotation of peaks can be performed using custom database search and online databases search (supported online database or implemented as additional plugins). **Database** Chemical formula prediction module to calculate all possible molecular formulas for every peak in a peaklist. Lipid Annotation Module to search for lipids. **In house library generation** The software provides a module to export MS/MS spectral library entries and directly submit them to the GNPS spectral library.	1. Processing of the data in MZmine. 2. Per compound spectra (i.e., selection of all ion adducts, in source fragments and multimers for one compound): select "export selected spectra as MS/MS library'' to add metadata (e.g., adduct, fragmentation method, formulas, SMILES) and apply filters (e.g., noise filter, minimal number of signals in MS/MS scans and whether the signals are sorted by maximum TIC or maximum number of signals). 3. Export MS/MS spectra as .json file (GNPS format) or .msp file. Entries can be directly submitted to GNPS.	(Pluskal et al., 2010)

Table 5.1 Continuation.

ADDITIONAL DATABASES AND SOFTWARE FOR METABOLITE ANNOTATION			
SOFTWARE	**AVAILABILITY**	**TOOL(S)***	**REFERENCES**
HMDB	Freely available	**Database** Experimental MS/MS data for over 5,700 compounds. *In silico* fragmentation available for all QTOF MS/MS spectra in both positive and negative ionization mode at three collision energies (10, 20 and 40 eV). MetCCS and DeepCCS (published CCS predictors) were used to generate CCS values for all metabolites (reported errors of <3-4%). **Comprehensive metabolite information** Chemical, clinical and molecular/biochemical data for more than 41,000 metabolites. Many data are hyperlinked to other databases (e.g., KEGG and GenBank) and a variety of structure tools, pathway visualization tools, and chemical taxonomy (ClassyFire).	(Wishart et al., 2022)
SIRIUS	Freely available	**Software** Molecular formula annotation. CSI:FingerID is used as a web service to search in databases. CANOPUS is used for *de novo* compound class prediction.	(Dührkop et al., 2019)
MoNA	Freely available	**Database** 2,042,858 mass spectral records from experimental, *in silico* libraries and from user contributions. **Software** Option to submit spectral library data on MoNa. Community curation and feedback via bar graph. "Clean" or "Noisy" feedback available for each spectrum. Spectral entropy and normalized entropy to label spectral quality. Libraries cannot be generated from raw data. The webtool supports .msp, .mgf, mass bank records (.txt) or spectral entries in [m/z]:[intensity] format. The spectral data can be manually annotated and filtered. Metadata can also be added including mobile phase composition, collision energy, CCS value, retention time, instrumental characteristics, etc.	(Y. Li et al., 2021)
METLIN Gen2	Commercial	**Database** Spectra derived from 860,000 standards (4 collision energies). *In silico* fragmentation when no experimental spectra are available. isoMETLIN enables annotation of isotopically labelled metabolites. Option to expand the library with the MassHunter Personal Compound Database (PCDL) commercial software for Agilent instruments.	(Smith et al., 2005a)

Table 5.1 Continuation.

SOFTWARE	AVAILABILITY	TOOL(S)*	REFERENCES
mzCloud	Freely available	**Database** Multi-stage tandem mass spectra and annotation of some of the fragment ions. MS^n information for 1,606 endogenous metabolites. CID and HCD breakdown curves. Library search by compound identifiers, structure or spectrum. Option to expand the library with the mzVault commercial software for Thermo Scientific instruments.	https://www.mzcloud.org/

* The database's content and workflow are current as of October 2022. The workflow presented to create in house libraries is a concise summary based on the author's experience, and it may include additional steps as a result of updates, particular data files and processing parameters.

In this study, a systematic workflow was developed to create in-house MS/MS metabolite libraries from analytical standards, using RMassBank, including RT and CCS values, and QC criteria. The proposed workflow can be applied by metabolomics groups that would like to share their data with the scientific community and improve metabolite annotation workflows. The selection of the software solution was based on compatibility with in-house untargeted workflows, accessibility and quality of results obtained.

5.2. Materials and methods

5.2.1. Chemicals and materials

Methanol ultrapure (MeOH), acetonitrile (ACN), and formic acid (99%, HCOOH) UPLC/MS grade were purchased from Biosolve (Valkenswaard, the Netherlands). Ammonium acetate LC-MS grade (CH_3COONH_4) and acetone (CH_3COCH_3, ACS reagent) were obtained from Sigma-Aldrich (Darmstadt, Germany). Acetic acid (100%, CH_3COOH) and ethanol (EtOH), all LC-MS grade, isopropanol for analysis (IPA, ACS reagent), ammonia solution (25%, LC-MS grade), and chloroform ($CHCl_3$, analytical grade) were purchased from Merck (Merck KGaA, Darmstadt, Germany). Ultrapure water (H_2O) used throughout the experiments was obtained from an Elga Pure Lab apparatus (Tienen, Belgium). Reference standards for the preparation of individual solutions mixtures and system suitability (SS) solution were obtained from various vendors (supplementary information (SI) 1), including the Mass Spectrometry Metabolite Library of Standards (MSMLS) from IROA Technologies (New York, USA).

5.2.2. Preparation of individual solutions, mixtures and system suitability solution

A solution of 5 µg/mL was prepared for each reference standard using a suitable solvent (SI-1). After drying under a stream of N_2 at room temperature, standards were reconstituted to 2 µg/mL IPA/MeOH (35/65, v/v). The SS mixture composed of 1 µg/mL of 2-octenoyl-L-carnitine (CAR 8:1), glycerol tripalmitate-[$^{13}C_3$] (TG 16:0/16:0/16:0-[$^{13}C_3$]), 1,2-dipalmitoyl-sn-glycero-3-phosphoethanolamine (PE 16:0/16:0), lithocholic acid, 1-stearoyl-phosphatidylethenolamine (LPE 18:1) and 1,2-dipalmitoyl-rac-glycero-3-phosphoinositol (PI 16:0/16:0) was prepared in IPA/MeOH (35/65, v/v).

5.2.3. Data acquisition

The analytical measurements were performed on an Agilent 1290 Infinity II LC system coupled to an Agilent 6560 Drift Tube-IM (DTIM)-Quadrupole-Time of Flight (QTOF)-HRMS with Dual Jet Stream electrospray ionization (ESI) in positive (+) and negative (-) modes. Instrumental parameters were obtained by previous in-house method

optimization (chapter 4). Data were acquired in 2 GHz extended dynamic mode with a scan range of 100-1700 *m/z* in MS1 (3 spectra/s) and 70-1700 *m/z* in MS2 (6 spectra/s). A maximum of 4 precursors per scan cycle was applied with a separate injection for each of the three used collision energies (CE 10, 20, and 40 eV). A narrow (1.3 amu) quadrupole isolation window was used in auto-MS/MS mode. Purine and hexakis(1H, 1H, 3H-tetrafluoropropoxy)phosphazine were constantly infused for recalibration of the mass axis (*m/z* 121.0508 and 922.0097 in ESI+, *m/z* 119.0363 and 980.0163 in ESI-). DTIMS analysis was performed using single pulse mode with a trap filling time of 20 ms and a trap release time of 200 µs.

To acquire RT information, a previously optimized LC method was used (da Silva, Iturrospe, Heyrman, et al., 2021). Three µL was injected onto an ACQUITY UPLC BEH C18 column (150 × 2.1 mm, 1.7 µm) maintained at 60 °C at a 0.2 mL/min flow rate. The mobile phase consisted of (A) ACN/5 mM of CH_3COONH_4 (30/70, v/v) and (B) IPA/ACN/5 mM CH_3COONH_4 (88/10/2, v/v/v). In ESI+, 0.1% (v/v) of CH_3COOH was added to the aqueous fraction. The gradient was set as follows: 15% (B) was kept constant for 2 min and increased to 30% at 3 min, to 60% at 5 min, which was kept constant for 3 min, to 100% at 20 min, and returned to 15% at 35 min for a 5 min equilibration. An isocratic condition at 50% B was kept for 1 min for direct injections to acquire MS/MS spectra and IM data.

5.2.4. Data processing

The raw MS/MS data files (Agilent .d format) were converted to an open-source format (.mzML) and centroided using peak picking (msLevel = 1-) with MSConvert (Holman et al., 2014). The converted data files were divided into folders by ESI mode and collision energy. The R package RMassBank (Stravs et al., 2013) v. 3.14 was used to generate MassBank records (.txt files). The data file names followed the same general naming conventions (compoundname_1001_neg.mzML) associated with the compound table, which contained an internal ID, name, and simplified molecular-input line-entry system (SMILES) for each compound. Processed acquisition files were renamed with Ant Renamer 2.12. The MassBank records for the same ionization mode and different CEs were merged and converted to a NIST format library (.msp) with the MassbankToMspConverter 1.04 tool. This NIST format can be used for library matching in open-source software such as MS-DIAL (Tsugawa et al., 2020). The NIST format converted library was imported into MS-LIMA 1.54, facilitating the examination of MS/MS spectra at different CEs. The .msp format allowed the addition of orthogonal data such as RT and CCS values. The detailed workflow is explained in SI-2. $^{DT}CCS_{N2}$ values were calculated using IM-MS Browser B.08.00 (Agilent). The calibration coefficients

enabling single-field CCS calculations were derived from infusion data of the Agilent tune mixture (G1969-85000).

5.3. Results and discussion

5.3.1. General workflow and implementation of QA/QC

One of the most important applications of an in-house library in untargeted metabolomics is the facilitation of obtaining a high confidence level of metabolite annotation. While there are several scales to report confidence in compound annotation, the highest level (1 or A) relies on confirming the structural information with authentic standards acquired under the same conditions (da Silva, Iturrospe, Bars, et al., 2021). Moreover, laboratories cannot obtain individual standards for each biologically significant metabolite, and therefore generating records of available standards is essential to predict the behavior of similar compounds and to retain chemical information (e.g., fragmentation patterns, retention time behavior in different chromatographic conditions, CCS values).

To generate a straightforward and flexible multidimensional spectral library workflow (Figure 5.1), a comprehensive set of 100 unique endogenous metabolites was used. The repertoire of metabolites included nine different super classes reflecting the large biological scope of the library.

A SS mixture of standards (distributed across the *m/z* and RT range) was injected at the beginning and end of each batch, to assess the instrumental performance over a complete analysis window. The SS acceptance criteria were based on the variation of repeated injections over time (e.g., every week, three injections per day for one month) and included: (i) peak height above 5,000 counts and without saturation, (ii) maximal mass error of 10 ppm, and (iii) RT deviation of maximum ± 0.2 min. The precision of the SS measurements can also be included as an evaluation criterium using the coefficient of variation (CV) of intra-assay (e.g., two injections before and after the assay) and inter-assay measurements (e.g., injections in the same system from different experiments over weeks, months, years). After establishing reference values, they can be monitored over time before and after each analysis.

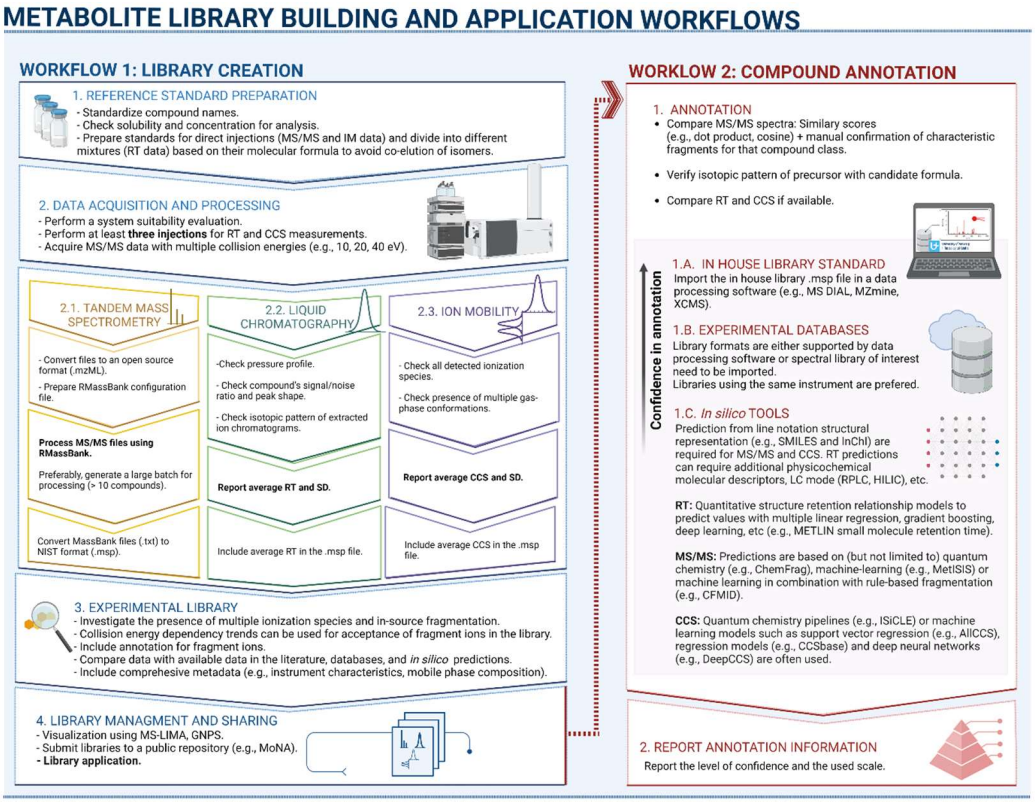

Figure 5.1 General workflow to build a multidimensional metabolite library. RT: Retention time. CCS: Collision cross-section. SD: Standard deviation. IM: Ion mobility. LC: Liquid chromatography. RPLC: Reversed-phase liquid chromatography. HILIC: Hydrophilic interaction liquid chromatography.

The standards for the metabolite library were prepared for direct injections (to obtain MS/MS and IM data) and divided into different mixtures (to obtain RT data) based on their molecular formula to avoid co-elution of isomers. First, MS/MS data were acquired in ESI+ and ESI− modes using three collision energies (10, 20, and 40 eV) to acquire compound-specific reference spectra. Data files were converted to an open-source format (.mzML) and separated into folders by ionization mode. Each compound identifier (filename with a 4-digit identification number, CE voltage, and polarity) and SMILES notation (neutral structure obtained from PubChem (Kim et al., 2021)) were curated. The RMassBank script, developed to generate high-quality MS/MS spectra using recalibration and formula annotation of product ions from Orbitrap mass spectrometers (Stravs et al., 2013), was applied. In order to use the script for a QTOF instrument, the configuration files were modified to work with the higher mass errors of low abundant ions in MS/MS (≤ 25 ppm). Given the lower mass accuracy of a QTOF instrument compared to an Orbitrap, annotation confidence can benefit from the

addition of orthogonal data. Therefore, the acquisition of RT and CCS values were included in the general workflow in order to increase the confidence in the annotation of metabolites.

As coupling of DTIMS to LC-MS inherently decreases sensitivity due to impaired duty cycles (da Silva, Iturrospe, Heyrman, et al., 2021), it is recommended to run DTIMS-MS separately from MS/MS and LC-MS for library building purposes. In addition, it should be noted that DTIMS can be coupled with data-independent acquisition (DIA), but is incompatible with data-dependent acquisition (DDA) (Agilent Technologies, 2017), while DDA is the MS/MS method of choice for library generation as this method results in cleaner fragmentation spectra due to more straightforward MS/MS deconvolution (Guo & Huan, 2020). In the scope of this latter phenomenon, it should be mentioned that coupling of DTIMS to MS/MS in All-ions fragmentation mode (AIF; DIA mode) enables a more straightforward deconvolution due to drift time-matching of fragments and precursors (Pezzatti et al., 2020). In addition, acquired DTIMS-AIF spectra can be matched with DDA spectra using software such as MS-DIAL (Tsugawa et al., 2020). Ideally LC-MS/MS acquisition is performed for each standard separately. However, as this latter can be very time-consuming, DDA MS/MS spectra can be acquired from direct injections of standards, while standard mixtures can be used to acquire RT information. In these standard mixtures, isomers should be separated to avoid wrong interpretations in case of co-elution.

A total of 539 MS/MS spectra of different ionization species and collision energies, 194 RT values, and 177 CCS values in ESI+ and ESI− were obtained from 100 molecules and added to the library. The detailed information regarding which adducts were detected, retention time and CCS values in each ionization mode can be found in SI-1. The CCS values acquired in single field were calculated in IM-Browser for three injections per compound. The RT and CCS values were added to the NIST converted .msp file. All metabolites included in the library showed mass errors < 15 ppm, a relative standard deviation (RSD) for CCS values < 0.5% (May & McLean, 2015) (SI-1) and a maximum RT shift < 0.2 min (in-house SS acceptance criteria). As RMassBank is based on R language, the suggested workflow in Figure 5.1 generates data that can be easily shared with the scientific community (MassBank records or .msp files) and coupled with computational tools that allow efficient evaluation of the experimental library and accurate matching of experimental data to library LC-(IM)-HRMS data.

5.3.2. Tandem mass spectrometry (MS/MS)

The MS/MS spectra of individual molecules in metabolomics libraries are typically acquired using high-resolution mass spectrometers which provide accurate mass measurements for precursor and product ions. The QTOF analyzers have less resolving

power and accuracy than Orbitrap instruments, therefore, the latter would be more beneficial for MS/MS library building. However, the QTOF instruments can operate at a higher scan speed which is advantageous for coupling with sub-2 µm LC-columns and IM separation for complex samples allowing high peak capacity (da Silva, Iturrospe, Heyrman, et al., 2021; Hopfgartner, 2011). Using data-dependent acquisition mode, the quality of the MS/MS spectra can be affected by the isolation window of the precursor ion and the total cycle time (Hopfgartner, 2011). As a result, MS/MS spectra were acquired in auto-MS/MS mode using one collision energy at a time and the number of precursors was limited to four per cycle, with a scan rate of 6 spectra/s in order to increase the number of transients per spectrum.

The optimization of these latter parameters can help to improve the MS/MS data from QTOF instruments, but the presence of background signals and contaminants, compounds with complex fragmentation mechanisms, and low abundant fragment ions (e.g., ions with signals close to experimental noise levels) makes assessing the quality of the MS/MS spectra extremely challenging. Therefore, in order to verify whether the chemical formula assignments performed by RMassBank retained important fragment ions, different strategies were used including rule-based and in-source fragmentation and the evaluation of multiple ionization species and radical ions.

5.3.2.1. Rule-based fragmentation as a tool to evaluate experimental libraries

Rule-based fragmentation is commonly used for lipid annotation using *in silico* software since many diagnostic lipid class fragments are well characterized by mass spectrometry (Koelmel, Kroeger, Ulmer, et al., 2017; R. C. Murphy, 2014). Therefore, the MS/MS spectra of several lipids can be used to verify whether relevant product ions were retained after data processing. In Figure 5.2 and Figure 5.3, the MS/MS spectra of the protonated and sodiated species of 1-octadecanoyl-sn-glycero-3-phosphocholine (LPC 18:0) are shown. The loss of H_2O (18 Da) can be observed at the three collision energies for $[M+H]^+$, a characteristic concerted mechanism of heterocyclization of acyl-linked LPC (driven by protonation of *sn*1 ester) (R. C. Murphy, 2014). In a recent study, alkyl and alkenyl-linked LPC did not show this neutral loss in ESI+ (Lange et al., 2021). The diagnostic ions of LPC include the formation of phosphocholine (*m/z* 184.0734), choline (*m/z* 104.1070), and a less abundant glycerophosphocholine that generates smaller product ions (*m/z* 124.9998 and *m/z* 86.0963), according to the mechanisms of dissociation proposed Colsch et al. 2017.

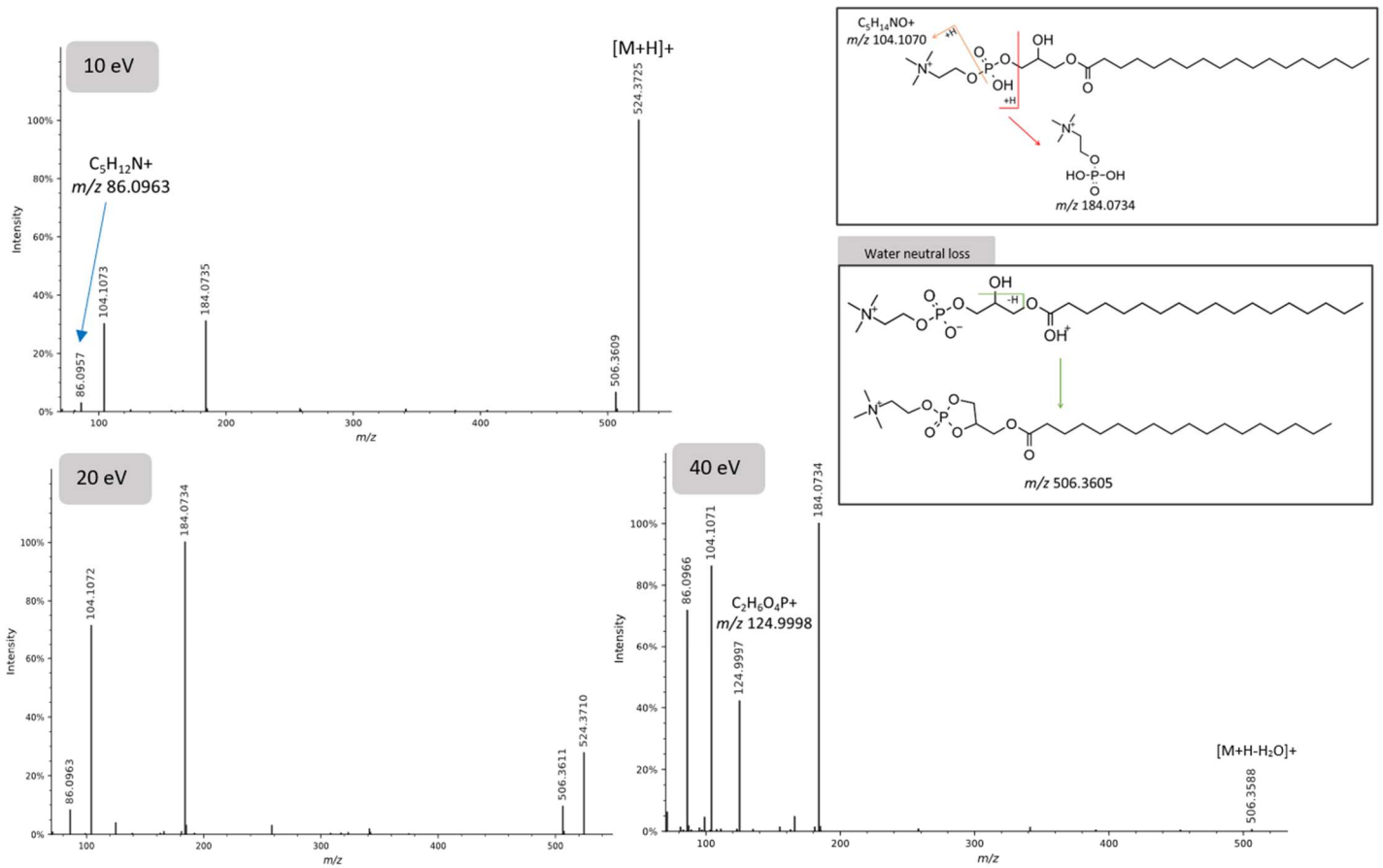

Figure 5.2 MS/MS spectra of the $[M+H]^+$ ion species of 1-octadecanoyl-sn-glycero-3-phosphocholine (LPC 18:0) at CID 10, 20 and 40 eV.

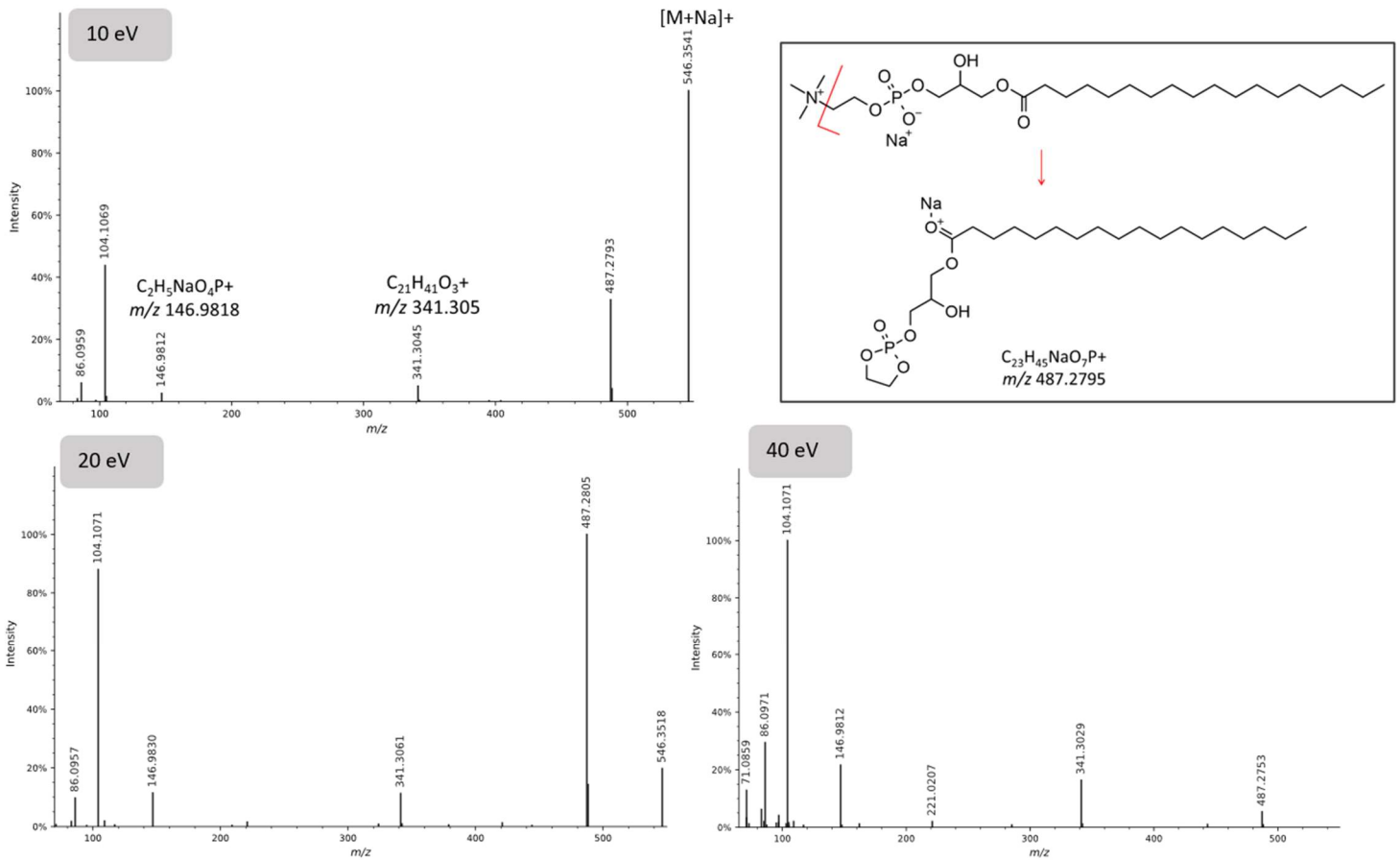

Figure 5.3 MS/MS spectra of the $[M+Na]^+$ ion species of 1-octadecanoyl-sn-glycero-3-phosphocholine (LPC 18:0) at CID 10, 20 and 40 eV.

The addition of different precursor ion species to the library can facilitate the structural elucidation of an unknown due to different dissociation mechanisms. As shown in the spectrum of $[LPC18:0+Na]^+$, the neutral loss of trimethylamine (59 Da) is preferred for this monoacylglycerophosphocholine through a rearrangement mechanism that involves folding of the side chain to form the ion at *m/z* 487.2795.

For carnitines, the spectra of CAR 14:0 are shown as an example in Figure 5.4. The characteristic oxonium ion at *m/z* 85.0288 is visible at the three collision energies. This latter ion is formed after the loss of the fatty acyl chain and subsequent loss of the trimethylamine moiety. The neutral loss of trimethylamine from the precursor ion showing an ion at *m/z* 313.2375 and the protonated fatty acyl chain after H_2O loss $[FA14:0+H-H2O]^+$ (*m/z* 211.2056) could be observed at 10 and 20 eV. This fragmentation pattern was already confirmed by several studies (Lange et al., 2021; R. C. Murphy, 2014; Yan et al., 2020) and the implementation of these additional ions in rule-based predictions could increase similarity matches with experimental MS/MS spectra. However, as of July 2022, on the LIPID MAPS (Sud et al., 2007) spectral database (e.g., LMFA07070102), the prediction from LipidBlast (also used by MS-DIAL (Tsugawa et al., 2020)) only uses *m/z* 85.0288 as characteristic ion for the acylcarnitines.

5.3.2.2. Compounds with multiple ionization species

In an untargeted metabolomics strategy, several compound classes are analyzed simultaneously and the addition of modifiers such as acids, bases, or salts to mobile phase solvents facilitates the ionization of neutral and polar lipids (e.g., the addition of CH_3COONH_4 facilitates ionization of triacylglycerols as $[M+NH_4]^+$). However, for metabolites that form multiple ions, the addition of modifiers can increase the complexity of data analysis and generate different MS/MS spectra for different adducts in the same ionization mode.

Ceramides (Cer) can ionize in both ionization polarities forming a diverse set of adduct ions and can also undergo in-source fragmentation. In Figure 5.5, the MS/MS spectra of N-palmitoyl-D-sphingosine are shown in ESI+ and in Figure 5.6 in ESI-. In Figure 5.5, the $[M+H]^+$ precursor ion can easily generate abundant ions due to one or two water losses and amide cleavage to generate N' ($-H_2O$) and N" ($-H_2O$) ions already at 10 eV (R. C. Murphy, 2014). However, for $[M+Na]^+$ adducts, this latter CE was not sufficient to generate *N*-ions and only a low abundant signal for water loss $[M+Na-H_2O]^+$ was noticed. Controversially, alkali ions of Cer, such as $[M+Li]^+$ can produce a series of diagnostic fragments due to charge remote fragmentation mechanisms (J. Adams & Ann, 1993), but this was not seen for the alkali adduct ion in the library, $[M+Na]^+$, even at a high collision energy (40 eV).

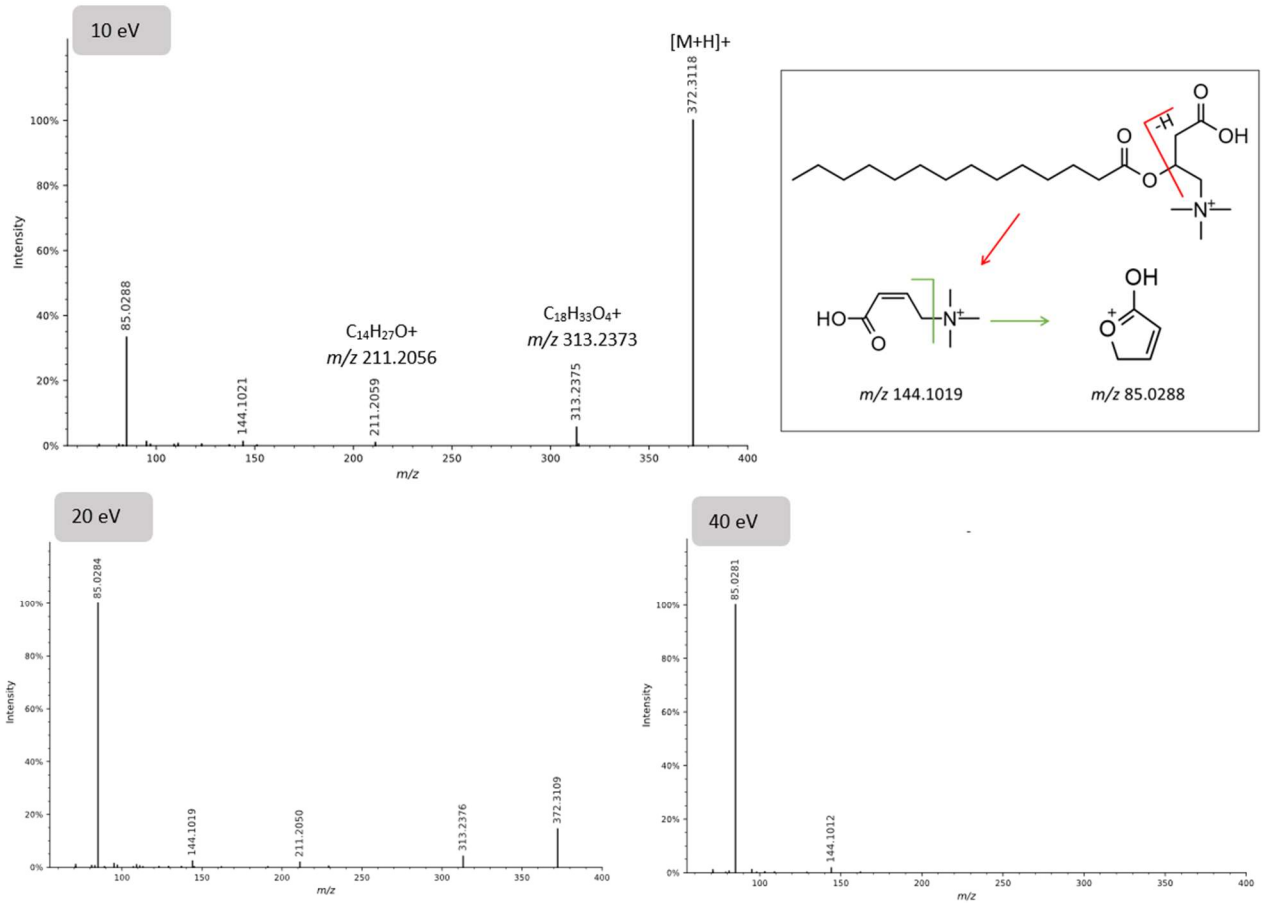

Figure 5.4 MS/MS spectra of the $[M+H]^+$ ion of myristoyl-carnitine (CAR 14:0) at CID 10, 20 and 40 eV.

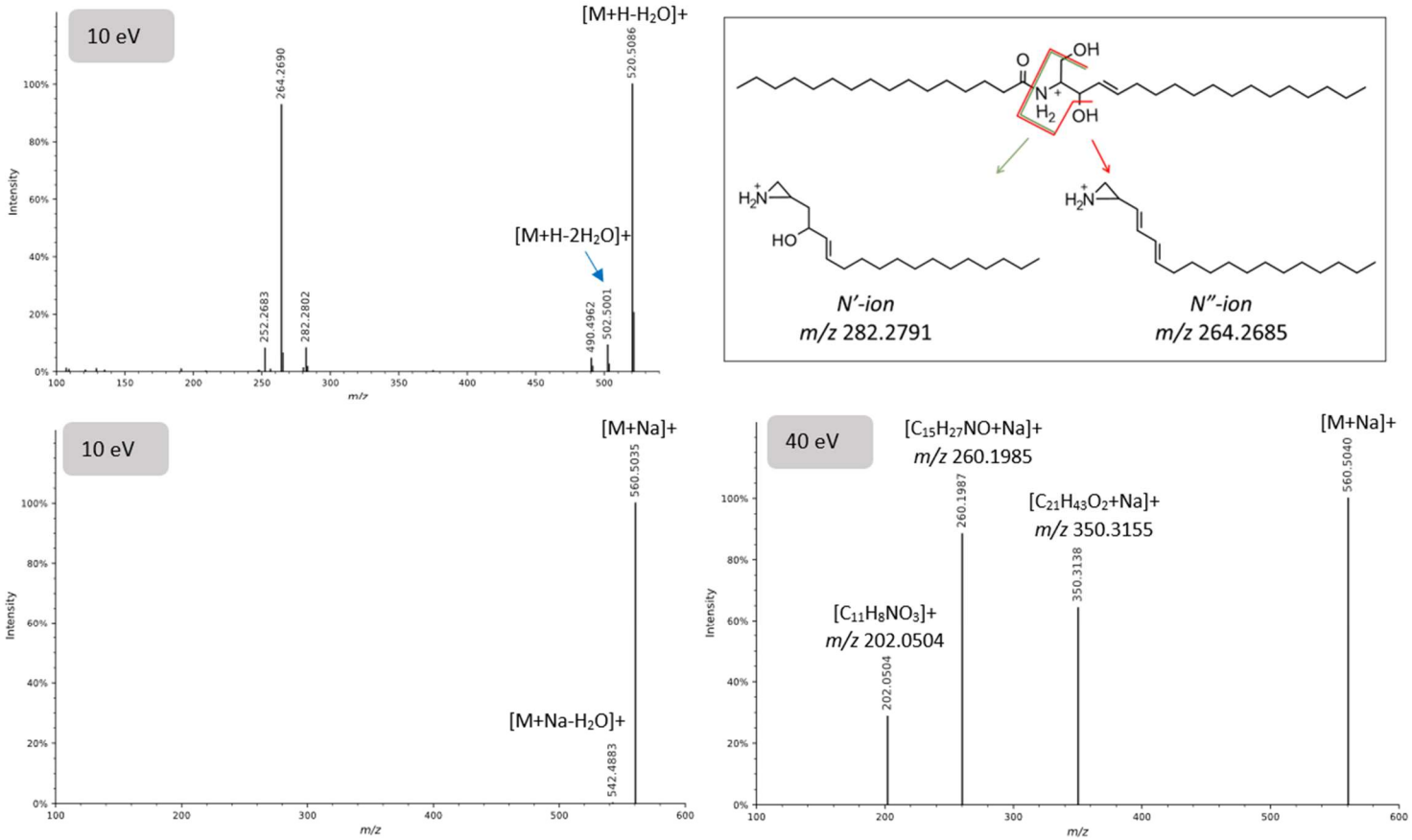

Figure 5.5 MS/MS spectra of N-palmitoyl-sphingosine $[M+H]^+$ at CID 10 eV and $[M+Na]^+$ at CID 10 eV and 40 eV.

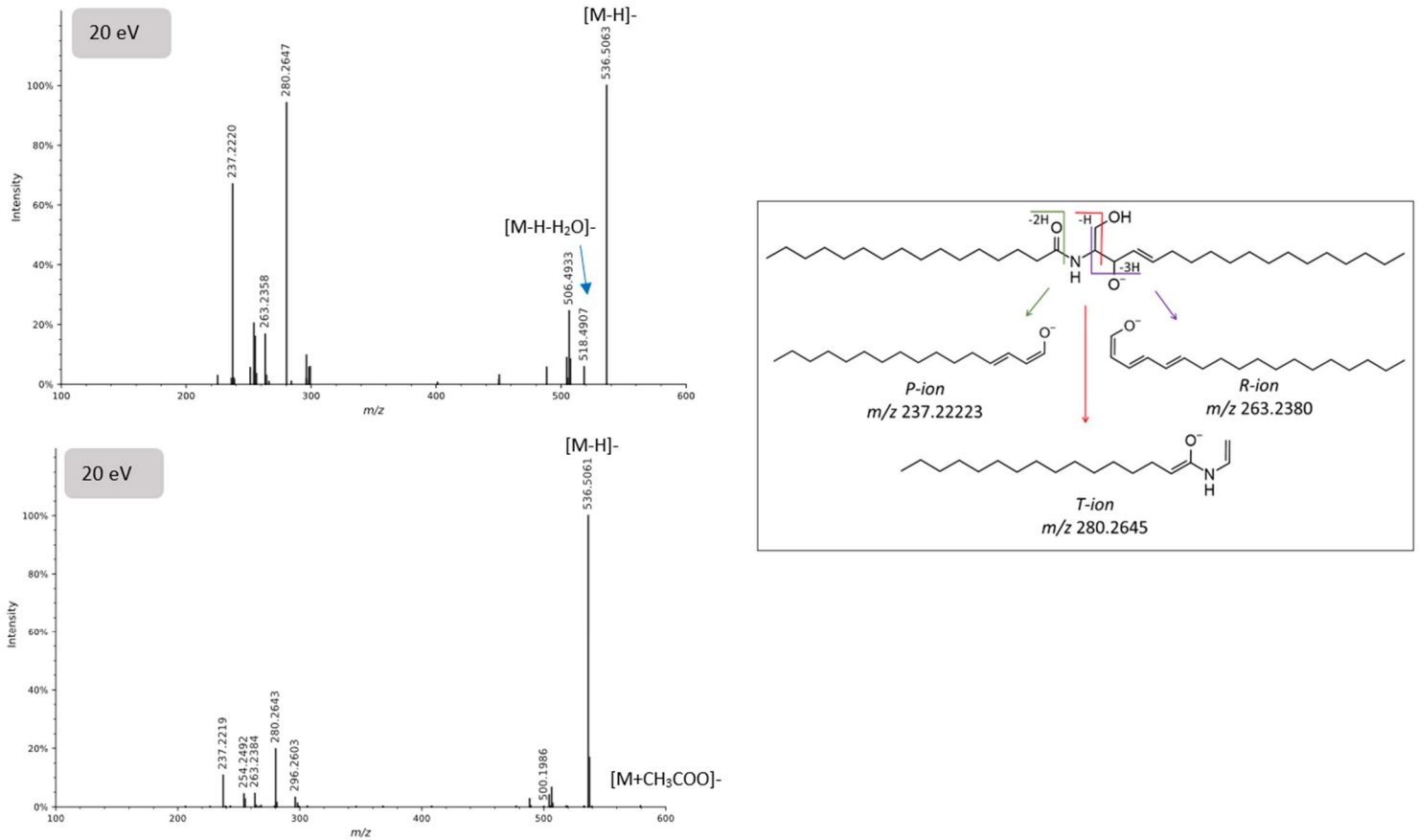

Figure 5.6 MS/MS spectra of N-palmitoyl-sphingosine $[M-H]^-$ and $[M+ CH_3COO]^-$ at CID 20 eV.

In Figure 5.6, N-palmitoyl-D-sphingosine generated $[M-H]^-$ and $[M+CH_3COO]^-$ ions. It is clear that the formation of different adduct types affects the energy state of the molecule as the characteristic series of ions P, T, and R (Domon & Costello, 1988) (Figure 5.6) have lower intensities at 20 eV for the acetate adduct in comparison to the deprotonated compound. While this is not problematic for an individually injected standard, several isobaric species can be selected for fragmentation in an untargeted metabolomics study, even with a narrow *m/z* window, and thus the intensity of fragment ions relative to the precursor will become more important. Therefore, the inclusion of reference MS/MS spectra, if possible, at different ionization polarities, is valuable for reliable annotation.

5.3.2.3. In-source fragments as precursor ions

In-source fragmentation (ISF) is a common effect in ESI for a wide range of molecules and can be reduced by optimization of instrumentation settings. However, ISF cannot be completely avoided since it usually occurs due to the pressure difference that ions experience when being transferred from the atmospheric pressure region to the low-pressure region in the first stage of the mass spectrometer (Criscuolo et al., 2020). To increase confidence in compound annotation, ISF MS/MS spectra were retained in the library since they contain important information to characterize the ionization behavior of different molecule classes and help to reduce false positives when combined with retention time information.

For instance, the analysis of cholesterol and cholesteryl esters using ESI is usually performed in positive mode with the formation of sodiated and/or ammonium adducts. The formation of the characteristic cholestene ion at *m/z* 369.3515 was observed during the injection of cholesterol (Figure 5.7). However, the latter ion is probably formed due to ISF of the $[M+NH_4]^+$ adduct which plays an important role in the mechanisms of formation of this ion (R. C. Murphy, 2014). Interestingly, the MS/MS spectra of cholesterol shown in Figure 5.7 had cholestene as a precursor ion which generated a myriad of fragment ions at lower mass ranges (< 200 Da).

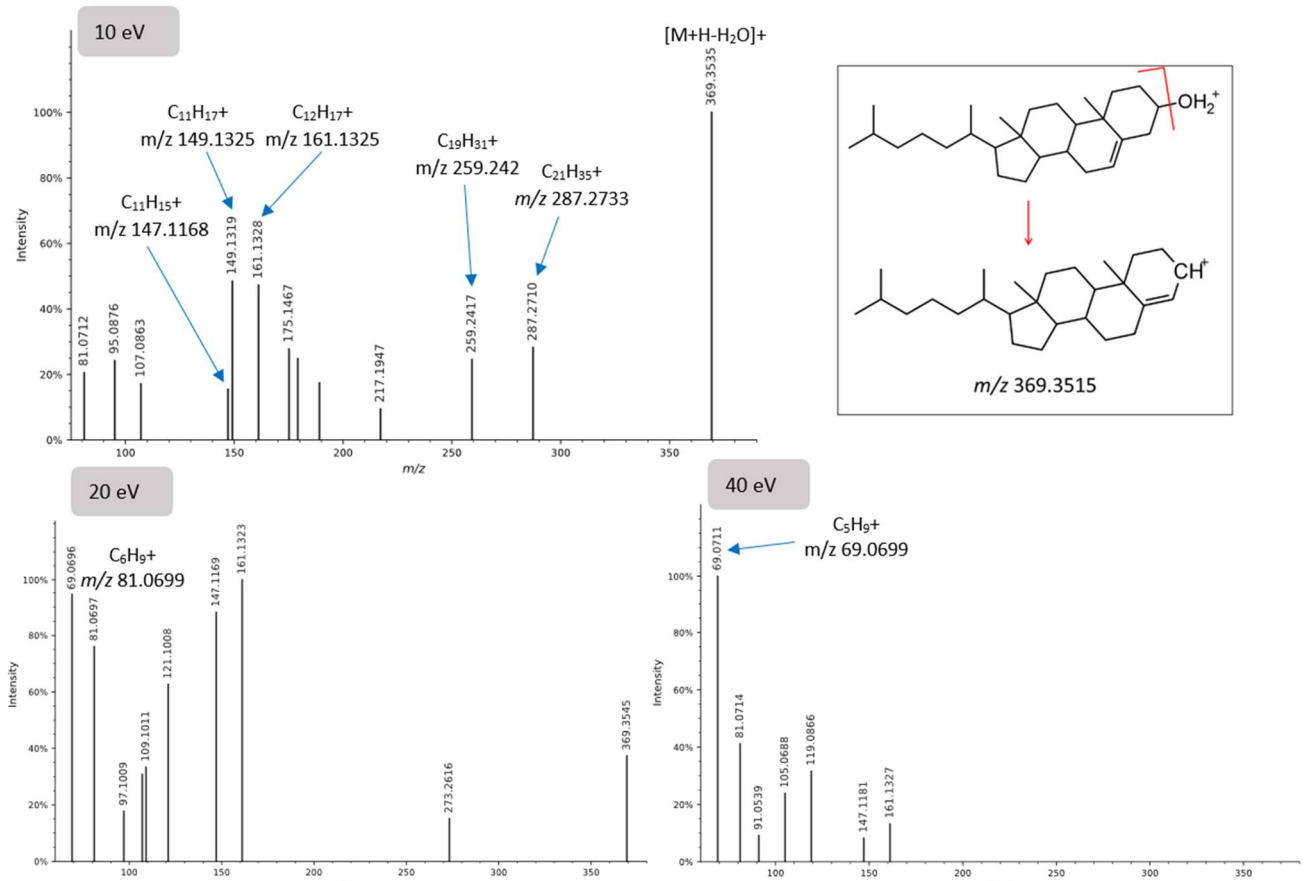

Figure 5.7 MS/MS spectra of the $[M+H-H_2O]^+$ ion of cholesterol at CID 10, 20 and 40 eV.

5.3.2.4. Radical ions in ESI and CID-based tandem mass spectrometry

A recent study showed that for different compound classes, even-electron precursor ions can also generate radical fragment ions representing a high percentage of their MS/MS spectrum (e.g., up to 30% for benzenoids (Djoumbou Feunang et al., 2016)), highlighting the importance of including these ions in experimental metabolite libraries for further implementation to *in silico* MS/MS spectra tools (Xing & Huan, 2022).

Radical ions ($M^{\bullet+}$) are usually formed by electron impact (EI). However, it was shown that odd-electron ions can dissociate forming odd and even-electron ions using CID-based fragmentation depending on the oxidation potential of the compound, mobile phase composition, and capillary voltage (Guaratini et al., 2004; Neto et al., 2016). In the metabolite library of this work, the prenol lipid β-carotene formed a $[M]^{\bullet+}$ under ESI conditions, and its MS/MS spectra are shown in Figure 5.8. As previously reported, an electrocyclic reaction with elimination of toluene (92 Da) can generate an ion at *m/z* 444.3743 $[C_{33}H_{48}]^{\bullet+}$ (double bond equivalent (DBE) number = 10) observed at both 10 and 20 eV (Guaratini et al., 2004; Neto et al., 2016). Alternatively, several ions in the MS/MS spectra are even-electron fragments such as *m/z* 119.0855 ($[C_9H_{11}]^+$, DBE = 4.5) formed by rearrangement and elimination in the central part of the polyene carbon chain that occurs in both $[M]^{\bullet+}$ and $[M+H]^+$ ion species (Rivera et al., 2014). As another example of radical ion fragment formation in ESI, the MS/MS spectra of the benzenoid liothyronine, a halogenated compound, are shown in Figure 5.9. The compound showed abundant radical fragment ions at *m/z* 478.8859 $[C_{14}H_{11}I_2NO_2]^{\bullet+}$ (DBE = 9) resulting from the loss of H_2O, CO, and one I, and at *m/z* 507.8663 $[C_{15}H_{10}I_2O_4]^{\bullet+}$ (DBE = 10) from the loss of NH_3 and I (Zhao et al., 2006). Bile acids, such as cholic acid, also showed minor ions originating from homolytic cleavage of carbon bonds (Figure 5.10), in addition to the generation of typical even-electron ions. The mechanisms for the formation of these ions for both free and conjugated species are well-known and depend on the applied collision energy (Griffiths, 2003). While only neutral losses, such as $[M\text{-}H\text{-}H_2O]^-$, $[M\text{-}H\text{-}2H_2O]^-$, $[M\text{-}H\text{-}H_2O\text{-}CO_2]^-$, were observed at lower collision energies (10 and 20 eV), radical ions were observed at 40 eV (Figure 5.10).

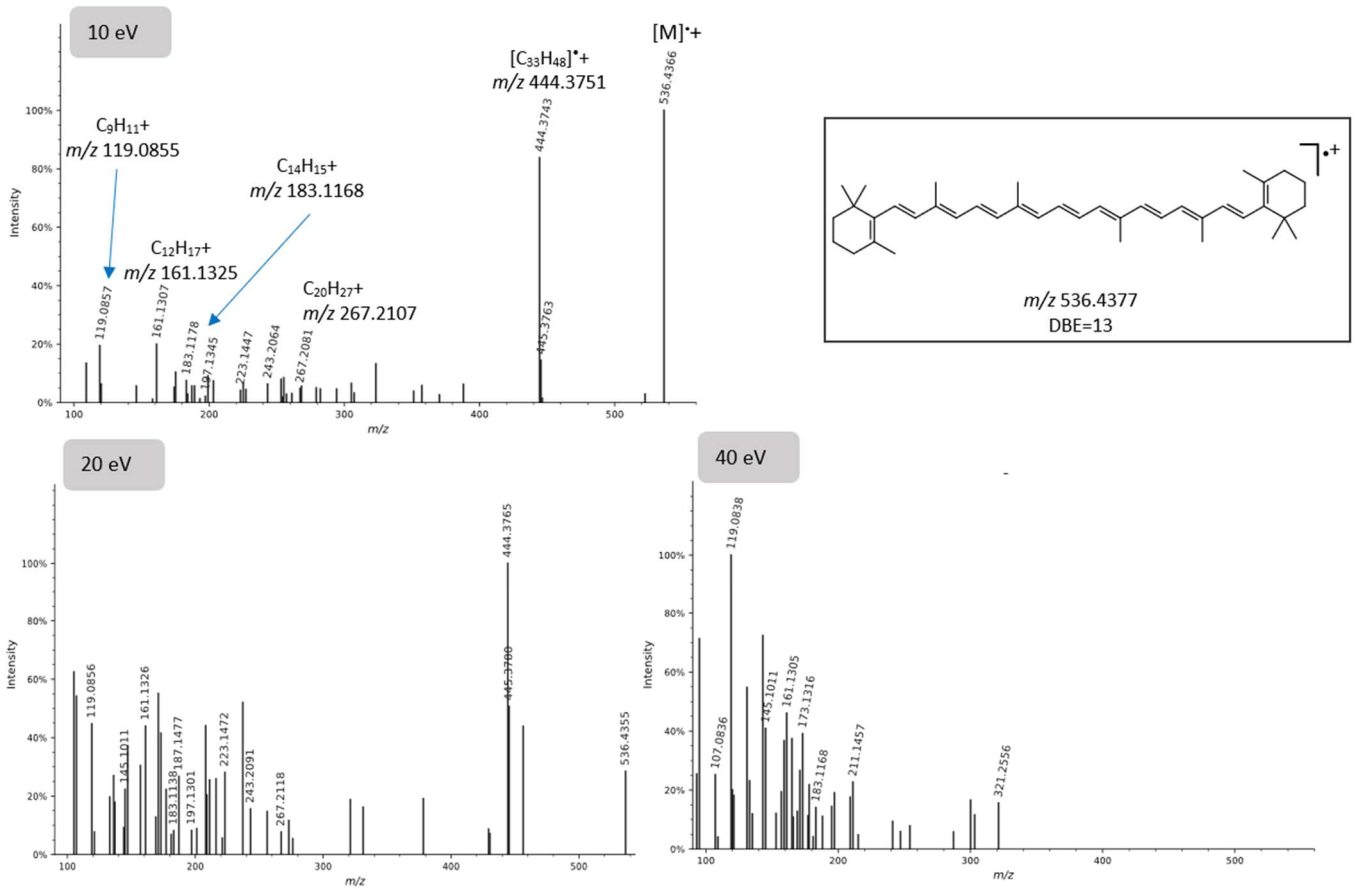

Figure 5.8 MS/MS spectra of β-carotene [M+•] ion at CID 10, 20 and 40 eV. The formula annotated fragment ions are present in at least two collision energies. DBE: double bond equivalent.

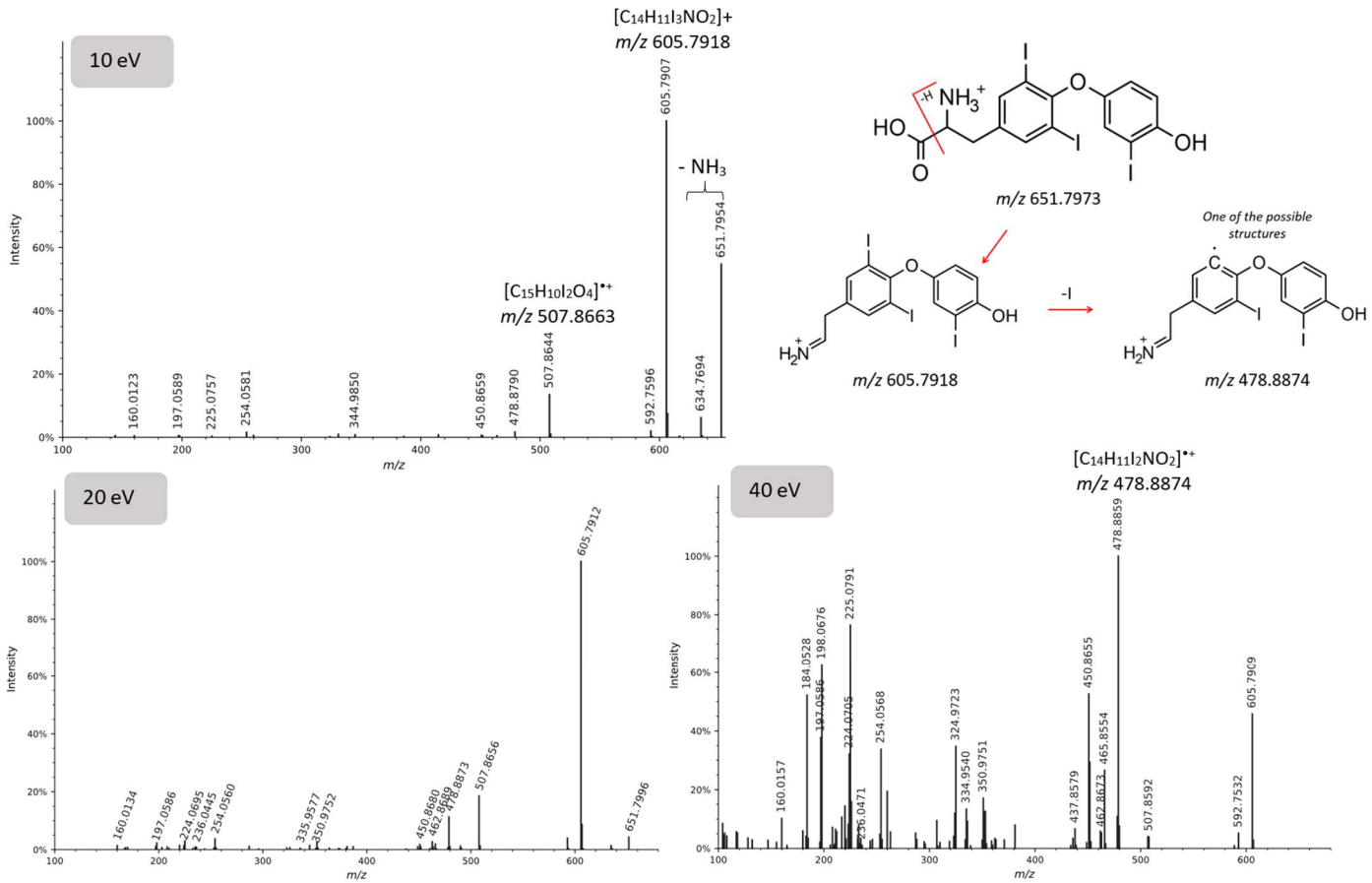

Figure 5.9 MS/MS spectra of liothyronine $[M+H]^+$ ion at CID 10, 20 and 40 eV.

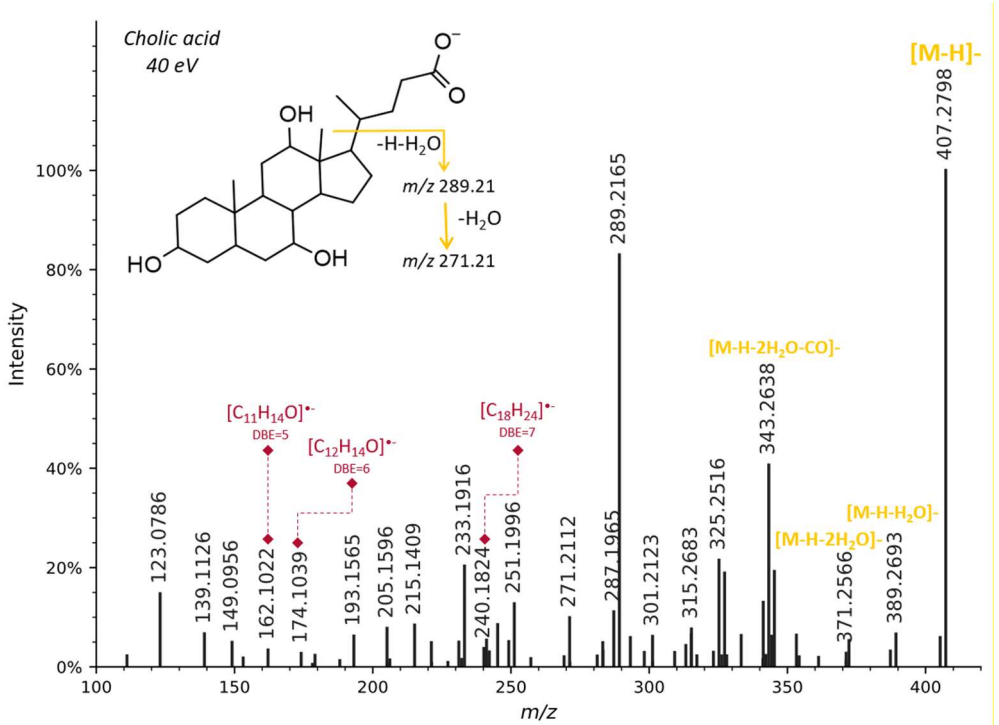

Figure 5.10 Example of fragment ions with integer double bond equivalents (DBE) in the MS/MS spectra of cholic acid at 40 eV.

5.3.3. Liquid chromatography

The use of RPLC can facilitate metabolite annotation by separating molecular isomers, reducing co-elution, and decreasing matrix effects. For example, *sn*-positional isomers of 1-octadecanoyl-glycero-3-phosphocholine and 1-octadecanoyl-glycerol could be resolved with the BEH C18 RPLC column used during this study (da Silva, Iturrospe, Heyrman, et al., 2021). Note that in biological samples, the separation of *sn*-positional isomers can become more difficult as chromatograms can be highly populated. Also, compounds that generate high abundant ISF ions, such as prostaglandins, can benefit from separation before MS/MS analysis. Prostaglandin E1 (PGE1) generates $[M\text{-}H\text{-}H_2O]^-$ in the source, which has a very similar fragmentation pattern compared to prostaglandin A1 (PGA1) (R. C. Murphy et al., 2005). Thus, RT information is crucial to assign a correct structure since PGE1 can be resolved from PGA1 by two minutes difference (3.2 and 5.0 min, respectively).

The separation mechanism in common C18-based columns is based on the hydrophobic interactions that can separate lipids by their carbon chain length, and the level of saturation (Lange et al., 2019). As a result, different classes can be mapped within RT ranges. These class-specific RT windows can then be used to filter false positive lipid annotations in complex matrices using Kendrick mass defect plotted against reversed-

phase RT values (da Silva, Iturrospe, et al., 2022; Lange et al., 2021; Lerno et al., 2010). When the RT of metabolites follows class-specific RT windows during the annotation of a metabolomics dataset, these RTs can be used as an additional confirmation for putative annotations (Ovčačíková et al., 2016). In addition, RT information can also be used to show the structural characteristic behavior within the same class. For fatty acyls in negative ionization mode, a RT window was observed from 3 minutes to 17 minutes. Within the same class, a larger carbon chain results in increased RT. The oxidized fatty acyls elute first, for example, prostaglandin E2 has lower retention on RPLC due to its higher polarity with a retention time of 3.0 min. Unsaturated fatty acyls elute earlier than their saturated carbon chain equivalents. For example, eicosapentaenoic acid (FA 20:5) elutes at 8.2 min, while eicosanoic acid (FA 20:0) has an RT of 13.5 min.

5.3.4. Ion mobility spectrometry

5.3.4.1. Additional separation and CCS for annotation

In addition to *m/z*, MS/MS spectra, and RT, ion mobility provides CCS values as an additional molecular descriptor, to further increase annotation confidence (Celma et al., 2020; Pičmanová et al., 2022). In addition, CCS values can be used as a class annotation filter (Qian Wu et al., 2020). When plotting CCS values in function of *m/z* values, metabolites within the same class will cluster together as their similarity in the chemical space is reflected in their ion mobility behavior. As a result of this clustering behavior, metabolites that show a large deviation in CCS within their class can be flagged as possible false positive annotations. In addition, CCS values can help in the structural characterization of lipids. Lipid species within the same class show increasing CCS values with increasing fatty acyl chain length as their increased size will cause slower passage through the ion mobility spectrometer. For example, the $^{DT}CCS_{N2}$ value for [Cer d18:1/16:0+H]$^+$ was determined to be 255.1 Å², while a $^{DT}CCS_{N2}$ value of 258.6 Å² was derived for [Cer d18:1/17:0+H]$^+$. In contrast to the direct relation between CCS value and fatty acyl chain length, there is an inverse relation with the degree of unsaturation, as an increasing degree of unsaturation can compact the conformation, increasing the speed of the analytical ions traveling through the buffer gas. This latter is shown in the IM separation of [Cer d18:1/16:0+H]$^+$ and [Cer d18:0/16:0+H]$^+$ providing $^{DT}CCS_{N2}$ values of 255.1 Å² and 257.4 Å², respectively.

Unlike LC where multiple ion species derived from the same compound show the same RT, the ion species will impact the ion mobility behavior. For example, [coenzyme Q10+Na]$^+$ and [coenzyme Q10+H]$^+$ showed a $^{DT}CCS_{N2}$ value of 307.6 Å² and 303.9 Å², respectively. The higher CCS value for the [M+Na]$^+$ adduct compared to [M+H]$^+$ could be explained by the larger size of the [M+Na]$^+$ adduct and was observed for all classes within the library. Interestingly, ceramides were the only class where the [M+Na]$^+$

adduct showed lower CCS values compared to $[M+H]^+$, which could be related to gas-phase conformational changes induced by adduct formation. This latter was consistently observed for all ceramides, while *in silico* tools always predicted a higher CCS value for the $[M+Na]^+$ adduct compared to $[M+H]^+$. High repeatability of the $^{DT}CCS_{N2}$ measurements is reflected by > 85% of $^{DT}CCS_{N2}$ showing an SD ≤ 0.1 Å² (*N*=3). The largest SD of 1.2 Å² was obtained for $[PGA1+H-H_2O]^+$. This latter SD can be explained by the broader peak of $[PGA1+H-H_2O]^+$ in the IM spectrum compared to for example $[PGA1+Na]^+$. As PGA1 contains both a carboxyl and a hydroxyl group, water loss could occur at two different positions. These two different isomers of $[PGA1+H-H_2O]^+$ could cause one broad peak when baseline separation did not occur. This behavior would be in line with the IM spectrum of $[aldosterone+H]^+$, where IM was able to provide different $^{DT}CCS_{N2}$ values for two protomers of aldosterone (Figure 5.11). Both CCS values were reported on PubChem. The $^{DT}CCS_{N2}$ value for the protomer generating the most intense signal was reported in the library.

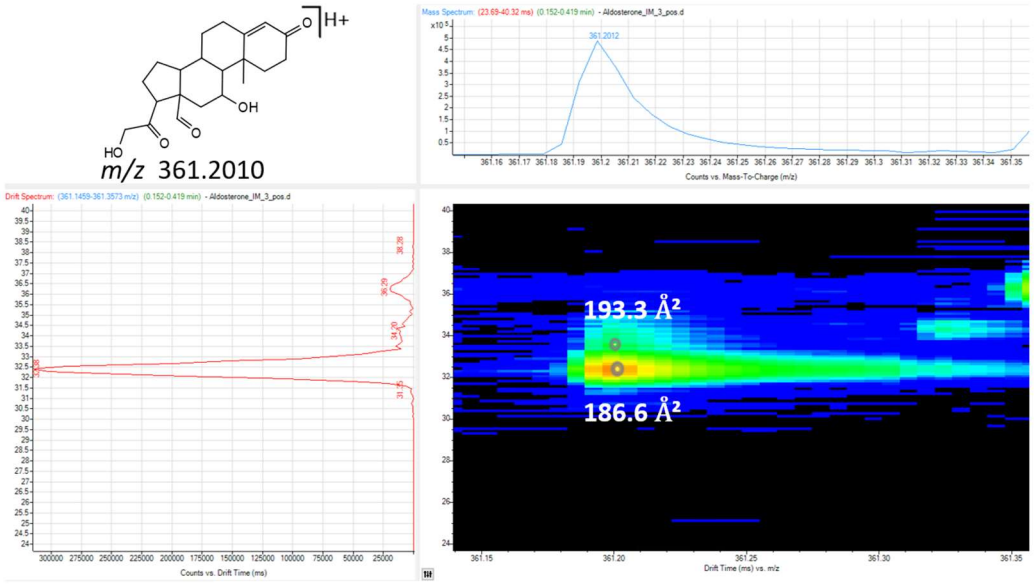

Figure 5.11 Ion mobility spectrum of $[aldosterone+H]^+$ showing different $^{DT}CCS_{N2}$ values for two protomers.

5.3.4.2. CCS predictions

After calculating single-field $^{DT}CCS_{N2}$ values from experimentally acquired drift times of reference standards, they were compared to *in silico* generated CCS values. For the prediction of CCS values, three different tools were used; AllCCS (Zhiwei Zhou et al., 2020), CCSbase (Ross et al., 2020), and DeepCCS (Plante et al., 2019). Compared to experimental single-field $^{DT}CCS_{N2}$ values, CCSbase predictions showed the highest

Pearson correlation coefficient of 0.995, followed by AllCCS with 0.987 and DeepCCS with 0.978 (Figure 5.12). For the generation of this figure, datapoints were only included when all three software were able to provide a CCS prediction. CCSbase and AllCCS showed similar median prediction errors (1.21% and 1.20% respectively), while the prediction error was larger for DeepCCS (2.09%). These results are in line with the root mean square error (RMSE) (Figure 5.12). Although the prediction capacity of the three tools was similar based on the Pearson correlation coefficients, differences were observed in prediction coverage. Considering all detected ionization species for all reference standards, 195 signals were detected. From these 195 ions, AllCCS was able to predict 174 CCS values, while CCSbase and DeepCCS were only able to predict 157 and 149 CCS values, respectively. When comparing the number of CCS errors below 3% within the predictions per tool, CCSbase showed the highest accuracy (87% of CCS errors < 3%), followed by AllCCS (81%) and DeepCCS (56%).

However, the complementarity of *in silico* tools needs to be highlighted as for example, AllCCS was not able to predict CCS values for cardiolipins, unlike CCSbase and DeepCCS. On the other hand, AllCCS was the only tool able to predict CCS values for $[M+H-H_2O]^+$ adducts. As AllCCS showed the highest prediction coverage, combined with the lowest median prediction error and a high Pearson correlation coefficient, the use of this prediction tool is suggested as primary tool for confirmation of CCS library entries. Multiple prediction tools may be screened for classes for which AllCCS is unable to predict CCS values. The primary aim of this simplified investigation was not to identify the most effective machine learning approach for predicting CCS values. This would require a thorough evaluation of prediction accuracy for a broader range of molecule classes. Instead, our emphasis was on investigating user-friendly and benchmarked tools that can offer predictions within the chemical space of a metabolomics experiment. Important to mention is the current absence of a tool to predict CCS values for $[M+CH_3COO]^-$ adducts, while this adduct is frequently detected and can provide important information on side chain composition, for example for glycerophospholipids.

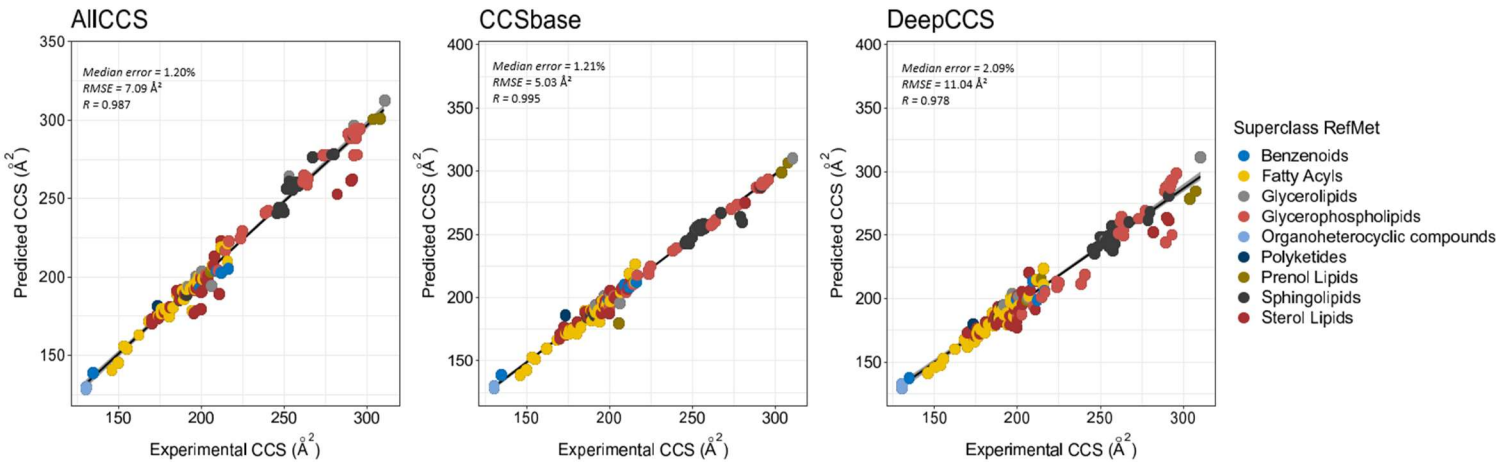

Figure 5.12 Correlation between experimental acquired $^{DT}CCS_{N2}$ values for reference standards and predicted CCS values using AllCCS, CCSbase, and DeepCCS. RefMet super classes were separated by color. RMSE: Root mean square error.

5.4. Conclusions

A multidimensional metabolite library workflow was created with open-source software to confidently annotate features resulting from untargeted metabolomics experiments. Although manual MS/MS spectra verification is still required when using experimental untargeted datasets, the level of confidence is increased by internal library annotation with multidimensional information. A total of 539 MS/MS spectra of different ionization species, 194 retention time values, and 177 CCS values derived from 100 authentic standards, were converted to an open-source format (NIST .msp) and shared via an open-access platform. Building and curating a metabolite library allow to obtain in-depth knowledge of class-specific retention time ranges, the ionization species formed by different compounds, in-source fragmentation, and trends in IM space. Moreover, sharing retention time values in public databases can aid in the development of prediction models to further characterize the overall retention patterns across different chromatographic systems.

5.5. Data availability

The NIST msp file can be accessed at Metabolomics Library Toxicology Centre (BE) [Data set]. Zenodo. https://doi.org/10.5281/zenodo.6979698

5.6. Supplementary information

SI-1 and SI-2 are available in the electronic supplementary information, which is accessible using the link below.
https://www.dropbox.com/sh/bvxln6vaf00q3hk/AABt5gt5XbDgsROqKY4w7Znla?dl=1

SI-1 (xlsx) provides a table of reference standards used in this chapter (sheet 1). Retention time, CCS values, suppliers, solubilization solvents and CCS predictions were described. In sheet 2, the composition of the SS sample is described, together with the acceptance criteria.
SI-2 provides the library creation workflow in a step-by-step manner.

PART B:
METABOLIC ALTERATIONS IN ETHANOL-INDUCED HEPATOTOXICITY

CHAPTER 6:
METHODOLOGY USED DURING HEPARG EXPERIMENTS

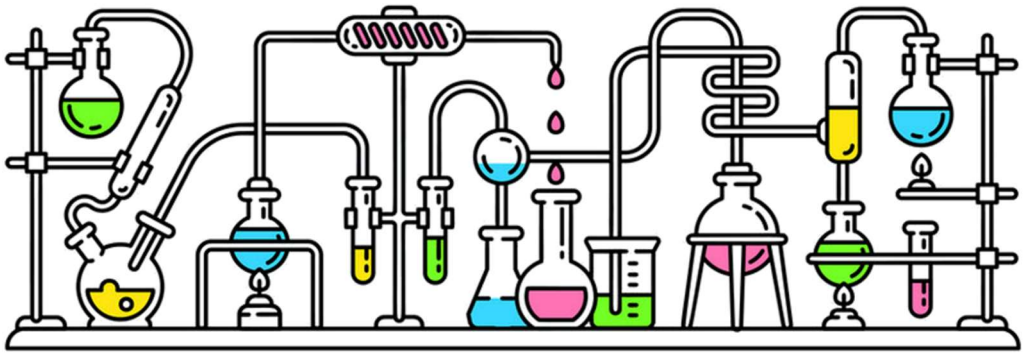

Based on the following publications

Iturrospe E, Da Silva KM, Van de Lavoir M, Robeyns R, Cuykx M, Vanhaecke T, van Nuijs A, Covaci A. Mass spectrometry-based untargeted metabolomics and lipidomics platforms to analyze cell culture extracts. In: González-Domínguez, R. (eds) Mass Spectrometry for Metabolomics. Methods in Molecular Biology, Springer Nature. 2023; 2571, 189-206. Humana, New York, NY. (DOI: 10.1007/978-1-0716-2699-3_19).

Iturrospe E, Da Silva KM, Robeyns R, Van de Lavoir M, Boeckmans J, Vanhaecke T, van Nuijs A, Covaci A. Metabolic signature of ethanol-induced hepatotoxicity in HepaRG cells by LC-MS-based untargeted metabolomics. Journal of Proteome Research. 2022; 21(4), 1153-1166. (DOI: 10.1021/acs.jproteome.2c00029).

Iturrospe E, Robeyns R, Da Silva KM, Van de Lavoir M, Boeckmans J, Vanhaecke T, van Nuijs A, Covaci A. Metabolic signature of HepaRG cells exposed to ethanol and tumor necrosis factor alpha to study alcoholic steatohepatitis by LC-MS-based untargeted metabolomics. Archives of Toxicology. 2023; 97, 1335-1353. (DOI: 10.1007/s00204-023-03470-y).

6.1. Introduction

This chapter extensively describes the methodology used for HepaRG experiments, while the metabolic signature of HepaRG exposure to ethanol and to ethanol combined with tumor necrosis factor alpha (TNF-α) are discussed in the following two chapters.
An overview is provided on dosage estimation of ethanol for cell exposure, as well as cell cultivation procedures and sample preparation methods. Analytical methods for untargeted metabolomics employing LC-(DTIMS)-QTOF-MS/MS, which were optimized in chapter 3 (polar metabolites) and chapter 4 (lipids), are summarized, including analytical QA/QC procedures. In addition, a method for ethanol quantification using headspace-gas chromatography-flame ionization detection is described. Employed data analysis, including data preprocessing, pretreatment, statistics and metabolite annotation methods are discussed.

6.2. Chemicals and materials

Internal standards hippuric acid-(phenyl-$^{13}C_6$), L-lysine-$^{13}C_6$-$^{15}N_2$, Leucine-5,5,5-D_3, glucose-$^{13}C_6$, glyceryl tri(palmitate-1-^{13}C) and cholic acid-2,2,4,4-D_4 were purchased from Sigma Aldrich (St. Louis, Missouri, USA). Lauric acid-12,12,12-D_3 was bought from CDN Isotopes (Pointe-Claire, Quebec, Canada), caffeine-$^{13}C_3$ from Cerilliant Corporation (Texas, USA), 18:1-D_7 lyso PE from Avanti Polar Lipids and octanoyl-L-carnitine-(N-methyl-D_3), ceramide (d18:1/18:1(9Z)-$^{13}C_{18}$) and L-phenylalanine-$^{13}C_9$-^{15}N from Cambridge Isotope Laboratories (Massachusetts, USA). Methanol (MeOH), acetonitrile (ACN) and formic acid (99%, HCOOH), all ULC/MS-CC/CSF grade, were purchased from Biosolve (Valkenswaard, The Netherlands). Ammonium formate (≥ 99%, $HCOONH_4$) LC-MS grade, ammonium carbonate HPLC grade ($(NH_4)_2CO_3$) and ammonium acetate LC-MS grade (CH_3COONH_4) were obtained from Sigma Aldrich. Acetic acid (100%, CH_3COOH) and ammonia solution (25%, $NH_{3(aq)}$), both LC-MS grade, isopropanol for analysis (ACS reagent) (IPA) and chloroform (analytical grade) ($CHCl_3$), were purchased from Merck (Darmstadt, Germany). Ultrapure water (H_2O) used throughout the experiments was obtained from an Elga Pure Lab apparatus (Tienen, Belgium). L-ascorbic acid (≥ 99%), butylated hydroxytoluene (≥ 99%, BHT), EDTA (99.995%) and neutral red (BioReagent) were purchased from Sigma Aldrich. Ethanol for cell exposure (≥ 99.8%, molecular biology, EtOH) was purchased from Sigma Aldrich, while recombinant human TNF-α was acquired from Prospec-Tany TechnoGene Ltd. (Rehovot, Israel). Eppendorf Safe-Lock tubes, reacti-vials and 0.2 µm nylon centrifugal filters were acquired from Eppendorf, Thermo Scientific and VWR (Pennsylvania, USA), respectively. Pure, dry nitrogen (AZOTE N28, N_2) used for solvent evaporation was obtained from Air

Liquide Belge (Liège, Belgium). 384-well plates (PS, small volume) were bought from Greiner Bio-One (Vilvoorde, Belgium).

6.3. Dosage estimation

The inhibitory concentration $(IC)_{10}$ of ethanol in HepaRG cells (i.e., concentration of ethanol that causes a decrease of 10% in HepaRG cell viability) was determined after 24 h and 48 h exposure via the neutral red uptake assay as described by Ates *et al.*(2017). Differentiated HepaRG cells (Biopredic International, Rennes, France) were seeded in 96-well plates (Falcon, Corning, New York, USA) at a concentration of 94 x 10^3 cells per well. The cells were incubated for 7 days at 37 °C, 5% CO_2, and saturated humidity. On day 7, cells were divided into equal groups I and II, which were subject to 24 h and 48 h of ethanol exposure, respectively. Cells from groups I and II were exposed to eight different concentrations of ethanol (range 250-950 mM, increments of 100 mM) for 24 h. For cells of group II, ethanol-containing media were renewed after 24 h and exposure was continued for another 24 h. In addition, unexposed negative controls and blanks were obtained.

After exposure, used media were replaced by neutral red-containing media (25 µg/mL) and incubation was continued for another 3 h. Media were washed away using phosphate-buffered saline (PBS, 37 °C), and a desorption solution was added to the cells (1 CH_3COOH, 50 EtOH and 49 H_2O, v/v/v) after which they were shaken for 30 min at 80 rpm in a dark environment. After 5 min equilibration, absorption was measured at 540 ± 10 nm using a victor³ 1420 multilabel counter (Perkin Elmer, Massachusetts, USA). Experiments were conducted in triplicate. To avoid cross-contamination due to the volatile nature of EtOH, separate well plates were used for each concentration of EtOH and PBS containing the same EtOH concentration was used to fill surrounding wells. Absorbance versus EtOH concentration was plotted using four-parameter logistics least squares regression in Graphpad Prism (v. 9.0) (Figure 6.1), which enabled the calculation of the IC_{50} and the Hill slope. The latter two parameters were used to calculate the IC_{10} value, according to equation 6.1.

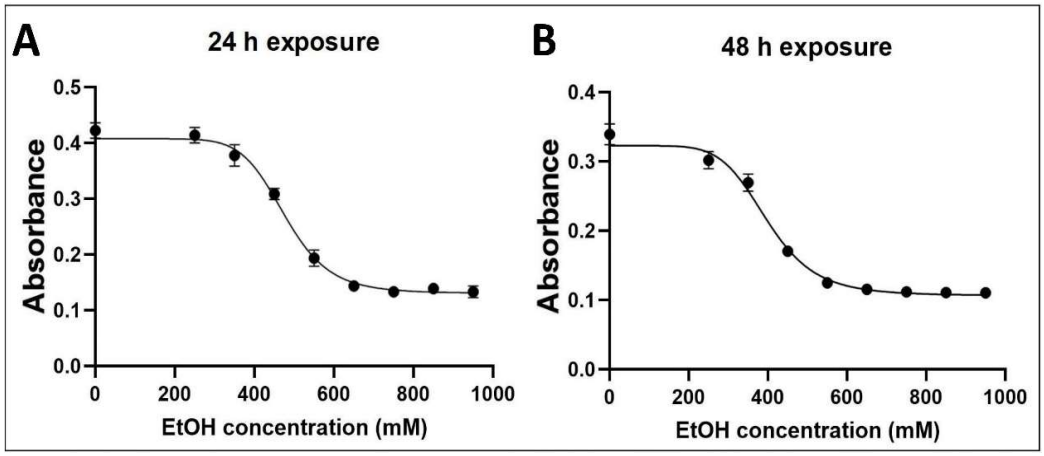

Figure 6.1 Absorbance measured during neutral red uptake assay for 24 h (A) and 48 h (B) of ethanol exposure. Cells were incubated using eight different ethanol concentrations (n = 3).

$$IC10 = \left(\frac{90}{100 - 90}\right)^{1/H} * IC50$$

Equation 6.1 IC_{10} calculation using IC_{50} and Hill slope.

The IC_{10} value for HepaRG cells exposed for 24 h and 48 h to EtOH was determined to be 368 mM and 284 mM, respectively.

6.4. Cell cultivation and exposure

Ethical approval for the use of HepaRG cells was provided by the Medical Ethics Committee of the University Hospital Brussels (reference number 143201941214). Differentiated HepaRG cells were seeded in collagen-coated Permanox 2-well Lab-Tek chamber slides (Nunc, Thermo Scientific, Rochester NY, USA) at a concentration of 1 x 10^6 cells per well (day 0). The chamber slides were coated with rat tail collagen type I (Corning, New York, USA). For seeding of the cells, Basal Hepatic Medium with HepaRG Thaw, Seed and General-Purpose Supplement (Biopredic International) was used. The cells were incubated at 37 °C, 5% CO_2 and saturated humidity using a Galaxy 170 S incubator (Eppendorf, Hamburg, Germany). On day 1 of incubation, the medium was replaced by Basal Hepatic Medium with HepaRG Maintenance and Metabolism Supplement (Biopredic International) (1.2 mL per well). On days 3 and 6, the medium was renewed and cell exposure to ethanol (or ethanol and TNF-α) was initiated on day 7.

All exposure experiments were repeated to validate the experiment, using a second batch of HepaRG cells (batch numbers were 116310 and 116308, respectively). Since cell samples (i.e., intracellular (IC) fraction) and conditioned media samples (i.e.,

extracellular (EC) fraction) were prepared separately (see 6.5), subsequent data acquisition and -analysis were used for metabolic fingerprinting and footprinting, respectively.

Due to the volatile nature of ethanol, concentration loss during cultivation was expected. More importantly, ethanol evaporation from cells exposed to a high concentration can cause cross-contamination of cells exposed to a low concentration or unexposed negative controls. Therefore, cells were cultivated in chamber slides within Petri dishes to minimize the risk of cross-contamination. Each chamber slide comprised two wells. Cells were exposed to ethanol-containing medium in one well, while PBS with the same ethanol concentration was added to the second well. In addition, the concentration of ethanol in the medium was determined before and after cultivation using headspace gas chromatography with flame ionization detection (HS-GC-FID).

6.5. Sample preparation

6.5.1. Intracellular HepaRG extracts

After cell exposure, media were collected (6.5.2) and the chamber slides were washed twice using PBS (37 °C) before snap-freezing with liquid N_2. Quenching was performed using 300 µL of a solution, which consisted of 80% (v/v) MeOH and 20% (v/v) of 10 mM CH_3COONH_4 at -80 °C. After 2 min, the cells were scraped and transferred to a vial for liquid-liquid extraction (LLE), which contained 500 µL of a polar mixture and 420 µL of an apolar mixture (at -20 °C). The polar mixture consisted out of 1 mM $(NH_4)_2EDTA$ and 0.5 mM ascorbic acid in 5 mM CH_3COONH_4 with 0.1% (v/v) CH_3COOH (pH 4.2). The apolar mixture consisted of 1 mM BHT in $CHCl_3$. Another 300 µL of the quenching solution was used for rinsing and was collected in the same LLE-vial.

Internal standard mixture 1 contained 22 µg/mL lauric acid-12,12,12-D_3, cholic acid-2,2,4,4-D_4, glyceryl tri(palmitate-1-^{13}C), 18:1-D_7 lyso PE, octanoyl-L-carnitine-(N-methyl-D_3) and ceramide (d18:1/18:1(9Z)-$^{13}C_{18}$) in $CHCl_3$. Internal standard mixture 2 contained 14 µg/mL hippuric acid-(phenyl-$^{13}C_6$), L-lysine-$^{13}C_6$-$^{15}N_2$, leucine-5,5,5-D_3, glucose-$^{13}C_6$, caffeine-$^{13}C_3$ and L-phenylalanine-$^{13}C_9$-^{15}N in H_2O/MeOH (1/1, v/v). Aliquots of 20 µL of internal standard mixtures 1 and 2 were added to each LLE-vial (final concentration after reconstitution 2 µg/mL). This latter concentration of internal standards is doubled compared to the concentrations used in chapter 3 and 4, to ensure easy evaluation and to minimize the risk of low S/N ratios due to poor ionization and/or ion suppression.

The extraction mixture was subsequently vortexed for 90 s, equilibrated for 10 min on ice, centrifuged at 2,200 g for 7 min at room temperature and again equilibrated for 10 min on ice. A volume of 900 µL of the polar fraction (upper phase) was transferred to an Eppendorf tube, without transferring solid particles from the protein disk. After

vortexing for 20 s, 450 µL was transferred to a second Eppendorf tube after which the liquid of both Eppendorf tubes was evaporated using pure, dry nitrogen at room temperature. 240 µL of the apolar fraction (lower phase) was transferred to a reacti-vial. After vortexing for 20 s, 120 µL was transferred to a second reacti-vial, after which the liquid was evaporated using pure, dry N_2 at room temperature. Dried extracts were stored at -80 °C and reconstituted directly before analysis. Each fraction (polar and apolar) was divided into two subfractions right before the evaporation step, in order to analyze each subfraction using a different polarity during liquid chromatography (LC) – (drift tube ion mobility (DTIM) –) high resolution mass spectrometry (HRMS) acquisitions. Extracts from the polar and apolar fractions were reconstituted on ice using 60 µL of ACN/H_2O (65/35, v/v) and IPA/MeOH (35/65, v/v), respectively. After vortexing for 90 s, samples were filtered using 0.2 µm nylon centrifugal filters and centrifugated at 14,000 g for 2 min at room temperature. Ten µL of each extract was transferred to an LC-vial to create a QC pool. Another 20 µL of each sample was transferred to a Greiner Bio-One 384-well plate (small volume). Surrounding wells were filled with solvent blanks and the well plate was sealed using aluminum adhesive. Both the well plate and the QC pool were transferred to the autosampler (4 °C) right before analysis.

6.5.2. Extracellular HepaRG extracts

After exposure of HepaRG cells, the incubation medium (1.2 mL per well) was extracted in separate Eppendorf tubes. Blank media were obtained after incubation without HepaRG cells and were treated identically to other samples. From the collected medium, 320 µL was transferred to a second Eppendorf tube, to which 725 µL of the -80 °C quenching solution was added (composition described in 6.5.1). After vortexing for 60 s, 980 µL of the quenched medium was transferred to an LLE-vial and LLE was performed as described in 6.5.1. The same internal standard mixtures were used to obtain a final concentration (i.e., after reconstitution) of 2 µg/mL. After LLE, higher volumes were extracted from the polar (1000 µL) and apolar fractions (290 µL), which were divided in two subfractions before drying. Subsequent sample preparation steps were identical to those for the intracellular extracts (6.5.1). Optimization of the dilution factor used during sample preparation was described in the supplementary information (6.10.1).

6.6. Analytical methods

6.6.1. Data acquisition using LC-(DTIMS)-QTOF-MS/MS

Analytical measurements of the polar fraction of the samples were carried out on an Agilent 1290 Infinity UPLC system coupled to an Agilent 6530 quadrupole-time-of-flight

(QTOF) HRMS with Agilent Jet Stream Electrospray Ionization (Agilent Technologies, Santa Clara, USA). In ESI (+), an iHILIC-Fusion column (100 x 2.1 mm, 1.8 µm, zwitterionic, charge modulated amide, silica-based, HILICON AB, Sweden) was used with 10 mM $HCOONH_4$ and 0.1% (v/v) HCOOH in H_2O/MeOH (9/1, v/v) as mobile phase A (MPA) and ACN as mobile phase B (MPB). In ESI (-), an iHILIC-Fusion(P) column (100 x 2.1 mm, 5 µm, zwitterionic, charge modulated amide, polymer-based, HILICON AB), was used with H_2O containing 2 mM CH_3COONH_4 and 2 mM $(NH_4)_2CO_3$ as MPA and ACN/MeOH (9/1, v/v) as MPB.

The analytical measurements of the apolar fraction of the samples were carried out on an Agilent 1290 Infinity II LC system coupled to an Agilent 6560 DTIM-QTOF-HRMS using Agilent Dual Jet Stream Electrospray Ionization. In both ESI (+) and ESI (-) modes, an ACQUITY UPLC BEH C18 column (150 x 2.1 mm, 1.7 µm, Waters Corporation, Massachusetts, USA) was used with 5 mM CH_3COONH_4 in H_2O/ACN (7/3, v/v) as MPA and 5 mM CH_3COONH_4 in H_2O/ACN/IPA (2/10/88, v/v/v) as MPB. In ESI (+) mode, 0.1% (v/v) CH_3COOH was added to the aqueous fraction of MPA and MPB.

Data were acquired in 2 GHz extended dynamic mode for all four analytical methods. Details on the LC and QTOF parameters can be found in Table 6.1.

Before each analytical run, a system suitability sample was injected which needed to fulfill preset criteria concerning peak height, mass error and RT deviation (6.9). All samples were randomized before injection, and data were acquired in full scan (MS1) profile mode. A QC pooled sample was injected at regular intervals (n = 6-7). Data-dependent acquisition (auto-MS/MS) with iterative exclusion (Koelmel, Kroeger, Gill, et al., 2017) was obtained during conditioning of the system by at least six injections of the QC pooled sample. In addition, fragmentation target lists were built for interesting features selected by the statistical workflow of the first experiment, and applied during data acquisition of the validation experiment. Since lipids comprise a wide variety of isomers and isobars, additional ion mobility (IM) data was acquired for the QC pool of the apolar fraction of the HepaRG samples, both in single pulse and 4-bit multiplexed mode. Details on the DTIMS parameters can be found in Table 6.1.

Table 6.1 Data acquisition parameters per sample fraction. For mobile phase compositions, modifier concentrations were calculated based on the volume of the aqueous fraction. For polar methods (ESI (+) and ESI (-)), additional MS2 runs were acquired using one collision energy at a time (10, 20 or 40 eV) with a maximum of 12 precursors per scan cycle (*). During validation experiments, fragmentation target lists were used based on interesting features elucidated from the first exposure experiments. ESI: Electrospray ionization. LC: Liquid chromatography. QTOF: Quadrupole-time-of-flight. DTIM: Drift tube ion mobility. BEH: Ethylene bridged hybrid. UPLC: Ultra performance liquid chromatography. MeOH: Methanol. ACN: Acetonitrile. IPA: Isopropanol.

Sample fraction	Polar	Polar	Apolar	Apolar
ESI mode	ESI (+)	ESI (-)	ESI (+)	ESI (-)
LC system	Agilent 1290 Infinity	Agilent 1290 Infinity	Agilent 1290 Infinity II	Agilent 1290 Infinity II
Detector	Agilent 6530 QToF	Agilent 6530 QToF	Agilent 6560 (DTIM)-QToF	Agilent 6560 (DTIM)-QToF
Column	iHILIC-Fusion	iHILIC-Fusion(P)	ACQUITY UPLC BEH C18	ACQUITY UPLC BEH C18
Column dimensions	100 x 2.1 mm, 1.8 µm	100 x 2.1 mm, 5 µm	150 x 2.1 mm, 1.7 µm	150 x 2.1 mm, 1.7 µm
Mobile phase A	10 mM $HCOONH_4$ + 0.1% (v/v) HCOOH in H_2O/MeOH (9/1, v/v)	2 mM CH_3COONH_4 + 2 mM $(NH_4)_2CO_3$ in H_2O	5 mM CH_3COONH_4 + 0.1% (v/v) CH_3COOH in H_2O/ACN (7/3, v/v)	5 mM CH_3COONH_4 in H_2O/ACN (7/3, v/v)
Mobile phase B	ACN	ACN/MeOH (9/1, v/v)	5 mM CH_3COONH_4 + 0.1% (v/v) CH_3COOH in H_2O/ACN/IPA (2/10/88, v/v/v)	5 mM CH_3COONH_4 in H_2O/ACN/IPA (2/10/88, v/v/v)
Flow rate (mL/min)	0.25	0.20	0.20	0.20

Table 6.1 Continuation.

Sample fraction	Polar	Polar	Apolar	Apolar
ESI mode	ESI (+)	ESI (-)	ESI (+)	ESI (-)
Gradient	Min - %B 0 – 95 4 – 95 12.5 – 60 20 – 60 21 – 95 26 – 95	Min - %B 0 – 95 1 – 95 10 – 20 14 – 20 15 – 95 20 – 95	Min - %B 0 – 15 2 – 15 3 – 30 5 – 60 8 – 60 20 – 100 30 – 100 35 – 15 40 – 15	Min - %B 0 – 15 2 – 15 3 – 30 5 – 60 8 – 60 20 – 100 30 – 100 35 – 15 40 – 15
Injection volume (µL)	3	3	3	2
Autosampler temperature (°C)	4	4	4	4
Column temperature	60	25, bypassing heat exchanger	60	60
Nozzle voltage (V)	0	0	500	500
Capillary voltage (V)	2000	2000	3500	3750
Fragmentor voltage (V)	150	100	200	200
Drying gas	Nitrogen	Nitrogen	Nitrogen	Nitrogen
Sheath gas	Nitrogen	Nitrogen	Nitrogen	Nitrogen
Drying gas temperature (°C)	250	250	325	350
Sheath gas temperature (°C)	350	350	325	350
Drying gas flow (L/min)	8	10	8	8

Table 6.1 Continuation.

Sample fraction	Polar	Polar	Apolar	Apolar
ESI mode	ESI (+)	ESI (-)	ESI (+)	ESI (-)
Sheath gas flow (L/min)	11	10	8	8
Nebulizer gas pressure (psig)	45	45	30	30
MS1 range (*m/z*)	60-1200	60-1200	100-1500	100-1500
MS1 acquisition mode	Profile	Profile	Profile	Profile
MS1 scan rate (spectra/s)	2	2	4	4
MS2 mass range (*m/z*)	40-1000	40-1000	60-1200	60-1200
MS2 acquisition mode	Profile (auto MS/MS + target MS/MS)	Profile (auto MS/MS + target MS/MS)	Profile (auto MS/MS with iterative exclusion + target MS/MS)	Profile (auto MS/MS with iterative exclusion + target MS/MS)
MS2 scan rate (spectra/s)	6	6	6	6
Max precursors/scan cycle	4*	4*	4	4
Collision energy (eV)	10-20-40*	10-20-40*	10-20-40	10-20-40
Quad width	Small (1.3 amu)	Small (1.3 amu)	Small (1.3 amu)	Small (1.3 amu)
DTIM drift entrance voltage (V)	/	/	1221	1273
DTIM drift exit voltage (V)	/	/	300	300
DTIM rear funnel entrance voltage (V)	/	/	200	216

Table 6.1 Continuation.

Sample fraction	Polar	Polar	Apolar	Apolar
ESI mode	ESI (+)	ESI (-)	ESI (+)	ESI (-)
DTIM rear funnel exit voltage (V)	/	/	49	47
DTIM single pulse trap filling time (µs)	/	/	30,000	30,000
DTIM single pulse trap release time (µs)	/	/	200	200
DTIM 4-bit multiplexing trap filling time (µs)	/	/	3,000	3,000
DTIM 4-bit multiplexing trap release time (µs)	/	/	200	200

6.6.2 Data acquisition using HS-GC-FID

To quantify ethanol in cell media, headspace analysis was performed on an Agilent 6890 gas chromatograph with a flame ionization detector (GC-FID) coupled to an Agilent 7697A headspace sampler (HS) (Agilent Technologies, Santa Clara, USA). An Agilent J&W DB-1 column (50 m x 0.32 mm x 1.2 µm) was used and the oven and detector temperatures were 175 and 250 °C, respectively. The validated method (Maudens et al., 2014) used hydrogen as a carrier gas (67.8 mL/min total flow, 30:1 split ratio). The detector gas comprised of hydrogen (40 mL/min), air (300 mL/min) and nitrogen makeup (5 mL/min). Calibration was performed using six aqueous ethanol standards within a range of 0.05-5 g/L (ACQ Science GmbH, Rottenburg, Germany). For determination of the ethanol concentration in cultivated media, 400 µL of the medium was added to 1.5 mL H_2O and 100 µL ACN was added as internal standard (0.786 g/L). Samples with ethanol concentrations higher than the highest calibrator of 5 g/L were diluted and re-analyzed. To ensure the analytical performance, ethanol QC solutions of 0.3 g/L and 4.0 g/L were analyzed before and after the analysis (ACQ Science GmbH). The acceptance criteria for the QC solutions included a maximal bias of 15% compared to the nominal concentration and for precision a coefficient of variation (CV) < 15%. These latter criteria were based on the guidelines for bioanalytical method validation of the European Medicines Agency (EMA) (European Medicines Agency, 2022).

6.7. Data processing and statistics

Raw LC-HRMS data files (.d) were converted to .mzML format using MSConvert (Kessner et al., 2008). Subsequently, peak picking and alignment were performed in MS-DIAL (v. 4.6/4.9) (Tsugawa et al., 2020). Details on used MS-DIAL parameters are provided in SI (Table SI-6.1). MS-FLO was used for additional deisotoping and removal of duplicates (DeFelice et al., 2017). To evaluate the data quality, the relative standard deviation (RSD) of the intensity of each feature was plotted for each sample group separately. Intensity drift was corrected using cubic spline drift correction (Klåvus et al., 2020). To avoid low-quality features, several filter steps were applied. Features present in at least 80% of an exposed or control sample group were retained. In addition, only features with an RSD < 30% in at least one exposure group were kept. For intracellular samples, features with maximum intensity lower than ten times the average intensity in the blank were removed. For extracellular samples, a fold change (FC) > 3 or < 0.33 between the average intensity in an exposure group and the average intensity in the blanks were used to retain a feature. In addition, features with maximal intensity in the QC pooled samples below 3000 were removed when no MS/MS data was acquired. Missing values were imputed using random forest, and intensity values were log-transformed (Klåvus

et al., 2020). Probabilistic quotient normalization (PQN) was performed using the median intensity of the QC pooled samples as a reference (Jankevics et al., 2022), followed by Pareto scaling (K. Murphy et al., 2020).

Principal component analysis (PCA) plots were built for visualization and removal of outliers. In addition, outlier samples were removed based on deviations in the detection of internal standards. Acceptance criteria for internal standards were the same as for system suitability samples (Table 6.2). Both univariate and multivariate statistics were applied because of their complementarity (Saccenti et al., 2014). Before log transformation, normalization and scaling, a Shapiro-Wilk test was performed using the intensity values for each feature separately as a test of normality. Depending on the significance ($p < 0.05$) of the Shapiro-Wilk test, a Mann-Whitney U-test or a Welch's t-test was performed (Gaude et al., 2013). The Benjamini-Hochberg procedure was used to correct for multiple testing (Benjamini & Hochberg, 1995). Features with $p < 0.05$ and a $FC > 5$ or < 0.2 compared to the control group (i.e., either negative or positive control group), were considered significant.

Multivariate statistics included a binary RF classifier (Beirnaert, Cuykx, et al., 2019) and partial least squares-discriminant analysis (PLS-DA) (Thévenot et al., 2015) with 7-fold cross-validation. The PLS-DA model was evaluated by permutation of the y-variable ($n = 1000$) and by the R^2 and Q^2 value of the model, while the RF model was evaluated by the area under the curve (AUC). Interesting features were selected based on their variable importance in projection (VIP) value for the PLS-DA model and their mean decrease in accuracy or variable importance measure (VIM) for the RF model. Interesting features selected by the univariate or the multivariate model were only kept when they were selected both in the original experiments and the validation experiments. In addition, boxplots based on intensity of the features in each group were created for each selected feature and manually evaluated to decrease the number of false positives.

For the ion mobility data of the apolar fraction, multiplexed data files were de-multiplexed using the vendor-supplied software Agilent deMP. Data files were smoothed with a kernel size of 3 for drift and retention time and saturation repaired for points over 40% of the abundance limit using PNNL Preprocessor (Bilbao et al., 2021). The collision cross-section ($^{DT}CCS_{N2}$) values were calculated using single-field calibration coefficients obtained by infusing the Agilent Tune Mix in IM-MS Browser B.08.00 (Agilent Technologies).

6.8. Metabolite annotation

For annotation of metabolites in the polar fractions, the All Public MS/MS libraries (v. 15) were used for MS/MS matching in MS-DIAL (Tsugawa et al., 2020), next to MS-Finder (v. 3.5) (Tsugawa et al., 2016), MassBank (Horai et al., 2010), NIST library (v.17) with MS Search (v. 2.3, National Institute of Standards and Technology, Gaithersburg, MD, USA), METLIN (Smith et al., 2005a), and GNPS (Nothias et al., 2020).

For annotation of features originating from the apolar sample fractions, the modified LipidBlast library was used for MS/MS matching in MS-DIAL (v. 4.6/4.9) (Tsugawa et al., 2020), next to LipidMatch (Koelmel, Kroeger, Ulmer, et al., 2017), LipidHunter (Ni et al., 2017), and Lipostar (v. 2) (Goracci et al., 2017). Matched MS/MS spectra were manually evaluated to improve annotation confidence, and in-house standards were used for confirmation when available. Confirmation of fragments using rule-based fragmentation was used for manual evaluation of annotated lipids (Lange et al., 2021; Pi et al., 2016). Only features that could be annotated with a level 3 (L3) confidence or higher, according to the annotation confidence system of Schymanski *et al*. (2014), were considered. L3 refers to tentative candidates (i.e., insufficient information for one exact structure, e.g., annotation until lipid class level), while level 2 (L2) refers to a probable structure and is divided into 2a (i.e., unambiguous library spectrum match) and 2b (i.e., unambiguous annotation e.g., based on diagnostic MS/MS fragments, without available standard or literature for confirmation). Level 1 (L1) refers to a confirmed structure (i.e., confirmation using a reference standard with MS, MS/MS and RT matching). To further increase the annotation confidence for annotated lipids, CCS values were searched in experimental databases (CCS compendium (Picache et al., 2019), CCSbase (Ross et al., 2020), MS-DIAL internal lipidomic library v. 4.6 or 4.9 (Tsugawa et al., 2020)) or *in silico* generated using AllCCS (Zhiwei Zhou et al., 2020), when experimental values were unavailable, and annotated lipids were only considered when the CCS error was below 3% (da Silva, Iturrospe, Heyrman, et al., 2021).

6.9. Analytical QA/QC procedures

During all experiments, standard operating procedures (SOPs) were used for cell cultivation and exposure, sample preparation, data acquisition and processing. Chromatographic column inventories were used to keep track of the purchase dates, sample types injected and to monitor the number of injections and backpressure throughout analytical batches.

During analytical runs on the Agilent 6530 and 6560 systems, reference masses (922.0098 *m/z* and 121.0508 *m/z* for ESI (+) and 966.0007 *m/z* and 119.0363 *m/z* for ESI (-)) were constantly infused with an additional isocratic pump, and used to correct the

mass axis during acquisition. Acquisition worklists were prepared as shown in Figure 6.2. The injection order of the samples was randomized to prevent bias. Chromatographic columns were equilibrated using the mobile phase start composition. Blank solvent samples (n = 3) were injected after the column pressure baseline was stable at the required flow rate for at least 10 min. Alignment of the pressure profiles of the blank samples was evaluated to ensure sufficient equilibration of the column. Before data acquisition of the test and QC samples, a system suitability (SS) sample was injected. The SS sample was applied to verify that the system would perform according to pre-defined acceptance criteria. The composition of the SS sample is given in Table 6.2, together with the acceptance criteria regarding mass accuracy, peak height and RT. In general, for each of the four analytical platforms, the SS sample was composed of 1 µg/mL of three standards which were selected based on their distribution across the RT (Figure 6.3) and *m/z* window (i.e., to assess the complete analysis window).

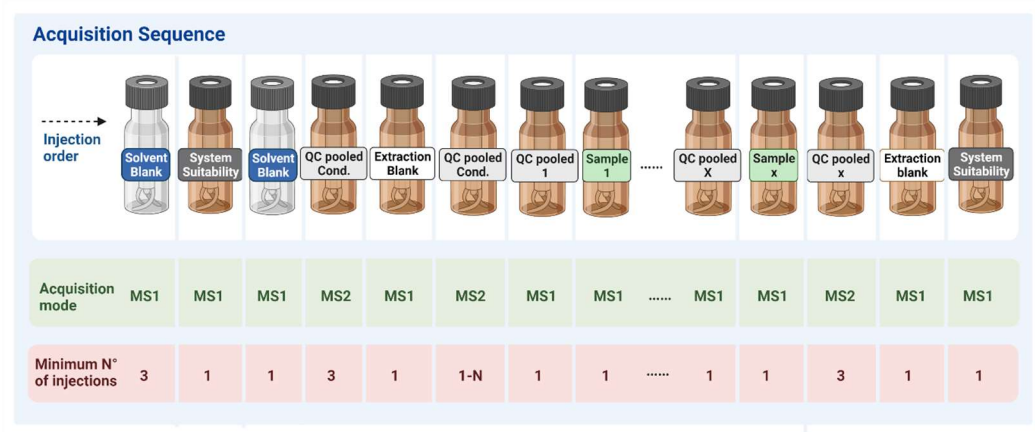

Figure 6.2 General overview of an acquisition sequence for untargeted metabolomics analysis. A system suitability (SS) sample is injected at the start and end of the analysis (MS1 data acquisition mode). Based on set acceptation criteria, the SS sample at the start of the analysis will be used to determine whether the instrumental performance is sufficient to start the worklist. When acceptance criteria are met for the SS sample, pooled QC samples are analyzed at the start to condition the system and to acquire MS2 spectra. In addition, pooled QC samples were run periodically, every 4-6 test samples, for QC processes (MS1 data acquisition mode). The minimum number of periodically injected QC samples was 6 per analytical batch.

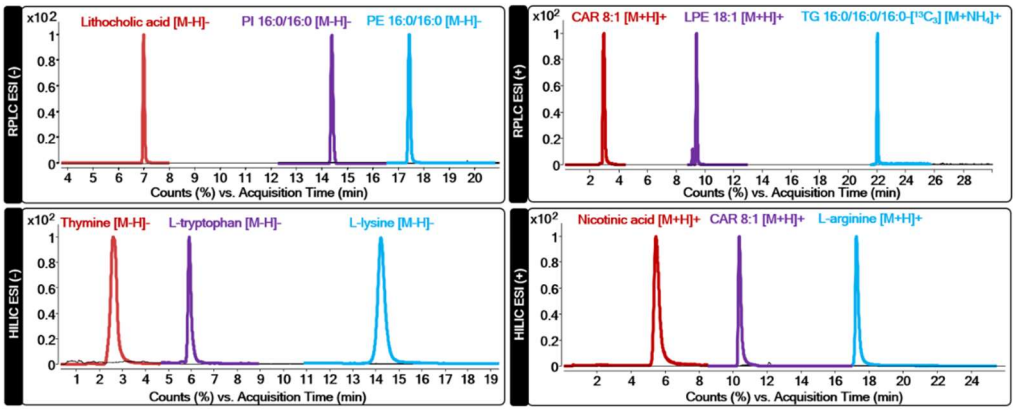

Figure 6.3 Chromatograms of the standards used in the system suitability sample. RPLC: Reversed-phase liquid chromatography. HILIC: Hydrophilic interaction liquid chromatography. ESI: Electrospray ionization. PI: Phosphatidylinositol. PE: Phosphatidylethanolamine. CAR: Carnitine. LPE: Lysophosphatidylethanolamine. TG: Triglyceride.

When the SS sample met all acceptance criteria, a pooled QC sample was used to condition the LC-MS system, during which MS/MS data were acquired (n_{inj} = 3). After conditioning, an extraction blank was injected to acquire MS1 data, followed by a second round of conditioning using the pooled QC sample with MS/MS acquisition (n_{inj} ≥ 5). The number of pooled QC injections necessary for conditioning the system is dependent on the samples under investigation. The number was optimized by iterative injections of the QC pooled sample. When the total ion current chromatogram, the RT and peak intensity/area of the internal standards become stable, acquisition of samples can be initiated.

Biological samples were injected in a randomized order and a QC pooled sample was injected minimum six times at regular intervals across the worklist. During these latter injections, data were acquired in MS1 mode. A second extraction blank was injected at the end of the worklist, followed by the SS sample. Injection of a SS sample both in the beginning and in the end of a worklist is necessary to estimate the maintenance of the instrumental performance during the run. During analytical runs, the column backpressure was monitored, as well as the signal intensities, RT and mass accuracy of the internal standards. Both the chromatographic column and LC-MS system were cleaned thoroughly after each analytical batch.

Table 6.2 System suitability mixture of standards for reversed-phase liquid chromatography (RPLC) and hydrophilic interaction liquid chromatography (HILIC) methods in ESI (+) and ESI (-) modes. The acceptance criteria used for the LC-HRMS methods are listed. ESI: Electrospray ionization. PI: Phosphatidylinositol. PE: Phosphatidylethanolamine. CAR: Carnitine. LPE: Lysophosphatidylethanolamine. TG: Triglyceride.

Compound name	Formula	Ionization species	*m/z*	Retention time (min)				Acceptance criteria		
				RPLC ESI (+)	RPLC ESI (-)	HILIC ESI (+)	HILIC ESI (-)	Peak height	Mass error (ppm)	RT deviation (min)
Lithocholic acid	$C_{24}H_{40}O_3$	$[M-H]^-$	375.2904		6.95			> 5,000 < Saturation	< 10	< 0.2
PI 16:0/16:0	$C_{41}H_{79}O_{13}P$	$[M-H]^-$	809.5185		14.22			> 5,000 < Saturation	< 10	< 0.2
PE 16:0/16:0	$C_{37}H_{74}NO_8P$	$[M-H]^-$	690.5079		17.49			> 5,000 < Saturation	< 10	< 0.2
CAR 8:1	$C_{15}H_{27}NO_4$	$[M+H]^+$	286.2013	3.12		10.44		> 5,000 < Saturation	< 10	< 0.5 HILIC < 0.2 RPLC
LPE 18:1	$C_{23}H_{46}NO_7P$	$[M+H]^+$	480.3085	9.40				> 5,000 < Saturation	< 10	< 0.2
TG 16:0/16:0/16:0-[$^{13}C_3$]	$C_{48}[^{13}C]_3H_{98}O_6$	$[M+NH_4]^+$	827.7802	21.87				> 5,000 < Saturation	< 10	< 0.2
Thymine	$C_5H_6N_2O_2$	$[M-H]^-$	125.0355				2.59	> 5,000 < Saturation	< 10	< 0.5
L-tryptophan	$C_{11}H_{12}N_2O_2$	$[M-H]^-$	203.0826				6.09	> 5,000 < Saturation	< 10	< 0.5
L-lysine	$C_6H_{14}N_2O_2$	$[M-H]^-$	145.0990				14.44	> 5,000 < Saturation	< 10	< 0.5
Nicotinic acid	$C_6H_5NO_2$	$[M+H]^+$	124.0393			5.71		> 5,000 < Saturation	< 10	< 0.5
L-arginine	$C_6H_{14}N_4O_2$	$[M+H]^+$	175.1190			17.50		> 5,000 < Saturation	< 10	< 0.5

6.10. Supplementary information

6.10.1. Optimization of dilution factor for extracellular HepaRG extracts

The sample preparation of the extracellular fraction of HepaRG samples was based on the method of Cuykx *et al.* (2017) and Dettmer *et al.* (2013). Because of the high dynamic range of metabolites, some metabolites are highly abundant and cause signal saturation during LC-MS analyses, which impairs mass accuracy and disables calculations of reliable fold changes between controls and exposed groups. Other metabolites are less abundant and cause low signal intensities or might be undetectable. In order to find a balance between the high and low abundant metabolites, the dilution factor used during sample preparation was optimized (Z. E. Wu et al., 2019).

During experiments for optimization of the dilution factor, the same sample preparation method was used as described in 6.5.2. The volume of cell medium, quenching solution and solutions used for LLE were multiplied by a factor of 3. After eight days of incubation of HepaRG cells, 960 µL of the medium was collected and 2175 µL of -80 °C quenching solution was added (80% (v/v) MeOH and 20% (v/v) of 10 mM CH_3COONH_4). After vortexing for 60 s, 2940 µL of the quenched medium was transferred to an LLE-vial, which contained 1560 µL of a polar mixture and 1320 µL of an apolar mixture (-20 °C). The polar mixture consisted out of 1 mM $(NH_4)_2EDTA$ and 0.5 mM ascorbic acid in 5 mM CH_3COONH_4 with 0.1% (v/v) CH_3COOH (pH 4.2). The apolar mixture consisted of 1 mM BHT in $CHCl_3$. The LLE vial was subsequently vortexed for 90 s, equilibrated for 10 min on ice, centrifuged at 2,200 g for 7 min at room temperature and again equilibrated for 10 min on ice. 3000 µL of the polar fraction (upper phase) was transferred to an Eppendorf tube, without transferring solid particles from the protein disk. After vortexing for 20 s, 1500 µL was transferred to a second Eppendorf tube after which the liquid of both Eppendorf tubes was evaporated using pure, dry nitrogen at room temperature. 870 µL of the apolar fraction (lower phase) was transferred to a reacti-vial. After vortexing for 20 s, 435 µL was transferred to a second reacti-vial, after which the liquid was evaporated using pure, dry N_2 at room temperature. Dried extracts were stored at -80 °C and reconstituted directly before analysis. Polar and apolar samples were reconstituted on ice using 60 µL of ACN/H_2O (65/35, v/v) and IPA/MeOH (35/65, v/v), respectively. The polar reconstitution solvent contained 1 µg/mL of hippuric acid-(phenyl-$^{13}C_6$), L-lysine-$^{13}C_6$-$^{15}N_2$, leucine-5,5,5-D_3, glucose-$^{13}C_6$, caffeine-$^{13}C_3$ and L-phenylalanine-$^{13}C_9$-^{15}N. The apolar reconstitution solvent contained 1 µg/mL of lauric acid-12,12,12-D_3, cholic acid-2,2,4,4-D_4, glyceryl tri(palmitate-1-^{13}C), 18:1-D_7 lyso PE, octanoyl-L-carnitine-(N-methyl-D_3) and ceramide (d18:1/18:1(9Z)-$^{13}C_{18}$). After vortexing for 90 s, serial dilutions were made from the original sample (Figure SI-6.1) using the

abovementioned polar and apolar reconstitution solvents as dilution solvents. All samples were filtered using 0.2 µm nylon centrifugal filters and centrifugated at 14,000 g for 2 min at room temperature. 20 µL of each sample from the dilution experiment was transferred to a Greiner Bio-One 384-well plate. Surrounding wells were filled with solvent blanks and the well plate was sealed using aluminum adhesive. The 384-well plate was transferred to the autosampler (4 °C) right before analysis. Samples were ordered from low to high concentration for instrumental injection and data acquisition. Each sample was injected *in duplo*.

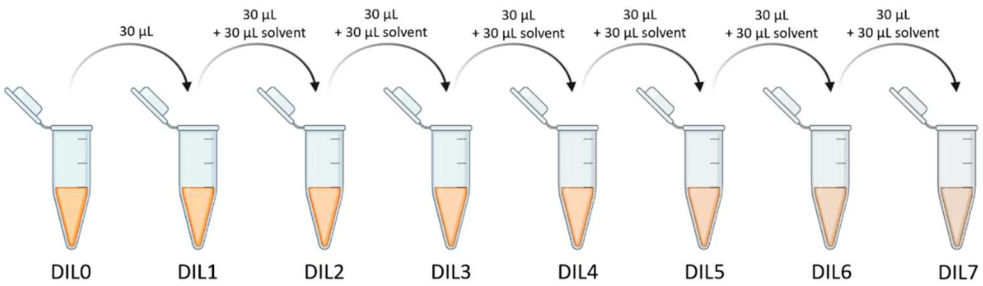

Figure SI-6.1 Dilution series used during optimization of the dilution factor for the extracellular fraction of HepaRG sample extracts.

After data-acquisition, data-preprocessing consisted of peak picking, alignment, missing value imputation and solvent blank subtraction (6.7). The mean of replicate intensity values was calculated and $\log_{10}$ transformed. For each feature, the Pearson correlation coefficients (r) were calculated based on the intensity for each combination of four or more consecutive dilution factors. Features with $r > 0.9$ for at least one of the combinations of ≥ 4 consecutive dilution factors were kept. After excluding the features with Pearson correlation coefficients ≤ 0.9, the mean intensity of features was plotted per dilution factor (Figure SI-6.2). For the apolar fraction (Figure SI-6.2-A) in ESI (-), there is only a small increase in mean intensity going from the highest dilution to dilution 3, indicating a high number of features at low intensity. In ESI (+), dilution 0 (i.e., the most concentrated sample) showed only a small increase in mean intensity compared to the other dilutions. This could indicate a larger number of features close to the detector saturation level in comparison to dilution 1. For the polar fraction (Figure SI-6.2-B), no indications for detector saturation could be observed in ESI (+). However, in ESI (-), dilution 0 showed a lower mean intensity in comparison to dilution 1. Based on these results, dilution 2 or dilution 1 would be suitable concentrations for the apolar fraction, while dilution 2 is preferred for the polar fraction. The sample preparation was adapted accordingly as explained in 6.5.2.

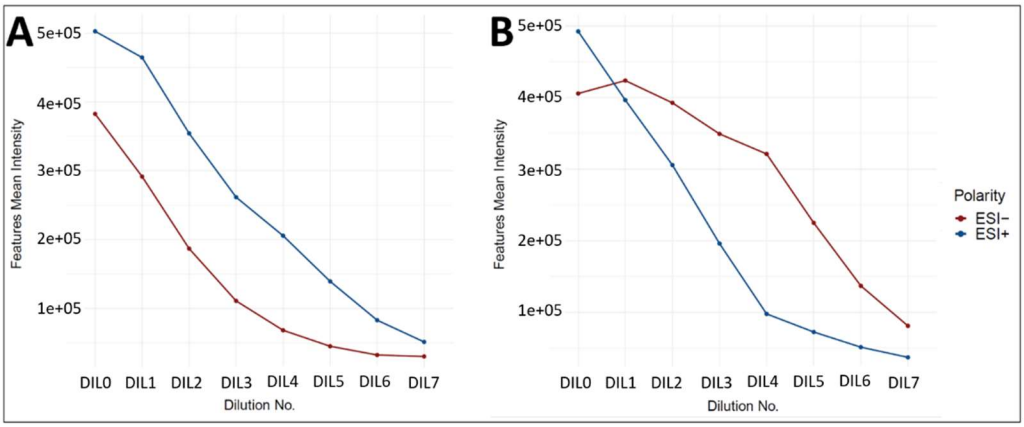

Figure SI-6.2 Mean intensity of features in relation to the dilution factor of the extracellular apolar (A) and polar (B) fractions of HepaRG cells.

6.10.2. MS-DIAL parameters used for data processing

Converted data files (.mzML format) were imported and processed using MS-DIAL. The following parameters were used for peak detection and alignment (Table SI-6.1).

Table SI-6.1 MS-DIAL parameters used for peak detection and alignment. ESI: Electrospray ionization. RT: Retention time.

Sample fraction	Polar	Polar	Apolar	Apolar
ESI mode	ESI (+)	ESI (-)	ESI (+)	ESI (-)
Mass range (Da)	60-1200	60-1200	100-1500	100-1500
RT range (min)	0.5-22	0.5-19.5	0.5-30	0.5-30
Accurate mass tolerance (MS1) (Da)	0.01	0.01	0.01	0.01
Accurate mass tolerance (MS2) (Da)	0.05	0.05	0.05	0.05
Maximum charged number	1	1	1	1
Smoothing method	linear weighted moving average	linear weighted moving average	linear weighted moving average	linear weighted moving average
Scans smoothing level	3	3	3	3
Scans minimum peak width	5	5	5	5
Mass slice width (Da)	0.1	0.1	0.1	0.1
Sigma window value	0.5	0.5	0.5	0.5
RT tolerance alignment (min)	0.2	0.2	0.15	0.15
MS1 tolerance alignment (Da)	0.015	0.015	0.01	0.01
Gap filling	Yes	Yes	Yes	Yes
Adduct ion setting	$[M+H]^+$, $[M+NH4]^+$, $[M+Na]^+$, $[M-H2O+H]^+$	$[M-H]^-$, $[M-H2O-H]^-$, $[M+HCOO]^-$, $[M+CH3COO]^-$	$[M+H]^+$, $[M+NH4]^+$, $[M+Na]^+$, $[M-H2O+H]^+$	$[M-H]^-$, $[M-H2O-H]^-$, $[M+HCOO]^-$, $[M+CH3COO]^-$

CHAPTER 7:
METABOLIC SIGNATURE OF ETHANOL-INDUCED HEPATOTOXICITY IN HEPARG CELLS

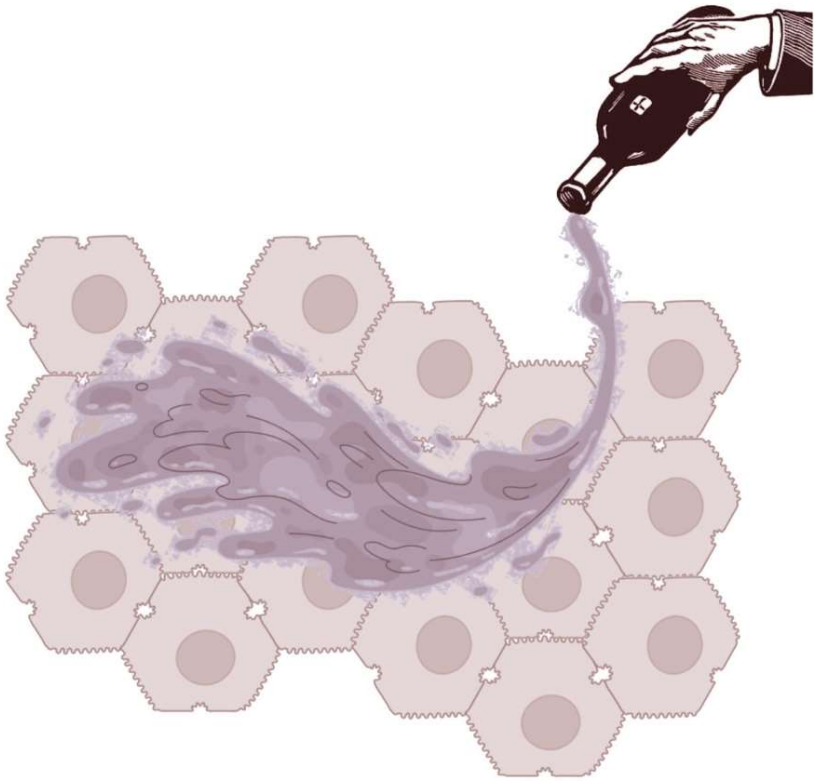

Based on the following publication

Iturrospe E, Da Silva KM, Robeyns R, Van de Lavoir M, Boeckmans J, Vanhaecke T, van Nuijs A, Covaci A. Metabolic signature of ethanol-induced hepatotoxicity in HepaRG cells by LC-MS-based untargeted metabolomics. Journal of Proteome Research. 2022; 21(4), 1153-1166. (DOI: 10.1021/acs.jproteome.2c00029).

7.1. Introduction

Alcohol-related disorders, which put individuals at high risk of developing ALD, are highly prevalent but poorly identified and characterized (Seitz et al., 2018). Symptoms tend to develop late in the course of disease progression and may only be apparent at the stage of irreversible cirrhosis (Seitz et al., 2018; Sheron et al., 2013). There are no early and specific biomarkers for the diagnosis of ALD, and currently, no single marker or combination of markers can be used to differentiate between different causes and stages of liver disease (European Association for the Study of the Liver, 2018; Vonghia et al., 2014). Because changes in the metabolome often are reflected in changes in the phenotype and vice-versa, metabolomics and its subdiscipline lipidomics offer the opportunity to identify diagnostic biomarkers, showcase potential pharmacotherapeutic targets and clarify the mechanism of action of ethanol-induced hepatotoxicity, with the overall objective to facilitate intervention in early stages of ALD. Based on relative differences in signal abundance between biological control samples and biological samples exposed to ethanol, the metabolic signature of ethanol exposure can be elucidated. Although animal models to study ethanol-induced hepatotoxicity are useful, they suffer from several drawbacks such as lower susceptibility of rodents to develop ALD and differences in the pathophysiological stages of ALD development compared to humans (Brandon-Warner et al., 2012; Lamas-Paz et al., 2018). *In vitro* hepatic metabolic research on the other hand enables mechanistic elucidation at the cellular level and circumvents the difficult accessibility of the liver through biopsies.

In this study, HepaRG cells, derived from a human hepatocellular carcinoma, were used to investigate the effects of ethanol exposure on cell metabolism using liquid chromatography (LC)-mass spectrometry (MS)-based untargeted metabolomics platforms. Extraction and analysis of intracellular metabolites were able to provide a metabolic fingerprint for ethanol-induced hepatotoxicity in HepaRG cells. In addition, conditioned cell media were analyzed to yield the metabolic footprint (i.e., provide information on metabolic secretion and consumption) (Kell et al., 2005). Dynamic changes of metabolites were elucidated in order to get a better understanding of early-stage indicators of AFLD. Due to the high diversity of lipid isomeric structures, these latter were further investigated using ion mobility spectrometry (IMS) to improve the level of confidence in annotation at species-level.

7.2. Materials and methods

The used materials and methods were extensively described in chapter 6, including chemicals and materials (6.2), dosage estimation (6.3), HepaRG cell cultivation regimen

(6.4), sample preparation (6.5), analytical methods (6.6), data processing and statistics (6.7), metabolite annotation (6.8) and analytical QA/QC procedures (6.9).

7.2.1. Cell exposure

After 7 days of incubation (i.e., needed for obtaining polarized hepatocyte colonies and biliary-like cells, see 6.4) HepaRG cell exposure was initiated (Figure 7.1). Differentiated HepaRG cells were exposed for 24 h to 368 mM of ethanol (i.e., IC_{10}, n = 6), 36.8 mM (i.e., 1/10 IC_{10}, n = 6) or no ethanol (i.e., negative control, n = 6). For the 48 h exposure group, cells were exposed to 284 mM of ethanol (i.e., IC_{10}, n = 6), 28.4 mM (i.e., 1/10 IC_{10}, n = 6) or no ethanol (i.e., negative control, n = 6) and ethanol containing media were renewed after 24 h. Negative control groups, sample groups exposed to the IC_{10} of ethanol and to 1/10 of the IC_{10} of ethanol will be further referred to as sample groups C (Control), H (High dose) and L (Low dose), respectively. In addition, two extraction blanks, not containing cells, were obtained for each exposure group using the same conditions.

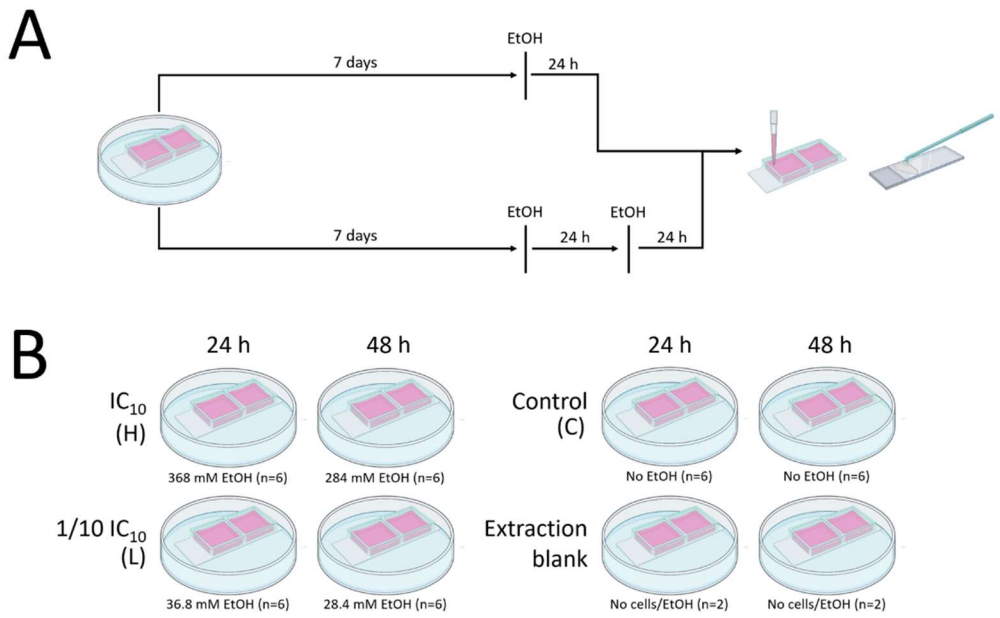

Figure 7.1 A) Graphical representation of the exposure experiment. HepaRG cells were exposed to ethanol for 24 h or for 48 h (with renewal of ethanol-containing media after 24 h). The same set-up was used for the validation experiment. **B)** Graphical representation of the used sample groups. Graphical icons in this figure were provided by BioRender, license n. 2641-5211.

7.3. Results

7.3.1. Influence of incubation conditions on ethanol concentration

During the exposure experiments, different sample groups were exposed to five different concentrations of ethanol (i.e., 368 mM – $IC_{10\text{-}24h}$, 284 mM – $IC_{10\text{-}48h}$, 36.8 mM – 1/10 $IC_{10\text{-}24h}$, 28.4 mM – 1/10 $IC_{10\text{-}48h}$, and 0 mM – control). The ethanol content of the media was determined pre- and post-incubation using HS-GC-FID. Results are presented in Figure 7.2. Incubation for 24 h caused an average decrease in ethanol concentration of 50% for the IC_{10} and 39% for 1/10 of the IC_{10}. Incubation for 48 h with renewal of ethanol containing media after 24 h showed a decrease of 49% for the IC_{10} and 35% for 1/10 of the IC_{10}. After 24 h and 48 h, control samples showed an ethanol content of 1.1% and 1.4% compared to the IC_{10}, respectively. Pre- and post-run ethanol QC solutions met the acceptance criteria (6.6.2) and were quantified both as 0.3 g/L for the 0.3 g/L solution (bias = 0%, CV = 0%) and 3.9 g/L and 4.0 g/L for the 4.0 g/L solution (max bias = 2.5%, CV = 1.8%), respectively. The monitoring of cross-contamination due to ethanol evaporation is important as complete avoidance of cross-contamination would only be possible when using closed systems to incubate cells, which would not allow necessary gas exchange, or when using separate incubators for each concentration. This latter would require a lab environment equipped with a dedicated incubator for each ethanol concentration and can increase non-biological inter-group variation due to variance in temperature, $\%CO_2$ and humidity between incubators.

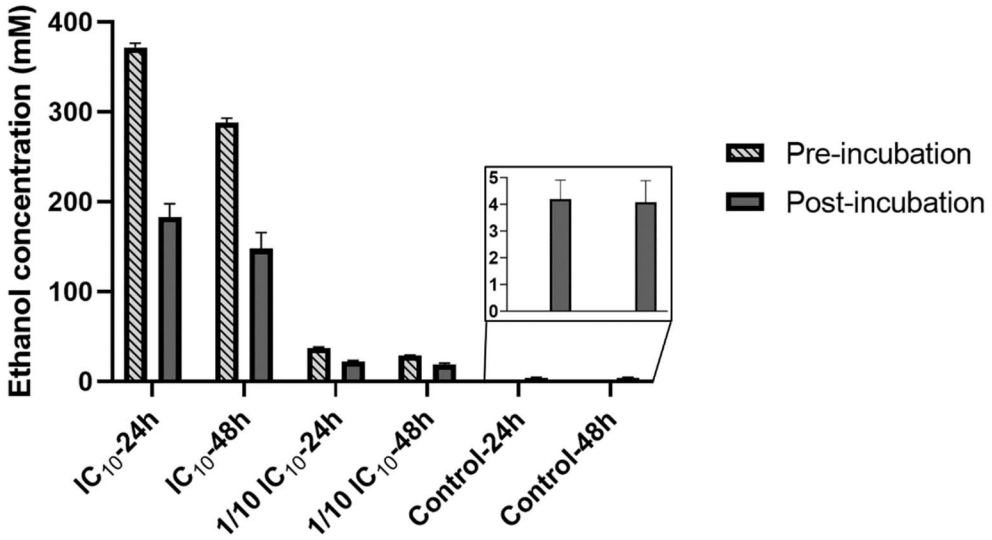

Figure 7.2 Decrease in ethanol concentration during incubation. Headspace gas chromatography with flame ionization detection (HS-GC-FID) was used to determine the ethanol concentration pre-incubation (n = 2) and post-incubation (n = 12).

7.3.2. Data quality

Post-run quality control included manual evaluation of extracted ion chromatograms of internal standards. Pre-set requirements for data quality of internal standards needed to be fulfilled for retaining a sample were the same as for the system suitability sample (Table 6.2).

For the intracellular samples, mRSDs were < 15% for all QC samples of the apolar fraction and < 20% for all QC samples of the polar fractions, with one exception (21% for ESI (+) after 24 h exposure – batch 1) (Table SI-7.1). Concordant with the intracellular fraction, mRSDs of the QC samples of the apolar fraction of the extracellular samples (Table SI-7.2) were all < 15%. While the mRSDs of the QC samples of the polar fraction in positive ionization modes were < 15%, higher mRSDs were seen for the polar fraction in negative ionization mode, with an average mRSD of 22%. All calculated mRSD values indicate a reliable analytical method as RSD values ≤ 30% are generally accepted in untargeted metabolomics (Naz et al., 2014). Biological and sample preparation variance is indicated by the increase in mRSD between QC samples and biological samples (i.e., sample groups C, H and L). For the intracellular samples, the average mRSD increased from 12% to 23% and from 16% to 23% for the apolar and polar fractions, respectively. The increase in average mRSD was slightly lower for the extracellular samples, with 11% to 20% for the apolar fractions and 17% to 20% for the polar fractions. The low increase in mRSD indicates little sample preparation and biological variance.

Principal component analysis (PCA) plots (Figure SI-7.1-SI-7.8) showed a clear separation in PC1 and/or PC2 between sample group H and the other sample groups indicating a high inter-group variability due to a strong metabolic impact of ethanol exposure. For example, the PCA plot of the apolar fraction of the intracellular samples of HepaRG cells exposed to ethanol for 24 h, in ESI (+) mode, is shown in Figure 7.3.

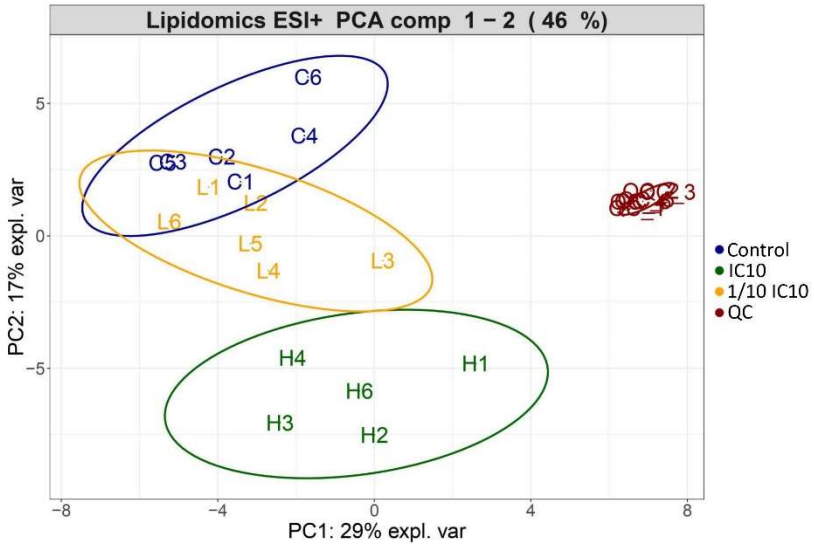

Figure 7.3 Example of a principal component analysis plot of the apolar fraction of intracellular samples of HepaRG cells analyzed in ESI (+) mode, after 24 h exposure to ethanol. There is a clear distinction between the control group (C, blue) and the sample group exposed to the IC_{10} of ethanol (H, green), while there is a slight overlap between the control group and the sample group exposed to 1/10 of the IC_{10} of ethanol (L, orange). This latter indicates a larger metabolic difference between control – IC_{10} compared to control – 1/10 IC_{10}. The clustering of pooled QC samples is shown in red.

For 24 h and 48 h exposure, inter-group variability between group C and group L was often insufficient to obtain a clear separation in PC1 and PC2. The higher similarity in metabolic profile can explain the overlap between these two groups. The degree of overlap between group C and L depended on the analyzed fraction, reflected by a higher overlap for the apolar fractions and a better separation for the polar fractions. There is a clear distinction between group C and L in PC1 and/or PC2 in ESI (+) mode, while more overlap is seen in ESI (-) mode.

In line with the trends observed during the PCA analysis, the evaluation parameters of the multivariate statistical models (i.e., R^2, Q^2, R^2_{PERM}, Q^2_{PERM} (n permutations = 1000) for the PLS-DA models and AUC for the RF models, Table SI-7.3-SI-7.6), showed high values for R^2 ($\bar{x}_{IC}$ = 0.95, $\bar{x}_{EC}$ = 0.95), Q^2 ($\bar{x}_{IC}$ = 0.83, $\bar{x}_{EC}$ = 0.86), and AUC ($\bar{x}_{IC}$ = 0.99, $\bar{x}_{EC}$ = 0.99) and low values for R^2_{PERM} ($\bar{x}_{IC}$ = 0.01, $\bar{x}_{EC}$ = 0.02) and Q^2_{PERM} ($\bar{x}_{IC}$ = 0.01, $\bar{x}_{EC}$ = 0.00) for the models comparing the group C with H. PLS-DA and RF models comparing the group C with L showed lower values for R^2 ($\bar{x}_{IC}$ = 0.92, $\bar{x}_{EC}$ = 0.85), Q^2 ($\bar{x}_{IC}$ = 0.55, $\bar{x}_{EC}$ = 0.52), and AUC ($\bar{x}_{IC}$ = 0.76, $\bar{x}_{EC}$ = 0.82) and higher values for R^2_{PERM} ($\bar{x}_{IC}$ = 0.31, $\bar{x}_{EC}$ = 0.20) and Q^2_{PERM} ($\bar{x}_{IC}$ = 0.18, $\bar{x}_{EC}$ = 0.09).

Post-exposure phase-contrast microscopic evaluation of the different sample groups (i.e., C, H and L for either 24 h or 48 h of exposure) was performed (Figure 7.4). No clear morphological differences could be observed between cells of group C and cells of group L. However, when comparing group C to group H, for both time points, the polarized hepatocyte colonies show faded lining and impaired organization of hepatic clusters in addition to accumulated debris.

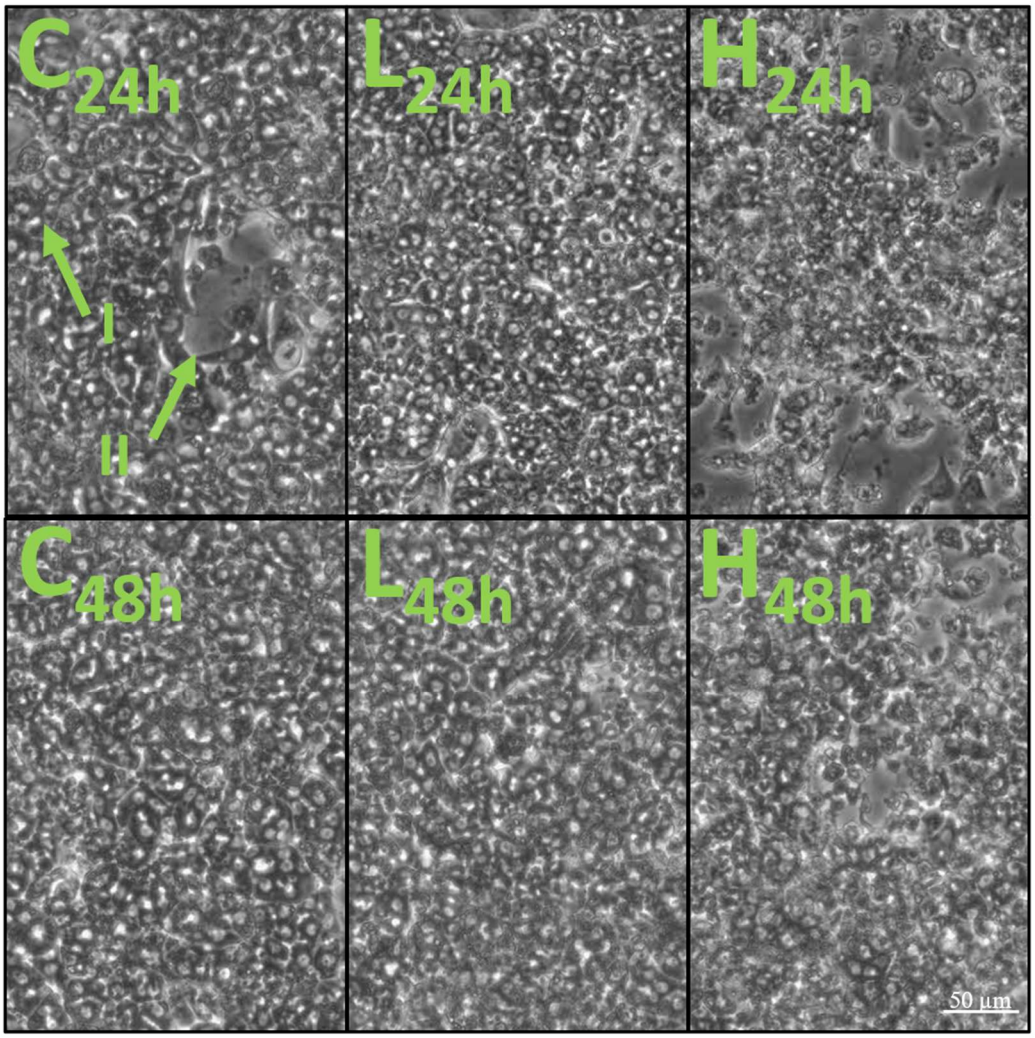

Figure 7.4 Phase-contrast microscopic pictures of HepaRG cells (10x10). C_{24h}-L_{24h}-H_{24h}: control, 1/10 IC_{10} and IC_{10} after 24 h of exposure. C_{48h}-L_{48h}-H_{48h}: control, 1/10 IC_{10} and IC_{10} after 48 h of exposure. Roman numbers refer to polarized hepatocyte colonies (I) and biliary canaliculi and biliary-like epithelial cells (II).

7.3.3. Metabolic fingerprint of ethanol-induced hepatotoxicity in HepaRG cells

Features selected by univariate (Mann-Whitney U-test or a Welch's t-test combined with FC cut-off) and/or multivariate statistical approaches (PLS-DA and RF) were only kept for annotation when selected in both the exposure experiment and the validation experiment. Annotated metabolites with their observed RT, *m/z* value, $^{DT}CCS_{N2}$ value and additional information are listed in Table SI-7.7. The effect of ethanol exposure on the intracellular metabolome of HepaRG cells is shown in Figure 7.5.

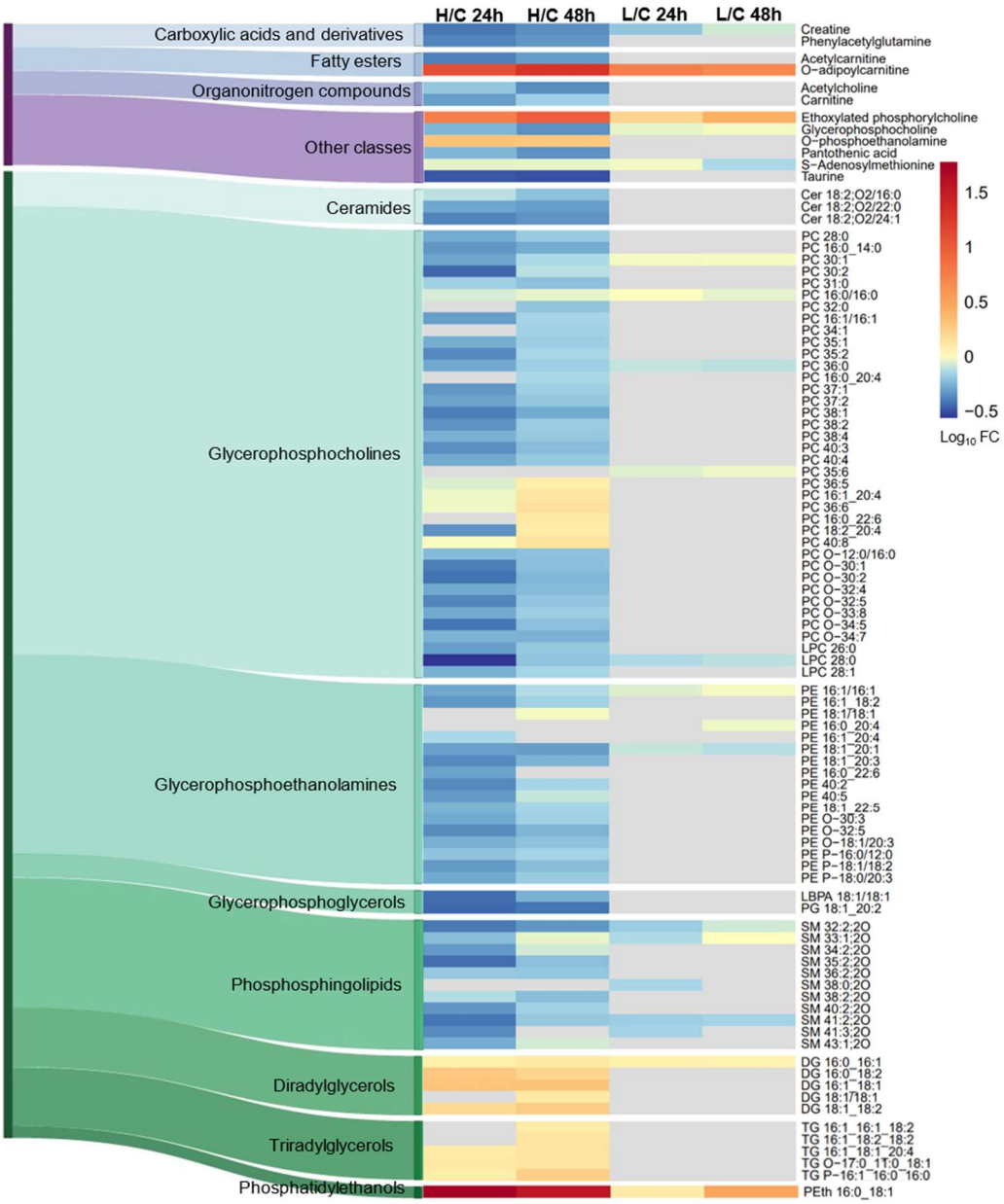

Figure 7.5 Sankey diagram combined with heatmaps to show the effect of ethanol exposure on the intracellular metabolome of HepaRG cells. Altered metabolites in the polar fraction of the samples are indicated by a blue-purple Sankey diagram, while a green Sankey diagram represents metabolites originating from the apolar fraction. Grey color in the heatmap was used when a metabolite was not selected during the statistical selection. H/C 24 h: IC_{10} vs control after 24 h of ethanol exposure. H/C 48 h: IC_{10} vs control after 48 h of ethanol exposure. L/C 24 h: 1/10 IC_{10} vs control after 24 h of ethanol exposure. L/C 48 h: 1/10 IC_{10} vs control after 48 h of ethanol exposure. FC: fold change.

In total, 94 altered metabolites selected during the statistical workflow could be annotated. Of the 82 lipids, 40 were annotated as L2 and 42 as L3, while of the 12 polar metabolites, 9 were annotated as L1 and three as L2. Annotation levels and libraries used for MS/MS matching per metabolite can be consulted in the supplementary spreadsheet (7.7.3). Usage of multiple libraries is recommended as their combination increases coverage. For example, 77% of annotated lipids were elucidated using the modified LipidBlast library of MS-DIAL (v. 4.6), while 49% and 25% of lipids were annotated using LipidMatch and LipidHunter respectively. The lower coverage of LipidHunter can be explained by the limited number of selectable ionization species. For polar metabolites, NIST (v. 17) and MassBank yielded the highest coverage (both 92%), followed by METLIN (69%), GNPS (61%), the All Public MS/MS library (v. 15) of MS-DIAL (54%) and MS-Finder (38%).

As expected, based on the results of the PCA analysis and the evaluation parameters of the PLS-DA and RF models, a more distinct metabolic pattern is observed after ethanol exposure at the IC_{10} than at 1/10 of the IC_{10}. In group H, upregulation was observed during 24 h and 48 h exposure for diacylglycerols (DG) and triacylglycerols (TG), with more TGs upregulated after 48 h exposure. At both time points, a downregulation was observed for ceramides with a d18:2 backbone (Cer d18:2), lysophosphatidylcholines (LPC), phosphatidylcholines (PC), phosphatidylethanolamines (PE) and sphingomyelins (SM). Interestingly, polyunsaturated PCs (≥ 5 double bonds) were slightly upregulated after 48 h exposure, while they were downregulated after 24 h exposure. In addition, two glycerophosphoglycerols (LBPA 18:1/18:1 and PG 18:1_20:2) were downregulated. PEth 16:0_18:1, as a marker of ethanol exposure, was detected at high intensity in all exposed samples.

Concerning polar metabolites, there was a downregulation of acetylcholine, creatine, glycerophosphocholine, pantothenic acid, phenylacetylglutamine, S-adenosylmethionine (SAM) and taurine. Upregulation was observed for O-phosphoethanolamine. While short-chain acylcarnitines (< C5) were downregulated, O-adipoylcarnitine, a medium-chain acylcarnitine (C6-C13), was strongly upregulated. Similar up- and downregulations were observed for group L during 24 h and 48 h exposure (Figure 7.5); although fewer metabolic classes were affected, fold changes were lower and affected classes were represented by a lower number of species. Ethylated phosphorylcholine was found highly upregulated in each exposure group. The high fold change was caused by its absence in the group C. Since no MS/MS library could be found for this latter metabolite, its fragmentation was matched using NIST (v.17) without accurate *m/z* matching, enabling fragmentation spectral matching with fragments of other metabolites with a higher *m/z* value. In addition, the fragmentation

spectra of ethylated phosphorylcholine were confirmed with *in silico* generated fragments using CFM-ID (v. 4.0) (F. Wang et al., 2021) (Figure SI-7.9-SI-7.12).

7.3.4. Metabolic footprint of ethanol-induced hepatotoxicity in HepaRG cells

As for elucidation of the metabolic fingerprint, features were selected by univariate and/or multivariate statistics and were only kept for annotation when selected in both the exposure and validation experiments. Annotated metabolites with their observed RT, *m/z* value, $^{DT}CCS_{N2}$ value and additional information are listed in supplementary Table SI-7.8. The effect of ethanol exposure on the extracellular metabolome of HepaRG cells is shown in Figure 7.6. The lower number of selected features in the extracellular fraction (Figure 7.6 shows 23 altered metabolites) compared to the intracellular fraction (Figure 7.5 shows 94 altered metabolites) can be explained by the complex extracellular matrix as incubation media contained calf serum among various other components. Of the 11 lipids, 1 was annotated as L1 and 10 as L2, while of the 12 polar metabolites, 5 were annotated as L1 and 7 as L2. Annotation levels and libraries used for MS/MS matching per metabolite can be consulted in the supplementary spreadsheet (7.7.3). From the annotated lipids, 71% could be elucidated using LipidMatch, 50% using the modified LipidBlast library of MS-DIAL (v. 4.6) and 21% using LipidHunter. For polar metabolites, the highest coverage was yielded by NIST (v. 17) (83%), followed by MassBank (67%), GNPS (58%), MS-Finder (50%), METLIN (42%) and the All Public MS/MS library (v. 15) of MS-DIAL (33%).

When comparing exposure vs control samples for metabolic footprinting, it is challenging to assign up- or downregulation to either changes in hepatic metabolite secretion or to changes in consumption of media components. In order to be able to distinguish altered secretion from altered consumption, Figure 7.6 shows the fold change differences between (I) exposure vs control, (II) exposure vs blank media and (III) control vs blank media, with blank media referring to extraction blanks (i.e., incubated media without cells). A negative fold change for all three groups indicates metabolites that show an increased consumption during ethanol exposure, while a positive fold change for all groups indicates an increased secretion. Metabolites downregulated in group (II) and (III) and upregulated in group (I), indicate metabolites that are less consumed by HepaRG cells. A fourth scenario is upregulation in group (II) and (III) and downregulation in group (I), indicating reduced secretion. As metabolomic studies provide a snapshot of metabolic patterns, the four described scenarios should be interpreted carefully since changes can be highly dynamic.

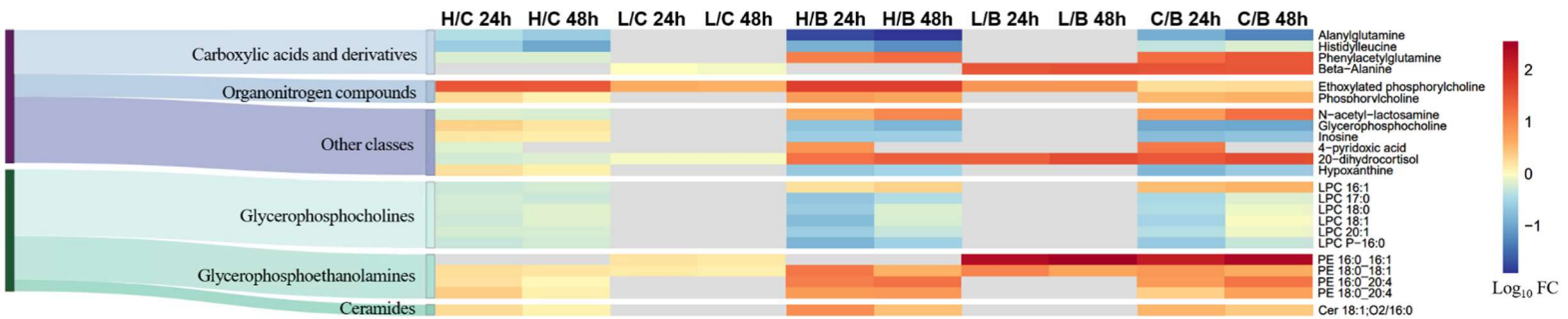

Figure 7.6 Sankey diagram combined with heatmaps to show the effect of ethanol exposure on the extracellular metabolome of HepaRG cells. Only annotated metabolites selected by univariate and/or multivariate statistics are shown. Altered metabolites in the polar fraction of the samples are indicated by a blue-purple Sankey diagram, while a green Sankey diagram represents metabolites originating from the apolar fraction. Grey color in the heatmap was used when a metabolite was not selected during the statistical selection. H/C 24 h: IC_{10} vs. control after 24 h of ethanol exposure. H/C 48 h: IC_{10} vs control after 48 h of ethanol exposure. L/C 24 h: 1/10 IC_{10} vs control after 24 h of ethanol exposure. L/C 48 h: 1/10 IC_{10} vs control after 48 h of ethanol exposure. H/B 24 h: IC_{10} vs blank media after 24 h of ethanol exposure. H/B 48 h: IC_{10} vs blank media after 48 h of ethanol exposure. L/B 24 h: 1/10 IC_{10} vs blank media after 24 h of ethanol exposure. L/B 48 h: 1/10 IC_{10} vs blank media after 48 h of ethanol exposure. C/B 24 h: Control vs blank media after 24 h of incubation. C/B 48 h: Control vs blank media after 48 h of incubation. FC: fold change.

For group H after 24 h and 48 h exposure, increased secretion was observed for PEs and Cer 18:1;O2/16:0, while LPCs were downregulated because of higher consumption. Concerning polar metabolites, there was a downregulation of N-acetyl-lactosamine, phenylacetylglutamine and 4-pyridoxic acid (only after 48 h exposure), due to a decreased secretion. Alanylglutamine and histidylleucine were downregulated due to higher consumption. Glycerophosphocholine, hypoxanthine and inosine were upregulated because of lower consumption, while phosphorylcholine was upregulated due to increased secretion. Metabolic changes in sample group L were less profound compared to group H, with only upregulation of PEs in the apolar sample fraction. Beta-alanine was downregulated due to less secretion only in group L. 20-dihydrocortisol was less secreted in all exposure groups. Interestingly, high secretion of ethylated phosphorylcholine was found in each exposure group.

7.4. Discussion

An overview of the most important metabolic changes due to ethanol exposure in HepaRG cells is presented in Figure 7.7.

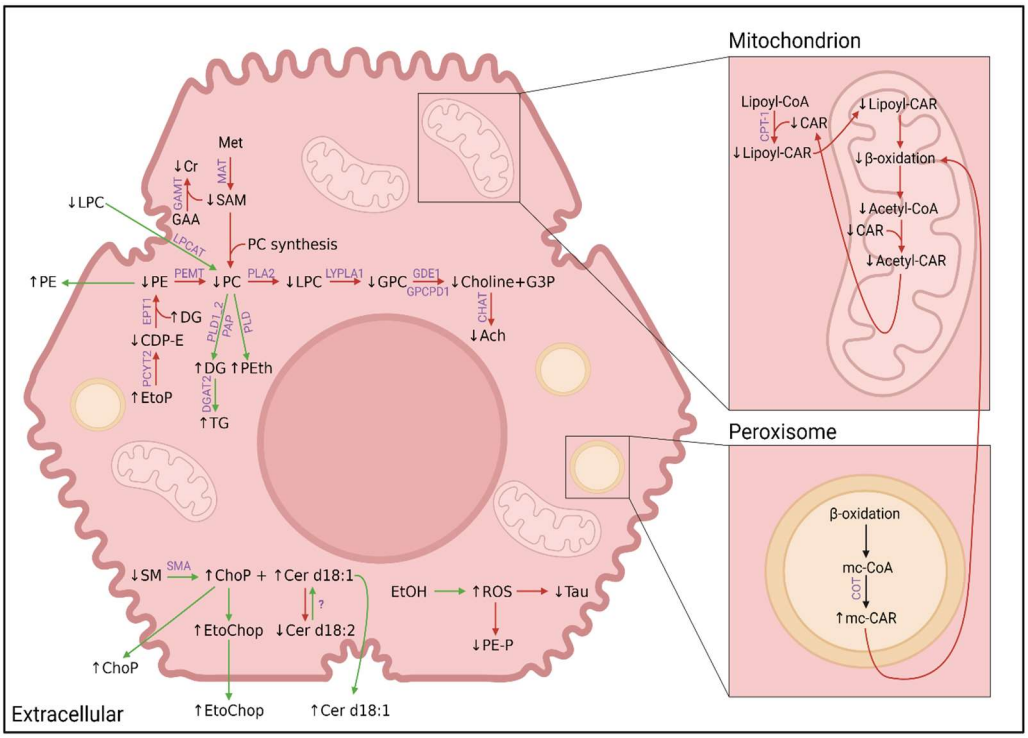

Figure 7.7 Metabolic changes in HepaRG cells after ethanol exposure. Intracellular green and red arrows were used to indicate increased and decreased biosynthesis/availability, respectively. Green arrows connecting the intracellular and extracellular compartment indicate increased secretion or uptake, depending on their direction. Graphical icons in this figure were provided by BioRender, license n. 2641-5211. Ach: Acetylcholine. CAR: Carnitine. CDP-E: CDP-ethanolamine. Cer: Ceramide. CHAT: Choline O-acetyltransferase. ChoP: Phosphorylcholine. CoA: Coenzyme A. COT: Carnitine octanoyltransferase. CPT-1: Carnitine palmitoyltransferase 1. Cr: Creatine. DG: Diglyceride. DGAT2: Diglyceride acyltransferase 2. EPT1: Ethanolaminephosphotransferase 1. EtOChoP: Ethylated phosphorylcholine. EtoP: O-phosphoethanolamine. G3P: Glycerol 3-phosphate. GAA: Guanidinoacetate. GAMT: Guanidinoacetate methyltransferase. GDE1: Glycerophosphodiester phosphodiesterase 1. GPC: Glycerophosphocholine. GPCPD1: Glycerophosphocholine phosphodiesterase 1. LPC: Lysophosphatidylcholine. LPCAT: Lysophosphatidylcholine acyltransferase. LYPLA1: Lysophospholipase 1. MAT: Methionine adenosyltransferase. mc-CAR: medium chain-CAR. mc-COA: medium chain-CoA. Met: Methionine. PAP: Phosphatidate phosphatase. PC: Phosphatidylcholine. PCYT2: Phosphoethanolamine cytidylyltransferase. PE: Phosphatidylethanolamine. PEMT: Phosphatidylethanolamine-N-methyltransferase. PE-P: Alkenyl ether phosphatidylethanolamine. PEth: Phosphatidylethanol. PLA2: Phospholipase A2. PLD: Phospholipase D. PLD1_2: Phospholipase D1/2. ROS: Reactive oxygen species. SAM: S-adenosyl methionine. SM: Sphingomyelin. SMA: Sphingomyelinase. Tau: Taurine. TG: Triglyceride.

7.4.1. Phosphatidylcholines and their relation to phosphatidylethanolamines, diglycerides, triglycerides, phosphatidylethanol and S-adenosyl methionine

It is known that ethanol exposure inhibits phosphatidylethanolamine-N-methyltransferase (PEMT), causing a lower production rate of PCs from PEs (Lieber et al., 1994). In addition, the accumulation of PEth reduces the PC content since PEth is formed by the exchange of ethanol for choline in PCs. PEth is a phospholipid only formed in the presence of ethanol in a reaction catalyzed by phospholipase D (PLD). Previously, hepatic PEth accumulation has been shown *in vivo* and *in vitro* (Aroor et al., 2002; Jaremek et al., 2013). A third effect that can explain the downregulation of hepatic PCs is the ethanol-induced reduction of SAM formation by the inhibition of methionine synthase and methionine adenosyltransferase, which disturbs hepatic methyl transfer necessary for the generation of PCs (Lieber et al., 1994; Stickel & Seitz, 2003). In addition, SAM reduction could explain the downregulation of intracellular creatine, as its hepatic synthesis is catalyzed by guanidinoacetate methyltransferase (GAMT), which uses SAM as a methyl donor (Ganesan et al., 2016). A fourth mechanism explaining decreased hepatic PC content is the shift towards TG synthesis through initial conversion of PCs to DGs, supported by the finding of upregulation of DG acyltransferase 2 (DGAT2) after ethanol consumption by mice (Z. Wang et al., 2010). The increase in DGs and TGs can additionally be explained by the ethanol-induced upregulation of lipin-1, which is considered a key enzyme in the pathogenesis of ALD and shows a dual function as phosphatidic acid phosphohydrolase enzyme and transcriptional coregulator (Hu et al., 2012, 2013). The general image showed a decrease of PCs in the intracellular fraction of HepaRGs after 24 h and 48 h of ethanol exposure. However, after 48 h, a slight increase of highly unsaturated PCs (≥ 5 double bonds) was observed. This might relate to the shift of saturated to unsaturated fatty acids as observed in ethanol-fed rodents (Jeon & Carr, 2020). Polyunsaturated fatty acids can be incorporated in DGs and subsequently in PCs through the CDP-choline pathway (Jeon & Carr, 2020).

7.4.2. Lysophosphatidylcholines and glycerophosphocholine

In addition to decreased hepatic PCs, a similar trend was observed for hepatic LPCs. Israelsen *et al.* observed a decrease of LPCs in human hepatic venous blood after ethanol intoxication in healthy volunteers and ALD patients, with only minor effects in patients suffering from non-alcoholic fatty liver disease (NAFLD) (Israelsen et al., 2021). These results are concordant with the reduction of LPCs caused by increased consumption in the extracellular fraction of HepaRG cells exposed to ethanol. The authors hypothesized that the reduction of circulating LPCs could be caused by an increased hepatic uptake, which was confirmed in this study. However, our results show

a decreased level of LPCs, both in the intracellular and extracellular fractions. The decrease of intracellular LPCs is in agreement with the findings of Puri *et al.* and Koelmel *et al.*, who reported a decreased hepatic LPC content in mice which were fed a diet rich in ethanol (Koelmel, Tan, et al., 2021; Puri et al., 2016). Puri *et al.* found that the decrease in hepatic LPCs was more pronounced in obese than lean mice. Additionally, Puri *et al.* saw a trend towards decrease in hepatic LPCs in human patients suffering from NAFLD, while they were significantly increased in non-alcoholic steatohepatitis (NASH), suggesting an important inflammatory component for LPC upregulation, which could contribute to lipoapoptosis of hepatocytes (Myoung et al., 2008; Puri et al., 2007). Stefanescu *et al.* suggested prognostic importance of LPC decrease in the serum of patients with ALD (Stefanescu et al., 2016). The downregulation of PCs due to a shift towards TG synthesis amongst others, could explain the reduced catabolism of PCs by deacylation to LPCs catalyzed by phospholipase A2 (PLA2). This hypothesis is supported by the intracellular decrease of glycerophosphocholine (GPC), the deacylation product of LPCs, formed in the second step of PC catabolism, catalyzed by lysophospholipase I (LYPLA1). Increased uptake of LPCs from the extracellular environment might be used to fuel the formation of GPC by LYPLA1 and/or to fuel the PC pool by lysophosphatidylcholine acyltransferase (LPCAT). Downregulation of GPC facilitates the observed intracellular reduction of acetylcholine, as GPC, formed during PC catabolism, can be converted into glycerol-3-phosphate and free choline, available for the biosynthesis of acetylcholine (Zhaoyu Li et al., 2005).

7.4.3. Phosphatidylethanolamines and their relation to diglycerides, triglycerides and O-phosphoethanolamine

Despite ethanol-induced inhibition of PEMT, a decrease in hepatic PEs was seen in intracellular HepaRG extracts. This is consistent with the significant decrease of hepatic PEs observed in human patients suffering from NAFLD and the decrease of PEs in HepaRG cells after steatosis induction using sodium valproate (Cuykx, Claes, et al., 2018; Puri et al., 2007). An impaired activity of phosphoethanolamine cytidylyltransferase (PCYT2) in the CDP-ethanolamine pathway might explain the decreased content of PEs. Impaired activity of the latter enzyme would also contribute to the accumulation of hepatic O-phosphoethanolamine (EtoP) and DGs, which are normally used for the synthesis of CDP-ethanolamine. In addition, accumulated DGs can be used for the synthesis of TGs, increasing the steatotic image (Calzada et al., 2016). In PCYT2 knockout mice, deletion of the PCYT2 allele caused the development of liver steatosis (Pavlovic & Bakovic, 2013). However, the hypothesis of impaired activity of phosphoethanolamine cytidylyltransferase does not explain the increase in extracellular PEs and could not be confirmed since the effect of ethanol exposure on this enzyme has not been studied.

Another possibility is that the decrease in intracellular PEs and the increase in extracellular PEs are related to the altered secretion of PEs in VLDL-type chylomicrons (Cuykx, Claes, et al., 2018). Dysregulation of phospholipid synthesis in hepatocytes, observed as deviations of PC and PE abundances and the molar ratio of PC/PE can affect cell membrane integrity, assembly and secretion of VLDL and mitochondrial bioenergetics (Ma et al., 2021; van der Veen et al., 2017).

7.4.4. Ether lipids and taurine

In addition to decreased hepatic PCs and PEs, ether lipids (e.g., ether-PC and ether-PE) were decreased in the intracellular fraction. This latter relates to both alkyl and alkenyl ether glycerophospholipids. Alkenyl ether lipids are important antioxidants, and the decrease could be explained by their involvement during the clearance of reactive oxygen species (ROS) generated during ethanol metabolism (Skaff et al., 2008). Although the understanding of the function of ether lipids is growing, there are still large knowledge gaps, especially in relation to pathophysiology (Dean & Lodhi, 2018). In addition to ether lipids, the intracellular decrease of taurine could also be related to the clearance of ROS, as Wu *et al.* demonstrated that taurine administration increased hepatic antioxidant capacity and reduced lipid peroxidation in ethanol-fed rats (G. Wu et al., 2018).

7.4.5. Sphingomyelins and their relation to ceramides and phosphorylcholine

The decrease of hepatic SMs is in accordance with the previously observed downregulation of SMs in human serum of heavy drinkers, which could be due to increased hydrolysis of SMs into Cers and phosphorylcholine (ChoP) by sphingomyelinase (SMA) (Jaremek et al., 2013). This decrease of SMs and increased activity of sphingomyelinase was also observed in ethanol-exposed HepG2 cells (Liu et al., 2000). In studies describing upregulation of hepatic Cers after ethanol exposure, Cers with a sphing-4-enine-backbone (d18:1) are listed, which could contribute to blocking fatty acid oxidation and promote its synthesis by inhibition of the phosphorylation of adenosine monophosphate-activated protein kinase (AMPK) (Liangpunsakul et al., 2010; L. Yang et al., 2016). During the present study, no increased hepatic Cer d18:1 species could be annotated after statistical selection, possibly because the FC differences were not large enough. However, three selected Cers with a sphingadienine-backbone (d18:2) were downregulated (FC between 0.4 and 0.7). Since data on Cer d18:2 species and their biological relevance is limited, an example MS/MS spectrum for Cer 18:2;O2/22:0 was included (Figure SI-7.13). Both Cer d18:1 species and phosphorylcholine were upregulated in the extracellular fraction due to increased secretion.

7.4.6. Carnitines and vitamins

As steatosis can impair hepatic biosynthesis of L-carnitine, which is necessary for the transfer of long-chain fatty acids to mitochondria, subsequent β-oxidation is reduced, leading to toxic cytoplasmatic accumulation of fatty acids (N. Li & Zhao, 2021; Savic et al., 2020). In addition, ethanol inhibits carnitine palmitoyltransferase 1 (CPT-1) activity, a rate-limiting step in fatty acid translocation for mitochondrial β-oxidation (Gao & Bataller, 2011). Under physiological conditions, carnitine can buffer excess acetyl-CoA in the mitochondria via the formation of acetyl-carnitine for mitochondrial export by carnitine acylcarnitine translocase (N. Li & Zhao, 2021). The reduction of acetyl-carnitine in the intracellular extracts after ethanol exposure of HepaRG cells can be explained by the impaired β-oxidation, reducing the biosynthesis of acetyl-CoA in mitochondria. Another possible contributing factor is the intracellular reduction of pantothenic acid, one of the precursors of CoA, which was also observed in the liver of ethanol-fed rats (Iannucci et al., 1982; Machado et al., 2016; Miyazaki et al., 2012). Next to a decrease of hepatic pantothenic acid in ethanol-fed rats, Miyazaki *et al.* targeted different B-group vitamins and observed a decreased excretion of 4-pyridoxic acid, a catabolite of vitamin B6. This result is concordant with the decreased hepatic secretion of 4-pyridoxic acid in HepaRG cells after 48 h of ethanol exposure. The authors hypothesized increased hepatic storage of vitamin B6 during ethanol exposure (Miyazaki et al., 2012).

Since acetyl-carnitine can provide acetyl groups for the production of acetylcholine catalyzed by choline acetyltransferase, the reduction of acetyl-carnitine facilitated downregulation of hepatic acetylcholine, which is also in line with the reduced uptake of extracellular GPC. However, as cytosolic acetyl-CoA can also be used as acetyl source, there is a strong likelihood for additional mechanisms of acetylcholine reduction (Onofrj et al., 2014). The strong intracellular upregulation of octanoyl-carnitine could also be explained by impaired β-oxidation. Very long-chain and branched-chain fatty acids are mainly oxidized in peroxisomes, while long-chain fatty acid are β-oxidized both in peroxisomes and mitochondria. As peroxisomal oxidation of fatty acids is incomplete, shortened medium-chain acyl-CoAs are generated that need to be transported to mitochondria for further oxidation. As the generated medium-chain acyl-CoAs are membrane-impermeable, they are converted to their respective carnitine esters by peroxisomal carnitine octanoyltransferase (COT) for transportation out of peroxisomes (Steiber et al., 2004).

7.4.7. 20-dihydrocortisol

Decreased hepatic secretion of 20-dihydrocortisol could be explained by decreased expression of AKR1D1. This latter gene encodes 3-oxo-5-beta-steroid 4-dehydrogenase, which is responsible for catalyzing the conversion of cortisol to 20-dihydrocortisol. In

human liver biopsies from NAFLD patients, a decrease of AKR1D1 expression was observed with advancing steatosis, fibrosis and inflammation and a relation with triglyceride accumulation and reduced beta-oxidation amongst others, was observed using human liver cell lines with AKR1D1 knockdown by Nikolaos *et al.* (2019).

7.4.8. Ethylated phosphorylcholine

Ethylated phosphorylcholine (EtOChoP, Figure 7.8 and Figure SI-7.9-SI-7.12), a previously unreported metabolite, might be a new marker of ethanol exposure. Due to its absence in the control samples, the metabolite showed similar large fold changes to PEth 16:0_18:1. Interestingly, unlike PEth 16:0_18:1, ethylated phosphorylcholine was found both in intracellular and extracellular samples due to a high level of hepatic secretion. Based on the structure of EtOChoP (Figure 7.8), it could be biosynthesized in a reaction using both phosphorylcholine and ethanol as precursors. As no commercial standard was available, both EtOChoP and EtOChoP-D_5 were synthesized by Dr. Vladimir N. Belov (Max Planck Institute, Göttingen, Germany). Analysis of the EtOChoP standard confirmed the HepaRG annotation, increasing the level of confirmation from L2b to L1 according to the annotation level system of Schymanski et al. (2014). In order to confirm whether EtOChoP can be considered as a marker of ethanol consumption in humans, a targeted LC-MS/MS method was developed and applied on human whole blood samples as a proof-of-concept (SI-7.7.5).

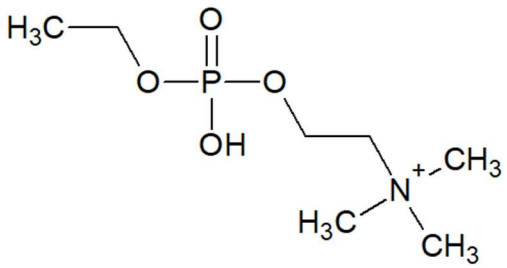

Figure 7.8 Structure of 2-[ethoxy(hydroxy)phosphoryl]oxyethyl-trimethylazanium or ethylated phosphorylcholine. The structure was drawn using ACD/ChemSketch (v. 2022.1.1).

7.5. Conclusions

HepaRG cells are considered as an appropriate surrogate for primary human hepatocytes when investigating liver metabolism and detoxification (Tascher et al., 2019), while untargeted metabolomics can be used to generate pathophysiological hypotheses and could pinpoint etiology-dependent metabolic differences in liver disease. Combining the elucidation of the metabolic fingerprint and footprint of

ethanol-induced hepatotoxicity in HepaRG cells facilitated the biological interpretation of results. Metabolic alterations showed only minor differences between 24 h and 48 h of exposure, with more upregulated TGs with a high level of confirmation and more upregulated polyunsaturated PCs after 48 h of exposure. However, metabolic alterations were strongly affected by the concentration of ethanol. Many altered metabolites were consistent with a steatotic image as seen in previous research, such as increased intracellular DGs and TGs, phosphorylcholine and Cers (d18:1), decreased PEs, PCs, LPCs, SMs, SAM and small chain CARs. Additional markers of toxicity have been observed such as downregulation of Cers (d18:2), creatine, O-phosphoethanolamine and acetylcholine and upregulation of octanoylcarnitine. Decreased catabolism of PCs to LPCs was supported by the decrease in GPC. In addition to detection of high levels of intracellular PEth 16:0_18:1, ethylated phosphorylcholine could be identified, both intra- and extracellular. Based on its absence in control samples, ethylated phosphorylcholine was considered as a potential new marker of ethanol exposure. Targeted analysis of ethylated phosphorylcholine showed the presence of ethylated phosphorylcholine in the blood of heavy drinkers, while it remained absent in negative controls. Although further validation is required, the proof-of-concept of ethylated phosphorylcholine as a marker of ethanol consumption was delivered.

7.6. Data availability

Raw datafiles are available through the MassIVE repository (https://massive.ucsd.edu/ProteoSAFe/) with the data set identifier MSV000088638.

7.7. Supplementary information

7.7.1. Data processing

Median relative standard deviation (mRSD) of the intensity of LC-MS features for each analytical platform and sample group of the intracellular and extracellular HepaRG fractions are given in Table SI-7.1 and SI-7.2. mRSD values were calculated after deisotoping and blank subtraction.

Table SI-7.1 Median relative standard deviation (mRSD) of the intensity of LC-MS features of the intracellular HepaRG fraction for each sample group and analytical platform. B1: Batch 1. B2: Batch 2. LIP+: Lipidomics in positive electrospray ionization mode. LIP-: Lipidomics in negative electrospray ionization mode. MET+: Metabolomics in positive electrospray ionization mode. MET-: Metabolomics in negative electrospray ionization mode.

	QC	Control	IC_{10}	1/10 IC_{10}
B1-24h-LIP+	12.8	17.8	26.0	20.1
B2-24h-LIP+	12.8	22.1	22.1	24.1
B1-48h-LIP+	9.3	17.8	22.7	25.6
B2-48h-LIP+	14.6	23.8	21.7	23.1
B1-24h-LIP-	11.2	22.9	32.4	25.7
B2-24h-LIP-	10.4	13.8	17.0	18.5
B1-48h-LIP-	10.8	25.9	21.4	28.3
B2-48h-LIP-	10.7	25.2	20.5	27.4
B1-24h-MET+	21.1	27.5	28.3	28.3
B2-24h-MET+	11.8	19.9	16.9	17.8
B1-48h-MET+	13.0	21.0	21.6	19.6
B2-48h-MET+	13.4	22.5	23.4	20.2
B1-24h-MET-	19.4	22.7	25.9	21.0
B2-24h-MET-	19.3	27.1	24.8	25.8
B1-48h-MET-	16.0	21.6	22.7	19.1
B2-48h-MET-	17.2	24.5	18.5	25.8

Table SI-7.2 Median relative standard deviation (mRSD) of the intensity of LC-MS features of the extracellular HepaRG fraction for each sample group and analytical platform. B1: Batch 1. B2: Batch 2. LIP+: Lipidomics in positive electrospray ionization mode. LIP-: Lipidomics in negative electrospray ionization mode. MET+: Metabolomics in positive electrospray ionization mode. MET-: Metabolomics in negative electrospray ionization mode.

	QC	Control	IC_{10}	1/10 IC_{10}
B1-24h-LIP+	11.0	20.5	25.4	20.3
B2-24h-LIP+	13.6	22.4	19.6	20.1
B1-48h-LIP+	10.7	19.6	23.2	17.7
B2-48h-LIP+	12.9	23.3	29.0	19.3
B1-24h-LIP-	10.1	21.6	16.1	22.0
B2-24h-LIP-	11.2	23.6	16.7	22.6
B1-48h-LIP-	10.3	14.8	19.7	18.0
B2-48h-LIP-	10.0	15.8	20.7	18.4
B1-24h-MET+	12.4	16.2	15.9	17.7
B2-24h-MET+	13.5	15.1	15.5	16.3
B1-48h-MET+	12.2	14.4	15.6	15.7
B2-48h-MET+	13.7	18.1	17.9	18.9
B1-24h-MET-	20.6	23.4	22.9	20.9
B2-24h-MET-	20.0	22.9	20.2	21.2
B1-48h-MET-	20.5	20.1	24.4	20.8
B2-48h-MET-	26.2	26.1	27.7	26.3

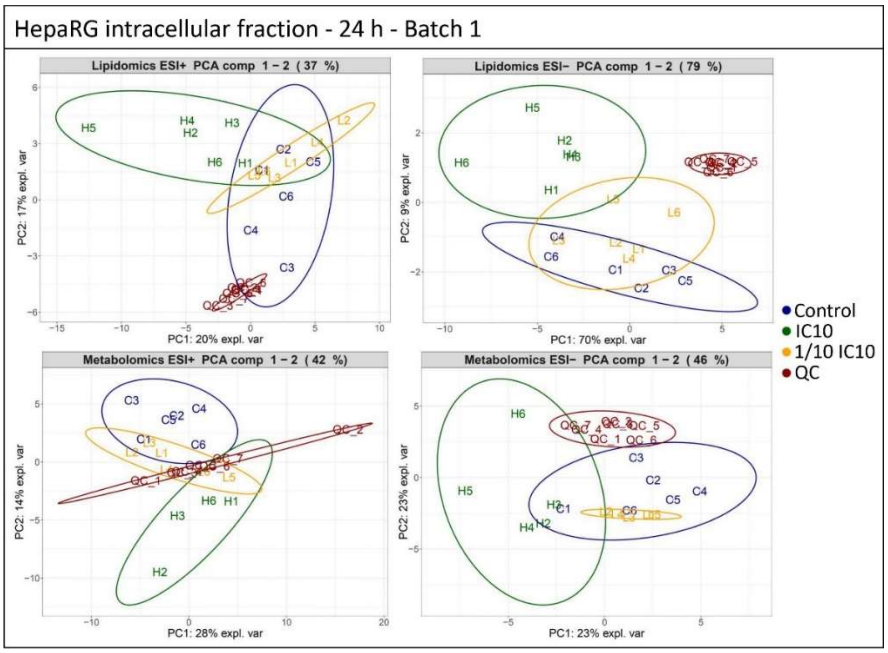

Figure SI-7.1 Principal component analysis plots of the intracellular fraction of HepaRG cells of batch 1 after 24 h exposure to ethanol. ESI+ and ESI- refer to electrospray ionization in positive and negative modes, respectively.

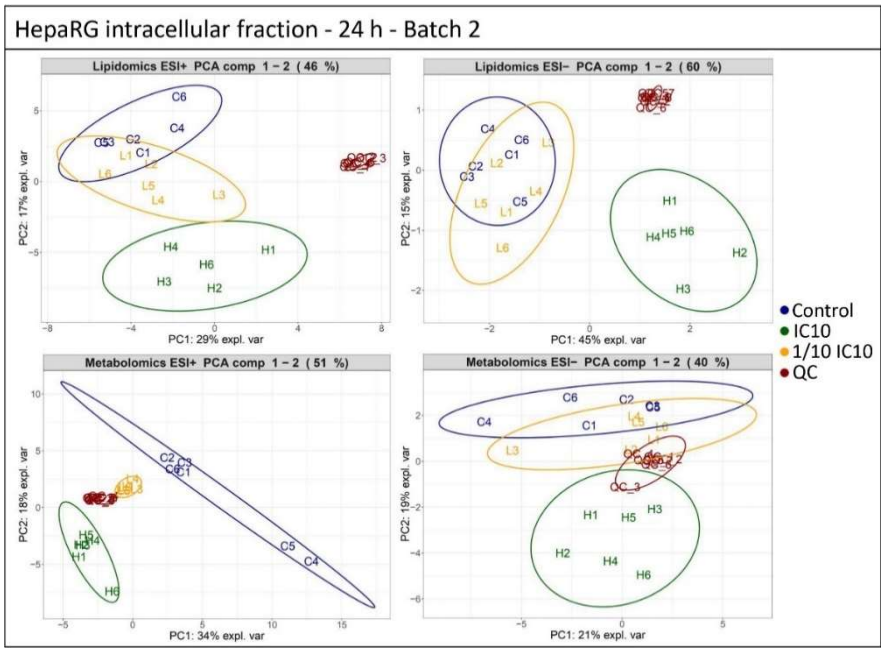

Figure SI-7.2 Principal component analysis plots of the intracellular fraction of HepaRG cells of batch 2 after 24 h exposure to ethanol. ESI+ and ESI- refer to electrospray ionization in positive and negative modes, respectively.

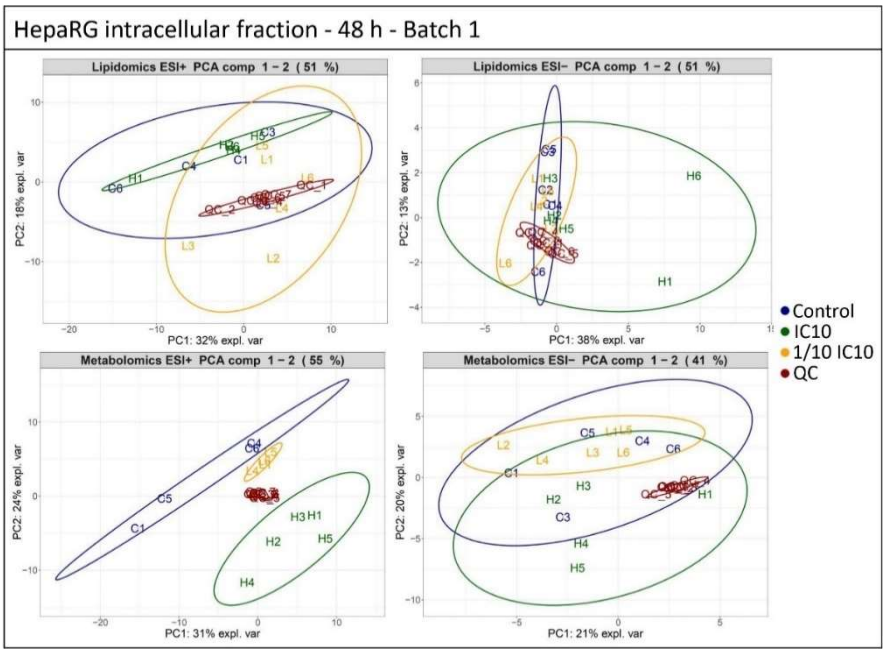

Figure SI-7.3 Principal component analysis plots of the intracellular fraction of HepaRG cells of batch 1 after 48 h exposure to ethanol. ESI+ and ESI- refer to electrospray ionization in positive and negative modes, respectively.

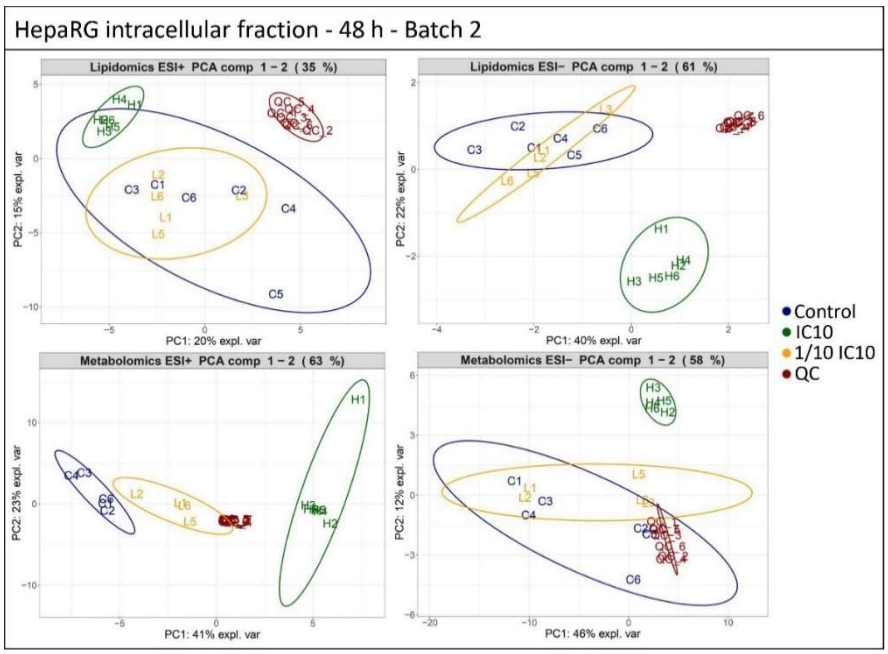

Figure SI-7.4 Principal component analysis plots of the intracellular fraction of HepaRG cells of batch 2 after 48 h exposure to ethanol. ESI+ and ESI- refer to electrospray ionization in positive and negative modes, respectively.

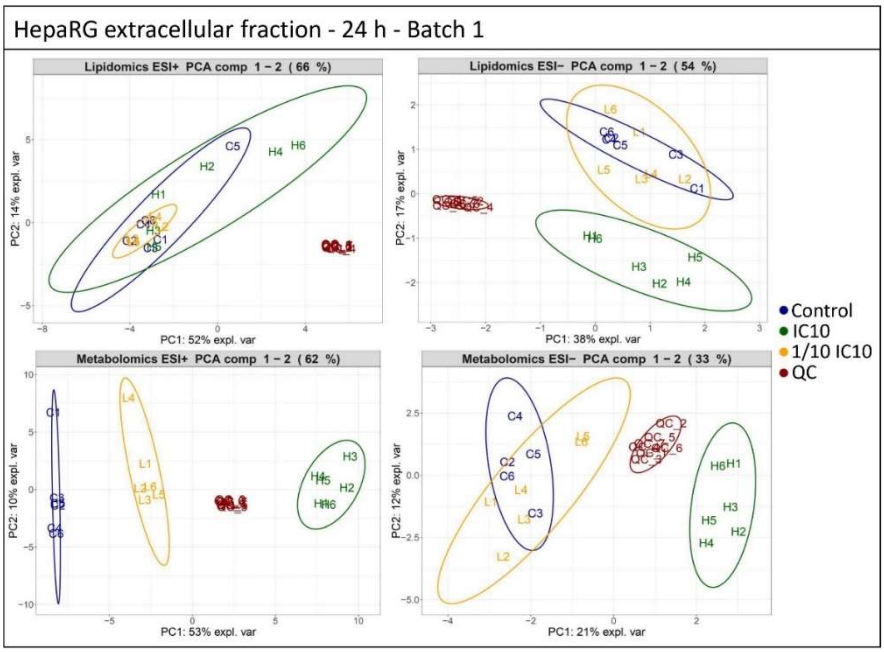

Figure SI-7.5 Principal component analysis plots of the extracellular fraction of HepaRG cells of batch 1 after 24 h exposure to ethanol. ESI+ and ESI- refer to electrospray ionization in positive and negative modes, respectively.

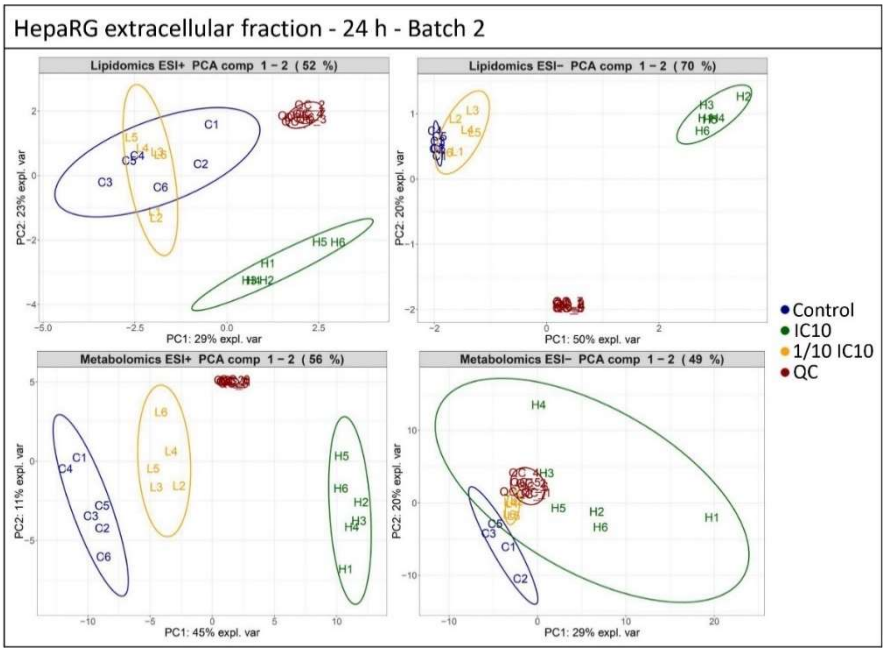

Figure SI-7.6 Principal component analysis plots of the extracellular fraction of HepaRG cells of batch 2 after 24 h exposure to ethanol. ESI+ and ESI- refer to electrospray ionization in positive and negative modes, respectively.

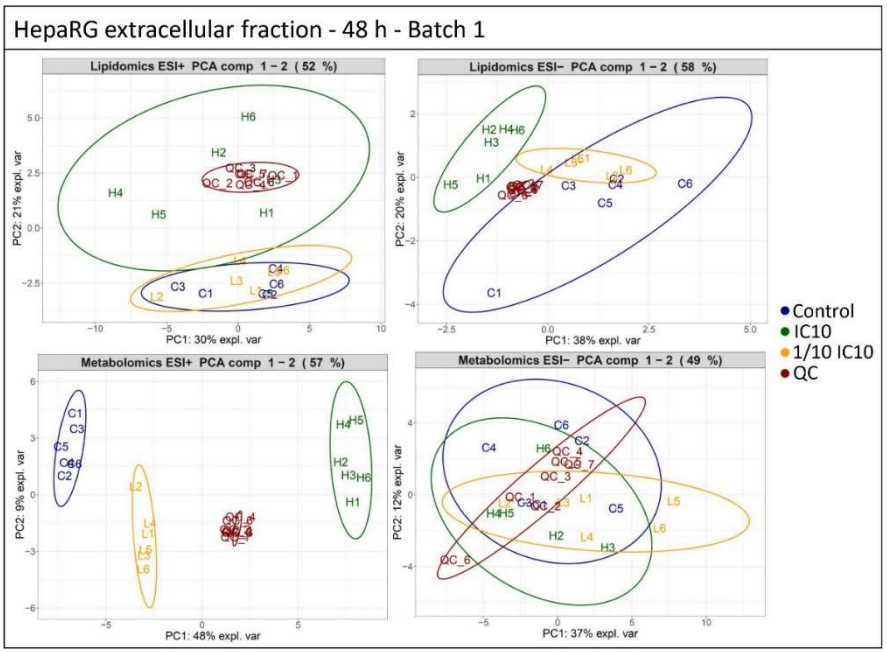

Figure SI-7.7 Principal component analysis plots of the extracellular fraction of HepaRG cells of batch 1 after 48 h exposure to ethanol. ESI+ and ESI- refer to electrospray ionization in positive and negative modes, respectively.

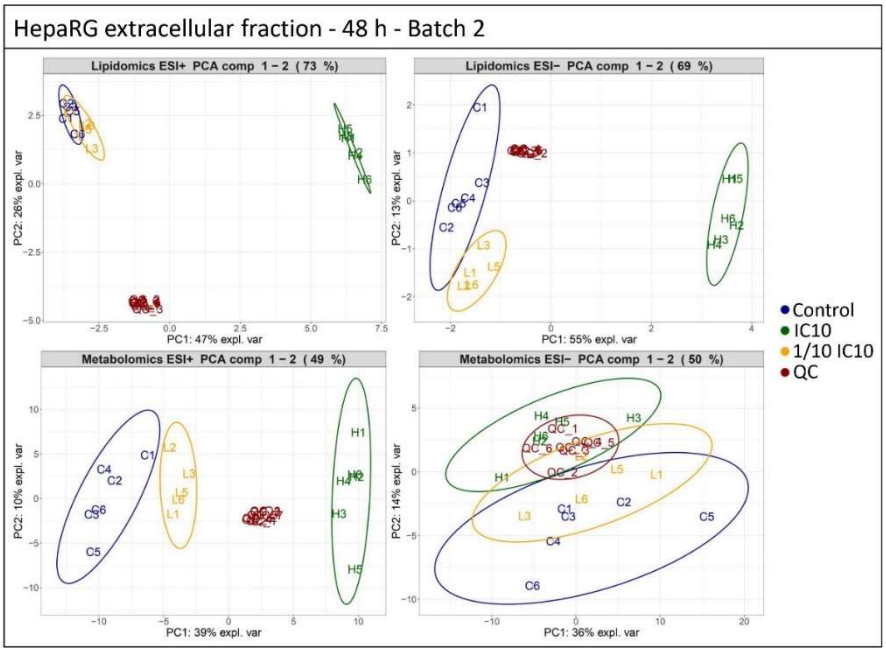

Figure SI-7.8 Principal component analysis plots of the extracellular fraction of HepaRG cells of batch 2 after 48 h exposure to ethanol. ESI+ and ESI- refer to electrospray ionization in positive and negative modes, respectively.

Table SI-7.3-SI-7.6 show the evaluation parameters of the multivariate statistical models for intracellular and extracellular fractions after exposure to ethanol (24 h and 48 h) at either IC_{10} concentration or 1/10 IC_{10} concentration. R^2, Q^2, R^2PERM and Q^2PERM (calculated after 1000 random permutations) were selected for evaluation of the PLS-DA model, while the area under the curve (AUC) was selected for evaluation of the random forest classification model.

Table SI-7.3 Evaluation parameters of multivariate statistical models for the intracellular fraction after exposure to the IC_{10} concentration of ethanol for 24 h and 48 h. B1: Batch 1. B2: Batch 2. LIP+: Lipidomics in positive electrospray ionization mode. LIP-: Lipidomics in negative electrospray ionization mode. MET+: Metabolomics in positive electrospray ionization mode. MET-: Metabolomics in negative electrospray ionization mode.

	R^2	Q^2	R^2_{PERM}	Q^2_{PERM}	AUC
B1-24h-LIP+	0.97	0.85	0.00	0.00	1.00
B2-24h-LIP+	1.00	0.96	0.01	0.00	1.00
B1-48h-LIP+	0.89	0.50	0.01	0.04	0.93
B2-48h-LIP+	0.96	0.85	0.00	0.00	1.00
B1-24h-LIP-	0.98	0.82	0.01	0.00	1.00
B2-24h-LIP-	0.99	0.90	0.03	0.00	1.00
B1-48h-LIP-	1.00	0.95	0.01	0.00	1.00
B2-48h-LIP-	0.91	0.86	0.02	0.00	1.00
B1-24h-MET+	1.00	0.86	0.01	0.01	1.00
B2-24h-MET+	0.99	0.95	0.00	0.00	1.00
B1-48h-MET+	0.93	0.86	0.01	0.01	1.00
B2-48h-MET+	0.95	0.92	0.00	0.00	1.00
B1-24h-MET-	0.87	0.78	0.04	0.00	1.00
B2-24h-MET-	0.95	0.87	0.00	0.00	1.00
B1-48h-MET-	0.89	0.75	0.02	0.01	1.00
B2-48h-MET-	0.96	0.88	0.00	0.00	1.00

Table SI-7.4 Evaluation parameters of multivariate statistical models for the intracellular fraction after exposure to 1/10 of the IC_{10} concentration of ethanol for 24 h and 48 h. B1: Batch 1. B2: Batch 2. LIP+: Lipidomics in positive electrospray ionization mode. LIP-: Lipidomics in negative electrospray ionization mode. MET+: Metabolomics in positive electrospray ionization mode. MET-: Metabolomics in negative electrospray ionization mode.

	R^2	Q^2	R^2_{PERM}	Q^2_{PERM}	AUC
B1-24h-LIP+	0.83	0.37	0.05	0.03	0.75
B2-24h-LIP+	0.99	0.73	0.13	0.02	0.97
B1-48h-LIP+	0.99	0.70	0.12	0.08	0.97
B2-48h-LIP+	1.00	0.15	0.94	0.75	0.62
B1-24h-LIP-	0.54	0.20	0.27	0.05	0.83
B2-24h-LIP-	1.00	0.83	0.03	0.00	0.88
B1-48h-LIP-	0.99	0.71	0.17	0.07	0.77
B2-48h-LIP-	0.95	0.76	1.00	0.86	0.56
B1-24h-MET+	1.00	0.74	0.68	0.12	0.91
B2-24h-MET+	0.63	0.49	0.16	0.01	0.92
B1-48h-MET+	0.99	0.50	0.32	0.06	0.61
B2-48h-MET+	0.96	0.66	0.09	0.01	0.65
B1-24h-MET-	1.00	0.89	0.01	0.00	0.80
B2-24h-MET-	1.00	0.57	0.06	0.03	0.86
B1-48h-MET-	0.84	0.30	0.18	0.07	0.79
B2-48h-MET-	1.00	0.27	0.71	0.79	0.31

Table SI-7.5 Evaluation parameters of multivariate statistical models for the extracellular fraction after exposure to the IC_{10} concentration of ethanol for 24 h and 48 h. B1: Batch 1. B2: Batch 2. LIP+: Lipidomics in positive electrospray ionization mode. LIP-: Lipidomics in negative electrospray ionization mode. MET+: Metabolomics in positive electrospray ionization mode. MET-: Metabolomics in negative electrospray ionization mode.

	R^2	Q^2	R^2_{PERM}	Q^2_{PERM}	AUC
B1-24h-LIP+	0.94	0.89	0.00	0.00	1.00
B2-24h-LIP+	0.94	0.89	0.00	0.00	1.00
B1-48h-LIP+	0.90	0.78	0.00	0.00	1.00
B2-48h-LIP+	0.90	0.78	0.00	0.00	0.99
B1-24h-LIP-	0.95	0.93	0.00	0.00	1.00
B2-24h-LIP-	0.95	0.93	0.00	0.00	1.00
B1-48h-LIP-	0.91	0.79	0.00	0.00	1.00
B2-48h-LIP-	0.91	0.79	0.00	0.00	1.00
B1-24h-MET+	0.97	0.95	0.00	0.00	1.00
B2-24h-MET+	0.97	0.95	0.00	0.00	1.00
B1-48h-MET+	0.96	0.91	0.00	0.00	1.00
B2-48h-MET+	0.96	0.91	0.00	0.00	1.00
B1-24h-MET-	0.94	0.70	0.14	0.00	1.00
B2-24h-MET-	0.94	0.70	0.14	0.00	0.99
B1-48h-MET-	0.99	0.92	0.01	0.00	0.94
B2-48h-MET-	0.99	0.92	0.01	0.00	0.95

Table SI-7.6 Evaluation parameters of multivariate statistical models for the extracellular fraction after exposure to 1/10 of the IC_{10} concentration of ethanol for 24 h and 48 h. B1: Batch 1. B2: Batch 2. LIP+: Lipidomics in positive electrospray ionization mode. LIP-: Lipidomics in negative electrospray ionization mode. MET+: Metabolomics in positive electrospray ionization mode. MET-: Metabolomics in negative electrospray ionization mode.

	R^2	Q^2	R^2_{PERM}	Q^2_{PERM}	AUC
B1-24h-LIP+	0.70	0.19	0.27	0.08	0.60
B2-24h-LIP+	0.62	0.40	0.17	0.01	0.87
B1-48h-LIP+	0.99	0.77	0.03	0.01	0.87
B2-48h-LIP+	0.86	0.70	0.04	0.01	0.86
B1-24h-LIP-	0.96	0.28	0.13	0.09	0.66
B2-24h-LIP-	0.25	0.10	0.29	0.03	0.69
B1-48h-LIP-	0.69	0.25	0.02	0.04	0.96
B2-48h-LIP-	0.70	0.22	0.03	0.03	0.84
B1-24h-MET+	0.99	0.71	0.15	0.01	0.93
B2-24h-MET+	1.00	0.83	0.16	0.00	0.99
B1-48h-MET+	0.98	0.88	0.04	0.00	1.00
B2-48h-MET+	1.00	0.79	0.34	0.03	0.88
B1-24h-MET-	0.89	0.15	0.31	0.13	0.55
B2-24h-MET-	0.99	0.46	0.02	0.04	0.85
B1-48h-MET-	1.00	0.92	0.15	0.00	0.75
B2-48h-MET-	1.00	0.59	1.00	0.88	0.75

7.7.2. Annotated metabolites

Information concerning annotated metabolites that were altered after ethanol exposure to HepaRG cells can be found in Table SI-7.7 and Table SI-7.8 of the electronic supplementary information 1 (SI-1) of chapter 7, which is available on the link below. In these SI tables, annotated metabolites are listed together with their metabolic class, formula, ionization species, *m/z*, RT, $^{DT}CCS_{N2}$, annotation level, mass error, CCS error and fold change direction per exposure timepoint and ethanol concentration.
https://www.dropbox.com/sh/bvxln6vaf00q3hk/AABt5gt5XbDgsROqKY4w7Znla?dl=1

7.7.3. Software and libraries used to annotate metabolites

A supplementary spreadsheet containing information on the software and libraries used per annotated metabolite can be consulted in electronic supplementary information 2 (SI-2) of chapter 7, which is available on the link below.
https://www.dropbox.com/sh/bvxln6vaf00q3hk/AABt5gt5XbDgsROqKY4w7Znla?dl=1

7.7.4. Examples of MS/MS spectra

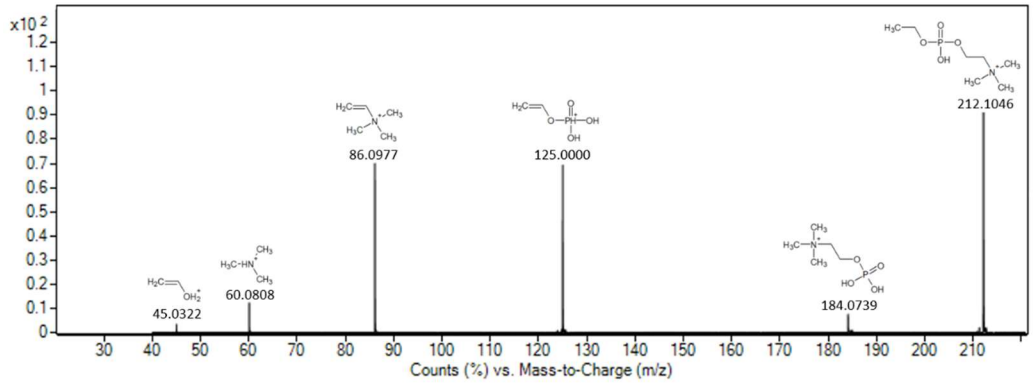

Figure SI-7.9 MS/MS spectrum of ethylated phosphorylcholine at 10 eV after maximum intensity normalization. The spectrum was measured in the extracellular polar fraction of HepaRG cells (ESI (+)). Fragment structures were derived from CFM-ID.

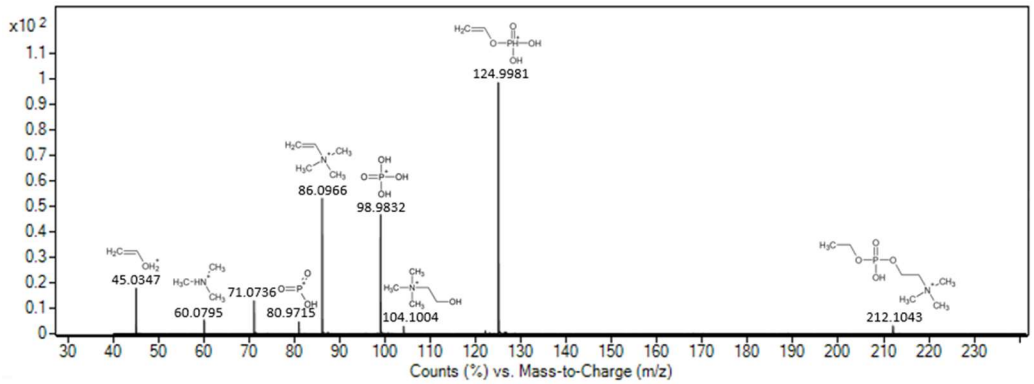

Figure SI-7.10 MS/MS spectrum of ethylated phosphorylcholine at 20 eV after maximum intensity normalization. The spectrum was measured in the extracellular polar fraction of HepaRG cells (ESI (+)). Fragment structures were derived from CFM-ID.

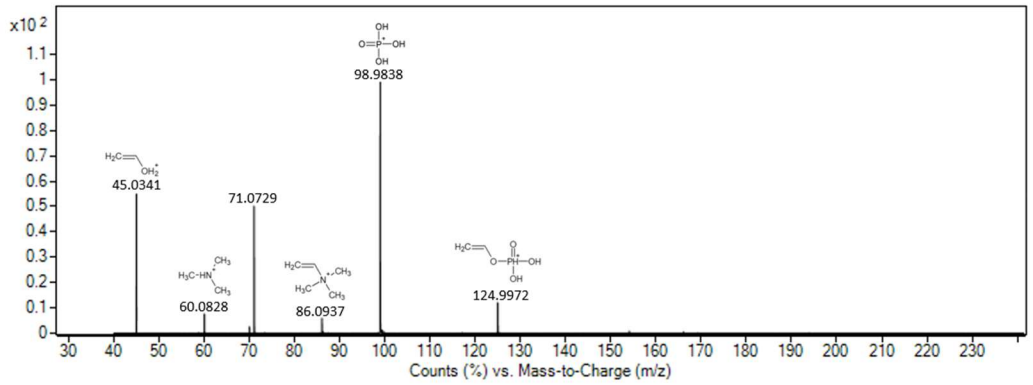

Figure SI-7.11 MS/MS spectrum of ethylated phosphorylcholine at 40 eV after maximum intensity normalization. The spectrum was measured in the extracellular polar fraction of HepaRG cells (ESI (+)). Fragment structures were derived from CFM-ID.

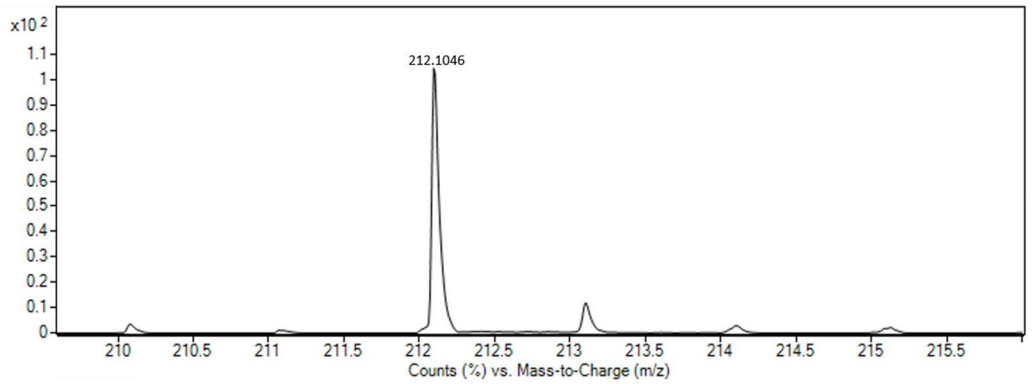

Figure SI-7.12 Isotopic pattern of ethylated phosphorylcholine. The spectrum was measured in the extracellular polar fraction of HepaRG cells (ESI (+)).

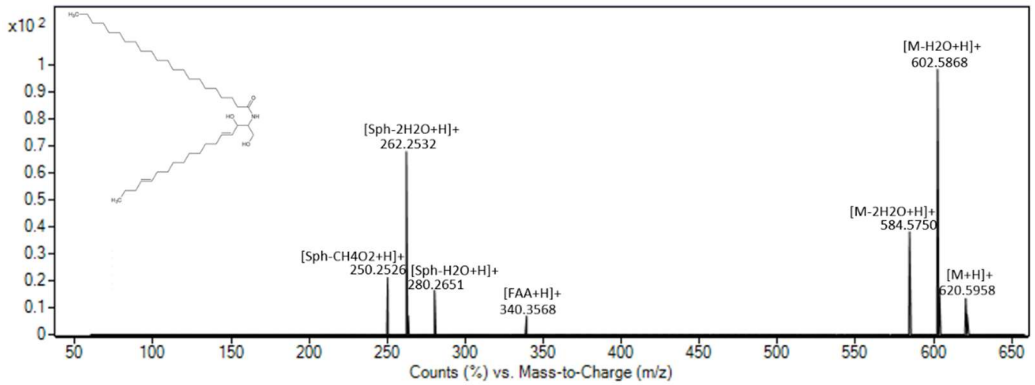

Figure SI-7.13 MS/MS spectrum of Cer 18:2;O2/22:0 at 10 eV after maximum intensity normalization. The spectrum was measured in the intracellular apolar fraction of HepaRG cells (ESI (+)). Fragment structures are not shown due to their size. FAA: fatty acid ammonia (i.e., FA-OH+NH3). Sph: Sphingoid base.

7.7.5. Ethylated phosphorylcholine in human whole blood

To determine whether EtOChoP can be considered a biomarker of ethanol consumption, the compound was targeted for quantification in human whole blood samples of teetotalers and ethanol consumers.

7.7.5.1. Human samples

Three post-mortem whole blood samples with high blood ethanol concentrations (range: 1.87 - 3.56 g/L) and 7 whole blood samples with high PEth 16:0/18:1 concentrations (range: 207 – (>)2000 ng/mL) were selected in addition to 4 control samples (no detectable ethanol or PEth 16:0/18:1). All whole blood samples were collected in EDTA tubes. A summary of the samples can be found in Table SI-7.9.

Table SI-7.9 Whole blood samples used for determination of EtOChoP. PEth: Phosphatidylethanol. NC: Negative control (i.e., teetotaler). HD: Heavy drinker (i.e., PEth 16:0_18:1 >200 ng/mL (Luginbühl et al., 2022)). PM: Post mortem. ND: Not detected. NA: Not available.

Sample ID	Ethanol (g/L)	PEth 16:0_18:1 (ng/mL)
NC-1	ND	ND
NC-2	ND	ND
NC-3	ND	ND
NC-4	ND	ND
HD-1	1.34	1400
HD-2	0.38	902
HD-3	0.20	>2000
HD-4	1.00	>1000
HD-5	0.86	>1000
HD-6	0.97	474
HD-7	0.32	207
PM-1	3.56	NA
PM-2	2.67	NA
PM-3	1.87	NA

7.7.5.2. Sample preparation

Sample preparation was based on the method of Gowda *et al*. (2017). A volume of 200 µL whole blood was quenched using 550 µL of MeOH (-80 °C), after which 50 µL of a 4 ppm solution of EtOChoP-D_5 in MeOH was added (to obtain a final concentration of 0.5 ppm). After vortexing for 30 s, samples were sonicated on ice for 2 min, followed by 20 min equilibration on ice and centrifugation at 16,000 g for 30 min at room temperature. From the supernatant, 400 µL was aliquoted and dried under a stream of pure, dry N_2 at room temperature. Dried extracts were stored at -80 °C and reconstituted directly before analysis. Dried extracts were reconstituted on ice using 200 µL of ACN/H_2O (65/35, v/v). After vortexing for 90 s, samples were filtered using 0.2 µm nylon centrifugal filters and centrifugated at 14,000 g for 2 min at room temperature. Sample extracts were transferred to LC vials and passed on to the autosampler (4 °C) right before analysis.

For each calibration point, the same sample preparation procedure was used with whole blood of a teetotaler. Eight calibration samples were used with a concentration of EtOChoP of 10, 20, 50, 100, 200, 500, 1000 and 2000 ng/mL. EtOChoP standard was added to the 50 µL of the EtOChoP-D_5 solution to spike each calibration point at a different concentration.

7.7.5.3. Analytical method

LC–MS/MS analyses were performed on a 1290 Infinity LC system connected to a 6460 triple quadrupole mass spectrometer from Agilent Technologies with an ESI interface operated in positive ionisation mode. An iHILIC-Fusion(+) column (100 x 2.1 mm, 1.8 µm; zwitterionic) was used at 60 °C. The mobile phase consisted of 10 mM HCOONH4 + 0.1% (v/v) HCOOH in H_2O/MeOH (9/1, v/v) (A) and ACN (B). The gradient profile was 0–4 min, 95% B; 4–12.5 min, 95-60% B; 12.5–20 min, 60% B; 20-21 min, 60-95% B; 21-26 min, 95% B. The mobile phase flow rate was set at 0.25 mL/min, and the injection volume was optimised at 1 µL.

The most abundant MRM transitions of EtOCHoP and EtOCHoP-D_5 were used for quantification (quantifier), while other transitions (qualifiers) were used for identity confirmation. Three transitions were selected for EtOCHoP (212.1 → 124.9 (quantifier), 212.1 → 86.1 (qualifier 1), and 212.1 → 98.9 (qualifier 2)), while two transitions were used for EtOChoP-D_5 (217.1 → 126.0 (quantifier) and 217.1 → 86.1 (qualifier)). For confirmation of the detected compound, both retention times and quantifier/qualifier ratios were used. The maximum allowed retention deviation from the internal standard was set at 2.5% and qualifier/quantifier ratios were not allowed to differ more than ±30%.

7.7.5.4. Results and discussion

An overview of the determined EtOChoP concentrations can be found in Table SI-7.10.

Table SI-7.10 Concentrations of ethylated phosphorylcholine (EtOChoP) determined in whole blood samples. PEth: Phosphatidylethanol. NC: Negative control (i.e., teetotaler). HD: Heavy drinker (i.e., PEth 16:0_18:1 >200 ng/mL (Luginbühl et al., 2022)). PM: Post mortem. ND: Not detected. NA: Not available.

Sample ID	Ethanol (g/L)	PEth 16:0_18:1 (ng/mL)	EtOChoP (ng/mL)
NC-1	ND	ND	ND
NC-2	ND	ND	ND
NC-3	ND	ND	ND
NC-4	ND	ND	ND
HD-1	1.34	1400	<10
HD-2	0.38	902	<10
HD-3	0.20	>2000	<10
HD-4	1.00	>1000	<10
HD-5	0.86	>1000	<10
HD-6	0.97	474	<10
HD-7	0.32	207	<10
PM-1	3.56	NA	153
PM-2	2.67	NA	91
PM-3	1.87	NA	<10

EtOChoP was absent in the whole blood samples of negative controls, while it could be detected in all whole blood samples of heavy drinkers. Unfortunately, the used calibration range (10 – 2000 ng/mL) was too high to quantify most samples. Only two post-mortem samples could be quantified using the calibration curve (R^2 = 0.98). Their concentrations were 153 ng/mL (3.56 g/L blood ethanol) and 91 ng/mL (2.67 g/L blood ethanol). Comparing the area ratio (EtOChoP/EtOChoP-D_5) in the samples to that of the lowest calibration standard of the calibration curve, the concentration in the other samples could be estimated in a range of 0.2 to 1.5 ng/mL. Although the targeted method requires further optimization, the analyses were able to show the presence of EtOChoP in the blood of heavy drinkers, while it remained absent in negative controls. Thus, the proof-of-concept of EtOChoP as a marker of ethanol consumption was delivered.

CHAPTER 8:
METABOLIC SIGNATURE OF HEPARG CELLS EXPOSED TO ETHANOL AND TUMOR NECROSIS FACTOR ALPHA

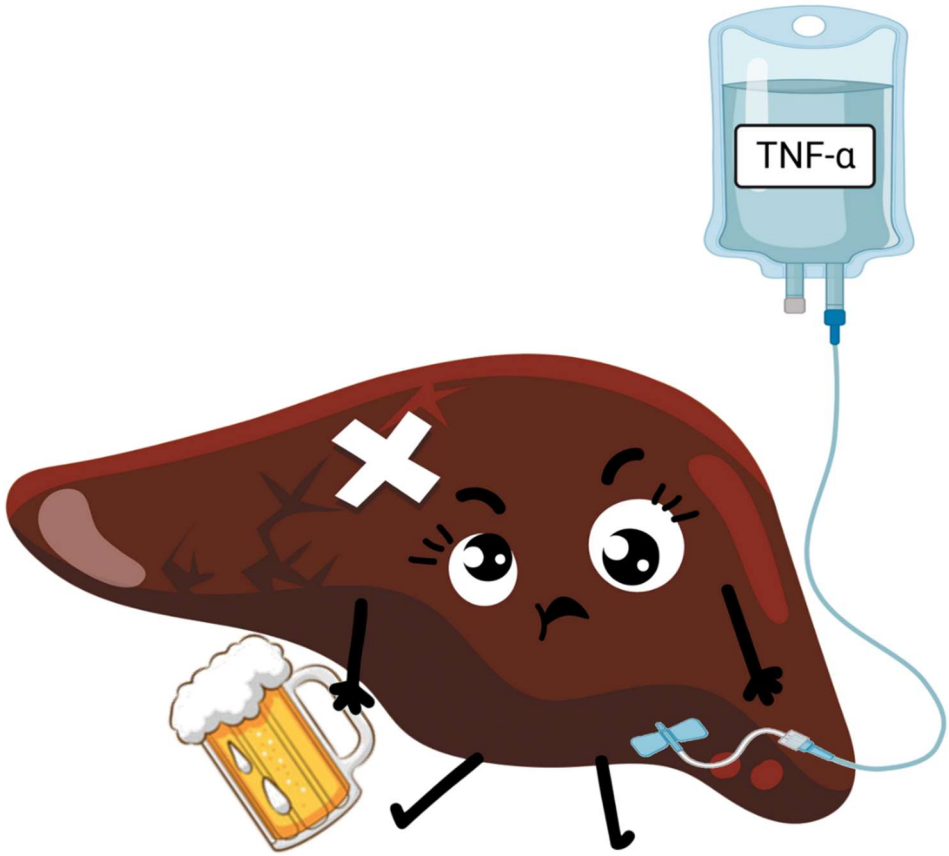

Based on the following publication

Iturrospe E, Robeyns R, Da Silva KM, Van de Lavoir M, Boeckmans J, Vanhaecke T, van Nuijs A, Covaci A. Metabolic signature of HepaRG cells exposed to ethanol and tumor necrosis factor alpha to study alcoholic steatohepatitis by LC-MS-based untargeted metabolomics. Archives of Toxicology. 2023; 97, 1335-1353. (DOI: 10.1007/s00204-023-03470-y).

8.1. Introduction

Alcoholic liver disease (ALD) can progress from alcoholic fatty liver disease (AFLD) to alcoholic steatohepatitis (ASH), while advanced stages include liver fibrosis, (de)compensated cirrhosis and hepatocellular cancer (HCC) (Sakhuja, 2014; Seitz et al., 2018; Shim & Jeong, 2020). The early stages of ALD are characterized by progressive intracellular lipid accumulation in the hepatocytes, while hepatic inflammation becomes apparent in the stage of ASH (Sakhuja, 2014; Seitz et al., 2018).

HepaRG cells were used in chapter 7 to simulate ALFD *in vitro*, by exposing the cells to ethanol at different concentrations for 24 h and 48 h. These experiments showed, among other, downregulation of hepatic phosphatidylcholines and -ethanolamines and alterations of carnitines depending on the size of their carbon chain. Ethylated phosphorylcholine was identified as a marker of ethanol exposure. Intracellular di- and triglycerides were upregulated, although the number of species selected by the statistical workflow were low. As the extrahepatic environment was absent in these *in vitro* experiments, ethanol exposure could not generate the inflammatory response caused by extrahepatic cytokines as seen in human ASH (Nagy, 2015). In this chapter, follow-up experiments were performed in which HepaRG cells were co-exposed to ethanol and tumor necrosis factor alpha (TNF-α) in order to obtain an improved *in vitro* simulation of ASH. TNF-α is considered the most important inflammatory cytokine in the progression of ALD (Kawaratani et al., 2013; Nagy, 2015; Seo & Jeong, 2016; Yin et al., 1999). Excessive consumption of ethanol alters the characteristics and composition of the microbiome in the gastrointestinal tract and augments permeability of the intestinal membrane, which increases the portal concentration of blood endotoxins (lipopolysaccharides; LPS) (Kawaratani et al., 2013; Nagy, 2015). LPS can activate Kupffer cells via the toll-like receptor 4 (TLR4) signaling pathway, resulting in secretion of TNF-α, which reacts with TNF-α receptors (TNF-R) on hepatocytes (Nagy, 2015; Seo & Jeong, 2016). In addition, ethanol consumption stimulates expression of TNF-α in immune cells of adipose tissue. TNF-α originating from adipose tissue can reach the liver through the portal circulation (Shim & Jeong, 2020). Ethanol also increases the susceptibility to TNF-α by increasing the levels of TNF-R1 on hepatocytes in a dose-dependent manner (Rodriguez et al., 2004). The activity of TNF-α significantly contributes to alcohol-induced liver damage by inducing apoptosis and necrosis, and increasing expression of intracellular adhesion molecules, which promote inflammation (Nagy, 2015; Rodriguez et al., 2004). Next to ALD, TNF-α is also associated with liver injury in non-alcoholic steatohepatitis (NASH) (Kawaratani et al., 2013).

After exposure of HepaRG cells to ethanol and TNF-α, metabolic alterations were elucidated using the LC-MS-based untargeted metabolomic platforms described in

chapter 6. In addition to untargeted screening, suspect screening was performed to compare fold change differences (i.e., based on differences in peak abundancies in different exposure groups) of previously elucidated metabolites after solely ethanol exposure (chapter 7) versus combined exposure to ethanol and TNF-α.
Extraction and analyses of intracellular metabolites were able to provide a metabolic fingerprint for hepatotoxicity induced by ethanol and TNF-α in HepaRG cells. In addition, conditioned cell media were analyzed to yield the metabolic footprint (i.e., provide information on metabolic secretion and consumption). Dynamic changes in metabolites were elucidated in order to get a better understanding of early-stage indicators of ASH.

8.2. Materials and methods

The used materials and methods were described earlier in chapter 6, including chemicals and materials (6.2), dosage estimation (6.3), HepaRG cell cultivation regimen (6.4), sample preparation (6.5), analytical methods (6.6), data processing and statistics (6.7), metabolite annotation (6.8) and analytical QA/QC procedures (6.9).
For suspect screening, annotated metabolites selected after ethanol exposure of HepaRG cells (chapter 7) were used to build a target list (*m/z* values to undergo fragmentation in a specific retention time window) for data acquisition.

8.2.1. Cell exposure

After 7 days of incubation (i.e., needed for obtaining polarized hepatocyte colonies and biliary-like cells, see 6.4) HepaRG cell exposure was initiated (Figure 8.1). Differentiated HepaRG cells were exposed for 24 h to 368 mM of ethanol (i.e., IC_{10}, positive control, n = 7), 368 mM of ethanol combined with 50 ng/mL TNF-α (1.2 mL/well, n = 7) or no ethanol or TNF-α (i.e., negative control, n = 7). Negative control groups, sample groups exposed to solely ethanol and to the combination of ethanol and TNF-α will be further referred to as sample groups C (Control), E (Ethanol) and T (TNF-α & ethanol), respectively. While ethanol was directly mixed with the incubation medium, TNF-α was firstly dissolved in double-filtered PBS to obtain a solution of 20 µg/mL. Twenty-five µL of this latter solution was added to 10 mL of incubation medium to obtain a final concentration of 50 ng/mL. The concentration of TNF-α was based on the protocol of Boeckmans *et al.* for *in vitro* simulation of non-alcoholic steatohepatitis (NASH) (2019, 2020). In addition, three extraction blanks, not containing cells, were obtained using the same incubation conditions.

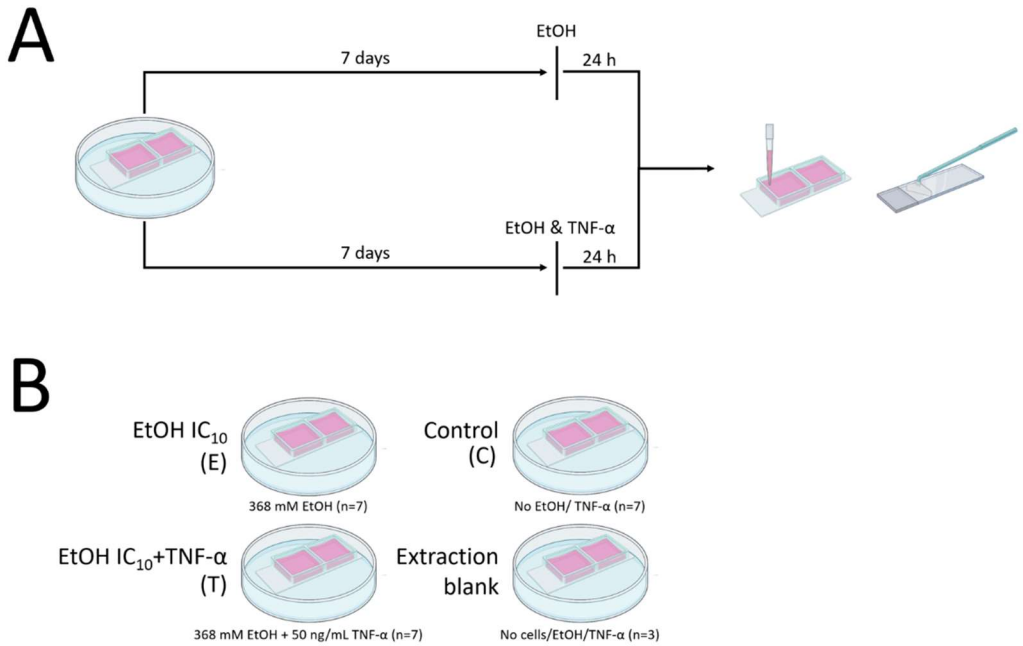

Figure 8.1 A) Graphical representation of the exposure experiment. HepaRG cells were exposed for 24 h to ethanol or to both ethanol and tumor necrosis factor alpha (TNF-α). The same set-up was used for the validation experiment. **B)** Graphical representation of the used sample groups. Graphical icons in this figure were provided by BioRender, license n. 2641-5211.

8.3. Results

8.3.1. Influence of incubation conditions on ethanol concentration

During exposure experiments, sample groups were exposed to either 368 mM of ethanol (with or without TNF-α) or no ethanol. The ethanol content of the media was determined pre- and post-incubation using headspace gas chromatography with flame ionization detection (HS-GC-FID). Results are presented in Figure 8.2. Incubation for 24 h caused an average decrease in ethanol concentration of 48% for the ethanol group and 47% for the group exposed to ethanol and TNF-α (for both n = 14, i.e., original and validation experiment combined). As the IC_{10} was determined over a time period of 24 h, this decrease in concentration did not influence the outcome. After 24 h, negative control samples (n = 14) showed an ethanol content of 2.4% compared to the IC_{10}. Pre- and post-run ethanol QC solutions met the acceptance criteria (6.6.2) and were quantified both as 0.3 g/L for the 0.3 g/L solution (bias = 0%, CV = 0%) and 4.1 g/L and 4.2 g/L for the 4.0 g/L solution (max bias = 5%, CV = 1.7%), respectively.

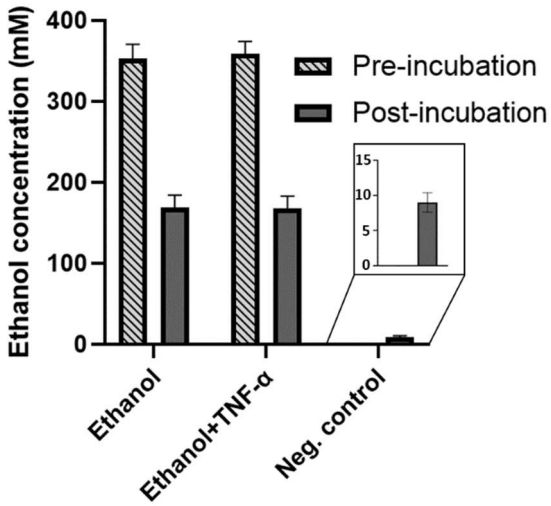

Figure 8.2 Decrease of ethanol concentration during incubation. Headspace gas chromatography with flame ionization detection (HS-GC-FID) was used to determine the ethanol concentration pre- (n = 2) and post-incubation (n = 14). The figure was made using Graphpad Prism (v. 9.0).

8.3.2. Data quality

Post-run quality control included manual evaluation of extracted ion chromatograms of internal standards. Pre-set requirements for data quality of internal standards needed to be fulfilled for retaining a sample were the same as for the system suitability sample (Table 6.2). For the intracellular samples, mRSDs were < 15% for all QC samples of the apolar fractions and < 20% for all QC samples of the polar fractions, with one exception (24% for ESI (-) – batch 2) (Table SI-8.1). For the extracellular samples, mRSDs of the QC samples of both the polar and apolar fractions were all < 20% (Table SI-8.2). All calculated mRSD values indicate a reliable analytical method as RSD values ≤ 30% are generally accepted in untargeted metabolomics (Naz et al., 2014). Biological and sample preparation variance is indicated by the increase in mRSD between QC samples and biological samples (i.e., sample groups C, E and T). For the intracellular samples, the average mRSD increased from 12% to 18% and from 18% to 25% for the apolar and polar fractions, respectively. The increase in average mRSD was slightly higher for the apolar fractions of the extracellular samples, with 15% to 25% and lower for the polar fractions from 15 to 18%. The low increase in mRSD indicates little sample preparation and biological variance.

Principal component analysis (PCA) plots (Figure SI-8.1-SI-8.4) showed a clear separation in PC1 and/or PC2 between the negative control group and the other sample groups, indicating a high inter-group variability due to a strong metabolic impact of ethanol or

combined ethanol and TNF-α exposure. For example, the PCA plots of the intracellular samples of HepaRG cells batch 1 are shown in Figure 8.3.

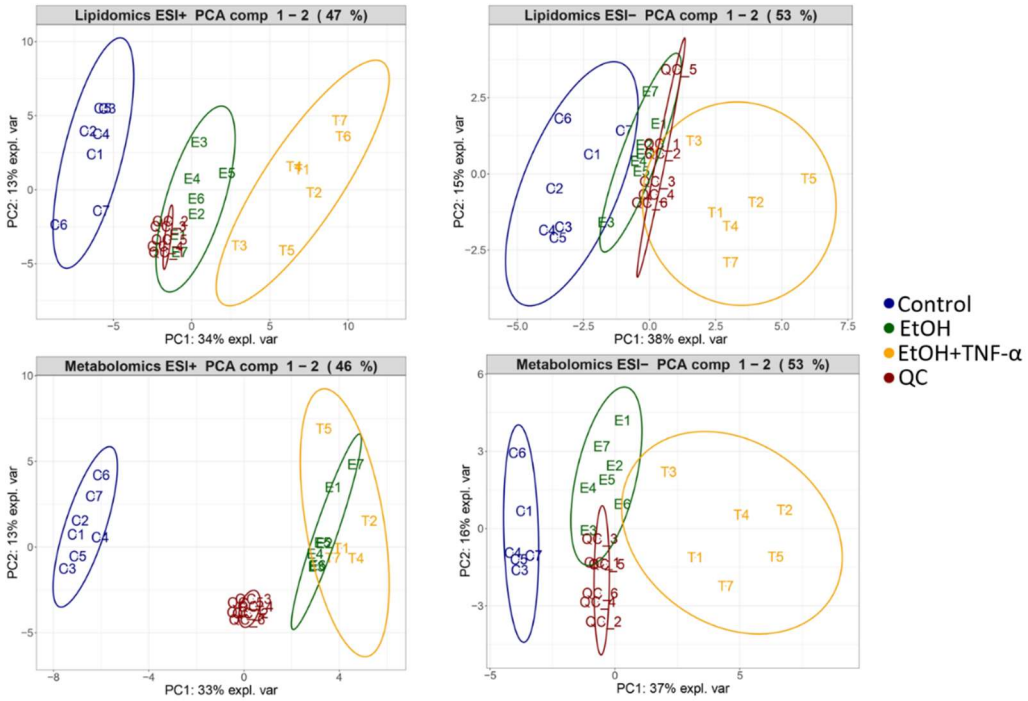

Figure 8.3 Example of a principal component analysis plots of intracellular samples of HepaRG cells analyzed in different ionization modes (ESI+ and ESI-), after 24 h exposure to ethanol and combined exposure to ethanol and TNF-α. The two PCA plots above were built using apolar sample fractions, while the two PCA plots below were generated using polar sample fractions. For all PCA plots, there is a clear distinction between the negative control group (C, blue), the sample group exposed to the IC_{10} of ethanol (E, green), and the sample group exposed to ethanol (IC_{10}) and TNF-α (T, orange). Only for the polar sample fraction is ESI+, overlap can be observed for sample groups E and T. The clustering of pooled QC samples is shown in red.

For the intracellular fractions, the inter-group variability between group E and T was sufficient to obtain a clear separation for all sample polarities, sample batches and ionization modes, except for ESI (+) for the polar samples (batch 1) and ESI (-) for the polar samples (batch 2). However, this overlap was directed by the QC samples as generation of PCA plots without QC samples rearranged the spatial orientation to a clear separation between E and T (data not shown). A similar effect was observed for extracellular samples. All sample groups (C, E, T) were clearly separated in all polarities (polar and apolar), ionization modes (ESI (+) and ESI (-)) and batches (1 and 2), with the exception of the polar fractions in ESI (-). In these latter PCA plots, both E and T were

clearly separated from C, but overlap between E and T was observed. This latter overlap resolved when QC samples were excluded from the PCA (data not shown).
In all PCA plots, sample group C and T showed the strongest separation, while sample group E was positioned in between sample group C and T. This latter is in line with the expected distinctiveness of the metabolic profile as combined exposure to ethanol and TNF-α was expected to generate a more distinctive metabolic profile compared to that of solely ethanol exposure. The evaluation parameters of the multivariate statistical models (i.e., R^2, Q^2, R^2_{PERM}, Q^2_{PERM} (n permutations = 1000) for the PLS-DA models and AUC for the RF models, Table SI-8.3-SI-8.6), were concordant with the trends observed during PCA analyses. High values were found for R^2 ($\bar{x}_{IC}$ = 1.00, $\bar{x}_{EC}$ = 0.98), Q^2 ($\bar{x}_{IC}$ = 0.95, $\bar{x}_{EC}$ = 0.95), and AUC ($\bar{x}_{IC}$ = 1.00, $\bar{x}_{EC}$ = 1.00) and low values for R^2_{PERM} ($\bar{x}_{IC}$ = 0.00, $\bar{x}_{EC}$ = 0.00) and Q^2_{PERM} ($\bar{x}_{IC}$ = 0.00, $\bar{x}_{EC}$ = 0.00) for the models comparing group C with T. PLS-DA and RF models comparing group E with T showed lower values for R^2 ($\bar{x}_{IC}$ = 0.94, $\bar{x}_{EC}$ = 0.99), Q^2 ($\bar{x}_{IC}$ = 0.79, $\bar{x}_{EC}$ = 0.85), and AUC ($\bar{x}_{IC}$ = 1.00, $\bar{x}_{EC}$ = 0.98) and higher values for R^2_{PERM} ($\bar{x}_{IC}$ = 0.01, $\bar{x}_{EC}$ = 0.04) and Q^2_{PERM} ($\bar{x}_{IC}$ = 0.00, $\bar{x}_{EC}$ = 0.00). Overall, the lowest predictive values were observed for polar fractions in ESI (-) mode comparing E versus T.
Post-exposure phase-contrast microscopic evaluation of the different HepaRG cultures was performed (Figure 8.4). Unexposed control cells showed clear clustering of hepatocytes and distinctive biliary cells. Going from sample group C to E and T, increased stress was observed as distortion of cytological morphology, faded lining of polarized hepatocyte colonies, accumulation of debris and impaired organization of hepatic clusters.

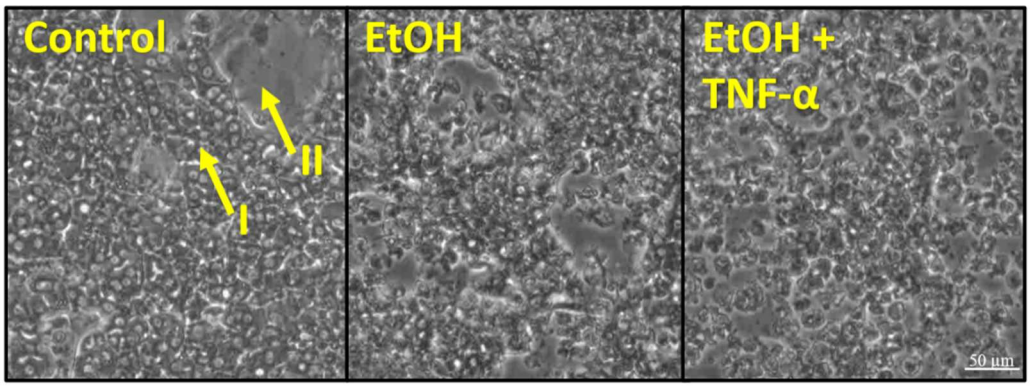

Figure 8.4 Phase-contrast microscopic pictures of HepaRG cells (10x10). Cells were not exposed to ethanol (Control), 368 mM of ethanol for 24 h (EtOH) or 368 mM of ethanol combined with 50 ng/mL TNF-α (1.2 mL/sample) for 24 h (TNF-α + EtOH). Roman numbers refer to polarized hepatocyte colonies (I) and biliary canaliculi and biliary-like epithelial cells (II).

8.3.3. Suspect screening of HepaRG cells exposed to ethanol with and without co-exposure to TNF-α

In chapter 7, a list was reported of 64 intracellular and 20 extracellular metabolites that were able to distinguish between HepaRG cells exposed to ethanol (IC_{10}) for 24 h and non-exposed control cells. This list was used to confirm the effects of ethanol in the positive control group (i.e., HepaRG cells exposed to ethanol (IC_{10}) for 24 h) (Figure 8.5 and Figure 8.6). In addition, the same metabolites were targeted in all other experimental groups in order to follow the effect of co-exposure to ethanol and TNF-α (Figure 8.5 and Figure 8.6). A detailed list of metabolites with their observed RT, *m/z* value, $^{DT}CCS_{N2}$ value, level of annotation confidence and additional information can be found in the supplementary Table SI-8.7 for intracellular metabolites and Table SI-8.8 for extracellular metabolites.

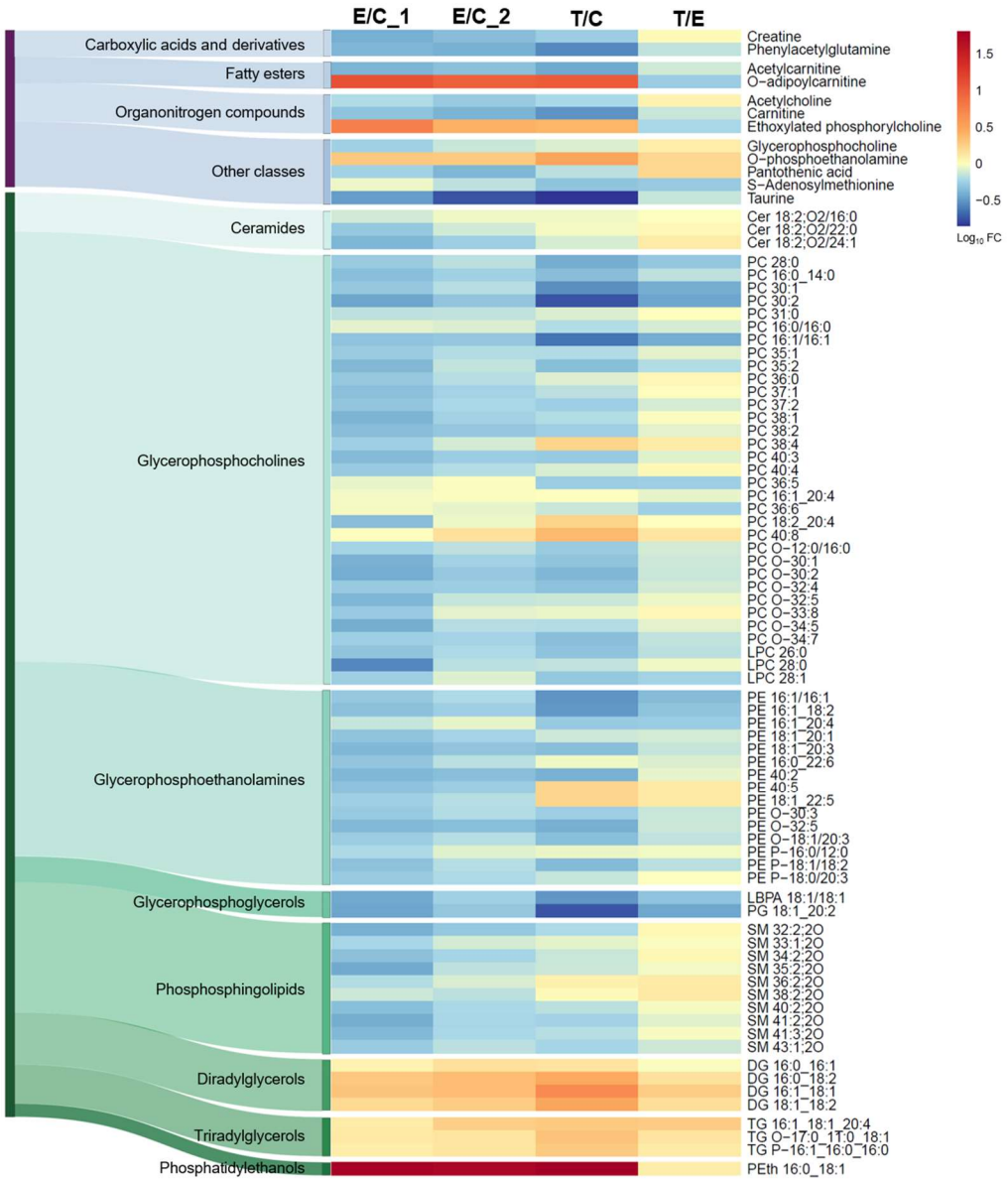

Figure 8.5 Intracellular suspect screening of HepaRG cells exposed to ethanol with and without co-exposure to TNF-α. A Sankey diagram combined with heatmaps was used to show the effect of ethanol exposure and TNF-α co-exposure on the intracellular metabolome of HepaRG cells. Metabolites in the polar fraction of the samples are indicated by a blue-purple Sankey diagram, while a green Sankey diagram represents metabolites originating from the apolar fraction. E/C_1: Ethanol (IC_{10}) vs. negative control after 24 h of exposure as previously reported in chapter 7. E/C_2: Ethanol (IC_{10}) vs. negative control after 24 h. T/C: Ethanol (IC_{10}) + TNF-α vs. negative control after 24 h. T/E: Ethanol (IC_{10}) + TNF-α vs. ethanol (IC_{10}) after 24 h. FC: Fold change.

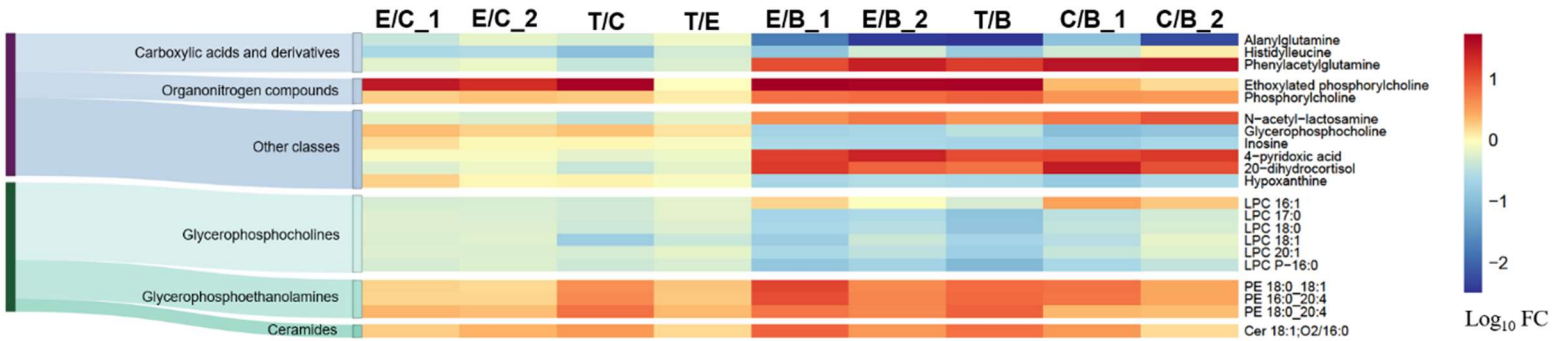

Figure 8.6 Extracellular suspect screening of HepaRG cells exposed to ethanol with and without co-exposure to TNF-α. A Sankey diagram combined with heatmaps was used to show the effect of ethanol exposure and TNF-α co-exposure on the extracellular metabolome of HepaRG cells. Metabolites in the polar fraction of the samples are indicated by a blue-purple Sankey diagram, while a green Sankey diagram represents metabolites originating from the apolar fraction. E/C_1: Ethanol (IC_{10}) vs. negative control after 24 h of exposure as previously reported in chapter 7. E/C_2: Ethanol (IC_{10}) vs. negative control after 24 h. T/C: Ethanol (IC_{10}) + TNF-α vs. negative control after 24 h. T/E: Ethanol (IC_{10}) + TNF-α vs. ethanol (IC_{10}) after 24 h. E/B_1: Ethanol (IC_{10}) vs. blank media after 24 h as previously reported in chapter 7. E/B_2: Ethanol (IC_{10}) vs. blank media after 24 h of exposure. T/B: Ethanol (IC_{10}) + TNF-α vs. blank media after 24 h. C/B_1: Negative control vs. blank media after 24 h as previously reported in chapter 7. C/B_2: Negative control vs. blank media after 24 h. FC: Fold change.

8.3.3.1. Metabolic fingerprint of HepaRG cells exposed to ethanol and effect of co-exposure to TNF-α

When comparing ethanol exposed versus non-exposed control cells, upregulation was observed for diglycerides (DG) and triglycerides (TG), while sphingomyelins (SM), phosphatidylethanolamines (PE) and phosphatidylcholines (PC) were downregulated, concordant with our previous findings (chapter 7). Also, other observations were consistent such as downregulation of ceramides (Cer) with a sphingadienine-backbone (d18:2), small-chain acylcarnitines, phenylacetylglutamine (PAG), creatine, acetylcholine, glycerophosphocholine (GPC), pantothenic acid, S-adenosylmethionine (SAM) and taurine. PEth 16:0_18:1, O-adipoylcarnitine, ethylated phosphorylcholine (EtOChoP) and O-phosphoethanolamine (EtoP) were upregulated. When comparing HepaRG cells exposed to solely ethanol versus cells exposed to both ethanol and TNF-α, the same fold change directions could be observed for nearly all metabolites. Only for polyunsaturated PCs, some species (e.g., PC 38:4, PC 18:2_20:4, PC 40:8) showed upregulation as was previously seen during HepaRG exposure to ethanol for 48 h (chapter 7). TNF-α co-exposure did influence the magnitude of up- or downregulation. The strongest shift in upregulation was observed for di- and triglycerides and EtoP. The strongest shift in downregulation was observed for saturated and low-level unsaturated PCs (< 4 double bonds), PEs, SAM and PAG.

8.3.3.2. Metabolic footprint of HepaRG cells exposed to ethanol and effect of co-exposure to TNF-α

In order to be able to distinguish between altered secretion and altered consumption, both incubation media from exposed cells, control cells and blank media (i.e., incubated media without cells) were analyzed (Figure 8.6). A negative metabolite fold change (FC) difference between (I) exposure versus control, (II) exposure versus blank media and (III) control versus blank media indicates increased consumption due to exposure. A positive FC for all three groups indicates increased secretion. Metabolites downregulated in groups II and III and upregulated in group I indicate metabolites that are less consumed by HepaRG cells. A fourth scenario is upregulation in groups II and III and downregulation in group I, indicating reduced secretion. As metabolomic studies provide a snapshot of metabolic patterns, the four described scenarios should be interpreted carefully because changes can be highly dynamic.

For the positive control, up- and downregulation of metabolites in the extracellular fraction was consistent with previous findings (chapter 7). Ethanol exposure did for example increase cellular consumption of lysoPCs (LPC) and secretion of PEs, Cers, phosphorylcholine (ChoP) and EtOChoP. Decreased consumption was observed for GPC, inosine and hypoxanthine, while extracellular PAG decreased due to decreased

secretion. When the metabolites of Figure 8.6 were targeted in extracellular media of HepaRG cells exposed to both ethanol and TNF-α, the same FC directions were observed as seen with solely ethanol exposure when comparing exposure to unexposed controls. The magnitude of the FC difference was comparable for many metabolites including ChoP and EtOChoP. However, addition of TNF-α resulted in a stronger increase in LPC consumption (+38% relative abundance) and PE secretion (+65% relative abundance). A nearly four times stronger decrease was observed in PAG secretion. In addition, TNF-α co-exposure resulted in increased consumption of inosine and hypoxanthine compared to solely ethanol exposure.

8.3.4. Untargeted metabolomics to elucidate the metabolic signature of HepaRG exposure to ethanol and TNF-α

Features distinctive for exposure to ethanol and TNF-α compared to negative controls were selected by univariate (Mann−Whitney U test or Welch's t-test combined with FC cut-off) and/or multivariate statistical approaches (PLS-DA and RF) (Figure 8.7 and Figure 8.8). They were kept for annotation only when they were selected in both the exposure experiment and the validation experiment. Annotated metabolites with their observed RT, *m/z* value, $^{DT}CCS_{N2}$ value, and additional information are listed in supplementary Table SI-8.9 for intracellular metabolites and Table SI-8.10 for extracellular metabolites.

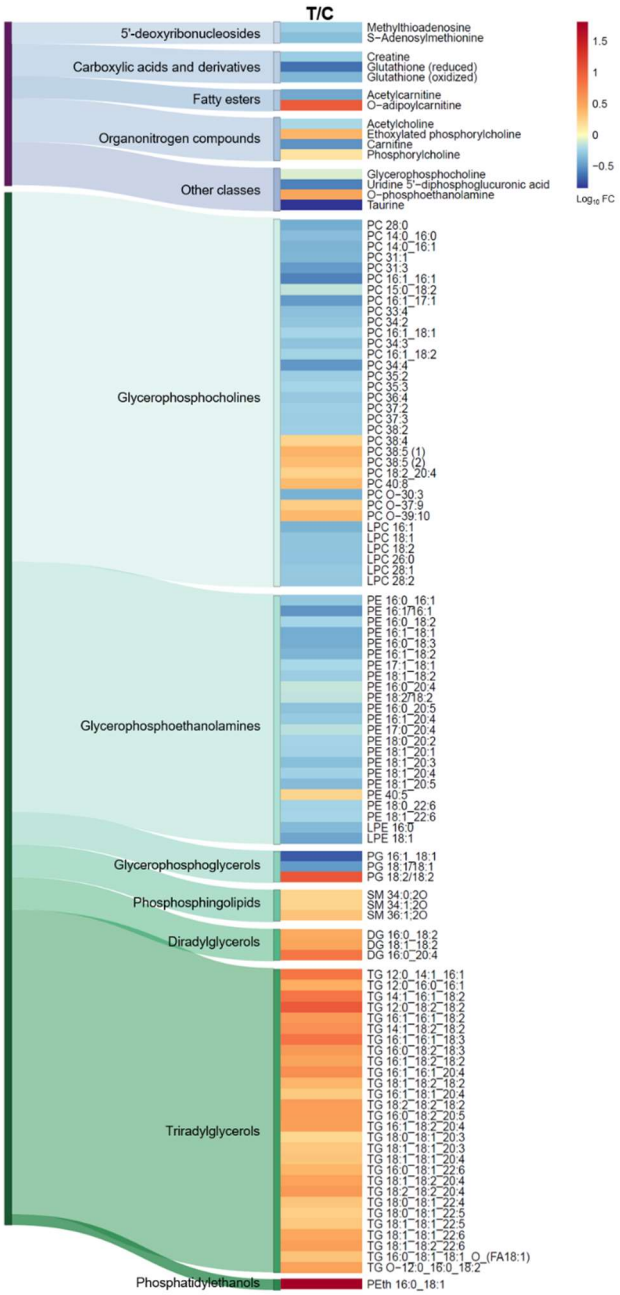

Figure 8.7 Intracellular untargeted metabolomics to elucidate the metabolic signature of HepaRG exposure to ethanol and TNF-α. A Sankey diagram combined with heatmaps was used to show the effect of combined ethanol and TNF-α exposure on the intracellular metabolome of HepaRG cells. Metabolites in the polar fraction of the samples are indicated by a blue-purple Sankey diagram, while a green Sankey diagram represents metabolites originating from the apolar fraction. T/C: Ethanol (IC_{10}) + TNF-α vs. negative control after 24 h of exposure. FC: Fold change.

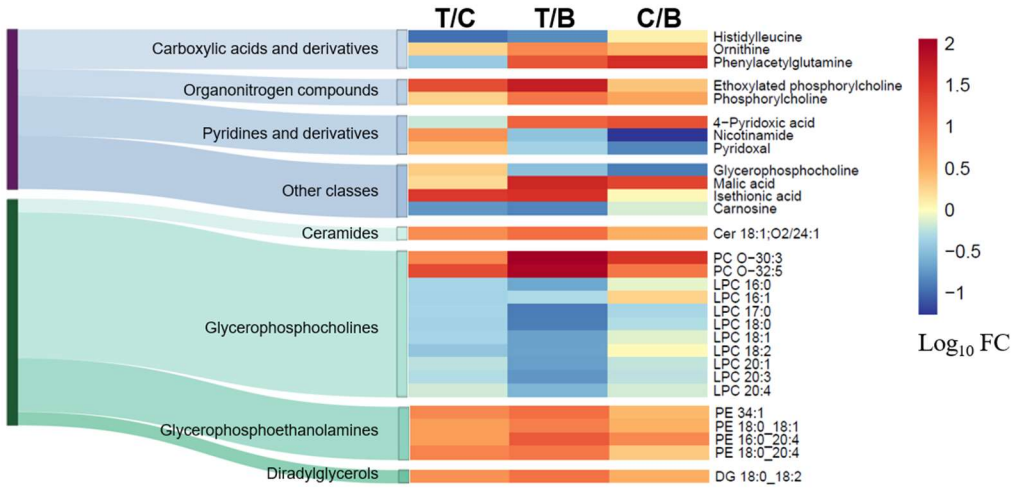

Figure 8.8 Extracellular untargeted metabolomics to elucidate the metabolic signature of HepaRG exposure to ethanol and TNF-α. A Sankey diagram combined with heatmaps was used to show the effect of combined ethanol and TNF-α exposure on the extracellular metabolome of HepaRG cells. Metabolites in the polar fraction of the samples are indicated by a blue-purple Sankey diagram, while a green Sankey diagram represents metabolites originating from the apolar fraction. T/C: Ethanol (IC_{10}) + TNF-α vs. negative control after 24 h of exposure. T/B: Ethanol (IC_{10}) + TNF-α vs. blank media after 24 h. C/B: Negative control vs. blank media after 24 h. FC: Fold change.

8.3.4.1. Metabolic fingerprint of HepaRG cells exposed to ethanol and TNF-α

In total, 110 altered metabolites selected during the statistical workflow could be annotated. Of the 95 lipids, one was annotated as L1, 70 were annotated as L2 and 24 as L3, while of the 15 polar metabolites, 12 were annotated as L1 and three as L2. When comparing annotation software for lipids (supplementary spreadsheet, 8.7.3), 81% could be annotated using Lipostar, 72% using LipidMatch, 59% using the modified LipidBlast library of MS-DIAL (v. 4.9) and 39% using LipidHunter. For polar metabolites, NIST (v. 17) yielded the highest coverage (100%), followed by MassBank (93%), the All Public MS/MS library (v. 15) of MS-DIAL (53%) and MS-Finder (20%).

When comparing HepaRG cells exposed to ethanol and TNF-α with unexposed control cells, LPEs, PEs, LPCs and PCs were downregulated. However, for PCs a trend of upregulation was observed when the number of double bonds increased (i.e., > 4 double bonds). Both DGs and TGs were upregulated. In comparison to solely ethanol exposure (chapter 7), the statistical workflow drastically increased the number of selected upregulated TGs after TNF-α co-exposure. PEth 16:0_18:1, a marker of ethanol exposure, was detected at high intensity in exposed samples. The three selected SMs were upregulated. However, as seen in the suspect screening experiment, SMs can be

down- or upregulated due to exposure to ethanol and TNF-α, depending on the specific species. Two diacylglycerophosphoglycerols were downregulated (i.e., PG 16:1_18:1 and PG 18:1/18:1), while one species was upregulated (i.e., PG 18:2/18:2). Concerning polar metabolites, there was a downregulation of SAM, methylthioadenosine (MTA), creatine, acetylcholine, taurine, GPC, carnitine, acetylcarnitine and uridine 5'-diphosphoglucuronic acid (UDPGA). In addition, glutathione, both in its reduced as oxidized form (GSH and GSSG, respectively), was downregulated. Upregulation was observed for ChoP, EtOChoP, EtoP and O-adipoylcarnitine.

8.3.4.2. Metabolic footprint of HepaRG cells exposed to ethanol and TNF-α

In total, 29 altered metabolites were annotated in the extracellular fraction of HepaRG cells. Of the 17 lipids, one was annotated as L1, 13 as L2 and three as L3, while 9 of the polar metabolites were annotated as L1 and three as L2. Annotation software used for MS/MS matching for each metabolite can be consulted in the supplementary spreadsheet (8.7.3). For the annotated lipids, LipidMatch and Lipostar yielded the highest coverage (both 86%), followed the modified LipidBlast library of MS-DIAL (v. 4.9) (68%) and LipidHunter (11%). For polar metabolites, 83% could be elucidated using MassBank, 75% using NIST (v. 17), 42% using MS-DIAL (v. 4.9) and 8% using MS-Finder.
Exposure to ethanol and TNF-α caused downregulation of LPCs due to increased consumption. PEs, Cer 18:1;O2/24:1, DG 18:0_18:2 and two alkyl ether PC species were upregulated due to increased secretion. Carnosine and histidylleucine were downregulated due to increased consumption, while PAG and 4-pyridoxic acid were downregulated due to decreased secretion. The consumption of nicotinamide, pyridoxal and GPC decreased, causing a positive fold change. Exposure to ethanol and TNF-α stimulated secretion of both ChoP and EtOChoP, ornithine and the acids malic acid and isethionic acid.

8.3.5. Untargeted metabolomics to elucidate the effect of co-exposure to TNF-α in ethanol exposed HepaRG cells

Features distinctive for combined exposure to ethanol and TNF-α compared to exposure to solely ethanol were selected by univariate (Mann−Whitney U test or Welch's t test combined with FC cut-off) and/or multivariate statistical approaches (PLS-DA and RF). They were kept for annotation only when they were selected in both the exposure experiment and the validation experiment. Annotated metabolites with their observed RT, *m/z* value, $^{DT}CCS_{N2}$ value, and additional information are listed in supplementary Table SI-8.11 for intracellular metabolites and Table SI-8.12 for extracellular metabolites. The magnitude of up- or downregulation is shown per metabolite in the form of heatmaps in the supplementary information (Figure SI-8.5-SI-8.6).

When using the statistical workflow described in chapter 6 (6.7) to compare HepaRG cells exposed to ethanol and TNF-α versus solely ethanol, 102 distinctive metabolites could be annotated in the intracellular fraction (Figure SI-8.5). TNF-α co-exposure resulted in a further decrease of LPEs, PEs, LPCs and PCs. As reported during the suspect screening, highly unsaturated PCs showed upregulation during TNF-α co-exposure. This latter was reflected in this untargeted experiment by upregulation of two PC 38:5 species. SM 36:1;2O, two Cers and PG 18:2/18:2 were upregulated, while PG 16:1_18:1 and PG 18:1/18:1 were downregulated. Both DGs and TGs showed stronger upregulation when TNF-α was used as inflammatory trigger. This latter is also reflected in the number of distinctive TGs elucidated when comparing (i) HepaRG cells exposed to ethanol versus negative control cells and (ii) HepaRG cells exposed to ethanol and TNF-α versus solely ethanol. In chapter 7, three upregulated TG species were elucidated when HepaRG cells were exposed to ethanol (IC_{10}) for 24 h, while TNF-α co-exposure resulted in upregulation of 28 distinctive TG species. Interestingly, TG estolides showed a negative fold change during TNF-α co-exposure compared to solely ethanol exposure. Concerning polar metabolites, carnitine, acetylcarnitine, O-octanoylcarnitine, taurine, UDPGA and GSSG were downregulated as well as the nucleosides SAM and MTA. ChoP, GPC, EtoP and pantothenic acid were upregulated.

In the extracellular fraction (Figure SI-8.6), TNF-α co-exposure increased consumption of LPCs and secretion of PEs, Cers and alkyl ether PCs. In addition, carnosine and histidylleucine were more consumed, and pyridoxal less. Secretion of ornithine and malic acid increased, while secretion decreased for isethionic acid, PAG and 4-pyridoxic acid.

8.4. Discussion

Findings, hypotheses and interpretation on the distinctive metabolic profile between 24 h of ethanol exposure and unexposed control cells originating from the suspect screening were discussed in chapter 7. The discussion in this chapter is limited to findings of new metabolites altered due to HepaRG co-exposure to ethanol and TNF-α, and to metabolites that were either stronger up- or downregulated or showed a fold change in opposite direction compared to solely ethanol exposure. An overview of the most important metabolic changes due to ethanol and TNF-α co-exposure in HepaRG cells is presented in Figure 8.9.

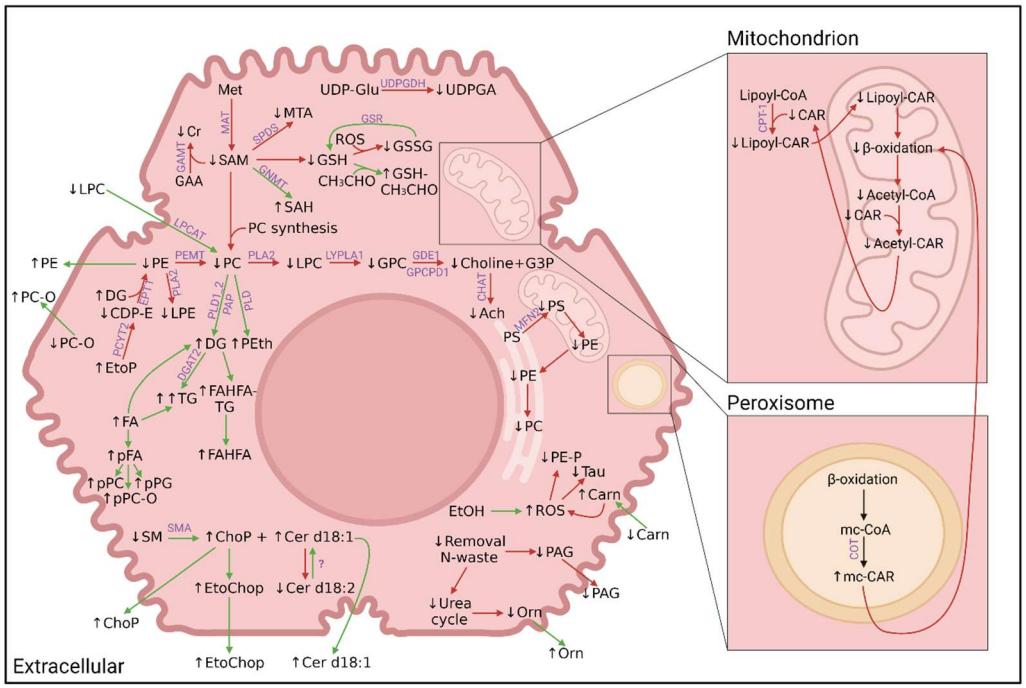

Figure 8.9 Metabolic changes in HepaRG cells after combined ethanol and TNF-α exposure for 24 h. New insights originating from TNF-α co-exposure were added to the figure of chapter 7 on metabolic changes in HepaRG cells after ethanol exposure (Figure 7.7). Intracellular green and red arrows were used to indicate increased and decreased biosynthesis/availability, respectively. Green arrows connecting the intracellular and extracellular compartment indicate increased secretion or uptake, depending on their direction, while red arrows connecting both compartments indicate decreased secretion. Graphical icons in this figure were provided by BioRender, license n. 2641-5211.

Ach: Acetylcholine. CAR: Carnitine. Carn: Carnosine. CDP-E: CDP-ethanolamine. Cer: Ceramide. CH_3CHO: Acetaldehyde. CHAT: Choline O-acetyltransferase. ChoP: Posphorylcholine. CoA: Coenzyme A. COT: Carnitine octanoyltransferase. CPT-1: Carnitine palmitoyltransferase 1. Cr: Creatine. DG: Diglyceride. DGAT2: Diglyceride acyltransferase 2. EPT1: Ethanolaminephosphotransferase 1. EtOChoP: Ethylated phosphorylcholine. EtoP: O-phosphoethanolamine. FA: Fatty acid. FAHFA: Fatty acyl esters of hydroxy fatty acid. G3P: Glycerol 3-phosphate. GAA: Guanidinoacetate. GAMT: Guanidinoacetate methyltransferase. GDE1: Glycerophosphodiester phosphodiesterase 1. GNMT: Glycine N-methyltransferase. GPC: Glycerophosphocholine. GPCPD1: Glycerophosphocholine phosphodiesterase 1. GSH: Glutathione (reduced). GSR: Glutathione reductase. GSSG: Glutathione (oxidized). LPC: Lysophosphatidylcholine. LPCAT: Lysophosphatidylcholine acyltransferase. LPE: Lysophosphatidylethanolamine. LYPLA1: Lysophospholipase 1. MAT: Methionine adenosyltransferase. mc-CAR: medium chain-CAR. mc-CoA: medium chain-CoA. Met: Methionine. MFN2: Mitochondrial protein mitofusin 2. MTA: Methylthioadenosine. Orn: Ornithine. PAG: Phenylacetylglutamine. PAP: Phosphatidate phosphatase. PC:

Phosphatidylcholine. PC-O: Alkyl ether PC. PCYT2: Phosphoethanolamine cytidylyltransferase. PE: Phosphatidylethanolamine. PEMT: Phosphatidylethanolamine-N-methyltransferase. PE-P: Alkenyl ether PE. PEth: Phosphatidylethanol. pFA: Polyunsaturated FA. PLA2: Phospholipase A2. PLD: Phospholipase D. PLD1_2: Phospholipase D1/2. pPC: Polyunsaturated PC. pPC-O: Polyunsaturated PC-O. pPG: Polyunsaturated phosphatidylglycerol. PS: Phosphatidylserine. ROS: Reactive oxygen species. SAH: S-adenosyl-homocysteine. SAM: S-adenosylmethionine. SM: Sphingomyelin. SMA: Sphingomyelinase. SPDS: Spermidine synthase. Tau: Taurine. TG: Triglyceride. UDPGA: Uridine 5'-diphosphoglucuronic acid. UDPGDH: UDP-glucose dehydrogenase. UDP-Glu: Uridine diphosphate glucose.

8.4.1. Diglycerides and triglycerides

As seen during both suspect screening and untargeted analyses, the magnitude of intracellular upregulation of DG and TG species increased during TNF-α co-exposure. In addition, the number of distinctive TG species increased significantly between solely ethanol exposure and combined exposure to ethanol and TNF-α, suggesting an important role of inflammation during steatosis progression. These findings are concordant with a significant increase of TG species in TNF-α-infused mice and rats (Raina et al., 1995; Tacer et al., 2007). In addition, ethanol can increase the susceptibility to TNF-α by increasing the levels of tumor necrosis factor-alpha receptor-1 (TNF-R1) (Rodriguez et al., 2004). TNF-α stimulated hepatic lipogenesis has been observed in both human and murine studies (Popa et al., 2007). It is believed that TNF-α induces *de novo* fatty acid synthesis in the liver, resulting in increased DG and TG synthesis, without increasing the enzymes involved in esterification with glycerol (Popa et al., 2007). Several mechanisms would feed *de novo* fatty acid synthesis, such as elevation of fatty acid synthetase (FAS) (Grunfeld et al., 1988) and increased expression and maturation of sterol regulatory element-binding protein-1c (SREBP-1c), a transcription factor regulating gene expression related to fatty acid metabolism (Endo et al., 2007; Lawler et al., 1998). TNF-α can induce insulin resistance through serine phosphorylation of insulin receptor substrate-1 (IRS-1) (Kanety et al., 1995; Popa et al., 2007) and insulin can activate the promotor of SREBP-1c (Dif et al., 2006). In addition, as seen in mice models and *in vitro* experiments, exposure to ethanol can induce lipin-1 (Hu et al., 2012), an important enzyme in TG biosynthesis, and DG acyltransferase 2 (DGAT2), which can result in shift towards TG synthesis through initial conversion of PCs to DGs (Z. Wang et al., 2010). Among the upregulated TG species, TG estolides, categorized as fatty acyl esters of hydroxy fatty acid (FAHFA)-containing triacylglycerols (FAHFA-TGs) were found. Interestingly, these TG estolides were the only TG species which were downregulated during exposure to ethanol and TNF-α compared to solely ethanol exposure. TG estolides are rather less investigated species of TG and to the authors knowledge, its presence in human hepatocytes is unreported. Their presence in mice

livers was previously reported (Saponara et al., 2022). Example MS/MS spectra of the FAHFA-TGs found in the HepaRG samples were added to the SI (Figure SI-8.7-SI-8.8). In 2015, TG estolides were reported for the first time in mammals, after GC-MS analyses of paracloacal glands of possums (McLean et al., 2015). Branched-chain FAHFAs have shown anti-diabetic and anti-inflammatory properties (Yore et al., 2014) and their biosynthesis can be augmented by oxidative stress (Kuda et al., 2018). These FAHFAs can acylate the free hydroxyl group of DGs to form a storage pool of FAHFAs under the form of FAHFA-TGs (Tan et al., 2019). The decrease of TG estolides during co-exposure of ethanol and TNF-α could be explained by a release of FAHFAs by lipolytic enzymes in order for the FAHFAs to exert their anti-inflammatory properties.

8.4.2. Phosphatidylcholines, lysophosphatidylcholines, phosphatidylglycerols, S-adenosylmethionine, and methylthioadenosine

TNF-α co-exposure decreased intracellular PCs stronger than solely ethanol exposure, concordant with the findings of Männistö *et al.* who saw a decrease of hepatic PCs in simple steatosis, which decreased further during non-alcoholic steatohepatitis (NASH) in humans (Männistö et al., 2019). The authors suggested a mechanism of altered expression of glycine N-methyltransferase (GNMT) for the hepatic decrease of PCs in NASH. GNMT catalyzes the conversion of SAM to S-adenosyl-homocysteine (SAH), which is an inhibitor of phosphatidylethanolamine-N-methyltransferase (PEMT) (Männistö et al., 2019). PEMT, which can also be inhibited by ethanol (Lieber et al., 1994), converts PEs to PCs. PEMT inhibition by ethanol and increased conversion of SAM to SAH, could reduce hepatic PC levels. Decrease of hepatic SAM can be explained by ethanol-induced inhibition of methionine synthase and methionine adenosyltransferase (Stickel & Seitz, 2003). Further decrease induced by TNF-α co-exposure could support the hypothesis of altered GNMT expression. In addition, downregulation of SAM can explain the intracellular decrease of methylthioadenosine (MTA), as it acts as a precursor during the polyamine biosynthetic pathway (Avila et al., 2004). It is believed that MTA has hepatoprotective effects and a role during the regeneration after partial hepatectomy, a process triggered by cytokines, such as TNF-α (Avila et al., 2004).

Next to downregulation of hepatic PCs, a decrease in intracellular LPCs was observed, as well as an increased consumption of extracellular LPCs during TNF-α co-exposure. In line with these results, Israelsen *et al.* observed a decrease in LPCs in human hepatic venous blood after ethanol intoxication in healthy volunteers and ALD patients (Israelsen et al., 2021). The authors hypothesized that the reduction of circulating LPCs could be caused by an increased hepatic uptake, which was confirmed both in the present study and during HepaRG exposure to solely ethanol (chapter 7). In addition,

Koelmel *et al.* observed a decrease of both hepatic and plasma PC and LPC levels in ethanol-fed mice, with a stronger decrease after prolonged consumption of ethanol (Koelmel, Tan, et al., 2021). Interestingly, Puri *et al.* observed a decrease of hepatic LPCs in NAFLD, while they were increased in NASH (Puri et al., 2007). This latter indicates a potential distinctive hepatic LPC metabolism in NASH versus ASH. As hypothesized in chapter 7, intracellular LPCs could be downregulated due to reduced PC catabolism through phospholipase A2, while increased hepatic uptake of LPCs could be used to fuel formation of the PC pool (LPCAT) and/or GPC (LYPLA1). The stronger decrease of hepatic PCs that was observed during TNF-α co-exposure, might explain the increased hepatic uptake of LPCs as a compensating mechanism.

The decrease of intracellular alkyl ether PCs is consistent with the finding of increased extracellular secretion. Meikle *et al.* reported an increased content of alkyl ether PCs in serum of patients suffering from alcoholic cirrhosis (Meikle et al., 2015). As the understanding of the function of ether lipids and their role in pathophysiology is still largely unknown (Dean & Lodhi, 2018), the mechanism or function of intracellular decrease and extracellular increase still remains unclear.

Upregulation of polyunsaturated PCs was only seen during TNF-α co-exposure or during prolonged ethanol exposure (chapter 7). Ethanol exposure can induce a shift of saturated to unsaturated fatty acids as observed in several studies (Clugston et al., 2017), e.g. in ethanol-fed rodents (Jeon & Carr, 2020). On the other hand, TNF-α infusion in rats increased production of hepatic polyunsaturated fatty acids (PUFAs) (Raina et al., 1995). These PUFAs can be incorporated in DGs and subsequently in PCs through the cytidine diphosphocholine (CDP-choline) pathway (Jeon & Carr, 2020). Although the number of elucidated distinctive PGs was rather low (Figure 8.7), there seemed to be a trend for downregulation of species with a lower level of unsaturation (i.e., PG 16:1_18:1 and PG 18:1/18:1) and upregulation of species with a higher level of unsaturation (i.e., PG 18:2/18:2). Puri *et al.* saw an overall increase of PGs after ethanol consumption in mice. However, when looking at the species level, some PGs were upregulated, while others were downregulated (Puri et al., 2016). Although no correlation between the degree of unsaturation and upregulation could be observed, tendency towards upregulation of more unsaturated species was noticeable, especially in lean mice. In analogy to the results in this study, Puri *et al.* reported PG 18:2/18:2 as the species which was strongest upregulated (Puri et al., 2016). While the exact mechanism remains unclear, an increased biosynthesis of PUFAs could be a contributing factor.

8.4.3. Phosphatidylethanolamines, lysophosphatidylethanolamines, and O-phosphoethanolamine

Although PEMT inhibition reduces consumption of hepatic PEs, an intracellular decrease was observed, which was stronger during TNF-α co-exposure. This finding is concordant with the extracellular metabolome, where PEs were upregulated due to increased secretion. In addition, impaired activity of phosphoethanolamine cytidylyltransferase (PCYT2) in the CDP-ethanolamine pathway might explain the decreased content of PEs, as impairment would contribute to accumulation of hepatic DGs and O-phosphoethanolamine (EtoP) (Calzada et al., 2016), which were more upregulated after TNF-α co-exposure. Increase in EtoP suggests either activation of PE metabolism or impairment of PE incorporation in membranes (Beatriz et al., 2011). In addition, development of a NAFLD/NASH phenotype was observed in mice after knocking out the mitochondrial protein mitofusin 2 (mfn2) (Hernández-Alvarez et al., 2019). Mfn2 is a mitochondrial membrane protein, connecting membranes of the endoplasmatic reticulum (ER) to mitochondria. The close apposition between the ER and the mitochondria allows transport of phosphatidylserines (PSs) from the ER to mitochondria, where they can be converted into PEs. These PEs can be transported back to the ER for conversion into PCs. Mfn2 facilitates the PS transport (Ventura et al., 2022). Compared to simple steatosis, significant downregulation of mfn2, leading to decrease of hepatic PEs and PCs, has been observed in patients with NASH (Hernández-Alvarez et al., 2019). Downregulation of intracellular LPE levels can be a direct effect of PE depletion, as LPEs are formed by deacylation of PEs in a reaction catalyzed by phospholipase A2 (PLA2). The decrease of hepatic LPEs is consistent with the findings of Koelmel *et al.* in the livers of ethanol-fed mice (Koelmel, Tan, et al., 2021).

8.4.4. Sphingomyelins, ceramides, and phosphorylcholine

Although some SM species were upregulated in exposed HepaRG cells, the overall effect of downregulation of SM species was clearly observed during the suspect screening. This latter downregulation affects both cells exposed to ethanol and combined exposure to ethanol and TNF-α. As reported by Koelmel *et al.*, the fold change direction can be dependent on the length and degree of saturation of the fatty acyl constituents (Koelmel, Tan, et al., 2021). Although these latter findings could explain the observed discrepancies in up- and downregulation of SM species, they could neither be confirmed nor denied during this study as confident annotation of SM species was limited to their bulk structures.

As seen during the suspect screening, co-exposure to TNF-α had only small effects on SM species with overall a slightly stronger downregulation. As previously reported in chapter 7, decrease of hepatic SMs is in accordance with downregulation of SMs in

human serum of heavy drinkers, which could be due to increased hydrolysis of SMs into Cers and phosphorylcholine (ChoP) by sphingomyelinase (SMA) (Jaremek et al., 2013). Increased SM hydrolysis was supported by elevated extracellular levels of Cers (d18:1) and ChoP due to increased secretion. The levels of Cer species (both d18:1 and d18:2) and ChoP were slightly higher during TNF-α co-exposure compared to solely ethanol exposure, both intra- and extracellular. Ethylated phosphorylcholine (EtOChoP), which was previously identified as a new biomarker of ethanol exposure (Iturrospe et al., 2022), was found both intra- and extracellular. This compound was present after exposure to ethanol and ethanol combined with TNF-α, and remained absent in unexposed control samples. EtOChoP could be formed in a reaction using both ChoP and ethanol.

8.4.5. Ornithine and phenylacetylglutamine

Concerning the extracellular metabolome, an increased secretion of ornithine was observed after exposure to ethanol and TNF-α. This increase is consistent with the finding of Shi *et al.* who observed increased plasma levels of ornithine in ethanol-fed rats (C. Shi et al., 2020). As the hepatic content of ornithine in these rats decreased, the authors hypothesized that the changes in ornithine were due to an impaired urea cycle (C. Shi et al., 2020). During this cycle, which primarily occurs in the liver, toxic ammonia is converted to urea. This latter impairment was confirmed during *in vitro* studies and in human patients suffering from alcoholic liver disease (Aagaard et al., 2004; Glavind et al., 2016; Holmuhamedov et al., 2012). In addition to urea, phenylacetylglutamine (PAG) has been proposed as a vehicle for waste nitrogen excretion (Brusilow, 1991). The hypothesis of an impaired urea cycle, in addition to downregulated intracellular PAG and decreased hepatic PAG secretion, indicate an impaired processing of nitrogen waste by the liver cells.

8.4.6. Reduced and oxidized glutathione

During HepaRG exposure to ethanol and TNF-α, an intracellular decrease was observed of both reduced and oxidized glutathione (GSH and GSSG, respectively). Viña *et al.* found that hepatic GSH depletion is not a direct effect of ethanol, but of its oxidized biotransformation product acetaldehyde, which could form adducts with GSH (Vina et al., 1980). In addition, reduced hepatic synthesis of SAM results in decreased GSH levels (Cederbaum, 2010). Next to decreased GSH levels, mitochondrial uptake of GSH, is reduced in response to ethanol exposure, increasing susceptibility to oxidative stress produced by reactive oxygen species (ROS) (Fernández-Checa et al., 1997). This reduced uptake was determined as an important sensitizing factor to TNF-α toxicity (Fernández-Checa et al., 1997). As GSH is oxidized to GSSG during the neutralization of ROS

(Fernández-Checa et al., 1997), a decrease of GSSG can be expected since its precursor GSH was depleted. However, ROS are generated during ethanol exposure (Cahill et al., 2002), which would lead to a hypothesis of increased hepatic GSSG. Unlike the apparent consensus on downregulation of GSH in literature, there seem to be differences in reported GSSG levels as they were reported to be increased (X. Sun et al., 2021), decreased (Robin et al., 2005) or unchanged (Callans et al., 1987; Jewell et al., 1986). Important to mention is that ethanol exposure can have a different effect on cytosolic and mitochondrial GSSG concentrations (Robin et al., 2005). Based on rodent studies, it is suggested that during ethanol exposure the rate of conversion of GSSG to GSH would be increased due to higher activity of glutathione reductase (GSR) (Bailey et al., 2001; Callans et al., 1987). This latter highlights the dynamic character of the metabolome and therefore it would be possible that the rate of oxidation of GSH to GSSG may be greater than reflected by snapshot GSSG levels.

8.4.7. Taurine and carnosine

The stronger decrease of intracellular taurine after TNF-α co-exposure could be explained by an increased production of ROS as was seen in mitochondria of murine hepatocytes and the human cell line Huh-7 (Kastl et al., 2014). Taurine administration can increase hepatic antioxidant capacity and reduce lipid peroxidation in ethanol-fed rats and primary rat hepatocytes cultured with ethanol (G. Wu et al., 2018). In addition, an increased consumption of carnosine from the extracellular environment was observed. Carnosine can act as an antioxidant through the mechanism of chelating divalent metal ions, possessing superoxide dismutase (SOD)-like activity and scavenging of ROS and free radicals (Guney et al., 2006). Carnosine has shown hepatoprotective effects in ethanol-fed rats by ameliorating toxic effects of ethanol such as decrease of GSH levels, increase of alanine aminotransferase (ALT) and aspartate aminotransferase (AST) (Baykara et al., 2012).

8.4.8. Uridine 5'-diphosphoglucuronic acid

The intracellular decrease of uridine 5'-diphosphoglucuronic acid (UDPGA) could reflect a decreased biotransformation capacity after ethanol and TNF-α exposure. UDPGA is used during phase II biotransformation reactions for glucuronidation of endogenous compounds, xenobiotics and toxic substances in order to turn them into harmless or easily excreted metabolites (Sanchez-Dominguez et al., 2018). As seen in rat liver and primary rat hepatocytes, ethanol exposure can increase UDP-glucuronosyltransferases (UGTs), which could explain reduced levels of UDPGA (Y. Q. Li et al., 2000). However, during ethanol and TNF-α co-exposure, a stronger decrease of UDPGA was observed and TNF-α would rather downregulate hepatic UGTs (T. A. Richardson et al., 2006). This

latter would suggest a decreased production of UDPGA. UDP-glucose dehydrogenase (UDPGDH) is the enzyme responsible for catalyzing the conversion of UDP-glucose to UDPGA. During ethanol exposure, an intracellular inhibition of UDPGDH has been observed in rat hepatocytes (Aw & Jones, 1983). The stronger decrease of UDPGA after TNF-α co-exposure could indicate an additive or synergistic effect on UDPGDH inhibition.

8.5. Conclusions

Compared to solely ethanol-exposed HepaRG cells, additional exposure to TNF-α resulted in a stronger downregulation of PCs and PEs and a stronger upregulation of DGs and TGs, indicating increased hepatotoxicity. The most upregulated intracellular metabolites included TG 12:0_18:2_18:2, TG 16:1_16:1_18:3 and TG 18:1_18:2_22:6, while the most downregulated metabolites included PC 34:4, PC 16:1/16:1 and uridine 5'-diphosphoglucuronic acid. Extracellular metabolites which were most impacted included the upregulated PE 34:1 and downregulated LPC 18:2. Comparing non-exposed control cells to combined exposure of ethanol and TNF-α, the strongest impact on intracellular metabolites was observed for PEth 16:0_18:1, TG 12:0_18:2_18:2 and O-adipoylcarnitine, which were among the most upregulated. Taurine and glutathione were among the most downregulated. Extracellularly, a strong upregulation was observed for ethylated phosphorylcholine.

FAHFA-TGs were reported for the first time in human hepatocytes. The decrease of FAHFA-TGs during TNF-α co-exposure could be explained by a release of FAHFAs by lipolytic enzymes to exert their anti-inflammatory properties. Polyunsaturated PCs, for which upregulation was observed after prolonged ethanol exposure, were upregulated twice as fast due to co-exposure to TNF-α. Downregulation of SAM showed to play an important role in ethanol-induced hepatotoxicity as its downregulation had multiple effects on for example biosynthesis of PC, MTA and GSH. Metabolic finger- and footprinting of LPCs highlighted a potential distinctive hepatic LPC metabolism in NASH versus ASH. As observed during our previous study exposing HepaRG cells to ethanol, ethylated phosphorylcholine was found both intra- and extracellularly. This latter metabolite was considered as a new biomarker of ethanol exposure based on its absence in control samples and its structure, which could be generated from a combination of ethanol and phosphorylcholine, the hydrolysis product of sphingomyelins.

8.6. Data availability

Raw datafiles are available through the MassIVE repository (https://massive.ucsd.edu/ProteoSAFe/) with the data set identifier MSV000090773.

8.7. Supplementary information

8.7.1. Data processing

Median relative standard deviation (mRSD) of the intensity of LC-MS features for each analytical platform and sample group of the intracellular and extracellular HepaRG fractions are given in Table SI-8.1 and SI-8.2. mRSD values were calculated after deisotoping and blank subtraction.

Table SI-8.1 Median relative standard deviation (mRSD) of the intensity of LC-MS features of the intracellular HepaRG fraction for each sample group and analytical platform. B1: Batch 1. B2: Batch 2. LIP+: Lipidomics in positive electrospray ionization mode. LIP-: Lipidomics in negative electrospray ionization mode. MET+: Metabolomics in positive electrospray ionization mode. MET-: Metabolomics in negative electrospray ionization mode.

	QC	Control	Ethanol	Ethanol + TNF-α
B1-LIP+	9.8	14.0	12.8	18.8
B2-LIP+	11.6	13.4	14.7	17.2
B1-LIP-	11.3	19.5	14.4	25.6
B2-LIP-	14.3	19.2	17.5	22.9
B1-MET+	17.1	25.2	26.6	30.2
B2-MET+	12.2	18.8	17.7	26.6
B1-MET-	16.5	18.5	19.2	23.8
B2-MET-	24.3	32.7	27.1	31.6

Table SI-8.2 Median relative standard deviation (mRSD) of the intensity of LC-MS features of the extracellular HepaRG fraction for each sample group and analytical platform. B1: Batch 1. B2: Batch 2. LIP+: Lipidomics in positive electrospray ionization mode. LIP-: Lipidomics in negative electrospray ionization mode. MET+: Metabolomics in positive electrospray ionization mode. MET-: Metabolomics in negative electrospray ionization mode.

	QC	Control	Ethanol	Ethanol + TNF-α
B1-LIP+	11.7	18.3	20.1	22.6
B2-LIP+	19.2	26.8	28.1	28.6
B1-LIP-	13.9	23.4	24.9	26.4
B2-LIP-	16.7	26.2	24.7	28.7
B1-MET+	12.9	16.1	18.8	17.2
B2-MET+	10.8	14.7	14.9	15.2
B1-MET-	15.6	17.8	17.2	17.2
B2-MET-	19.9	23.2	22.5	22.6

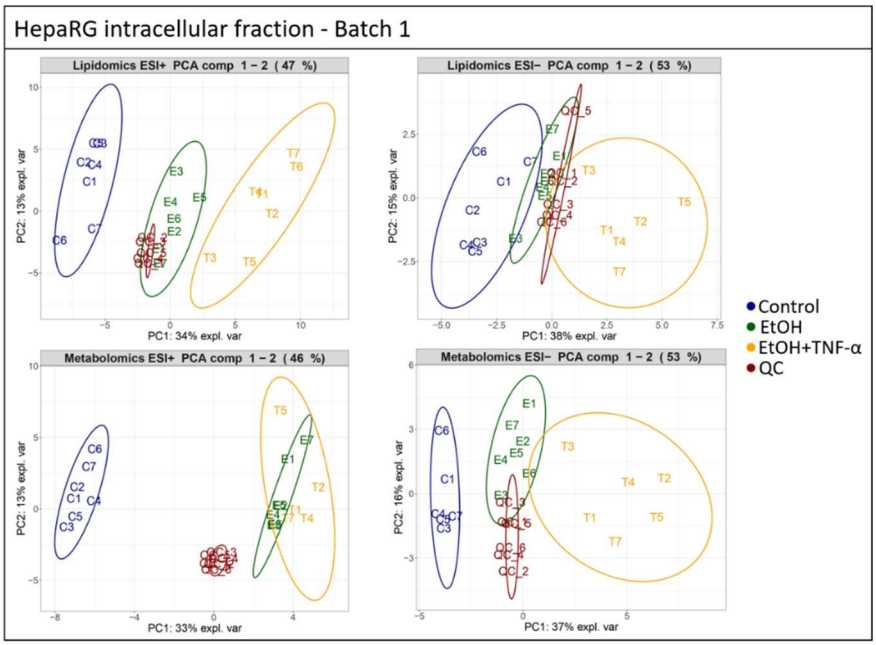

Figure SI-8.1 Principal component analysis plots of the intracellular fraction of HepaRG cells of batch 1 after 24 h exposure to ethanol and TNF-α. ESI+ and ESI- refer to electrospray ionization in positive and negative modes, respectively.

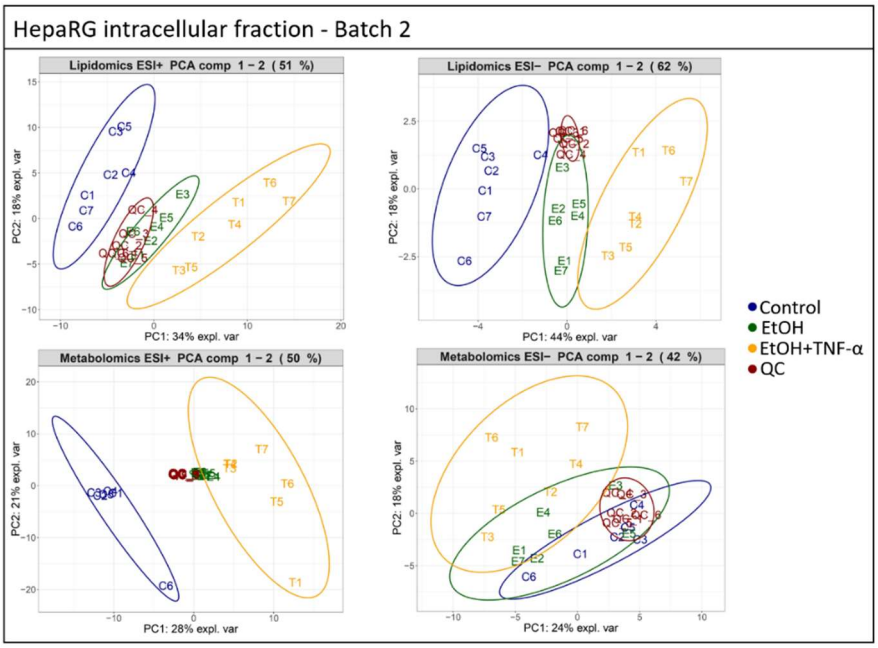

Figure SI-8.2 Principal component analysis plots of the intracellular fraction of HepaRG cells of batch 2 after 24 h exposure to ethanol and TNF-α. ESI+ and ESI- refer to electrospray ionization in positive and negative modes, respectively.

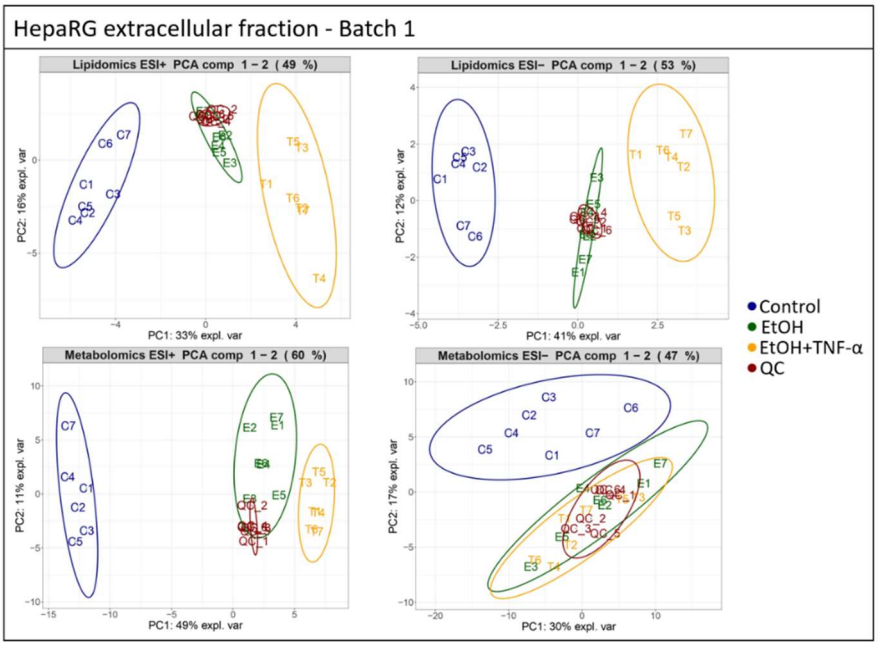

Figure SI-8.3 Principal component analysis plots of the extracellular fraction of HepaRG cells of batch 1 after 24 h exposure to ethanol and TNF-α. ESI+ and ESI- refer to electrospray ionization in positive and negative modes, respectively.

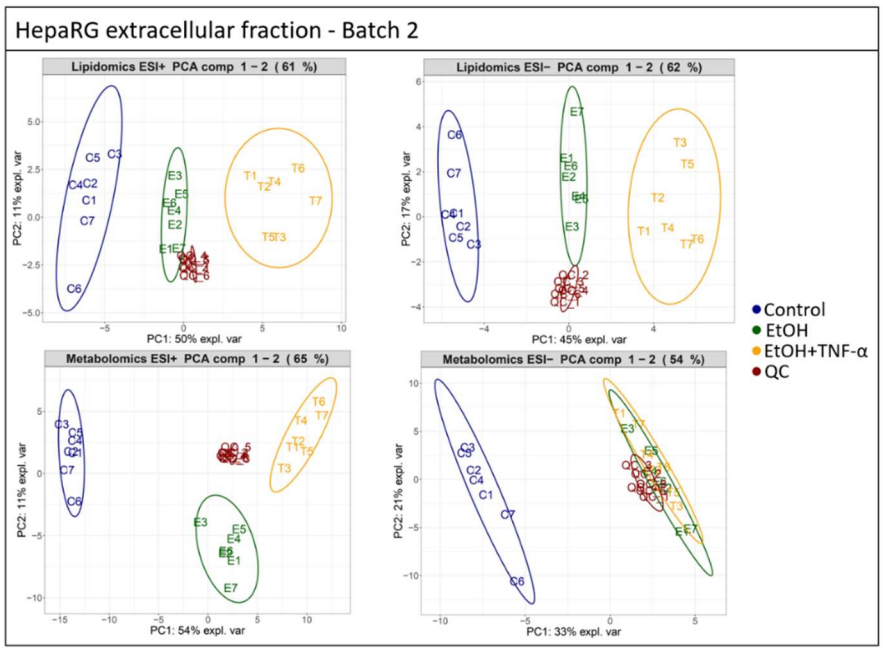

Figure SI-8.4 Principal component analysis plots of the extracellular fraction of HepaRG cells of batch 2 after 24 h exposure to ethanol and TNF-α. ESI+ and ESI- refer to electrospray ionization in positive and negative modes, respectively.

Table SI-8.3-SI-8.6 show the evaluation parameters of the multivariate statistical models for intracellular and extracellular fractions after exposure to ethanol and/or TNF-α. R^2, Q^2, R^2PERM and Q^2PERM (calculated after 1000 random permutations) were selected for evaluation of the PLS-DA model, while the area under the curve (AUC) was selected for evaluation of the random forest classification model.

Table SI-8.3 Evaluation parameters of multivariate statistical models for the intracellular fraction comparing exposure to ethanol (IC_{10}) and TNF-α to unexposed controls. B1: Batch 1. B2: Batch 2. LIP+: Lipidomics in positive electrospray ionization mode. LIP-: Lipidomics in negative electrospray ionization mode. MET+: Metabolomics in positive electrospray ionization mode. MET-: Metabolomics in negative electrospray ionization mode.

	R^2	Q^2	R^2_{PERM}	Q^2_{PERM}	AUC
B1-LIP+	1.00	0.98	0.00	0.00	1.00
B2-LIP+	1.00	0.98	0.00	0.00	1.00
B1-LIP-	0.99	0.94	0.00	0.00	1.00
B2-LIP-	1.00	0.97	0.00	0.00	1.00
B1-MET+	0.99	0.93	0.00	0.00	1.00
B2-MET+	0.99	0.94	0.00	0.00	1.00
B1-MET-	0.99	0.95	0.00	0.00	1.00
B2-MET-	1.00	0.92	0.00	0.00	1.00

Table SI-8.4 Evaluation parameters of multivariate statistical models for the extracellular fraction comparing exposure to ethanol (IC_{10}) and TNF-α to unexposed controls. B1: Batch 1. B2: Batch 2. LIP+: Lipidomics in positive electrospray ionization mode. LIP-: Lipidomics in negative electrospray ionization mode. MET+: Metabolomics in positive electrospray ionization mode. MET-: Metabolomics in negative electrospray ionization mode.

	R^2	Q^2	R^2_{PERM}	Q^2_{PERM}	AUC
B1-LIP+	0.98	0.96	0.00	0.00	1.00
B2-LIP+	0.99	0.97	0.00	0.00	1.00
B1-LIP-	1.00	0.97	0.00	0.00	1.00
B2-LIP-	0.98	0.97	0.00	0.00	1.00
B1-MET+	0.99	0.98	0.00	0.00	1.00
B2-MET+	1.00	0.99	0.00	0.00	1.00
B1-MET-	0.98	0.84	0.00	0.00	1.00
B2-MET-	0.95	0.90	0.00	0.00	1.00

Table SI-8.5 Evaluation parameters of multivariate statistical models for the intracellular fraction comparing exposure to ethanol (IC_{10}) and TNF-α to exposure to solely ethanol (IC_{10}). B1: Batch 1. B2: Batch 2. LIP+: Lipidomics in positive electrospray ionization mode. LIP-: Lipidomics in negative electrospray ionization mode. MET+: Metabolomics in positive electrospray ionization mode. MET-: Metabolomics in negative electrospray ionization mode.

	R^2	Q^2	R^2_{PERM}	Q^2_{PERM}	AUC
B1-LIP+	0.99	0.78	0.00	0.00	1.00
B2-LIP+	0.99	0.78	0.00	0.00	1.00
B1-LIP-	0.97	0.89	0.02	0.00	1.00
B2-LIP-	0.99	0.86	0.00	0.00	1.00
B1-MET+	0.99	0.86	0.01	0.00	1.00
B2-MET+	0.97	0.82	0.00	0.00	1.00
B1-MET-	0.99	0.88	0.00	0.00	1.00
B2-MET-	0.71	0.49	0.03	0.01	0.98

Table SI-8.6 Evaluation parameters of multivariate statistical models for the extracellular fraction comparing exposure to ethanol (IC_{10}) and TNF-α to exposure to solely ethanol (IC_{10}). B1: Batch 1. B2: Batch 2. LIP+: Lipidomics in positive electrospray ionization mode. LIP-: Lipidomics in negative electrospray ionization mode. MET+: Metabolomics in positive electrospray ionization mode. MET-: Metabolomics in negative electrospray ionization mode.

	R^2	Q^2	R^2_{PERM}	Q^2_{PERM}	AUC
B1-LIP+	1.00	0.93	0.00	0.00	1.00
B2-LIP+	0.97	0.84	0.00	0.00	1.00
B1-LIP-	0.97	0.84	0.01	0.00	1.00
B2-LIP-	1.00	0.95	0.01	0.00	1.00
B1-MET+	1.00	0.94	0.00	0.00	0.99
B2-MET+	1.00	0.97	0.00	0.00	1.00
B1-MET-	0.99	0.78	0.16	0.01	0.89
B2-MET-	0.99	0.65	0.13	0.01	0.99

8.7.2. Annotated metabolites

8.7.2.1. Suspect screening of HepaRG cells exposed to ethanol with and without co-exposure to TNF-α

Information concerning annotated metabolites originating from the suspect screening of HepaRG cells exposed to ethanol with and without co-exposure to TNF-α can be found in Table SI-8.7 and Table SI-8.8 of the electronic supplementary information 1 (SI-1) of chapter 8, which is available on the link below.

https://www.dropbox.com/sh/bvxln6vaf00q3hk/AABt5gt5XbDgsROqKY4w7Znla?dl=1

In these SI tables, annotated metabolites are listed together with their metabolic class, formula, ionization species, *m/z*, RT, $^{DT}CCS_{N2}$, annotation level, mass error, CCS error and fold change direction comparing (i) ethanol exposure versus negative controls, (ii)

ethanol + TNF-α exposure versus negative controls, and (iii) ethanol + TNF-α exposure versus solely ethanol exposure.

8.7.2.2. Metabolic alterations resolved by untargeted analyses in HepaRG cells exposed to ethanol and TNF-α compared to unexposed controls

Information concerning annotated metabolites originating from the untargeted analyses comparing HepaRG cells exposed to ethanol and TNF-α with unexposed controls can be found in Table SI-8.9 and Table SI-8.10 of the electronic supplementary information 1 (SI-1) of chapter 8, which is available on the link below.
https://www.dropbox.com/sh/bvxln6vaf00q3hk/AABt5gt5XbDgsROqKY4w7Znla?dl=1

8.7.2.3. Metabolic alterations resolved by untargeted analyses in HepaRG cells exposed to ethanol and TNF-α compared to solely ethanol

Information concerning annotated metabolites originating from the untargeted analyses comparing HepaRG cells exposed to ethanol and TNF-α with cells exposed to solely ethanol can be found in Table SI-8.11 and Table SI-8.12 of the electronic supplementary information 1 (SI-1) of chapter 8, which is available on the link below.
https://www.dropbox.com/sh/bvxln6vaf00q3hk/AABt5gt5XbDgsROqKY4w7Znla?dl=1
In addition, in Figure SI-8.5 and Figure SI-8.6, heatmaps were used to represent the metabolic alterations in the intracellular and extracellular fractions, respectively.

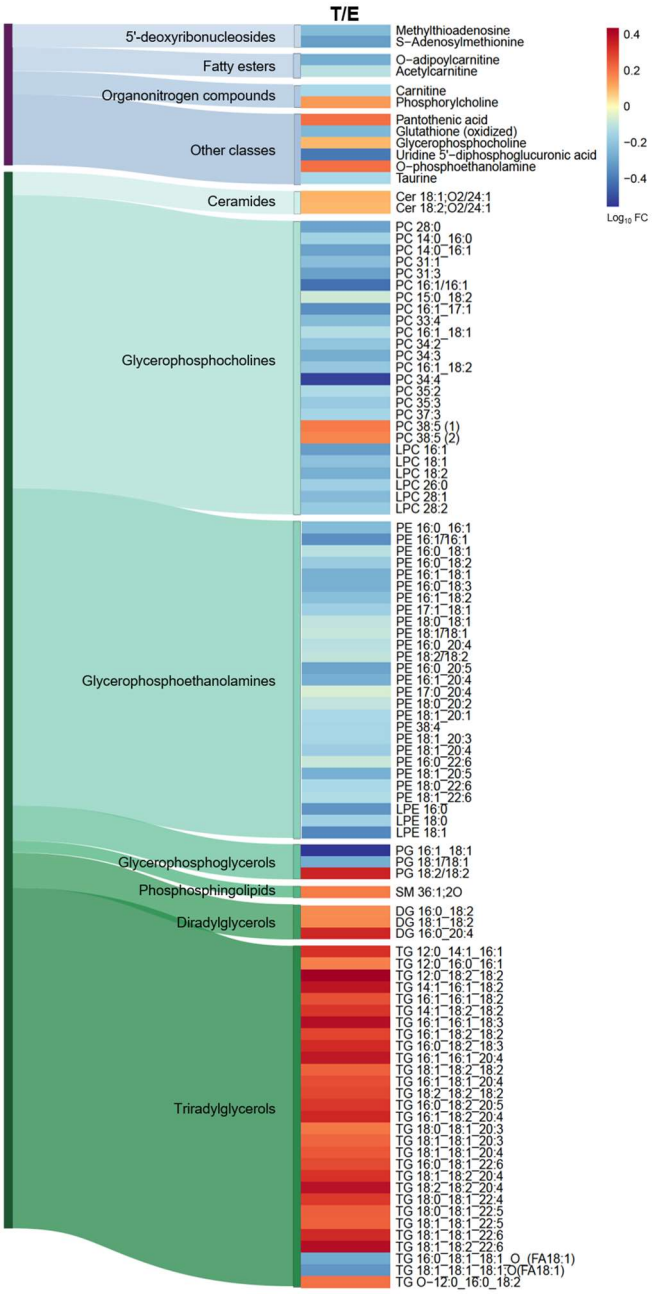

Figure SI-8.5 Intracellular untargeted metabolomics to elucidate the effect of co-exposure to TNF-α in ethanol exposed HepaRG cells. A Sankey diagram combined with heatmaps was used to show the effect of combined ethanol and TNF-α exposure vs solely ethanol exposure on the intracellular metabolome of HepaRG cells. Metabolites in the polar fraction of the samples are indicated by a blue-purple Sankey diagram, while a green Sankey diagram represents metabolites originating from the apolar fraction. T/E: Ethanol (IC_{10}) + TNF-α vs ethanol (IC_{10}) after 24 h of exposure. FC: Fold change.

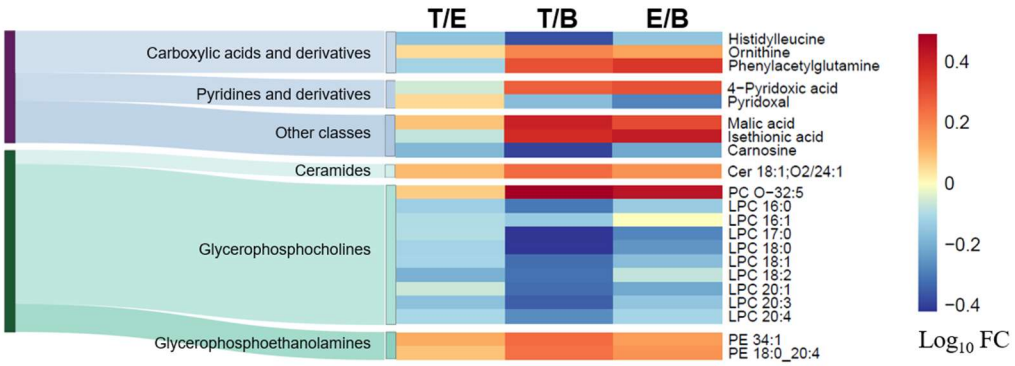

Figure SI-8.6 Extracellular untargeted metabolomics to elucidate the effect of co-exposure to TNF-α in ethanol exposed HepaRG cells. A Sankey diagram combined with heatmaps was used to show the effect of combined ethanol and TNF-α exposure vs solely ethanol exposure on the extracellular metabolome of HepaRG cells. Metabolites in the polar fraction of the samples are indicated by a blue-purple Sankey diagram, while a green Sankey diagram represents metabolites originating from the apolar fraction. T/E: Ethanol (IC_{10}) + TNF-α vs ethanol (IC_{10}) after 24 h of exposure. T/B: Ethanol (IC_{10}) + TNF-α vs blank media after 24 h. E/B: Ethanol (IC_{10}) vs blank media after 24 h. FC: Fold change.

8.7.3. Software and libraries used to annotate metabolites

A supplementary spreadsheet containing information on the software and libraries used per annotated metabolite can be consulted in electronic supplementary information 2 (SI-2) of chapter 8, which is available on the link below.

https://www.dropbox.com/sh/bvxln6vaf00q3hk/AABt5gt5XbDgsROqKY4w7Znla?dl=1

8.7.4. MS/MS spectra of triglyceride estolides

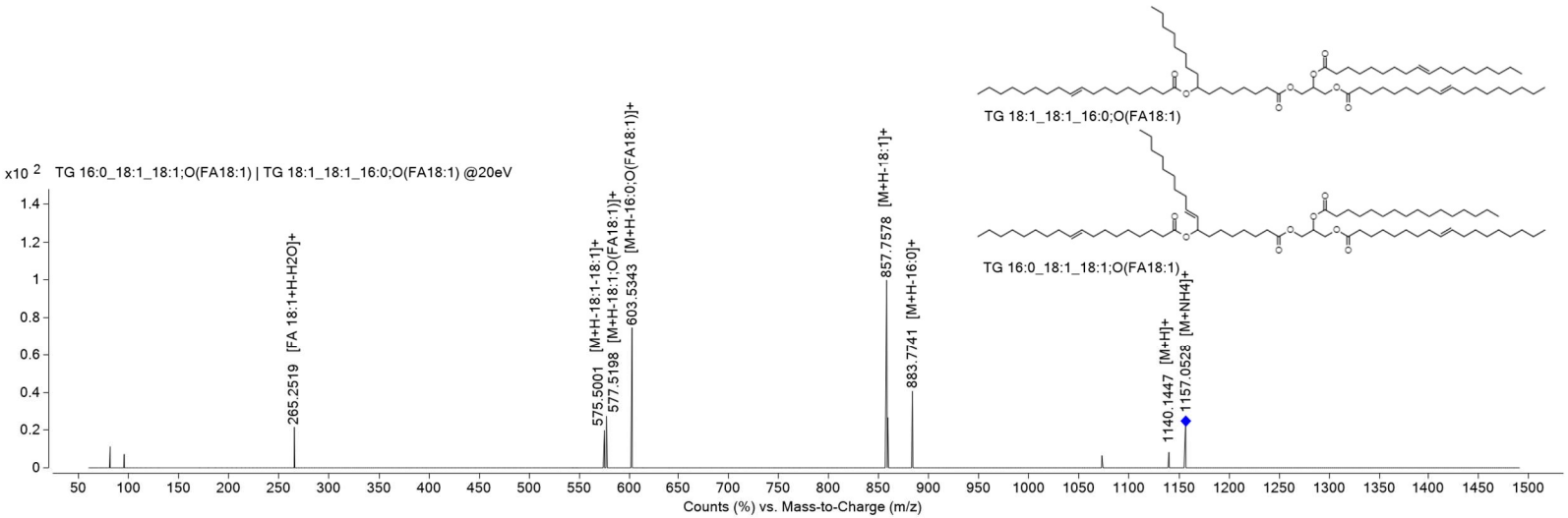

Figure SI-8.7 MS/MS spectrum of TG 16:0_18:1_18:1_O_(FA 18:1) at 20eV after maximum intensity normalization. The spectrum was measured in the intracellular apolar fraction of HepaRG cells (ESI(+)). The spectrum was derived from two different species, namely TG 16:0_18:1_18:1;O(FA 18:1) and TG 18:1_18:1_16:0;O(FA 18:1).

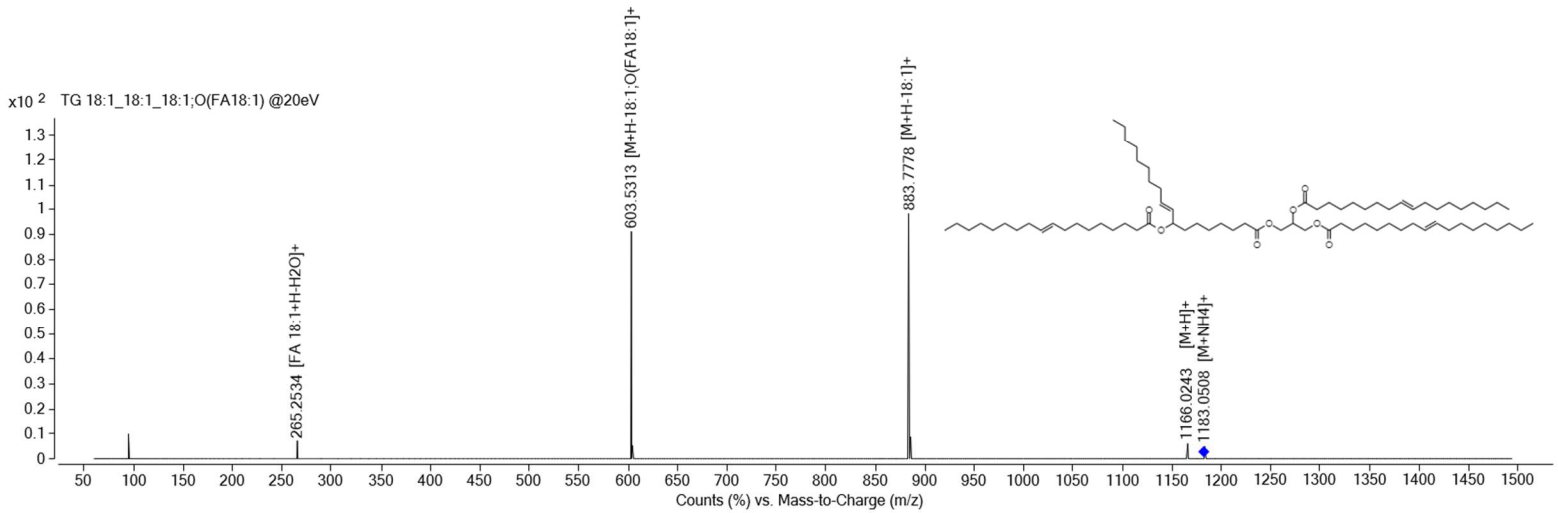

Figure SI-8.8 MS/MS spectrum of TG 18:1/18:1/18:1;O(FA 18:1) at 20eV after maximum intensity normalization. The spectrum was measured in the intracellular apolar fraction of HepaRG cells (ESI(+)).

CHAPTER 9:
GENERAL DISCUSSION

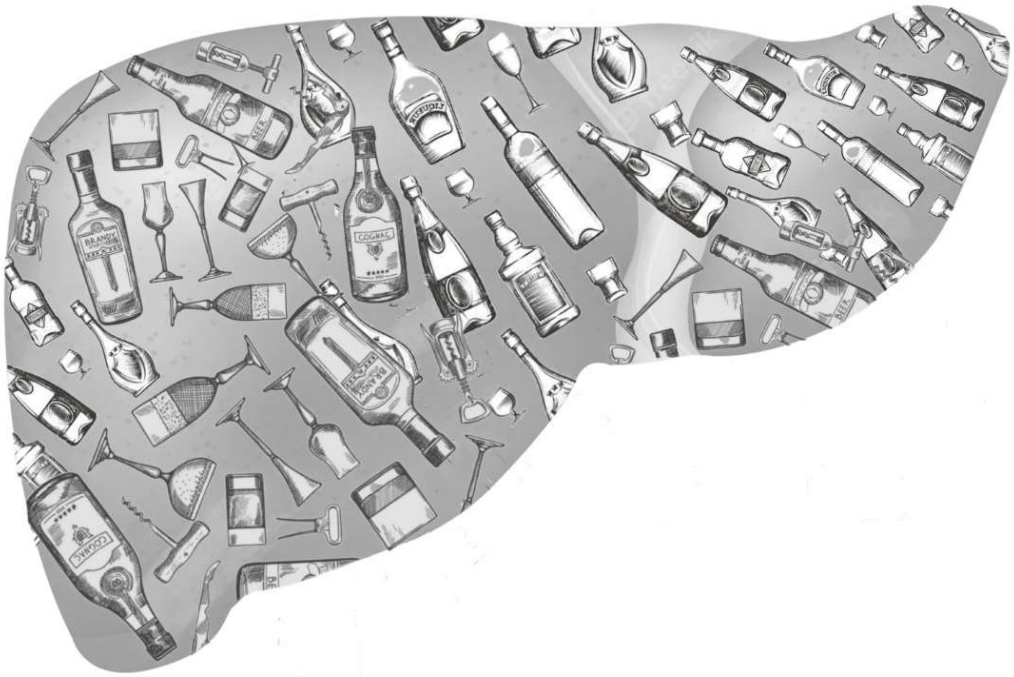

9.1. Analytical method development

In this PhD thesis, four untargeted analytical LC-QTOF-MS/MS platforms were developed. For polar metabolites, HILIC-based methods were used in ESI (+) and ESI (-), while RPLC was used in both ionization modes for lipids. As discussed in chapter 3, HILIC columns have the potential to retain and separate polar metabolites that show no retention or co-elute in RPLC. The combination of both HILIC and RPLC is a comprehensive strategy for untargeted metabolomics, providing a broad metabolite coverage. Unlike available method validation guidelines for targeted metabolomics, such guidelines are not fully developed for the untargeted approach, which aims at generation of hypotheses through a global unbiased analysis of all small-molecule metabolites present within a biological system, under a given set of conditions (Naz et al., 2014). For this latter reason, a predefined set of analytical standards of metabolites was selected for method optimization (80 polar metabolites and 50 lipids), which showed high coverage of metabolic pathways in addition to diversity in polarity, *m/z* and structure. After method optimization using standards, biological samples were analyzed to determine the precision of the methods, in addition to the number of detectable features and annotated metabolites.

For polar metabolites, six HILIC columns and one RPLC column were selected for a screening experiment using generic methods. Based on metabolite coverage, peak shape, S/N ratio and retention factor, generic methods were optimized in terms of mobile phase composition (solvents, pH, modifiers), temperature, gradient and flow rate. Separate analytical methods were optimized in ESI (+) and ESI (-) mode, as combination of these ionization modes benefits analysis of acidic and basic functional groups (Banerjee & Mazumdar, 2012). During column screening, the advantage of HILIC over RPLC to retain polar metabolites became clear. In RPLC, short retention times were observed with a substantial degree of co-elution between 1.5-4 minutes and elution close to the void time (34% showed $t_0 \leq RT \leq 1.1\ t_0$ in ESI (-) mode).

For the HILIC methods, no analytical standards eluted close to the void time. The better separation capacity for polar metabolites of HILIC compared to RPLC outweigh drawbacks such as longer equilibration times and lower precision of retention times. However, these latter disadvantages highlight the importance of implementing appropriate QA/QC procedures to ensure reliable data when using HILIC-MS methods. The final selected columns in ESI (+) and ESI (-) were both zwitterionic HILIC columns. Their stationary phases carry both positive and negative charges, making these columns highly versatile for retention of a wide range of polar metabolites. Using the two final optimized methods, biological samples were analyzed and the precision of the datasets was defined by the mRSD of the feature intensity in QC pooled samples. For each

dataset, the mRSD value was below 30%, which is a threshold often used to define a high-quality dataset for untargeted analysis and which reflects a good method stability over runs with different matrices (Cuykx, Negreira, et al., 2017; Naz et al., 2014).

To analyze lipids, three RPLC columns were subjected to a screening experiment (chapter 4). Although HILIC-based methods can be useful for lipidomics applications, separation of lipids is mostly limited to differences in polarity of the lipid head groups leading to co-elution of all lipids of a specific class (A. Li et al., 2020). This co-elution can cause ion suppression, favoring detection of high abundant lipid species over low abundant ones (Lange & Fedorova, 2020). In addition, MS/MS deconvolution to facilitate annotation at a species level is impaired. In RPLC, lipids are separated based on chain length and degree of unsaturation of fatty acyl chains (Lange & Fedorova, 2020; A. Li et al., 2020). The advantage of RPLC-based analysis is that lipids can be annotated more easily at a species level, enabling to showcase trends of up- or downregulation of lipids based on the size of their side chain and/or level of unsaturation. In addition, it provides a higher resolution separation than HILIC, with narrower peaks and a greater mass loading capacity (Plumb et al., 2022). For lipidomics analysis, the LC method optimization strategy was the same as for polar metabolites in chapter 3. The ACQUITY BEH C18 column was selected in both ESI (+) and ESI (-) modes. The optimized mobile phase was the same for both modes, with exception of the addition of 0.1% (v/v) CH_3COOH to the aqueous fraction for ESI (+) mode. Combining both ionization polarities, all lipid standards could be detected with an excellent peak shape (FWHM < 0.2, tailing factor < 2 and > 0.8, and no elution close to t_0) in addition to separation of *sn*-positional isomers. However, as RPLC-HRMS and MS/MS cannot separate all lipid isomers, DTIM was added as an additional dimension of separation to increase peak capacity (Causon & Hann, 2015; Kyle et al., 2016). In addition, DTIM provides CCS values as an additional molecular descriptor, to further increase annotation confidence (Figure 9.1) (Celma et al., 2020; Pičmanová et al., 2022).

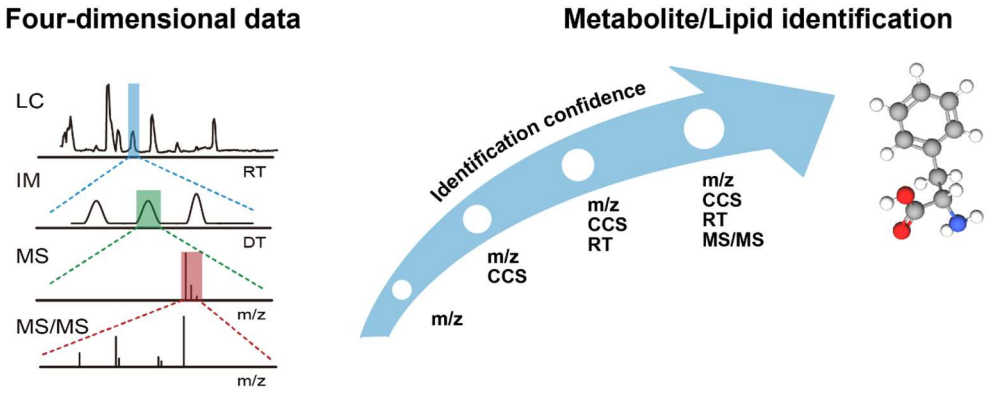

Figure 9.1 Integration of multi-dimensional information to support metabolite annotation in IM-HRMS-based lipidomics (Zhiwei Zhou et al., 2019).

CCS values can also be used as a class annotation filter (Qian Wu et al., 2020). When plotting CCS values in function of *m/z* values, metabolites within the same class will follow a trendline as their similarity in the chemical space is reflected in their ion mobility behavior. A major challenge of DTIM is an impairment of sensitivity as a result of reduced duty cycles (a continuous ionization source is coupled with the pulsed nature of IMS). In chapter 4, an in-depth sensitivity optimization of IMS was performed by evaluating the drift tube and rear funnel voltages with a chemometrics approach and by increasing duty cycles through usage of Hadamard multiplexing and manipulation of trap filling/release events, in the scope of finding a balance between sensitivity and detector saturation. Higher trap filling times resulted in higher signal intensities in single pulse mode, while no significant differences were detected in multiplexing mode. The tested range of trap filling times might be too small on the theoretical duty cycle in multiplexing mode to show a significant effect. When comparing the S/N ratio between single pulse and multiplexed mode, most lipids showed higher S/N in single pulse mode. This finding is inconsistent with a sensitivity gain factor of 2-8 for metabolites in multiplexing mode (Baker et al., 2014; Causon et al., 2019; Reinecke et al., 2019). Important to mention is that this sensitivity gain was observed for small polar metabolites with a *m/z* value below 250 and multiplexing techniques have not been fully explored for lipidomics applications. In this study, no trend between S/N and *m/z* value of lipids or lipid category could be observed. However, multiplexed mode reduced detector saturation which improves the dynamic linear range and mass accuracy.

9.2. Building metabolite libraries

Metabolite annotation remains a bottleneck in metabolomics, due to limited availability of high-quality MS/MS spectra in public databases and limited accuracy of *in silico*

fragmentation as metabolites show high structural diversity and complex fragmentation patterns (Ivanisevic & Want, 2019; Scheubert et al., 2013).

In chapter 5, a multidimensional library was built using RMassBank. MS/MS fragmentation spectra, RT and CCS values of 100 metabolites were acquired and used to build a metabolite library. In addition to the construction of this in-house library, MS/MS spectra and RT values were acquired for 653 polar metabolite standards. Raw analytical data and metadata of these acquisitions were shared with the mFam Consortium (Leibniz Institute of Plant Biochemistry (IPB), Halle, Germany, https://github.com/ipb-halle/mFam-Classifier). This consortium is a collaboration of 40 international research groups and the final goal is the building and sharing of a large high-resolution MS/MS library for metabolites as well as using these spectra as training data to improve the prediction quality of MS/MS spectra. For processing of the data, IPB uses MS-DIAL and in-house scripts to generate MassBank and msp files. An example of one of the MS/MS spectra can be seen in Figure 9.2. All mass spectral data processed by the mFam Consortium were shared with its contributors.

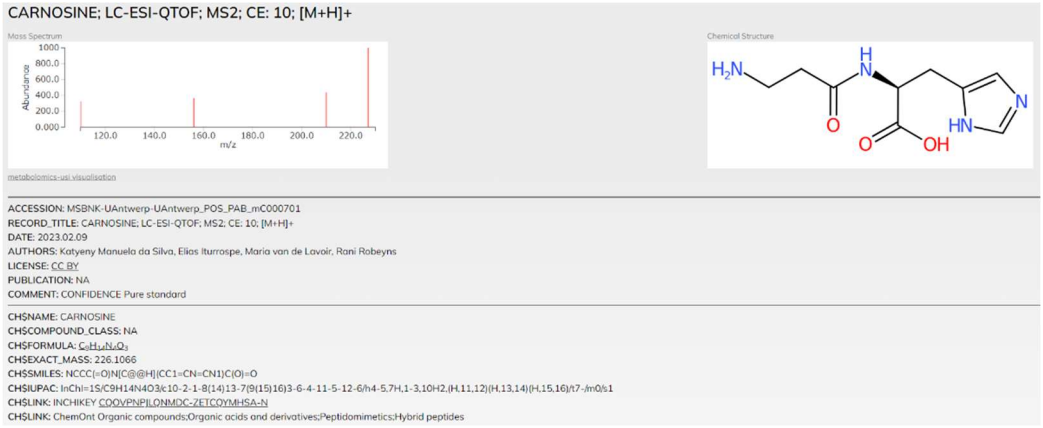

Figure 9.2 MS/MS spectrum of carnosine $[M+H]^+$ at 10 eV. The MS/MS spectrum was acquired by the Toxicological Centre of the University of Antwerp and processed by the mFam Consortium (IPB & UA, 2023).

During data acquisition of metabolite standards, MS/MS and DTIM data were acquired for each standard separately using FIA. DTIM-MS and MS/MS runs were performed separately as DTIM decreases sensitivity and is incompatible with DDA, which generally results in cleaner MS/MS spectra (da Silva, Iturrospe, Heyrman, et al., 2021). FIA was preferred over LC-MS/MS and LC-DTIM-MS acquisitions as these latter two would drastically increase the acquisition time. In addition to FIA, standard mixtures were injected using LC-MS to acquire RT information. Isomers were injected in separate mixtures to avoid misinterpretations. Other QA/QC strategies included usage of system

suitability samples, triplicate injections for RT and CCS measurements to enable calculation of the average and SD, usage of multiple collision energies for MS/MS mode, extensive reporting of metadata, manual control of pressure profiles, isotopic pattern, S/N, peak shape, MS/MS spectra, RT values, CCS values, and presence of multiple gas-phase conformations during DTIM.

Generation of in-house mass spectral libraries facilitates high confidence during metabolite annotation (Schymanski et al., 2014). Manual evaluation of MS/MS spectra and observing trends in RT and DTIM behavior helped in improving personal skills useful in future metabolite annotations.

During RMassBank processing, large batches of MS/MS data were used to improve recalibration. During MS/MS recalibration, MS1 datapoints of all spectra are used to calculate mass errors and to generate an MS/MS calibration curve to correct mass errors of all spectra (Stravs et al., 2013). Recalibration can correct for systematic deviations in MS/MS spectra, which otherwise would impede the performance of database searches and comparability with other HRMS instruments. Following recalibration, denoising was performed by removing MS/MS fragments when no subformulas could be generated. Meringer *et al.* showed that MS/MS fragments without the possibility to assign a subformula are an indication of instrument noise or interfering peaks (2011). A limitation of the library built in chapter 4 is that only single MS/MS spectra were acquired per collision energy. Multiple acquisitions per collision energy would increase acquisition time, but also facilitate multiplicity filtering as a second denoising step. During this process, peaks are only retained when they have at least one possible formula and occur in at least two spectra from the same metabolite (Stravs et al., 2013). Denoising using fragment subformulas and the possibility to perform subsequent multiplicity filtering are alternatives to denoising using absolute or relative intensity cut-offs, which are commonly used for removal of random noise. However, usage of such cut-offs is at risk of removing fragment peaks originating from the actual precursor.

In order to evaluate MS/MS spectra processing, special attention was given to rule-based fragmentation, multiple ionization species, in-source fragmentation (ISF), and radical ions. Multiple ionization species for one metabolite can provide different MS/MS fragmentation and the resulting spectra can be complementary for structure elucidation. ISF is important to recognize as e.g., PGE1 can generate $[M\text{-}H\text{-}H_2O]^-$ in the source, which has a very similar fragmentation pattern compared to PGA1 (R. C. Murphy et al., 2005).

9.3. Experimental design to study ethanol-induced hepatotoxicity

To study ethanol-induced hepatotoxicity *in vitro* using untargeted metabolomics, HepaRG cells were used. These cells were chosen over primary human hepatocytes as the latter are difficult to standardize, have limited *in vitro* stability and unpredictable availability (Guillouzo et al., 2007; Zeilinger et al., 2016). Liver cell lines on the other hand, show good availability, high proliferation activity and stable metabolic performance (Zeilinger et al., 2016), however, mostly at a lower level than *in vivo* as many have lost major liver-like functions (Tascher et al., 2019). For example, HepG2 cells show loss of crucial CYP enzymes (Zeilinger et al., 2016). On the other hand, HepaRG cells maintain expression of most liver-specific functions, including CYP activity and bile acid synthesis, and are capable of differentiating towards hepatocyte-like cells and biliary-like cells, mimicking the *in vivo* situation (Guillouzo et al., 2007; Marion et al., 2010). Within hepatoma cell lines, the HepaRG cell line shows a phenotype most close to that of the *in vivo* organ and is well accepted to study disease-related mechanisms (Guguen-Guillouzo & Guillouzo, 2010; McGill et al., 2011; Tascher et al., 2019).

In addition, HepaRG cells are suitable to explore ethanol biotransformation as they express enzymes involved in the oxidative biotransformation of ethanol, such as CYP2E1, ADH and ALDH (Hugbart et al., 2020). Hugbart *et al.* exposed HepaRG cells to 25 and 50 mM of ethanol for 8-72 h and studied the non-oxidative biotransformation of ethanol. Exposure led to a significant induction of CYP2E1 mRNA and a dose- and time-dependent production of ethylglucuronide (EtG) and ethylsulfate (EtS) (2020).

For cellular exposure, ethanol was used at its sub-cytotoxic IC_{10} concentration, as higher concentrations such as IC_{50} have such a strong impact that only alterations to general toxicity can be observed, impeding mechanistic fingerprinting (Cuykx, Rodrigues, et al., 2018). As combination of different exposure concentrations can be useful to investigate trends of toxicity markers, HepaRG cells were exposed to ethanol both at IC_{10} and 1/10 of the IC_{10} concentrations. A second and lower concentration is often applied to investigate metabolic alterations before any (substantial) cell death occurs (Cuykx, Rodrigues, et al., 2018). To be able to calculate the IC_{10} concentration of ethanol, a NRU assay was used, which is based on lysosomal storage of a cationic dye (Ates et al., 2017; S. Z. Zhang et al., 1990). This cell viability assay was chosen over the more commonly used MTT assay or assays using water soluble tetrazolium salts (e.g., WST-1) as these assays are dependent on the mitochondrial function of the cells under investigation (Kamiloglu et al., 2020) and previous research showed that hepatic mitochondria are an important target for ethanol-induced tissue injury (Das et al., 2012). Indeed, several studies in both animal and human models have demonstrated that ethanol intake or exposure alters mitochondrial morphology and function by causing, among others,

impairment of mitochondrial biogenesis, mitochondrial DNA damage, and oxidative stress (Abdallah & Singal, 2020; Das et al., 2012; Mansouri et al., 1999; Singal et al., 2011).

In chapter 7, HepaRG cells were exposed to ethanol during a time period of 24 h and 48 h. Usage of different exposure times enables investigation of time-related differences in metabolite levels. Within *in vitro* hepatotoxicity analyses, multiple timepoint investigations with a final endpoint of 24 h or 48 h are often used (Balcke et al., 2011; Kalkhof et al., 2015; Knockaert et al., 2012; X. Li et al., 2017; Zhonghuang Li et al., 2015; Meissen et al., 2015; Minsart et al., 2020). As longer exposure times could result in more pronounced differences and as differentiated HepaRG cells show long-term stability (i.e., many liver-specific functions such as CYP activity and membrane transporters remain relatively stable for up to four weeks), the NRU assay was conducted for 168 h of ethanol exposure (in addition to 24 h and 48 h). Despite several NRU assays with different concentration ranges and renewal of ethanol-containing media every 24 h, the results of these NRU assays were rejected as too much variability in cell viability made IC_x calculations unreliable. The failing of these latter experiments could be due to loss of long-term stability due to ethanol-induced cellular changes and/or difficulties related to the volatile nature of ethanol. As a result, only two exposure times (i.e., 24 h and 48 h) were retained. In chapter 8, cells were exposed to both ethanol and TNF-α in order to investigate the effect of this inflammation inducer, which is considered to be the most important inflammatory cytokine in the progression of ALD (Kawaratani et al., 2013; Nagy, 2015; Seo & Jeong, 2016; Yin et al., 1999). During these experiments, only an exposure time of 24 h was used as the differences in metabolic alteration between 24 h and 48 h of ethanol exposure (chapter 7) were rather small.

Per sample group (i.e., exposure and control), 6 to 7 replicates were used. As the growth of cells in culture can be carefully controlled, a sample size of three to five per group may already give useful data (Barnes et al., 2016a). The majority of experiments report no more than 6 replicates per group and although 3 replicates is considered as the minimum, ≥ 5 replicates are recommended for reliable *in vitro* metabolomics applications by the metabolomics standards initiative (MSI) (Martano et al., 2014; Sumner et al., 2007). These guidelines were proposed as sample size calculation remains a difficult topic in untargeted metabolomics (Ivanisevic & Want, 2019). When solely univariate statistics are used to select relevant features, sample size can be calculated using power analysis, which requires the estimation of population means, standard deviations and effect sizes. As metabolomics generally provides high-dimensional data, average power is used, the significance level needs to take multiple testing into account and both effect sizes and variances take multiple values. Unfortunately, this power calculation can only be used post-hoc and for univariate statistical analysis (Vinaixa et

al., 2012). Power calculation was not used in this thesis as omics data are multivariate in nature (Ivanisevic & Want, 2019) and multivariate statistical analysis was needed in order to provide mechanistic information on ethanol-induced hepatotoxicity. Univariate statistical analysis was solely used as an additional tool to select relevant features that could escape the multivariate selection of relevant features. The ideal sample size will depend on the intrinsic variation in the biological samples as well as the magnitude of the observed metabolic perturbations (Gertsman & Barshop, 2018). One of the advantages of using cell lines is the low biological variation compared to animal models and human subjects, which are prone to inter-individual variation and confounding factors, such as age, sex, overall health status, and varying environmental exposures (Hounoum et al., 2016). The low biological variation of cell lines decreases the number of replicates needed to observe important changes in the cellular profile (Hounoum et al., 2016).

As metabolite changes are typically unknown and may be numerous, data usually shows high dimensionality and a large degree of correlation between variables, a pilot study can be used to evaluate sample size requirements (Ivanisevic & Want, 2019). For example, differences in RSD calculated for feature intensities in pooled QC samples compared to those in biological samples can be evaluated to ensure the essential separation between technical and biological variance (Kuhring et al., 2020). The degree of sample group separation in PCA plots can give an indication on within-group and between-group variability.

Another important aspect in the experimental design was randomization. Cell samples were randomized prior to exposure and sample collection, during sample preparation and instrumental injection. These randomization steps were applied to minimize generation of non-biological variance (Barnes et al., 2016a).

As mentioned in chapter 6, sample preparation of HepaRG extracts was based on the optimized in-house method of Cuykx *et al.* (Cuykx, Mortelé, et al., 2017). Chamber slides were used for cell cultivation instead of well plates, as these slides facilitate washing after cultivation and enable a higher extraction efficiency (Cuykx, Mortelé, et al., 2017). In order to increase metabolite coverage, sample extracts were fractionated in a polar and apolar fraction, which were analyzed with separate analytical platforms. As these analytical platforms used different instrumentation, data for polar and apolar fractions could be acquired simultaneously, decreasing acquisition time.

9.4. Statistical interpretation

As metabolomics analysis usually generates thousands of features for a single sample, data processing is of vital importance to extract useful information from this big data. Feature reduction was performed using:

(i) a frequency filter; features needed to be present in ≥ 80% of an exposed or control sample group. A frequency filter makes sure that only features which are present in a minimum percentage of samples are selected for downstream analysis. This type of filtering is used to generate a consensus peak table and excludes features with a large number of missing values, which can be due to e.g., sample contaminants (Alonso et al., 2015; X. Zhang et al., 2020).

(ii) a filter based on intensity variation; feature intensity needed to have a RSD < 30% in at least one exposure group. RSD filters can be applied using QC pooled samples to exclude features with large intensity fluctuations due to analytical variation introduced during data acquisition (Godzien et al., 2015). However, RSD filters can also be applied based on the intensity fluctuations within biological sample groups, to remove the most variable (i.e., irreproducible) signals between replicates (i.e., due to either technical or biological variability or a combination). This latter reduces the risk of false positives when comparing intensity differences between exposed and control samples (Jankevics, 2013; Schiffman et al., 2019).

(iii) a filter to remove background noise; maximal feature intensity of a biological sample/average intensity of the extraction blanks needed to be > 10 (for intracellular samples) or average intensity in an exposure group/ average intensity in the extraction blanks needed to show a fold change > 3 or < 0.33 (for extracellular samples). Different blank subtraction thresholds were used for intracellular and extracellular samples, as extraction blanks for extracellular samples contained incubated cell medium.

Prior to applying multivariate statistical methods to metabolomics data, pretreatment steps are needed. For instance, 5000-fold differences in concentration for different metabolites can be present in a metabolomics data set, while these differences are not proportional to the biological relevance of these metabolites. Data analysis methods are not able to make this distinction and pretreatment of data can correct for aspects that hinder the biological interpretation (van den Berg et al., 2006).

Both univariate and multivariate statistics were applied because of their complementarity (Saccenti et al., 2014). Univariate approaches can rather easily be interpretated. Significance indicates a difference in average metabolite intensities between sample groups. However, when relevant information is available in a set of metabolites, this does not necessarily mean that each of the individual metabolites

isolated from the others also contains this relevant information (Saccenti et al., 2014). In contrary to univariate methods, multivariate methods make use of all variables simultaneously and take into account the relationship among variables (Dillon & Goldstein, 1984). In this thesis, PLS-DA was used as a statistical tool to select features based on their importance in sample class separation. However, as supervised multivariate approaches are prone to overfitting, cross-validation of the built PLS-DA models was performed, and the models were subjected to permutation tests (Ruiz-Perez et al., 2020). In addition, to decrease the risk of false positively selecting a feature as relevant, a random forest binary classifier was used (Beirnaert, Cuykx, et al., 2019). Only features relevant according to both the PLS-DA and RF models were considered. Features selected by univariate and/or multivariate workflows were used to construct boxplots based on their intensities per sample group. Manual evaluation of these boxplots was used to further reduce potential false positives by exclusion (e.g., when variation in the exposed group was substantially large compared to the control group or when discrimination was due to outliers).

9.5. Metabolomics to investigate early ALD *in vitro*

Alcoholic liver disease (ALD) is a major problem with over 2 billion people consuming ethanol, 75 million diagnoses of ethanol-use disorders, and many people that remain undiagnosed (Asrani et al., 2019; de Wit et al., 2010). A major issue of ALD is that symptoms tend to develop late in the course of disease progression and most patients are only diagnosed in advanced and irreversible stages (Seitz et al., 2018; Sheron et al., 2013; Singal et al., 2018). Despite their high prevalence, ethanol-related disorders remain poorly identified and characterized (Seitz et al., 2018). At present, there are no early and specific biomarkers for the diagnosis of ALD and therapeutical options are lacking, especially in early stages. Corticosteroids can be used in severe alcoholic hepatitis, although data from clinical trials and meta-analyses of corticosteroids have been conflicting (Saberi et al., 2016).

The importance of ethanol consumption in liver disease was recently highlighted by Staufer *et al.* (2022). In their publication, Staufer *et al*. included 184 patients suffering from either NALFD, AFLD or metabolic dysfunction-associated fatty liver disease (MAFLD) and questioned the possibility to distinguish NAFLD and AFLD by diagnostic means. By determining EtG in hair and urine, they classified 29% of presumed NAFLD patients and 25% of presumed MAFLD patients as moderate to excessive ethanol consumers (Staufer et al., 2022).

In this thesis, the research goal of identifying small-molecule biomarkers to characterize early stages of alcoholic liver disease (AFLD and ASH) was set as the limited

understanding of ALD pathogenesis hampers development of novel therapies and diagnostic improvements (Hyun et al., 2021). By exposing HepaRG cells to ethanol and TNF-α, biochemical biomarkers could be identified at a mechanistic cellular level. Other arguments for using an *in vitro* set up are the difficult accessibility of ALD patient samples and the lack of reliable animal models for ALD that reflect human ALD. Using ethanol-exposed HepaRG cells, metabolic fingerprinting was performed to pinpoint intracellular alterations. In addition, metabolic footprinting was used to observe changes in secretion and consumption of metabolites. As untargeted metabolomics only provides a snapshot of the current composition of a cell, it does not show active metabolite fluxes. Nevertheless, this static image can provide hypothesis-generating data, help in expanding adverse outcome pathways (AOPs) and support or reject current mechanistic explanations.

9.5.1. Simulation of AFLD in HepaRG cells

In chapter 7, metabolomics and lipidomics analyses were performed on the intra- and extracellular fractions of ethanol-exposed HepaRG cells. These cells were exposed to ethanol at their IC_{10} and 1/10 of the IC_{10} concentration for 24 h and 48 h (i.e., with renewal of ethanol-containing media after 24 h). Based on relative differences in signal abundance between biological control samples and ethanol-exposed biological samples, the metabolic signature of ethanol exposure was elucidated. Although a list of metabolites can be sufficient for the distinguishment between control and exposed cells, this list was used for the mechanistic interpretation to offer additional value and to improve the confidence of the results. Dynamic changes of metabolites were unravelled in order to get a better understanding of early-stage indicators of AFLD.

To the best of our knowledge, no AOPs are defined for ALD. However, 10 AOPs on hepatic steatosis as adverse outcome are under development in the AOP knowledge database (AOP-KB) (Gijbels & Vinken, 2017; Society for Advancement of AOPs, 2023). In addition, an AOP network on hepatic steatosis was proposed by Mellor *et al*. (2016) and Escher *et al.* (2022). AOPs provide a conceptual framework that links the molecular initiating event (MIE) to an adverse outcome through key events (KEs), based on organized toxicological knowledge, bridging the gap from chemistry to toxicological effect (Mellor et al., 2016). The AOP-KB database was introduced by the Organization for Economic Cooperation and Development together with the U.S. Environmental Protection Agency, the U.S. Army Engineer Research and Development Center, and the European Joint Research Center, in response to the increasing use of AOPs (Gijbels & Vinken, 2017). Each of the steatosis AOPs considers a different MIE, including modulation of nuclear receptors (e.g., constitutive androstane receptor, liver X receptor), suppression of transcription factors (e.g., nuclear erythroid 2-related factor),

and activation or inhibition of specific enzymes. All these MIEs trigger an array of effects, such as enhanced transcription of genes encoding mediators of lipid metabolism. As a result, *de novo* lipid synthesis is enhanced, lipid fluxes are changed,… Consequently, normal processes of triglyceride synthesis and elimination are impaired leading to their accumulation in hepatocytes. This hepatocellular lipid accumulation and its ability to provoke cytoplasm displacement, nucleus distortion, mitochondrial toxicity, and endoplasmic reticulum stress are characteristic for the fatty liver cell phenotype (Gijbels & Vinken, 2017).

Eight out of ten publicly available AOPs in construction (Society for Advancement of AOPs, 2023) contain one or more KEs that were confirmed during HepaRG experiments, either by direct results or as part of hypothesis generation to discuss the observed results. These KEs included inhibition of mitochondrial β-oxidation (AOP 36, 57, 58, 60, 61, 232, 318), fatty acid accumulation (AOP 36, 57, 58, 60), *de novo* fatty acid synthesis (AOP 34, 61, 58), triglyceride accumulation (AOP 34, 57, 58, 60, 61, 318), activation of SREBP-1c (AOP 34), and elevation of FAS (AOP 34, 58).

As shown by these examples, metabolomics can provide important information concerning key events in AOPs, highlight affected pathways and provide further evidence for existing AOPs. As an untargeted approach was used, it can (i) reveal effects that were previously undetected (e.g., the alterations in peroxisomal β-oxidation as a result of inhibited mitochondrial β-oxidation), and (ii) confirm and/or clarify effects that were previously (in full or in part) published (e.g., increased catabolism of sphingomyelins, downregulation of phosphatidylcholines as a result of PEMT inhibition and impaired formation of S-adenosylmethionine, and increased consumption of lysophosphatidylcholines), which can, after further in-depth investigation, be used to expand existing AOPs.

In summary, exposing HepaRG cells to ethanol increased di- and triglycerides, concordant with a steatotic image. Phosphatidylcholines decreased and could be used for di- and subsequent triglyceride synthesis, facilitating fat accumulation (Z. Wang et al., 2010). Intracellular phosphatidylethanolamines decreased, possibly due to reduced synthesis as its precursors (diglycerides and O-phosphoethanolamine) increased and diglycerides can fuel triglyceride synthesis. In addition, intracellular decrease could be explained by increased secretion into the extracellular environment.

Several intracellular metabolic patterns could be related to changes in the extracellular environment, such as increased intracellular hydrolysis of sphingomyelins, leading to increased phosphorylcholine secretion. Carnitines showed alterations depending on the size of their carbon chain, which highlighted the interplay between β-oxidation in mitochondria and peroxisomes. The capacity of HepaRG cells to non-oxidatively

biotransform ethanol was previously explored by Hugbart *et al*, who measured EtG and EtS in ethanol-exposed HepaRG cells (Hugbart et al., 2020). During this thesis, it was observed that HepaRG cells are also capable of synthesizing PEth 16:0_18:1, which is formed in a reaction utilizing phosphatidylcholine 16:0_18:1 and ethanol.

When comparing HepaRG exposure to ethanol at the IC_{10} concentration and at 1/10 of the IC_{10} concentration, a similar image was observed although less metabolic classes could be selected by the statistical workflow at the low concentration. In addition to fewer affected classes, fold changes were lower and affected classes were represented by a lower number of species. These results were concordant with the exploratory PCA plots that showed a higher resemblance in the metabolome of ethanol exposure at 1/10 IC_{10} versus negative controls in comparison to exposure at IC_{10} versus negative controls. Ethanol exposure to either 24 h or 48 h showed a similar metabolic effect for most metabolic classes. However, for phosphatidylcholines time-related differences were observed. The general image showed a decrease of phosphatidylcholines in the intracellular fraction of HepaRGs after 24 h and 48 h of ethanol exposure. However, after 48 h, a slight increase of highly unsaturated phosphatidylcholines (≥ 5 double bonds) was observed. This might relate to the shift of saturated to polyunsaturated fatty acids (PUFAs) as observed in ethanol-fed rodents (Jeon & Carr, 2020).

9.5.2. Simulation of ASH in HepaRG cells

In chapter 8, follow-up experiments were performed exposing HepaRG cells to both ethanol and TNF-α in order to obtain an improved *in vitro* simulation of ASH. TNF-α is considered the most important inflammatory cytokine in the progression of ALD (Kawaratani et al., 2013; Nagy, 2015; Seo & Jeong, 2016; Yin et al., 1999) and significantly contributes to ethanol-induced liver damage by inducing inflammation, apoptosis and necrosis (Nagy, 2015; Rodriguez et al., 2004). Excessive consumption of ethanol increases gut-derived LPS in the portal circulation (Kawaratani et al., 2013; Nagy, 2015), which can activate Kupffer cells to secrete TNF-α for interaction with hepatocytes (Nagy, 2015; Seo & Jeong, 2016). In addition, ethanol consumption increases the susceptibility to TNF-α by increasing the levels of its receptors on hepatocytes (Rodriguez et al., 2004), and stimulates TNF-α expression in adipose tissue (Shim & Jeong, 2020).

Untargeted metabolomics was used to compare the metabolic profile of HepaRG cells exposed to ethanol and TNF-α with (i) negative controls, and (ii) HepaRG cells exposed to solely ethanol. In addition, suspect screening was performed to compare fold change differences of previously elucidated metabolites after solely ethanol exposure (chapter 7) versus combined exposure to ethanol and TNF-α.

There is only one AOP publicly available for steatohepatitis (AOP 213) (Society for Advancement of AOPs, 2023). This latter AOP was defined for NASH and is currently in construction. The MIE of this AOP is inhibition of β-oxidation. In chronological order, KEs include an increase in cytosolic fatty acids, increased steatosis, increased production of ROS, and increased oncotic necrosis.

As seen during both suspect screening and untargeted analyses, the magnitude of intracellular upregulation of di- and triglyceride species increased during TNF-α co-exposure, with an average factor of 1.7 and 2.0 compared to solely ethanol exposure, respectively. In addition, the number of distinctive triglyceride species increased significantly between solely ethanol exposure and combined exposure to ethanol and TNF-α, suggesting an important role of inflammation during steatosis progression. A possible explanation is the capability of TNF-α to induce *de novo* fatty acid synthesis (Popa et al., 2007). Of all triglyceride species, only FAHFA triglycerides were downregulated during exposure to ethanol and TNF-α compared to solely ethanol exposure. FAHFA triglycerides, which were previously unreported in human hepatocytes, can form a storage pool of FAHFAs (Tan et al., 2019). The decrease of FAHFA triglycerides during co-exposure of TNF-α could be explained by a release of FAHFAs by lipolytic enzymes in order for the FAHFAs to exert their anti-inflammatory properties.

For (lyso)phosphatidylcholines, a further intracellular decrease was observed during TNF-α co-exposure, which could be explained by altered GNMT expression (Männistö et al., 2019). In the HepaRG model of AFLD and ASH, an intracellular decrease was observed for lysophosphatidylcholines, concordant with findings in NAFLD (Puri et al., 2007). However, hepatic lysophosphatidylcholines in NASH are upregulated (Puri et al., 2007), indicating a potential distinctive hepatic lysophosphatidylcholine metabolism in NASH versus ASH. In chapter 7, polyunsaturated phosphatidylcholines were upregulated after 48 h of ethanol exposure. The same effect was observed after 24 h when ethanol exposure was combined with TNF-α. These findings could be explained by increased production of PUFAs as seen after TNF-α infusion in rats (Raina et al., 1995). These PUFAs can be incorporated in phosphatidylcholines through the CDP-choline pathway (Jeon & Carr, 2020). Increased levels of PUFAs could also explain the trend of up- and downregulation of phosphatidylglycerols, which was dependent on the level of unsaturation. Next to phosphatidylcholines, phosphatidylethanolamines decreased further due to TNF-α co-exposure, concordant with increased secretion and intracellular increase of its precursors (diglycerides and O-phosphoethanolamine). Increased secretion of ornithine and phenylacetylglutamine, and downregulation of intracellular phenylacetylglutamine could indicate an impaired processing of nitrogen waste. Other findings indicated a decreased biotransformation capacity (intracellular

decrease of 5'-diphosphoglucuronic acid) and increased susceptibility for oxidative stress (intracellular decrease of glutathione).

9.5.3. Ethylated phosphorylcholine: a potential new marker of ethanol consumption

Ethylated phosphorylcholine (EtOChoP), a previously unreported metabolite, was suggested to be a new marker of ethanol exposure. EtOChoP was elucidated in chapter 7 in HepaRG samples exposed to ethanol. Since no MS/MS library entry could be found for this latter metabolite, its fragmentation was matched using NIST (v.17) without accurate *m/z* matching, enabling fragmentation spectral matching with fragments of other metabolites with a higher *m/z* value (e.g., 1,2-dipalmitoyl-sn-glycero-O-ethyl-3-phosphatidylcholine). In addition, the fragmentation spectra of EtOChoP were confirmed with *in silico* generated fragments using CFM-ID (v. 4.0) (F. Wang et al., 2021). Due to its absence in the negative control samples, the metabolite showed similar large fold changes to PEth 16:0_18:1. Interestingly, unlike PEth 16:0_18:1, ethylated phosphorylcholine was found both in intracellular and extracellular samples due to a high level of hepatic secretion. To increase confidence in the annotation of EtOChoP, the standard was synthesized by Dr. Vladimir N. Belov (Max Planck Institute, Göttingen, Germany). After analysis of this latter standard, an L1 level of confirmation could be assigned to the annotation (Schymanski et al., 2014). Targeted analyses (SI-7.7.5) were able to show the presence of EtOChoP in whole blood of heavy drinkers, while it remained absent in negative controls. Although (i) the used method needs further optimization (e.g., decrease of the lower limit of quantification) and validation, and (ii) additional samples should be analyzed (e.g., comparing social and heavy drinkers), the proof-of-concept of EtOChoP as a marker of ethanol consumption was delivered.

CHAPTER 10:
CONCLUSIONS AND FUTURE PERSPECTIVES

10.1. Conclusions

The first part of this thesis (i.e., major objective 1) focused on developing untargeted metabolomics and lipidomics platforms using LC-HRMS, and creating a multidimensional metabolite library workflow to confidently annotate features resulting from untargeted experiments. The developed platforms consisted of four complementary methods, two HILIC-based methods for polar metabolites, and two RPLC-based methods for lipids. For method optimization, a variety of analytical standards was used, which showed high coverage of metabolic pathways in addition to diversity in polarity, *m/z* and structure. Although untargeted metabolomics should be as unbiased as possible, the usage of analytical standards benefits the optimization of platforms. In addition, biological samples were used to evaluate the performance of the optimized methods. HILIC columns showed superiority over RPLC to retain polar metabolites. The mix-mode interaction mechanisms of two generations of HILIC columns were investigated and enabled successful retainment and separation of nearly 100% of polar standards, covering key pathways of the polar human metabolome. For lipids, the ACQUITY UPLC BEH C18 column provided satisfactory results in terms of lipid coverage and its ability to separate critical pairs. DTIMS was hyphenated to LC-HRMS for lipid analysis as it can improve separation capacity and annotation confidence. Sensitivity of the LC-DTIMS-HRMS platform could be increased for lipidomics purposes by optimizing several parameters. The multidimensional metabolite library workflow helped to obtain in-depth knowledge of class-specific retention time ranges, ionization species, fragmentation mechanisms, and trends in IM space. Overall, the first part of this thesis provides valuable insights and tools for untargeted metabolomics and lipidomics research.

The optimized analytical platforms allowed to cater to the second major objective: the investigation of AFLD and ASH in an *in vitro* model using the HepaRG liver cell line. Firstly, ethanol-induced hepatotoxicity in HepaRG cells was studied to generate pathophysiological hypotheses for AFLD. Combining the elucidation of the metabolic fingerprint and footprint of ethanol exposure facilitated the biological interpretation of results. Metabolic alterations showed only minor differences between 24 h and 48 h of ethanol exposure, with more upregulated triglycerides and higher fold changes of polyunsaturated phosphatidylcholines after 48 h of exposure. However, metabolic alterations were strongly affected by the concentration of ethanol. Many altered metabolites were consistent with a steatotic image as seen in previous research, such as lipid accumulation and depletion of S-adenosylmethionine. Further metabolic alterations included depletion of ceramides (d18:2), O-phosphoethanolamine and upregulation of octanoylcarnitine. In addition to the detection of high levels of

intracellular PEth 16:0_18:1, ethylated phosphorylcholine could be identified as a new marker of ethanol exposure.

Follow-up experiments were performed whereby HepaRG cells were exposed to both ethanol and TNF-α in order to obtain an improved *in vitro* simulation of ASH. Compared to solely ethanol-exposed HepaRG cells, additional co-exposure to TNF-α resulted in a stronger lipid accumulation, indicating increased hepatotoxicity. The downregulation of FAHFA triglycerides seen during TNF-α co-exposure could be a compensating mechanism to counteract liver inflammation. Downregulation of S-adenosylmethionine showed to play an important role in ethanol-induced hepatotoxicity as its downregulation had multiple effects on for example biosynthesis of phosphatidylcholines, methylthioadenosine and glutathione. Metabolic finger- and footprinting of lysophosphatidylcholines highlighted a potential distinctive hepatic metabolism in NASH versus ASH. Overall, subjecting the HepaRG liver cell line to metabolomics analyses proved to be a valuable tool to obtain mechanistic insight in ethanol-induced hepatotoxicity. Usage of this tool facilitates future *in vivo* research by pinpointing interesting metabolites and pathways.

10.2. Future perspectives

10.2.1. Analytical perspectives

As untargeted metabolomics aims to separate and detect as many metabolites as possible, additional analytical platforms could be considered to analyze samples. For example, GC-MS is a useful platform for untargeted metabolomics as it generates robust retention times and highly reproducible mass spectra (within and between instruments). For untargeted purposes, GC-HRMS shows a higher metabolic coverage and potential to elucidate unknowns compared to commonly used unit-mass resolution single-quadrupole GC-MS instruments (Stettin et al., 2020). Electron impact (EI) ionization, used in GC-MS, is a hard ionization technique that generates complex and rich fragmentation patterns which can be exploited to increase the specificity in mass spectral matching. Large transferable EI-mass spectral libraries are available for metabolite annotation (Fiehn, 2016; Lynch, 2017). A downside of GC-MS is that many metabolites require derivatization in order to increase volatility and thermal stability. The most common derivatization methods, such as trimethylsilylation, remove acidic protons from hydroxyl-, carboxyl-, amino- or thiol-groups, are performed under mild conditions and obtain high yields (Fiehn, 2016). However, during untargeted metabolomics there are important considerations such as different derivatization kinetics between metabolites (i.e., depending on the sample, different derivatization times can be necessary) and the absence of a derivatization method that leads to one

derivative type per metabolite for all compound classes (Papadimitropoulos et al., 2018). The most widely used derivatization method in untargeted GC-MS metabolomics is a two-step procedure, to improve the range of metabolite classes. This latter method includes (i) methoximation of the ketone group-containing metabolites, and (ii) silylation of all metabolites, including the methoximes formed in the previous step, into their trimethylsilyl (TMS) derivatives (Papadimitropoulos et al., 2018). Although silylation would be sufficient for many metabolites, prior methoximation can be needed for specific classes such as sugars.

GC-MS analysis is useful for robust analysis of, among others, organic acids, sugars, fatty acids, and sterols (Fiehn, 2016). GC-MS is considered the gold standard methodology for neutral cholesterol metabolites as neutral sterols are relatively resistant to electrospray ionization, causing low sensitivity during LC-MS (Griffiths et al., 2017; Honda et al., 2010). GC-MS is preferred over LC-MS for analysis of fatty acids as low-energy (< 100 eV) CID conditions are typical to most commercial LC-MS instruments, which result in little to no fragmentation for many fatty acids. Unsaturated fatty acids can undergo fragmentation to some extent, but the abundances of these fragments are generally low and highly sensitive instruments and methods are needed to enable reliable detection (Bollinger et al., 2013; Koch et al., 2021; Thomas et al., 2014). A possible solution to improve diagnostic fragmentation of fatty acids in LC-MS is post-column infusion of barium ions (Zehethofer et al., 2008) or derivatization (e.g., using pyrolidides or dimethyloxazolines). However, the harsh conditions used for many derivatization methods can result in unwanted oxidation, isomerization or degradation of some fatty acids (Bollinger et al., 2013).

Two dimensional LC could be another analytical improvement. Ideally, the ^{2}D column is able to separate all the unresolved analytes present in each fraction of the ^{1}D effluent based on the differences in the selectivity of the two dimensions (Stoll & Carr, 2017). As shown in Figure 10.1, 2D-LC instrumentation can be used for (i) single heartcutting 2D-LC (i.e., LC-LC; a single fraction of the ^{1}D effluent is injected into the ^{2}D column for further separation), (ii) multiple heartcutting 2D-LC (i.e., mLC-LC; single fractions from several ^{1}D peaks are transferred one at a time into the ^{2}D column for further separation), and (iii) comprehensive 2D-LC (i.e., LCxLC; the complete effluent of the ^{1}D column is transferred to the ^{2}D column) (Sandra et al., 2017; Stoll & Carr, 2017).

While (m)LC-LC is useful when analyzing a small number of target compounds in a complex matrix, LCxLC has potential to increase peak capacity in untargeted analysis (Navarro-Reig et al., 2017; Stoll & Carr, 2017). As LCxLC usually is achieved by collecting the ^{1}D effluent in two loops which are alternatively transferred to the ^{2}D column, fast ^{2}D separations (typically < 1 min) are needed to facilitate a high sampling frequency and

maintain the ^{1}D separation (Sandra et al., 2017). To obtain orthogonal 2D-LC separations, different separation mechanisms should be used in the separate dimensions. For example, usage of HILICxRPLC, but also RPLCxRPLC with mobile phases at different pH values can be used to obtain complementarity of the two separation dimensions (Foster et al., 2022; Gilar et al., 2005).

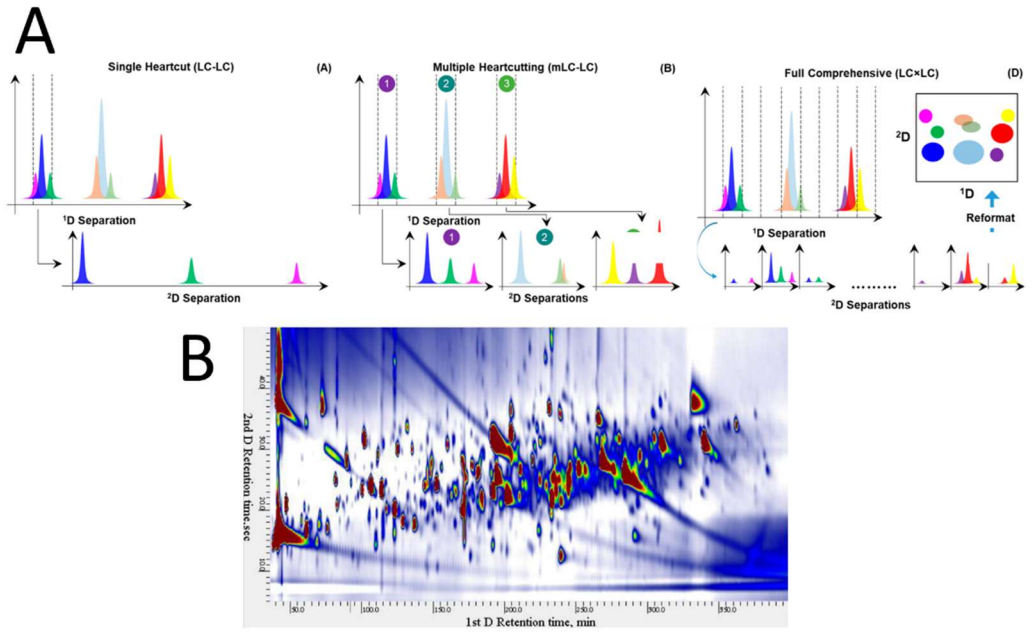

Figure 10.1 A) Different modes of two-dimensional liquid chromatography separation. Adapted from Pirok et al. (2019). **B)** Example of an LCxLC chromatogram (Zhu et al., 2020).

A downside of LCxLC is that analytes separated in the ^{1}D column get remixed prior to being sent to the ^{2}D column, resulting in a loss of resolution of the ^{1}D separation (Stoll & Carr, 2017). In addition, detection sensitivity is challenging in 2D-LC as the analyte zone eluted from the ^{1}D columns gets further diluted during the ^{2}D separation and the volume of ^{1}D effluent that will be injected into the ^{2}D column requires optimization (Stoll & Carr, 2017). Two dimensional LC comes with many analytical and bioinformatical challenges, especially when coupled to MS and/or when combined with additional separation techniques such as DTIM. While algorithms for treating 1D chromatograms are well established after many years of developed and refinement, such algorithms for processing 2D chromatograms are much younger and will benefit from further development and refinement in e.g., peak-tracking algorithms and automated feature mining (Molenaar et al., 2021, 2022; Pirok et al., 2019; Stoll & Carr, 2017).

10.2.2. Biological perspectives

10.2.2.1. Usage of multiomics

In addition to metabolomics, other -omics techniques are needed to understand the flow of information that underlies ethanol-induced hepatotoxicity and to confirm or reject generated hypotheses. Hence, next to metabolomics, genomics, transcriptomics and proteomics can be used to build a multiomics platform to enable a comprehensive understanding of molecular changes contributing to cellular response and to connect genotype to phenotype (Hasin et al., 2017). In chapter 7 and 8, several hypotheses for metabolite alterations were based on alterations in enzymatic activity after exposure to ethanol and/or TNF-α. While the effect of ethanol and/or TNF-α on enzymatic activity is well studied for several enzymes (e.g., ethanol-induced inhibition of PEMT (Lieber et al., 1994) or DGAT2 (Z. Wang et al., 2010)), the influence on many others still needs to be evaluated. Interesting enzymes for this latter evaluation include, for example, PLA2, LYPLA1 and LPCAT involved in phosphatidylcholine metabolism, PCYT2 in the CDP-ethanolamine pathway, GNMT involved in SAM metabolism, and mfn2 involved in metabolism of phosphatidylethanolamines and -cholines.

10.2.2.2. Comparison of AFLD/ASH to NAFLD/NASH

In addition to simulation of AFLD and ASH in HepaRG cells and elucidation of the metabolic fingerprint, similar experiments can be conducted simulating NALFD and NASH in order to elucidate potential discriminating biomarkers. For these latter experiments, either suspect screening can be performed on the NAFLD/NASH model to search for biomarkers elucidated in chapter 7 and 8 or an untargeted approach can be used to select discriminating markers between an AFLD/ASH and a NALFD/NASH model. Thomas Addison was the first to describe fatty liver in 1836 (Addison, 1836). His discovery was followed by several pathologists pinpointing similarities of liver histology seen in diabetic and morbidly obese individuals with those of alcoholics (Lonardo et al., 2020). In 1980, Ludwig *et al.* introduced the "term non-alcoholic steatohepatitis" to describe the progressive form of fatty liver disease histologically resembling ASH though observed in patients who denied any ethanol abuse (Lonardo et al., 2020; Ludwig et al., 1980). Schaffner and Thaler (1986) were the first to use the name "non-alcoholic fatty liver disease" in 1986 (Lonardo et al., 2020). The similarities in NALFD and AFLD were recently highlighted by Staufer *et al*. (2022), who classified nearly 30% of presumed NAFLD patients as moderate to excessive ethanol consumers by determination of EtG in hair and urine. However, histological differences between NAFLD/NASH and AFLD/NAFLD have been observed (Sakhuja, 2014). For example, fat infiltration of liver cells occurs generally at a greater degree in NAFLD/NASH compared to ALD, while inflammatory cell infiltration is more pronounced during ALD (Toshikuni et al., 2014). In

addition, there are several lesions of ALD that are not observed in NAFLD/NASH, including sclerosing hyaline necrosis (i.e., pericentral fibrosis), phlebosclerosis (i.e., fibrotic degeneration of the venous wall) and alcoholic foamy degeneration (i.e., significant microvesicular, foamy-appearing steatosis) (Brunt, 2007; Sakhuja, 2014). On the other hand, there are several biopsies of fatty liver disease for which the pathologist cannot be sure of the true etiology of liver disease, and cases in which obesity, diabetes and ethanol are all likely contributing factors (Brunt, 2007).

Despite the similar profile of NAFLD/NASH compared to AFLD/ASH, metabolomics offers the potential to elucidate discriminating biomarkers as the metabolic phenotype is a product of many interactions among a variety of factors. For example, NALFD could be induced in HepaRG cells by exposure to insulin and glucose, while NASH could be induced by additional exposure to oleic acid and palmitic acid in combination with pro-inflammatory triggers such as TNF-α (Boeckmans, 2020). Although using only TNF-α as an inflammatory trigger is interesting from a fundamental perspective, additional inflammatory triggers can be used when relevant for the pathology of interest. For example, in ASH (and NASH), additional exposure to IL-1β could be explored. In ASH, LPS-induced TLR4 activation stimulates the production of IL-1β, in addition to TNF-α (Nagy, 2015; Tilg et al., 2016). IL-1β has pleiotropic effects including induction of steatosis, involvement in hepatocyte death, and increasing the activity of pro-inflammatory monocyte chemoattractant protein-1 (MCP-1) in hepatocytes (Kawaratani et al., 2013; Nagy, 2015; Tilg et al., 2016).

10.2.2.3. *In vitro – in vivo* correlation

An important question is whether *in vitro* generated results using HepaRG cells are representative for the *in vivo* situation in humans. Kanebratt and Andersson (2008) showed that HepaRG cells are a valuable model for prediction of induction of drug-metabolizing P450 enzymes *in vivo* in humans. While the HepaRG cell line is well accepted to study disease-related mechanisms (Guguen-Guillouzo & Guillouzo, 2010; McGill et al., 2011; Tascher et al., 2019), the *in vitro – in vivo* correlation for metabolomics applications remains unexplored. The number of publicly available studies investigating metabolomics in human (N)ALFD or (N)ASH is limited.

For example, using “alcoholic fatty liver” and “metabolomics” or “lipidomics” as Mesh terms in PubMed generated 4 hits in human species. Changing “alcoholic fatty liver” to “non-alcoholic fatty liver disease” resulted in 164 hits. However, within the limited studies, consistency was observed with several HepaRG results listed in this thesis. A summary can be found in Table 10.1. For example, several studies report the accumulation of triglyceride species in liver biopsies from NAFLD and NASH patients (Gorden et al., 2015; Puri et al., 2007). Additionally, Puri *et al.* (2007) observed a

decrease of phosphatidylcholines, and an increase of diglyceride levels in the same liver biopsy samples. Concordant with the reduction of lysophosphatidylcholines in the extracellular fraction of ethanol-exposed HepaRG cells (i.e., due to increased consumption), Israelsen *et al.* (2021) observed a decrease of lysophosphatidylcholines in human hepatic venous blood after ethanol intoxication in healthy volunteers and ALD patients. Additionally, intracellular decreases of lysophosphatidylcholines, sphingomyelins and phosphatidylethanolamines were observed in NAFLD (Puri et al., 2007). Sphingomyelins were found to be downregulated in the serum of heavy drinkers (Jaremek et al., 2013). Combined HepaRG exposure to ethanol and TNF-α resulted in a stronger upregulation of triglyceride species and the number of distinctive triglyceride species increased significantly between solely ethanol exposure and combined exposure to ethanol and TNF-α. These findings are consistent with increased hepatic triglyceride production in humans after TNF-α administration (Popa et al., 2007; Sherman et al., 1988). TNF-α co-exposure also decreased intracellular phosphatidylcholines stronger than solely ethanol exposure in HepaRG cells, in line with the findings of Männistö *et al.* (2019) who saw a decrease of hepatic phosphatidylcholines in simple steatosis, which decreased further during NASH in humans. Puri *et al.* (2007) also observed a decrease of hepatic phosphatidylcholines in NASH. However, the authors observed a slightly stronger decrease in NALFD biopsies compared to NASH biopsies. These latter inconsistencies could be due to small sample sizes and/or lack of proper experimental design for human metabolomics studies. Hernández-Alvarez *et al.* (2019) discovered downregulation of mfn2 in human liver during progression from steatosis to NASH. As mfn2 is a mitochondrial membrane protein involved in transport of phosphatidylserines necessary for mitochondrial production of phosphatidylethanolamines and subsequent conversion to -cholines, its downregulation could explain decrease of hepatic phosphatidylcholines and -ethanolamines (Hernández-Alvarez et al., 2019; Ventura et al., 2022).

As mentioned earlier, EtOChoP was identified in ethanol-exposed HepaRG cells as a marker of ethanol exposure. Confirmation of the presence of EtOChoP in whole blood samples of heavy drinkers showed additional proof for the relevance of HepaRG cells as a human model organism. Recently Thiele *et al.* (2023) compared the lipid profile of liver tissue and plasma samples of 315 ALD patients in different stadia. The authors confirmed increased di- and triglycerides in liver samples of AFLD and ASH, in addition to decreased phosphatidylcholines and -ethanolamines. Sphingomyelins showed a progressive depletion in hepatic inflammation, consistent with the stronger overall downregulation of sphingomyelins in HepaRG cells when TNF-α was added, additional to ethanol. In contrast with the HepaRG results, the authors reported a progressive decrease of hepatic ceramides during inflammation. In addition, this finding was not

supported by previous literature describing upregulation of hepatic ceramides (d18:1) (Apostolopoulou et al., 2018; Jaremek et al., 2013; Longato et al., 2012; Luukkonen et al., 2016; Mühle et al., 2018; Reichel et al., 2010; L. Yang et al., 2016). However, Thiele *et al.* did not distinguish between ceramides (d18:1) and (d18:2), which were respectively up- and downregulated in HepaRG cells.

Table 10.1 Alterations in HepaRG cells exposed to ethanol or ethanol and TNF-α confirmed in literature by usage of patient samples. ALD: Alcoholic liver disease. Cer: Ceramides. DG: Diglycerides. EtOChoP: Ethylated phosphorylcholine. LPC: Lysophosphatidylcholines. (N)AFLD: (Non-)alcoholic fatty liver disease. (N)ASH: (Non-)alcoholic steatohepatitis. PC: Phosphatidylcholines. PC-O: Alkyl ether posphatidylcholines. PE: Phosphatidylethanolamines. SM: Sphingomyelins. TG: Triglycerides. TNF-α: Tumor necrosis factor alpha.

Observation	Sample type	Reference
↑TG	Liver, NAFLD, NASH	Gorden et al., 2015; Puri et al., 2007
↑DG, ↓PC	Liver, NAFLD, NASH	Puri et al., 2007
↓LPC	Hepatic venous blood after ethanol intoxication in healthy volunteers and ALD	Israelsen et al., 2021
↓LPC, ↓SM, ↓PE	Liver, NAFLD	Puri et al., 2007
↓SM	Serum, heavy drinkers	Jaremek et al., 2013
↑TG	Liver, post-TNF-α administration	Popa et al., 2007; Sherman et al., 1988
↓PC	Liver, NAFLD (↓), NASH (↓↓)	Männistö et al., 2019
↑EtOChoP	Whole blood heavy drinkers	In-house, not published
↑TG, ↑DG, ↓PC, ↓PE	Liver, AFLD, ASH	Thiele et al., 2023
↓SM	Liver, ASH	Thiele et al., 2023
↑PE	Plasma, AFLD	Thiele et al., 2023
↑Cer, ↑PC-O, ↓LPC	Plasma, ASH	Thiele et al., 2023

Concerning the plasma lipidome, Thiele *et al.* reported upregulation of phosphatidylethanolamines in AFLD, consistent with elevated secretion in ethanol-exposed HepaRG cells. However, their reported increase of lysophosphatidylcholines was in contrast to our finding of decreased lysophosphatidylcholines due to increased hepatic consumption. For ASH, increased ceramides and alkyl ether phosphatidylcholines, and decreased lysophosphatidylcholines were consistent with the findings of the extracellular metabolome of HepaRG cells after exposure to ethanol and TNF-α (i.e., increased secretion of ceramides (d18:1) and alkyl ether phosphatidylcholines, and increased consumption of lysophosphatidylcholines). However, the reliability of the data of Thiele *et al.* is questionable from an analytical perspective. Their annotations did not include confidence levels and they did not report mass errors or retention times. The authors did not mention the use of MS/MS data and as their annotations were limited to bulk names, usage of MS/MS data is rather unlikely, as fragmentation spectra generally provide information for annotation at a species level. While putative identities can be based on accurate mass searching, usage of this tool alone provides poor evidence for metabolite annotation (Domingo-Almenara et al., 2018).

Although a literature search is very useful to compare results, a full exploration of the in *vitro – in vivo* correlation of the HepaRG results requires a suspect screening using samples of patients suffering from AFLD and ASH. A collaboration with the department of gastro-enterology and hepatology of the Antwerp University Hospital was initiated to obtain liver biopsies, blood and hair samples of AFLD and ASH patients. Liver and blood samples could be used for future suspect screening. In addition, the Toxicological Centre of the University of Antwerp initiated a project to elucidate biomarkers of AFLD and ASH in hair. Ethical approval was granted by the Antwerp University Hospital (Project ID 1975 - EDGE 2067). Moreover, contracts were finalized with the biobank of the Antwerp University Hospital, a clinical study site agreement was completed and informed consent forms (ICF) and questionnaires were developed. A suspect screening of these samples can estimate the *vitro – in vivo* correlation of the HepaRG results and pinpoint metabolites that are interesting to use as biomarkers in the clinic. After selection of these biomarkers, a targeted method can be developed for quantification. The most promising biomarkers for screening or diagnosis can be elucidated using classification models to predict class membership. For example, univariate regression can be used to select the most promising biomarker according to its predictive power, while multivariate regression is useful to select a panel of discriminating biomarkers (McDermott et al., 2013). Other approaches that have led to successful biomarker identification include machine learning algorithms such as random forest (McDermott et al., 2013). As models to select biomarkers are prone to overestimation of

performance results, independent test data should be used for evaluation. While a limited number of patients samples can be sufficient to demonstrate clinical validity (i.e., to establish an association between biomarkers and the endpoint of interest), large multiple studies are needed to demonstrate clinical utility (i.e., to establish the clinical usefulness of markers; whether the use of the markers in clinical care result in improved patient outcomes) (Ou et al., 2021). Biomarker validation includes estimation of the sensitivity, specificity, positive and negative predictive value and receiver operating characteristic (ROC) curve, in an internal and external setting (Ou et al., 2021). Finding an early, sensitive and specific biomarker would allow detection before the occurrence of irreversible liver damage, allowing a correction in ethanol abuse and preventing further disease progression.

10.2.2.4. *Ethylated phosphorylcholine*

While EtOCHoP most probably does not translate into active liver disease, but rather can be used as a marker of exposure or consumption, follow-up experiments can be conducted. As the currently used targeted method is not ideal with its runtime of 26 min, method optimization should be used to obtain a faster method enabling a high throughput. Ideally RPLC methods should be explored as HILIC generally leads to broader peaks and less stable retention times, which are not ideal for a targeted method. Furthermore, the calibration range should be lowered and a full method validation should be performed. Different matrices can be explored for EtOChoP detection such as plasma/serum, urine and hair. In addition, whole blood should not be neglected. As the proof-of-concept experiment only included a limited number of samples, more samples with a wide range in blood ethanol concentration and PEth 16:0/18:1 concentration should be explored. In addition, studies can be performed to determine pharmacokinetics of EtOChoP, including the rate of formation and elimination using experiments where volunteers drink standard doses of ethanol, as self-reported ethanol use may not be accurate (Hahn et al., 2016).

REFERENCES

Aagaard, N. K., Thøgersen, T., Grøfte, T., Greisen, J., & Vilstrup, H. (2004). Alcohol Acutely Down-Regulates Urea Synthesis in Normal Men. *Alcoholism: Clinical and Experimental Research*, *28*(5), 697–701. https://doi.org/10.1097/01.ALC.0000125355.31808.DC

Abdallah, M. A., & Singal, A. K. (2020). Mitochondrial dysfunction and alcohol-associated liver disease: a novel pathway and therapeutic target. *Signal Transduction and Targeted Therapy*, *5*(1), 26. https://doi.org/10.1038/s41392-020-0128-8

Adams, J., & Ann, Q. (1993). Structure determination of sphingolipids by mass spectrometry. *Mass Spectrometry Reviews*, *12*(1), 51–85. https://doi.org/10.1002/mas.1280120103

Adams, K. J., Pratt, B., Bose, N., Dubois, L. G., St. John-Williams, L., Perrott, K. M., Ky, K., Kapahi, P., Sharma, V., Maccoss, M. J., Moseley, M. A., Colton, C. A., Maclean, B. X., Schilling, B., & Thompson, J. W. (2020). Skyline for Small Molecules: A Unifying Software Package for Quantitative Metabolomics. *Journal of Proteome Research*, *19*(4), 1447–1458. https://doi.org/10.1021/ACS.JPROTEOME.9B00640

Addison, T. (1836). Observations on fatty degeneration of the liver. *Guys Hosp Rep*, *1*(476), 485.

Addolorato, G., Leggio, L., Ferrulli, A., Cardone, S., Vonghia, L., Mirijello, A., Abenavoli, L., D'Angelo, C., Caputo, F., Zambon, A., Haber, P. S., & Gasbarrini, G. (2007). Effectiveness and safety of baclofen for maintenance of alcohol abstinence in alcohol-dependent patients with liver cirrhosis: randomised, double-blind controlled study. *Lancet*, *370*(9603), 1915–1922. https://doi.org/10.1016/S0140-6736(07)61814-5

Agilent Technologies. (2016). *Agilent 6560 Ion Mobility Q-TOF Specifications Data Sheet*. www.agilent.com/Library/usermanuals

Agilent Technologies. (2017). *Agilent 6200 Series TOF and 6500 Series Q-TOF LC/MS System Concept Guide*. https://doi.org/G3335-90193

Alonso, A., Marsal, S., & Julià, A. (2015). Analytical methods in untargeted metabolomics: State of the art in 2015. *Frontiers in Bioengineering and Biotechnology*, *3*, 23. https://doi.org/10.3389/FBIOE.2015.00023

Alseekh, S., Aharoni, A., Brotman, Y., Contrepois, K., D'Auria, J., Ewald, J., C. Ewald, J., Fraser, P. D., Giavalisco, P., Hall, R. D., Heinemann, M., Link, H., Luo, J., Neumann, S., Nielsen, J., Perez de Souza, L., Saito, K., Sauer, U., Schroeder, F. C., … Fernie, A. R. (2021). Mass spectrometry-based metabolomics: a guide for annotation, quantification and best reporting practices. *Nature Methods*, *18*(7), 747–756. https://doi.org/10.1038/s41592-021-01197-1

Alseekh, S., & Fernie, A. R. (2018). Metabolomics 20 years on: what have we learned and what hurdles remain? *Plant Journal*, *94*(6), 933–942. https://doi.org/10.1111/tpj.13950

Ankley, G. T., Bennett, R. S., Erickson, R. J., Hoff, D. J., Hornung, M. W., Johnson, R. D., Mount, D. R., Nichols, J. W., Russom, C. L., Schmieder, P. K., Serrrano, J. A., Tietge, J. E., & Villeneuve, D. L. (2010). Adverse outcome pathways: A conceptual framework to support ecotoxicology research and risk assessment. *Environmental Toxicology and Chemistry*, *29*(3), 730–741. https://doi.org/10.1002/ETC.34

Apostolopoulou, M., Gordillo, R., Koliaki, C., Gancheva, S., Jelenik, T., De Filippo, E., Herder, C., Markgraf, D., Jankowiak, F., Esposito, I., Schlensak, M., Scherer, P. E., & Roden, M. (2018). Specific Hepatic Sphingolipids Relate to Insulin Resistance, Oxidative Stress, and Inflammation in Nonalcoholic Steatohepatitis. *Diabetes Care*, *41*(6), 1235–1243. https://doi.org/10.2337/dc17-1318

Aroor, A. R., Custer, G. W., Weng, Y. I., Lee, Y. J., & Shukla, S. D. (2002). Phosphatidylethanol mimics ethanol modulation of p42/44 mitogen-activated protein kinase signalling in hepatocytes. *Alcohol and Alcoholism*, *37*(6), 534–539. https://doi.org/10.1093/ALCALC/37.6.534

Arteel, G. E. (2010). Animal Models of Alcoholic Liver Disease. *Digestive Diseases*, *28*(6), 729–736. https://doi.org/10.1159/000324280

Aske, K. C., & Waugh, C. A. (2017). Expanding the 3R principles: More rigour and transparency in research using animals. *EMBO Reports*, *18*(9), 1490–1492. https://doi.org/10.15252/EMBR.201744428

Asrani, S. K., Devarbhavi, H., Eaton, J., & Kamath, P. S. (2019). Burden of liver diseases in the world. *Journal of Hepatology*, *70*(1), 151–171. https://doi.org/10.1016/J.JHEP.2018.09.014

Ates, G., Vanhaecke, T., Rogiers, V., & Rodrigues, R. M. (2017). Assaying Cellular Viability Using the Neutral

Red Uptake Assay. In D. F. Gilbert & O. Friedrich (Eds.), *Methods in Molecular Biology, Cell Viability Assays* (pp. 19–26). Humana Press, New York, NY. https://doi.org/10.1007/978-1-4939-6960-9_2

Avila, M. A., García-Trevijano, E. R., Lu, S. C., Corrales, F. J., & Mato, J. M. (2004). Methylthioadenosine. *The International Journal of Biochemistry & Cell Biology*, *36*(11), 2125–2130. https://doi.org/10.1016/J.BIOCEL.2003.11.016

Aw, T. Y., & Jones, D. P. (1983). Intracellular inhibition of UDP-glucose dehydrogenase during ethanol oxidation. *Chemico-Biological Interactions*, *43*(3), 283–288. https://doi.org/10.1016/0009-2797(83)90112-6

Bahureksa, W., Borch, T., Young, R. B., Weisbrod, C. R., Blakney, G. T., & McKenna, A. M. (2022). Improved Dynamic Range, Resolving Power, and Sensitivity Achievable with FT-ICR Mass Spectrometry at 21 T Reveals the Hidden Complexity of Natural Organic Matter. *Analytical Chemistry*, *94*(32), 11382–11389. https://doi.org/10.1021/acs.analchem.2c02377

Bailey, S. M., Patel, V. B., Young, T. A., Asayama, K., & Cunningham, C. C. (2001). Chronic Ethanol Consumption Alters the Glutathione/Glutathione Peroxidase-1 System and Protein Oxidation Status in Rat Liver. *Alcoholism: Clinical and Experimental Research*, *25*(5), 726–733. https://doi.org/10.1111/J.1530-0277.2001.TB02273.X

Baker, E. S., Burnum-Johnson, K. E., Jacobs, J. M., Diamond, D. L., Brown, R. N., Ibrahim, Y. M., Orton, D. J., Piehowski, P. D., Purdy, D. E., Moore, R. J., Danielson, W. F., Monroe, M. E., Crowell, K. L., Slysz, G. W., Gritsenko, M. A., Sandoval, J. D., LaMarche, B. L., Matzke, M. M., Webb-Robertson, B. J. M., … Smith, R. D. (2014). Advancing the high throughput identification of liver fibrosis protein signatures using multiplexed ion mobility spectrometry. *Molecular and Cellular Proteomics*, *13*(4), 1119–1127. https://doi.org/10.1074/mcp.M113.034595

Balcke, G. U., Kolle, S. N., Kamp, H., Bethan, B., Looser, R., Wagner, S., Landsiedel, R., & van Ravenzwaay, B. (2011). Linking energy metabolism to dysfunctions in mitochondrial respiration – A metabolomics in vitro approach. *Toxicology Letters*, *203*(3), 200–209. https://doi.org/10.1016/j.toxlet.2011.03.013

Banerjee, S., & Mazumdar, S. (2012). Electrospray Ionization Mass Spectrometry: A Technique to Access the Information beyond the Molecular Weight of the Analyte. *International Journal of Analytical Chemistry*, *2012*, 282574. https://doi.org/10.1155/2012/282574

Baraona, E., & Lieber, C. S. (1979). Effects of ethanol on lipid metabolism. *Journal Lipid Research*, *20*(3), 289–315. https://doi.org/10.1016/S0022-2275(20)40613-3

Barnes, S., Benton, H. P., Casazza, K., Cooper, S. J., Cui, X., Du, X., Engler, J., Kabarowski, J. H., Li, S., Pathmasiri, W., Prasain, J. K., Renfrow, M. B., & Tiwari, H. K. (2016a). Training in metabolomics research. I. Designing the experiment, collecting and extracting samples and generating metabolomics data. *Journal of Mass Spectrometry*, *51*(7), 461–475. https://doi.org/10.1002/jms.3782

Barnes, S., Benton, H. P., Casazza, K., Cooper, S. J., Cui, X., Du, X., Engler, J., Kabarowski, J. H., Li, S., Pathmasiri, W., Prasain, J. K., Renfrow, M. B., & Tiwari, H. K. (2016b). Training in metabolomics research. II. Processing and statistical analysis of metabolomics data, metabolite identification, pathway analysis, applications of metabolomics and its future. *Journal of Mass Spectrometry : JMS*, *51*(8), 535–548. https://doi.org/10.1002/jms.3780

Baykara, B., Mıcılı, S. C., Tugyan, K., Tekmen, I., Bagriyanik, H., Sonmez, U., Sonmez, A., Oktay, G., Yener, N., & Ozbal, S. (2012). The protective effects of carnosine in alcohol-induced hepatic injury in rats. *Toxicology and Industrial Health*, *30*(1), 25–32. https://doi.org/10.1177/0748233712446722

Beatriz, M. G., Morales, J. M., Rodrigo, J. M., Del Olmo, J., Serra, M. A., Ferrández, A., Celda, B., & Monleón, D. (2011). Metabolic profile of chronic liver disease by NMR spectroscopy of human biopsies. *International Journal of Molecular Medicine*, *27*(1), 111–117. https://doi.org/10.3892/IJMM.2010.563

Beger, R. D., Dunn, W. B., Bandukwala, A., Bethan, B., Broadhurst, D., Clish, C. B., Dasari, S., Derr, L., Evans, A., Fischer, S., Flynn, T., Hartung, T., Herrington, D., Higashi, R., Hsu, P.-C., Jones, C., Kachman, M., Karuso, H., Kruppa, G., … Zanetti, K. A. (2019). Towards quality assurance and quality control in untargeted metabolomics studies. *Metabolomics*, *15*(1), 1–5. https://doi.org/10.1007/S11306-018-1460-7

Beirnaert, C., Cuykx, M., & Bijtebier, S. (2019). *MetaboMeeseeks: Helper functions for metabolomics*

analysis. https://github.com/Beirnaert/MetaboMeeseeks/

Beirnaert, C., Peeters, L., Meysman, P., Bittremieux, W., Foubert, K., Custers, D., van der Auwera, A., Cuykx, M., Pieters, L., Covaci, A., & Laukens, K. (2019). Using expert driven machine learning to enhance dynamic metabolomics data analysis. *Metabolites*, *9*(3), 1–13. https://doi.org/10.3390/metabo9030054

Bellentani, S., & Tiribelli, C. (2001). The spectrum of liver disease in the general population: lesson from the Dionysos study. *Journal of Hepatology*, *35*(4), 531–537. https://doi.org/10.1016/S0168-8278(01)00151-9

Benito, S., Sánchez-Ortega, A., Unceta, N., Andrade, F., Aldámiz-Echevarria, L., Goicolea, M. A., & Barrio, R. J. (2018). Untargeted metabolomics for plasma biomarker discovery for early chronic kidney disease diagnosis in pediatric patients using LC-QTOF-MS. *Analyst*, *143*(18), 4448–4458. https://doi.org/10.1039/C8AN00864G

Benjamini, Y., & Hochberg, Y. (1995). Controlling the False Discovery Rate: A Practical and Powerful Approach to Multiple Testing. *Journal of the Royal Statistical Society: Series B (Methodological)*, *57*(1), 289–300. https://doi.org/10.1111/J.2517-6161.1995.TB02031.X

Bernardo-bermejo, S., Sánchez-lópez, E., Tan, L., Benito-martínez, S., Jiang, Z., Castro-puyana, M., Lucio-cazaña, F. J., & Marina, M. L. (2021). Exploratory metabolomic analysis based on reversed-phase liquid chromatography–mass spectrometry to study an in vitro model of hypoxia-induced metabolic alterations in hk-2 cells. *International Journal of Molecular Sciences*, *22*(14). https://doi.org/10.3390/IJMS22147399

Bertola, A., Mathews, S., Ki, S. H., Wang, H., & Gao, B. (2013). Mouse model of chronic and binge ethanol feeding (the NIAAA model). *Nature Protocols*, *8*(3), 627–637. https://doi.org/10.1038/NPROT.2013.032

Bilbao, A., Gibbons, B. C., Stow, S. M., Kyle, J. E., Bloodsworth, K. J., Payne, S. H., Smith, R. D., Ibrahim, Y. M., Baker, E. S., & Fjeldsted, J. C. (2021). A Preprocessing Tool for Enhanced Ion Mobility-Mass Spectrometry-Based Omics Workflows. *Journal of Proteome Research*, *21*(3), 798–807. https://doi.org/10.1021/ACS.JPROTEOME.1C00425

Bishop, M., Fody, E., & Schoeff, L. (2017). *Clinical Chemistry: Principles, Techniques, Correlations* (8th ed.). Wolters Kluwer, Philadelphia.

Blaženović, I., Shen, T., Mehta, S. S., Kind, T., Ji, J., Piparo, M., Cacciola, F., Mondello, L., & Fiehn, O. (2018). Increasing Compound Identification Rates in Untargeted Lipidomics Research with Liquid Chromatography Drift Time-Ion Mobility Mass Spectrometry. *Analytical Chemistry*, *90*(18), 10758–10764. https://doi.org/10.1021/acs.analchem.8b01527

Bligh, E. G., & Dyer, W. J. (1959). A rapid method of total lipid extraction and purification. *Canadian Journal of Biochemistry and Physiology*, *37*(8), 911–917. https://doi.org/10.1139/O59-099

Boeckmans, J. (2020). *Development and characterization of a human stem cell-based in vitro model for anti-NASH drug testing*. Vrije Universiteit Brussel.

Boeckmans, J., Buyl, K., Natale, A., Vandenbempt, V., Branson, S., De Boe, V., Rogiers, V., De Kock, J., Rodrigues, R. M., & Vanhaecke, T. (2019). Elafibranor restricts lipogenic and inflammatory responses in a human skin stem cell-derived model of NASH. *Pharmacological Research*, *144*, 377–389. https://doi.org/10.1016/J.PHRS.2019.04.016

Boeckmans, J., Natale, A., Rombaut, M., Buyl, K., Vanhaecke, T., Rogiers, V., Rodrigues, R. M., & De Kock, J. (2020). Flow cytometric quantification of neutral lipids in a human skin stem cell-derived model of NASH. *MethodsX*, *7*, 101068. https://doi.org/10.1016/J.MEX.2020.101068

Bohm, M. K., Liu, Y., Esser, M. B., Mesnick, J. B., Lu, H., Pan, Y., & Greenlund, K. J. (2021). Binge Drinking Among Adults, by Select Characteristics and State-United States, 2018. *Morbidity and Mortality Weekly Report*, *70*(41), 1441–1446. https://doi.org/10.15585/mmwr.mm7041a2

Bollinger, J. G., Rohan, G., Sadilek, M., & Gelb, M. H. (2013). LC/ESI-MS/MS detection of FAs by charge reversal derivatization with more than four orders of magnitude improvement in sensitivity. *Journal of Lipid Research*, *54*(12), 3523–3530. https://doi.org/10.1194/jlr.D040782

Brandon-Warner, E., Schrum, L. W., Schmidt, C. M., & McKillop, I. H. (2012). Rodent Models of Alcoholic Liver Disease: Of Mice and Men. *Alcohol*, *46*(8), 715–725. https://doi.org/10.1016/J.ALCOHOL.2012.08.004

Bravo-Veyrat, S., & Hopfgartner, G. (2022). Mass spectrometry based high-throughput bioanalysis of low molecular weight compounds: are we ready to support personalized medicine? *Analytical and Bioanalytical Chemistry*, *414*(1), 181–192. https://doi.org/10.1007/S00216-021-03583-2

Broadhurst, D., Goodacre, R., Reinke, S. N., Kuligowski, J., Wilson, I. D., Lewis, M. R., & Dunn, W. B. (2018). Guidelines and considerations for the use of system suitability and quality control samples in mass spectrometry assays applied in untargeted clinical metabolomic studies. *Metabolomics*, *14*(6), 72. https://doi.org/10.1007/s11306-018-1367-3

Bruce, S. J., Tavazzi, I., Parisod, V., Rezzi, S., Kochhar, S., & Guy, P. A. (2009). Investigation of human blood plasma sample preparation for performing metabolomics using ultrahigh performance liquid chromatography/mass spectrometry. *Analytical Chemistry*, *81*(9), 3285–3296. https://doi.org/10.1021/ac8024569

Brunt, E. M. (2007). Pathology of fatty liver disease. *Modern Pathology*, *20*(1), S40–S48. https://doi.org/10.1038/modpathol.3800680

Brunt, E. M., Neuschwander-Tetri, B. A., Oliver, D., Wehmeier, K. R., & Bacon, B. R. (2004). Nonalcoholic steatohepatitis: Histologic features and clinical correlations with 30 blinded biopsy specimens. *Human Pathology*, *35*(9), 1070–1082. https://doi.org/10.1016/j.humpath.2004.04.017

Brusilow, S. W. (1991). Phenylacetylglutamine May Replace Urea as a Vehicle for Waste Nitrogen Excretion. *Pediatric Research*, *29*(2), 147–150. https://doi.org/10.1203/00006450-199102000-00009

Burnette, E. M., Nieto, S. J., Grodin, E. N., Meredith, L. R., Hurley, B., Miotto, K., Gillis, A. J., & Ray, L. A. (2022). Novel Agents for the Pharmacological Treatment of Alcohol Use Disorder. *Drugs*, *82*(3), 251–274. https://doi.org/10.1007/s40265-021-01670-3

Burnum-Johnson, K. E., Zheng, X., Dodds, J. N., Ash, J., Fourches, D., Nicora, C. D., Wendler, J. P., Metz, T. O., Waters, K. M., Jansson, J. K., Smith, R. D., & Baker, E. S. (2019). Ion mobility spectrometry and the omics: Distinguishing isomers, molecular classes and contaminant ions in complex samples. *TrAC - Trends in Analytical Chemistry*, *116*, 292–299. https://doi.org/10.1016/j.trac.2019.04.022

Buszewski, B., & Noga, S. (2012). Hydrophilic interaction liquid chromatography (HILIC) - a powerful separation technique. *Analytical and Bioanalytical Chemistry*, *402*(1), 231–247. https://doi.org/10.1007/s00216-011-5308-5

Cahill, A., Cunningham, C. C., Adachi, M., Ishii, H., Bailey, S. M., Fromenty, B., & Davies, A. (2002). Effects of Alcohol and Oxidative Stress on Liver Pathology: The Role of the Mitochondrion. *Alcoholism: Clinical and Experimental Research*, *26*(6), 907–915. https://doi.org/10.1111/J.1530-0277.2002.TB02621.X

Cajka, T., & Fiehn, O. (2014). Comprehensive analysis of lipids in biological systems by liquid chromatography-mass spectrometry. *TrAC Trends in Analytical Chemistry*, *61*, 192–206. https://doi.org/10.1016/J.TRAC.2014.04.017

Cajka, T., Smilowitz, J. T., & Fiehn, O. (2017). Validating Quantitative Untargeted Lipidomics Across Nine Liquid Chromatography–High-Resolution Mass Spectrometry Platforms. *Analytical Chemistry*, *89*(22), 12360–12368. https://doi.org/10.1021/acs.analchem.7b03404

Callans, D. J., Wacker, L. S., & Mitchell, M. C. (1987). Effects of ethanol feeding and withdrawal on plasma glutathione elimination in the rat. *Hepatology*, *7*(3), 496–501. https://doi.org/10.1002/HEP.1840070314

Calzada, E., Onguka, O., & Claypool, S. M. (2016). Phosphatidylethanolamine Metabolism in Health and Disease. *International Review of Cell and Molecular Biology*, *321*, 29–88. https://doi.org/10.1016/BS.IRCMB.2015.10.001

Candioti, L. V., De Zan, M. M., Cámara, M. S., & Goicoechea, H. C. (2014). Experimental design and multiple response optimization. Using the desirability function in analytical methods development. *Talanta*, *124*, 123–138. https://doi.org/10.1016/j.talanta.2014.01.034

Cao, W., Cheng, S., Yang, J., Feng, J., Zhang, W., Li, Z., Chen, Q., Xia, Y., Ouyang, Z., & Ma, X. (2020). Large-scale lipid analysis with C=C location and sn-position isomer resolving power. *Nature Communications*, *11*(1), 1–11. https://doi.org/10.1038/s41467-019-14180-4

Causon, T. J., & Hann, S. (2015). Theoretical evaluation of peak capacity improvements by use of liquid chromatography combined with drift tube ion mobility-mass spectrometry. *Journal of Chromatography A*, *1416*, 47–56. https://doi.org/10.1016/j.chroma.2015.09.009

Causon, T. J., Si-Hung, L., Newton, K., Kurulugama, R. T., Fjeldsted, J., & Hann, S. (2019). Fundamental study

of ion trapping and multiplexing using drift tube-ion mobility time-of-flight mass spectrometry for non-targeted metabolomics. *Analytical and Bioanalytical Chemistry*, *411*(24), 6265–6274. https://doi.org/10.1007/s00216-019-02021-8

Cederbaum, A. I. (2010). Hepatoprotective effects of S-adenosyl-L-methionine against alcohol- and cytochrome P450 2E1-induced liver injury. *World Journal of Gastroenterology*, *16*(11), 1366–1376. https://doi.org/10.3748/WJG.V16.I11.1366

Celma, A., Sancho, J. V., Schymanski, E. L., Fabregat-Safont, D., Ibáñez, M., Goshawk, J., Barknowitz, G., Hernández, F., & Bijlsma, L. (2020). Improving Target and Suspect Screening High-Resolution Mass Spectrometry Workflows in Environmental Analysis by Ion Mobility Separation. *Environmental Science & Technology*, *54*(23), 15120–15131. https://doi.org/10.1021/acs.est.0c05713

Chacko, K. R., & Reinus, J. (2016). Spectrum of Alcoholic Liver Disease. *Clinics in Liver Disease*, *20*(3), 419–427. https://doi.org/10.1016/J.CLD.2016.02.002

Chen, Y., Xu, J., Zhang, R., & Abliz, Z. (2016). Methods used to increase the comprehensive coverage of urinary and plasma metabolomes by MS. *Bioanalysis*, *8*(9), 981–997. https://doi.org/10.4155/bio-2015-0010

Chirita, R.-I., West, C., Finaru, A.-L., & Elfakir, C. (2010). Approach to hydrophilic interaction chromatography column selection: Application to neurotransmitters analysis. *Journal of Chromatography A*, *1217*(18), 3091–3104. https://doi.org/10.1016/j.chroma.2010.03.001

Clowers, B. H., Ibrahim, Y. M., Prior, D. C., Danielson, W. F., Belov, M. E., & Smith, R. D. (2008). Enhanced ion utilization efficiency using an electrodynamic ion funnel trap as an injection mechanism for ion mobility spectrometry. *Analytical Chemistry*, *80*(3), 612–623. https://doi.org/10.1021/ac701648p

Clugston, R. D., Gao, M. A., & Blaner, W. S. (2017). The hepatic lipidome: a gateway to understanding the pathogenesis of alcohol-induced fatty liver. *Current Molecular Pharmacology*, *10*(3), 195–206. https://doi.org/10.2174/1874467208666150817111419

Colsch, B., Fenaille, F., Warnet, A., Junot, C., & Tabet, J. C. (2017). Mechanisms governing the fragmentation of glycerophospholipids containing choline and ethanolamine polar head groups. *European Journal of Mass Spectrometry*, *23*(6), 427–444. https://doi.org/10.1177/1469066717731668

Copeland, S., Shaw Warren, H., Lowry, S. F., Galvano, S. E., & Remick, D. (2005). Acute inflammatory response to endotoxin in mice and humans. *Clinical and Diagnostic Laboratory Immunology*, *12*(1), 60–67. https://doi.org/10.1128/CDLI.12.1.60-67.2005

Corradi, M. P. F., de Haan, A. M., Staumont, B., Piersma, A. H., Geris, L., Pieters, R. H. H., Krul, C. A. M., & Teunis, M. A. T. (2022). Natural language processing in toxicology: Delineating adverse outcome pathways and guiding the application of new approach methodologies. *Biomaterials and Biosystems*, *7*, 100061. https://doi.org/10.1016/j.bbiosy.2022.100061

Criscuolo, A., Zeller, M., & Fedorova, M. (2020). Evaluation of Lipid In-Source Fragmentation on Different Orbitrap-based Mass Spectrometers. *Journal of the American Society for Mass Spectrometry*, *31*(2), 463–466. https://doi.org/10.1021/jasms.9b00061

Cuykx, M., Claes, L., Rodrigues, R. M., Vanhaecke, T., & Covaci, A. (2018). Metabolomics profiling of steatosis progression in HepaRG® cells using sodium valproate. *Toxicology Letters*, *286*, 22–30. https://doi.org/10.1016/j.toxlet.2017.12.015

Cuykx, M., Mortelé, O., Rodrigues, R. M., Vanhaecke, T., & Covaci, A. (2017). Optimisation of: In vitro sample preparation for LC-MS metabolomics applications on HepaRG cell cultures. *Analytical Methods*, *9*(24), 3704–3712. https://doi.org/10.1039/c7ay00573c

Cuykx, M., Negreira, N., Beirnaert, C., Van den Eede, N., Rodrigues, R., Vanhaecke, T., Laukens, K., & Covaci, A. (2017). Tailored liquid chromatography-mass spectrometry analysis improves the coverage of the intracellular metabolome of HepaRG cells. *Journal of Chromatography A*, *1487*, 168–178. https://doi.org/10.1016/j.chroma.2017.01.050

Cuykx, M., Rodrigues, R. M., Laukens, K., Vanhaecke, T., & Covaci, A. (2018). In vitro assessment of hepatotoxicity by metabolomics: a review. *Archives of Toxicology*, *92*(10), 3007–3029. https://doi.org/10.1007/s00204-018-2286-9

da Silva, K. M., Iturrospe, E., Bars, C., Knapen, D., Van Cruchten, S., Covaci, A., & van Nuijs, A. L. N. (2021). Mass Spectrometry-Based Zebrafish Toxicometabolomics: A Review of Analytical and Data Quality Challenges. *Metabolites*, *11*(9), 635. https://doi.org/10.3390/metabo11090635

da Silva, K. M., Iturrospe, E., Heyrman, J., Koelmel, J. P., Cuykx, M., Vanhaecke, T., Covaci, A., & van Nuijs, A. L. N. (2021). Optimization of a liquid chromatography-ion mobility-high resolution mass spectrometry platform for untargeted lipidomic and application to HepaRG cell extracts. *Talanta*, *235*, 122808. https://doi.org/10.1016/j.talanta.2021.122808

da Silva, K. M., Iturrospe, E., van den Boom, R., van de Lavoir, M., Robeyns, R., Vergauwen, L., Knapen, D., Cuykx, M., Covaci, A., & van Nuijs, A. L. N. (2022). Lipidomics profiling of zebrafish liver through untargeted liquid chromatography-high resolution mass spectrometry. *Journal of Separation Science*, *45*, 2935–2945. https://doi.org/10.1002/jssc.202200214

da Silva, K. M., van de Lavoir, M., Robeyns, R., Iturrospe, E., Verheggen, L., Covaci, A., & van Nuijs, A. L. N. (2022). Guidelines and considerations for building multidimensional libraries for untargeted MS-based metabolomics. *Metabolomics*, *19*(1), 1–15. https://doi.org/10.1007/S11306-022-01965-W

Das, S., Hajnóczky, N., Antony, A. N., Csordás, G., Gaspers, L. D., Clemens, D. L., Hoek, J. B., & Hajnóczky, G. (2012). Mitochondrial morphology and dynamics in hepatocytes from normal and ethanol-fed rats. *Pflügers Archiv - European Journal of Physiology*, *464*(1), 101–109. https://doi.org/10.1007/s00424-012-1100-4

de Wit, M., Jones, D. G., Sessler, C. N., Zilberberg, M. D., & Weaver, M. F. (2010). Alcohol-Use Disorders in the Critically Ill Patient. *Chest*, *138*(4), 994–1003. https://doi.org/10.1378/chest.09-1425

Dean, J. M., & Lodhi, I. J. (2018). Structural and functional roles of ether lipids. *Protein & Cell*, *9*(2), 196–206. https://doi.org/10.1007/S13238-017-0423-5

DeCarli, L. M., & Lieber, C. S. (1967). Fatty Liver in the Rat after Prolonged Intake of Ethanol with a Nutritionally Adequate New Liquid Diet. *The Journal of Nutrition*, *91*(3), 331–336. https://doi.org/10.1093/JN/91.3_SUPPL.331

DeFelice, B. C., Mehta, S. S., Samra, S., Čajka, T., Wancewicz, B., Fahrmann, J. F., & Fiehn, O. (2017). Mass Spectral Feature List Optimizer (MS-FLO): A Tool To Minimize False Positive Peak Reports in Untargeted Liquid Chromatography–Mass Spectroscopy (LC-MS) Data Processing. *Analytical Chemistry*, *89*(6), 3250–3255. https://doi.org/10.1021/acs.analchem.6b04372

Demelenne, A., Nys, G., Nix, C., Fjeldsted, J. C., Crommen, J., & Fillet, M. (2022). Separation of phosphorothioated oligonucleotide diastereomers using multiplexed drift tube ion mobility mass spectrometry. *Analytica Chimica Acta*, *1191*, 339297. https://doi.org/10.1016/J.ACA.2021.339297

Derringer, G., & Suich, R. (1980). Simultaneous Optimization of Several Response Variables. *Journal of Quality Technology*, *12*(4), 214–219. https://doi.org/10.1080/00224065.1980.11980968

Desmet, G., Clicq, D., & Gzil, P. (2005). Geometry-Independent Plate Height Representation Methods for the Direct Comparison of the Kinetic Performance of LC Supports with a Different Size or Morphology. *Analytical Chemistry*, *77*(13), 4058–4070. https://doi.org/10.1021/ac050160z

Dettmer, K., Vogl, F. C., Ritter, A. P., Zhu, W., Nürnberger, N., Kreutz, M., Oefner, P. J., Gronwald, W., & Gottfried, E. (2013). Distinct metabolic differences between various human cancer and primary cells. *Electrophoresis*, *34*(19), 2836–2847. https://doi.org/10.1002/elps.201300228

Di Guida, R., Engel, J., Allwood, J. W., Weber, R. J. M., Jones, M. R., Sommer, U., Viant, M. R., & Dunn, W. B. (2016). Non-targeted UHPLC-MS metabolomic data processing methods: a comparative investigation of normalisation, missing value imputation, transformation and scaling. *Metabolomics*, *12*(5), 1–14. https://doi.org/10.1007/s11306-016-1030-9

Dif, N., Euthine, V., Gonnet, E., Laville, M., Vidal, H., & Lefai, E. (2006). Insulin activates human sterol-regulatory-element-binding protein-1c (SREBP-1c) promoter through SRE motifs. *Biochemical Journal*, *400*(1), 179–188. https://doi.org/10.1042/BJ20060499

Dilley, J. E., Nicholson, E. R., Fischer, S. M., Zimmer, R., & Froehlich, J. C. (2018). Alcohol Drinking and Blood Alcohol Concentration Revisited. *Alcoholism, Clinical and Experimental Research*, *42*(2), 260–269. https://doi.org/10.1111/ACER.13549

Dillon, W. R., & Goldstein, M. (1984). Multivariate analysis : methods and applications. In *Wiley series in probability and mathematical statistics. Applied probability and statistics*. Wiley, New York, NY. https://doi.org/ISBN: 0471083178

Dinh, N. P., Jonsson, T., & Irgum, K. (2011). Probing the interaction mode in hydrophilic interaction chromatography. *Journal of Chromatography A*, *1218*(35), 5880–5891. https://doi.org/10.1016/j.chroma.2011.06.037

Djoumbou Feunang, Y., Eisner, R., Knox, C., Chepelev, L., Hastings, J., Owen, G., Fahy, E., Steinbeck, C., Subramanian, S., Bolton, E., Greiner, R., & Wishart, D. S. (2016). ClassyFire: automated chemical classification with a comprehensive, computable taxonomy. *Journal of Cheminformatics*, *8*(1), 1–20. https://doi.org/10.1186/s13321-016-0174-y

Domingo-Almenara, X., Montenegro-Burke, J. R., Benton, H. P., & Siuzdak, G. (2018). Annotation: A Computational Solution for Streamlining Metabolomics Analysis. *Analytical Chemistry*, *90*(1), 480–489. https://doi.org/10.1021/acs.analchem.7b03929

Domon, B., & Costello, C. E. (1988). Structure elucidation of glycosphingolipids and gangliosides using high-performance tandem mass spectrometry. *Biochemistry*, *27*(5), 1534–1543. https://doi.org/10.1021/bi00405a021

Dührkop, K., Fleischauer, M., Ludwig, M., Aksenov, A. A., Melnik, A. V, Meusel, M., Dorrestein, P. C., Rousu, J., & Böcker, S. (2019). SIRIUS 4: a rapid tool for turning tandem mass spectra into metabolite structure information. *Nature Methods*, *16*(4), 299–302. https://doi.org/10.1038/s41592-019-0344-8

Emwas, A. H., Szczepski, K., Al-Younis, I., Lachowicz, J. I., & Jaremko, M. (2022). Fluxomics - New Metabolomics Approaches to Monitor Metabolic Pathways. *Frontiers in Pharmacology*, *13*, 805782. https://doi.org/10.3389/FPHAR.2022.805782

Endo, M., Masaki, T., Seike, M., & Yoshimatsu, H. (2007). TNF-α Induces Hepatic Steatosis in Mice by Enhancing Gene Expression of Sterol Regulatory Element Binding Protein-1c (SREBP-1c). *Experimental Biology and Medicine*, *232*(5), 614–621. https://doi.org/10.3181/00379727-232-2320614

Escher, S. E., Aguayo-Orozco, A., Benfenati, E., Bitsch, A., Braunbeck, T., Brotzmann, K., Bois, F., van der Burg, B., Castel, J., Exner, T., Gadaleta, D., Gardner, I., Goldmann, D., Hatley, O., Golbamaki, N., Graepel, R., Jennings, P., Limonciel, A., Long, A., … Fisher, C. (2022). Integrate mechanistic evidence from new approach methodologies (NAMs) into a read-across assessment to characterise trends in shared mode of action. *Toxicology in Vitro*, *79*, 105269. https://doi.org/10.1016/j.tiv.2021.105269

European Association for the Study of the Liver. (2018). EASL Clinical Practice Guidelines: Management of alcohol-related liver disease. *Journal of Hepatology*, *69*(1), 154–181. https://doi.org/10.1016/J.JHEP.2018.03.018

European Commission. (2021). *Food-Based Dietary Guidelines in Europe - table 17 | Knowledge for policy*. https://knowledge4policy.ec.europa.eu

European Medicines Agency, E. M. A. (2022). *ICH guideline M10 on bioanalytical method validation and study sample analysis*. https://www.ema.europa.eu

Evans, A. M., O'Donovan, C., Playdon, M., Beecher, C., Beger, R. D., Bowden, J. A., Broadhurst, D., Clish, C. B., Dasari, S., Dunn, W. B., Griffin, J. L., Hartung, T., Hsu, P. C., Huan, T., Jans, J., Jones, C. M., Kachman, M., Kleensang, A., Lewis, M. R., … Vuckovic, D. (2020). Dissemination and analysis of the quality assurance (QA) and quality control (QC) practices of LC–MS based untargeted metabolomics practitioners. *Metabolomics*, *16*(10), 113. https://doi.org/10.1007/s11306-020-01728-5

Faber, J., & Fonseca, L. M. (2014). How sample size influences research outcomes. *Dental Press Journal of Orthodontics*, *19*(4), 27–29. https://doi.org/10.1590/2176-9451.19.4.027-029.ebo

Fahy, E., Cotter, D., Sud, M., & Subramaniam, S. (2011). Lipid classification, structures and tools. *Biochimica et Biophysica Acta*, *1811*(11), 637–647. https://doi.org/10.1016/j.bbalip.2011.06.009

Fernández-Checa, J. C., Kaplowitz, N., García-Ruiz, C., Colell, A., Miranda, M., Marí, M., Ardite, E., & Morales, A. (1997). GSH transport in mitochondria: defense against TNF-induced oxidative stress and alcohol-induced defect. *American Journal of Physiology-Gastrointestinal and Liver Physiology*, *273*(1), G7–G17. https://doi.org/10.1152/AJPGI.1997.273.1.G7

Fernández-Peralbo, M. A., & Luque de Castro, M. D. (2012). Preparation of urine samples prior to targeted or untargeted metabolomics mass-spectrometry analysis. *TrAC Trends in Analytical Chemistry*, *41*, 75–85. https://doi.org/10.1016/j.trac.2012.08.011

Fiehn Lab. (2020). *Mass Spectrometry Adduct Calculator*. https://fiehnlab.ucdavis.edu

Fiehn, O. (2016). Metabolomics by gas chromatography-mass spectrometry: Combined targeted and untargeted profiling. *Current Protocols in Molecular Biology*, *114*, 30.4.1-30.4.32. https://doi.org/10.1002/0471142727.mb3004s114

Fjeldsted, J. C. (2016). Advances in Time-of-Flight Mass Spectrometry. In S. Pérez, P. Eichhorn, & D. Barceló (Eds.), *Comprehensive Analytical Chemistry* (Vol. 71, pp. 19–49). Elsevier. https://doi.org/10.1016/BS.COAC.2016.01.002

Foster, S. W., Parker, D., Kurre, S., Boughton, J., Stoll, D. R., & Grinias, J. P. (2022). A review of two-dimensional liquid chromatography approaches using parallel column arrays in the second dimension. *Analytica Chimica Acta*, *1228*, 340300. https://doi.org/10.1016/j.aca.2022.340300

Francque, S., & Vonghia, L. (2017). The future of diagnosing NASH - could a simple blood test be the key? *Expert Review of Gastroenterology & Hepatology*, *11*(11), 995–997. https://doi.org/10.1080/17474124.2017.1374851

Galli, A., Pinaire, J., Fischer, M., Dorris, R., & Crabb, D. W. (2001). The Transcriptional and DNA Binding Activity of Peroxisome Proliferator-activated Receptor α Is Inhibited by Ethanol Metabolism. *Journal of Biological Chemistry*, *276*(1), 68–75. https://doi.org/10.1074/jbc.m008791200

Ganesan, M., Feng, D., Barton, R. W., Thomes, P. G., McVicker, B. L., Tuma, D. J., Osna, N. A., & Kharbanda, K. K. (2016). Creatine Supplementation Does Not Prevent the Development of Alcoholic Steatosis. *Alcoholism, Clinical and Experimental Research*, *40*(11), 2312–2319. https://doi.org/10.1111/ACER.13214

Gao, B., & Bataller, R. (2011). Alcoholic Liver Disease: Pathogenesis and New Therapeutic Targets. *Gastroenterology*, *141*(5), 1572–1585. https://doi.org/10.1053/J.GASTRO.2011.09.002

Gao, B., Xu, M. J., Bertola, A., Wang, H., Zhou, Z., & Liangpunsakul, S. (2017). Animal Models of Alcoholic Liver Disease: Pathogenesis and Clinical Relevance. *Gene Expression*, *17*(3), 173–186. https://doi.org/10.3727/105221617X695519

García-Reyes, J. F., Moreno-González, D., Nortes-Méndez, R., Gilbert-López, B., & Molina Díaz, A. (2017). HRMS: Hardware and Software. In R. Romero-González & A. G. Frenich (Eds.), *Applications in High Resolution Mass Spectrometry: Food Safety and Pesticide Residue Analysis* (pp. 15–57). Elsevier. https://doi.org/10.1016/B978-0-12-809464-8.00002-6

Gaude, E., Chignola, F., Spiliotopoulos, D., Spitaleri, A., Ghitti, M., M Garcia-Manteiga, J., Mari, S., & Musco, G. (2013). muma, An R Package for Metabolomics Univariate and Multivariate Statistical Analysis. *Current Metabolomics*, *1*(2), 180–189. https://doi.org/10.2174/2213235x11301020005

Gertsman, I., & Barshop, B. A. (2018). Promises and pitfalls of untargeted metabolomics. In *Journal of Inherited Metabolic Disease* (Vol. 41, Issue 3, pp. 355–366). Springer Netherlands. https://doi.org/10.1007/s10545-017-0130-7

Ghaste, M., Mistrik, R., & Shulaev, V. (2016). Applications of Fourier Transform Ion Cyclotron Resonance (FT-ICR) and Orbitrap Based High Resolution Mass Spectrometry in Metabolomics and Lipidomics. *International Journal of Molecular Sciences*, *17*(6), 816. https://doi.org/10.3390/IJMS17060816

Gijbels, E., & Vinken, M. (2017). An Update on Adverse Outcome Pathways Leading to Liver Injury. *Applied in Vitro Toxicology*, *3*(4), 283–285. https://doi.org/10.1089/aivt.2017.0027

Gika, H. G., Virgiliou, C., Theodoridis, G., Plumb, R. S., & Wilson, I. D. (2019). Untargeted LC/MS-based metabolic phenotyping (metabonomics/metabolomics): The state of the art. *Journal of Chromatography B*, *1117*, 136–147. https://doi.org/10.1016/j.jchromb.2019.04.009

Gika, H. G., Zisi, C., Theodoridis, G., & Wilson, I. D. (2016). Protocol for quality control in metabolic profiling of biological fluids by U(H)PLC-MS. *Journal of Chromatography B*, *1008*, 15–25. https://doi.org/10.1016/j.jchromb.2015.10.045

Gilar, M., Olivova, P., Daly, A. E., & Gebler, J. C. (2005). Orthogonality of Separation in Two-Dimensional Liquid Chromatography. *Analytical Chemistry*, *77*(19), 6426–6434. https://doi.org/10.1021/ac050923i

Giles, K., Ujma, J., Wildgoose, J., Pringle, S., Richardson, K., Langridge, D., & Green, M. (2019). A Cyclic Ion Mobility-Mass Spectrometry System. *Analytical Chemistry*, *91*(13), 8564–8573. https://doi.org/10.1021/ACS.ANALCHEM.9B01838

Glavind, E., Aagaard, N. K., Grønbæk, H., Møller, H. J., Orntoft, N. W., Vilstrup, H., & Thomsen, K. L. (2016). Alcoholic Hepatitis Markedly Decreases the Capacity for Urea Synthesis. *PLOS ONE*, *11*(7), e0158388. https://doi.org/10.1371/JOURNAL.PONE.0158388

Godzien, J., Alonso-Herranz, V., Barbas, C., & Armitage, E. G. (2015). Controlling the quality of metabolomics data: new strategies to get the best out of the QC sample. *Metabolomics*, *11*(3), 518–528.

https://doi.org/10.1007/s11306-014-0712-4
Gong, Z. G., Hu, J., Wu, X., & Xu, Y. J. (2017). The Recent Developments in Sample Preparation for Mass Spectrometry-Based Metabolomics. *Critical Reviews in Analytical Chemistry*, *47*(4), 325–331. https://doi.org/10.1080/10408347.2017.1289836
González-Domínguez, R., Sayago, A., & Fernández-Recamales, Á. (2016). Direct infusion mass spectrometry for metabolomic phenotyping of diseases. *Bioanalysis*, *9*(1), 131–148. https://doi.org/10.4155/BIO-2016-0202
Goodacre, R., Broadhurst, D., Smilde, A. K., Kristal, B. S., Baker, J. D., Beger, R., Bessant, C., Connor, S., Capuani, G., Craig, A., Ebbels, T., Kell, D. B., Manetti, C., Newton, J., Paternostro, G., Somorjai, R., Sjöström, M., Trygg, J., & Wulfert, F. (2007). Proposed minimum reporting standards for data analysis in metabolomics. *Metabolomics*, *3*(3), 231–241. https://doi.org/10.1007/s11306-007-0081-3
Goracci, L., Tortorella, S., Tiberi, P., Pellegrino, R. M., Di Veroli, A., Valeri, A., & Cruciani, G. (2017). Lipostar, a Comprehensive Platform-Neutral Cheminformatics Tool for Lipidomics. *Analytical Chemistry*, *89*(11), 6257–6264. https://doi.org/10.1021/ACS.ANALCHEM.7B01259
Gorden, D. L., Myers, D. S., Ivanova, P. T., Fahy, E., Maurya, M. R., Gupta, S., Min, J., Spann, N. J., McDonald, J. G., Kelly, S. L., Duan, J., Sullards, M. C., Leiker, T. J., Barkley, R. M., Quehenberger, O., Armando, A. M., Milne, S. B., Mathews, T. P., Armstrong, M. D., … Brown, H. A. (2015). Biomarkers of NAFLD progression: a lipidomics approach to an epidemic. *Journal of Lipid Research*, *56*(3), 722–736. https://doi.org/10.1194/jlr.P056002
Greco, G., & Letzel, T. (2013). Main interactions and influences of the chromatographic parameters in HILIC separations. *Journal of Chromatographic Science*, *51*(7), 684–693. https://doi.org/10.1093/chromsci/bmt015
Griffiths, W. J. (2003). Tandem mass spectrometry in the study of fatty acids, bile acids, and steroids. *Mass Spectrometry Reviews*, *22*(2), 81–152. https://doi.org/10.1002/mas.10046
Griffiths, W. J., Abdel-Khalik, J., Yutuc, E., Morgan, A. H., Gilmore, I., Hearn, T., & Wang, Y. (2017). Cholesterolomics: An update. *Analytical Biochemistry*, *524*, 56–67. https://doi.org/10.1016/j.ab.2017.01.009
Gritti, F., Hölttzel, A., Tallarek, U., & Guiochon, G. (2015). The relative importance of the adsorption and partitioning mechanisms in hydrophilic interaction liquid chromatography. *Journal of Chromatography A*, *1376*, 112–125. https://doi.org/10.1016/j.chroma.2014.11.087
Gromski, P. S., Muhamadali, H., Ellis, D. I., Xu, Y., Correa, E., Turner, M. L., & Goodacre, R. (2015). A tutorial review: Metabolomics and partial least squares-discriminant analysis - a marriage of convenience or a shotgun wedding. *Analytica Chimica Acta*, *879*, 10–23. https://doi.org/10.1016/j.aca.2015.02.012
Grunfeld, C., Verdier, J. A., Neese, R., Moser, A. H., & Feingold, K. R. (1988). Mechanisms by which tumor necrosis factor stimulates hepatic fatty acid synthesis in vivo. *Journal Lipid Research*, *29*(10), 1327–1335. https://doi.org/10.1016/S0022-2275(20)38435-2
Guaratini, T., Vessecchi, R. L., Lavarda, F. C., Maia Campos, P. M. B. G., Naal, Z., Gates, P. J., & Lopes, N. P. (2004). New chemical evidence for the ability to generate radical molecular ions of polyenes from ESI and HR-MALDI mass spectrometry. *The Analyst*, *129*(12), 1223–1226. https://doi.org/10.1039/b412154f
Guguen-Guillouzo, C., & Guillouzo, A. (2010). General review on in vitro hepatocyte models and their applications. In P. Maurel (Ed.), *Methods in Molecular Biology, Hepatocytes* (Vol. 640, pp. 1–40). Humana Press, New Jersey. https://doi.org/10.1007/978-1-60761-688-7_1
Guillouzo, A., Corlu, A., Aninat, C., Glaise, D., Morel, F., & Guguen-Guillouzo, C. (2007). The human hepatoma HepaRG cells: a highly differentiated model for studies of liver metabolism and toxicity of xenobiotics. *Chemico-Biological Interactions*, *168*(1), 66–73. https://doi.org/10.1016/j.cbi.2006.12.003
Guney, Y., Ozel Turkcu, U., Hicsonmez, A., Nalca Andrieu, M., Guney, H. Z., Bilgihan, A., & Kurtman, C. (2006). Carnosine may reduce lung injury caused by radiation therapy. *Medical Hypotheses*, *66*(5), 957–959. https://doi.org/10.1016/J.MEHY.2005.11.023
Guo, J., & Huan, T. (2020). Comparison of Full-Scan, Data-Dependent, and Data-Independent Acquisition Modes in Liquid Chromatography-Mass Spectrometry Based Untargeted Metabolomics. *Analytical Chemistry*, *92*(12), 8072–8080. https://doi.org/10.1021/acs.analchem.9b05135

Hahn, J. A., Anton, R. F., & Javors, M. A. (2016). The Formation, Elimination, Interpretation, and Future Research Needs of Phosphatidylethanol for Research Studies and Clinical Practice. *Alcohol: Clinical and Experimental Research*, *40*(11), 2292–2295. https://doi.org/10.1111/acer.13213

Han, L., Matarrita, J., Sapozhnikova, Y., & Lehotay, S. J. (2016). Evaluation of a recent product to remove lipids and other matrix co-extractives in the analysis of pesticide residues and environmental contaminants in foods. *Journal of Chromatography A*, *1449*, 17–29. https://doi.org/10.1016/j.chroma.2016.04.052

Hao, Z., Xiao, B., & Weng, N. (2008). Impact of column temperature and mobile phase components on selectivity of hydrophilic interaction chromatography (HILIC). *Journal of Separation Science*, *31*(9), 1449–1464. https://doi.org/10.1002/jssc.200700624

Harrieder, E. M., Kretschmer, F., Böcker, S., & Witting, M. (2022). Current state-of-the-art of separation methods used in LC-MS based metabolomics and lipidomics. *Journal of Chromatography B*, *1188*, 123069. https://doi.org/10.1016/J.JCHROMB.2021.123069

Hasin, Y., Seldin, M., & Lusis, A. (2017). Multi-omics approaches to disease. *Genome Biology*, *18*(1), 83. https://doi.org/10.1186/s13059-017-1215-1

Hernández-Alvarez, M. I., Sebastián, D., Vives, S., Ivanova, S., Bartoccioni, P., Kakimoto, P., Plana, N., Veiga, S. R., Hernández, V., Vasconcelos, N., Peddinti, G., Adrover, A., Jové, M., Pamplona, R., Gordaliza-Alaguero, I., Calvo, E., Cabré, N., Castro, R., Kuzmanic, A., … Zorzano, A. (2019). Deficient Endoplasmic Reticulum-Mitochondrial Phosphatidylserine Transfer Causes Liver Disease. *Cell*, *177*(4), 881-895.e17. https://doi.org/10.1016/j.cell.2019.04.010

Hinnenkamp, V., Klein, J., Meckelmann, S. W., Balsaa, P., Schmidt, T. C., & Schmitz, O. J. (2018). Comparison of CCS Values Determined by Traveling Wave Ion Mobility Mass Spectrometry and Drift Tube Ion Mobility Mass Spectrometry. *Analytical Chemistry*, *90*(20), 12042–12050. https://doi.org/10.1021/acs.analchem.8b02711

Ho, C. S., Lam, C. W. K., Chan, M. H. M., Cheung, R. C. K., Law, L. K., Lit, L. C. W., Ng, K. F., Suen, M. W. M., & Tai, H. L. (2003). Electrospray Ionisation Mass Spectrometry: Principles and Clinical Applications. *The Clinical Biochemist Reviews*, *24*(1), 3–12. PMC1853331

Holman, J. D., Tabb, D. L., & Mallick, P. (2014). Employing ProteoWizard to Convert Raw Mass Spectrometry Data. *Current Protocols in Bioinformatics*, *46*, 13.24.1-13.24.9. https://doi.org/10.1002/0471250953.bi1324s46

Holmuhamedov, E. L., Czerny, C., Beeson, C. C., & Lemasters, J. J. (2012). Ethanol Suppresses Ureagenesis in Rat Hepatocytes: role of acetaldehyde. *The Journal of Biological Chemistry*, *287*(10), 7692–7700. https://doi.org/10.1074/JBC.M111.293399

Honda, A., Miyazaki, T., Ikegami, T., Iwamoto, J., Yamashita, K., Numazawa, M., & Matsuzaki, Y. (2010). Highly sensitive and specific analysis of sterol profiles in biological samples by HPLC–ESI–MS/MS. *The Journal of Steroid Biochemistry and Molecular Biology*, *121*(3), 556–564. https://doi.org/10.1016/j.jsbmb.2010.03.030

Hopfgartner, G. (2011). Can MS fully exploit the benefits of fast chromatography ? *Bioanalysis*, *3*(2), 121–123. https://doi.org/10.4155/bio.10.191

Horai, H., Arita, M., Kanaya, S., Nihei, Y., Ikeda, T., Suwa, K., Ojima, Y., Tanaka, K., Tanaka, S., Aoshima, K., Oda, Y., Kakazu, Y., Kusano, M., Tohge, T., Matsuda, F., Sawada, Y., Hirai, M. Y., Nakanishi, H., Ikeda, K., … Nishioka, T. (2010). MassBank: a public repository for sharing mass spectral data for life sciences. *Journal of Mass Spectrometry*, *45*(7), 703–714. https://doi.org/10.1002/JMS.1777

Hounoum, B. M., Blasco, H., Emond, P., & Mavel, S. (2016). Liquid chromatography–high-resolution mass spectrometry-based cell metabolomics: Experimental design, recommendations, and applications. *TrAC Trends in Analytical Chemistry*, *75*, 118–128. https://doi.org/10.1016/j.trac.2015.08.003

Hu, M., Wang, F., Li, X., Rogers, C. Q., Liang, X., Finck, B. N., Mitra, M. S., Zhang, R., Mitchell, D. A., & You, M. (2012). Regulation of Hepatic Lipin-1 by Ethanol: Role of AMPK-SREBP-1 Signaling. *Hepatology*, *55*(2), 437–446. https://doi.org/10.1002/HEP.24708

Hu, M., Yin, H., Mitra, M. S., Liang, X., Ajmo, J. M., Nadra, K., Chrast, R., Finck, B. N., & You, M. (2013). Hepatic-specific lipin-1 deficiency exacerbates experimental alcohol-induced steatohepatitis in mice. *Hepatology*, *58*(6), 1953–1963. https://doi.org/10.1002/HEP.26589

Hugbart, C., Verres, Y., Le Daré, B., Bucher, S., Vène, E., Bodin, A., Lagente, V., Fromenty, B., Bouvet, R.,

Morel, I., Loyer, P., & Gicquel, T. (2020). Non-oxidative ethanol metabolism in human hepatic cells in vitro: Involvement of uridine diphospho-glucuronosyltransferase 1A9 in ethylglucuronide production. *Toxicology in Vitro*, *66*, 104842. https://doi.org/10.1016/j.tiv.2020.104842

Hyun, J., Han, J., Lee, C., Yoon, M., & Jung, Y. (2021). Pathophysiological Aspects of Alcohol Metabolism in the Liver. *International Journal of Molecular Sciences*, *22*(11), 5717. https://doi.org/10.3390/IJMS22115717

Iannucci, J., Milner, R., Arbizo, M. V., & Smith, C. M. (1982). The effect of ethanol and acetaldehyde on [14C]pantothenate incorporation into CoA in cultured rat liver parenchymal cells. *Archives of Biochemistry and Biophysics*, *217*(1), 15–29. https://doi.org/10.1016/0003-9861(82)90474-X

Ibrahim, Y. M., Baker, E. S., Danielson, W. F., Norheim, R. V., Prior, D. C., Anderson, G. A., Belov, M. E., & Smith, R. D. (2015). Development of a New Ion Mobility (Quadrupole) Time-of-Flight Mass Spectrometer. *International Journal of Mass Spectrometry*, *377*(1), 655–662. https://doi.org/10.1016/J.IJMS.2014.07.034

Ikegami, T. (2019). Hydrophilic interaction chromatography for the analysis of biopharmaceutical drugs and therapeutic peptides: A review based on the separation characteristics of the hydrophilic interaction chromatography phases. *Journal of Separation Science*, *42*(1), 130–213. https://doi.org/10.1002/jssc.201801074

IPB, & UA. (2023). *MassBank - mFam record: Carnosine MS2 spectrum 10 eV*. https://msbi.ipb-halle.de/MassBank-mFam

Israelsen, M., Kim, M., Suvitaival, T., Madsen, B. S., Hansen, C. D., Torp, N., Trost, K., Thiele, M., Hansen, T., Legido-Quigley, C., & Krag, A. (2021). Comprehensive lipidomics reveals phenotypic differences in hepatic lipid turnover in ALD and NAFLD during alcohol intoxication. *JHEP Reports*, *3*(5), 100325. https://doi.org/10.1016/J.JHEPR.2021.100325

Iturrospe, E., Da Silva, K. M., Robeyns, R., van de Lavoir, M., Boeckmans, J., Vanhaecke, T., van Nuijs, A. L. N., & Covaci, A. (2022). Metabolic Signature of Ethanol-Induced Hepatotoxicity in HepaRG Cells by Liquid Chromatography–Mass Spectrometry-Based Untargeted Metabolomics. *Journal of Proteome Research*, *21*(4), 1153–1166. https://doi.org/10.1021/acs.jproteome.2c00029

Iturrospe, E., Da Silva, K. M., Talavera Andújar, B., Cuykx, M., Boeckmans, J., Vanhaecke, T., Covaci, A., & van Nuijs, A. L. N. (2021). An exploratory approach for an oriented development of an untargeted hydrophilic interaction liquid chromatography-mass spectrometry platform for polar metabolites in biological matrices. *Journal of Chromatography A*, *1637*, 461807. https://doi.org/10.1016/j.chroma.2020.461807

Ivanisevic, J., & Want, E. J. (2019). From samples to insights into metabolism: Uncovering biologically relevant information in LC-HRMS metabolomics data. *Metabolites*, *9*(12), 1–30. https://doi.org/10.3390/metabo9120308

Jankevics, A. (2013). *Extreme Metabolomics: Developing a high-performance computational pipeline for high-resolution LC-MS data sets* [University of Groningen]. https://pure.rug.nl/ws/files/14414080

Jankevics, A., Lloyd, G. R., & Weber, R. J. M. (2022). *pmp: Peak Matrix Processing and signal batch correction for metabolomics datasets* (R package version 1.10.0.). https://doi.org/10.18129/B9.bioc.pmp

Jaremek, M., Yu, Z., Mangino, M., Mittelstrass, K., Prehn, C., Singmann, P., Xu, T., Dahmen, N., Weinberger, K. M., Suhre, K., Peters, A., Döring, A., Hauner, H., Adamski, J., Illig, T., Spector, T. D., & Wang-Sattler, R. (2013). Alcohol-induced metabolomic differences in humans. *Translational Psychiatry*, *3*(7), e276–e276. https://doi.org/10.1038/tp.2013.55

Jenner, A. M., & Brown, S. H. J. (2017). Sterol analysis by quantitative mass spectrometry. In A. Gelissen, I., Brown (Ed.), *Methods in Molecular Biology, Cholesterol Homeostasis* (Vol. 1583, pp. 221–239). Humana Press, New York, NY. https://doi.org/10.1007/978-1-4939-6875-6_17

Jeon, S., & Carr, R. (2020). Alcohol effects on hepatic lipid metabolism. *Journal of Lipid Research*, *61*(4), 470–479. https://doi.org/10.1194/JLR.R119000547

Jewell, S. A., Di Monte, D., Gentile, A., Guglielmi, A., Altomare, E., & Albano, O. (1986). Decreased hepatic glutathione in chronic alcoholic patients. *Journal of Hepatology*, *3*(1), 1–6. https://doi.org/10.1016/S0168-8278(86)80139-8

Jiang, W., Fischer, G., Girmay, Y., & Irgum, K. (2006). Zwitterionic stationary phase with covalently bonded phosphorylcholine type polymer grafts and its applicability to separation of peptides in the

hydrophilic interaction liquid chromatography mode. *Journal of Chromatography A*, *1127*(1–2), 82–91. https://doi.org/10.1016/j.chroma.2006.05.080

Johnson, A. R., & Carlson, E. E. (2015). Collision-Induced Dissociation Mass Spectrometry: A Powerful Tool for Natural Product Structure Elucidation. *Analytical Chemistry*, *87*(21), 10668–10678. https://doi.org/10.1021/ACS.ANALCHEM.5B01543

Johnson, C. H., Ivanisevic, J., & Siuzdak, G. (2016). Metabolomics: beyond biomarkers and towards mechanisms. *Nature Reviews. Molecular Cell Biology*, *17*(7), 451–459. https://doi.org/10.1038/NRM.2016.25

Kalkhof, S., Dautel, F., Loguercio, S., Baumann, S., Trump, S., Jungnickel, H., Otto, W., Rudzok, S., Potratz, S., Luch, A., Lehmann, I., Beyer, A., & von Bergen, M. (2015). Pathway and Time-Resolved Benzo[a]pyrene Toxicity on Hepa1c1c7 Cells at Toxic and Subtoxic Exposure. *Journal of Proteome Research*, *14*(1), 164–182. https://doi.org/10.1021/pr500957t

Kamiloglu, S., Sari, G., Ozdal, T., & Capanoglu, E. (2020). Guidelines for cell viability assays. *Food Frontiers*, *1*(3), 332–349. https://doi.org/10.1002/fft2.44

Kanebratt, K. P., & Andersson, T. B. (2008). HepaRG Cells as an in Vitro Model for Evaluation of Cytochrome P450 Induction in Humans. *Drug Metabolism and Disposition*, *36*(1), 137 LP – 145. https://doi.org/10.1124/dmd.107.017418

Kanehisa, M., & Goto, S. (2000). KEGG: Kyoto Encyclopedia of Genes and Genomes. *Nucleic Acids Research*, *28*(1), 27–30. https://doi.org/10.1093/NAR/28.1.27

Kanety, H., Feinstein, R., Papa, M. Z., Hemi, R., & Karasik, A. (1995). Tumor necrosis factor alpha-induced phosphorylation of insulin receptor substrate-1 (IRS-1). Possible mechanism for suppression of insulin-stimulated tyrosine phosphorylation of IRS-1. *The Journal of Biological Chemistry*, *270*(40), 23780–23784. https://doi.org/10.1074/JBC.270.40.23780

Karaca, G., Xie, G., Moylan, C., Swiderska-Syn, M., Guy, C. D., Krüger, L., Machado, M. V., Choi, S. S., Michelotti, G. A., Burkly, L. C., & Diehl, A. M. (2015). Role of Fn14 in acute alcoholic steatohepatitis in mice. *American Journal of Physiology - Gastrointestinal and Liver Physiology*, *308*(4), G325–G334. https://doi.org/10.1152/AJPGI.00429.2013

Karaman, I., Climaco Pinto, R., & Graça, G. (2018). Metabolomics Data Preprocessing: From Raw Data to Features for Statistical Analysis. *Comprehensive Analytical Chemistry*, *82*, 197–225. https://doi.org/10.1016/BS.COAC.2018.08.003

Kastl, L., Sauer, S. W., Ruppert, T., Beissbarth, T., Becker, M. S., Süss, D., Krammer, P. H., & Gülow, K. (2014). TNF-α mediates mitochondrial uncoupling and enhances ROS-dependent cell migration via NF-κB activation in liver cells. *FEBS Letters*, *588*(1), 175–183. https://doi.org/10.1016/J.FEBSLET.2013.11.033

Kawaratani, H., Tsujimoto, T., Douhara, A., Takaya, H., Moriya, K., Namisaki, T., Noguchi, R., Yoshiji, H., Fujimoto, M., & Fukui, H. (2013). The effect of inflammatory cytokines in alcoholic liver disease. *Mediators of Inflammation*, *2013*, 495156. https://doi.org/10.1155/2013/495156

Kebarle, P., & Verkcerk, U. H. (2009). Electrospray: From ions in solution to ions in the gas phase, what we know now. *Mass Spectrometry Reviews*, *28*(6), 898–917. https://doi.org/10.1002/MAS.20247

Kell, D. B., Brown, M., Davey, H. M., Dunn, W. B., Spasic, I., & Oliver, S. G. (2005). Metabolic footprinting and systems biology: the medium is the message. *Nature Reviews Microbiology*, *3*(7), 557–565. https://doi.org/10.1038/nrmicro1177

Kessner, D., Chambers, M., Burke, R., Agus, D., & Mallick, P. (2008). ProteoWizard: open source software for rapid proteomics tools development. *Bioinformatics*, *24*(21), 2534–2536. https://doi.org/10.1093/BIOINFORMATICS/BTN323

Kim, S., Chen, J., Cheng, T., Gindulyte, A., He, J., He, S., Li, Q., Shoemaker, B. A., Thiessen, P. A., Yu, B., Zaslavsky, L., Zhang, J., & Bolton, E. E. (2021). PubChem in 2021: New data content and improved web interfaces. *Nucleic Acids Research*, *49*(D1), D1388–D1395. https://doi.org/10.1093/nar/gkaa971

Kind, T., Tsugawa, H., Cajka, T., Ma, Y., Lai, Z., Mehta, S. S., Wohlgemuth, G., Barupal, D. K., Showalter, M. R., Arita, M., & Fiehn, O. (2018). Identification of small molecules using accurate mass MS/MS search. *Mass Spectrometry Reviews*, *37*(4), 513–532. https://doi.org/10.1002/MAS.21535

Klåvus, A., Kokla, M., Noerman, S., Koistinen, V. M., Tuomainen, M., Zarei, I., Meuronen, T., Häkkinen, M. R., Rummukainen, S., Babu, A. F., Sallinen, T., Kärkkäinen, O., Paananen, J., Broadhurst, D., Brunius,

C., & Hanhineva, K. (2020). “Notame”: Workflow for Non-Targeted LC–MS Metabolic Profiling. *Metabolites*, *10*(4), 135. https://doi.org/10.3390/METABO10040135

Klein, C. (2020). Recent Advances to Conquer Analytical Challenges with High-Resolution, Accurate Mass Spectrometry. *Chromatography Today, Buyers’ Guide 2020*, 34–37.

Knockaert, L., Berson, A., Ribault, C., Prost, P.-E., Fautrel, A., Pajaud, J., Lepage, S., Lucas-Clerc, C., Bégué, J.-M., Fromenty, B., & Robin, M.-A. (2012). Carbon tetrachloride-mediated lipid peroxidation induces early mitochondrial alterations in mouse liver. *Laboratory Investigation*, *92*(3), 396–410. https://doi.org/10.1038/labinvest.2011.193

Koch, E., Wiebel, M., Hopmann, C., Kampschulte, N., & Schebb, N. H. (2021). Rapid quantification of fatty acids in plant oils and biological samples by LC-MS. *Analytical and Bioanalytical Chemistry*, *413*(21), 5439–5451. https://doi.org/10.1007/s00216-021-03525-y

Koelmel, J. P., Aristizabal-Henao, J. J., Ni, Z., Fedorova, M., Kato, S., Otoki, Y., Nakagawa, K., Lin, E. Z., Godri Pollitt, K. J., Vasiliou, V., Guingab, J. D., Garrett, T. J., Williams, T. L., Bowden, J. A., & Penumetcha, M. (2021). A Novel Technique for Redox Lipidomics Using Mass Spectrometry: Application on Vegetable Oils Used to Fry Potatoes. *Journal of the American Society for Mass Spectrometry*, *32*(7), 1798–1809. https://doi.org/10.1021/jasms.1c00150

Koelmel, J. P., Kroeger, N. M., Gill, E. L., Ulmer, C. Z., Bowden, J. A., Patterson, R. E., Yost, R. A., & Garrett, T. J. (2017). Expanding Lipidome Coverage Using LC-MS/MS Data-Dependent Acquisition with Automated Exclusion List Generation. *Journal of the American Society for Mass Spectrometry*, *28*(5), 908–917. https://doi.org/10.1007/s13361-017-1608-0

Koelmel, J. P., Kroeger, N. M., Ulmer, C. Z., Bowden, J. A., Patterson, R. E., Cochran, J. A., Beecher, C. W. W., Garrett, T. J., & Yost, R. A. (2017). LipidMatch: An automated workflow for rule-based lipid identification using untargeted high-resolution tandem mass spectrometry data. *BMC Bioinformatics*, *18*(1), 331. https://doi.org/10.1186/s12859-017-1744-3

Koelmel, J. P., Li, X., Stow, S. M., Sartain, M. J., Murali, A., Kemperman, R., Tsugawa, H., Takahashi, M., Vasiliou, V., Bowden, J. A., Yost, R. A., Garrett, T. J., & Kitagawa, N. (2020). Lipid annotator: Towards accurate annotation in non-targeted liquid chromatography high-resolution tandem mass spectrometry (LC-HRMS/MS) lipidomics using a rapid and user-friendly software. *Metabolites*, *10*(3), 101. https://doi.org/10.3390/metabo10030101

Koelmel, J. P., Tan, W. Y., Li, Y., Bowden, J. A., Ahmadireskety, A., Patt, A. C., Orlicky, D. J., Mathé, E., Kroeger, N. M., Thompson, D. C., Cochran, J. A., Golla, J. P., Kandyliari, A., Chen, Y., Charkoftaki, G., Guingab-Cagmat, J. D., Tsugawa, H., Arora, A., Veselkov, K., … Vasilou, V. (2021). Lipidomics and Redox Lipidomics Indicate Early Stage Alcohol-Induced Liver Damage. *Hepatology Communications*, *6*, 513–525. https://doi.org/10.1002/HEP4.1825

Koelmel, J. P., Ulmer, C. Z., Jones, C. M., Yost, R. A., & Bowden, J. A. (2017). Common cases of improper lipid annotation using high-resolution tandem mass spectrometry data and corresponding limitations in biological interpretation. *Biochimica et Biophysica Acta*, *1862*(8), 766–770. https://doi.org/10.1016/j.bbalip.2017.02.016

Krettler, C. A., & Thallinger, G. G. (2021). A map of mass spectrometry-based in silico fragmentation prediction and compound identification in metabolomics. *Briefings in Bioinformatics*, *22*(5), bbab073. https://doi.org/10.1093/BIB/BBAB073

Kuda, O., Brezinova, M., Silhavy, J., Landa, V., Zidek, V., Dodia, C., Kreuchwig, F., Vrbacky, M., Balas, L., Durand, T., Hübner, N., Fisher, A. B., Kopecky, J., & Pravenec, M. (2018). Nrf2-Mediated Antioxidant Defense and Peroxiredoxin 6 Are Linked to Biosynthesis of Palmitic Acid Ester of 9-Hydroxystearic Acid. *Diabetes*, *67*(6), 1190–1199. https://doi.org/10.2337/DB17-1087

Kuhring, M., Eisenberger, A., Schmidt, V., Kränkel, N., Leistner, D. M., Kirwan, J., & Beule, D. (2020). Concepts and Software Package for Efficient Quality Control in Targeted Metabolomics Studies: MeTaQuaC. *Analytical Chemistry*, *92*(15), 10241–10245. https://doi.org/10.1021/acs.analchem.0c00136

Kyle, J. E., Zhang, X., Weitz, K. K., Monroe, M. E., Ibrahim, Y. M., Moore, R. J., Cha, J., Sun, X., Lovelace, E. S., Wagoner, J., Polyak, S. J., Metz, T. O., Dey, S. K., Smith, R. D., Burnum-Johnson, K. E., & Baker, E. S. (2016). Uncovering biologically significant lipid isomers with liquid chromatography, ion mobility spectrometry and mass spectrometry. *Analyst*, *141*(5), 1649–1659.

https://doi.org/10.1039/c5an02062j
Lai, Z., Tsugawa, H., Wohlgemuth, G., Mehta, S., Mueller, M., Zheng, Y., Ogiwara, A., Meissen, J., Showalter, M., Takeuchi, K., Kind, T., Beal, P., Arita, M., & Fiehn, O. (2017). Identifying metabolites by integrating metabolome databases with mass spectrometry cheminformatics. *Nature Methods*, *15*(1), 53–56. https://doi.org/10.1038/nmeth.4512
Lamas-Paz, A., Hao, F., Nelson, L. J., Vázquez, M. T., Canals, S., Moral, M. G. del, Martínez-Naves, E., Nevzorova, Y. A., & Cubero, F. J. (2018). Alcoholic liver disease: Utility of animal models. *World Journal of Gastroenterology*, *24*(45), 5063–5075. https://doi.org/10.3748/WJG.V24.I45.5063
Lange, M., Angelidou, G., Ni, Z., Criscuolo, A., Schiller, J., Blüher, M., & Fedorova, M. (2021). AdipoAtlas: A Reference Lipidome for Human White Adipose Tissue. *Cell Reports Medicine*, *2*(10), 100407. https://doi.org/10.1101/2021.01.20.427444
Lange, M., & Fedorova, M. (2020). Evaluation of lipid quantification accuracy using HILIC and RPLC MS on the example of NIST® SRM® 1950 metabolites in human plasma. *Analytical and Bioanalytical Chemistry*, *412*(15), 3573–3584. https://doi.org/10.1007/s00216-020-02576-x
Lange, M., Ni, Z., Criscuolo, A., & Fedorova, M. (2019). Liquid Chromatography Techniques in Lipidomics Research. *Chromatographia*, *82*(1), 77–100. https://doi.org/10.1007/s10337-018-3656-4
Lawler, J. F., Yin, M., Diehl, A. M., Roberts, E., & Chatterjee, S. (1998). Tumor necrosis factor-α stimulates the maturation of sterol regulatory element binding protein-1 in human hepatocytes through the action of neutral sphingomyelinase. *Journal of Biological Chemistry*, *273*(9), 5053–5059. https://doi.org/10.1074/jbc.273.9.5053
Le Faouder, P., Baillif, V., Spreadbury, I., Motta, J. P., Rousset, P., Chêne, G., Guigné, C., Tercé, F., Vanner, S., Vergnolle, N., Bertrand-Michel, J., Dubourdeau, M., & Cenac, N. (2013). LC-MS/MS method for rapid and concomitant quantification of pro-inflammatory and pro-resolving polyunsaturated fatty acid metabolites. *Journal of Chromatography B: Analytical Technologies in the Biomedical and Life Sciences*, *932*, 123–133. https://doi.org/10.1016/j.jchromb.2013.06.014
Le Faouder, P., Soullier, J., Tremblay-Franco, M., Tournadre, A., Martin, J.-F., Guitton, Y., Carlé, C., Caspar-Bauguil, S., Denechaud, P.-D., & Bertrand-Michel, J. (2021). Untargeted Lipidomic Profiling of Dry Blood Spots Using SFC-HRMS. *Metabolites*, *11*(5), 305. https://doi.org/10.3390/metabo11050305
Leggio, L., Kenna, G. A., & Swift, R. M. (2008). New developments for the pharmacological treatment of alcohol withdrawal syndrome. A focus on non-benzodiazepine GABAergic medications. *Progress in Neuro-Psychopharmacology and Biological Psychiatry*, *32*(5), 1106–1117. https://doi.org/10.1016/J.PNPBP.2007.09.021
Lerno, L. A., German, J. B., & Lebrilla, C. B. (2010). Method for the Identification of Lipid Classes Based on Referenced Kendrick Mass Analysis. *Analytical Chemistry*, *82*(10), 4236–4245. https://doi.org/10.1021/ac100556g
Letzel, T. (2019). Specifications of Gradients in Hydrophilic Interaction Liquid Chromatography (HILIC). In S. Kromidas (Ed.), *Gradient HPLC for Practitioners* (pp. 175–182). Wiley-Vch Verlag Gmbh. https://doi.org/doi:10.1002/9783527812745.ch6
Levsen, K., Schiebel, H.-M., Terlouw, J. K., Jobst, K. J., Elend, M., Preiß, A., Thiele, H., & Ingendoh, A. (2007). Even-electron ions: a systematic study of the neutral species lost in the dissociation of quasi-molecular ions. *Journal of Mass Spectrometry*, *42*(8), 1024–1044. https://doi.org/10.1002/jms.1234
Li, A., Hines, K. M., & Xu, L. (2020). Lipidomics by HILIC-Ion Mobility-Mass Spectrometry. In *Methods in molecular biology* (Vol. 2084, pp. 119–132). NIH Public Access. https://doi.org/10.1007/978-1-0716-0030-6_7
Li, L., Zhong, S., Shen, X., Li, Q., Xu, W., Tao, Y., & Yin, H. (2019). Recent development on liquid chromatography-mass spectrometry analysis of oxidized lipids. *Free Radical Biology and Medicine*, *144*, 16–34. https://doi.org/10.1016/j.freeradbiomed.2019.06.006
Li, N., & Zhao, H. (2021). Role of Carnitine in Non-alcoholic Fatty Liver Disease and Other Related Diseases: An Update. *Frontiers in Medicine*, *8*, 689042. https://doi.org/10.3389/FMED.2021.689042
Li, Q., Dhyani, M., Grajo, J. R., Sirlin, C., & Samir, A. E. (2018). Current status of imaging in nonalcoholic fatty liver disease. *World Journal of Hepatology*, *10*(8), 530–542. https://doi.org/10.4254/WJH.V10.I8.530
Li, X., Li, X., Lu, J., Huang, Y., Lv, L., Luan, Y., Liu, R., & Sun, R. (2017). Saikosaponins induced hepatotoxicity in mice via lipid metabolism dysregulation and oxidative stress: a proteomic study. *BMC*

Complementary and Alternative Medicine, *17*(1), 219. https://doi.org/10.1186/s12906-017-1733-0

Li, Y., Kind, T., Folz, J., Vaniya, A., Mehta, S. S., & Fiehn, O. (2021). Spectral entropy outperforms MS/MS dot product similarity for small-molecule compound identification. *Nature Methods*, *18*(12), 1524–1531. https://doi.org/10.1038/s41592-021-01331-z

Li, Y. Q., Prentice, D. A., Howard, M. L., Mashford, M. L., Wilson, J. S., & Desmond, P. V. (2000). Alcohol up-regulates udp-glucuronosyltransferase mrna expression in rat liver and in primary rat hepatocyte culture. *Life Sciences*, *66*(7), 575–584. https://doi.org/10.1016/S0024-3205(99)00630-X

Li, Zhaoyu, Agellon, L. B., & Vance, D. E. (2005). Phosphatidylcholine Homeostasis and Liver Failure. *Journal of Biological Chemistry*, *280*(45), 37798–37802. https://doi.org/10.1074/JBC.M508575200

Li, Zhonghuang, Zheng, L., Shi, J., Zhang, G., Lu, L., Zhu, L., Zhang, J., & Liu, Z. (2015). Toxic Markers of Matrine Determined Using ^{1}H-NMR-Based Metabolomics in Cultured Cells *In Vitro* and Rats *In Vivo*. *Evidence-Based Complementary and Alternative Medicine*, *2015*, 598412. https://doi.org/10.1155/2015/598412

Liangpunsakul, S., Haber, P., & McCaughan, G. W. (2016). Alcoholic Liver Disease in Asia, Europe, and North America. *Gastroenterology*, *150*(8), 1786–1797. https://doi.org/10.1053/J.GASTRO.2016.02.043

Liangpunsakul, S., Sozio, M. S., Shin, E., Zhao, Z., Xu, Y., Ross, R. A., Zeng, Y., & Crabb, D. W. (2010). Inhibitory effect of ethanol on AMPK phosphorylation is mediated in part through elevated ceramide levels. *American Journal of Physiology - Gastrointestinal and Liver Physiology*, *298*(6), 1004–1012. https://doi.org/10.1152/AJPGI.00482.2009

Lieber, C. S., Leo, M. A., Mak, K. M., Decarli, L. M., & Sato, S. (1985). Choline fails to prevent liver fibrosis in ethanol-fed baboons but causes toxicity. *Hepatology*, *5*(4), 561–572. https://doi.org/10.1002/HEP.1840050407

Lieber, C. S., Robins, S. J., & Leo, M. A. (1994). Hepatic phosphatidylethanolamine methyltransferase activity is decreased by ethanol and increased by phosphatidylcholine. *Alcoholism, Clinical and Experimental Research*, *18*(3), 592–595. https://doi.org/10.1111/J.1530-0277.1994.TB00915.X

Lieber, C. S., Rubin, E., & DeCarli, L. M. (1970). Hepatic microsomal ethanol oxidizing system (MEOS): Differentiation from alcohol dehydrogenase and NADPH oxidase. *Biochemical and Biophysical Research Communications*, *40*(4), 858–865. https://doi.org/10.1016/0006-291X(70)90982-4

Liebisch, G., Fahy, E., Aoki, J., Dennis, E. A., Durand, T., Ejsing, C. S., Fedorova, M., Feussner, I., Griffiths, W. J., Köfeler, H., Merrill, A. H., Murphy, R. C., O'Donnell, V. B., Oskolkova, O., Subramaniam, S., Wakelam, M. J. O., & Spener, F. (2020). Update on LIPID MAPS classification, nomenclature, and shorthand notation for MS-derived lipid structures. *Journal of Lipid Research*, *61*(12), 1539–1555. https://doi.org/10.1194/jlr.S120001025

Liu, J. J., Wang, J. Y., Hertervig, E., Cheng, Y., Nilsson, Å. K. E., & Duan, R. D. (2000). Activation of neutral sphingomyelinase participates in ethanol-induced apoptosis in HepG2 cells. *Alcohol and Alcoholism*, *35*(6), 569–573. https://doi.org/10.1093/ALCALC/35.6.569

Lonardo, A., Leoni, S., Alswat, K. A., & Fouad, Y. (2020). History of Nonalcoholic Fatty Liver Disease. In *International Journal of Molecular Sciences* (Vol. 21, Issue 16). https://doi.org/10.3390/ijms21165888

Longato, L., Ripp, K., Setshedi, M., Dostalek, M., Akhlaghi, F., Branda, M., Wands, J. R., & de la Monte, S. M. (2012). Insulin resistance, ceramide accumulation, and endoplasmic reticulum stress in human chronic alcohol-related liver disease. *Oxidative Medicine and Cellular Longevity*, *2012*, 479348. https://doi.org/10.1155/2012/479348

Louvet, A., & Mathurin, P. (2015). Alcoholic liver disease: mechanisms of injury and targeted treatment. *Nature Reviews Gastroenterology & Hepatology*, *12*(4), 231–242. https://doi.org/10.1038/nrgastro.2015.35

Lu, S. C., Huang, Z. Z., Yang, H., Mato, J. M., Avila, M. A., & Tsukamoto, H. (2000). Changes in methionine adenosyltransferase and S-adenosylmethionine homeostasis in alcoholic rat liver. *American Journal of Physiology. Gastrointestinal and Liver Physiology*, *279*(1), G178–G185. https://doi.org/10.1152/AJPGI.2000.279.1.G178

Lu, W., Su, X., Klein, M. S., Lewis, I. A., Fiehn, O., & Rabinowitz, J. D. (2017). Metabolite Measurement: Pitfalls to Avoid and Practices to Follow. *Annual Review of Biochemistry*, *86*(1), 277–304. https://doi.org/10.1146/annurev-biochem-061516-044952

Ludwig, J., Viggiano, T. R., McGill, D. B., & Oh, B. J. (1980). Nonalcoholic steatohepatitis: Mayo Clinic experiences with a hitherto unnamed disease. *Mayo Clinic Proceedings*, *55*(7), 434–438. https://doi.org/PMID: 7382552

Luginbühl, M., Wurst, F. M., Stöth, F., Weinmann, W., Stove, C. P., & Van Uytfanghe, K. (2022). Consensus for the use of the alcohol biomarker phosphatidylethanol (PEth) for the assessment of abstinence and alcohol consumption in clinical and forensic practice. *Drug Testing and Analysis*, *14*(10), 1800–1802. https://doi.org/10.1002/dta.3340

Luukkonen, P. K., Zhou, Y., Sädevirta, S., Leivonen, M., Arola, J., Orešič, M., Hyötyläinen, T., & Yki-Järvinen, H. (2016). Hepatic ceramides dissociate steatosis and insulin resistance in patients with non-alcoholic fatty liver disease. *Journal of Hepatology*, *64*(5), 1167–1175. https://doi.org/10.1016/j.jhep.2016.01.002

Lynch, K. L. (2017). Toxicology: Liquid chromatography mass spectrometry. In H. Nair & W. Clarke (Eds.), *Mass Spectrometry for the Clinical Laboratory* (pp. 109–130). Elsevier Inc. https://doi.org/10.1016/B978-0-12-800871-3.00006-7

Ma, X., Qian, H., Chen, A., Ni, H. M., & Ding, W. X. (2021). Perspectives on Mitochondria–ER and Mitochondria–Lipid Droplet Contact in Hepatocytes and Hepatic Lipid Metabolism. *Cells*, *10*(9), 2273. https://doi.org/10.3390/CELLS10092273

Machado, M. V., Kruger, L., Jewell, M. L., Michelotti, G. A., Pereira, T. de A., Xie, G., Moylan, C. A., & Diehl, A. M. (2016). Vitamin B5 and N-acetylcysteine in nonalcoholic steatohepatitis: a pre-clinical study in a dietary mouse model. *Digestive Diseases and Sciences*, *61*(1), 137–148. https://doi.org/10.1007/S10620-015-3871-X

Malm, L., Palm, E., Souihi, A., Plassmann, M., Liigand, J., & Kruve, A. (2021). Guide to Semi-Quantitative Non-Targeted Screening Using LC/ESI/HRMS. *Molecules*, *26*(12), 3524. https://doi.org/10.3390/MOLECULES26123524

Männistö, V., Kaminska, D., Kärjä, V., Tiainen, M., de Mello, V. D., Hanhineva, K., Soininen, P., Ala-Korpela, M., & Pihlajamäki, J. (2019). Total liver phosphatidylcholine content associates with non-alcoholic steatohepatitis and glycine N-methyltransferase expression. *Liver International*, *39*(10), 1895–1905. https://doi.org/10.1111/LIV.14174

Mansouri, A., Gaou, I., de Kerguenec, C., Amsellem, S., Haouzi, D., Berson, A., Moreau, A., Feldmann, G., Lettéron, P., Pessayre, D., & Fromenty, B. (1999). An alcoholic binge causes massive degradation of hepatic mitochondrial DNA in mice. *Gastroenterology*, *117*(1), 181–190. https://doi.org/10.1016/S0016-5085(99)70566-4

Marion, M.-J., Hantz, O., & Durantel, D. (2010). The HepaRG cell line: biological properties and relevance as a tool for cell biology, drug metabolism, and virology studies. In P. Maurel (Ed.), *Methods in molecular biology, Hepatocytes* (Vol. 640, pp. 261–272). Humana Press, New Jersey. https://doi.org/10.1007/978-1-60761-688-7_13

Martano, G., Delmotte, N., Kiefer, P., Christen, P., Kentner, D., Bumann, D., & Vorholt, J. A. (2014). Fast sampling method for mammalian cell metabolic analyses using liquid chromatography–mass spectrometry. *Nature Protocols*, *10*(1), 1–11. https://doi.org/10.1038/nprot.2014.198

Martin, P. R., Singleton, C. K., & Hiller-Sturmhöfel, S. (2003). The role of thiamine deficiency in alcoholic brain disease. *Alcohol Research & Health : The Journal of the National Institute on Alcohol Abuse and Alcoholism*, *27*(2), 134–142. https://doi.org/PMC6668887

Martínez-Sena, T., Luongo, G., Sanjuan-Herráez, D., Castell, J. V., Vento, M., Quintás, G., & Kuligowski, J. (2019). Monitoring of system conditioning after blank injections in untargeted UPLC-MS metabolomic analysis. *Scientific Reports*, *9*(1), 1–9. https://doi.org/10.1038/s41598-019-46371-w

Matyash, V., Liebisch, G., Kurzchalia, T. V, Shevchenko, A., & Schwudke, D. (2008). Lipid extraction by methyl-tert-butyl ether for high-throughput lipidomics. *Journal of Lipid Research*, *49*(5), 1137–1146. https://doi.org/10.1194/jlr.D700041-JLR200

Maudens, K. E., Patteet, L., van Nuijs, A. L. N., Van Broekhoven, C., Covaci, A., & Neels, H. (2014). The influence of the body mass index (BMI) on the volume of distribution of ethanol. *Forensic Science International*, *243*, 74–78. https://doi.org/10.1016/J.FORSCIINT.2014.04.036

May, J. C., & McLean, J. A. (2015). Ion mobility-mass spectrometry: Time-dispersive instrumentation. *Analytical Chemistry*, *87*(3), 1422–1436. https://doi.org/10.1021/ac504720m

McCalley, D. V. (2017). Understanding and manipulating the separation in hydrophilic interaction liquid chromatography. *Journal of Chromatography A*, *1523*, 49–71. https://doi.org/10.1016/j.chroma.2017.06.026

McDermott, J. E., Wang, J., Mitchell, H., Webb-Robertson, B.-J., Hafen, R., Ramey, J., & Rodland, K. D. (2013). Challenges in biomarker discovery: combining expert insights with statistical analysis of complex omics data. *Expert Opinion on Medical Diagnostics*, *7*(1), 37–51. https://doi.org/10.1517/17530059.2012.718329

McGill, M. R., Yan, H.-M., Ramachandran, A., Murray, G. J., Rollins, D. E., & Jaeschke, H. (2011). HepaRG cells: A human model to study mechanisms of acetaminophen hepatotoxicity. *Hepatology*, *53*(3), 974–982. https://doi.org/10.1002/hep.24132

McLean, S., Davies, N. W., Nichols, D. S., & McLeod, B. J. (2015). Triacylglycerol Estolides, a New Class of Mammalian Lipids, in the Paracloacal Gland of the Brushtail Possum (Trichosurus vulpecula). *Lipids*, *50*(6), 591–604. https://doi.org/10.1007/S11745-015-4025-9

Meikle, P. J., Mundra, P. A., Wong, G., Rahman, K., Huynh, K., Barlow, C. K., Duly, A. M. P., Haber, P. S., Whitfield, J. B., & Seth, D. (2015). Circulating Lipids Are Associated with Alcoholic Liver Cirrhosis and Represent Potential Biomarkers for Risk Assessment. *PLOS ONE*, *10*(6), e0130346. https://doi.org/10.1371/JOURNAL.PONE.0130346

Meissen, J. K., Hirahatake, K. M., Adams, S. H., & Fiehn, O. (2015). Temporal metabolomic responses of cultured HepG2 liver cells to high fructose and high glucose exposures. *Metabolomics*, *11*(3), 707–721. https://doi.org/10.1007/s11306-014-0729-8

Mellor, C. L., Steinmetz, F. P., & Cronin, M. T. D. (2016). The identification of nuclear receptors associated with hepatic steatosis to develop and extend adverse outcome pathways. *Critical Reviews in Toxicology*, *46*(2), 138–152. https://doi.org/10.3109/10408444.2015.1089471

Meringer, M., Reinker, S., Zhang, J., & Muller, A. (2011). *MS/MS Data Improves Automated Determination of Molecular Formulas by Mass Spectrometry*. https://doi.org/Corpus ID: 5917602

Mestas, J., & Hughes, C. C. W. (2004). Of Mice and Not Men: Differences between Mouse and Human Immunology. *The Journal of Immunology*, *172*(5), 2731–2738. https://doi.org/10.4049/JIMMUNOL.172.5.2731

Michelmann, K., Silveira, J. A., Ridgeway, M. E., & Park, M. A. (2014). Fundamentals of trapped ion mobility spectrometry. *Journal of the American Society for Mass Spectrometry*, *26*(1), 14–24. https://doi.org/10.1007/S13361-014-0999-4

Minsart, C., Liefferinckx, C., Lemmers, A., Dressen, C., Quertinmont, E., Leclercq, I., Devière, J., Moreau, R., & Gustot, T. (2020). New insights in acetaminophen toxicity: HMGB1 contributes by itself to amplify hepatocyte necrosis in vitro through the TLR4-TRIF-RIPK3 axis. *Scientific Reports*, *10*(1), 5557. https://doi.org/10.1038/s41598-020-61270-1

Misra, B. B. (2021). New software tools, databases, and resources in metabolomics: updates from 2020. *Metabolomics*, *17*(5), 49. https://doi.org/10.1007/S11306-021-01796-1

Miyazaki, A., Sano, M., Fukuwatari, T., & Shibata, K. (2012). Effects of ethanol consumption on the B-group vitamin contents of liver, blood and urine in rats. *The British Journal of Nutrition*, *108*(6), 1034–1041. https://doi.org/10.1017/S0007114511006192

Molenaar, S. R. A., Dahlseid, T. A., Leme, G. M., Stoll, D. R., Schoenmakers, P. J., & Pirok, B. W. J. (2021). Peak-tracking algorithm for use in comprehensive two-dimensional liquid chromatography – Application to monoclonal-antibody peptides. *Journal of Chromatography A*, *1639*, 461922. https://doi.org/10.1016/j.chroma.2021.461922

Molenaar, S. R. A., van de Put, B., Desport, J. S., Samanipour, S., Peters, R. A. H., & Pirok, B. W. J. (2022). Automated Feature Mining for Two-Dimensional Liquid Chromatography Applied to Polymers Enabled by Mass Remainder Analysis. *Analytical Chemistry*, *94*(14), 5599–5607. https://doi.org/10.1021/acs.analchem.1c05336

Mühle, C., Weinland, C., Gulbins, E., Lenz, B., & Kornhuber, J. (2018). Peripheral Acid Sphingomyelinase Activity Is Associated with Biomarkers and Phenotypes of Alcohol Use and Dependence in Patients and Healthy Controls. In *International Journal of Molecular Sciences* (Vol. 19, Issue 12). https://doi.org/10.3390/ijms19124028

Muñoz, N. M., Katz, L. H., Shin, J. H., Gi, Y. J., Menon, V. K., Gagea, M., Rashid, A., Chen, J., & Mishra, L.

(2014). Generation of a mouse model of T-cell lymphoma based on chronic LPS challenge and TGF-β signaling disruption. *Genes & Cancer*, *5*(9–10), 348–352. https://doi.org/10.18632/GENESANDCANCER.32

Murphy, K., Viroli, C., & Gormley, I. C. (2020). Infinite Mixtures of Infinite Factor Analysers. *Bayesian Analysis*, *15*(3), 937–963. https://doi.org/10.1214/19-BA1179

Murphy, R. C. (2014). Tandem Mass Spectrometry of Lipids. In *New Developments in Mass Spectrometry*. Royal Society of Chemistry. https://doi.org/10.1039/9781782626350

Murphy, R. C., Barkley, R. M., Berry, K. Z., Hankin, J., Harrison, K., Johnson, C., Krank, J., McAnoy, A., Uhlson, C., & Zarini, S. (2005). Electrospray ionization and tandem mass spectrometry of eicosanoids. *Analytical Biochemistry*, *346*(1), 1–42. https://doi.org/10.1016/J.AB.2005.04.042

Myoung, S. H., Sun, Y. P., Shinzawa, K., Kim, S., Kun, W. C., Lee, J. H., Choon, H. K., Lee, K. W., Lee, J. H., Cheol, K. P., Woo, J. C., Jae, S. H., Yan, J. J., Song, D. K., Tsujimoto, Y., & Lee, M. S. (2008). Lysophosphatidylcholine as a death effector in the lipoapoptosis of hepatocytes. *Journal of Lipid Research*, *49*(1), 84–97. https://doi.org/10.1194/JLR.M700184-JLR200

Nagana Gowda, G. A., & Raftery, D. (2017). Whole Blood Metabolomics by 1H NMR Spectroscopy Provides a New Opportunity To Evaluate Coenzymes and Antioxidants. *Analytical Chemistry*, *89*(8), 4620–4627. https://doi.org/10.1021/acs.analchem.7b00171

Naghavi, M., Abajobir, A. A., Abbafati, C., Abbas, K. M., Abd-Allah, F., Abera, S. F., Aboyans, V., Adetokunboh, O., Ärnlöv, J., Afshin, A., Agrawal, A., Kiadaliri, A. A., Ahmadi, A., Ahmed, M. B., Aichour, A. N., Aichour, I., Aichour, M. T. E., Aiyar, S., Al-Eyadhy, A., … Murray, C. J. L. (2017). Global, regional, and national age-sex specific mortality for 264 causes of death, 1980–2016: a systematic analysis for the Global Burden of Disease Study 2016. *The Lancet*, *390*(10100), 1151–1210. https://doi.org/10.1016/S0140-6736(17)32152-9

Nagy, L. E. (2015). The Role of Innate Immunity in Alcoholic Liver Disease. *Alcohol Research : Current Reviews*, *37*(2), 237–250. PMC4590620

Navarro-Reig, M., Jaumot, J., Baglai, A., Vivó-Truyols, G., Schoenmakers, P. J., & Tauler, R. (2017). Untargeted Comprehensive Two-Dimensional Liquid Chromatography Coupled with High-Resolution Mass Spectrometry Analysis of Rice Metabolome Using Multivariate Curve Resolution. *Analytical Chemistry*, *89*(14), 7675–7683. https://doi.org/10.1021/acs.analchem.7b01648

Nawrocki, J. (1997). The silanol group and its role in liquid chromatography. *Journal of Chromatography A*, *779*(1), 29–71. https://doi.org/10.1016/S0021-9673(97)00479-2

Naz, S., Vallejo, M., García, A., & Barbas, C. (2014). Method validation strategies involved in non-targeted metabolomics. *Journal of Chromatography A*, *1353*, 99–105. https://doi.org/10.1016/j.chroma.2014.04.071

Neto, F. C., Guaratini, T., Costa-Lotufo, L., Colepicolo, P., Gates, P. J., & Lopes, N. P. (2016). Re-investigation of the fragmentation of protonated carotenoids by electrospray ionization and nanospray tandem mass spectrometry. *Rapid Communications in Mass Spectrometry*, *30*(13), 1540–1548. https://doi.org/10.1002/rcm.7589

Ni, Z., Angelidou, G., Lange, M., Hoffmann, R., & Fedorova, M. (2017). LipidHunter Identifies Phospholipids by High-Throughput Processing of LC-MS and Shotgun Lipidomics Datasets. *Analytical Chemistry*, *89*(17), 8800–8807. https://doi.org/10.1021/ACS.ANALCHEM.7B01126

NIAA. (2010). *Rethinking Drinking: Alcohol and Your Health*. https://www.rethinkingdrinking.niaaa.nih.gov

Nikolaou, N., Gathercole, L. L., Marchand, L., Althari, S., Dempster, N. J., Green, C. J., van de Bunt, M., McNeil, C., Arvaniti, A., Hughes, B. A., Sgromo, B., Gillies, R. S., Marschall, H. U., Penning, T. M., Ryan, J., Arlt, W., Hodson, L., & Tomlinson, J. W. (2019). AKR1D1 is a novel regulator of metabolic phenotype in human hepatocytes and is dysregulated in non-alcoholic fatty liver disease. *Metabolism*, *99*, 67–80. https://doi.org/10.1016/J.METABOL.2019.153947

Nothias, L.-F., Petras, D., Schmid, R., Dührkop, K., Rainer, J., Sarvepalli, A., Protsyuk, I., Ernst, M., Tsugawa, H., Fleischauer, M., Aicheler, F., Aksenov, A. A., Alka, O., Allard, P.-M., Barsch, A., Cachet, X., Caraballo-Rodriguez, A. M., Da Silva, R. R., Dang, T., … Dorrestein, P. C. (2020). Feature-based molecular networking in the GNPS analysis environment. *Nature Methods*, *17*(9), 905–908. https://doi.org/10.1038/s41592-020-0933-6

O'Donnell, V. B., Dennis, E. A., Wakelam, M. J. O., & Subramaniam, S. (2019). LIPID MAPS: Serving the next

generation of lipid researchers with tools, resources, data, and training. *Science Signaling*, *12*(563), eaaw2964. https://doi.org/10.1126/scisignal.aaw2964

Olesti, E., Boccard, J., Visconti, G., González-Ruiz, V., & Rudaz, S. (2021). From a single steroid to the steroidome: Trends and analytical challenges. *Journal of Steroid Biochemistry and Molecular Biology*, *206*, 105797. https://doi.org/10.1016/j.jsbmb.2020.105797

Onofrj, M., Ciccocioppo, F., Varanese, S., Di Muzio, A., Calvani, M., Chiechio, S., Osio, M., & Thomas, A. (2014). Acetyl-L-carnitine: from a biological curiosity to a drug for the peripheral nervous system and beyond. *Expert Review of Neurotherapeutics*, *13*(8), 925–936. https://doi.org/10.1586/14737175.2013.814930

Oshea, R. S., Dasarathy, S., & McCullough, A. J. (2010). Alcoholic liver disease. *American Journal of Gastroenterology*, *105*(1), 14–32. https://doi.org/10.1038/AJG.2009.593

Ou, F.-S., Michiels, S., Shyr, Y., Adjei, A. A., & Oberg, A. L. (2021). Biomarker Discovery and Validation: Statistical Considerations. *Journal of Thoracic Oncology*, *16*(4), 537–545. https://doi.org/10.1016/j.jtho.2021.01.1616

Ovčačíková, M., Lísa, M., Cífková, E., & Holčapek, M. (2016). Retention behavior of lipids in reversed-phase ultrahigh-performance liquid chromatography-electrospray ionization mass spectrometry. *Journal of Chromatography. A*, *1450*, 76–85. https://doi.org/10.1016/j.chroma.2016.04.082

Owens, R. E., Snyder, H. S., Twilla, J. D., & Satapathy, S. K. (2016). Pharmacologic Treatment of Alcoholic Hepatitis: Examining Outcomes Based on Disease Severity Stratification. *Journal of Clinical and Experimental Hepatology*, *6*(4), 275–281. https://doi.org/10.1016/J.JCEH.2016.07.003

Öztas, Y., & Bosgelmez, I. (2017). An Introduction to Lipidomics : From Laboratory to Clinic. *Acta Medica*, *48*(1), 14–23. https://doi.org/actamedica.org/index.php/actamedica/article/view/18

Paglia, G., Smith, A. J., & Astarita, G. (2021). Ion mobility mass spectrometry in the omics era: Challenges and opportunities for metabolomics and lipidomics. *Mass Spectrometry Reviews*, *41*, 722–765. https://doi.org/10.1002/mas.21686

Paik, Y. H., Schwabe, R. F., Bataller, R., Russo, M. P., Jobin, C., & Brenner, D. A. (2003). Toll-like receptor 4 mediates inflammatory signaling by bacterial lipopolysaccharide in human hepatic stellate cells. *Hepatology*, *37*(5), 1043–1055. https://doi.org/10.1053/jhep.2003.50182

Papadimitropoulos, M. E. P., Vasilopoulou, C. G., Maga-Nteve, C., & Klapa, M. I. (2018). Untargeted GC-MS metabolomics. *Methods in Molecular Biology*, *1738*, 133–147. https://doi.org/10.1007/978-1-4939-7643-0_9

Park, P. H., Lim, R. W., & Shukla, S. D. (2005). Involvement of histone acetyltransferase (HAT) in ethanol-induced acetylation of histone H3 in hepatocytes: Potential mechanism for gene expression. *American Journal of Physiology - Gastrointestinal and Liver Physiology*, *289*(6), G1124–G1136. https://doi.org/10.1152/ajpgi.00091.2005

Parker, R., Kim, S. J., & Gao, B. (2017). Alcohol, adipose tissue and liver disease: mechanistic links and clinical considerations. *Nature Reviews Gastroenterology & Hepatology*, *15*(1), 50–59. https://doi.org/10.1038/nrgastro.2017.116

Patti, G. J. (2011). Separation strategies for untargeted metabolomics. *Journal of Separation Science*, *34*(24), 3460–3469. https://doi.org/10.1002/jssc.201100532

Pavlovic, Z., & Bakovic, M. (2013). Regulation of Phosphatidylethanolamine Homeostasis—The Critical Role of CTP:Phosphoethanolamine Cytidylyltransferase (Pcyt2). *International Journal of Molecular Sciences*, *14*(2), 2529–2550. https://doi.org/10.3390/IJMS14022529

Peng, B., Kopczynski, D., Pratt, B. S., Ejsing, C. S., Burla, B., Hermansson, M., Benke, P. I., Tan, S. H., Chan, M. Y., Torta, F., Schwudke, D., Meckelmann, S. W., Coman, C., Schmitz, O. J., MacLean, B., Manke, M. C., Borst, O., Wenk, M. R., Hoffmann, N., & Ahrends, R. (2020). LipidCreator workbench to probe the lipidomic landscape. *Nature Communications*, *11*(1), 1–14. https://doi.org/10.1038/s41467-020-15960-z

Perez De Souza, L., Alseekh, S., Brotman, Y., & Fernie, A. R. (2020). Network-based strategies in metabolomics data analysis and interpretation: from molecular networking to biological interpretation. *Expert Review of Proteomics*, *17*(4), 243–255. https://doi.org/10.1080/14789450.2020.1766975

Pesek, J. J., Matyska, M. T., & Fischer, S. M. (2011). Improvement of peak shape in aqueous normal phase

analysis of anionic metabolites. *Journal of Separation Science*, *34*(24), 3509–3516. https://doi.org/10.1002/jssc.201100607

Pezzatti, J., González-Ruiz, V., Boccard, J., Guillarme, D., & Rudaz, S. (2020). Evaluation of Different Tandem MS Acquisition Modes to Support Metabolite Annotation in Human Plasma Using Ultra High-Performance Liquid Chromatography High-Resolution Mass Spectrometry for Untargeted Metabolomics. *Metabolites*, *10*(11), 1–17. https://doi.org/10.3390/METABO10110464

Pezzatti, J., González-Ruiz, V., Codesido, S., Gagnebin, Y., Joshi, A., Guillarme, D., Schappler, J., Picard, D., Boccard, J., & Rudaz, S. (2019). A scoring approach for multi-platform acquisition in metabolomics. *Journal of Chromatography A*, *1592*, 47–54. https://doi.org/10.1016/j.chroma.2019.01.023

Pi, J., Wu, X., & Feng, Y. (2016). Fragmentation patterns of five types of phospholipids by ultra-high-performance liquid chromatography electrospray ionization quadrupole time-of-flight tandem mass spectrometry. *Analytical Methods*, *8*(6), 1319–1332. https://doi.org/10.1039/C5AY00776C

Picache, J. A., Rose, B. S., Balinski, A., Leaptrot, K. L., Sherrod, S. D., May, J. C., & McLean, J. A. (2019). Collision cross section compendium to annotate and predict multi-omic compound identities. *Chemical Science*, *10*(4), 983–993. https://doi.org/10.1039/C8SC04396E

Pičmanová, M., Moses, T., Cortada-Garcia, J., Barrett, G., Florance, H., Pandor, S., & Burgess, K. (2022). Rapid HILIC-Z ion mobility mass spectrometry (RHIMMS) method for untargeted metabolomics of complex biological samples. *Metabolomics*, *18*(3), 16. https://doi.org/10.1007/s11306-022-01871-1

Pirok, B. W. J., Stoll, D. R., & Schoenmakers, P. J. (2019). Recent Developments in Two-Dimensional Liquid Chromatography: Fundamental Improvements for Practical Applications. *Analytical Chemistry*, *91*(1), 240–263. https://doi.org/10.1021/acs.analchem.8b04841

Plante, P.-L., Francovic-Fontaine, É., May, J. C., McLean, J. A., Baker, E. S., Laviolette, F., Marchand, M., & Corbeil, J. (2019). Predicting Ion Mobility Collision Cross-Sections Using a Deep Neural Network: DeepCCS. *Analytical Chemistry*, *91*(8), 5191–5199. https://doi.org/10.1021/acs.analchem.8b05821

Plumb, R. S., Isaac, G., Rainville, P. D., Hill, J., Gethings, L. A., Johnson, K. A., Lauterbach, J., & Wilson, I. D. (2022). High Throughput UHPLC-MS-Based Lipidomics Using Vacuum Jacketed Columns. *Journal of Proteome Research*, *21*(3), 691–701. https://doi.org/10.1021/acs.jproteome.1c00836

Pluskal, T., Castillo, S., Villar-Briones, A., & Orešič, M. (2010). MZmine 2: Modular framework for processing, visualizing, and analyzing mass spectrometry-based molecular profile data. *BMC Bioinformatics*, *11*, 395. https://doi.org/10.1186/1471-2105-11-395

Popa, C., Netea, M. G., Van Riel, P. L. C. M., Van Der Meer, J. W. M., & Stalenhoef, A. F. H. (2007). The role of TNF-α in chronic inflammatory conditions, intermediary metabolism, and cardiovascular risk. *Journal of Lipid Research*, *48*(4), 751–762. https://doi.org/10.1194/JLR.R600021-JLR200

Prost, S. A., Crowell, K. L., Baker, E. S., Ibrahim, Y. M., Clowers, B. H., Monroe, M. E., Anderson, G. A., Smith, R. D., & Payne, S. H. (2014). Detecting and removing data artifacts in Hadamard transform ion mobility-mass spectrometry measurements. *Journal of the American Society for Mass Spectrometry*, *25*(12), 2020–2027. https://doi.org/10.1007/s13361-014-0895-y

Puri, P., Baillie, R. A., Wiest, M. M., Mirshahi, F., Choudhury, J., Cheung, O., Sargeant, C., Contos, M. J., & Sanyal, A. J. (2007). A lipidomic analysis of nonalcoholic fatty liver disease. *Hepatology*, *46*(4), 1081–1090. https://doi.org/10.1002/HEP.21763

Puri, P., Xu, J., Vihervaara, T., Katainen, R., Ekroos, K., Daita, K., Min, H. K., Joyce, A., Mirshahi, F., Tsukamoto, H., & Sanyal, A. J. (2016). Alcohol produces distinct hepatic lipidome and eicosanoid signature in lean and obese. *Journal of Lipid Research*, *57*(6), 1017–1028. https://doi.org/10.1194/JLR.M066175

R Core Team. (2018). *R: A Language and Environment for Statistical Computing*. R Foundation for Statistical Computing, Vienna, Austria. https://www.r-project.org

Raina, N., Matsui, J., Cunnane, S. C., & Jeejeebhoy, K. N. (1995). Effect of tumor necrosis factor-α on triglyceride and phospholipid content and fatty acid composition of liver and carcass in rats. *Lipids*, *30*(8), 713–718. https://doi.org/10.1007/BF02537797

Ramaiah, S. K., & Jaeschke, H. (2007). Role of Neutrophils in the Pathogenesis of Acute Inflammatory Liver Injury. *Toxicologic Pathology*, *35*(6), 757–766. https://doi.org/10.1080/01926230701584163

Ramani Venkata, A., & Ramesh, M. (2021). A concise review on lipidomics analysis in biological samples. *ADMET & DMPK*, *9*(1), 1–22. https://doi.org/10.5599/ADMET.913

Rathahao-Paris, E., Alves, S., Junot, C., & Tabet, J. C. (2015). High resolution mass spectrometry for structural

identification of metabolites in metabolomics. *Metabolomics*, *12*(1), 1–15. https://doi.org/10.1007/S11306-015-0882-8

Reichel, M., Greiner, E., Richter-Schmidinger, T., Yedibela, Ö., Tripal, P., Jacobi, A., Bleich, S., Gulbins, E., & Kornhuber, J. (2010). Increased Acid Sphingomyelinase Activity in Peripheral Blood Cells of Acutely Intoxicated Patients With Alcohol Dependence. *Alcohol: Clinical and Experimental Research*, *34*(1), 46–50. https://doi.org/10.1111/j.1530-0277.2009.01064.x

Reinecke, T., Naylor, C. N., & Clowers, B. H. (2019). Ion multiplexing: Maximizing throughput and signal to noise ratio for ion mobility spectrometry. *TrAC Trends in Analytical Chemistry*, *116*, 340–345. https://doi.org/10.1016/j.trac.2019.03.014

Reynaud, M., Aubin, H. J., Trinquet, F., Zakine, B., Dano, C., Dematteis, M., Trojak, B., Paille, F., & Detilleux, M. (2017). A Randomized, Placebo-Controlled Study of High-Dose Baclofen in Alcohol-Dependent Patients-The ALPADIR Study. *Alcohol and Alcoholism*, *52*(4), 439–446. https://doi.org/10.1093/ALCALC/AGX030

Richardson, K., Langridge, D., & Giles, K. (2018). Fundamentals of travelling wave ion mobility revisited: I. Smoothly moving waves. *International Journal of Mass Spectrometry*, *428*, 71–80. https://doi.org/10.1016/J.IJMS.2018.03.007

Richardson, T. A., Sherman, M., Kalman, D., & Morgan, E. T. (2006). Expression of UDP-Glucuronosyltransferase Isoform mRNAs during Inflammation and Infection in Mouse Liver and Kidney. *Drug Metabolism and Disposition: The Biological Fate of Chemicals*, *34*(3), 351–353. https://doi.org/10.1124/DMD.105.007435

Riquelme, G., Zabalegui, N., Marchi, P., Jones, C. M., & Monge, M. E. (2020). A Python-Based Pipeline for Preprocessing LC–MS Data for Untargeted Metabolomics Workflows. *Metabolites*, *10*(10), 1–14. https://doi.org/10.3390/metabo10100416

Rivera, S. M., Christou, P., & Canela-Garayoa, R. (2014). Identification of carotenoids using mass spectrometry. *Mass Spectrometry Reviews*, *33*(5), 353–372. https://doi.org/10.1002/mas.21390

Robin, M. A., Demeilliers, C., Sutton, A., Paradis, V., Maisonneuve, C., Dubois, S., Poirel, O., Lettéron, P., Pessayre, D., & Fromenty, B. (2005). Alcohol increases tumor necrosis factor α and decreases nuclear factor-κb to activate hepatic apoptosis in genetically obese mice. *Hepatology*, *42*(6), 1280–1290. https://doi.org/10.1002/HEP.20949

Rodriguez, D. A., Moncada, C., Núñez, M. T., Lavandero, S., Ponnappa, B. C., & Israel, Y. (2004). Ethanol increases tumor necrosis factor-alpha receptor-1 (TNF-R1) levels in hepatic, intestinal, and cardiac cells. *Alcohol*, *33*(1), 9–15. https://doi.org/10.1016/J.ALCOHOL.2004.03.001

Ross, D. H., Cho, J. H., & Xu, L. (2020). Breaking Down Structural Diversity for Comprehensive Prediction of Ion-Neutral Collision Cross Sections. *Analytical Chemistry*, *92*(6), 4548–4557. https://doi.org/10.1021/ACS.ANALCHEM.9B05772

Ruiz-Perez, D., Guan, H., Madhivanan, P., Mathee, K., & Narasimhan, G. (2020). So you think you can PLS-DA? *BMC Bioinformatics*, *21*(Suppl 1), 2. https://doi.org/10.1186/s12859-019-3310-7

Rush, B. (1785). *An Inquiry Into the Effects of Ardent Spirits Upon the Human Body and Mind: with an account of the means of preventing, and of the remedies for curing them*. Printed for Cornelius Davis, New York. https://doi.org/resource.nlm.nih.gov/2569025R

Saberi, B., Dadabhai, A. S., Jang, Y.-Y., Gurakar, A., & Mezey, E. (2016). Current Management of Alcoholic Hepatitis and Future Therapies. *Journal of Clinical and Translational Hepatology*, *4*(2), 113–122. https://doi.org/10.14218/JCTH.2016.00006

Saccenti, E., Hoefsloot, H. C. J., Smilde, A. K., Westerhuis, J. A., & Hendriks, M. M. W. B. (2014). Reflections on univariate and multivariate analysis of metabolomics data. *Metabolomics*, *10*(3), 361–374. https://doi.org/10.1007/S11306-013-0598-6

Sakhuja, P. (2014). Pathology of alcoholic liver disease, can it be differentiated from nonalcoholic steatohepatitis? *World Journal of Gastroenterology*, *20*(44), 16474–16479. https://doi.org/10.3748/WJG.V20.I44.16474

Sakodynskii, K. (1972). The life and scientific works of Michael Tswett. *Journal of Chromatography A*, *73*(2), 303–360. https://doi.org/10.1016/S0021-9673(01)91213-0

Sampsonidis, I., Witting, M., Koch, W., Virgiliou, C., Gika, H. G., Schmitt-Kopplin, P., & Theodoridis, G. A. (2015). Computational analysis and ratiometric comparison approaches aimed to assist column

selection in hydrophilic interaction liquid chromatography-tandem mass spectrometry targeted metabolomics. *Journal of Chromatography. A*, *1406*, 145–155. https://doi.org/10.1016/j.chroma.2015.06.008

Sanchez-Dominguez, C. N., Gallardo-Blanco, H. L., Salinas-Santander, M. A., & Ortiz-Lopez, R. (2018). Uridine 5'-diphospho-glucronosyltrasferase: Its role in pharmacogenomics and human disease. *Experimental and Therapeutic Medicine*, *16*(1), 3–11. https://doi.org/10.3892/ETM.2018.6184

Sandra, K., Steenbeke, M., Vandenheede, I., Vanhoenacker, G., & Sandra, P. (2017). The versatility of heart-cutting and comprehensive two-dimensional liquid chromatography in monoclonal antibody clone selection. *Journal of Chromatography A*, *1523*, 283–292. https://doi.org/10.1016/j.chroma.2017.06.052

Saponara, E., Penno, C., Orsini, V., Wang, Z.-Y., Fischer, A., Aebi, A., Matadamas-Guzman, M. L., Brun, V., Fischer, B., Brousseau, M., O'donnell, P., Turner, J., Meyer, A. G., Bollepalli, L., D'ario, G., Roma, G., Carbone, W., Annunziato, S., Obrecht, M., … Ruffner, H. (2022). Loss of Hepatic Leucine-Rich Repeat-Containing G-Protein–Coupled Receptors 4 and 5 Promotes Nonalcoholic Fatty Liver Disease. *The American Journal of Pathology*, *193*(2), 161–181. https://doi.org/10.1016/J.AJPATH.2022.10.008

Savic, D., Hodson, L., Neubauer, S., & Pavlides, M. (2020). The Importance of the Fatty Acid Transporter L-Carnitine in Non-Alcoholic Fatty Liver Disease (NAFLD). *Nutrients*, *12*(8), 1–17. https://doi.org/10.3390/NU12082178

Schaffner, F., & Thaler, H. (1986). Nonalcoholic fatty liver disease. *Progress in Liver Diseases*, *8*, 283–298. https://doi.org/PMID: 3086934

Schellinger, A. P., & Carr, P. W. (2004). Solubility of Buffers in Aqueous – Organic Eluents for Reversed-Phase Liquid Chromatography. *Liquid Chromatography Gas Chromatography North America*, *22*(6), 544–548.

Scheubert, K., Hufsky, F., & Böcker, S. (2013). Computational mass spectrometry for small molecules. *Journal of Cheminformatics*, *5*(1), 12. https://doi.org/10.1186/1758-2946-5-12

Schiffman, C., Petrick, L., Perttula, K., Yano, Y., Carlsson, H., Whitehead, T., Metayer, C., Hayes, J., Rappaport, S., & Dudoit, S. (2019). Filtering procedures for untargeted LC-MS metabolomics data. *BMC Bioinformatics*, *20*(1), 1–10. https://doi.org/10.1186/S12859-019-2871-9

Schymanski, E. L., Jeon, J., Gulde, R., Fenner, K., Ruff, M., Singer, H. P., & Hollender, J. (2014). Identifying Small Molecules via High Resolution Mass Spectrometry: Communicating Confidence. *Environmental Science & Technology*, *48*(4), 2097–2098. https://doi.org/10.1021/es5002105

Seitz, H. K., Bataller, R., Cortez-Pinto, H., Gao, B., Gual, A., Lackner, C., Mathurin, P., Mueller, S., Szabo, G., & Tsukamoto, H. (2018). Alcoholic liver disease. *Nature Reviews. Disease Primers*, *4*(1), 16. https://doi.org/10.1038/S41572-018-0014-7

Seitzer, P., Bennett, B., & Melamud, E. (2022). MAVEN2: An Updated Open-Source Mass Spectrometry Exploration Platform. *Metabolites*, *12*(8), 684. https://doi.org/10.3390/metabo12080684

Seo, W., & Jeong, W. Il. (2016). Hepatic non-parenchymal cells: Master regulators of alcoholic liver disease? *World Journal of Gastroenterology*, *22*(4), 1348–1356. https://doi.org/10.3748/WJG.V22.I4.1348

Sherman, M. L., Spriggs, D. R., Arthur, K. A., Imamura, K., Frei, E., & Kufe, D. W. (1988). Recombinant human tumor necrosis factor administered as a five-day continuous infusion in cancer patients: phase I toxicity and effects on lipid metabolism. *Journal of Clinical Oncology*, *6*(2), 344–350. https://doi.org/10.1200/JCO.1988.6.2.344

Sheron, N., Moore, M., O'Brien, W., Harris, S., & Roderick, P. (2013). Feasibility of detection and intervention for alcohol-related liver disease in the community: the Alcohol and Liver Disease Detection study (ALDDeS). *The British Journal of General Practice : The Journal of the Royal College of General Practitioners*, *63*(615), e698–e705. https://doi.org/10.3399/BJGP13X673711

Shi, C., Wang, L., Zhou, K., Shao, M., Lu, Y., & Wu, T. (2020). Targeted Metabolomics Identifies Differential Serum and Liver Amino Acids Biomarkers in Rats with Alcoholic Liver Disease. *Journal of Nutritional Science and Vitaminology*, *66*(6), 536–544. https://doi.org/10.3177/JNSV.66.536

Shi, J., Zhou, J., Ma, H., Guo, H., Ni, Z., Duan, J., Tao, W., & Qian, D. (2016). An in vitro metabolomics approach to identify hepatotoxicity biomarkers in human L02 liver cells treated with pekinenal, a natural compound. *Analytical and Bioanalytical Chemistry*, *408*(5), 1413–1424. https://doi.org/10.1007/S00216-015-9202-4

Shim, Y. R., & Jeong, W. Il. (2020). Recent advances of sterile inflammation and inter-organ cross-talk in alcoholic liver disease. *Experimental & Molecular Medicine*, *52*(5), 772–780. https://doi.org/10.1038/s12276-020-0438-5

Sillner, N., Walker, A., Harrieder, E.-M., Schmitt-Kopplin, P., & Witting, M. (2019). Development and application of a HILIC UHPLC-MS method for polar fecal metabolome profiling. *Journal of Chromatography B*, *1109*, 142–148. https://doi.org/10.1016/j.jchromb.2019.01.016

Singal, A. K., Bataller, R., Ahn, J., Kamath, P. S., & Shah, V. H. (2018). ACG clinical guideline: Alcoholic liver disease. *American Journal of Gastroenterology*, *113*(2), 175–194. https://doi.org/10.1038/ajg.2017.469

Singal, A. K., Jampana, S. C., & Weinman, S. A. (2011). Antioxidants as therapeutic agents for liver disease. *Liver International*, *31*(10), 1432–1448. https://doi.org/10.1111/j.1478-3231.2011.02604.x

Singh, S., Osna, N. A., & Kharbanda, K. K. (2017). Treatment options for alcoholic and non-alcoholic fatty liver disease: A review. *World Journal of Gastroenterology*, *23*(36), 6549–6570. https://doi.org/10.3748/wjg.v23.i36.6549

Skaff, O., Pattison, D. I., & Davies, M. J. (2008). The Vinyl Ether Linkages of Plasmalogens Are Favored Targets for Myeloperoxidase-Derived Oxidants: A Kinetic Study†. *Biochemistry*, *47*(31), 8237–8245. https://doi.org/10.1021/BI800786Q

Smith, C. A., O'Maille, G., Want, E. J., Qin, C., Trauger, S. A., Brandon, T. R., Custodio, D. E., Abagyan, R., & Siuzdak, G. (2005a). METLIN: a metabolite mass spectral database. *Therapeutic Drug Monitoring*, *27*(6), 747–751. https://doi.org/10.1097/01.ftd.0000179845.53213.39

Smith, C. A., O'Maille, G., Want, E. J., Qin, C., Trauger, S. A., Brandon, T. R., Custodio, D. E., Abagyan, R., & Siuzdak, G. (2005b). METLIN: a metabolite mass spectral database. *Therapeutic Drug Monitoring*, *27*(6), 747–751. https://doi.org/10.1097/01.FTD.0000179845.53213.39

Smith, C. A., Want, E. J., O'Maille, G., Abagyan, R., & Siuzdak, G. (2006). XCMS: Processing mass spectrometry data for metabolite profiling using nonlinear peak alignment, matching and identification. *Analytical Chemistry*, *78*(3), 779–787. https://doi.org/10.1021/ac051437y

Society for Advancement of AOPs. (2023). *AOP-Wiki*. AOP-Wiki. http://aopwiki.org

Soga, T., Igarashi, K., Ito, C., Mizobuchi, K., Zimmermann, H.-P., & Tomita, M. (2009). Metabolomic Profiling of Anionic Metabolites by Capillary Electrophoresis Mass Spectrometry. *Analytical Chemistry*, *81*(15), 6165–6174. https://doi.org/10.1021/ac900675k

Spicer, R., Salek, R. M., Moreno, P., Cañueto, D., & Steinbeck, C. (2017). Navigating freely-available software tools for metabolomics analysis. *Metabolomics*, *13*(9), 1–16. https://doi.org/10.1007/s11306-017-1242-7

Staufer, K., Huber-Schönauer, U., Strebinger, G., Pimingstorfer, P., Suesse, S., Scherzer, T.-M., Paulweber, B., Ferenci, P., Stimpfl, T., Yegles, M., Datz, C., & Trauner, M. (2022). Ethyl glucuronide in hair detects a high rate of harmful alcohol consumption in presumed non-alcoholic fatty liver disease. *Journal of Hepatology*, *77*(4), 918–930. https://doi.org/10.1016/j.jhep.2022.04.040

Stefanescu, H., Suciu, A., Romanciuc, F., Crisan, D., Procopet, B., Radu, C., Tantau, M., Socaciu, C., & Grigorescu, M. (2016). Lyso-phosphatidylcholine: A potential metabolomic biomarker for alcoholic liver disease? *Hepatology*, *64*(2), 678–679. https://doi.org/10.1002/HEP.28630

Steiber, A., Kerner, J., & Hoppel, C. L. (2004). Carnitine: a nutritional, biosynthetic, and functional perspective. *Molecular Aspects of Medicine*, *25*(5–6), 455–473. https://doi.org/10.1016/J.MAM.2004.06.006

Stettin, D., Poulin, R. X., & Pohnert, G. (2020). Metabolomics Benefits from Orbitrap GC-MS-Comparison of Low- and High-Resolution GC-MS. *Metabolites*, *10*(4). https://doi.org/10.3390/metabo10040143

Stickel, F., Moreno, C., Hampe, J., & Morgan, M. Y. (2017). The genetics of alcohol dependence and alcohol-related liver disease. *Journal of Hepatology*, *66*(1), 195–211. https://doi.org/10.1016/J.JHEP.2016.08.011

Stickel, F., & Seitz, H. (2003). Ethanol and Methyl Transfer: Its Role in Liver Disease and Hepatocarcinogenesis. In R. R. Watson & V. R. Preedy (Eds.), *Nutrition and Alcohol* (pp. 57–71). CRC Press, Florida. https://doi.org/10.1201/9780203507636.CH4

Stoll, D. R., & Carr, P. W. (2017). Two-Dimensional Liquid Chromatography: A State of the Art Tutorial. *Analytical Chemistry*, *89*(1), 519–531. https://doi.org/10.1021/acs.analchem.6b03506

Stow, S. M., Causon, T. J., Zheng, X., Kurulugama, R. T., Mairinger, T., May, J. C., Rennie, E. E., Baker, E. S., Smith, R. D., McLean, J. A., Hann, S., & Fjeldsted, J. C. (2017). An Interlaboratory Evaluation of Drift Tube Ion Mobility-Mass Spectrometry Collision Cross Section Measurements. *Analytical Chemistry*, *89*(17), 9048–9055. https://doi.org/10.1021/acs.analchem.7b01729

Strassburg, K., Huijbrechts, A. M. L., Kortekaas, K. A., Lindeman, J. H., Pedersen, T. L., Dane, A., Berger, R., Brenkman, A., Hankemeier, T., Van Duynhoven, J., Kalkhoven, E., Newman, J. W., & Vreeken, R. J. (2012). Quantitative profiling of oxylipins through comprehensive LC-MS/MS analysis: Application in cardiac surgery. *Analytical and Bioanalytical Chemistry*, *404*(5), 1413–1426. https://doi.org/10.1007/s00216-012-6226-x

Stravs, M. A., Schymanski, E. L., Singer, H. P., & Hollender, J. (2013). Automatic recalibration and processing of tandem mass spectra using formula annotation. *Journal of Mass Spectrometry*, *48*(1), 89–99. https://doi.org/10.1002/jms.3131

Su Jung, K., Su Hee, K., Ji Hyun, K., Shin, H., & Hyun Ju, Y. (2016). Understanding Metabolomics in Biomedical Research. *Endocrinology and Metabolism*, *31*(1), 7–16. https://doi.org/10.3803/ENM.2016.31.1.7

Sud, M., Fahy, E., Cotter, D., Brown, A., Dennis, E. A., Glass, C. K., Merrill, A. H., Murphy, R. C., Raetz, C. R., Russell, D. W., & Subramaniam, S. (2007). LMSD: LIPID MAPS structure database. *Nucleic Acids Research*, *35*, D527–D532. https://doi.org/10.1093/NAR/GKL838

Sumner, L. W., Amberg, A., Barrett, D., Beale, M. H., Beger, R., Daykin, C. A., Fan, T. W.-M., Fiehn, O., Goodacre, R., Griffin, J. L., Hankemeier, T., Hardy, N., Harnly, J., Higashi, R., Kopka, J., Lane, A. N., Lindon, J. C., Marriott, P., Nicholls, A. W., … Viant, M. R. (2007). Proposed minimum reporting standards for chemical analysis. *Metabolomics*, *3*(3), 211–221. https://doi.org/10.1007/s11306-007-0082-2

Sun, J., Fu, J., Li, L., Chen, C., Wang, H., Hou, Y., Xu, Y., & Pi, J. (2018). Nrf2 in alcoholic liver disease. *Toxicology and Applied Pharmacology*, *357*, 62–69. https://doi.org/10.1016/j.taap.2018.08.019

Sun, X., Ye, C., Deng, Q., Chen, J., & Guo, C. (2021). Contribution of glutaredoxin-1 to Fas s-glutathionylation and inflammation in ethanol-induced liver injury. *Life Sciences*, *264*, 118678. https://doi.org/10.1016/J.LFS.2020.118678

Tacer, K. F., Kuzman, D., Seliškar, M., Pompon, D., & Rozman, D. (2007). TNF-α interferes with lipid homeostasis and activates acute and proatherogenic processes. *Physiological Genomics*, *31*(2), 216–227. https://doi.org/10.1152/PHYSIOLGENOMICS.00264.2006

Tada, I., Tsugawa, H., Meister, I., Zhang, P., Shu, R., Katsumi, R., Wheelock, C. E., Arita, M., & Chaleckis, R. (2019). Creating a Reliable Mass Spectral-Retention Time Library for All Ion Fragmentation-Based Metabolomics. *Metabolites*, *9*(11), 251. https://doi.org/10.3390/metabo9110251

Tan, D., Ertunc, M. E., Konduri, S., Zhang, J., Pinto, A. M., Chu, Q., Kahn, B. B., Siegel, D., & Saghatelian, A. (2019). Discovery of FAHFA-Containing Triacylglycerols and Their Metabolic Regulation. *Journal of the American Chemical Society*, *141*(22), 8798–8806. https://doi.org/10.1021/JACS.9B00045

Tang, D.-Q., Zou, L., Yin, X.-X., & Ong, C. N. (2016). HILIC-MS for metabolomics: An attractive and complementary approach to RPLC-MS. *Mass Spectrometry Reviews*, *35*(5), 574–600. https://doi.org/10.1002/mas.21445

Tascher, G., Burban, A., Camus, S., Plumel, M., Chanon, S., Guevel, R. Le, Shevchenko, V., Dorsselaer, A. Van, Lefai, E., Guguen-Guillouzo, C., & Bertile, F. (2019). In-Depth Proteome Analysis Highlights HepaRG Cells as a Versatile Cell System Surrogate for Primary Human Hepatocytes. *Cells*, *8*(2), 192. https://doi.org/10.3390/CELLS8020192

Thévenot, E. A., Roux, A., Xu, Y., Ezan, E., & Junot, C. (2015). Analysis of the Human Adult Urinary Metabolome Variations with Age, Body Mass Index, and Gender by Implementing a Comprehensive Workflow for Univariate and OPLS Statistical Analyses. *Journal of Proteome Research*, *14*(8), 3322–3335. https://doi.org/10.1021/acs.jproteome.5b00354

Thiele, M., Rausch, V., Fluhr, G., Kjærgaard, M., Piecha, F., Mueller, J., Straub, B. K., Lupșor-Platon, M., De-Ledinghen, V., Seitz, H. K., Detlefsen, S., Madsen, B., Krag, A., & Mueller, S. (2018). Controlled attenuation parameter and alcoholic hepatic steatosis: Diagnostic accuracy and role of alcohol detoxification. *Journal of Hepatology*, *68*(5), 1025–1032. https://doi.org/10.1016/j.jhep.2017.12.029

Thiele, M., Suvitaival, T., Trošt, K., Kim, M., de Zawadzki, A., Kjaergaard, M., Rasmussen, D. N., Lindvig, K. P., Israelsen, M., Detlefsen, S., Andersen, P., Juel, H. B., Nielsen, T., Georgiou, S., Filippa, V., Kuhn, M.,

Nishijima, S., Moitinho-Silva, L., Rossing, P., … Krag, A. (2023). Sphingolipids are depleted in alcohol-related liver fibrosis. *Gastroenterology*, *S0016-5085*(23), 00162–2. https://doi.org/10.1053/j.gastro.2023.02.023

Thomas, M. C., Altvater, J., Gallagher, T. J., & Nette, G. W. (2014). Collision-Induced Dissociation of Fatty Acid [M – 2H + Na]– Ions: Charge-Directed Fragmentation and Assignment of Double Bond Position. *Journal of the American Society for Mass Spectrometry*, *25*(11), 1917–1926. https://doi.org/10.1007/s13361-014-0966-0

Thursz, M., Gual, A., Lackner, C., Mathurin, P., Moreno, C., Spahr, L., Sterneck, M., & Cortez-Pinto, H. (2018). EASL Clinical Practice Guidelines: Management of alcohol-related liver disease. *Journal of Hepatology*, *69*(1), 154–181. https://doi.org/10.1016/j.jhep.2018.03.018

Tilg, H., Moschen, A. R., & Szabo, G. (2016). Interleukin-1 and inflammasomes in alcoholic liver disease/acute alcoholic hepatitis and nonalcoholic fatty liver disease/nonalcoholic steatohepatitis. *Hepatology*, *64*(3), 955–965. https://doi.org/10.1002/hep.28456

Toshikuni, N., Tsutsumi, M., & Arisawa, T. (2014). Clinical differences between alcoholic liver disease and nonalcoholic fatty liver disease. *World Journal of Gastroenterology*, *20*(26), 8393–8406. https://doi.org/10.3748/wjg.v20.i26.8393

Treutler, H., & Neumann, S. (2016). Prediction, Detection, and Validation of Isotope Clusters in Mass Spectrometry Data. *Metabolites*, *6*(4), 37. https://doi.org/10.3390/metabo6040037

Treyer, A., & Müsch, A. (2013). Hepatocyte Polarity. *Comprehensive Physiology*, *3*(1), 243–287. https://doi.org/10.1002/CPHY.C120009

Tsugawa, H., Cajka, T., Kind, T., Ma, Y., Higgins, B., Ikeda, K., Kanazawa, M., VanderGheynst, J., Fiehn, O., & Arita, M. (2015). MS-DIAL: data-independent MS/MS deconvolution for comprehensive metabolome analysis. *Nature Methods*, *12*(6), 523–526. https://doi.org/10.1038/nmeth.3393

Tsugawa, H., Ikeda, K., Takahashi, M., Satoh, A., Mori, Y., Uchino, H., Okahashi, N., Yamada, Y., Tada, I., Bonini, P., Higashi, Y., Okazaki, Y., Zhou, Z., Zhu, Z. J., Koelmel, J., Cajka, T., Fiehn, O., Saito, K., Arita, M., & Arita, M. (2020). A lipidome atlas in MS-DIAL 4. *Nature Biotechnology*, *38*(10), 1159–1163. https://doi.org/10.1038/s41587-020-0531-2

Tsugawa, H., Kind, T., Nakabayashi, R., Yukihira, D., Tanaka, W., Cajka, T., Saito, K., Fiehn, O., & Arita, M. (2016). Hydrogen Rearrangement Rules: Computational MS/MS Fragmentation and Structure Elucidation Using MS-FINDER Software. *Analytical Chemistry*, *88*(16), 7946–7958. https://doi.org/10.1021/ACS.ANALCHEM.6B00770

Tsukamoto, H., Reidelberger, R. D., French, S. W., & Largman, C. (1984). Long-term cannulation model for blood sampling and intragastric infusion in the rat. *American Journal of Physiology-Regulatory, Integrative and Comparative Physiology*, *16*(3), R595–R599. https://doi.org/10.1152/AJPREGU.1984.247.3.R595

U.S. Department of Health and Human Services, D. H. H. S., & U.S. Department of Agriculture, D. O. A. (2020). *2015–2020 Dietary Guidelines for Americans* (8th ed.). https://health.gov/our-work/food-nutrition/previous-dietary-guidelines/2015

Ulmer, C. Z., Koelmel, J. P., Jones, C. M., Garrett, T. J., Aristizabal-Henao, J. J., Vesper, H. W., & Bowden, J. A. (2021). A Review of Efforts to Improve Lipid Stability during Sample Preparation and Standardization Efforts to Ensure Accuracy in the Reporting of Lipid Measurements. *Lipids*, *56*(1), 3–16. https://doi.org/10.1002/lipd.12263

VAD. (2016). *Richtlijn voor alcoholgebruik*. www.alcoholhulp.be.

van den Berg, R. A., Hoefsloot, H. C. J., Westerhuis, J. A., Smilde, A. K., & van der Werf, M. J. (2006). Centering, scaling, and transformations: Improving the biological information content of metabolomics data. *BMC Genomics*, *7*, 142. https://doi.org/10.1186/1471-2164-7-142

Van den Eede, N., Cuykx, M., Rodrigues, R. M., Laukens, K., Neels, H., Covaci, A., & Vanhaecke, T. (2015). Metabolomics analysis of the toxicity pathways of triphenyl phosphate in HepaRG cells and comparison to oxidative stress mechanisms caused by acetaminophen. *Toxicology in Vitro*, *29*(8), 2045–2054. https://doi.org/10.1016/j.tiv.2015.08.012

van der Veen, J. N., Kennelly, J. P., Wan, S., Vance, J. E., Vance, D. E., & Jacobs, R. L. (2017). The critical role of phosphatidylcholine and phosphatidylethanolamine metabolism in health and disease. *Biochimica et Biophysica Acta - Biomembranes*, *1859*(9), 1558–1572.

https://doi.org/10.1016/J.BBAMEM.2017.04.006
Ventura, R., Martínez-Ruiz, I., & Hernández-Alvarez, M. I. (2022). Phospholipid Membrane Transport and Associated Diseases. *Biomedicines*, *10*(5), 1201. https://doi.org/10.3390/biomedicines10051201
Vina, J., Estrela, J. M., Guerri, C., & Romero, F. J. (1980). Effect of ethanol on glutathione concentration in isolated hepatocytes. *Biochemical Journal*, *188*(2), 549–552. https://doi.org/10.1042/BJ1880549
Vinaixa, M., Samino, S., Saez, I., Duran, J., Guinovart, J. J., & Yanes, O. (2012). A guideline to univariate statistical analysis for LC/MS-based untargeted metabolomics-derived data. *Metabolites*, *2*(4), 775–795. https://doi.org/10.3390/metabo2040775
Vinaixa, M., Schymanski, E. L., Neumann, S., Navarro, M., Salek, R. M., & Yanes, O. (2016). Mass spectral databases for LC/MS- and GC/MS-based metabolomics: State of the field and future prospects. *TrAC Trends in Analytical Chemistry*, *78*, 23–35. https://doi.org/10.1016/J.TRAC.2015.09.005
Vinken, M., Knapen, D., Vergauwen, L., Hengstler, J. G., Angrish, M., & Whelan, M. (2017). Adverse outcome pathways: a concise introduction for toxicologists. *Archives of Toxicology*, *91*(11), 3697–3707. https://doi.org/10.1007/S00204-017-2020-Z
Vonghia, L., Michielsen, P., Dom, G., & Francque, S. (2014). Diagnostic challenges in alcohol use disorder and alcoholic liver disease. *World Journal of Gastroenterology*, *20*(25), 8024–8032. https://doi.org/10.3748/WJG.V20.I25.8024
Vorrink, S. U., Ullah, S., Schmidt, S., Nandania, J., Velagapudi, V., Beck, O., Ingelman-Sundberg, M., & Lauschke, V. M. (2017). Endogenous and xenobiotic metabolic stability of primary human hepatocytes in long-term 3D spheroid cultures revealed by a combination of targeted and untargeted metabolomics. *FASEB Journal*, *31*(6), 2696–2708. https://doi.org/10.1096/fj.201601375R
Vosse, C., Wienken, C., Cadenas, C., & Hayen, H. (2018). Separation and identification of phospholipids by hydrophilic interaction liquid chromatography coupled to tandem high resolution mass spectrometry with focus on isomeric phosphatidylglycerol and bis(monoacylglycero)phosphate. *Journal of Chromatography A*, *1565*, 105–113. https://doi.org/10.1016/j.chroma.2018.06.039
Vuittonet, C. L., Halse, M., Leggio, L., Fricchione, S. B., Brickley, M., Haass-Koffler, C. L., Tavares, T., Swift, R. M., & Kenna, G. A. (2014). Pharmacotherapy for alcoholic patients with alcoholic liver disease. *American Journal of Health-System Pharmacy*, *71*(15), 1265–1276. https://doi.org/10.2146/AJHP140028
Wagner, G. R., Bhatt, D. P., O'Connell, T. M., Thompson, J. W., Dubois, L. G., Backos, D. S., Yang, H., Mitchell, G. A., Ilkayeva, O. R., Stevens, R. D., Grimsrud, P. A., & Hirschey, M. D. (2017). A Class of Reactive Acyl-CoA Species Reveals the Non-enzymatic Origins of Protein Acylation. *Cell Metabolism*, *25*(4), 823-837.e8. https://doi.org/10.1016/j.cmet.2017.03.006
Wang, F., Liigand, J., Tian, S., Arndt, D., Greiner, R., & Wishart, D. S. (2021). CFM-ID 4.0: More Accurate ESI-MS/MS Spectral Prediction and Compound Identification. *Analytical Chemistry*, *93*(34), 11692–11700. https://doi.org/10.1021/ACS.ANALCHEM.1C01465
Wang, M., Carver, J. J., Phelan, V. V., Sanchez, L. M., Garg, N., Peng, Y., Nguyen, D. D., Watrous, J., Kapono, C. A., Luzzatto-Knaan, T., Porto, C., Bouslimani, A., Melnik, A. V., Meehan, M. J., Liu, W. T., Crüsemann, M., Boudreau, P. D., Esquenazi, E., Sandoval-Calderón, M., … Bandeira, N. (2016). Sharing and community curation of mass spectrometry data with Global Natural Products Social Molecular Networking. *Nature Biotechnology*, *34*(8), 828–837. https://doi.org/10.1038/NBT.3597
Wang, Y., Zhu, W., Qiu, J., Wang, X., Zhang, P., Yan, J., & Zhou, Z. (2015). Monitoring tryptophan metabolism after exposure to hexaconazole and the enantioselective metabolism of hexaconazole in rat hepatocytes in vitro. *Journal of Hazardous Materials*, *295*, 9–16. https://doi.org/10.1016/J.JHAZMAT.2015.04.006
Wang, Z., Yao, T., & Song, Z. (2010). Involvement and mechanism of DGAT2 upregulation in the pathogenesis of alcoholic fatty liver disease. *Journal of Lipid Research*, *51*(11), 3158–3165. https://doi.org/10.1194/JLR.M007948
Want, E. J., Masson, P., Michopoulos, F., Wilson, I. D., Theodoridis, G., Plumb, R. S., Shockcor, J., Loftus, N., Holmes, E., & Nicholson, J. K. (2013). Global metabolic profiling of animal and human tissues via UPLC-MS. *Nature Protocols*, *8*(1), 17–32. https://doi.org/10.1038/nprot.2012.135
Wei, R., Wang, J., Su, M., Jia, E., Chen, S., Chen, T., & Ni, Y. (2018). Missing Value Imputation Approach for Mass Spectrometry-based Metabolomics Data. *Scientific Reports*, *8*(1), 1–10.

https://doi.org/10.1038/s41598-017-19120-0
Wernisch, S., & Pennathur, S. (2016). Evaluation of coverage, retention patterns, and selectivity of seven liquid chromatographic methods for metabolomics. *Analytical and Bioanalytical Chemistry*, *408*(22), 6079–6091. https://doi.org/10.1007/s00216-016-9716-4
Wieder, C., Frainay, C., Poupin, N., Rodríguez-Mier, P., Vinson, F., Cooke, J., Lai, R. P. J., Bundy, J. G., Jourdan, F., & Ebbels, T. (2021). Pathway analysis in metabolomics: Recommendations for the use of over-representation analysis. *PLoS Computational Biology*, *17*(9), e1009105. https://doi.org/10.1371/JOURNAL.PCBI.1009105
Wilkin, R. J. W., Lalor, P. F., Parker, R., & Newsome, P. N. (2016). Murine Models of Acute Alcoholic Hepatitis and Their Relevance to Human Disease. *The American Journal of Pathology*, *186*(4), 748–760. https://doi.org/10.1016/J.AJPATH.2015.12.003
Wishart, D. S., Guo, A. C., Oler, E., Wang, F., Anjum, A., Peters, H., Dizon, R., Sayeeda, Z., Tian, S., Lee, B. L., Berjanskii, M., Mah, R., Yamamoto, M., Jovel, J., Torres-Calzada, C., Hiebert-Giesbrecht, M., Lui, V. W., Varshavi, D., Varshavi, D., … Gautam, V. (2022). HMDB 5.0: the Human Metabolome Database for 2022. *Nucleic Acids Research*, *50*(D1), D622–D631. https://doi.org/10.1093/NAR/GKAB1062
World Health Organization. (2018). *Global status report on alcohol and health 2018*. https://doi.org/9789241565639
Wu, G., Yang, J., Lv, H., Jing, W., Zhou, J., Feng, Y., Lin, S., Yang, Q., & Hu, J. (2018). Taurine prevents ethanol-induced apoptosis mediated by mitochondrial or death receptor pathways in liver cells. *Amino Acids*, *50*(7), 863–875. https://doi.org/10.1007/S00726-018-2561-3
Wu, Qian, Wang, J. Y., Han, D. Q., & Yao, Z. P. (2020). Recent advances in differentiation of isomers by ion mobility mass spectrometry. *TrAC Trends in Analytical Chemistry*, *124*, 115801. https://doi.org/10.1016/J.TRAC.2019.115801
Wu, Qiong, Zhang, H., Dong, X., Chen, X.-F., Zhu, Z.-Y., Hong, Z.-Y., & Chai, Y.-F. (2014). UPLC-Q-TOF/MS based metabolomic profiling of serum and urine of hyperlipidemic rats induced by high fat diet. *Journal of Pharmaceutical Analysis*, *4*(6), 360–367. https://doi.org/10.1016/j.jpha.2014.04.002
Wu, Z. E., Kruger, M. C., Cooper, G. J. S., Poppitt, S. D., & Fraser, K. (2019). Tissue-specific sample dilution: An important parameter to optimise prior to untargeted LC-MS metabolomics. *Metabolites*, *9*(7), 1–19. https://doi.org/10.3390/metabo9070124
Xing, S., & Huan, T. (2022). Radical fragment ions in collision-induced dissociation-based tandem mass spectrometry. *Analytica Chimica Acta*, *1200*, 339613. https://doi.org/10.1016/j.aca.2022.339613
Xu, T., Hu, C., Xuan, Q., & Xu, G. (2020). Recent advances in analytical strategies for mass spectrometry-based lipidomics. *Analytica Chimica Acta*, *1137*, 156–169. https://doi.org/10.1016/j.aca.2020.09.060
Xue, J., Guijas, C., Benton, H. P., Warth, B., & Siuzdak, G. (2020). METLIN MS2 molecular standards database: a broad chemical and biological resource. *Nature Methods*, *17*(10), 953–954. https://doi.org/10.1038/s41592-020-0942-5
Yan, X., Markey, S. P., Marupaka, R., Dong, Q., Cooper, B. T., Mirokhin, Y. A., Wallace, W. E., & Stein, S. E. (2020). Mass Spectral Library of Acylcarnitines Derived from Human Urine. *Analytical Chemistry*, *92*(9), 6521–6528. https://doi.org/10.1021/acs.analchem.0c00129
Yanes, O., Tautenhahn, R., Patti, G. J., & Siuzdak, G. (2011). Expanding coverage of the metabolome for global metabolite profiling. *Analytical Chemistry*, *83*(6), 2152–2161. https://doi.org/10.1021/ac102981k
Yang, K., & Han, X. (2016). Lipidomics: Techniques, applications, and outcomes related to biomedical sciences. *Trends in Biochemical Sciences*, *41*(11), 954–969. https://doi.org/10.1016/J.TIBS.2016.08.010
Yang, L., Jin, G. H., & Zhou, J. Y. (2016). The Role of Ceramide in the Pathogenesis of Alcoholic Liver Disease. *Alcohol and Alcoholism*, *51*(3), 251–257. https://doi.org/10.1093/ALCALC/AGV119
Yang, X., Neta, P., & Stein, S. E. (2014). Quality control for building libraries from electrospray ionization tandem mass spectra. *Analytical Chemistry*, *86*(13), 6393–6400. https://doi.org/10.1021/AC500711M
Yetukuri, L., Ekroos, K., Vidal-Puig, A., & Orešič, M. (2008). Informatics and computational strategies for the study of lipids. *Molecular BioSystems*, *4*(2), 121–127. https://doi.org/10.1039/b715468b
Yin, M., Wheeler, M. D., Kono, H., Bradford, B. U., Gallucci, R. M., Luster, M. I., & Thurman, R. G. (1999).

Essential role of tumor necrosis factor α in alcohol-induced liver injury in mice. *Gastroenterology*, *117*(4), 942–952. https://doi.org/10.1016/S0016-5085(99)70354-9

Yore, M. M., Syed, I., Moraes-Vieira, P. M., Zhang, T., Herman, M. A., Homan, E. A., Patel, R. T., Lee, J., Chen, S., Peroni, O. D., Dhaneshwar, A. S., Hammarstedt, A., Smith, U., McGraw, T. E., Saghatelian, A., & Kahn, B. B. (2014). Discovery of a class of endogenous mammalian lipids with anti-diabetic and anti-inflammatory effects. *Cell*, *159*(2), 318–332. https://doi.org/10.1016/j.cell.2014.09.035

You, M., Fischer, M., Deeg, M. A., & Crabb, D. W. (2002). Ethanol induces fatty acid synthesis pathways by activation of sterol regulatory element-binding protein (SREBP). *The Journal of Biological Chemistry*, *277*(32), 29342–29347. https://doi.org/10.1074/JBC.M202411200

Zehethofer, N., Pinto, D. M., & Volmer, D. A. (2008). Plasma free fatty acid profiling in a fish oil human intervention study using ultra-performance liquid chromatography/electrospray ionization tandem mass spectrometry. *Rapid Communications in Mass Spectrometry*, *22*(13), 2125–2133. https://doi.org/10.1002/rcm.3597

Zeilinger, K., Freyer, N., Damm, G., Seehofer, D., & Knöspel, F. (2016). Cell sources for in vitro human liver cell culture models. *Experimental Biology and Medicine*, *241*(15), 1684–1698. https://doi.org/10.1177/1535370216657448

Zhang, S. Z., Lipsky, M. M., Trump, B. F., & Hsu, I. C. (1990). Neutral red (NR) assay for cell viability and xenobiotic-induced cytotoxicity in primary cultures of human and rat hepatocytes. *Cell Biology and Toxicology*, *6*(2), 219–234. https://doi.org/10.1007/BF00249595

Zhang, X., Dong, J., & Raftery, D. (2020). Five Easy Metrics of Data Quality for LC–MS-Based Global Metabolomics. *Analytical Chemistry*, *92*(19), 12925–12933. https://doi.org/10.1021/acs.analchem.0c01493

Zhang, Y., Fowler, K. J., Hamilton, G., Cui, J. Y., Sy, E. Z., Balanay, M., Hooker, J. C., Szeverenyi, N., & Sirlin, C. B. (2018). Liver fat imaging—a clinical overview of ultrasound, CT, and MR imaging. *The British Journal of Radiology*, *91*(1089), 20170959. https://doi.org/10.1259/BJR.20170959

Zhao, J., Shoeib, T., Siu, K. W. M., & Hopkinson, A. C. (2006). The fragmentation of protonated tyrosine and iodotyrosines: The effect of substituents on the losses of NH3 and of H2O and CO. *International Journal of Mass Spectrometry*, *255–256*, 265–278. https://doi.org/10.1016/J.IJMS.2006.03.012

Zheng, R., Stejskal, K., Pynn, C., Mechtler, K., & Boychenko, A. (2022). Deep Single-Shot NanoLC-MS Proteome Profiling with a 1500 Bar UHPLC System, Long Fully Porous Columns, and HRAM MS. *Journal of Proteome Research*, *21*(10), 2545–2551. https://doi.org/10.1021/ACS.JPROTEOME.2C00270

Zheng, X., Aly, N. A., Zhou, Y., Dupuis, K. T., Bilbao, A., Paurus, V. L., Orton, D. J., Wilson, R., Payne, S. H., Smith, R. D., & Baker, E. S. (2017). A structural examination and collision cross section database for over 500 metabolites and xenobiotics using drift tube ion mobility spectrometry. *Chem. Sci.*, *8*(11), 7724–7736. https://doi.org/10.1039/C7SC03464D

Zhou, Zhi, Chen, Y., He, J., Xu, J., Zhang, R., Mao, Y., & Abliz, Z. (2017). Systematic evaluation of serum and plasma collection on the endogenous metabolome. *Bioanalysis*, *9*(3), 239–250. https://doi.org/10.4155/bio-2016-0078

Zhou, Zhiwei, Luo, M., Chen, X., Yin, Y., Xiong, X., Wang, R., & Zhu, Z. J. (2020). Ion mobility collision cross-section atlas for known and unknown metabolite annotation in untargeted metabolomics. *Nature Communications*, *11*(1), 4334. https://doi.org/10.1038/S41467-020-18171-8

Zhou, Zhiwei, Shen, X., Chen, X., Tu, J., Xiong, X., & Zhu, Z. J. (2019). LipidIMMS Analyzer: Integrating multi-dimensional information to support lipid identification in ion mobility - Mass spectrometry based lipidomics. *Bioinformatics*, *35*(4), 698–700. https://doi.org/10.1093/bioinformatics/bty661

Zhou, Zhiwei, Tu, J., Xiong, X., Shen, X., & Zhu, Z.-J. (2017). LipidCCS: Prediction of Collision Cross-Section Values for Lipids with High Precision To Support Ion Mobility–Mass Spectrometry-Based Lipidomics. *Analytical Chemistry*, *89*(17), 9559–9566. https://doi.org/10.1021/ACS.ANALCHEM.7B02625

Zhou, Zhiwei, Xiong, X., & Zhu, Z.-J. (2017). MetCCS predictor: a web server for predicting collision cross-section values of metabolites in ion mobility-mass spectrometry based metabolomics. *Bioinformatics*, *33*(14), 2235–2237. https://doi.org/10.1093/BIOINFORMATICS/BTX140

Zhu, K., Pursch, M., Eeltink, S., & Desmet, G. (2020). Maximizing two-dimensional liquid chromatography peak capacity for the separation of complex industrial samples. *Journal of Chromatography A*, *1609*,

460457. https://doi.org/10.1016/j.chroma.2019.460457

SUMMARY

Despite the high prevalence of alcoholic liver disease, its identification and characterization remain poor, especially in early stages such as alcoholic fatty liver disease and alcoholic steatohepatitis. This latter implies diagnostic difficulties, few therapeutic options and unclear mechanisms of action. In this thesis, LC-MS-based metabolomics was used in an *in vitro* set-up to identify biochemical biomarkers able to elucidate the mechanism of ethanol-induced hepatotoxicity at a mechanistic cellular level. HepaRG, a human hepatocyte cell line was used to elucidate metabolic alterations and pinpoint affected metabolic pathways after exposure to ethanol in order to simulate alcoholic fatty liver disease. Combined exposure to ethanol and tumor necrosis factor alpha was used to simulate alcoholic steatohepatitis *in vitro*.

Part A of this thesis (i.e., chapter 3-5) was dedicated to development of analytical methods using liquid chromatography-quadrupole-time-of-flight high-resolution mass spectrometry (LC-QTOF-HRMS) and the hyphenation to drift tube ion mobility spectrometry (DTIMS) was explored. In addition, a multidimensional library for untargeted MS-based metabolomics was constructed and guidelines and consideration were formulated. Part B of this thesis (i.e., chapter 6-8) describes the application of the optimized metabolomics methods to study ethanol-induced hepatotoxicity in an *in vitro* set-up.

In chapter 3, a metabolomics platform was optimized to be able to analyze polar metabolites in HepaRG extracts. The analysis of polar metabolites based on LC-MS methods should take into consideration the complexity of interactions in LC columns to be able to cover a broad range of metabolites of key biological pathways. Therefore, in chapter 3, different chromatographic columns were tested for polar metabolites including reversed-phase and hydrophilic interaction liquid chromatography (HILIC) columns. Based on a column screening, two new generations of zwitterionic HILIC columns were selected for further evaluation. A tree-based method optimization was applied to investigate the chromatographic factors affecting the retention mechanisms of polar metabolites with zwitterionic stationary phases. The results were evaluated based on a scoring system which was applied for more than 80 polar metabolites with a high coverage of key human metabolic pathways. The final optimized methods showed high complementarity to analyze a wide range of metabolic classes including amino acids, small peptides, sugars, amino sugars, phosphorylated sugars, organic acids, nucleobases, nucleosides, nucleotides and acylcarnitines. Optimized methods were applied to analyze different biological matrices, including HepaRG extracts, human urine

and plasma using an untargeted approach. The number of high-quality features (< 30% median relative standard deviation) ranged from 3,755 for urine to 5,402 for the intracellular metabolome of HepaRG cells, showing the potential of the methods for untargeted purposes.

In chapter 4, a lipidomics platform was optimized to be able to analyze lipids in HepaRG extracts. There are thousands of lipids in most biological samples, and therefore separation methods before introduction to the mass spectrometer are key for relative quantitation and identification. Chromatographic methods differ across laboratories, without any consensus on the best methodologies. Therefore, we designed an experiment to determine the optimal LC methodology, and assessed the value of ion mobility as an additional dimension of separation. To apply an untargeted method for hypothesis generation focused on lipidomics, LC-HRMS parameters were optimized based on the measurement of 50 panel lipids covering key human metabolic pathways. Similar to the approach in chapter 3, reversed-phase liquid chromatography columns were compared based on a quality scoring system considering the signal-to-noise ratio, peak shape, and retention factor. DTIMS was implemented to increase peak capacity and confidence during annotation by providing collision cross section (CCS) values for the analytes under investigation. However, hyphenating DTIMS to LC-HRMS may result in a reduced sensitivity due to impaired duty cycles. To increase the signal intensity, a Box-Behnken design (BBD) was used to optimize four key factors; drift entrance voltage, drift exit voltage, rear funnel entrance, and rear funnel exit voltages. Application of a maximized desirability function provided voltages for the above-mentioned parameters resulting in higher signal intensity compared to each combination of parameters used during the BBD. In addition, the influence of single pulse and Hadamard 4-bit multiplexed modes on signal intensity was explored and different trap filling and release times of ions were evaluated. The optimized LC-DTIM-HRMS platform was applied to extracts from HepaRG cells and resulted in 3912 high-quality features. From these features, 436 lipid species could be annotated (i.e., matching based on accurate mass <5 ppm, isotopic pattern, MS/MS fragmentation, and CCS database matching <3%).

As feature annotation is crucial in untargeted metabolomics and remains a major challenge, chapter 5 was dedicated to the construction of multidimensional libraries for untargeted MS-based metabolomics. The large pool of metabolites collected under various instrumental conditions is underrepresented in publicly available databases. Retention time (RT) and CCS measurements from liquid chromatography ion mobility high-resolution mass spectrometers can be employed in addition to MS/MS spectra to improve the confidence of metabolite annotation. Recent advancements in machine

learning focus on improving the accuracy of predictions for CCS and RT values. Therefore, high-quality experimental data are crucial to be used either as training datasets or as a reference for high-confidence matching. Chapter 5 provides an easy-to-use workflow for the creation of an in-house metabolite library, offers an overview of alternative solutions, and discusses the challenges and advantages of building in-house libraries. A total of 100 metabolite standards from various classes were analyzed and subjected to the described workflow for library generation. The outcome was an open-access available NIST format metabolite library (.msp) with multidimensional information. The library was used to evaluate CCS prediction tools, MS/MS spectra heterogeneities (e.g., multiple adducts, in-source fragmentation, and radical fragment ions using collision-induced dissociation), and the reporting of RT.

Chapter 6 provides a summary of the optimized analytical methods that were used to study ethanol-induced hepatotoxicity in HepaRG cells, in addition to a description of experimental exposure conditions, procedures for sample preparation, data processing, statistics and metabolite annotation. Sample preparation was based on a liquid-liquid extraction with H_2O/MeOH/$CHCl_3$ and was used to divide each biological sample in 2 polar and 2 apolar subfractions, which were analyzed using separate corresponding analytical methods to increase metabolite coverage. Throughout the analytical workflow, comprehensive quality assurance and quality control measures were implemented to ensure high reproducibility. These latter measures included, for example, usage of standardized acquisition sequences, pooled quality control samples, and system suitability samples.

Alcoholic fatty liver disease was simulated in HepaRG cells in chapter 7 by exposure of these cells to ethanol at different concentrations and exposure times. Excessive ethanol consumption is known to alter lipid metabolism, followed by progressive intracellular lipid accumulation, resulting in alcoholic fatty liver disease. In chapter 7, HepaRG cells were exposed to ethanol at IC_{10} and 1/10 IC_{10} for 24 and 48 h. Metabolic alterations were investigated intra-and extracellularly with LC-HRMS. Ion mobility was added as an extra separation dimension for untargeted lipidomics to improve annotation confidence. Distinctive patterns between exposed and control cells were consistently observed, with intracellular upregulation of di- and triglycerides, downregulation of phosphatidylcholines and -ethanolamines, sphingomyelins, and S-adenosylmethionine, among others. Several intracellular metabolic patterns could be related to changes in the extracellular environment, such as increased intracellular hydrolysis of sphingomyelins, leading to increased phosphorylcholine secretion. Carnitines showed alterations depending on the size of their carbon chain, which highlights the interplay

between β-oxidation in mitochondria and peroxisomes. Potential new biomarkers of ethanol-induced hepatotoxicity have been observed, such as ceramides with a sphingadienine backbone, octanoylcarnitine, creatine, acetylcholine, and ethylated phosphorylcholine. The combination of the metabolic fingerprint and footprint enabled a comprehensive investigation of the pathophysiology behind ethanol-induced hepatotoxicity.

In chapter 8, HepaRG cells were exposed for 24 h to both ethanol (IC_{10}, 368 mM) and tumor necrosis factor alpha (TNF-α, 50 ng/mL), in order to improve *in vitro* simulation of alcoholic steatohepatitis. This combined exposure was compared to solely ethanol-exposed as well as -nonexposed cells. As in chapter 7, LC-(DTIMS)-HRMS was used to elucidate both intracellular and extracellular metabolic alterations. Some of the key findings include the influence of TNF-α in the upregulation of hepatic triglycerides and the downregulation of hepatic phosphatidylcholines and -ethanolamines. S-adenosylmethionine showed to play a central role in the progression of alcoholic steatohepatitis. In addition, fatty acyl esters of hydroxy fatty acid (FAHFA)-containing triglycerides were detected for the first time in human hepatocytes and their alterations showed a potentially important role during the progression of alcoholic steatohepatitis. As in chapter 7, ethylated phosphorylcholine was observed as a potential new biomarker of ethanol exposure. In order to evaluate the biomarker potential of this latter compound in humans, a targeted method was developed. As a proof-of-concept, the presence of ethylated phosphorylcholine was confirmed in whole blood samples of heavy drinkers. Details on these latter findings are described in the supplementary information of chapter 7.

SAMENVATTING

Ondanks de hoge prevalentie van alcoholische leverziekte zijn de identificatie en karakterisering ervan ondermaats, en dan voornamelijk in vroege stadia zoals alcoholische leververvetting en alcoholische steatohepatitis. Dit laatste impliceert diagnostische moeilijkheden, weinig therapeutische opties en onduidelijke werkingsmechanismen. In dit proefschrift werd op LC-MS-gebaseerde metabolomics gebruikt in een *in vitro* opstelling om biochemische biomarkers te identificeren die ethanol-geïnduceerde hepatotoxiciteit op mechanistisch cellulair niveau kunnen ophelderen. HepaRG, een cellijn van menselijke hepatocyten, werd gebruikt om metabole veranderingen op te helderen en aangetaste metabole routes te lokaliseren tijdens alcoholische leververvetting. Gecombineerde blootstelling aan ethanol en tumornecrosefactor-alfa werd gebruikt om *in vitro* alcoholische steatohepatitis te simuleren.

Deel A van dit proefschrift (d.w.z. hoofdstuk 3-5) werd gewijd aan de ontwikkeling van analytische methoden met behulp van vloeistofchromatografie-quadrupool-time-of-flight hoge-resolutie massaspectrometrie (LC-QTOF-HRMS) en de koppeling met drift tube ionenmobiliteitsspectrometrie (DTIMS) werd onderzocht. Daarnaast werd een multidimensionale bibliotheek voor untargeted MS-gebaseerde metabolomics geconstrueerd en werden richtlijnen en overwegingen geformuleerd. Deel B van dit proefschrift (d.w.z. hoofdstuk 6-8) beschrijft de toepassing van de geoptimaliseerde metabolomics methoden om ethanol-geïnduceerde hepatotoxiciteit te bestuderen in een *in vitro* opstelling.

In hoofdstuk 3 werd een metabolomics-platform geoptimaliseerd om polaire metabolieten in HepaRG-extracten te kunnen analyseren. Bij de analyse van polaire metabolieten op basis van LC-MS-methoden moet rekening worden gehouden met de complexiteit van interacties in LC-kolommen om een breed scala aan metabolieten van belangrijke biologische routes te kunnen dekken. Daarom werden in hoofdstuk 3 verschillende chromatografische kolommen getest voor polaire metabolieten, waaronder reversed-phase en hydrofiele interactie vloeistofchromatografie (HILIC) kolommen. Op basis van een kolomscreening werden twee nieuwe generaties zwitterionische HILIC-kolommen geselecteerd voor verdere evaluatie. Een tree-based methodeoptimalisatie werd toegepast om de chromatografische factoren te onderzoeken die de retentiemechanismen van polaire metabolieten met zwitterionische stationaire fasen beïnvloeden. De resultaten werden geëvalueerd op basis van een scoresysteem dat werd toegepast voor meer dan 80 polaire metabolieten

met een hoge dekking van belangrijke menselijke metabole routes. De uiteindelijk geoptimaliseerde methoden vertoonden een hoge complementariteit om een breed scala aan metabole klassen te analyseren, waaronder aminozuren, kleine peptiden, suikers, aminosuikers, gefosforyleerde suikers, organische zuren, nucleobasen, nucleosiden, nucleotiden en acylcarnitines. De geoptimaliseerde methoden werden toegepast om verschillende biologische matrices, waaronder HepaRG-extracten, menselijke urine en plasma, te analyseren met behulp van een untargeted benadering. Het aantal features met hoge kwaliteit (< 30% mediane relatieve standaarddeviatie) varieerde van 3.755 voor urine tot 5.402 voor het intracellulaire metaboloom van HepaRG cellen, wat het potentieel van de methoden voor untargeted doeleinden aantoont.

In hoofdstuk 4 werd een lipidomics-platform geoptimaliseerd om lipiden in HepaRG-extracten te kunnen analyseren. In de meeste biologische stalen zijn duizenden lipiden aanwezig, waardoor scheidingsmethoden alvorens MS-analyse belangrijk zijn voor relatieve kwantificering en identificatie. Chromatografische methoden verschillen tussen laboratoria, zonder enige consensus over de beste methodologieën. Omwille hiervan hebben we een experiment ontworpen om de optimale LC-methodologie te bepalen en de waarde van ionenmobiliteit als een extra dimensie van scheiding beoordeeld. Om een untargeted methode toe te passen voor het ontwikkelen van hypothesen gericht op lipidomics, werden de LC-HRMS-parameters geoptimaliseerd op basis van de meting van 50 panel lipiden die de belangrijkste menselijke metabole routes dekken. Vergelijkbaar met de benadering in hoofdstuk 3, werden reversed-phase vloeistofchromatografiekolommen vergeleken op basis van een kwaliteitsscoresysteem waarbij rekening werd gehouden met de signaal-ruisverhouding, piekvorm en retentiefactor. DTIMS werd geïmplementeerd om de piekcapaciteit en het vertrouwen tijdens annotatie te vergroten door collision cross section (CCS) waarden te bepalen voor de te onderzoeken analieten. Het koppelen van DTIMS met LC-HRMS kan resulteren in een verminderde gevoeligheid als gevolg van verminderde duty cycles. Om de signaalintensiteit te verhogen, werd een Box-Behnken-design (BBD) gebruikt om vier sleutelfactoren te optimaliseren; drift entrance voltage, drift exit voltage, rear funnel entrance en rear funnel exit voltages. Toepassing van een maximale desirability functie leverde voltages op voor de bovengenoemde parameters, wat resulteerde in een hogere signaalintensiteit in vergelijking met elke combinatie van parameters die tijdens de BBD werden gebruikt. Daarnaast werd de invloed van single puls en Hadamard 4-bit multiplexed modi op de signaalintensiteit onderzocht en werden verschillende trap vullingstijden en vrijgavetijden van ionen geëvalueerd. Het geoptimaliseerde LC-DTIM-HRMS-platform werd toegepast op extracten van HepaRG-cellen en resulteerde in 3912

features van hoge kwaliteit. Van deze features konden 436 lipide species worden geannoteerd (d.w.z. matching op basis van nauwkeurige massa <5 ppm, isotopisch patroon, MS/MS-fragmentatie en CCS-database-matching <3%).

Omdat annotatie van features cruciaal is in untargeted metabolomics en een grote uitdaging blijft, werd hoofdstuk 5 gewijd aan de constructie van multidimensionale bibliotheken voor untargeted MS-gebaseerde metabolomics. De grote verzameling metabolieten, die onder verschillende instrumentele omstandigheden zijn gecollecteerd, is ondervertegenwoordigd in openbaar beschikbare databases. Retentietijd (RT) en CCS-metingen van vloeistofchromatografie-ionenmobiliteit massaspectrometers met hoge resolutie kunnen in additie van MS/MS-spectra worden gebruikt om de betrouwbaarheid van metabolietannotatie te verbeteren. Recente ontwikkelingen in machine learning richten zich op het verbeteren van de nauwkeurigheid van voorspellingen voor CCS- en RT-waarden. Daarom zijn experimentele gegevens van hoge kwaliteit cruciaal om te worden gebruikt als trainingsdatasets of als referentie voor betrouwbare matching. Hoofdstuk 5 biedt een gebruiksvriendelijke workflow voor de constructie van een interne metabolietbibliotheek, biedt een overzicht van alternatieve oplossingen en bespreekt de uitdagingen en voordelen van de constructie van interne bibliotheken. In totaal werden 100 metabolietstandaarden uit verschillende klassen geanalyseerd en onderworpen aan de beschreven workflow voor het genereren van bibliotheken. Het resultaat was een vrij toegankelijke metabolietbibliotheek (.msp) in NIST-formaat met multidimensionale informatie. De bibliotheek werd gebruikt voor de evaluatie van CCS-voorspellingstools, MS/MS-spectra-heterogeniteiten (bijv. meerdere adducten, fragmentatie in de bron en radicale fragmentionen met behulp van door collisie geïnduceerde dissociatie) en de rapportering van RT.

Hoofdstuk 6 geeft een samenvatting van de geoptimaliseerde analytische methoden die werden gebruikt om ethanol-geïnduceerde hepatotoxiciteit in HepaRG-cellen te bestuderen. Verder bevat dit hoofdstuk een beschrijving van experimentele blootstellingsomstandigheden, procedures voor monstervoorbereiding, dataverwerking, statistieken en annotatie van metabolieten. De monstervoorbereiding was gebaseerd op een vloeistof-vloeistofextractie met H_2O/MeOH/$CHCl_3$ en werd gebruikt om elk biologisch staal te verdelen in 2 polaire en 2 apolaire subfracties, dewelke werden geanalyseerd met afzonderlijke overeenkomstige analytische methoden om de metabolietdekking te vergroten. Gedurende de hele analytische workflow werden uitgebreide maatregelen voor kwaliteitsborging en kwaliteitscontrole geïmplementeerd om een hoge reproduceerbaarheid te garanderen. Deze laatste

maatregelen omvatten bijvoorbeeld het gebruik van gestandaardiseerde acquisitiesequenties, gepoolde kwaliteitscontrolestalen en stalen om de systeemgeschiktheid te evalueren.

Alcoholische leververvetting werd gesimuleerd in HepaRG-cellen in hoofdstuk 7 door deze cellen bloot te stellen aan ethanol in verschillende concentraties en met verschillende blootstellingstijden. Van overmatig ethanolgebruik is bekend dat deze het vetmetabolisme verandert, gevolgd door progressieve intracellulaire vetophoping, resulterend in alcoholische leververvetting. In hoofdstuk 7 werden HepaRG-cellen gedurende 24 en 48 uur blootgesteld aan ethanol bij IC_{10} en 1/10 IC_{10} concentraties. Metabolische veranderingen werden intra- en extracellulair onderzocht met LC-HRMS. Ionenmobiliteitsspectrometrie werd toegevoegd als een extra scheidingsdimensie voor untargeted lipidomics om het annotatievertrouwen te verbeteren. Discriminerende patronen tussen blootgestelde en controlecellen werden consistent waargenomen, met intracellulaire opregulatie van onder andere di- en triglyceriden, neerwaartse regulatie van fosfatidylcholines en -ethanolamines, sfingomyelines en S-adenosylmethionine. Verschillende intracellulaire metabole patronen konden in verband worden gebracht met veranderingen in de extracellulaire omgeving, zoals een verhoogde intracellulaire hydrolyse van sfingomyelines, wat leidde tot een verhoogde secretie van fosforylcholine. Carnitines vertoonden veranderingen afhankelijk van de grootte van hun koolstofketen, wat de wisselwerking tussen β-oxidatie in mitochondriën en peroxisomen benadrukt. Er werden potentiële nieuwe biomarkers van ethanol-geïnduceerde hepatotoxiciteit waargenomen, zoals ceramiden met een sfingadienine-ruggengraat, octanoylcarnitine, creatine, acetylcholine en geëthyleerde fosforylcholine. De combinatie van de metabole vinger- en voetafdruk maakte een uitgebreid onderzoek mogelijk naar de pathofysiologie achter ethanol-geïnduceerde hepatotoxiciteit.

In hoofdstuk 8 werden HepaRG-cellen gedurende 24 uur blootgesteld aan zowel ethanol (IC_{10}, 368 mM) als tumornecrosefactor-alfa (TNF-α, 50 ng/ml), om de *in vitro* simulatie van alcoholische steatohepatitis te verbeteren. Deze gecombineerde blootstelling werd vergeleken met uitsluitend aan ethanol blootgestelde en niet-blootgestelde cellen. Net als in hoofdstuk 7 werd LC-(DTIMS)-HRMS gebruikt om zowel intracellulaire als extracellulaire metabole veranderingen op te helderen. Enkele van de belangrijkste bevindingen waren de invloed van TNF-α op de opwaartse regulatie van hepatische triglyceriden en de neerwaartse regulatie van hepatische fosfatidylcholines en -ethanolamines. S-adenosylmethionine bleek een centrale rol te spelen in de progressie van alcoholische steatohepatitis. Bovendien werden voor het eerst fatty acyl esters van hydroxyvetzuur (FAHFA)-bevattende triglyceriden gedetecteerd in menselijke

hepatocyten en hun veranderingen toonden een potentieel belangrijke rol tijdens de progressie van alcoholische steatohepatitis. Net als in hoofdstuk 7 werd geëthyleerd fosforylcholine waargenomen als een potentiële nieuwe biomarker voor blootstelling aan ethanol. Om het biomarkerpotentieel van deze laatste compound bij mensen te evalueren, werd een targeted methode ontwikkeld. Als proof-of-concept werd de aanwezigheid van geëthyleerde fosforylcholine bevestigd in volbloedstalen van zware drinkers. Details over deze laatste bevindingen werden beschreven in de appendix van hoofdstuk 7.

CURRICULUM VITAE

Personal information

Name	Iturrospe, Elias
Date of birth	12/19/1995
E-mail	elias.iturrospe@uantwerpen.be
	elias.iturrospe@vub.be
	elias_iturrospe@hotmail.com

Education

Oct. 2019 – Oct. 2023	Joint-PhD in Pharmaceutical Sciences (UA – VUB) FWO Fundamental Research Grant
Sept. 2019 – present	Master of Science in Laboratory Medicine (UA)
Sept. 2017 – Jun. 2019	Master of Science in Drug Development – Pharmacist (UA) Degree: Greatest distinction (86.0%)
Sept. 2014 – Jun. 2017	Bachelor of Science in Pharmaceutical Sciences (UA) Degree: Greatest distinction (85.4%)

Work experience

Oct. 2019 – Oct. 2023	Joint-PhD researcher (TC-UA & IVTD-VUB). Toxicological Centre, University of Antwerp (TC-UA). *In Vitro* Toxicology & Dermato-cosmetology research group, Vrije Universiteit Brussels (IVTD-VUB). Topic: Untargeted metabolomics to study ethanol-induced hepatotoxicity. Promotor: Prof. Adrian Covaci (TC-UA). Co-promotor: Prof. Alexander van Nuijs (TC-UA). Co-promotor: Prof. Tamara Vanhaecke (IVTD-VUB).
Aug. 2019 – Sept. 2019	Research internship (TC-UA). Urine metabolomics to study the fate of organic metabolites during (partial) nitrification.
Jan. 2019 – May 2019	Pharmacist trainee (Apotheek Kapelfarma, Kontich, Belgium).
Sept. 2018- Jan. 2019	Research internship (TC-UA). Identification of colonic metabolites of chlorogenic acid by LC-QTOF-MS/MS (optimization of sample preparation and

	development of suspect and non-targeted screening workflows).
Jul. 2018 – Sept. 2019	Pharmacist trainee (Apotheek Kapelfarma, Kontich, Belgium).

Peer-reviewed articles

FIRST AUTHOR

Iturrospe E, Robeyns R, Da Silva KM, Van de Lavoir M, Boeckmans J, Vanhaecke T, van Nuijs A, Covaci A. Metabolic signature of HepaRG cells exposed to ethanol and tumor necrosis factor alpha to study alcoholic steatohepatitis by LC-MS-based untargeted metabolomics. Archives of Toxicology. 2023; 97(5), 1335-1353. (DOI: 10.1007/s00204-023-03470-y).

Da Silva KM*, Van de Lavoir M*, Robeyns R*, **Iturrospe E***, Verheggen L, Covaci A, Van Nuijs A. Guidelines and considerations for building multidimensional libraries for untargeted MS-based metabolomics. Metabolomics. 2023; 19(1), 4. (DOI: 10.1007/s11306-022-01965-w). *Shared first authors.

Iturrospe E, Da Silva KM, Van de Lavoir M, Robeyns R, Cuykx M, Vanhaecke T, van Nuijs A, Covaci A. Mass spectrometry-based untargeted metabolomics and lipidomics platforms to analyze cell culture extracts. In: González-Domínguez, R. (eds) Mass Spectrometry for Metabolomics. Methods in Molecular Biology, Springer Nature. 2023; 2571, 189-206. Humana, New York, NY. (DOI: 10.1007/978-1-0716-2699-3_19).

Iturrospe E, Da Silva KM, Robeyns R, Van de Lavoir M, Boeckmans J, Vanhaecke T, van Nuijs A, Covaci A. Metabolic signature of ethanol-induced hepatotoxicity in HepaRG cells by LC-MS-based untargeted metabolomics. Journal of Proteome Research. 2022; 21(4), 1153-1166. (DOI: 10.1021/acs.jproteome.2c00029).

Da Silva KM*, **Iturrospe E***, Heyrman J, Koelmel JP, Cuykx M,, Vanhaecke T, Covaci A, Van Nuijs A. Optimization of a liquid chromatography-ion mobility-high resolution mass spectrometry platform for untargeted lipidomics and application to HepaRG cell extracts. Talanta. 2021; 235, 122808. (DOI: 10.1016/j.talanta.2021.122808). *Shared first authors.

Iturrospe E*, Da Silva KM*, Andujar BT, Cuykx M, Boeckmans J, Vanhaecke T, Covaci A, Van Nuijs A. An exploratory approach for an oriented development of an untargeted hydrophilic interaction liquid chromatography-mass spectrometry platform for polar metabolites in biological matrices. Journal of Chromatography A. 2021; 1637, 461807. (DOI: 10.1016/j.chroma.2020.461807). *Shared first authors.

CO-AUTHOR

Robeyns R, Sisto A, **Iturrospe E**, Da Silva KM, Van de Lavoir M, Timmermans V, Stroobants S, Covaci A, van Nuijs A. The metabolic and lipidomic fingerprint of Torin1 exposure in mouse embryonic fibroblasts using LC-HRMS-based untargeted metabolomics. Submitted to Metabolomics.

Da Silva KM, Wölk M, Nepachalovich P, **Iturrospe E**, Covaci A, van Nuijs A, Federova M. Investigating the potential of drift tube ion mobility to analyze oxidized lipids. Analytical Chemistry. 2023. (DOI: 10.1021/acs.analchem.3c02213).

Van de Lavoir M, da Silva KM, **Iturrospe E**, Robeyns R, van Nuijs A, Covaci A. Untargeted hair lipidomics: Comprehensive evaluation of the hair-specific lipid signature using LC-MS and considerations for retrospective analysis. Analytical and Bioanalytical Chemistry. 2023; 415(23), 5589-5604. (DOI: 10.1007/s00216-023-04851-z).

Peeters M, **Iturrospe E**, Jans D, van Nuijs A, De Loof H. Incorporating 'reason for use' into the prescribing process of medication: a survey on the opinion of patients in Flanders, Belgium. BMC Health Services Research. 2022; 22(1), 1216. (DOI: 10.1186/s12913-022-08596-w).

Jeong Y, Da Silva KM, **Iturrospe E**, Fuiji Y, Boogaerts T, Van Nuijs A, Koelmel J, Covaci A. Occurrence and contamination profile of legacy and emerging per- and polyfluoroalkyl substances (PFAS) in Belgian wastewater using target, suspect and non-target screening approaches. Journal of Hazardous Materials. 2022; 437, 129378. (DOI: 10.1016/j.jhazmat.2022.129378).

Da Silva KM, **Iturrospe E**, van den Boom R, van de Lavoir M, Robeyns R, Vergauwen L, Knapen D, Cuykx M, Covaci A, van Nuijs A. Lipidomics profiling of zebrafish liver through untargeted liquid chromatography-high resolution mass spectrometry. Journal of Separation Science. 2022; 45(15), 2935-2945. (DOI: 10.1002/jssc.202200214).

Poma G, Cuykx M, Da Silva KM, **Iturrospe E**, Van Nuijs A, Van Huis A, Covaci A. Edible insects in the metabolomics era. First steps towards the implementation of entometabolomics in food systems. Trends in Food Science & Technology. 2022; 119, 371-377. (DOI: 10.1016/j.tifs.2021.12.018).

Da Silva KM, **Iturrospe E**, Bars C, Knapen D, Van Cruchten S, Covaci A, Van Nuijs A. Mass spectrometry-based zebrafish toxicometabolomics: A review of analytical and data quality challenges. Metabolites 2021; 11(9), 635. (DOI: 10.3390/metabo11090635).

Mortelé O, **Iturrospe E**, Breynaert A, Verdickt E, Xavier BB, Lammens C, et al. Optimization of an in vitro gut microbiome biotransformation platform with chlorogenic acid as model compound: From fecal sample to biotransformation product identification. Journal of Pharmaceutical and Biomedical Analysis. 2019; 175, 112768. (DOI: 10.1016/j.jpba.2019.07.016).

Mortelé O, **Iturrospe E**, Breynaert A, Lammens C, Xavier B, Malhotra-kumar S, et al. Chlorogenic Acid as a Model Compound for Optimization of an In Vitro Gut Microbiome-Metabolism Model †. 2019; 11(1), 31. (DOI: 10.3390/proceedings2019011031).

Oral presentations

2023 Conference of The International Association of Forensic Toxicologists. **Iturrospe E**, Dumitrascu C, Vanhaecke T, van Nuijs A, Covaci A. Ethylated phosphorylcholine as a new marker for ethanol consumption: Discovery and proof-of-concept.

2022 Research day Faculty of Pharmaceutical, Biomedical and Veterinary Sciences – University of Antwerp. **Iturrospe E**, Covaci A, Van Nuijs A, Vanhaecke T. Untargeted metabolomics to study ethanol-induced hepatotoxicity.

2021 International Scientific Seminar CEHS-UA: **Iturrospe E**, Da Silva KM, Van de Lavoir A, Robeyns R, Van Nuijs A, Covaci A. (1) Metabolomics – general aspects. (2) Metabolomics – applications – In vitro biomarker elucidation of ethanol-induced hepatotoxicity.

2021 LIPID MAPS Spring School: **Iturrospe E**, Da Silva KM, Heyrman J, Cuykx M, Vanhaecke T, Covaci A, Van Nuijs A. Optimization of a liquid chromatography-ion mobility-mass spectrometry platform in untargeted lipidomics: Exploring ion mobility sensitivity.

Poster presentations

FIRST AUTHOR

2022 International Mass Spectrometry Conference 2022: **Iturrospe E**, Robeyns R, Da Silva KM, Van de Lavoir M, Boeckmans J, Vanhaecke T, Van Nuijs A, Covaci A. Metabolic alterations of HepaRG cells in response to ethanol and TNF-α co-exposure.

2022 18th Annual Conference of the Metabolomics Society: **Iturrospe E**, Da Silva KM, Robeyns R, Van de Lavoir M, Vanhaecke T, Van Nuijs A, Covaci A. Metabolic signature of ethanol induced hepatotoxicity in HepaRG Cells by LC-MS based untargeted metabolomics.

2021 17th Annual Conference of the Metabolomics Society: **Iturrospe E**, Da Silva KM, Vanhaecke T, Van Nuijs A, Covaci A. Lipidomic biomarkers of ethanol induced hepatotoxicity in human HepaRG liver cells.

CO-AUTHOR

2022 24th Annual Meeting Belgian Society for Mass Spectrometry: Da Silva KM, **Iturrospe E**, Covaci A, van Nuijs A. Optimization of a liquid chromatography-ion mobility-high resolution mass spectrometry (LC-IM-HRMS) platform for untargeted lipidomics.

2022 24th Annual Meeting Belgian Society for Mass Spectrometry: Robeyns R, **Iturrospe E**, Sisto A, Da Silva KM, Van de Lavoir M, Covaci A, van Nuijs A. The Fingerprint of Torin1 Induced Autophagy in MEF Cells by Liquid Chromatography−Mass Spectrometry-Based Untargeted Metabolomics.

2022 International Mass Spectrometry Conference 2022: Van de Lavoir M, Da Silva KM, **Iturrospe E**, Robeyns R, Van Nuijs A, Covaci A. Lipidomics profiling of human hair.

2022 International Mass Spectrometry Conference 2022: Da Silva KM, Van de Lavoir M, Robeyns R, **Iturrospe E**, Verheggen L, Covaci A, Van Nuijs A. Building multidimensional in-house metabolomics libraries for untargeted metabolomics with open-source tools.

2022 18th Annual Conference of the Metabolomics Society: Da Silva KM, Wölk M, Nepachalovich P, **Iturrospe E**, Covaci A, Van Nuijs A, Fedorova M. Investigating the potential of ion mobility to oxidized lipids using high resolution demultiplexing.

2022 18th Annual Conference of the Metabolomics Society: Robeyns R, **Iturrospe E**, Sisto A, Da Silva KM, Van de Lavoir M, Covaci A, Van Nuijs A. The lipidomic fingerprint of torin1 induced autophagy in mouse embryonic fibroblast cells.

2022 18th Annual Conference of the Metabolomics Society: Van de Lavoir M, Da Silva KM, **Iturrospe E**, Robeyns R, Van Nuijs A, Covaci A. Revealing the complexity of the hair lipidome.

2021 17th Annual Conference of the Metabolomics Society: Da Silva KM, **Iturrospe E**, Logie E, Van De Lavoir M, Cuykx M, Covaci A, Vanden Berghe W, Van Nuijs A. Liquid chromatography – mass spectrometry (LC-MS) based untargeted lipidomics platform to investigate ferroptosis in multiple myeloma cells.

2020 16th Annual Conference of the Metabolomics Society: Da Silva KM, **Iturrospe E**, Cuykx M, Covaci A, van Nuijs A. Enhancing the chromatographic separation of polar metabolites using new generation HILIC columns.

2020 MELiSSA Conference: Van Malderen V, Sachdeva N, Wattiez R, Belova L, **Iturrospe E**, Mortelé O, Covaci A, Van Nuijs A, Vlaeminck SE. Opening the 'yellow box': Main organics in urine and their fate during nitrification and microalgae cultivation.

Participation at workshops and conferences

2023 Conference of The International Association of Forensic Toxicologists 2023: Rome (Italy).
2022 International Mass Spectrometry Conference 2022: Maastricht (The Netherlands).
2022 18th Annual Conference of the Metabolomics Society: Valencia (Spain).
2021 Hackathon 2021 in Computational Metabolomics (German Network for Bioinformatics Infrastructure): Wittenberg (Germany).
2021 17th Annual Conference of the Metabolomics Society: online.
2021 LIPID MAPS Spring School: online.
2020 Lipidomics Meeting: 8th European Lipidomics Meeting (ELM) 2020: online.
2020 Multivariate statistics workshop StatUA: Antwerp (Belgium).
2020 Ion Mobility (IM) Meeting: 6th International Ion Mobility Spectrometry Meeting: Essen (Germany).
2020 Ion Mobility (IM) workshop at BOKU (Universität für Bodenkultur Wien): Vienna (Austria).
2019 R workshop StatUA: Antwerp (Belgium).
2019 Metabolomics Seminar: 2nd Agilent European Metabolomics Seminar Tour: Brussels (Belgium).

Awards

2019 Best master thesis in research and development awarded by the prize of Bank J. Van Breda & C°
2017 Highest distinction of Bachelor of Science in 2017 awarded by the yearly faculty prize FBD

Supervised theses

2023 **Gridda Yasmine, Peeters Annouk, Tobback Maarten, Van Hoof Caro**: A metabolomics cell-based approach for identifying and investigating xenobiotic-induced-hepatotoxicity. Bsc. Thesis at University of Antwerp.

2021 **Vermuyten Marijke**: Evaluation of iterative data dependent acquisition (DDA) techniques to improve metabolite coverage in untargeted metabolomics. Msc. Thesis at University of Antwerp.

2021 **Van Delen Mats**: Metabolomic and lipidomic analysis of vitamin D3 treated tolerogenic dendritic cells. Msc. Thesis at University of Antwerp.

2021 **Heyrman Joris**: Increasing compound coverage and identification confidence in lipidomics using ion mobility spectrometry and iterative tandem mass spectrometry. Msc. Thesis at University of Antwerp.

2021 **Peeters Marijke**: Indication on medicinal prescriptions: a step forward or a step too far? Literature study and qualitative research into the opinion of the Flemish population. Msc. Thesis at University of Antwerp.

2020 **Danen Caroline, Noens Hanna, Van Hooydonck Amber, Van Lerberghe Eline**: Biomarkers of alcohol abuse. Bsc. Thesis at University of Antwerp.

Reviewer activities

Reviewer of scientific manuscripts for
- Analytica Chimica Acta
- Analytical & Bioanalytical Chemistry
- Environmental Health Perspectives
- Journal of Proteome Research
- Journal of Insects as Food and Feed
- Toxicology

Jury member MSc. thesis Medicine Development: Pharmacist 2023

Van Loo Lies: Persistence in Streptococcus pneumoniae: Characterization of persistence in S. pneumoniae clinical isolates and biofilms

Leong Evy: Evaluation of mass spectrometry response prediction

ACKNOWLEDGEMENTS

Conducting this research and completing this thesis would not have been possible without the help and support of several people. First of all, I am extremely grateful to my promotor Prof. Dr. Adrian Covaci for giving me the opportunity to start a PhD and for his excellent support and guidance during this research. Adrian was available for support 24/7 and always willing to share his extensive scientific experience, as well as the newest albums in progrock and metal. Nearly each Friday, I could expect an email with new songs or albums, proving his passion not only for science, but also for music. His dedication to science is of a very high level, yet he remains very humble and easily accessible.

I'm deeply indebted to Prof. Dr. Alexander van Nuijs, my co-promotor, for his guidance, the many valuable discussions and his encouragement. Thank you for your contributions which were always to-the-point, without cutting hairs. This was very important for me as losing yourself in details can happen quickly, especially in a field such as metabolomics.

I would also like to express my deepest appreciation to Prof. Dr. Tamara Vanhaecke, my co-promotor from the *Vrije Universiteit Brussel*. Although I worked mostly at the University of Antwerp on the metabolomics analyses, I am very grateful as without your collaboration, this thesis would not be possible. Thank you for welcoming me to your research group, introducing me to the world of *in vitro* research and guiding me throughout these four years of the PhD project.

To Adrian, Alexander and Tamara, also my sincere thanks for your help in obtaining a PhD fellowship of the FWO. As I was still in my masters when writing the proposal, your extensive expertise was extremely helpful and your faith in me highly appreciated.

I would like to express my gratitude and respect to the members of the internal jury, Prof. Dr. Luc Pieters, Prof. Dr. Ann van Eeckhaut and Prof. Dr. Luisa Vonghia for devoting their time to revise the present thesis. In addition, I would like to thank Luisa and her colleagues, among others, Prof. Dr. Sven Francque, Marijke Rotsaert and Zouhir Gadi for helping to establish a collaboration between the department of gastroenterology – hepatology of the Antwerp University Hospital and the Toxicological Centre of the University of Antwerp. A sincere thank you to Prof. Dr. Pim E.G. Leonards and Prof. Dr. Jef Verbeek for agreeing to be an external member of the PhD jury and evaluating my thesis.

To continue, I would like to thank Prof. Dr. Hugo Neels for his advice and motivating scientific passion. Also, a major thank you to Dr. Matthias Cuykx, as he introduced me in the world of metabolomics. Even after his PhD, Matthias was always available for help

and advice despite his busy agenda. I started my PhD together with Manuela Da Silva, at that moment the only two researchers on the topic of metabolomics. However, the metabolomics department within the Toxicological Centre grew over the years and Annemieke van de Lavoir and Rani Robeyns joined the department. I would like to mention a special thank you to all for the many collaborations and fruitful discussions. In addition, a big thanks goes to Manuela for her contributions to the development of the analytical platforms. Recently, Dr. Ting Zeng started as a postdoctoral researcher in our laboratory in the field of metabolomics. I wish her the best of luck in this interesting, yet challenging topic. Special thanks also to Catalina Dumitrascu for sharing her expertise on targeted forensic analyses.

A big thank you to Dr. Joost Boeckmans for his help and ideas concerning the experimental design of the exposure experiments. Also, thank you to Anja Heymans and Dinja De Win for their help during the differentiation of cells.

I would like to mention and thank all the important researchers and colleagues I met during the PhD. For the University of Antwerp these include Adam Cseresznye, Alicia Macan Schonleben, Allen Jun Anies, Anna Klimowska, Begoña Talavera Andújar, Beibei Gao, Celine Gys, Christina Christia, Dahye Kim, Eleanor Berry, Elvio Amato, Eveline Nelen, Evi De Voecht, Fatima den Ouden, Francesca Cappelli, Giulia Poma, Glenn Van Nieuwenhove, Govindan Malarvannan, Jasper Bombeke, Karina Crols, Kelly Allains, Lidia Belova, Lotte Van Dyck, Maarten Degreef, Maarten Quireyns, Maarten Roggeman, Maryline Busschots, Matthias Van Puymbroeck, Michiel Bastiaensen, Natan Van Wichelen, Noelia Caballero Casero, Olivier Mortelé, Paulien Cleys, Philippe Vervliet, Shanshan Yin, Siebe Lievens, Sofie Abrahams, Stephanie Ceusters, Steven Andries, Thomas McGrath, Tim Boogaerts, Yu Ait Bamai, Yukiko Kobayashi and Yunsun Jeong. In addition, I would like to thank all important researchers and collegeagues from the *Vrije Universiteit Brussel*: Alexandra Gatzios, Amy Maerten, Andres Tabernilla Garcia, Ania Stras, Anne Caufriez, Anouck Thienpont, Anouk Verhoeven, Arne Loosen, Axelle Cooreman, Batuhan Yildiz, Bruna dos Santos Rodrigues, Elif Ince Ergüc, Ellen Callewaert, Emmanuel Demuynck, Fabienne Van Bamis, Fareed Chowdary, Fien Haenen, Gigly Del'Haye, Gunther Bal, Haaike Colemonts-Vroninks, Ine Nulmans, Jan Maushagen, Jenny De Visscher, Jessie Neuckermans, Jian Jiang, Joery De Kock, Jonas van Ertvelde, Julen Sanz Serrano, Julia Dominika Zajac, Julie Sanders, Kaat Leroy, Karolien Buyl, Kristiaan Demeyer, Kristien De Paepe, Lisbeth Desmet, Lorna Divida P. Marchandise, Marth Stinckens, Mathieu Vinken, Matthias Rombaut, Maude Everaert, Maxim Pauwels, Mieke Van Mulders, Milos Mihajlovic, Mona Delagrange, Paul Claes, Prashant Kadam, Quinten Marcelis, Raf Van Campenhout, Robim Marcelino Rodrigues, Santina Gorsen,

Sara Sepehri, Sien Lequeue, Sybren De Boever, Vera Rogiers, Walter Van der Eycken and Yoni Baert.

Finally, I would like to thank the people closest to me including my parents, my brothers and sister and my friends. Thank you for believing in me and for your endless and unconditional support. I am very grateful that I can always count on you! You were always there when I needed you and you never wavered in your support.

Last but most important, I would like to thank my wonderful girlfriend Mariel for her support, patience and love during my PhD and during all other aspects of life. Your presence always puts a smile on my face and makes life more beautiful. Gracias amigita!